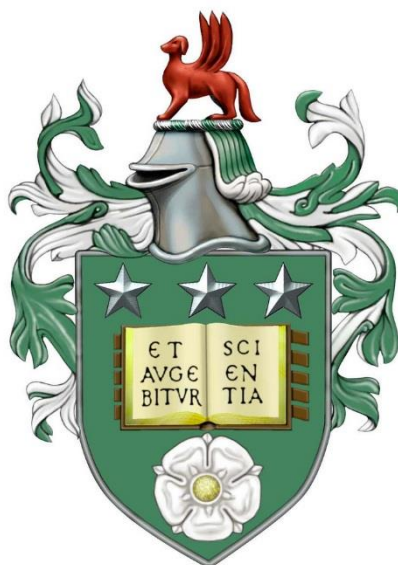


*FABRICATION AND CHARACTERISATION  
OF AN ADAPTABLE PLASMONIC  
NANOROD ARRAY*



*JOSHUA WILLIAM COTTOM*

**Doctoral Training Centre in Low Carbon Technologies**

**School of Chemical and Process Engineering**

**University of Leeds**

**Submitted in accordance with the requirements for the degree of**

**Doctor of Philosophy**

**September 2017**

*Dedicated to my parents*

## DECLARATION

The candidate confirms that the work submitted is his own, except where work which has formed part of jointly authored publications has been included. The contribution of the candidate and the other authors to this work has been explicitly indicated below. The candidate confirms that appropriate credit has been given within the thesis where reference has been made to the work of others.

The finite element model outlined in Chapter 5 was published in *Analyst*:

El-Khoury, P.Z., Abellan, P., Gong, Y., Hage, F.S., Cottom, J. Joly, A.G., Brydson, R. Ramasse, Q.M., Hess, W.P. Visualizing surface plasmons with photons, photoelectrons, and electrons. *Analyst*, 2016, **141**, pp. 3562-3572. DOI: 10.1039/c6an00308g

The candidate undertook the finite element simulations of a supported silver nanobar and assisted in the writing of this section. The majority of the writing was performed by El-Khoury and Abellan. The remaining authors provided assistance in the experiments, analysis and technical advice.

Sections of Chapter 6 are published in *Journal of Physics: Conference Series (JPCS)*:

Cottom, J., Abellan, P., Hage, F.S., Ramasse, Q.M., Critchley, K., Brydson, R. Fabrication and Characterisation of an adaptable plasmonic nanorod array for solar energy conversion. *Journal of Physics: Conference Series*, 2017, **902**(1), pp.012025. DOI: 10.1088/1742-6596/902/1/012025

The candidate wrote the paper and undertook the modelling, data analysis and assisted in the EELS experiments. Abellan carried out the experimental EELS experiments and assisted with data analysis. Hage and Ramasse assisted in the EELS experiments and analysis. Critchley and Brydson were involved with writing and technical assistance.

This copy has been supplied on the understanding that it is copyright material and that no quotation from the thesis may be published without proper acknowledgement.

© 2017 The University of Leeds and Joshua William Cottom

## ACKNOWLEDGEMENTS

I would firstly like to thank my academic supervisors, Rik Brydson and Kevin Critchley for their support and guidance throughout my PhD. They were invaluable in their knowledge and assisted me throughout my time at Leeds. In particular, whenever I was stressing over a problem, their positive approach in meetings always guaranteed I left more relaxed. I would also like to pay my upmost gratitude to Patricia Aballen for all the help she has given me in numerous areas of my work. Her continual dedication to support me is thoroughly appreciated and allowed me to achieve many of the results in this thesis.

I would also like to thank the following people who collaborated with me and gave me assistance and advice over the course of my PhD. Firstly, I would like to thank Prof. Holger Schönherr and Haider Bayat for their help on AAO production and for their friendly and accommodating nature during my time in Siegen. Additionally, the LEMAS team are greatly appreciated for their continual help with my SEM and TEM exploits. The group at SuperSTEM including Patricia Abellan, Fredrik Hage and Quintin Ramasse were also wonderful in all their EELS help, and were truly welcoming and inspiring. Special thanks also goes to Ben Johnson and all the technicians for supporting me with my experimental work. Additionally, my sincerest thanks also go to Mark Rosamond for his help and guidance in performing ALD, as well as Alisdair Macpherson at the University of Manchester for allowing me to use their optical equipment. Richard Douthwaite and Ben Coulson at the University of York also were very accommodating and their help with the photocatalytic experiments is greatly appreciated. Furthermore, I would like to thank the all the staff members of the DTC for their continual support. Lastly, I would like to acknowledge my thanks to the funders of this project, the Engineering and Physical Science Research Council (EPSRC).

In addition to the above staff members, I would like to thank my fellow PhD students both in the Low Carbon DTC and within Physics for their much needed distractions from work, many laughs and continued friendship. I also appreciate the contribution from my other friends and family, where their constant questioning of “are you a doctor yet?” motivated me during the long days of writing up. In particular, I am deeply grateful to my parents for their continued inspiration, and who will forever be my role models. Lastly, I am eternally grateful to my girlfriend Coralie for her amazing support and encouragement these last few years. Despite my constant complaining, she always took the time to listen to me vent and gave me a reason to leave work behind at the end of the day.

## ABSTRACT

This thesis focused on the fabrication and characterisation of an adaptable plasmonic platform consisting of a regular array of vertically aligned gold nanorods, supported on a gold substrate. The research aimed to understand the optical properties of the array, with particular emphasis on determining the coupling effects between the plasmonic nanorods. Characterisation was performed, both in the near and far-field, by means of optical spectroscopy, finite element modelling (FEM) and electron energy loss spectroscopy (EELS). The work subsequently aimed to use the knowledge gained from characterisation to optimise the absorption of visible light and enhancement of the electric-fields surrounding the plasmonic nanoparticles by controlling the geometrical factors of the array. Lastly, the nanorod arrays were then utilised for photocatalytic applications following their coating in a semiconductor material.

During this research, gold nanorod arrays were successfully fabricated by means of electrodeposition in anodic aluminium oxide (AAO) membranes, with accurate control over the geometrical factors. UV-Vis measurements revealed that coupling within the array resulted in the higher wavelength longitudinal mode of the nanorods blue-shifting considerably to occur within the visible spectrum. For short aspect ratio (AR) nanorods, this mode overlapped with that of the transverse mode, however for longer ARs the mode could be tuned throughout the visible spectrum. This was in agreement with FEM results, however, it was additionally revealed that strongly coupled nanorod arrays undergo a redistribution in their electric field from localisation at the end of the nanorods, to one within the middle or base of the nanorods for unsupported and supported arrays respectively. It was further found that the presence of the substrate led to the nanorods coupling with their substrate image leading to greatly red-shifted resonances. Through experimental EELS measurements it was confirmed that this red-shift is due to coupling with the substrate, in addition to further analysing the particle coupling effects for both dimers, and larger arrays of nanorods. It was found that for dimers with strong coupling the longitudinal mode splits into both a bright mode with symmetrically aligned dipoles, and a dark mode with anti-symmetrically aligned dipoles, thereby agreeing with plasmon hybridisation theory. Furthermore, as the number of particles within the array increases, the modes split to form hybridised bright and dark modes consisting of elements of each. An initial attempt at photocatalysis was also performed based on the degradation of methylene blue by injection of hot-electrons into  $\text{TiO}_2$ . No significant increase in activity was found, attributed to the semiconductor layer completely covering the nanorods thereby not allowing available sites for the oxidation reaction to replenish lost electrons in the metal.

# TABLE OF CONTENTS

<b>DECLARATION</b> .....	<b>III</b>
<b>ACKNOWLEDGEMENTS</b> .....	<b>IV</b>
<b>ABSTRACT</b> .....	<b>V</b>
<b>TABLE OF CONTENTS</b> .....	<b>VI</b>
<b>LIST OF TABLES</b> .....	<b>IX</b>
<b>LIST OF FIGURES</b> .....	<b>X</b>
<b>LIST OF ABBREVIATIONS</b> .....	<b>XXV</b>
<b>LIST OF SYMBOLS</b> .....	<b>XXVII</b>
<b>1 INTRODUCTION</b> .....	<b>1</b>
1.1 The Nanoscale World .....	1
1.2 The Rise of Plasmonics .....	3
1.3 Applications of Plasmonics .....	5
1.4 Overview of the Research.....	7
1.4.1 <i>The Challenge</i> .....	7
1.4.2 <i>Objectives</i> .....	9
1.4.3 <i>Thesis Structure</i> .....	10
<b>2 THEORETICAL BACKGROUND &amp; LITERATURE REVIEW</b> .....	<b>11</b>
2.1 Electromagnetic Radiation and its Interaction with Matter .....	12
2.1.1 <i>Fundamentals of Electromagnetic Radiation</i> .....	12
2.1.2 <i>Permittivity</i> .....	14
2.1.3 <i>Absorption, Scattering, and Transmission</i> .....	18
2.2 Mie Theory and Nanoscale Optics .....	19
2.3 Localised Surface Plasmon Resonances .....	22
2.4 Effect of Nanoparticle Environment.....	27
2.4.1 <i>Effect of Homogeneous Medium</i> .....	27
2.4.2 <i>Effect of Dielectric Shell</i> .....	28
2.5 Effect of Material and Size .....	33
2.6 Effect of Geometry .....	39
2.7 Effect of Substrates.....	47
2.7.1 <i>Dielectric Substrates</i> .....	47
2.7.2 <i>Metallic Substrates</i> .....	57
2.8 Effect of Coupling .....	65
2.8.1 <i>Coupling in Nanoparticle Dimers</i> .....	66

2.8.2	<i>Coupling in Nanoparticle Arrays</i> .....	75
<b>3</b>	<b>FABRICATION METHODOLOGY</b> .....	<b>86</b>
3.1	Production of Nanorod Arrays by Template Electrochemical Deposition .....	87
3.2	Methodology for Fabrication of AAO Templates .....	93
3.3	Methodology for Electrodeposition of Nanorod Arrays.....	97
3.4	Methodology for Preparation of TEM Cross Section.....	101
3.5	Methodology for Coating in Titanium Dioxide.....	102
<b>4</b>	<b>CHARACTERISATION AND OPTICAL PROPERTIES</b> .....	<b>105</b>
4.1	Characterisation of AAO Templates .....	105
4.2	Characterisation of Nanorod Arrays.....	113
4.2.1	<i>SEM Analysis of Nanorod Arrays</i> .....	114
4.2.2	<i>Optical Properties of Nanorod Arrays</i> .....	123
4.3	Summary of Results.....	133
<b>5</b>	<b>MODELLING OF PLASMONIC RESONANCES</b> .....	<b>135</b>
5.1	Aims of Modelling.....	135
5.2	Review of Plasmonic Modelling Techniques .....	136
5.2.1	<i>Discrete Dipole Approximation (DDA)</i> .....	137
5.2.2	<i>Finite Element Modelling (FEM)</i> .....	138
5.2.3	<i>Finite Difference Time Domain (FDTD)</i> .....	139
5.2.4	<i>Boundary Element Method (BEM)</i> .....	140
5.3	Modelling Methodology and Validation .....	141
5.3.1	<i>Nanoparticle in a Homogeneous Medium Model</i> .....	142
5.3.2	<i>Nanoparticle on a Substrate Model</i> .....	144
5.3.3	<i>Nanoparticle Array Model</i> .....	149
5.4	Validation of Model.....	150
5.4.1	<i>Mesh Independence</i> .....	150
5.4.2	<i>Comparison to Mie Data</i> .....	152
5.4.3	<i>Near Field Validation</i> .....	154
5.5	Modelling of Isolated Nanorods .....	155
5.6	Modelling of Coupled Nanoparticles.....	163
5.6.1	<i>Particle - Substrate Coupling</i> .....	164
5.6.2	<i>Particle - Particle Coupling</i> .....	172
5.6.3	<i>Plasmonic Nanorod Arrays on Gold Substrates</i> .....	185
5.7	Summary of Results.....	190
<b>6</b>	<b>ELECTRON ENERGY LOSS SPECTROSCOPY</b> .....	<b>193</b>
6.1	Overview of Transmission Electron Microscopy .....	195

6.1.1	<i>Basics of TEM and STEM</i> .....	195
6.1.2	<i>Improving Resolution</i> .....	198
6.1.3	<i>Imaging</i> .....	198
6.2	Overview of Electron Energy Loss Spectroscopy (EELS) .....	200
6.2.1	<i>Introduction to EELS</i> .....	200
6.2.2	<i>Measuring Plasmons with EELS</i> .....	202
6.2.3	<i>Operating Concept</i> .....	203
6.2.4	<i>Data Analysis</i> .....	204
6.3	Electron Energy Loss Spectroscopy Methodology .....	206
6.3.1	<i>Experimental Methodology</i> .....	206
6.3.2	<i>Modelling Methodology</i> .....	207
6.4	EELS Results .....	209
6.4.1	<i>Isolated Nanorods</i> .....	209
6.4.2	<i>Unsupported Nanorod Arrays</i> .....	213
6.4.3	<i>Supported Nanorod Dimers</i> .....	224
6.4.4	<i>Supported Nanorod Arrays</i> .....	234
6.5	Summary of Results .....	247
<b>7</b>	<b>NANOROD ARRAYS FOR PHOTOCATALYTIC REACTIONS</b> .....	<b>250</b>
7.1	Review of Plasmonics for Photocatalytic Reactions .....	250
7.1.1	<i>Increased Plasmonic Scattering</i> .....	251
7.1.2	<i>Hot Electron Transfer</i> .....	252
7.1.3	<i>Plasmon-Induced Resonant Energy Transfer (PIRET)</i> .....	254
7.1.4	<i>Localised Heating by Plasmonic Nanoparticles</i> .....	256
7.1.5	<i>Plasmonic Photocatalysis in Gold Nanorod Arrays</i> .....	257
7.2	Characterisation of Titanium Dioxide Shell .....	259
7.3	Photocatalytic Abilities of Nanorod Arrays .....	265
7.3.1	<i>Methylene Blue Degradation Methodology</i> .....	265
7.3.2	<i>Methylene Blue Degradation Results</i> .....	266
7.4	Summary .....	269
	<b>CONCLUSIONS AND FUTURE WORK</b> .....	<b>270</b>
7.5	Novelty of Results .....	270
7.6	Fulfilment of Research Objectives .....	271
7.7	Recommendations for Future Work .....	273
	<b>BIBLIOGRAPHY</b> .....	<b>275</b>
	<b>APPENDICES</b> .....	<b>298</b>

## LIST OF TABLES

Table 1: Electrodeposition conditions for nanorod growth.....	99
Table 2: Diameter and spacing of the arrays analysed by UV-Vis spectroscopy .....	126
Table 3: Definitions for the calculation of the optical cross sections .....	143
Table 4: Elemental analysis showing the atomic percent of each element. ....	263
Table 5: Elemental analysis showing the atomic ratios relative to titanium. ....	264

## LIST OF FIGURES

Figure 1.1: Change in colour of gold nanoparticles in solution due to variation in size <sup>(8)</sup> .....	3
Figure 1.2: Lycurgus Cup showing change in colour due to plasmonic particles <sup>(10)</sup> .....	4
Figure 1.3: Number of publications with ‘surface plasmon’ in the article title, abstract or keywords (data obtained from scopus.com).....	5
Figure 2.1: Diagram of a localised surface plasmon resonance (LSPR) of a sphere where the conduction electrons couple to the oscillating E-field <sup>(45)</sup> .....	22
Figure 2.2: Schematic of homogenous sphere of radius a, located in a isotropic non-absorbing medium and in the presence of an electrostatic field <sup>(36)</sup> .....	23
Figure 2.3: a) Calculated absorption spectra of gold colloids with 8.0 nm radius and changing refractive index, b) UV-Vis spectra of gold colloids with refractive index, c) Changing colour of gold colloids with increasing refractive index of solvent from left to right. Adapted from ref <sup>(49)</sup> .....	28
Figure 2.4: Calculated Extinction efficiency of a 50 nm silver sphere with a SiO <sub>2</sub> shell varying in thickness from 1 nm to 50 nm. The dashed line and the double dotted dashed line represent an uncoated sphere and a sphere fully embedded in SiO <sub>2</sub> respectively, the latter spectrum has been divided by 5.1 for comparison <sup>(48)</sup> .....	30
Figure 2.5: a) Normalised absorption spectra of Ag@TiO <sub>2</sub> core-shell nanoparticles with varying TiO <sub>2</sub> thickness, b) Simulated resonance position with TiO <sub>2</sub> shell thickness using 3 separate values for the refractive index of the TiO <sub>2</sub> . The squares represent the experimental data from a) <sup>(52)</sup> .....	31
Figure 2.6: E-Field distribution of a Au-Ag nanoparticle with SiO <sub>2</sub> shell thicknesses of 2, 5, 8, 15, 20 and 35 nm. The colour bar represents the local magnetic field divided by the incident electromagnetic field $ E/E_0 $ <sup>(54)</sup> .....	32
Figure 2.7: Electric field distribution of a Au nanorod with SiO <sub>2</sub> shell of varying thickness at its two resonant wavelengths <sup>(55)</sup> .....	33
Figure 2.8: Spectral range of plasmonic materials and geometries within the visible region <sup>(53)</sup> .....	34
Figure 2.9: Graph of Mie calculation results for extinction cross section of gold spheres with diameters between 20 nm and 140 nm in a vacuum. The arrows act as a guide for the eye showing the peak red-shift. Calculations were performed using the software MiePlot <sup>(57)</sup> .....	35
Figure 2.10: Graph of Mie calculation results for absorption efficiency (left) and scattering efficiency (right) of gold spheres with diameters between 20 nm and 400 nm in a vacuum. Calculations were performed using the software MiePlot <sup>(57)</sup> .....	36

Figure 2.11: A) Extinction spectra map showing the evolution of higher order modes. B-H) E-Field maps of field arrangements for dipoles ( $l=1$ ), quadrupoles ( $l=2$ ) and octupoles ( $l=3$ ) <sup>(30)</sup> .....	37
Figure 2.12: Comparison between experimental data from ref <sup>(65)</sup> and theoretical data using a modified permittivity from equation (58), for various Au sphere sizes embedded in glass <sup>(63)</sup> .....	39
Figure 2.13: Experimental absorption spectra for gold nanorods with AR of 2.7 and 3.3 showing the two modes. Inset is of the SPR wavelength with AR showing a positive linear relationship for the longitudinal mode and negligible change for the transverse mode <sup>(59)</sup> .....	40
Figure 2.14: a) Extinction spectrum of gold nanorods with aspect ratios between 2 – 4, b) the relationship between aspect ratio and peak longitudinal resonance wavelength <sup>(66)</sup> . ....	41
Figure 2.15: Comparison of DDA simulations to experimental data for AR vs $\lambda_{\max}$ (left) for three different geometry configurations (right) <sup>(70)</sup> .....	42
Figure 2.16: Schematic charge distributions, electric field distribution and far-field scattering plots for a gold nanorods a) dipole mode, b) quadrupole mode and c) sextuple mode <sup>(76)</sup> . .....	44
Figure 2.17: EELS spectra before and after annealing of the gold nanorods and their corresponding plasmon maps <sup>(77)</sup> .....	45
Figure 2.18: FDTD simulation results for gold nanorods with a) an arrow head end cap, and b) a hemispherical end cap, showing E-Field enhancements <sup>(78)</sup> .....	45
Figure 2.19: EELS maps of an a) nanoprism <sup>(82)</sup> , b) nanocube <sup>(83)</sup> , and c) nanostar <sup>(84)</sup> . This figure highlights the localisation of the plasmons but does not allude to the enhancement levels due to varying intensity scale from different work being used.....	46
Figure 2.20: Extinction cross section of a Ag sphere on a dielectric substrate with increasing permittivity, calculated using the polarizability of a sphere on a substrate method <sup>(48, 88)</sup> .....	48
Figure 2.21: Extinction cross sections of 10nm Au (a-c) and Ag (d-f) spheres on a substrate of refractive index $N_2$ , including all substrate effect (a,d), excluding extrinsic substrate effects such as reflections from the substrate altering the local field intensity (b,e), and excluding intrinsic substrate effects such as coupling (c,f). Adapted from <sup>(91)</sup> . ....	51
Figure 2.22: Method of image charges for a nanoparticle above a substrate with a-b) varying separation from the substrate and c-d) showing the presence of the induced local field at c) p-polarised light and d) s-polarised light <sup>(92)</sup> . ....	52
Figure 2.23: DDA results for a silver sphere becoming increasingly embedded in mica <sup>(45)</sup> . 54	

Figure 2.24: DDA results for a truncated tetrahedron without a substrate and on a mica substrate compared to experimental data <sup>(94)</sup> . .....	54
Figure 2.25: Experimental dark field spectroscopy spectra for Au/silica nanoshells on glass (n=1.52), sapphire (n=1.77) and ZnSe (n=2.67). Blue curves represent p-polarised incident light where as black curves represent s-polarised incident light. Adapted from <sup>(99)</sup> . .....	56
Figure 2.26: E-Field distribution of a Ag nanoparticle of radius 25 nm in a) air and b) 2 nm above a dielectric substrate (n=2). c) E-Field enhancements for separations varying from 20 nm to 0.6 nm. The inset represents the maximum field enhancements in the middle of the gap (rectangles) and 0.3 nm below the nanoparticle (circles) <sup>(100)</sup> . .....	56
Figure 2.27: a-b) Experimental EELS probability maps for the substrate localised dipole corner mode for the Ag nanocubes supported on a) SiO <sub>2</sub> insulator and b) a-Si semiconductor. c-d) Simulated EELS probability map for the same dipolar mode on a c) insulator and d) semiconductor showing the presence of PIET. Adapted from <sup>(103)</sup> . .....	57
Figure 2.28: a) Calculated scattering efficiencies for an aluminium nanoparticle approaching an aluminium film showing the emergence of the higher order modes and a subsequent narrowing of the dipolar linewidth. b) Experimental (left panel) and FDTD simulations (right panel) of an aluminium nanoparticle on an aluminium film of varying thickness. As the film thickness decreases to that of its skin depth, the dipolar linewidth broadens and reduces in amplitude <sup>(106)</sup> . .....	59
Figure 2.29: Far-Field spectra for a gold nanoparticle separated by a distance, d from a gold film with a SPP mode. a) Spectra for distances of 0 nm – 50 nm, b) spectra for distances from 100 nm – 900 nm. Here the intensity has been normalised by the local intensity of the electric field to accurately show comparisons between separation distances <sup>(109)</sup> . ..	61
Figure 2.30: Schematic of a) total internal reflection method and b) dark-field method <sup>(110)</sup> . ..	61
Figure 2.31: Scattering spectra for gold nanoparticles, a) directly supported on a gold film (red curve) compared to a dielectric (green curve), b) using dark-field illumination method with the nanoparticle a distance above the gold substrate, and c) as with b but using the total internal reflection illumination method thereby exciting both LSPR and SPP <sup>(110)</sup> . .....	63
Figure 2.32: Schematic energy-level diagram showing the plasmon hybridisation principle for a metallic substrate plasmons interacting with the plasmons of a gold sphere. The green lines represent hybridisation between plasmons of different angular momentum <i>l</i> <sup>(112)</sup> . .....	64
Figure 2.33: a) Schematic of the plasmon hybridisation theory for a nanoparticle dimer whereby the plasmonic modes of each nanoparticle are shown to hybridise with the	

others giving rise to bonding and anti-bonding modes. At small separations, mixing between modes of different angular momentum will also occur (green lines), as shown here for the dipole mode ( $l=1$ ) interacting with those of higher order, leading to a greater shift in energy <sup>(113)</sup> . b) Schematic representation of the $l=1$ bright and dark modes for a sphere dimer. ....	66
Figure 2.34: Induced field model for a dimer of nanoparticles with polarisation a) parallel to the inter-particle axis, and b) perpendicular to the inter-particle axis <sup>(92)</sup> .....	67
Figure 2.35: Exciton coupling diagram showing the coupling of the a nanorod dimers longitudinal modes for both an end to end and side by side orientation <sup>(115)</sup> .....	69
Figure 2.36: DDA simulations of AR=4 nanorod dimers showing the extinction efficiency for a side by side arrangement with a) longitudinal mode excitation and b) transverse mode excitation. Alternatively for an end to end arrangement with c) longitudinal mode excitation and d) transverse mode excitation <sup>(115)</sup> .....	70
Figure 2.37: a) UV-VIS of gold nanorods with different sodium citrate concentrations leading to aggregation in a side by side manner as shown in the TEM images in b) <sup>(115)</sup> .....	71
Figure 2.38: a) FDTD simulations of gold nanorods of varying number interacting in a side by side arrangement leading to a blue-shift and decrease in amplitude with increasing number of rods. b) Schematic of destructive interference between the radial E-Field components of two side by side rods with accompanying electric field intensity profiles from c) above for two rods and d) side on for four rods <sup>(120)</sup> .....	72
Figure 2.39: EFTEM image of coupling for the longitudinal mode in an end to end nanorod dimer with a 5 nm gap (left). DDA simulation for the same geometry showing the enhanced E-Fields (middle). Comparison of the plasmon decay between the experimental EFTEM data and the DDA results for the longitudinal mode of a single Au nanorod (right) <sup>(121)</sup> .....	73
Figure 2.40: Simulated electric field profiles for the connected gold nanoprisms using local (black) and non-local (red) conditions. b) Electric field maps using local conditions and c) non-local conditions clearly showing the reduction in field strength at the small bridge <sup>(125)</sup> .....	74
Figure 2.41: (Left) TEM image of the nanorod / alumina composite material, where the arrow highlights the embedded gold nanorods. (Right) Absorbance spectra taken at normal incidence for gold nanorod/ alumina composite with (A) AR of 1, (B) AR of 6 <sup>(128)</sup> ... ..	76
Figure 2.42: (Left) Schematic diagram of nanorod array in alumina <sup>(132)</sup> , (right) SEM image of gold nanorods after removal of alumina template, inset is a TEM cross section of the arrays in the alumina <sup>(133)</sup> .....	78

Figure 2.43: Transmission data for a gold nanorod array of AR=16.5 at varying angle of incidence with (a) s-polarised light, and (b) p-polarised light <sup>(132)</sup> .....	78
Figure 2.44: a) Extinction spectra for gold nanorod arrays with varying AR embedded in alumina. The incident light is p-polarised at 40° angle of incidence and the centre to centre inter-rod spacing is about 100 nm <sup>(134)</sup> . b) Resonant wavelength of the longitudinal mode with AR for both isolated rods (blue) and nanorod arrays (red) <sup>(133)</sup> .....	79
Figure 2.45: a) Calculated refractive indices for the principal axes x and z for the composite material with 75nm long gold nanorods. b) Effective refractive index for the p-polarised wave within the nanorod array. Both calculations are performed assuming an angle of 60° <sup>(132)</sup> .....	81
Figure 2.46: Schematic diagram for the plasmonic resonance energy levels of a nanorod array compared to its isolated modes. The top diagram refers to the longitudinal mode which under a strong coupling strength (J) splits to form a low and high energy mode. The bottom schematic represents that of the transverse mode coupling <sup>(133)</sup> .....	82
Figure 2.47: Electric field distribution and power flow vectors for the longitudinal mode of a nanorod array (30 nm x 300 nm), at an inter-rod spacing of a) 500 nm, b) 200 nm, c) 150 nm, d) 100 nm. A shift in the electric field spatial distribution occurred with decreasing separation between rods, from being localised at the rod ends to localisation in the middle of the rods.....	82
Figure 2.48: Simulations of a hexagonally periodic gold nanorod array in alumina showing the electric field plots at varying wavelengths. All plots shown are for p-polarised light at 20° <sup>(136)</sup> .....	83
Figure 3.1: Current-time curve showing the different stages of anodisation, along with schematic diagrams representing each. Adapted from <sup>(161)</sup> .....	88
Figure 3.2: Schematic diagram of the a) arrangement of pores, b) structural parameters <sup>(165)</sup> .....	89
Figure 3.3: (Left) Schematic diagram showing the two-step mild anodisation process. a-c) SEM images relating to schematic diagram steps i-iii respectively. d) A colour coded SEM image of the 2-step AAO showing the distribution of domains. Here white resembles defect pores, whereas the colours indicate the average angle to their six nearest neighbours <sup>(160)</sup> .....	90
Figure 3.4: a) Schematic of the three electrode system used for electrodeposition within AAO templates, b) Current-time curve of electrodeposition in AAO templates <sup>(174)</sup> .....	92
Figure 3.5 Schematic diagram of experimental rig used in production of AAO templates. ...	94
Figure 3.6: Mass loss with time of the first anodisation AAO layer showing complete removal of the layer by 120 minutes.....	95

Figure 3.7: Production steps in fabrication of AAO templates for nanoparticle growth. ....	97
Figure 3.8: Schematic diagram of electrodeposition setup including close up of how the AAO template is secured. ....	98
Figure 3.9: Schematic diagram of fabrication steps for electrodeposition within AAO templates .....	100
Figure 3.10: Schematic diagram of a single ALD deposition cycle with precursors A and B. The shapes of the reactants highlight the self-limiting surface chemistry <sup>(182, 185)</sup> .....	103
Figure 4.1: SEM images of a commercial Whatman AAO with quoted pore diameter of 20 nm for a) top and b) bottom surface and their respective pore diameter histograms (c,d) determined using image processing software.....	106
Figure 4.2: SEM images and pore measurements for left: 0.3 M sulphuric acid at 25 V, and right: 0.3 M oxalic acid at 40 V. The images at the top are for a plan view whereas the bottom images are cross-sectional views showing the barrier layer. All images are without any pore widening.....	107
Figure 4.3: SEM images and pore measurements for a hard anodisation using 0.3 M oxalic acid at 145 V. The left-hand image is the plan view of the pores whereas the right-hand image is a cross-sectional view of the barrier layer. All images are without any pore widening.....	108
Figure 4.4: SEM image of the top of an AAO template created using 0.1 M phosphoric acid electrolyte at 195 V and subsequently widened in 5 wt% phosphoric acid at 37°C for 90 minutes. ....	109
Figure 4.5: SEM images for the barrier layer side of an AAO template produced using 0.3 M sulphuric acid at 25 V and widened in 5 wt% phosphoric at 35°C for varying times. The inset in the 10 minutes image shows a magnified view of the small pores just after the barrier layer is removed.....	110
Figure 4.6: AAO pore diameters for both the top and barrier layer side with pore widening etching time. The AAO was produced using a 0.3 M sulphuric acid electrolyte at 25 V. ....	111
Figure 4.7: SEM images for the top surface of AAO templates using various electrolytes, voltages and pore widening times. ....	113
Figure 4.8: SEM images of the nanorod arrays produced using Whatman AAO templates. ....	114
Figure 4.9: SEM image showing widespread deposition in pores of homemade AAO template over large areas. The inset shows a picture of typical templates before and after deposition where the colour changes from gold to red due to the plasmonic properties of	

the gold. The green around the outside is the nail varnish used to insulate the aluminium supporting ring. ....	116
Figure 4.10: SEM images for short nanorod arrays with aspect ratios between 1 and 4. ....	117
Figure 4.11: SEM image for a nanorod array with the hexagonal ordered arrangement highlighted by the drawn lines. ....	118
Figure 4.12: SEM images of nanorod arrays produced with aspect ratios of 5, 7 and 9. The left-hand images show the plan view whereas the right-hand images are with the sample tilted.....	119
Figure 4.13: Cross-Sectional SEM image of nanorods supported in AAO template.....	120
Figure 4.14: SEM images showing long nanorods with AR=18 including a cross sectional view to enable accurate measurement of the lengths. ....	121
Figure 4.15: SEM images showing the ability to control the spacing of the nanorod arrays. ....	122
Figure 4.16: SEM image of Au-Ag multi-material nanorod array grown in a Whatman 20 nm commercial template (left), and accompanying SEM-EDX layered image highlighting the two materials (right). ....	123
Figure 4.17: Schematic diagram of the 150 mm integrating sphere. The numbers 1-4 represent possible positions the sample may be placed and the resultant optical properties they probe, as discussed within the text. ....	124
Figure 4.18: Extinction data for nanorod arrays in AAO with varying aspect ratios and at 0° and 20° angle of incidence. Unpolarised light was used for all measurements shown. ....	127
Figure 4.19: Extinction data for a nanorod array with AR=18 at 20° angle of incidence for S and P polarised light.....	129
Figure 4.20: Polarisation scan of nanorod array with AR=18 at a wavelength of 660 nm and angle of incidence of 20°. In this figure, 0° and 180° represent the light being completely s-polarised, whereas 90° and 270° represents the light being completely p-polarised. ....	129
Figure 4.21: Extinction data for a nanorod array with aspect ratio of 18 using p-polarised light at varying angles of incidence.....	130
Figure 4.22: Absorption data for a nanorod array with aspect ratio of 18 using p-polarised light at varying angles of incidence.....	131
Figure 4.23: Reflectance data for a bare gold substrate and a supported gold nanorod array at 8° angle of incidence using unpolarised light. ....	132

Figure 4.24: Reflectance data for a supported gold nanorod array at 8° angle of incidence using unpolarised light considering both diffuse reflection and total (diffuse + specular) reflection. ....	133
Figure 5.1: Comparison between course (left) and fine (right) meshing of a sphere showing sufficiently small elements are needed to accurately represent geometries. ....	138
Figure 5.2 – Coordinate system for a wave in a medium of refractive index $n_a$ incident on a substrate with refractive index $n_b$ at an angle of incidence $\theta_a$ , angle of refraction $\theta_b$ , and azimuthal angle $\phi$ . $k_a$ and $k_b$ refer to the wavenumber above and in the substrate respectively. ....	145
Figure 5.3: Schematic diagram showing the allocation of periodic boundary conditions under various incident conditions. a) s-polarised light with both $\theta$ and $\phi > 0$ , b) s-polarised light with $\phi = 0$ and $\theta > 0$ , c) p-polarised light with $\phi = 0$ and $\theta > 0$ . ....	148
Figure 5.4: Mesh independence test for a 40nm gold sphere in a vacuum at a wavelength of 510nm. a) Comparison of absorption efficiency with mesh size and degrees of freedom, b) time taken to solve for each mesh size and with the number of degrees of freedom. ....	151
Figure 5.5: Comparison of absorption and scattering cross section for both Mie Theory and the FEM solution for a 40 nm gold nanosphere in a homogeneous medium ( $\epsilon_m = 5$ ). ....	152
Figure 5.6: a) The absorption and b) scattering cross section FEM solution for a 40nm gold nanosphere in a homogeneous medium with changing permittivity from $\epsilon_m = 1$ to 8. c) A comparison of the absorption resonant wavelength ( $\lambda_{max}$ ) with Mie theory. ....	153
Figure 5.7: Normalised electric field with distance from the surface of a 40 nm sphere in vacuum at a wavelength of 508 nm. The inset shows the normalised electric field distribution. ....	154
Figure 5.8: Absorption efficiency spectra for a gold nanorods (40 nm x 120 nm) in water ( $n=1.33$ ) at 45°. The insets show the electric field distribution for the transverse and longitudinal modes. ....	156
Figure 5.9: Absorption efficiency spectra for spherically capped gold nanorods and flat-ended nanorods compared to Gans theory. The maps at the bottom show the electric field distribution for each of the rod end geometries (30 nm x 90 nm in vacuum). ....	157
Figure 5.10: Effect of diameter on the longitudinal modes absorption efficiency for a gold nanorod of AR=3. The inset shows the dependence on diameter for the transverse mode (diameter 10 nm – 50 nm). ....	158
Figure 5.11: Absorption efficiency with AR for a gold nanorod in a vacuum with diameter of 30nm. The field plots on the right show the electric field distribution for the longitudinal mode ( $\lambda=1285$ nm) and the sextuple mode ( $\lambda=605$ nm) of an AR=10 nanorod. ....	159

Figure 5.12: Average surface electric field strengths for a 30 nm x 90 nm gold nanorod with a TiO <sub>2</sub> shell on its surface varying from 2 nm to 10 nm in thickness. ....	160
Figure 5.13: Electric field distributions of 30 nm x 90 nm gold nanorod coated in TiO <sub>2</sub> of varying thickness. The plots are taken at the longitudinal resonance wavelength with a scale of 0-9 V/m apart from the plot at 650 nm which is taken at the peak of a lower wavelength resonance with a scale from 0-3 V/m. ....	161
Figure 5.14: Absorption efficiency for the transverse mode of a Au-Ag bimetallic nanorod with varying size of each material. The nanorod is kept at a constant diameter of 30 nm and AR=3. ....	162
Figure 5.15: Absorption efficiency for the longitudinal mode of a Au-Ag bimetallic nanorod with varying size of each material. The nanorod is kept at a diameter of 30 nm and AR=3. ....	163
Figure 5.16: a) Absorption efficiency spectra of a 40 nm gold sphere on top of a gold substrate, dielectric substrate and within a vacuum. S-polarised light is used incident normal to the substrate. b) Electric field plots for the background field (E <sub>y</sub> ) and the scattered field at $\lambda_{\max}$ from a side on view. ....	165
Figure 5.17: a) Absorption efficiency of a 40 nm gold sphere with distance above a 150 nm thick gold substrate for both s and p-polarised light at 45° angle of incidence. b) Resonant wavelength with distance above substrate. c) Electric field plots for both a 5 nm and 1 nm gap from the substrate when using s and p-polarised light at 45°. ....	166
Figure 5.18: Absorption efficiency spectra for 30 nm diameter gold nanorods supported on a 150 nm thick gold substrate with varying aspect ratios. 45° angle of incidence plane waves were used under a) s-polarisation or b) p-polarisation. The field distributions on the right are for both a “with substrate” and “without-substrate” scenario. ....	168
Figure 5.19: Absorption Efficiency spectra for an AR=3 gold nanorod with its long-axis perpendicular to a 150nm thick gold substrate at various particle-substrate gap sizes. ....	170
Figure 5.20: Electric field distribution plots for the longitudinal mode and higher order modes at decreasing wavelengths (left to right). The nanorod is 30 nm diameter with an aspect ratio of 8 and is supported on a 150 nm thick gold substrate. ....	171
Figure 5.21: Absorption efficiency for a 30 nm x 90 nm gold nanorod stood vertically on a gold substrate and illuminated by an s or p-polarised plane wave with varying angle of incidences. ....	171
Figure 5.22: Effect of spacing on the absorption efficiency for a trimer of side-by-side aligned gold nanorods of AR=3 and diameter 30 nm, excited using p-polarised light at 45°. The	

isolated curve represents that of a single gold nanorod therefore with no inter-particle coupling.....	172
Figure 5.23: Electric field distribution for a trimer of side-by-side nanorods showing the constructive interference between the transverse modes and destructive interference between the longitudinal modes.....	173
Figure 5.24: Dependence of the longitudinal modes optical cross section efficiencies on the inter-particle spacing for a trimer of gold nanorods (30 nm diameter, AR=3). .....	174
Figure 5.25: Effect of number of interacting nanorods on the absorption efficiency for an array of side-by-side aligned gold nanorods of AR=3 and diameter 30 nm, excited using p-polarised light at 45°. The periodic array curve represents that of an infinite array of gold nanorods. ....	175
Figure 5.26: Extinction cross sections for a 30 nm diameter nanorod array with a spacing of 40nm and varying aspect ratio. The array is excited by p-polarised light at an angle of incidence of 20° in a vacuum. ....	177
Figure 5.27: Effect of spacing on the absorption efficiency of a periodic array of nanorods with aspect ratio three in a vacuum (diameter of 30 nm). ....	179
Figure 5.28: Effect of spacing on the absorption efficiency of a periodic array of nanorods with aspect ratio seven in a vacuum (diameter of 30 nm). ....	180
Figure 5.29: Optical cross section efficiencies for gold nanorod arrays of aspect ratio 3,7,11 and 15. The diameter of the nanorods is 30 nm with 40 nm spacing and embedded in a vacuum. 20° angle of incidence p-polarised light is used to excite the plasmonic modes. ....	181
Figure 5.30: Resonant wavelength of the longitudinal mode with angle of incidence for an aspect ratio 3 nanorod array using p-polarised light. The nanorod diameter is 30 nm and the spacing is 80 nm. ....	182
Figure 5.31: Electric field distributions for the longitudinal mode of periodic gold nanorod arrays with spacing. The nanorods are 30 nm in diameter and AR=7. The incident light is p-polarised at 20°.....	183
Figure 5.32: Electric field distribution (colour plot) and Poynting vector (arrows) for an a) isolated and b) periodic array of nanorods of aspect ratio 7. The diameter of the nanorods is 30 nm and the incident light is p-polarised at an angle of 20°. ....	184
Figure 5.33: Comparison of absorption efficiency for a periodic array of nanorods (solid lines), both in a homogeneous medium (n=1) and supported on a 150 nm thick gold substrate. Additional dashed lines represent single nanorods not in an array, again in a homogeneous medium and supported on a gold substrate. P-polarised light at an angle	

of incidence of 20° was used in all these simulations. The nanorods in the arrays had a spacing of 80 nm. ....	186
Figure 5.34: Absorption efficiency for a gold nanorod array stood vertically on a gold substrate at varying spacing. Here the aspect ratio of the nanorods is three and the substrate thickness is 150 nm. The dashed and dotted line represent isolated unsupported nanorods of aspect ratio three and four respectively.....	188
Figure 5.35: Electric field distributions for the longitudinal mode of periodic gold nanorod arrays stood vertically on a 150 nm thick gold substrate with spacing. The nanorods are 30 nm in diameter and AR=7. The incident light is p-polarised at an angle of 20°. Each plot is taken at the resonant wavelength of the lowest energy peak, therefore representing the longitudinal mode.....	189
Figure 5.36: Electric field distribution for a) a single supported nanorod, b) a periodic array of supported nanorods, both at their longitudinal resonant wavelengths. The arrows represent the Poynting vector for each scenario. P-polarised light is incident at 20° angle of incidence. All nanorods are 30 nm in diameter and AR=7. ....	190
Figure 6.1: Schematic diagram of an electron beam interacting with a thin sample. $E_{\text{beam}}$ is the energy of the incident beam, whereas $E$ is the energy lost during an interaction. ....	196
Figure 6.2: a) Schematic diagram of the components in a CTEM and STEM <sup>(223)</sup> , b) Schematic representation of the electron beam in both a CTEM and STEM instrument <sup>(222)</sup> .....	197
Figure 6.3: Schematic diagram highlighting the parallel imaging capabilities of STEM along with examples of BF and HAADF images. $L$ represents the camera length which is the distance or magnification between the sample and detector <sup>(230)</sup> .....	199
Figure 6.4: Typical EELS spectrum with linear intensity showing the zero-loss peak (ZLP), plasmonic modes of the low loss region, and ionisation edges of the atoms in the higher energy core loss region <sup>(223)</sup> . ....	200
Figure 6.5: Schematic representation of a STEM-EELS instrument highlighting the operating principle of the spectrometer and EELS detector <sup>(241)</sup> . ....	203
Figure 6.6: Illustration of the concept behind the SI mapping of plasmon resonances acquired using a STEM-EELS technique. A gold nanorod is used as the example where the energies relating to the longitudinal mode are mapped.....	204
Figure 6.7: a) Bright field image of the nanorod also showing the silicon substrate. b) HAADF image of the nanorod where the coloured boxes represent the two locations the spectra was integrated over. c) EELS spectra with colours relating to the electron probe locations shown in the HAADF image. The text refers to the peak positions, found by applying a Gaussian fit to the curves. d) SI maps over the stated energy ranges showing both plasmonic modes.....	209

Figure 6.8: Comparison between experimental EELS spectra to that of modelled EELS spectra where the gold nanorod is either in vacuum, supported horizontally on a 5 nm thick Si substrate, or supported horizontally on a 5 nm thick Si substrate with a 3.2 nm CTAB layer on the nanorod surface. The nanorod has a diameter of 27.4 nm and length of 60.3 nm (AR=2.2). The arrows in the schematic diagram insets represent the position and direction of the electron beam in the simulations. In all cases this was placed 5 nm from the edge of the nanorod. The experimental EELS spectra is the same data as shown in Figure 6.7c (blue line). ..... 211

Figure 6.9: Modelled EELS intensity for a dimer of side-by-side aligned gold nanorods (30 nm x 90 nm) at varying spacing compared to an isolated nanorod. The nanorods are modelled within a vacuum with the electron beam aligned 5 nm above the left nanorod as demonstrated by the cross in the inset. Each curve has been offset in the y-direction. .... 213

Figure 6.10: a) Induced electric field plots for a gold nanorod dimer spaced 5nm based upon the data from Figure 6.9. The plots on the nanorod surface shows the surface charge distribution. b) Plots of the induced electric field modulus  $E_{zind} = E_{zind} \times E_{zind}$ , where  $E_{zind}$  is the complex conjugate of the induced electric field. c) Schematic representation of the surface charge distribution based upon the results from (a). .... 214

Figure 6.11: Schematic illustrations showing which modes may be excited when the electron beam is located in the dimer gap for a a) nanosphere dimer, b) end to end nanorod dimer, and c) side by side nanorod dimer. d) Modelling results for a side by side nanorod dimer (AR=3, 20 nm gap) with the electron beam located above a nanorod and in centre of the dimer gap..... 216

Figure 6.12: Modelled EELS intensity for a dimer of side-by-side nanorods of diameter 30 nm and with varying aspect ratios. The spacing within the array was kept constant at 30 nm. The array was excited with the electron beam located 5 nm below the left nanorod.. 218

Figure 6.13: a) Experimental EELS spectra for a dimer of nanorods half in AAO, compared to b) Simulated EELS spectra for the same dimer. The coloured blocks relate to the area integrated for the various spectra, and therefore the position of the electron beam c) SI and normalised SI map over the energy range 1.61-1.66 eV showing the nanorods dipole modes. .... 220

Figure 6.14: a) EELS spectra and corresponding bright field image showing the locations the spectra was integrated over. b) Normalised SI maps according to the energy range stated. .... 221

Figure 6.15: Modelled EELS intensity for a dimer of side-by-side aligned gold nanorods (30 nm x 90 nm) supported on a 150 nm thick gold substrate at varying spacing and

compared to an isolated nanorod. The nanorods are modelled within a vacuum with the electron beam positioned 5 nm above the left nanorod as demonstrated by the cross in the inset. Each curve has been offset in the y-direction to highlight the development of the modes. .... 224

Figure 6.16: a) Induced electric field plots for an AR=3 gold nanorod dimer supported on a 150 nm thick gold substrate and spaced 10 nm apart. The plots on the nanorod surface shows the surface charge distribution, however the view is tilted so as to also see the charge distribution on the substrate surface b) Plots of the induced electric field modulus. c) Schematic representation of the surface charge distribution based upon the results from (a)..... 226

Figure 6.17: a) Modelled EELS intensity for a dimer of side-by-side nanorods of diameter 30 nm and with varying aspect ratio. The nanorods are stood vertically on a 150 nm gold substrate with a spacing of 30 nm. The array was excited with the electron beam located 5 nm above the right nanorod. b) Induced electric field plots, c) modulus of induced electric field..... 227

Figure 6.18: EELS spectra for a supported nanorod dimer. The inset shows a bright field image whereby the coloured squares represent the regions integrated for the spectra shown. The SI maps are taken over the energy window stated and as shown by the dashed boxes. .... 228

Figure 6.19: Modelling of the experimental nanorod dimer comparing resonant wavelengths for nanorods that were a) unsupported and isolated, b) supported but isolated, and c) supported and in a dimer separated by 32 nm. .... 230

Figure 6.20: EELS spectra for a supported nanorod dimer in AAO. The inset shows a HAADF image whereby the coloured squares represent the regions integrated for the spectra shown. The SI maps for each peak are taken over the energy window stated and as shown in the spectra by the dashed boxes. .... 232

Figure 6.21: Modelling of a nanorod dimer with a) varying aspect ratio and b) varying diameter. The dimer was excited with an electron beam located in the centre of the dimer gap and has a spacing of 20 nm. Each spectra has been offset so as to assess the change in peak intensities. .... 233

Figure 6.22: a) Modelling of EELS spectra for a nanorod array with increasing number of interacting nanorods. The solid lines were modelled with the electron beam located above the centre most nanorod in the array, the dashed lines were for the electron beam located above the end nanorod, and the dotted line is with the electron beam above the 2<sup>nd</sup> from the end nanorod. The arrows help show the splitting and hybridisation of the modes with increasing number of nanorods, whereas the numbers aim to help identify

the peaks. b) Induced electric field plots for each mode of the nanorod trimer. The aspect ratio of the rods used in all these simulations was 3, along with a diameter of 30 nm and a spacing of 20 nm. ....	235
Figure 6.23: Plasmon hybridisation diagram for a side by side nanorod array with increasing number of nanorods. The aspect ratio of the nanorods was 3 whereas the spacing and diameter of the rods was 20 nm and 30 nm respectively. The relative energy positions of the above modes are located based upon the data from Figure 6.22a. The black dots refer to the location of the electron beam according to the configuration shown. ....	237
Figure 6.24: Induced electric field plots of the bright mode for an a) unsupported nanorod array, and b) supported nanorod array showing the electric field distribution altering to the centre or bottom of the nanorod. ....	239
Figure 6.25: EELS data for a nanorod array of AR ~ 2.5-4 on a 150 nm gold substrate. a) EELS spectra obtained from integrating over all pixels in the corresponding SI b) Individual EELS spectra for each nanorod, integrated over a region as represented by the coloured blocks in the HAADF image. The coloured dashed lines represent the dominant mode for the nanorod principally excited in that location c) SI maps for the energy windows 0.7-1.6 eV and 1.6-2.1 eV. ....	240
Figure 6.26: Normalised EELS measurements for a gold nanorod array embedded in AAO. a) Normalised EELS spectra for each nanorod, integrated over a region as represented by the coloured blocks in the HAADF image. The coloured dashed lines represent the dominant mode for the nanorod principally excited in that location. The inset shows the lower wavelengths peaks based on integrating a region spanning the bottom of all the nanorods (black box). b) SI maps over the energy windows 0.6-1.0 eV and 1.8-2.2 eV, and c) their normalised equivalents. ....	245
Figure 6.27: EELS spectra and SI maps showing the dipole and higher order modes of the gold substrate. The spectra was acquired by integrating the region as shown by the white square in the HAADF image. ....	247
Figure 7.1: a) Schematic of the generation of a hot electron b) Diagram of hot electron excitation and injection in to an adjacent semiconductor. CB and VB are the conduction and valence bands of the semiconductor respectively, whereas $E_F$ is the Fermi energy level. Adapted from <sup>(22)</sup> . ....	252
Figure 7.2: Schematic of the electron-hole formation in a semiconductor based upon plasmonic near field enhancement. Greater electron-hole formation occurs in the region close to the metal nanoparticle. Adapted from <sup>(22)</sup> . ....	255
Figure 7.3: Schematic illustrations of the PIRET and FRET processes. a) In PIRET the LSPR is excited and transfers its energy to an overlapping higher energy semiconductor,	

whereas in FRET the semiconductor is excited and transfers its energy to the overlapping lower energy metal. b) In both cases the donor has to have an overlapping energy with the acceptor. <sup>(279)</sup>..... 255

Figure 7.4: SEM images of a nanorod array both before (left) and after (right) TiO<sub>2</sub> deposition (Sample 1). The top row shows a top down view of the nanorods whereas the bottom row shows a tilted view..... 260

Figure 7.5: Tilted SEM images of Sample 1 showing the presence of a layer on the surface of the nanorods when using an accelerating voltage of 20 kV. With thanks to Dr. Mark Rosamond, University of Leeds..... 261

Figure 7.6: XPS survey of Sample 2 showing the presence of both titanium and oxygen. The inset shows the corresponding high resolution Ti2p Scan. .... 262

Figure 7.7: PAXPS spectra for the Ti2p and Au4f peaks at varying collection angles relative to the surface normal. The spectra have been normalised based upon their atomic percent concentration and offset from each other in the y-direction. .... 265

Figure 7.8: Methylene blue dye degradation percentage for Sample 1, Sample 2 and a control with no sample. A linear fit is added to the control sample so as to clearly see the typical self-degradation rate..... 267

Figure 7.9: Wu et. al. <sup>(301)</sup> experimental results for a) H<sub>2</sub> production via water splitting and b) methylene blue dye degradation. AuNR@TiO<sub>2</sub> refers to a completely covered core shell particle (see d), AuNR/TiO<sub>2</sub> is for coverage of TiO<sub>2</sub> only the ends (see c), and AuNR and TiO<sub>2</sub> refers to a physical mixture of nanorods and amorphous TiO<sub>2</sub>. c) Schematic illustration of photocatalysis for anisotropic TiO<sub>2</sub> coverage compared to d) lack of photocatalysis for completely coated nanorods..... 268

## LIST OF ABBREVIATIONS

<b>AAO</b>	Anodic Aluminum Oxide
<b>ALD</b>	Atomic Layer Deposition
<b>AR</b>	Aspect Ratio
<b>BEM</b>	Boundary Element Method
<b>BF</b>	Bright Field
<b>CB</b>	Conduction band
<b>CTAB</b>	Cetrimonium Bromide
<b>CTEM</b>	Conventional Transmission Electron Microscopy
<b>DDA</b>	Discrete Dipole Approximation
<b>DET</b>	Direct Electron Transfer
<b>DIM</b>	Dipolar Interaction Model
<b>EDX</b>	Energy-Dispersive X-Ray Spectroscopy
<b>EELS</b>	Electron Energy Loss Spectroscopy
<b>EFTEM</b>	Energy Filtered Transmission Electron Microscopy
<b>ELNES</b>	Electron Energy Loss Near Field Structure
<b>EXELFS</b>	Extended Electron Energy Loss Fine Structure
<b>FDTD</b>	Finite Difference Time Domain
<b>FEG</b>	Field Emission Gun
<b>FEM</b>	Finite Element Modelling
<b>FIB</b>	Focused Ion Beam
<b>FRET</b>	Förster Resonant Energy Transfer
<b>FWHM</b>	Full Width Half Maximum
<b>GNOR</b>	Generalised Nonlocal Optical Response
<b>HA</b>	Hard Anodisation
<b>HAADF</b>	High Angle Annular Dark Field
<b>LAADF</b>	Low Angle Annular Dark Field
<b>LSPR</b>	Localised Surface Plasmon Resonance
<b>MA</b>	Mild Anodisation
<b>MAADF</b>	Medium Angle Annular Dark Field
<b>NIR</b>	Near-Infrared
<b>OCP</b>	Open Circuit Potential
<b>PARDISO</b>	Parallel Sparse Direct Solver
<b>PAXPS</b>	Parallel Angle Resolved X-ray Photoelectron Spectroscopy
<b>PBC</b>	Periodic Boundary Condition

<b>PE-ALD</b>	Plasma Enhanced Atomic Layer Deposition
<b>PEC</b>	Perfect Electrical Conductor
<b>PIRET</b>	Plasmon-Induced Resonant Energy Transfer
<b>PMC</b>	Perfectly Magnetic Conductor
<b>PML</b>	Perfectly Matched Layer
<b>PRET</b>	Plasmon Resonant Energy Transfer
<b>PTFE</b>	Polytetrafluoroethylene
<b>ROI</b>	Region of Interest
<b>SEM</b>	Scanning Electron Microscope
<b>SERS</b>	Surface Enhanced Raman Spectroscopy
<b>SI</b>	Spectroscopic Image
<b>SNOM</b>	Scanning Near-Field Optical Microscopy
<b>SPP</b>	Surface Plasmon Polariton
<b>SPR</b>	Surface Plasmon Resonance
<b>STEM</b>	Scanning Transmission Electron Microscope
<b>TEM</b>	Transmission Electron Microscope
<b>VB</b>	Valence Band
<b>XPS</b>	X-Ray Photoelectron Microscope
<b>ZLP</b>	Zero Loss Peak

# LIST OF SYMBOLS

## CHAPTER 2: THEORETICAL BACKGROUND AND LITERATURE REVIEW

<b>D</b>	Electric displacement field	$\rho_v$	Charge Density
<b>B</b>	Magnetic flux density	<b>E</b>	Electric field
<b>H</b>	Magnetic field	<b>J</b>	Electric current density
$\epsilon_0$	Permittivity of free space	$\mu_0$	Magnetic permeability of free space
<b>P</b>	Polarisation	<b>M</b>	Magnetisation
$f$	Scalar wave amplitude	$v$	Velocity
$c$	Speed of light	$\epsilon$	Permittivity
$\mu$	Permeability	$n$	Refractive index
$\lambda$	Wavelength	$\nu$	Frequency
$h$	Planks constant	eV	Electron volts
$m$	Mass of an electron	$r$	Displacement of the electron
$\Gamma$	Damping rate	$\omega_0$	Natural resonant frequency
$q$	Charge	$\omega$	Angular frequency
<b>p</b>	Dipole moment	$N$	Number of atoms per unit volume
$\chi$	Susceptibility	$\omega_p$	Plasma frequency
$\tilde{\epsilon}_r$	Relative permittivity (complex)	$\epsilon_r'$	Real part of permittivity
$\epsilon_r''$	Imaginary part of permittivity	$f_n$	Oscillator strength
$\tilde{n}$	Complex refractive index	$k$	Extinction coefficient
$A$	Absorbance	$T$	Transmittance
$I$	Transmitted radiation	$I_0$	Incident radiation
$\sigma_{ext}$	Extinction cross section	$\sigma_{abs}$	Absorption cross section
$\sigma_{sca}$	Scattering cross section	$\sigma_{ext,eff}$	Extinction efficiency
$\sigma_{abs,eff}$	Absorption efficiency	$\sigma_{sca,eff}$	Scattering efficiency
$\sigma_{geom}$	Geometric cross section	$k$	Wave number
$R$	Sphere radius	$\epsilon_p$	Particle permittivity
$\epsilon_m$	Medium permittivity	$D$	Nanoparticle diameter
$E_0$	Incident electric field strength	$a$	Radius of sphere
<b>r</b>	Position vector	$P$	Point
$\theta$	Angle	$\phi$	Scalar function of azimuth angle
$\phi_{in}$	Potential inside sphere	$\phi_{out}$	Potential outside sphere
$\alpha$	Polarisability	<b>n</b>	Unit vector in direction of point P
$\lambda_{max}$	Resonant wavelength	$\epsilon_{core}$	Permittivity of core

$\epsilon_{sh}$	Permittivity of shell	$d$	Film thickness
$h$	Volume fraction of shell	$\lambda_p$	Plasma wavelength
$v_F$	Fermi velocity	$\tau$	Damping rate of free electron gas
$L$	Length	$V$	Volume
$P_j$	Depolarisation factors	$e$	Aspect ratio factor
$\epsilon_{sub}$	Permittivity of substrate	$\epsilon_{m,eff}$	Effective permittivity of medium
$\rho$	Substrate occupancy factor	$l$	Angular momentum
$\sigma$	Bonding mode	$\sigma^*$	Anti-bonding mode
$\pi$	Pi or Bonding mode	$\pi^*$	Anti-bonding mode
$n_a$	Refractive index of medium	$J$	Coupling Strength
$R_{12}$	Distance between dipole centres	$\kappa$	Orientation factor
$ \mu $	Modulus of transition dipole moment	$f_m$	Volume fraction of metal
$j$	Imaginary number		

### **CHAPTER 3: FABRICATION METHODOLOGY**

$U$	Potential	$Q$	Charge passed
$F$	Faradays constant	$M$	Molar mass
$z$	Valency number	$m$	Mass of material

### **CHAPTER 5: MODELLING OF PLASMONIC RESONANCES**

$E_0$	Incident electric field strength	$n_a$	Refractive index of medium
$I_0$	Incident intensity	$w$	Width of domain
$\phi$	Azimuth angle	$\theta_a$	Angle of incidence
$\theta_b$	Refraction angle	$\mathbf{k}_a$	Wavenumber in medium
$\mathbf{k}_b$	Wavenumber in substrate	$n_b$	Refractive index of substrate
$\epsilon_r'$	Real part of permittivity	$\epsilon_r''$	Imaginary part of permittivity
$d$	Periodic distance	$\lambda$	Wavelength

### **CHAPTER 6: ELECTRON ENERGY LOSS SPECTROSCOPY**

$v$	Electron velocity	$e$	Electron charge
$U$	Accelerating voltage	$m$	Mass of an electron
$j$	Electric current density	$c$	Speed of light
$R_0$	Impact parameter	$\omega$	Angular frequency
$E_z^{ind}$	Induced field	$E(z,\omega)$	Full field
$E_0(z,\omega)$	Background field	$\bar{E}_z^{ind}$	Complex conjugate of $E_z^{ind}$

### **CHAPTER 7: NANOROD ARRAYS FOR PHOTOCATALYTIC REACTIONS**

$A_0$	Initial absorbance	$A_t$	Absorbance at time, t
-------	--------------------	-------	-----------------------

# 1 INTRODUCTION

## 1.1 The Nanoscale World

The last century has seen huge technological advancements alongside ground-breaking scientific discoveries. We've been to the moon, created computers, and even developed technologies to replace damaged organs. A critical step in many of these advancements has been due to material research and our ability to understand, utilise, and control their properties. It is therefore undoubtable that our progression in the future will also depend on materials research and the unique new materials, properties and functions that arise.

At the heart of materials research is nanotechnology. This field was pioneered by the ideas of physicist Richard Feynman who proposed that atoms could be arranged in a bottom-up approach so as to build useful structures <sup>(1)</sup>. In general this remains the main role of nanotechnology, namely to control the nanoscale properties and effects so as govern the bulk material. By definition nanotechnology refers to *“The branch of technology that deals with dimensions and tolerances of less than 100 nanometres, especially the manipulation of individual atoms and molecules”* <sup>(2)</sup>.

These nanoscale effects referred to can be both incredibly unique and beneficial. At the length scales involved, forces do not act the same as we are used to in macroscopic environments. For example, gravity is a function of mass and therefore its effect on nanoscale objects is often negligible. On the other hand, electrostatic forces such as van der Waals interactions, which are strongly reliant on distance, are crucial at the nanoscale <sup>(3)</sup>.

Another major difference at the nanoscale is that the surface to volume ratio increases dramatically, meaning that forces such as surface energy become increasingly important. For example, nanoparticles in a solution have a large surface to volume ratio and therefore have a high surface energy. To minimise this energy, the nanoparticles will readily join with each other to form agglomerates, a process that is generally undesirable and must be overcome by a variety of means. The increase in surface to volume ratio can also mean that the chemical reactivity of the species increases. This is due to the atoms at the surface differing from those in the bulk owing to the reduced number of nearest neighbour atoms. This results in free valence electrons that can contribute to bonding and therefore provide a higher chemical reactivity <sup>(4)</sup>. Gold for instance is considered inert as a bulk material, however when in nanoparticle form it can show excellent catalytic activity, for instance in the oxidation of CO <sup>(5)</sup>. Care must be taken however with certain species that the increased reactivity and higher surface area does not mean undesired reactions occur, such as the formation of a stable oxide layer on metallic nanoparticles. This unreactive oxide layer would be more prominent in nanomaterials as there is more surface to react resulting in the potential for the reactivity to decrease compared to the bulk <sup>(4)</sup>.

Another important advantage of nanomaterials is the potential ability to adopt different crystal structures and geometries when in nanoparticle form. This can be particularly advantageous for the development of improved catalysts. As adsorbates can have varying affinities for different adsorption sites, control of the nanoparticle structure and geometry, including the presence of defect sites, corners, and edges, can lead to improvements in reaction rates, selectivity, and stability <sup>(6, 7)</sup>.

The optical properties of materials are also greatly affected when the size is reduced down to the nanoscale. Gold nanoparticles are a classical example. The characteristic shiny yellow colour seen in bulk gold is lost, and instead they can appear as a variety of different colours depending on its size. For example, for small gold nanoparticles around 30nm in size, the gold absorbs the blue and green portions of the light and reflects the red thereby appearing red in colour. In contrast, for larger sized gold nanoparticles around 100nm in size, the absorption of light occurs within the red region of the spectra resulting in a blue or purple colour <sup>(8)</sup>. The reasoning behind this change in colour is due to a nanoscale optical phenomenon termed surface plasmon resonance (SPR). This occurs when nanoparticles have dimensions small in comparison to the wavelength of incident light. The oscillating electric field of the light causes the conduction electrons in the nanoparticle to collectively oscillate around the surface of the

nanoparticle. This excitation of a surface plasmon resonance leads to the absorption of the light at a resonant wavelength that for gold is in the visible region. Other factors such as the size, shape and environment of the nanoparticle can also alter this resonant frequency however, which is why a variation in colour is seen for the different sized gold colloids as seen in Figure 1.1.



**Figure 1.1: Change in colour of gold nanoparticles in solution due to variation in size <sup>(8)</sup>.**

This fascinating nanoscale phenomenon will be the main focus of this work due to the advantages it provides for a wide range of applications. A more detailed explanation of surface plasmon resonances is given in Chapter 2, whereas here I provide a historical overview and an indication of their application areas.

## 1.2 The Rise of Plasmonics

The use of plasmonics and the interesting optical properties that they possess dates back to at least Roman times (4<sup>th</sup> Century AD), where colloidal gold and silver nanoparticles were built into the Lycurgus Cup as seen in Figure 1.2. When ambient light is reflected off the glass, the excited plasmonic particles scatter the green light resulting in an opaque green colour. On the other hand, when light is transmitted through the glass the plasmonic nanoparticles absorb the short wavelengths resulting in the observed bright red colour <sup>(9)</sup>.



**Figure 1.2: Lycurgus Cup showing change in colour due to plasmonic particles <sup>(10)</sup>.**

Although the Romans were able to take advantage of nanotechnology and the interesting optical properties plasmonics offers, it is doubtful they truly understood why the colour change occurred, or even that gold was critical in its formation <sup>(11)</sup>. This property was in fact only discovered in the 1850's by Michael Faraday's experiments with chemically produced gold leaf colloids <sup>(12)</sup>. This work was later built upon by Mie in 1908 who managed to theoretically describe the absorption and scattering of light by spherical metallic particles including gold <sup>(13)</sup>. This revolutionary work later became known as Mie theory and can be read about in more detail in Chapter 2.

While Mie theory could successfully describe the optical properties of isolated spherical particles, further unexplained observations of SPR effects were seen throughout the start of the 20<sup>th</sup> century. In fact it took until 1968 for the explanation of surface plasmons to arise when Otto successfully shone polarised light through a prism onto a thin metal film, and over certain resonance angles, witnessed a dip in reflected light intensity attributed to the formation of surface plasmons <sup>(14)</sup>. Unlike the surface plasmons present on individual nanoparticles termed localised surface plasmon resonances (LSPR), these plasmons propagate over a flat metal – dielectric interface and are referred to as surface plasmon polaritons (SPP).

Both these types of surface plasmon resonances have received much attention since their discovery, particularly since the late 1980's when technology advancements allowed better characterisation of nanoparticles along with improved control of their fabrication. Since then the subject has gone from strength to strength as new and interesting optical behaviours and applications have been identified. This can be seen in the dramatic rise of number of publications associated with the term '*surface plasmon*' as shown in Figure 1.3.

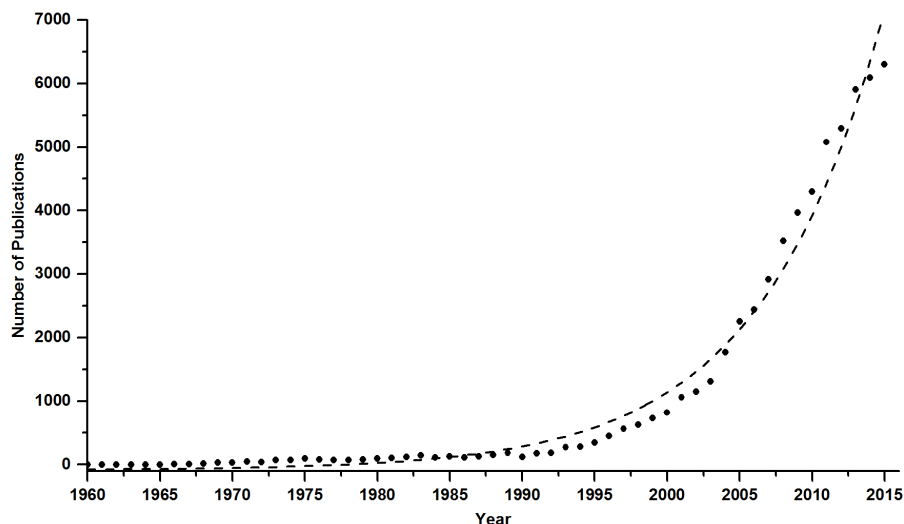


**Figure 1.3: Number of publications with ‘surface plasmon’ in the article title, abstract or keywords (data obtained from scopus.com).**

### 1.3 Applications of Plasmonics

The single largest use of plasmonics since their discovery has been in the development of analytical techniques such as Raman Spectroscopy. This is a process where a sample is excited by a monochromatic laser. Typically the light undergoes elastic Rayleigh scattering whereby the wavelength of the light remains constant. Occasionally however, the light will scatter inelastically (Raman scattering) as it induces atomic vibrations, with a resulting change in wavelength. This change can be detected and used to identify the molecules and structure of the substance. Unfortunately, the signal intensity received by Raman scattering is often a factor of  $10^{-6}$  weaker relative to the elastic scattering, and therefore difficult to detect. Plasmonics has assisted this technique by providing a metallic nanoparticle surface on which the molecules are adsorbed. The SPR effect upon this metallic surface gives rise to an enhanced electric field which in turn drastically increases the amount of inelastically scattered light and therefore the Raman signal. This technique is referred to as Surface Enhanced Raman Spectroscopy (SERS) and can give enhancement factors as high as  $\sim 10^{10}$  meaning detection of single molecules is possible <sup>(15, 16)</sup>. Similarly, plasmonic nanoparticles can also be used for the detection of biomolecules binding to a plasmonic surface based upon their large sensitivity to the dielectric properties of the environment. The specifics of this sensitivity will be discussed in detail with Chapter 2, however it may be noted here that the sensing of single molecules is increasingly becoming a reality <sup>(17)</sup>. Indeed, plasmonic sensing is already an area commercialised by companies such as Biacore (GE Healthcare) <sup>(18)</sup>.

In addition, much interest is currently being directed towards the use of plasmonics for medical procedures. This arises from the ability of plasmonic nanoparticles to generate large amounts of heat in a very concentrated area due to their thermo-electrical properties. It is hypothesised this thermal energy, produced by exciting LSPR modes of injected nanoparticles, may be harnessed to irreversibly destroy cancerous cells, if the nanoparticle can be successfully localised at a cancerous tumour. This has the advantage of targeting just the surrounding cancerous cells, unlike chemotherapy, and would not require surgical methods. So far a number of studies in this area have shown promising results such as Hirsch *et. al* <sup>(19)</sup> who experimented both *in vitro* and *in vivo* with gold / silica nanoshells. On illumination with infra-red radiation, temperature increase of  $37.4 \pm 6.6^{\circ}\text{C}$  was achieved thereby causing irreversible tissue damage within the tumour.

Another discipline that aims to utilise plasmonics is the electronics industry. Currently there is a great demand to find a mechanism capable of transferring data around a computer chip in much larger quantities than current wiring can provide. Fibre optic cables offer one solution however their size is limited by the diffraction limit, making the dimensions required too large for modern computer chips <sup>(20)</sup>. By instead putting a thin dielectric material between two metal plates and exciting an SPP along the interface, the wavelength may be shrunk by a factor of 10 whilst keeping the frequency the same. This technology is referred to as plasmon slot waveguides and shows massive potential for integration into modern circuits.

Plasmonic effects also show potential in enabling semiconductors to utilise visible light. This is desirable due to the restraint that semiconductors need a photon with energy equal or higher than its bandgap to generate electron-hole pairs, and that in general most semiconductors have relatively large bandgaps located within the UV region. Unfortunately, these wavelength have a particularly low irradiance on the earth's surface due to adsorption by the atmosphere and ozone layer. In contrast, visible light is far more abundant on the earth's surface and therefore if semiconductors could utilise this region potentially large increases in efficiency could be obtained for various applications. Typically this is achieved by coating the plasmonic nanoparticles in a semiconductor. The plasmonic resonance of the nanoparticles then allows absorption of the light at a controllable wavelength based upon its properties, followed by subsequent transfer of this energy into the semiconductor <sup>(21)</sup>. Additionally, the presence of metallic nanoparticles and the strong electric fields surrounding them also play a role by increasing charge separation and electron hole production <sup>(21, 22)</sup>. The specifics of these interactions are complex and discussed in more detail in Chapter 7.

These processes have a great deal of promise for a number of semiconductor related applications including photovoltaic thin film solar cells whereby increasing light absorption is essential. Here, plasmonic nanoparticles are typically used to extend the path lengths in the semiconductor due to their high scattering, in addition to the advantages described above <sup>(23)</sup>.

Plasmonic nanoparticles unique properties are also being harnessed in photocatalytic applications. This is where light is used to drive chemical reactions, which with the presence of a catalyst is done at enhanced rates. In this sense, the semiconductor and plasmonic nanoparticles would be the catalyst which absorb the light and create electron hole pairs that participate in the reaction. This has many uses but is particular popular in applications relating to the degradation of pollutants or the generation of hydrogen by water splitting <sup>(22)</sup>.

## 1.4 Overview of the Research

An overview of the work in this thesis is given below. An introduction to the problem will first be described, before highlighting the aims and objectives I hoped to achieve. Lastly, an overall outline of the thesis and its layout will be given.

### 1.4.1 The Challenge

Since the industrial revolution, the growth of civilisation has predominantly been fuelled by the use of carbon intensive energy sources such as coal and oil. These fossil fuels inevitably lead to the emission of carbon dioxide and as such have caused global CO<sub>2</sub> concentrations to dramatically increase. These higher concentrations have in turn raised the global temperature at unprecedented levels, the consequences of which could be devastating for the planet <sup>(24)</sup>.

To combat global warming, a switch to a low carbon society is essential. Based upon our current progress however we are set to fall short of the levels needed to limit this temperature increase to 2°C and thereby avoid the most devastating effects <sup>(25, 26)</sup>. In order to halt this trend, improvements need to be made in the uptake of low carbon technologies, something best achieved by making them competitive with the traditional methods.

Plasmonics is one of the many routes explored that hopes to do this by using its unique advantages, particularly in both photovoltaic and photocatalytic applications. Unfortunately, plasmonic research into these areas is still in its relative infancy, with lots more work required to fully understand the processes involved. For instance, it is known that the size and shape

of nanoparticles is critical to its plasmonic response, however aside from the basic geometries, which may be described by theoretical methods, more needs to be understood about complex geometries and arrangements. This is particularly difficult for a number of reasons. Firstly, typical synthesis routes of plasmonic nanoparticles have relied on wet chemical methods. Although this often allows nanoparticles to be grown with good control over the size and shape, the separation between the nanoparticles is almost impossible to control, a condition which can be incredibly important with regards to plasmonic coupling. Similarly, nanoparticles are often immobilised on substrates for their application. This can drastically alter the local environment of the nanoparticle and lead to changes in its plasmonic resonance, a factor that is often neglected. These difficulties have led to numerous authors concluding that better control of the size, shape and separation distances of the nanoparticles is required in the synthesis methods so as to better optimise photocatalytic reactions <sup>(21, 22, 27, 28)</sup>.

In addition, the characterisation of the nanoparticles can be equally as challenging due to their scale and the high number of variables the plasmonic properties depend on. This is also made more complicated by them showing both strong near and far-field effects, often which can be different <sup>(29)</sup>. Far-field effects have typically been explored by techniques such as UV-Vis spectroscopy and dark field microscopy, allowing information on the particles absorption and scattering properties to be determined relatively easy. On the other hand, the near field properties, being those less than a wavelength away from the particle, are often more difficult to probe, yet just as crucial due to the spatial dependence of the surface plasmons. This is particularly the case for photocatalytic applications when the near field electric field enhancements are required to effectively combine with semiconductor layers. Fortunately, both scanning near-field optical microscopy (SNOM) and electron energy loss spectroscopy (EELS) are capable of analysing these properties. EELS in particular is a promising method to explore the near field due to the rich information it gives, however excellent energy and spatial resolutions are often needed, requiring state of the art aberration corrected microscopes with monochromated electron sources.

Modelling is also playing an increasing role in understanding plasmonic nanoparticles properties in both the near and far-field. Its popularity is due to the ability to obtain rich information relatively easy, thereby probing the fundamental physics and supporting experimental work. For example, information on the absorption and scattering cross sections from nanoparticles may be calculated, in addition to simultaneously being able to describe the electric fields immediately surrounding the particles. Unfortunately, modelling can be

particularly susceptible to errors and therefore care must be taken that the results obtained are indeed accurate. Similarly, it is important to understand the validity and limits of simulations when dealing with nanoscale objects. For instance, when dealing with particularly small nanoparticles less than 10nm in size, quantum and non-local effects may become prominent, and therefore would need to be addressed within the model <sup>(30)</sup>.

## 1.4.2 Objectives

Considering the problems outlined above, the aim of this thesis is:

*“To fabricate a regular array of plasmonic nanostructures with accurate control over their size, shape and separation. This geometric order will then be utilised to characterise both the near and far-field properties of the plasmonic nanoparticles, specifically focusing on the absorption of the array and coupling effects. The photocatalytic properties should then also be determined by coating the plasmonic nanoparticles with a semiconductor, and conducting photocatalytic experiments.”*

The above aims can be further broken down in to a number of specific objectives, as follows:

- 1. To fabricate porous membranes with accurate control over the size, separation and arrangement of the pores for use as templates in the growth of plasmonic nanostructures.**
- 2. To fabricate regular arrays of plasmonic nanorods using the above mentioned templates, with control over their diameter, aspect ratio, spacing, arrangement and the area over which they are grown.**
- 3. To characterise the absorption and scattering properties of the nanorod arrays by UV-Vis spectroscopy, and tune the absorption to the visible region.**
- 4. To characterise the near-field electric field enhancements and coupling effects in nanorod arrays by the use of electron energy loss spectroscopy.**
- 5. To perform thorough simulations on the properties of plasmonic nanospheres and nanorods so as gain a deeper understanding of the fundamental mechanisms of operation and to guide the experimental work.**
- 6. To coat the nanorod array in a homogeneous thin layer of titanium dioxide.**
- 7. To perform photocatalytic dye degradation experiments using the TiO<sub>2</sub> coated nanorod arrays, and show activation in the visible region of the spectrum.**

### 1.4.3 Thesis Structure

The structure of this thesis is set out in the following manner. Firstly, a theoretical background is given in Chapter 2. This briefly covers the fundamentals behind electromagnetic radiation and its interaction with matter, including an explanation of Maxwell's Equations and Mie theory, before then reviewing the theory of localised surface plasmon resonances. A literature review of research focussing on plasmonic nanoparticles is then also included, with particular emphasis given to noble metal nanorods, and how their resonance wavelength may be controlled and optimised. An in-depth review of work focussing on the coupling properties of nanoparticles is also incorporated, which for simplicity is split into both particle-substrate coupling and particle-particle coupling. This review includes findings from both experimental and simulation based work with an aim of helping explain the experimental results that follow.

Chapter 3, outlines the methodology employed for fabrication of the arrays and subsequent coating in a semiconductor, with Chapter 4 then beginning their characterisation. The size and geometry is first assessed by means of SEM imaging, before characterisation of the far field optical properties by UV-Vis spectroscopy. Chapter 5 then aims to complement this experimental work and gain a deeper understanding of the results by focussing on the modelling of plasmonic nanoparticles and arrays using a finite element model. This increases in complexity, starting with the simulation of basic nanospheres to validate the model, before moving on to nanorods and the optimisation of their plasmonic properties with regards to absorption within the visible spectrum. Finally, an in-depth look at the coupling effects of particles within an array and on a substrate is addressed.

The near field properties of the nanoparticles and arrays are then determined in Chapter 6 using EELS. This EELS analysis of nanorod arrays is believed to be a particularly novel result. In addition to this, to support the EELS results I have also developed a FEM simulation of the EELS experiment so as to compare and analyse the results it provides. Finally, Chapter 7 discusses the application of the nanorod arrays for photocatalytic purposes. This initially reviews the various plasmonic photocatalytic mechanisms, before then highlighting the photocatalytic properties of the arrays from the degradation of an organic dye under visible light. I conclude the work with a summary of the findings and prospects for the future.

# 2 THEORETICAL BACKGROUND & LITERATURE REVIEW

This chapter aims to give an overview of the field of plasmonics so as to provide an understanding of its concepts and an appreciation of current developments. It will begin by outlining the fundamental theories that are vital to its understanding and on which the plasmonic concept is based, before moving on to specifically outline the theory behind plasmonics in relation to localised surface plasmon resonances (LSPRs). This will also include a description of relevant and important work by means of a literature review. Emphasis is given to research focused on the optical properties of plasmonic nanorods, including factors that determine the resonant frequency and strength, plus the effects of inter-particle coupling and the presence of substrates.

The work discussed in this chapter will be referred to later on so as better understand my own results. In addition however, it is also critiqued so an appreciation of gaps in the knowledge and flaws in current research may be identified. For conciseness, the theory and literature review on the application of plasmonic nanoparticles for photocatalytic purposes will not be discussed here, but is instead included within its relevant section; Chapter 7: Photocatalytic Applications.

## 2.1 Electromagnetic Radiation and its Interaction with Matter

### 2.1.1 Fundamentals of Electromagnetic Radiation

Electromagnetic radiation in its simplest term is the propagation of both an electric and magnetic field whereby both these fields are perpendicular to the direction of travel and to each other. An electromagnetic wave is characterised by the distance between two successive identical parts of the wave known as the wavelength ( $\lambda$ ). These can range from sub atomic sizes on the order of less than  $1 \times 10^{-12}$  metres for gamma rays, up to kilometres for radio waves. The narrow visible region, which accounts for the light able to be detected by our eyes, has wavelengths between approximately 400 nm and 800 nm and will be the main part of the spectrum focused upon within this work.

A large part of the explanation of electromagnetic waves was first achieved by James Maxwell in 1865 within his paper entitled “*A Dynamical Theory of the Electromagnetic Field*”<sup>(31)</sup>. In this historic paper, Maxwell successfully unified already known laws such as Ampere’s Law, Faraday’s Law, and Gauss’s Law, into a set of four equations known as Maxwell’s equations. These equations are shown in their differential form below where  $\mathbf{D}$  is the electric displacement field,  $\rho_v$  is the charge density,  $\mathbf{B}$  is the magnetic flux density,  $\mathbf{E}$  is the electric field,  $\mathbf{H}$  is the magnetic field and  $\mathbf{J}$  is the electric current density. The operators  $\nabla \cdot$  and  $\nabla \times$  refer to the divergence and curl of a vector function respectively.

$$\nabla \cdot \mathbf{D} = \rho_v \quad (1) \qquad \nabla \cdot \mathbf{B} = 0 \quad (2)$$

$$\nabla \times \mathbf{E} = -\frac{\partial \mathbf{B}}{\partial t} \quad (3) \qquad \nabla \times \mathbf{H} = \frac{\partial \mathbf{D}}{\partial t} + \mathbf{J} \quad (4)$$

These equations opened up a breadth of understanding of electromagnetic waves including their ability to propagate through different media, and the velocity at which they travel. For instance, using the relationships for the electric displacement field and magnetic field within a medium, defined as:

$$\mathbf{D} = \epsilon_0 \mathbf{E} + \mathbf{P} \quad (5)$$

$$\mathbf{B} = \mu_0 \mathbf{H} + \mathbf{M} \quad (6)$$

Here epsilon ( $\epsilon_0$ ) and mu ( $\mu_0$ ) represents the constants of electric permittivity and magnetic permeability of free space respectively, whereas  $\mathbf{P}$  and  $\mathbf{M}$  represent the polarisation and magnetisation of the medium. Assuming free space conditions, no charges exist ( $\mathbf{J}, \rho_v = 0$ ), plus  $\mathbf{P}$  and  $\mathbf{M}$  may be neglected. This allows equations (1) and (4) to become:

$$\nabla \cdot \mathbf{E} = \frac{\rho_v}{\epsilon_0} = 0 \quad (7)$$

$$\nabla \times \mathbf{B} = \mu_0 \epsilon_0 \frac{\delta \mathbf{E}}{\delta t} \quad (8)$$

By taking the curl of both sides of (3):

$$\nabla \times (\nabla \times \mathbf{E}) = - \frac{\delta(\nabla \times \mathbf{B})}{\delta t} \quad (9)$$

followed by substitution into (8), gives:

$$\nabla \times (\nabla \times \mathbf{E}) = -\mu_0 \epsilon_0 \frac{\delta^2 \mathbf{E}}{\delta t^2} \quad (10)$$

Using the vector calculus relationship for the curl of a curl, plus the condition that in free space  $\nabla \cdot \mathbf{E} = 0$ , as seen in equation (7), we get to the three-dimensional wave equation:

$$\nabla^2 \mathbf{E} = \mu_0 \epsilon_0 \frac{\delta^2 \mathbf{E}}{\delta t^2} \quad (11)$$

This can also be written in one dimension with a velocity term in its generalised form of:

$$\frac{\delta^2 f}{\delta x^2} = \frac{1}{v^2} \frac{\delta^2 f}{\delta t^2} \quad (12)$$

Whereby  $f$  is the scalar wave amplitude and  $v$  is the velocity of the wave, which in a vacuum is the speed of light ( $c$ ):

$$c = \frac{1}{\sqrt{\epsilon_0 \mu_0}} = 299,792,458 \text{ m/s} \quad (13)$$

In medium other than a vacuum, the velocity of the wave is related to the permittivity and permeability ( $\epsilon$ ,  $\mu$ ) of that medium. Comparing these velocities to the speed of light then gives rise to the dimensionless quantity of the refractive index ( $n$ ):

$$n = \frac{c}{v} \quad (14)$$

The velocity can further be related to the wavelength ( $\lambda$ ) and frequency ( $\nu$ ) of the wave via:

$$c = \lambda \nu \quad (15)$$

Alternatively, the electromagnetic wave can also be viewed using quantum mechanics as a packet of energy called a photon. The energy of these photons is quantised based upon the equation:

$$\text{Energy} = h\nu \quad (16)$$

Where  $h$  is Planck's constant equal to  $6.626 \times 10^{-34} \text{ m}^2\text{kg/s}$ . This means that by these relationships the electromagnetic spectrum can be based upon either the wavelength, frequency, or energy, often measured in units of electron-volts (eV).

### 2.1.2 Permittivity

At the heart of understanding how electromagnetic waves interact with matter is the idea of permittivity. This represents how difficult it is to establish an electric field within a medium. Generally the permittivity of a dielectric material can be predicted based upon the work of

Hendrik Lorentz towards the end of the 19<sup>th</sup> Century in the Lorentz Classical Oscillator Model <sup>(32)</sup>. Here Lorentz described the interaction between atoms and electric fields by relating the electron cloud to a mass on a spring. When the atom is polarised by an electric field, it becomes equivalent to stretching the spring. When released this sets off an oscillating motion of the electron cloud with damping forces acting to decay the oscillation and restoring forces according to Hooke's Law.

This model uses a simple equation of motion for an electron as shown below whereby the first term represents the acceleration; the second term is the damping losses, and the third term is the restoring force. These are balanced by the driving force of an electric field:

$$m \frac{\partial^2 \mathbf{r}}{\partial t^2} + m\Gamma \frac{\delta \mathbf{r}}{\delta t} + m\omega_0^2 \mathbf{r} = -q\mathbf{E} \quad (17)$$

Where  $m$  is the mass of an electron,  $\mathbf{r}$  is the displacement of the electron,  $\Gamma$  is the damping rate,  $\omega_0$  is the natural resonant frequency and  $q$  is the charge. Performing a Fourier transform and rearranging for the displacement ( $\mathbf{r}$ ) then gives the following, where  $\omega$  is the angular frequency:

$$\mathbf{r}(\omega) = -\frac{q}{m} \frac{\mathbf{E}(\omega)}{\omega_0^2 - \omega^2 - j\omega\Gamma} \quad (18)$$

The definition of a dipole moment ( $\mathbf{p}$ ) is the charge multiplied by the distance it is displaced, i.e.  $\mathbf{p}(\omega) = -q\mathbf{r}(\omega)$ . This can then be substituted into equation (18) to give:

$$\mathbf{p}(\omega) = \frac{q^2}{m} \frac{\mathbf{E}(\omega)}{\omega_0^2 - \omega^2 - j\omega\Gamma} \quad (19)$$

Now considering each atom in a material has its own dipole moment, it is useful to instead define the polarisation ( $\mathbf{P}$ ) of the material per unit volume. This becomes the summation of all the individual dipole moments divided by the volume. A macroscopic viewpoint is taken

for this whereby a statistical approach is used to approximate the average polarisation of the material, where  $N$  is the number of atoms per unit volume.

$$\mathbf{P}(\omega) = N\mathbf{p}(\omega) \quad (20)$$

Alternatively, we can also define the polarisation using a term called the susceptibility ( $\chi$ ). This relates how easily a material will have its electrons displaced under the presence of an electric field:

$$\mathbf{P}(\omega) = \epsilon_0\chi\mathbf{E} \quad (21)$$

Combining equations (20) and (21), followed by substituting in equation (19) then gives us the equation for the susceptibility of the dielectric material:

$$\chi(\omega) = \frac{\omega_p^2}{\omega_0^2 - \omega^2 - j\omega\Gamma} \quad (22)$$

Here the term ( $\omega_p$ ) is known as the plasma frequency and defines the frequency at which a materials plasma naturally oscillates around the heavy nucleus of the atom, determined as shown below:

$$\omega_p^2 = \frac{Nq^2}{\epsilon_0 m} \quad (23)$$

As a final step, the relative permittivity ( $\tilde{\epsilon}_r$ ) of the material may now be determined due to the relationship that it is equal to one plus the materials susceptibility:

$$\tilde{\epsilon}_r(\omega) = 1 + \frac{\omega_p^2}{\omega_0^2 - \omega^2 - j\omega\Gamma} \quad (24)$$

The relative permittivity is the permittivity of the material compared to that of free space and is a complex number having both real ( $\epsilon_r'$ ) and imaginary parts ( $\epsilon_r''$ ), where in general the imaginary part accounts for loss. In addition, it is clear to see that the relative permittivity varies with frequency. To determine the real and imaginary parts of the complex permittivity, the following equations may be used:

$$\epsilon_r'(\omega) = 1 + \omega_p^2 \frac{\omega_0^2 - \omega^2}{(\omega_0^2 - \omega^2)^2 + \omega^2 \Gamma^2} \quad (25)$$

$$\epsilon_r''(\omega) = \omega_p^2 \frac{\omega \Gamma}{(\omega_0^2 - \omega^2)^2 + \omega^2 \Gamma^2} \quad (26)$$

Unfortunately for metals, the Lorentz Classical Oscillator Model by itself is not sufficient to explain their optical properties and needs to be expanded. This is due to metals not having their electrons bound to the heavy nucleus of the atoms, therefore meaning there is no restoring force (i.e.  $\omega_0 = 0$ ). This instead leads to what is known as the Drude model for metals<sup>(33)</sup>, leading to a complex relative permittivity of:

$$\tilde{\epsilon}_r(\omega) = 1 - \frac{\omega_p^2}{\omega^2 - j\omega\Gamma} \quad (27)$$

To improve upon the accuracy of this it is possible to include the frequency dependent contributions from interband transitions. This is done by combining the Drude and the Lorentz equations, forming the Drude-Lorentz Model as seen below:

$$\tilde{\epsilon}_r(\omega) = \tilde{\epsilon}_r(\infty) - \frac{\omega_p^2}{\omega^2 + j\Gamma\omega} - \sum \frac{f_n \omega_n^2}{\omega^2 - \omega_n^2 + j\Gamma_n \omega} \quad (28)$$

Although materials can have only one plasma frequency, they may have multiple resonances. These are each of different strength related to each other by the factor  $f$  known as the oscillator strength. These resonances can then be summed up to the desired number of resonances you want to account for. In addition, the  $\epsilon(\infty)$  term is brought in to account for the static dielectric constant at an infinite frequency thereby representing the resonances above what is summed.

The complex permittivity determined above may also be linked to the complex refractive index ( $\tilde{n} = n + ik$ ), where the real part of the refractive index  $n(\omega)$  controls the dispersion in the medium, and the imaginary part  $k(\omega)$ , also known as the extinction coefficient, dictates the absorption. They are related via the formulas:

$$n = \sqrt{\frac{\sqrt{\epsilon'^2 + \epsilon''^2} + \epsilon'}{2}} \quad (29)$$

$$k = \frac{\epsilon''}{2n} \quad (30)$$

### 2.1.3 Absorption, Scattering, and Transmission

When an electromagnetic wave is impinged on a medium, one of three outcomes are possible. The radiation energy is either absorbed by the species, reflected away, or transmitted through it. If absorption occurs, the electromagnetic energy is converted to another form, typically heat, and the incident light never emerges from the species. In contrast, with transmission of the light, the incident radiation passes straight through the material and out the other side. Lastly, with reflection the incident wave is re-emitted from the substance. If the reflected beam displays the same angle as the incident beam relative to the normal of the surface, it is known as specular reflection, whereas if it reflects in all directions it is known as diffuse reflection or scattering.

Considering the above, the amount of light that interacts with a particle is equal to the incident light minus the light that is transmitted straight through the sample. The amounts of these may be found using the Beer Lambert law <sup>(34)</sup> as shown below:

$$A = -\log(T) = -\log\left(\frac{I}{I_0}\right) \quad (31)$$

Where the absorbance ( $A$ ) is the attenuation of the radiation by both absorption and scattering events,  $T$  is the transmittance, and  $I/I_0$  is the transmitted radiation over the incident radiation. The attenuation is also commonly referred to as the extinction of the beam. One useful way of representing the probability of extinction is the extinction cross section ( $\sigma_{\text{ext}}$ ) with units of area. Essentially this takes into account the geometric dependence and material properties of

a substance with regard to its probability to scatter or absorb radiation. This extinction cross section is made up from the summation of the absorption ( $\sigma_{\text{abs}}$ ) and scattering cross sections ( $\sigma_{\text{sca}}$ ) as follows:

$$\sigma_{\text{abs}} + \sigma_{\text{sca}} = \sigma_{\text{ext}} \quad (32)$$

Interestingly, the optical cross sections above may actually have areas larger than their geometric cross section, as is the case with plasmonic nanoparticles. For this reason it is often useful to refer to the cross sections instead as efficiencies whereby the optical cross section is divided by the geometric cross section:

$$\sigma_{\text{abs, eff}} = \sigma_{\text{abs}} / \sigma_{\text{geom}} \quad (33)$$

$$\sigma_{\text{sca, eff}} = \sigma_{\text{sca}} / \sigma_{\text{geom}} \quad (34)$$

$$\sigma_{\text{ext, eff}} = \sigma_{\text{ext}} / \sigma_{\text{geom}} \quad (35)$$

## 2.2 Mie Theory and Nanoscale Optics

In 1908, Gustav Mie used the knowledge gained from both Maxwell's equations and Lorentz theory to derive the light scattering and absorption from a sphere. This was achieved by directly solving Maxwell's equations to produce spectra for gold nanoparticles, and in doing so, predict the size-dependent colour variations seen in gold colloids <sup>(59)</sup>.

When first developed, Mie theory had a number of limitations towards its use. For instance, it was only applicable to the scattering and absorption of plane waves by a homogeneous isotropic spherical particle in a non-absorbing embedding medium. However, unlike Rayleigh scattering theory before it, whereby only small dielectric spherical particles much smaller than the wavelength of light were applicable, Mie theory could be applied to particles of any size and be composed of absorbing or non-absorbing materials. This gave it great practical application from nanoparticles, up to the order of millimetre scales for atmospheric chemistry <sup>(59, 60)</sup>.

The use of Mie theory and the mathematics behind it requires an in-depth and time consuming explanation, and therefore only the basics and the results are discussed here. Additional description of the procedure however can be read in several textbooks <sup>(59, 61)</sup>. Mie theory operates by calculating the electromagnetic field within the particle and within the medium it is embedded in. It stands to reason that to do this the permittivity of the materials is of critical importance. The solution requires the incident and scattered field to be expanded for each polarisation into spherical harmonic functions. The boundary conditions around the particle then need to be accounted for by ensuring the tangential components of the fields are continuous and finite at large distances. This is particularly challenging as it results in four equations where an infinite sum is present <sup>(59)</sup>.

Although developed in 1908, only recently has the true value of Mie theory been harnessed due to the increases in computational power allowing solutions to be calculated relatively quickly <sup>(35)</sup>. On the other hand, by making a few assumptions the absorption and scattering cross sections based upon Mie theory may be easily calculated. The assumptions made are that firstly a quasi-static approach is taken whereby the particle is said to be much smaller than the wavelength of light incident upon it, thereby allowing the electric field to be considered static. Secondly, we assume the sphere is isotropic and homogeneous, and that the medium it is embedded in is also isotropic and non-absorbing. This leads to the following equations for the absorption and scattering cross sections:

$$\sigma_{\text{abs}} \approx \sigma_{\text{ext}} = 4\pi k R^3 \text{Im} \left( \frac{\epsilon_p - \epsilon_m}{\epsilon_p + 2\epsilon_m} \right) \quad (36)$$

$$\sigma_{\text{scat}} = 8\pi k^4 R^6 \left| \frac{\epsilon_p - \epsilon_m}{\epsilon_p + 2\epsilon_m} \right|^2 \quad (37)$$

In the above equations,  $k$  is the wave number,  $R$  is the sphere radius, and  $\epsilon_p$  and  $\epsilon_m$  refer to the permittivity of the particle and medium respectively. It can be seen that the absorption scales with  $R^3$  whereas the scattering scales with  $R^6$ . This therefore shows how at small sizes the absorption dominates allowing the absorption and extinction cross sections to approximated equal, however at larger sizes, the scattering becomes prominent. Although these equations are only theoretically true for vanishingly small particles, it has been found to provide good approximations for dimensions below that of around 100nm. For dimensions above this, a rigorous solution using the full Mie Theory must be used <sup>(36)</sup>. Another important

aspect to take from the above equations is how the maximum of both the absorption and scattering cross sections occurs as the denominator reaches a minimum. In a vacuum this is therefore at a wavelength when the real part of the metals permittivity is equal to negative two i.e.  $\epsilon_p' = -2$ . Alternatively, for particles in other media, this becomes  $\frac{\epsilon_p'}{\epsilon_m} = -2$ .

One major limitation with the original Mie theory was the inability to alter the geometry of the particle from something other than a perfect sphere. In real life situations however, particles are generally not perfectly symmetrical and therefore extension of Mie theory was necessary. This came in 1912 by Richard Gans<sup>(37)</sup> whereby the solution was altered to account for prolate and oblate spheroids. Since then, further extensions have also been added to account for the addition of coated spheres<sup>(38)</sup>, inhomogeneous media such as supporting substrates<sup>(39)</sup>, and lastly charged particles<sup>(40)</sup>. Despite this, to determine the absorption and scattering from more complicated geometries and environments, modelling by numerical methods is often deemed necessary. These techniques will be discussed in more detail in Chapter 5.

In addition to Mie Theory, a brief explanation of some nanoscale optical theories, specifically focussing on the diffraction limit and the confinement of electromagnetic waves, is now discussed. The diffraction limit refers to the principle that an electromagnetic wave cannot be localised to a distance less than around half its vacuum wavelength due to diffraction of the wave<sup>(41)</sup>. This has consequences for optical microscopy whereby the resolution of the microscope is limited to this value. Similarly it also has negative effects for techniques which harness electromagnetic waves for carrying information instead of the more traditional electron signals<sup>(20)</sup>. This latter application is of particular importance due to us quickly approaching the limit for the speed and amount of data which electronic signals may carry<sup>(20, 41)</sup>. Electromagnetic waves on the other hand are capable of carrying much more information with less loss, for instance in fibre optic cables. The diffraction limit however limits the miniaturisation of this technology and deters its deployment into integrated circuits.

Fortunately however, new methods are realising ways in which we may beat the diffraction limit and localise the light to dimensions much smaller than its wavelength. One such method is by using materials with a negative permittivity, as is the case for certain metals such as gold and silver in the visible spectrum. At these frequencies the electrons of the metal experience a resonance whereby their conduction electrons collectively oscillate and are bound to the

surface between the metal and a dielectric, known as a surface plasmon resonance. These surface plasmon resonances may be split into two categories; surface plasmon polaritons (SPPs), and localised surface plasmon resonances (LSPRs). The former is related to a plasmonic resonance that propagates along a metal dielectric interface and therefore is particularly interesting for optical waveguides, whereas the latter occurs for nanoparticles that are much smaller than the wavelength of the incident light. Only LSPRs are considered within this work due to their ability to increase the optical cross sections, and greatly enhance the electric field strengths surrounding the nanoparticle, however details of SPPs are addressed in the following work <sup>(36, 42-44)</sup>.

## 2.3 Localised Surface Plasmon Resonances

LSPRs may occur when a metal nanoparticle is much smaller than the wavelength of incident light. At the resonant frequency, the conduction electrons collectively oscillate around the nanoparticle, driven by the incident oscillating electromagnetic field, as seen in Figure 2.1.

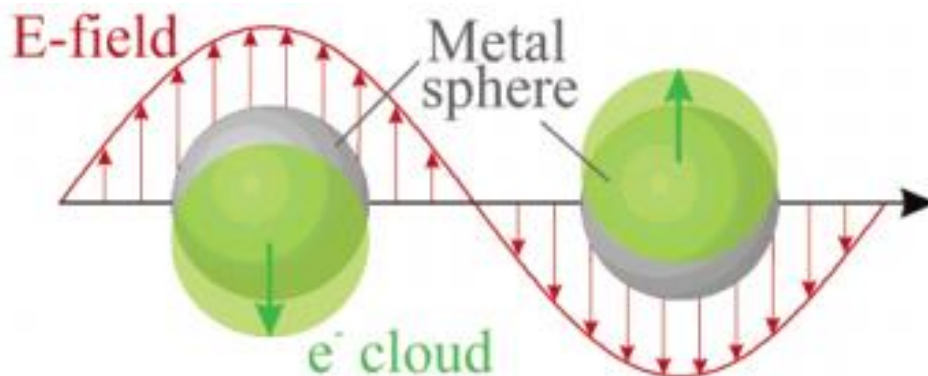


**Figure 2.1: Diagram of a localised surface plasmon resonance (LSPR) of a sphere where the conduction electrons couple to the oscillating E-field <sup>(45)</sup>.**

Considering the nanoparticles size ( $D$ ) is considerably less than that of the wavelength of light in the surrounding medium (i.e.  $D \ll \lambda$ ) then the quasi-static approximation may be assumed whereby the oscillating electromagnetic field is taken as constant over the particle volume and therefore the field is considered electrostatic <sup>(36)</sup>. Based on this assumption, a simple example will be shown below as outlined by Maier <sup>(36)</sup>. Firstly a homogenous, isotropic sphere with radius  $a$ , and dielectric function  $\epsilon(\omega)$  situated in an isotropic, non-absorbing medium with dielectric constant  $\epsilon_m$  is assumed. As the sphere dimensions are significantly less than the wavelength of incident light, a static electric field  $\mathbf{E} = E_0 \hat{z}$  can be assigned in the  $z$ -direction, as seen in Figure 2.2:

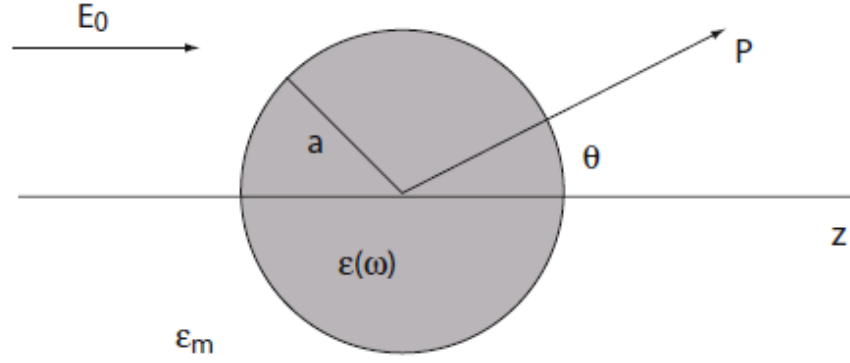


**Figure 2.2: Schematic of homogenous sphere of radius  $a$ , located in a isotropic non-absorbing medium and in the presence of an electrostatic field <sup>(36)</sup>.**

Due to the problem being an electrostatic one, a solution to the Laplace equation for the potential  $\nabla^2\Phi = 0$  needs to be found in order to calculate the electric field  $\mathbf{E} = -\nabla\Phi$ . As the system has azimuthal symmetry, according to Jackson <sup>(46)</sup>, the general solution is:

$$\Phi(\mathbf{r}, \theta) = \sum_{l=0}^{\infty} [A_l r^l + B_l r^{-(l+1)}] P_l(\cos \theta) \quad (38)$$

Here the angle  $\theta$ , as seen in Figure 2.2 is that between the position vector  $\mathbf{r}$  at point P and the z-axis. In addition,  $P_l(\cos\theta)$  are the Legendre Polynomials of order  $l$ . Following this, the solution of the potentials both inside  $\Phi_{in}$  and outside  $\Phi_{out}$  of the sphere can be expressed as seen below due to the fact that the potentials must remain finite at the origin:

$$\Phi_{in}(\mathbf{r}, \theta) = \sum_{l=0}^{\infty} A_l r^l P_l(\cos \theta) \quad (39)$$

$$\Phi_{out}(\mathbf{r}, \theta) = \sum_{l=0}^{\infty} [B_l r^l + C_l r^{-(l+1)}] P_l(\cos \theta) \quad (40)$$

The deduction of the coefficients  $A_l$ ,  $B_l$  and  $C_l$  can now be achieved from the boundary conditions at the surface of the sphere ( $r = a$ ) and at  $r \rightarrow \infty$ . Equality of the tangential components of the electric field demands that:

$$-\frac{1}{a} \frac{\delta\Phi_{\text{in}}}{\delta r} \Big|_{r=a} = -\frac{1}{a} \frac{\delta\Phi_{\text{out}}}{\delta\theta} \Big|_{r=a} \quad (41)$$

whereas the equality of the normal components of the displacement field gives:

$$-\varepsilon_0 \varepsilon \frac{\delta\Phi_{\text{in}}}{\delta r} \Big|_{r=a} = -\varepsilon_0 \varepsilon_m \frac{\delta\Phi_{\text{out}}}{\delta r} \Big|_{r=a} \quad (42)$$

With the boundary conditions the potentials become:

$$\Phi_{\text{in}} = -\frac{3\varepsilon_m}{\varepsilon + 2\varepsilon_m} E_0 r \cos\theta \quad (43)$$

$$\Phi_{\text{out}} = -E_0 r \cos\theta + \frac{\varepsilon - \varepsilon_m}{\varepsilon + 2\varepsilon_m} E_0 a^3 \frac{\cos\theta}{r^2} \quad (44)$$

Physically, equation (44) represents the superposition of the applied field  $E_0$  and the dipole field located at the centre of the sphere. Introducing this dipole moment,  $\mathbf{p}$  into the above gives:

$$\Phi_{\text{out}} = -E_0 r \cos\theta + \frac{\mathbf{p} \cdot \mathbf{r}}{4\pi\varepsilon_0\varepsilon_m r^3} \quad (45)$$

where the dipole moment is:

$$\mathbf{p} = 4\pi a^3 \varepsilon_0 \varepsilon_m \frac{\varepsilon - \varepsilon_m}{\varepsilon + 2\varepsilon_m} \mathbf{E}_0 \quad (46)$$

These equations signify that by applying an electric field, a dipole moment is induced within the sphere with its magnitude proportional to  $|\mathbf{E}_0|$ . If we now replace the dipole moment by its polarisability  $\alpha$ , defined as the ease at which a material may become polarised and related via  $\mathbf{p} = \varepsilon_0 \varepsilon_m \alpha \mathbf{E}_0$ , equation (46) becomes:

$$\alpha = 4\pi a^3 \frac{\epsilon - \epsilon_m}{\epsilon + 2\epsilon_m} \quad (47)$$

Studying this equation it is clear to see that as the denominator reaches a minimum, the polarisability obtains a resonant enhancement. Therefore, for a small or slowly varying imaginary permittivity, ( $\epsilon''(\omega)$ ) this simplifies to instead occur when:

$$\epsilon'(\omega) = -2\epsilon_m \quad (48)$$

Known as the Fröhlich condition, this important equation governs at what frequency the resonance occurs. For example, assuming the particle has a permittivity described by the Drude model (see equation (27)) with negligible damping, the Fröhlich condition is met when:

$$2\epsilon_m = -1 + \frac{\omega_p^2}{\omega^2} \quad (49)$$

Which if located within a vacuum is satisfied when:

$$\omega = \frac{\omega_p^2}{\sqrt{3}} \quad (50)$$

From these equations it is therefore possible to see how the frequency at which the resonance condition occurs is strongly dependant on the surrounding mediums dielectric constant. This strong dependence and ability to control the resonance is particularly useful for a number of applications and is covered in more detail in the following section.

Additionally, the electric field distribution both in and outside the sphere may be determined by:

$$\mathbf{E}_{in} = \frac{3\epsilon_m}{\epsilon + 2\epsilon_m} \mathbf{E}_0 \quad (51)$$

$$\mathbf{E}_{\text{out}} = \mathbf{E}_0 + \frac{3\mathbf{n}(\mathbf{n} \cdot \mathbf{p}) - \mathbf{p}}{4\pi\epsilon_0\epsilon_m} \frac{1}{r^3} \quad (52)$$

where  $\mathbf{n}$  is the unit vector in direction of point P. As can be seen in these equations, at resonance conditions both the internal and external electric fields achieve an enhancement. It is this enhancement that also proves particularly useful in plasmonic applications such as in the production of charge carriers in adjacent semiconductors, or large field strengths for SERS <sup>(47)</sup>.

So far the theory behind surface plasmon resonances has been discussed in terms of solving Maxwell's Equations and using Mie Theory. This approach is generally restricted to simple situations, such as for small spheres in a homogeneous medium, however several developments to the theory have been performed to approximate for complexities such as changes to the shape of the particle or inhomogeneous environments. Despite this, the vast majority of the work has been experimentally derived, and therefore requires a literature review covering the findings.

As our work focusses on the use of nanorod arrays coated in a semiconductor, there are many complex factors involved that influence the resonance wavelength, optical cross sections, and field enhancements. This includes the effects of their surrounding medium, including how the presence of a semiconductor shell may alter their response. Additionally, their size, material and geometry also dictates the plasmonic properties of the particle. Lastly, as the nanorod arrays are supported on a substrate and have small separation distances between each rod, the effects of both particle-substrate coupling and particle-particle coupling may also be prominent.

The following sections will address both adaptations to the theory and review the findings from experimental work focussing on the above factors. This will highlight the interesting and unique features of plasmonic resonances and show how with careful fabrication, the properties may be tuned for use in applications.

## 2.4 Effect of Nanoparticle Environment

### 2.4.1 Effect of Homogeneous Medium

It has been shown in the previous section that the environment in which the particle is situated is of critical importance to the wavelength at which the plasmonic resonance occurs, commonly referred to as  $\lambda_{\text{max}}$ . To recap, in order to sustain a plasmonic resonance whereby the electromagnetic waves are confined to the surface, the particle must be a conductive one with free conduction electrons that are able to oscillate, plus also have a negative real part of its complex dielectric function. In contrast, for the dielectric constant of the surrounding medium, its value must be positive as is the case for typical dielectrics such as air or water. Although plasmon resonances can occur if both these conditions are met, particular interest is focused around noble metals nanoparticles such as Au, Ag and Cu due to their resonances typically being present within the visible spectrum. As a reminder, this wavelength dependence is reliant on the condition that the real part of the particles dielectric function is equal to negative two times the dielectric constant of the medium:

$$\varepsilon'(\omega) = -2\varepsilon_m \quad (48)$$

Considering this, by altering the dielectric environment the particle is surrounded by you may tune the peak resonance condition. With an increase in relative permittivity a red shift is acquired, whereas oppositely a blue shift is achieved with decreasing relative permittivity of the medium. Building upon this theory, the difference in permittivity between the surrounding medium and the particle  $\varepsilon_p - \varepsilon_m$ , known as the optical contrast, also plays an important role not only in defining the resonant wavelength, but also on its magnitude. For instance, as the medium's dielectric constant increases, the resonance is known to red-shift to longer wavelengths and the magnitude is drastically increased <sup>(48)</sup>.

This theory was supported with experimental work by Underwood and Mulvaney <sup>(49)</sup> who placed gold colloids in solvents with varying refractive index and measured both a red-shift and an increase in magnitude with the higher refractive index solvents. A change in colour of the solution from red to purple was seen, as shown in Figure 2.3. In addition, the theoretical  $\lambda_{\text{max}}$  values matched very well with the experimental ones, with any error attributed mainly to the accuracy of the data of the metals permittivity.

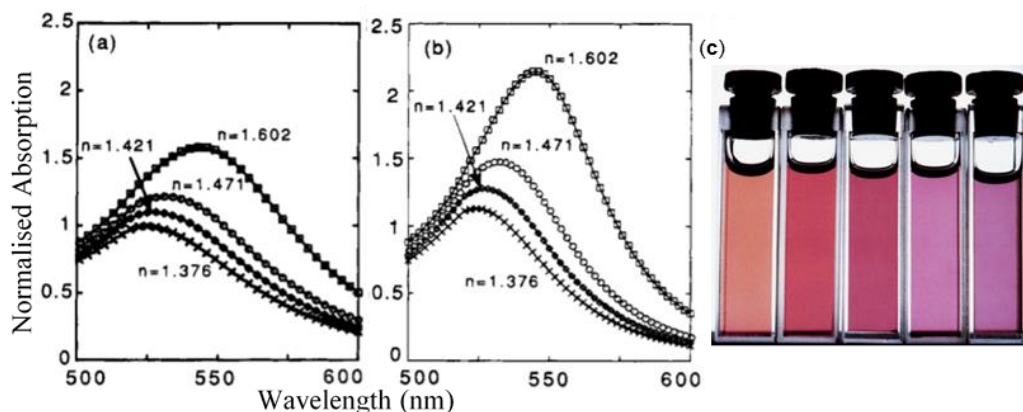


**Figure 2.3:** a) Calculated absorption spectra of gold colloids with 8.0 nm radius and changing refractive index, b) UV-Vis spectra of gold colloids with refractive index, c) Changing colour of gold colloids with increasing refractive index of solvent from left to right. Adapted from ref <sup>(49)</sup>.

## 2.4.2 Effect of Dielectric Shell

In real life conditions, a nanoparticle will often quickly gain a thin layer on its surface from either condensation of gaseous products or from natural oxidation. Similarly, nanoparticles may often have thin layers, such as that of surfactants or semiconductors, added to stop agglomeration or utilise the high absorption and strong electric fields surrounding the particle respectively. As the environment has shown to be important with regards to both the resonant position and its amplitude, these thin layers must be accounted for.

There are a number of possible core-shell particle arrangements depending not only on the material of the core and shell, but also on the number of shell layers and their relative thicknesses. Although Mie Theory is able to solve for these many arrangements, here we will only discuss with regards to a single dielectric layer on the surface of a metallic nanoparticle, as is the focus of this work.

Consider a geometry whereby a spherical core of radius  $R$  and permittivity  $\epsilon_c$  is surrounded by a single shell of thickness  $d$  and permittivity  $\epsilon_{sh}$ , which itself is surrounded by a homogeneous medium of permittivity  $\epsilon_m$ . It can be shown through an extension of Mie Theory that this core-shell nanoparticle, if small compared to the wavelength, has an extinction cross section equal to <sup>(48)</sup>:

$$\sigma_{\text{ext}}(\lambda, R, d) = \frac{8\pi^2(R+d)^3\sqrt{\epsilon_m}}{3\lambda} \text{Im} \left[ \frac{(\epsilon_{\text{sh}} - \epsilon_m)(\epsilon_c - 2\epsilon_{\text{sh}}) + \left(\frac{R}{R+d}\right)^3 (\epsilon_c - \epsilon_{\text{sh}})(\epsilon_m - 2\epsilon_{\text{sh}})}{(\epsilon_c + 2\epsilon_{\text{sh}})(\epsilon_{\text{sh}} + 2\epsilon_m) + 2\left(\frac{R}{R+d}\right)^3 (\epsilon_c - \epsilon_{\text{sh}})(\epsilon_{\text{sh}} - 2\epsilon_m)} \right] \quad (53)$$

A resonance is achieved when the denominator in equation (53) is zero. It can be seen that for a metallic core,  $\epsilon_c$ , with a dielectric shell,  $\epsilon_{\text{sh}}$ , this occurs when <sup>(48, 50)</sup>:

$$\epsilon_c = -2\epsilon_{\text{sh}} \frac{(\epsilon_{\text{sh}} + 2\epsilon_m) - \left(\frac{R}{R+d}\right)^3 (\epsilon_{\text{sh}} - \epsilon_m)}{(\epsilon_{\text{sh}} + 2\epsilon_m) + 2\left(\frac{R}{R+d}\right)^3 (\epsilon_{\text{sh}} - \epsilon_m)} \quad (54)$$

Applying limiting conditions to the above equation, it can be determined that for the case of a vanishingly small shell thickness ( $d \rightarrow 0$ ), the resonance occurs in the same manner as that for a sphere in a homogeneous environment,  $\epsilon_c = -2\epsilon_m$ . Alternatively, for a large shell thickness ( $d \rightarrow \infty$ ), the resonance occurs when:

$$\epsilon_c = -2\epsilon_{\text{sh}} \quad (55)$$

This latter limiting case is never fully valid as with a large increase in the shell thickness, the particle is no longer small compared to the wavelength and therefore the quasi-static approximation on which this equation was derived, no longer holds. Despite this, it can be hypothesised that as the thickness of the shell increases, its contribution to the resonance position also increases compared with the contribution from the surrounding medium. In addition, it is also noteworthy mentioning that unlike for the surrounding medium which has to have a real valued permittivity, the shell may instead have a complex valued permittivity meaning absorption within the shell is possible. Assuming a core metal whose permittivity may be described by the Drude model, as shown in equation (27), the resonance position becomes <sup>(51)</sup>:

$$\frac{\lambda^2}{\lambda_p^2} = \epsilon_\infty + \frac{2(1-h)\epsilon_{\text{sh}}(\epsilon_{\text{sh}} - \epsilon_m) + 6\epsilon_{\text{sh}}\epsilon_m}{3\epsilon_{\text{sh}} - 2(1-h)(\epsilon_{\text{sh}} - \epsilon_m)} \quad (56)$$

Here  $\lambda_p$  is the plasma wavelength of the metal,  $\epsilon_\infty$  is high frequency permittivity of gold and  $h$  represents the volume fraction of the shell,  $h = 1 - (R/R + d)^3$ . Equation (56) shows that if the permittivity of the shell is greater than that of the medium, a red-shift will be found with increasing shell thickness.

Calculating the extinction cross section for a silver nanoparticle with a diameter of 50 nm and SiO<sub>2</sub> shell of varying thicknesses, as seen in Figure 2.4, shows how important the thickness of the shell is on the resonance position. In fact, the sensitivity is such that even a 1 nm SiO<sub>2</sub> layer can cause a red-shift in the resonant position. This red-shift continues with increasing thickness of the shell, until eventually it matches the resonant position of the silver sphere completely embedded in silica.

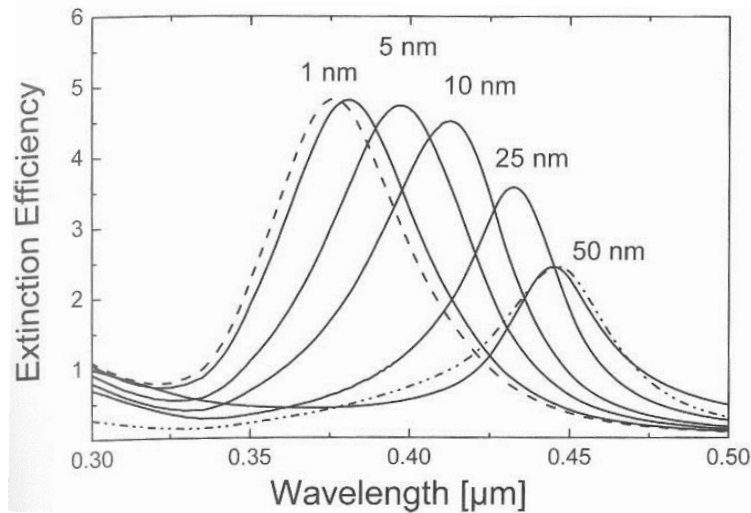


**Figure 2.4:** Calculated Extinction efficiency of a 50 nm silver sphere with a SiO<sub>2</sub> shell varying in thickness from 1 nm to 50 nm. The dashed line and the double dotted dashed line represent an uncoated sphere and a sphere fully embedded in SiO<sub>2</sub> respectively, the latter spectrum has been divided by 5.1 for comparison <sup>(48)</sup>.

In addition to the red-shift, a decrease in amplitude of the extinction efficiency is seen as the shell thickness increases. Based upon the concept of optical contrast, you would expect the SiO<sub>2</sub> shell to give an enhancement of the extinction due to a greater difference in the permittivity of the shell and core. The added thickness of the shell however, along with the fact that it doesn't contribute to the plasmon resonance, means the geometrical cross section is increased relative to the increased extinction cross section, thereby giving a decrease in amplitude of its efficiency.

The experimental results from Du et. al <sup>(52)</sup> support the above red-shift with shell thickness as seen in Figure 2.5a. By using a sol-gel method they were able to grow controlled shells of TiO<sub>2</sub> on silver nanoprisms with thickness tuned from 1 to 15 nm. A much greater red-shift however is observed compared those seen in Figure 2.4 for similar sized shells. This is allocated to the higher refractive index of the TiO<sub>2</sub> shell (~2.2) compared with that of a SiO<sub>2</sub> shell (~1.43).

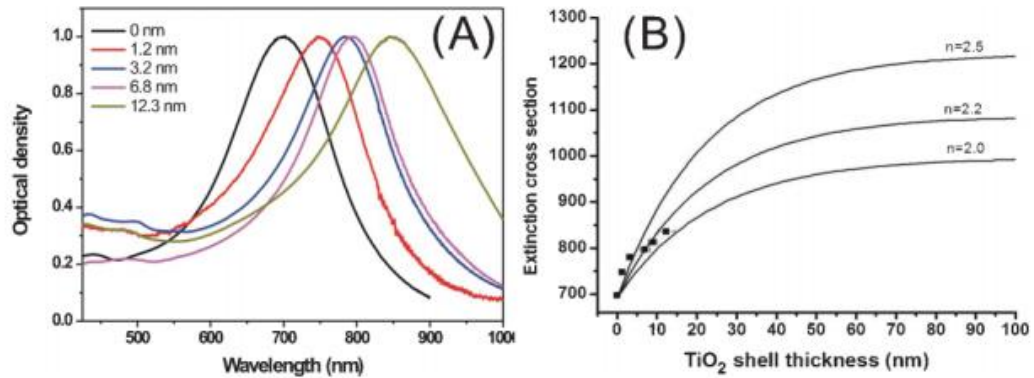


**Figure 2.5:** a) Normalised absorption spectra of Ag@TiO<sub>2</sub> core-shell nanoparticles with varying TiO<sub>2</sub> thickness, b) Simulated resonance position with TiO<sub>2</sub> shell thickness using 3 separate values for the refractive index of the TiO<sub>2</sub>. The squares represent the experimental data from a) <sup>(52)</sup>.

The simulated spectra in Figure 2.5b show that at small shell thicknesses, the red-shift is very sensitive, however as the layer gets larger this sensitivity decreases until almost no change with shell thickness is seen. This matches the theory in that a maximum shift would be seen as the shell thickness gets very large ( $d \rightarrow \infty$ ), as  $\lambda_{\max}$  becomes dependent only on the refractive index of the shell and not on the medium, as in equation (55).

In addition, the experimental results (squares) match reasonably well with the simulated results, however a certain degree of error in the resonance position is noted. The authors attribute this to the variance of sizes and shapes in the samples, as both triangular and spherical nanoparticles are present with different degrees of truncation and eccentricity along the edges. As will be shown later, these changes in geometry can have significant effect on the resonance positions and therefore may alter the accuracy of these results.

Thiele et. al. <sup>(53)</sup> fabricated silver triangular nanoparticles that were coated in SiO<sub>2</sub> for increased stability of the particle. These nanoparticles were synthesised for their application as refractive index sensors, whereby shifts in  $\lambda_{\max}$  could be attributed to changes in the dielectric environment. It was found that at a shell thickness of 83 nm, the particle was less sensitive to the refractive index of the medium than an uncoated particle. This also follows the principle that the red-shift slows with increasing shell thickness. Similarly, Peng et. al. <sup>(51)</sup> also analysed the effect of SiO<sub>2</sub> shells on gold spheres finding that at a thickness of 80 nm, energy transfer across the shell became negligible and the observed red-shift ceased.

We will now turn our attention to the near-field, focusing on the electric field distribution in the core@shell nanoparticles. It has been shown that the electric field surrounding the plasmonic particle is enhanced at the surface and decays exponentially away. Zhang et. al. <sup>(54)</sup> used finite element modelling to assess how the electric field distribution alters for a Au-Ag alloy nanoparticle surrounded by a SiO<sub>2</sub> shell of varying thickness. As seen in Figure 2.6, it was found that at small shell thicknesses the electric field was particularly enhanced around the outside of the shell. As the thickness of the shell increased however, the enhancement became more localised to metal surface and the field strength at the edge of the shell reduced.

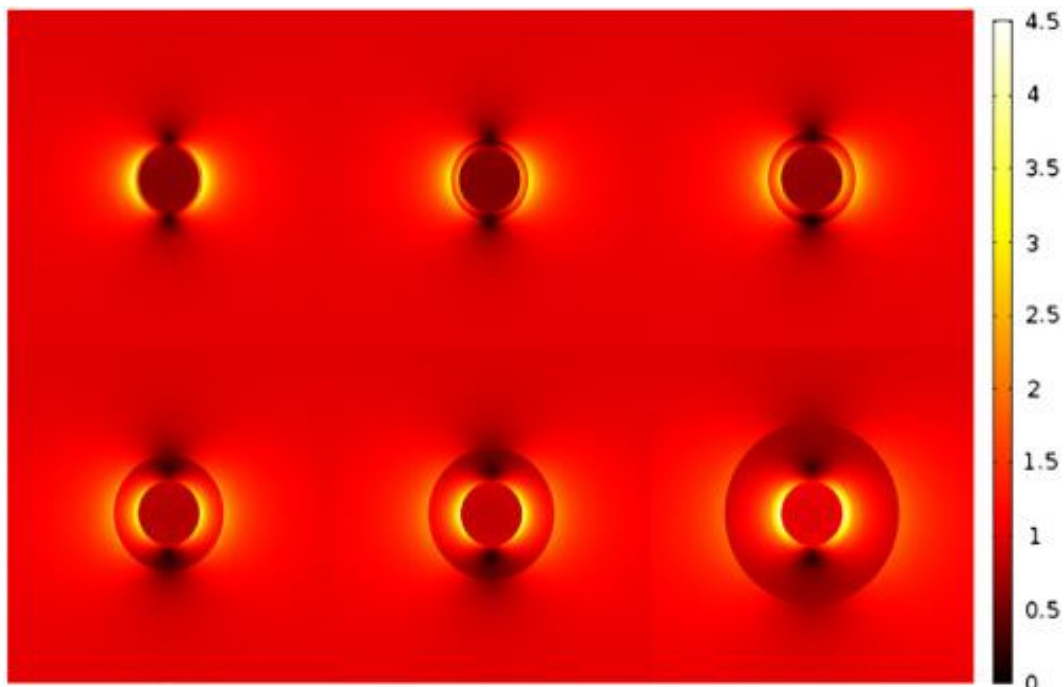


**Figure 2.6: E-Field distribution of a Au-Ag nanoparticle with SiO<sub>2</sub> shell thicknesses of 2, 5, 8, 15, 20 and 35 nm. The colour bar represents the local magnetic field divided by the incident electromagnetic field  $|E/E_0|$  <sup>(54)</sup>.**

Xu et. al. <sup>(55)</sup> also studied the effect of a silica shell of thicknesses of 5, 7 and 10 nm on a gold rod using finite difference time domain modelling as seen in Figure 2.7. Although the authors support the above result in claiming that a thinner shell leads to higher electric field around the outside of silica shell, it is possible to see the field distribution looks dissimilar. Unlike the above, the highest field strengths are consistently localised on the metal surface regardless of the thickness of the shell. The higher fields noted at the shell surface for thin shells may then simply due to the decay length of the plasmon. Considering this contrast in results, it is clear that the field distribution for core@shell particles is complex and may depend on factors other than the thickness of the shell.

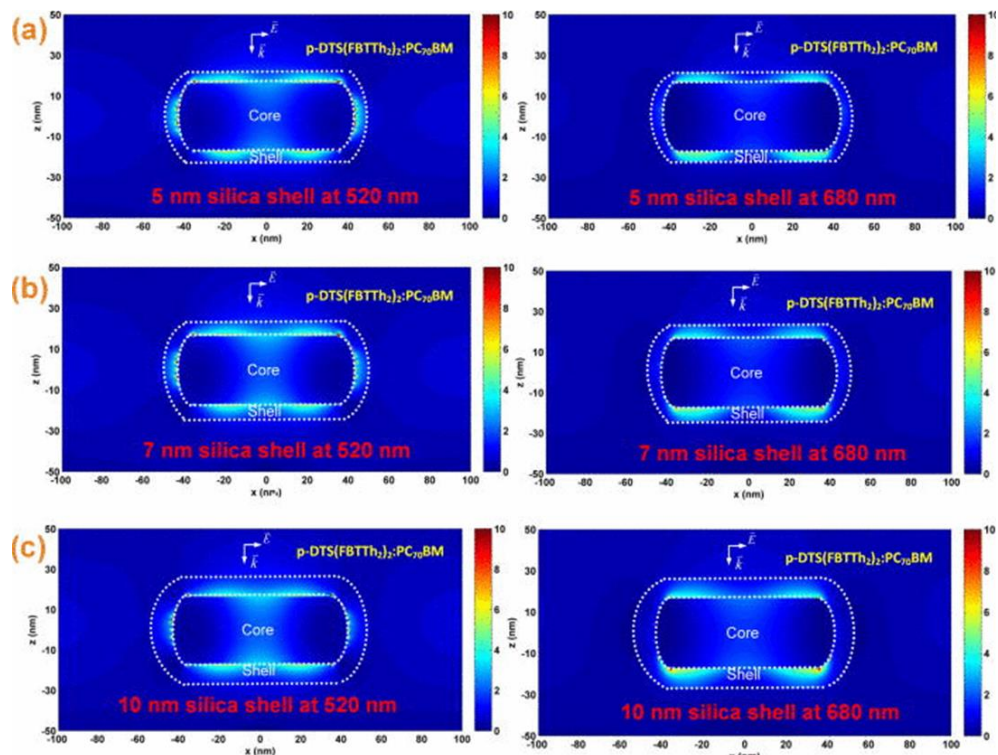
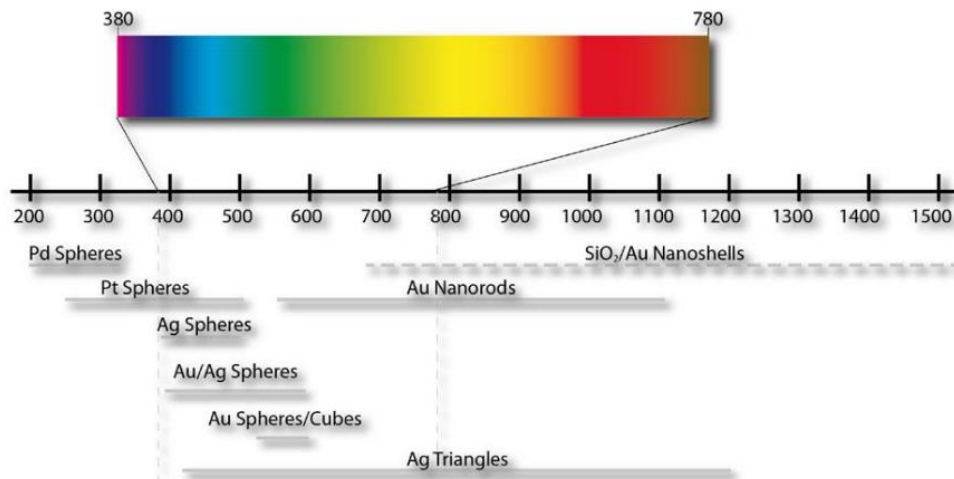


Figure 2.7: Electric field distribution of a Au nanorod with SiO<sub>2</sub> shell of varying thickness at its two resonant wavelengths <sup>(55)</sup>.

## 2.5 Effect of Material and Size

It has already been discussed that a plasmonic resonance can only occur for a metal when its real part of the permittivity is negative. For applications that aim to utilise the abundant visible spectrum of light, this limits the choice of metals that are applicable. The more common plasmonic materials that are applied in the visible region, plus the geometry and wavelength range at which they occur are shown in Figure 2.8. Gold and silver are typically the material of choice as they can be tuned across the entire visible spectrum and even into the NIR.



**Figure 2.8: Spectral range of plasmonic materials and geometries within the visible region** <sup>(53)</sup>

The disadvantage of silver nanoparticles is their surface readily oxidises to form what is essentially a core@shell nanoparticle of Ag@Ag<sub>2</sub>O. As shown in the previous section, this alters the plasmonic response and causes a red-shift, plus it has also been noted to decrease the intensity <sup>(56)</sup>. Gold on the other hand is very stable and does not oxidise making it an excellent choice for plasmonic applications.

Alongside the dielectric environment and material, the size of the plasmonic nanoparticles is also crucial in controlling the SPR. Firstly, as previously mentioned, in order to obtain a plasmonic response on a nanoparticle the dimensions must be significantly smaller than the wavelength of the incident light, which when looking at the visible spectrum, means on the nanoscale.

Firstly, it was shown in section 2.2 that under the quasi-static approximation the optical cross sections resonance position of spheres, and therefore the position of maximum absorption, depends only on the condition that the real part of the permittivity is equal to negative two. This however was only valid for vanishingly small particles. If the quasi-static approximation is dropped and instead the full Mie solution is determined, the results are as shown in Figure 2.9.

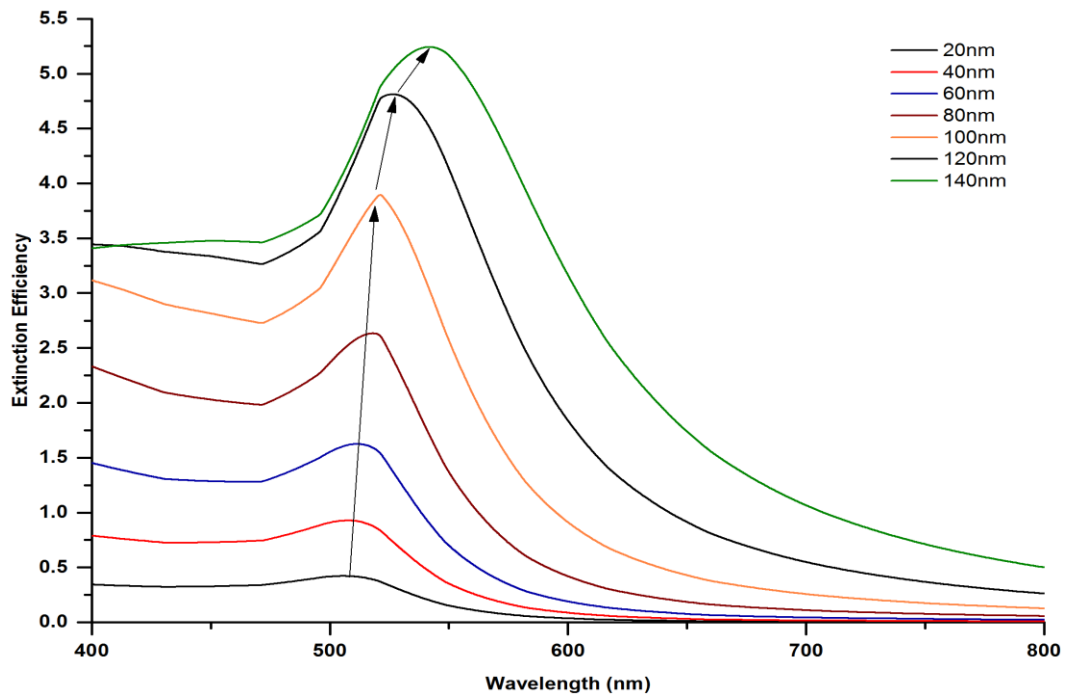


**Figure 2.9: Graph of Mie calculation results for extinction cross section of gold spheres with diameters between 20 nm and 140 nm in a vacuum. The arrows act as a guide for the eye showing the peak red-shift. Calculations were performed using the software MiePlot <sup>(57)</sup>.**

Mie theory predicts that with increasing diameter, the SPR peak red shifts and the peaks broaden. The red shift is negligible for small diameters, whereby the quasi-static approximation is roughly valid, however as the sphere increases in size, this simplification breaks down and larger red-shifts occur. This increase in wavelength with diameter explains the change in colour associated with different sized gold colloid solutions. The red-shift noted may be explained qualitatively as larger particles require the electrons to oscillate over a larger distance resulting in a reduction in the frequency and therefore a shift to longer wavelengths <sup>(58)</sup>. Although for spheres this red shift with diameter is relatively small, it can be much more pronounced for other geometries, such as for nanorods, whereby one dimension is considerably longer than the others. This can be particularly useful for tuning the optical properties over large areas of the spectra as will be discussed in more in the following section.

If we extend our Mie calculations to show the absorption and scattering cross section, as shown in Figure 2.10, plus include the result for a much larger 400 nm diameter sphere, a number of other deductions can be made.

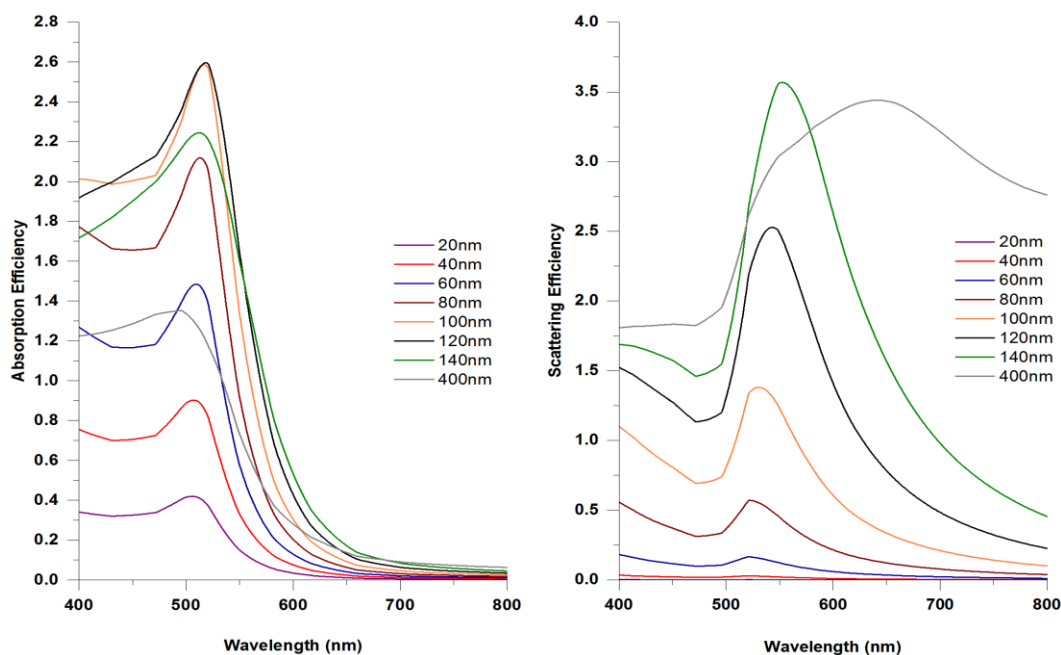


**Figure 2.10: Graph of Mie calculation results for absorption efficiency (left) and scattering efficiency (right) of gold spheres with diameters between 20 nm and 400 nm in a vacuum. Calculations were performed using the software MiePlot <sup>(57)</sup>.**

Firstly it can be seen that a maximum in the absorption efficiency for a sphere in a vacuum is seen at around a diameter of 100-120 nm. An increase in size beyond this causes a reduction in the efficiency and a substantial broadening of the peaks. Similarly the scattering efficiency also broadens with increasing diameter. This can be attributed to both radiative damping and the presence of higher order modes <sup>(30)</sup>.

Radiative damping refers to the process whereby energy is lost due to re-radiation from the particle and therefore coincides with the previously shown relationship from equation (37) that the scattering scales with the radius to the 6<sup>th</sup> power. Alternatively, the higher order modes come about as retardation effects become prominent. For instance, when the particle radius is substantial compared to that of the wavelength, typically quoted as around a tenth of the medium's wavelength, the light is unable to homogeneously polarise the particle causing the creation of additional modes <sup>(59)</sup>. These modes begin at shorter wavelengths and red-shift with increasing size, along with the production of further modes. The presence of one of these modes can be seen in the scattering spectra of the 400 nm sphere in Figure 2.10 at around 500 nm with the original dipole mode red-shifted to around 650 nm. These higher order modes can be allocated a number depending on the order they are produced with a dipole set as  $l=1$ , the quadrupole as  $l=2$ , and increasing thereafter.

Myroshnychenko *et al.* <sup>(30)</sup> used Mie theory to map the presence of these higher order modes against wavelength and diameter for gold spheres in water, as shown in Figure 2.11 a, and also produced near field plots of the resonances (B-H). It can clearly be seen that the higher order modes are created at larger diameters and red-shift similarly to the dipole mode. The near field distribution of these modes is then also represented by the creation of additional nodes evenly spaced on the surface of the particle.

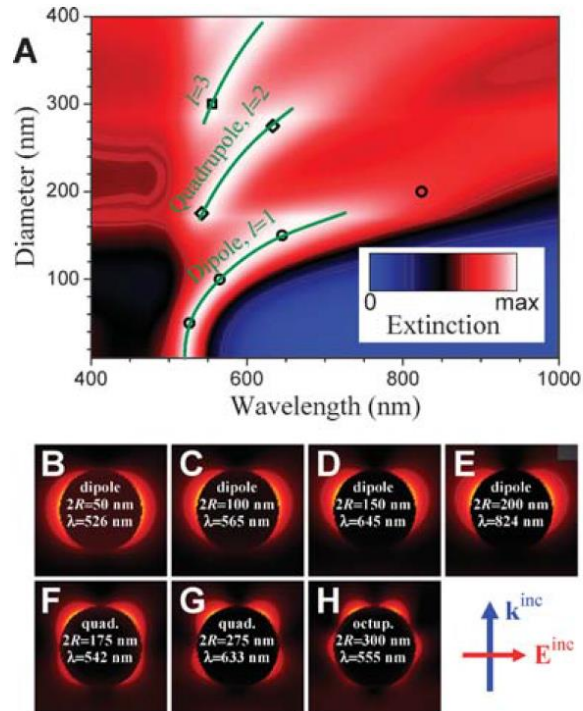


**Figure 2.11: A) Extinction spectra map showing the evolution of higher order modes. B-H) E-Field maps of field arrangements for dipoles ( $l=1$ ), quadrupoles ( $l=2$ ) and octupoles ( $l=3$ ) <sup>(30)</sup>.**

These higher order modes are not limited to just spheres but instead can occur for any geometry when the length scales are comparable to the incident light. For example, Payne *et al.* <sup>(60)</sup> fabricated nanorods with an average diameter of 85 nm and lengths from 96 nm up to 1175 nm. They found the presence of higher order modes began at an aspect ratio of around 4. The number of these modes increased for longer nanorods to the point where  $l=7$  modes were visible at an aspect ratio of  $\sim 14$ . Similar to the case for spheres, they show a trend where an increase in the length leads to a red shift in the position of the modes. Furthermore, it can also be observed that each additional mode is weaker than the one before it.

We will now briefly focus on the lower size limit of plasmonic nanoparticles. Here the higher order modes are non-existent and instead only the dipole mode is of importance. Mie theory predicts that with a decrease in size the quasi-static approximation once again becomes valid and the plasmonic peaks width and position becomes static. It has been shown experimentally however, by Alvarez *et al.* <sup>(61)</sup>, that at sizes below around 5 nm the absorption peak broadens and becomes considerably damped until around a diameter of 2 nm whereby it disappears completely. This can be attributed to a number of reasons. Firstly as the nanoparticle size reduces to just a few nanometres, the number of its conduction electrons also rapidly reduces. As a surface plasmon is caused by the collective oscillation of its conduction electrons, it is therefore reasonable to expect a decrease. Similarly, Mie theory breaks down as it uses bulk dielectric data which is no longer valid at these length scales <sup>(59)</sup>. The reasoning behind this deviation from the bulk dielectric data was proposed by Kreibig and von Fragstein <sup>(62)</sup> to be due to the mean free path of the electrons being limited by the size of the particle. As the particle gets smaller, the surface increasingly scatters the electrons randomly, thereby losing the coherent nature they require to form plasmons and also broadening the peak and dampening the oscillation <sup>(59)</sup>.

These deviations from the local dielectric data and the responses seen is commonly referred to as non-local effects. They can be somewhat accounted for by altering the dielectric function so that it accounts for the increased loss by changing the damping rate of the free electron gas ( $\tau$ ) as seen below, where  $v_F$  is the Fermi velocity <sup>(30)</sup>:

$$\varepsilon(\omega) + \frac{\omega_p^2}{\omega(\omega + i\tau^{-1})} - \frac{\omega_p^2}{\omega(\omega + i\tau^{-1} + iv_F/R)} \quad (57)$$

This allows better prediction of the optical cross sections for small spherical particles as seen in Figure 2.12 where the dashed lines represent calculated spectra using the above dielectric functions, and the solid lines represent experimental results. This method is only suitable for spheres however non-local effects can be prominent in other geometries as well as in sharp corners and small gaps <sup>(63)</sup>. For these, more in-depth methods such as the hydrodynamic Drude model or the generalised nonlocal optical response (GNOR) model may be used <sup>(64)</sup>.

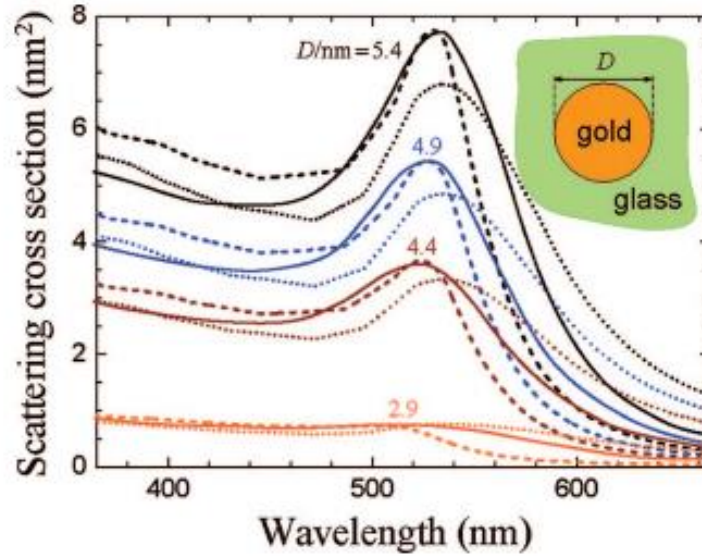


**Figure 2.12: Comparison between experimental data from ref <sup>(65)</sup> and theoretical data using a modified permittivity from equation (58), for various Au sphere sizes embedded in glass <sup>(63)</sup>.**

## 2.6 Effect of Geometry

In addition to the material, size, and dielectric environment of the particle, another important factor in dictating the plasmon resonance of a particle is its geometry. So far the discussion has mainly been directed towards perfect spheres due to the ability of solving these via Mie theory. By expanding into other geometries however, many interesting and advantageous properties may be realised.

Other than a sphere, another typical geometry for plasmonic particles is that of nanorods. These will be defined as having length  $L$ , and radius  $R$ , resulting in its aspect ratio (AR) being equal to:

$$AR = \frac{L}{2R} \quad (58)$$

These have grown in popularity due to their relative stability compared to other nanoparticle geometries and their anisotropic optical properties <sup>(66)</sup>. For example, an interesting thing to note with nanorods is the presence of two modes depending on its orientation relative to the polarisation of the incident light, namely being the transverse and longitudinal modes (Figure 2.13). This additional mode arises as one of the axis of a sphere is elongated, causing the plasmonic resonance to split. The transverse mode occurs when the electric field is polarised

perpendicular to the nanorods long axis, causing an oscillation over the nanorods width. This occurs at similar wavelengths to that of a sphere of the same diameter. Alternatively, the longitudinal mode occurs when the electric field is polarised parallel to the nanorods long axis causing an oscillation of the electrons over the length of the rod. Similarly to that seen with an increase in diameter of a sphere, the resonance over the longer distance requires a reduction in the frequency and therefore a red-shift of the resonance position.

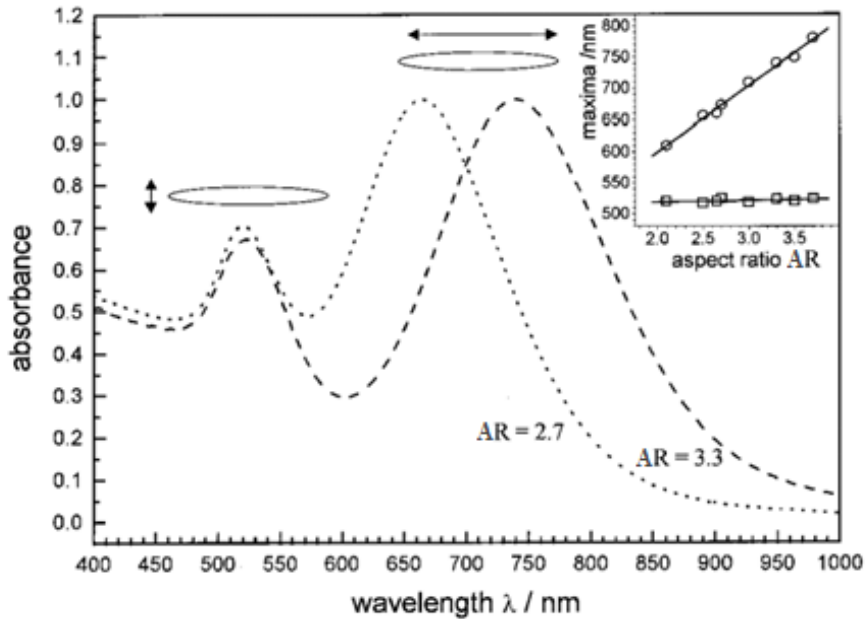


**Figure 2.13: Experimental absorption spectra for gold nanorods with AR of 2.7 and 3.3 showing the two modes. Inset is of the SPR wavelength with AR showing a positive linear relationship for the longitudinal mode and negligible change for the transverse mode <sup>(59)</sup>.**

These two modes were initially predicted in 1912 by Richard Gans in an adaption of Mie theory which has since become to be known as Gans theory <sup>(37)</sup>. Although this was originally developed to predict oblate and prolate ellipsoids extinction spectra, it can also be applied to approximate nanorods <sup>(66)</sup>. The extinction cross section is given by:

$$\sigma_{\text{ext}} = \frac{\omega}{3c} \varepsilon_m^{3/2} V \sum_j \frac{(1/P_j^2) \varepsilon_2}{\{\varepsilon_1 + [(1 - P_j)/P_j] \varepsilon_m\}^2 + \varepsilon_2^2}, \quad (59)$$

Where V is the particle volume and  $P_j$  represents the depolarisation factors for the three axes A, B and C of the nanorod with  $A > B = C$ , defined as <sup>(59)</sup>:

$$P_A = \frac{1 - e^2}{e^2} \left[ \frac{1}{2e} \ln \left( \frac{1 + e}{1 - e} \right) - 1 \right], \quad (60)$$

$$P_B = P_C = \frac{1 - P_A}{2}, \quad (61)$$

$$e = \left[ 1 - \left( \frac{2R}{L} \right)^2 \right]^{1/2} = \left( 1 - \frac{1}{R^2} \right)^{1/2} \quad (62)$$

Here the factor  $e$  accounts for the aspect ratio of the nanorod. Studying these equations along with Figure 2.13 shows that the transverse mode is fairly independent of aspect ratio with only a slight blue shift seen with increasing AR. Instead, this transverse resonance is more dependent on the diameter of the nanorod. On the other hand, the longitudinal plasmon mode, which occurs at higher wavelengths, depends on the aspect ratio with a linear relationship<sup>(67)</sup>. This can be seen clearer in Figure 2.14 from work by Tao et, al.<sup>(66)</sup>.

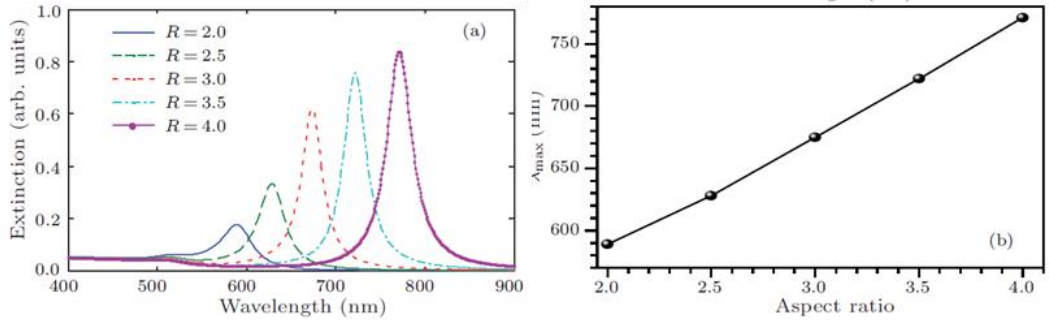


**Figure 2.14: a) Extinction spectrum of gold nanorods with aspect ratios between 2 – 4, b) the relationship between aspect ratio and peak longitudinal resonance wavelength<sup>(66)</sup>.**

Not only does the resonance position red-shift linearly with AR but there also appears to be an increase in the amplitude of the peaks with AR. This can be explained by its dependence on the volume term as seen in equation (59). On the other hand, we have seen previously that an increase in the diameter of a sphere above around 100 nm leads to a broadening of the peak and a decrease in the amplitude due to radiative damping. This is not the case for the longitudinal mode of nanorods however as although their length is increasing, the volume of the nanorod stays small compared to that of a sphere and therefore does not suffer from the same degree of radiative damping and broadening<sup>(68)</sup>. This enables long aspect ratio nanorods to have exceptionally high enhancements levels which along with their tunability from the visible into the infra-red, makes these excellent choices for surface-enhanced Raman spectroscopy and photocatalytic applications.

Bryant *et al.* <sup>(69)</sup> modelled nanorods using the boundary element method (an overview of which is given in Chapter 5). Although they also found a linear dependence with aspect ratio they concluded that it is not always as straightforward, as rods with different dimensions but the same aspect ratio can have significantly altered resonance positions. For instance, it is found that a rod with an AR of 2 but with different radii from 5 nm to 100 nm can observe over a 500 nm redshift for the larger diameter. This effect is also accelerated for larger aspect ratios. This red-shift with increasing diameter of the nanorod is attributed to the onset of retardation effects, similar to that with spheres.

Prescott and Mulvaney <sup>(70)</sup> also found this dependence of the resonance position with radius and not just aspect ratio of the rod. In addition, they concluded that although Gans theory may provide a rough estimation for a nanorods optical properties, significant differences in the estimated and actual resonance positions exist. Using the discrete dipole approximation (DDA) method, also outlined in Chapter 5, they further studied the effect of shape and end cap geometry. It was found that as the rod changed from that of a spheroid as in Gans theory, to a spherically capped cylinder and then a flat ended cylinder, a red-shift with each was seen. By comparing the results for the different rod end cap styles to experimental data, a counter intuitive outcome was found whereby flat ended cylinders better correlated with experimental data than round-ended cylinders, even though TEM analysis showed the geometry to be more like the latter. This result can be seen within Figure 2.15. In contrast, Pecharroman *et al.* <sup>(71)</sup> suggests that nanorods are instead modelled more accurately by spherically capped cylinders and that any additional red-shift arises from the surface roughness of the rod.

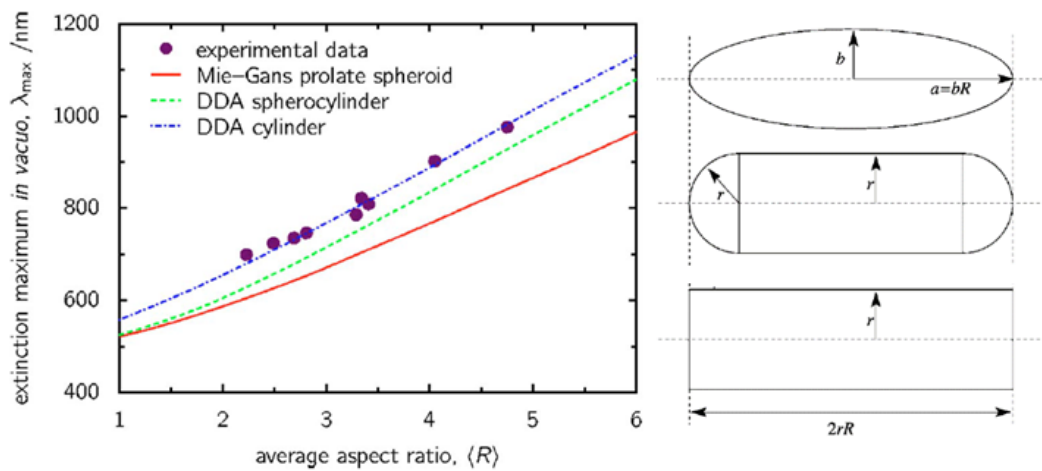


**Figure 2.15: Comparison of DDA simulations to experimental data for AR vs  $\lambda_{\max}$  (left) for three different geometry configurations (right) <sup>(70)</sup>.**

The work by Trugler *et al.* <sup>(72)</sup> contradicts the finding that surface roughness of a nanorod can cause a significant red-shift. Instead they claim by using both experimental work and modelling using the Boundary Element Method, that surface roughness has little effect on the far-field optical properties. Their reasoning behind this is due to motional narrowing whereby the random height fluctuations lead to destructive interference and an overall small dependence. Despite this claim, it is still possible to see in their results that a small red-shift occurs with surface roughness. This red-shift is drastically amplified for rippled rods whereby the height fluctuations are constant and periodic along the length of the rod as the random nature is lost and destructive interference no longer occurs.

From the above findings, it is possible to conclude that the optical properties of nanorods cannot be simplified by its aspect ratio and an analytic theory such as Gans theory. Instead the optical properties depend on many other factors such as the diameter of the rod, the end cap geometry and its surface roughness. This is in addition to other known factors that can affect the resonance of a nanorod such as the effect of surfactants commonly used in their fabrication <sup>(73)</sup>, the effect of plasmon coupling <sup>(74)</sup>, and polydispersity in the sample <sup>(75)</sup>.

The near field distribution of electric fields surrounding nanorods is critical to many applications and therefore a review of findings will be included here. With the development of modelling based approaches, the derivation of the electric fields surrounding particles of arbitrary shape has become commonplace. For instance, Yong *et al.* <sup>(76)</sup> used finite element modelling (FEM) to simulate the electric field enhancements of gold nanorods for the longitudinal dipole mode, quadrupole mode and sextuple mode, as seen in Figure 2.16. It is clear to see that the longitudinal dipole mode has the electric field maxima located around either end of the rod as one would expect and occurs at a wavelength of 2060 nm for the nanorod shown. Alternatively, the quadrupole mode is formed when the nanorod is long enough so that a further mode can be sustained in the middle of the rod, as shown in the schematic diagrams. This quadrupole mode, which in a similar manner to that for spheres, occurs at a lower wavelength than the dipole (1030 nm), has its biggest enhancement when the incident light has an angle of 39°, as shown in the far-field scattering plot.

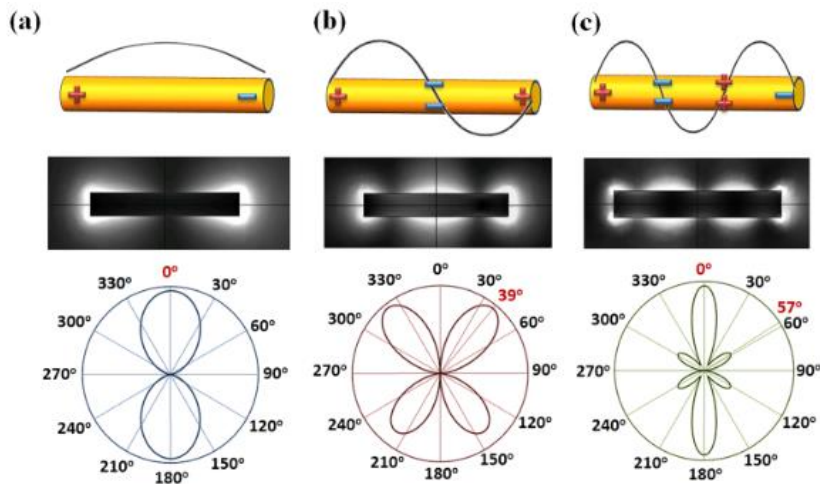


**Figure 2.16: Schematic charge distributions, electric field distribution and far-field scattering plots for a gold nanorods a) dipole mode, b) quadrupole mode and c) sextuple mode <sup>(76)</sup>.**

Its electric field distribution also shows differences whereby an enhancement is also seen at the centre of the rod in addition to the previously described dipole mode which is now weakened. Lastly, the sextuple mode (734 nm) shows similar behaviour, however, this time two enhanced modes are clearly visible towards the centre of the rod and once again the dipole mode is weakened.

These results are supported by the experimental work of Bosman *et al.* <sup>(77)</sup>. Here they used electron energy loss spectroscopy (EELS) to image the multiple plasmon modes of long gold nanorods. EELS is a technique that utilises an electron beam with a known and narrow kinetic energy. As the electrons pass the nanorod, the plasmonic modes are excited and the electrons have a subsequent loss in energy. This loss of energy can be measured and used to produce both spectra and maps of the energy loss, thereby allowing analysis of the plasmonic modes. A more thorough description of EELS is given in Chapter 6 since this technique has been used for this thesis to provide a detailed study of the fabricated nanorod arrays.

It can be seen in Figure 2.17 that a number of higher order modes are produced along the length of the nanorod and have very similar electric field distributions to those modelled in Figure 2.16. Similarly, each higher order mode occurs at decreased wavelengths and has a weaker intensity than the last. The two lines in the spectra refer to measurements both before and after annealing of the rod. The blue shift seen after annealing is attributed to a slight shortening of the nanorod <sup>(77)</sup>.

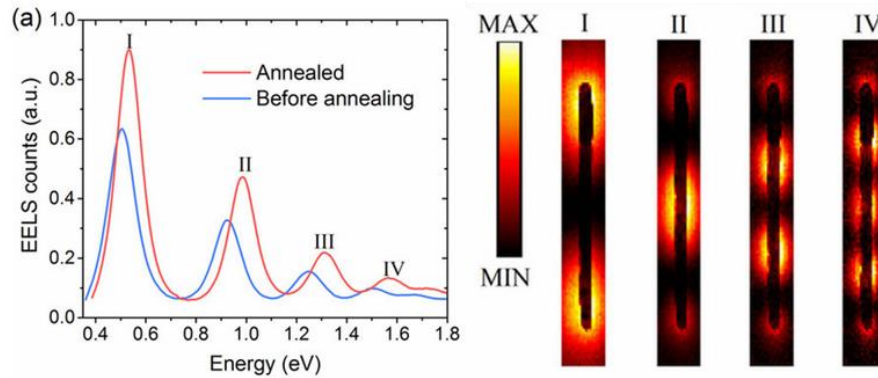


**Figure 2.17: EELS spectra before and after annealing of the gold nanorods and their corresponding plasmon maps <sup>(77)</sup>.**

As previously alluded to, the end cap geometry of nanorods can have a substantial effect on the resonance position of the longitudinal mode. Liu *et al.* <sup>(78)</sup> used Finite Difference Time Domain (FDTD) modelling of nanorods with both a curved surface and an arrowhead geometry to assess how the change in geometry affected the enhancement of the electric fields. The results, as seen in Figure 2.18, show that the arrow head geometry has considerably larger E-Field strengths compared to the rod with the hemispherical end cap. The distribution of the electric fields shows that although there is still a characteristic dipole in both geometries, the highest enhancements are located at the sharp corners of the arrowhead. In contrast, the electric fields in the hemispherical cap are more dispersed over the surface.

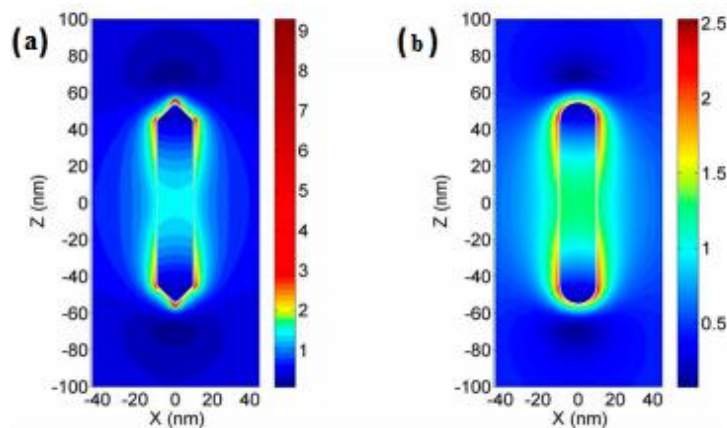


**Figure 2.18: FDTD simulation results for gold nanorods with a) an arrow head end cap, and b) a hemispherical end cap, showing E-Field enhancements <sup>(78)</sup>.**

This observed enhancement at the sharp corners of nanoparticles is a common feature that has been reported for many different types of geometry. For instance Zhang and Zhao <sup>(79)</sup> used

the DDA method to model the effect of a number of different nanorod shapes ranging from simple cylinders to more complicated castellated structures and y-shaped rods. They too found the electric field distribution depends on the shape of the nanorod with the highest enhancements once again noted at the corners of the nanorod. This however was also found to be polarisation dependent whereby a change in the incident angle can further alter both the location and magnitude of the electric fields. Additionally it was found that the sharp corners also led to subsequent red-shift of the plasmon resonance position.

Sturman *et al.* <sup>(80)</sup> also investigated the effect of sharp corners on the plasmonic resonance using a surface integral eigenvalue based technique. It was concluded that as the corner curvature increases, a red-shift of the resonant wavelength occurs. Additionally, for large curvatures the dipolar resonant wavelength is predominantly dictated by this curvature alone. Lastly, they further observed that the increased corner curvature leads to a localisation and enhancement of the electric fields, matching that seen previously.

This ability to control not only the resonant position but also the enhancement levels of the electric field using the geometry of the particle, has made the fabrication of new and exotic nanoparticle shapes an important area of research. The high electric fields in particular can be extremely useful in SERS applications due to the relationship that Raman scattering scales to the fourth power of the electric field <sup>(81)</sup>. Figure 2.19 gives examples of some of the unique geometries that are able to be fabricated which include nanoprisms, nanocubes and nanostars. Although these geometries can show several plasmonic modes, we have highlighted those whereby strong localisation occurs at their sharp corners.

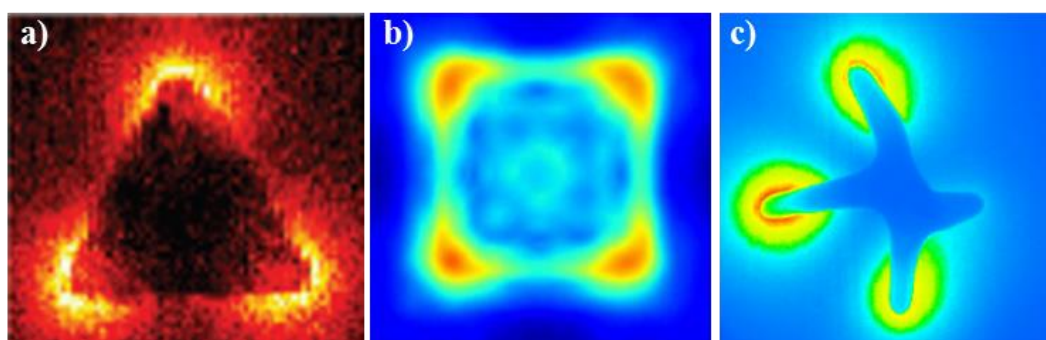


**Figure 2.19: EELS maps of an a) nanoprism <sup>(82)</sup>, b) nanocube <sup>(83)</sup>, and c) nanostar <sup>(84)</sup>. This figure highlights the localisation of the plasmons but does not allude to the enhancement levels due to varying intensity scale from different work being used.**

This localisation and the electric field enhancement can often be overestimated by simulations and theory, particularly for small sharp corners, due to non-local effects becoming prominent as previously discussed. Moskovits <sup>(85)</sup> states that non-local effects in general decrease the sharpness of the resonance and reduce the calculated enhancements by a magnitude of 2-3 for an isolated sphere. This was supported by the work of Ruppin <sup>(86)</sup> who found that when accounting for non-local effects in a conical tip, the electric field intensity is reduced by a factor of 2.64 when compared to the local calculations. Similarly, Toscano *et al.* <sup>(87)</sup> studied the non-local response of a groove whereby the gap reduced to infinitely sharp levels. In addition to a finite E-Field strength being observed, which was limited to enhancement factors below 10 orders of magnitude, a blue shift of the resonant position compared to that predicted with the local approximation is also observed.

## 2.7 Effect of Substrates

The optical properties of plasmonic nanoparticles are commonly obtained with them in suspension within a solution due to the ease of measurement by methods such as UV-Vis spectroscopy. Despite this, for the application of the nanoparticles it is often required for them to be immobilised upon a substrate causing an inhomogeneity in the surrounding dielectric constant. As it has already been observed, plasmonic nanoparticles are highly sensitive to their local environment, and therefore it is expected that this proximity to a substrate will result in a deviation of their optical properties. This topic will be discussed here, with focus first addressing the effect of plasmonic nanoparticles on dielectric substrates, followed by assessing the effects of metallic substrates whereby plasmonic coupling may play a role.

### 2.7.1 Dielectric Substrates

The first attempts made to account for the presence of a substrate involved averaging the surrounding mediums dielectric constant with that of the substrate, a method known as the homogeneous matrix model <sup>(48)</sup>. This is seen in equations (63) and (64) where the former is preferred for s-polarised light and the latter for p-polarised light.

$$\epsilon_{m,eff} = \rho\epsilon_{sub} + (1 - \rho)\epsilon_m \quad (63)$$

$$\frac{1}{\epsilon_{m,av}} = \frac{\rho}{\epsilon_{sub}} + \frac{(1 - \rho)}{\epsilon_m} \quad (64)$$

Where  $\epsilon_{m,eff}$  is the effective dielectric constant and  $\rho$  is a factor between 0 and 1 accounting for the relative occupancy of the substrate, typically around 0.5. Although this approximation qualitatively accounts for the effect of the substrate, the complexities of the electromagnetic wave and surface plasmon interactions within the vicinity of a substrate are not truly accounted for. Instead, Wind *et al.* <sup>(88)</sup> aimed to improve this method by including the substrate – embedding medium interface in the polarisation, similar to that performed for the sphere. The polarisability of the sphere on the substrate is then:

$$\alpha = 4\pi R^3 \frac{\epsilon - \epsilon_m}{\epsilon_m + L(\epsilon_m, \epsilon_{sub})(\epsilon - \epsilon_m)} \quad (65)$$

where the factor L is given by:

$$L = \frac{1}{3} \left( 1 - \frac{1}{8} \frac{\epsilon_{sub} - \epsilon_m}{\epsilon_{sub} + \epsilon_m} \right) \quad (66)$$

The results from this theory show that once again a red shift in peak resonance and an increase in magnitude is seen with increasing optical contrast between that of the substrate and the embedding medium,  $\epsilon_{sub} - \epsilon_m$ , as seen in Figure 2.20.

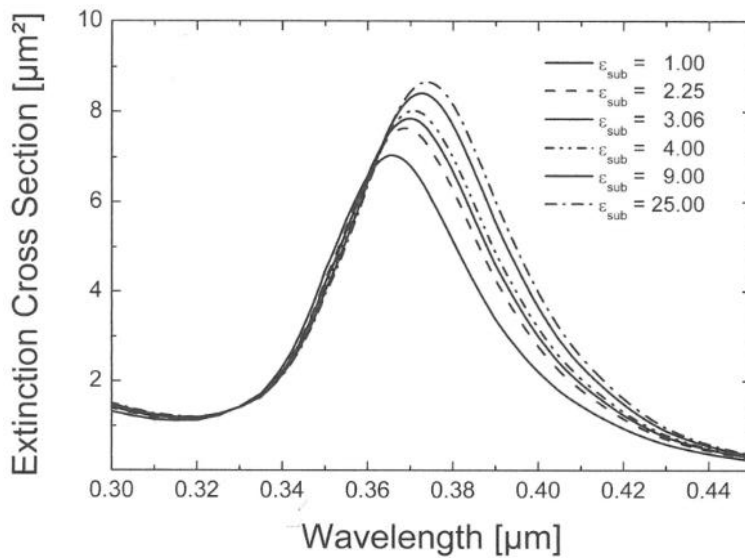


**Figure 2.20: Extinction cross section of a Ag sphere on a dielectric substrate with increasing permittivity, calculated using the polarizability of a sphere on a substrate method <sup>(48, 88)</sup>**

The above method is valid only when that particles are much smaller than the wavelength of light. Furthermore, it fails to fully account for all the complexities you get when a particle is near a substrate. For instance, considering just a planar substrate without an adjacent particle, the incident light will partly be reflected by the substrate leading to a superposition of both the incident and reflected waves. This leads to the formation of standing waves above the substrate that alter the intensity of the incident field. Further complications also arise when one considers that the particle above a substrate will scatter light. Under this scenario there are three possible outcomes for the scattered light. Firstly, the simplest option is that the scattered light directly travels to the far field and does not interact with the substrate. Secondly, the scattered light may impinge on the substrate and reflect back off it to the far field. Finally, the last case is one where the scattered light reflects back off the substrate and onto the particle again. This latter option is the major complication when deriving analytical solutions to the problem and accounts primarily for any particle – substrate coupling <sup>(89)</sup>.

Considering the above, it is now also noted that the solution does not simply depend on the permittivity of the materials as with previous methods, but also on the location of the particle with respect to the substrate, as well as the polarisation and angle of the incident light. Despite this added intricacy, a rigorous solution was developed by Johnson <sup>(89)</sup> that takes all of these factors into account using the so called multipole expansion method. One limitation of this method, however, is that the solution is only valid for perfectly reflective substrates, and not dielectric ones. This limitation was addressed by applying an approximation originally considered by Videen <sup>(39)</sup> and built upon by Johnson <sup>(89)</sup> whereby it states the field being reflected back on to the particle can be accounted for using the Fresnel reflection coefficients at normal incidence. It is assumed however that the maximum incident angle of the reflected wave on to the particle is limited to 30°, and that in the 0° - 30° range the coefficient can be approximated constant. Fucile *et al.* <sup>(90)</sup> later expanded this to account more precisely for the angle, however at the expense of much greater calculation effort <sup>(48)</sup>.

By implementing the later, more refined models, which account for the previous mentioned complexities, a number of differences compared to the former relatively simpler models was found. For instance, it can be seen that both the polarisation and angle of incidence play an important role in the optical properties of a sphere on a substrate. Additionally, although a noticeable red-shift with increasing permittivity of the substrate was still predicted, it was less pronounced than before <sup>(48)</sup>.

To better understand the effects that a substrate has on the optical properties of plasmonic nanospheres, a more rigorous examination that breaks down the various substrate effects was performed by Lermé *et al.* <sup>(91)</sup>. Here the exact multipole expansion method was once again used, however, the results were split into extrinsic substrate effects and intrinsic substrate effects. The former relates to the effects seen due to reflections from the surface of the substrate resulting in alterations of the local electric field, where as the later relates to the scattering of light from the nanoparticle being reflected back on to it.

Firstly, it was found that for a gold nanosphere on a substrate, an increase in the refractive index of the substrate causes a red-shift and a decrease in the extinction cross section (see Figure 2.21). The red-shift is predicted by simpler models such as the homogeneous matrix model, however the decrease in the extinction cross section is contradictory. By normalising the cross sections to the local field intensity however, thereby removing any extrinsic substrate effects, the extinction cross sections now match those of the homogeneous matrix model (Figure 2.21b). Similarly, by removing only the intrinsic substrate effects, the decrease is once again seen, however there is no observed red-shift in the resonance position (Figure 2.21c). This therefore highlights that the extrinsic substrate effects dictate the amplitude of the cross sections, whereas the intrinsic coupling effects control the associated red-shift.

When considering a silver nanoparticle instead of gold, as seen in Figure 2.21d-f, it can be seen that the inclusion of intrinsic effects results once again in a red-shift but also in the generation of additional modes. These additional modes therefore arise from coupling between the particle and the substrate. Furthermore, this splitting of the modes, and a resultant sharing of the oscillator strength, causes a decrease in the amplitudes with increasing refractive index, even when removing the extrinsic effects. This is in contrast to that predicted by the homogeneous matrix model and illustrates the importance of accounting accurately for factors such as reflection from the substrate, or coupling between the particle and the substrate.

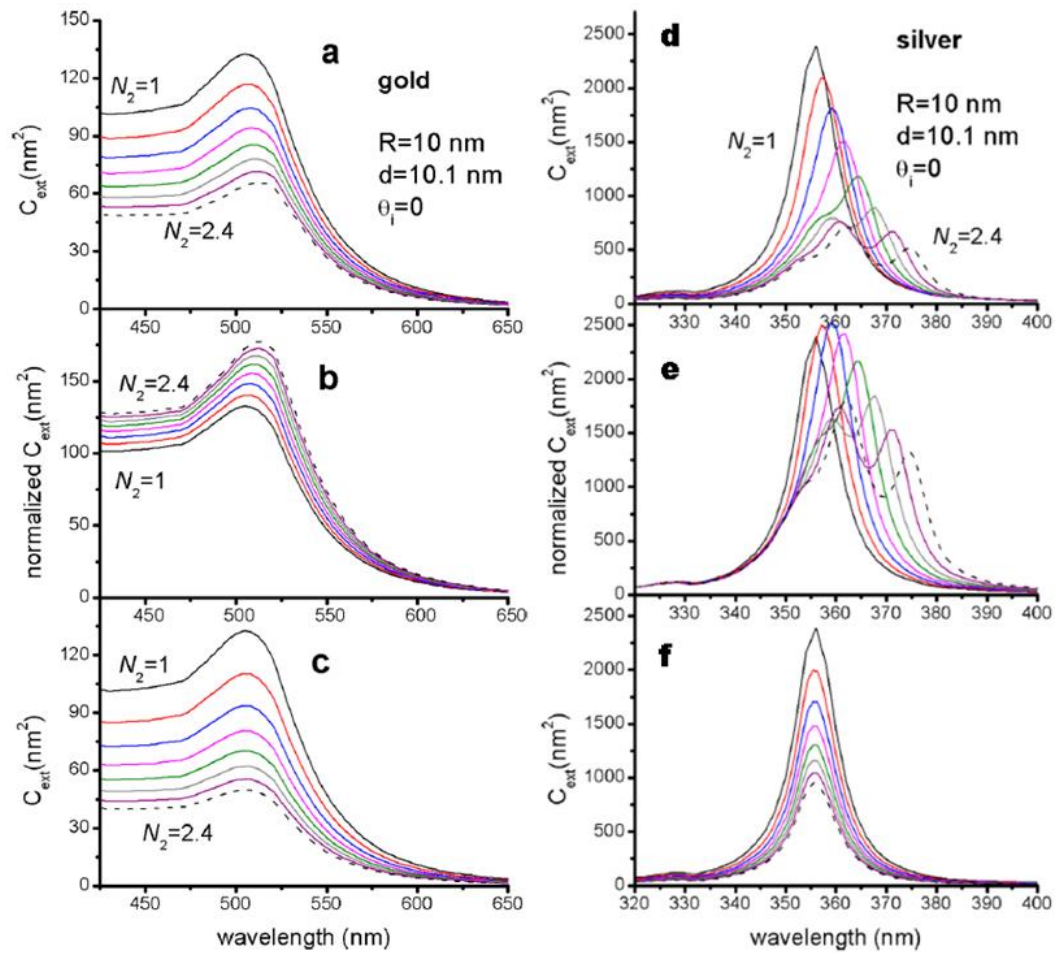


**Figure 2.21: Extinction cross sections of 10nm Au (a-c) and Ag (d-f) spheres on a substrate of refractive index  $N_2$ , including all substrate effect (a,d), excluding extrinsic substrate effects such as reflections from the substrate altering the local field intensity (b,e), and excluding intrinsic substrate effects such as coupling (c,f). Adapted from <sup>(91)</sup>.**

In addition to the effect of the substrates refractive index, Lermé *et al.* <sup>(91)</sup> also investigated the effect of polarisation, incident angle and the distance the particle is above the substrate. It was found that p-polarised light at oblique angles of incidence lead to much higher intrinsic substrate effects than with s-polarised light due to the charge distributions being located towards the bottom of the nanoparticle. Similarly, as a nanosphere approaches the substrate, the intrinsic substrate effects are predicted to increase, leading to a further red-shift and the generation of higher order modes.

Focussing on these intrinsic substrate effects in more detail, with an electrostatic viewpoint these effects are all accounted for by a variety of terms such as induced surface charge

distributions, plasmon hybridisation, the coupling or splitting of modes, and interaction with image charges <sup>(91)</sup>. This last term is particularly useful in explaining the particle-substrate interactions, as can be seen in Figure 2.22. For example, when a particle becomes polarised by an electric field, the substrate also undergoes an alteration in its charge distribution, which in turn may interact with that of the nanoparticle again. Using the image charge method it becomes possible to determine these charge distribution of the nanoparticle by specifying an imaginary image charge an equal but negative distance away from the substrate interface. The interaction of these two images can be solved whilst still satisfying the boundary conditions of the original solution.

When a particle is sufficiently far away from the substrate so that its field lines do not interact with those of its substrate image, the particle essentially acts as one in a homogeneous environment (Figure 2.22a). However, when the particle is located on the substrate, there is a hybridisation with its substrate image leading to the generation of higher order modes, non-uniform field distributions, and shifts within the spectra (Figure 2.22b) <sup>(92, 93)</sup>.

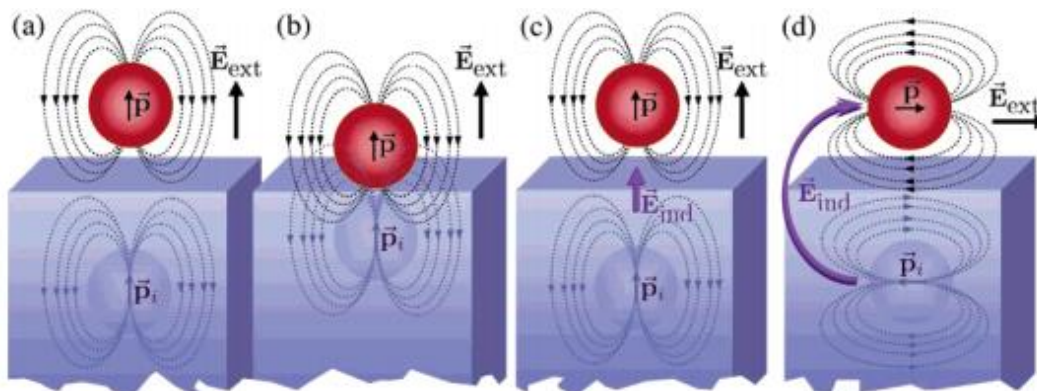


**Figure 2.22: Method of image charges for a nanoparticle above a substrate with a-b) varying separation from the substrate and c-d) showing the presence of the induced local field at c) p-polarised light and d) s-polarised light <sup>(92)</sup>.**

The observed red-shift seen as particles are brought closer to a substrate regardless of the polarisation of light, can also be explained by the method of image charges. For example, Figure 2.22c shows the situation for a nanoparticle above a substrate where the electric field is normal to the surface (p polarised). Here the substrate image and the particle are polarised in the same direction, with the resulting induced field supporting that of the applied electric field. Alternatively, in Figure 2.22d, the electric field is parallel to the substrate (s polarised), and the particle and substrate image polarisations are opposite. Despite this, the induced field

still acts along the same direction as that of the incident electric field. In both cases the induced field matches that of the applied field and acts against the restoring forces, thereby leading to a shift to higher wavelengths <sup>(92)</sup>.

The above derivations have been in regards to spheres above substrate. In contrast, Noguez <sup>(92)</sup> used the spectral representation method to derive theoretical solutions to the problem of prolate and oblate spheroids at a finite distance above a TiO<sub>2</sub> substrate, and under different polarisations of incident light, therefore representing something similar to a supported nanorod. It was found that as the aspect ratio of the spheroids increased, the longitudinal modes are red-shifted, however, the transverse modes are blue shifted, similar to that predicted by Gans Theory. Interestingly however they note that at larger aspect ratios, (AR > 3), the dipolar resonance dominates and is at a similar wavelength to that of an isolated particle, suggesting that as the particle's AR grows, the particle–substrate coupling becomes less dominant.

The above analytical results are useful in terms of gaining a deeper understanding of how particles may interact with substrates, however, they are limited to certain theoretical assumptions such as being only applicable for spheres or spheroids, being above infinitely large substrates, or only accounting for a finite number of multipolar modes. To test the validity of these predictions, a comparison between the theoretical predictions and those found by numerical modelling and experimental work is now given.

Myroshnychenko *et al.* <sup>(30)</sup> performed boundary element modelling of a gold nanoparticle on a silica substrate. They found the presence of the substrate decreased the scattering intensity, and that larger diameter particles were influenced more by the substrate than smaller ones. Alternatively, Kelly *et al.* <sup>(45)</sup> used the DDA modelling method to test numerically the red-shift seen as a 20 nm silver sphere came in contact with a mica substrate, as seen in Figure 2.23. An initial large red-shift is noted as the particle becomes partially embedded in the mica, compared to its vacuum resonance wavelength. This red-shift then slows becoming approximately linear, until it is completely embedded and represents that of a core-shell nanoparticle. The mica substrate in these models, however, has a thickness of only 10 nm and therefore it is questionable as to whether the complexities seen with real substrates, such as the presence of standing waves for instance, are truly represented.

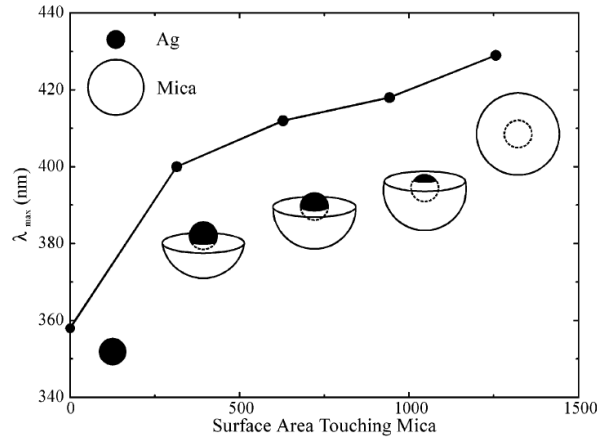


Figure 2.23: DDA results for a silver sphere becoming increasingly embedded in mica <sup>(45)</sup>.

Similarly, Jensen *et al.* <sup>(94)</sup> used a DDA approach to model a truncated tetrahedron both without a substrate, and supported on a mica slab, as seen in Figure 2.24. Comparing their results to experimental data, they found the presence of the mica substrate gave a substantial 100 nm red-shift of the resonance position and matched the experimental results uncharacteristically well, thereby concluding that substrate effects must be accounted for. They also noted that for accurate representation of the substrate, it should have a depth at least equal to the thickness of the particle and should extend a minimum of the radius of the particle past its edge. Despite this conclusion, I am sceptical that the full complexities of the substrate are once again truly modelled over such a short area. This partly is at fault of the DDA method which requires the entire simulation be constructed from a cubic lattice of polarisable dipoles, therefore making large areas extremely computational expensive.

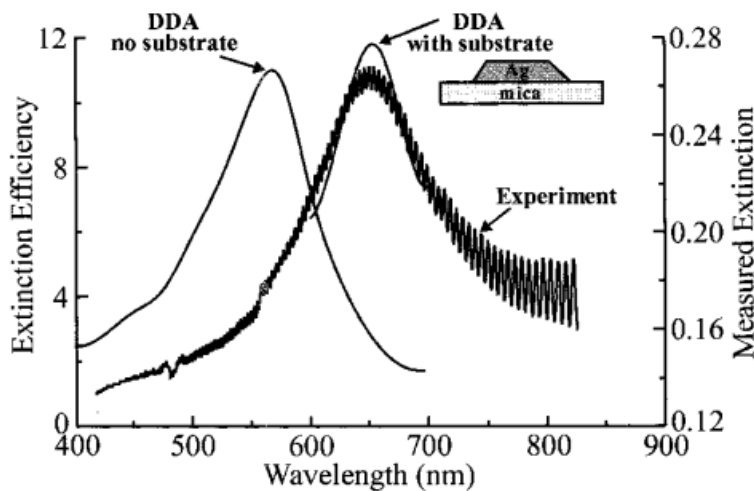


Figure 2.24: DDA results for a truncated tetrahedron without a substrate and on a mica substrate compared to experimental data <sup>(94)</sup>.

Yang *et al.* <sup>(95)</sup> performed FEM simulations of a 200 nm silver sphere on a silicon substrate of varying thickness, including the presence of a thin 10 nm SiO<sub>2</sub> layer separating them. They found that the thickness of the silicon substrate is critical to its scattering properties, with higher thicknesses leading to a larger red-shift of the resonance. They further propose that this may be a preferential method to tune the resonance positions of nanoparticles compared to altering their diameter. This was only performed however up to thicknesses equivalent to the sphere radius, and therefore may differ for larger substrates. Rui *et al.* <sup>(96)</sup> corrected for this by performing similar simulations using a finite difference time domain (FDTD) method, however they used smaller particles of 60 nm diameter and instead altered the thickness of the SiO<sub>2</sub> spacer layer. They found that adjusting the spacer thickness between 0 nm and 60 nm led to a large blue-shift in the resonance as the particle moved further away from the high refractive index silicon layer. This was quick at small thicknesses but slowed after around 15 nm due to the localised nature of the surface plasmon no longer interacting strongly with the silicon substrate.

On the other hand, Ringe *et al.* <sup>(97)</sup> studied the presence of a 72 nm silver nanocube on silicon nitride substrates of different thicknesses, ranging from 25 nm to 200 nm using a FDTD method. Although they found a red-shift in the resonance position with the addition of the 25 nm substrate, they also noted that further increases in thickness had negligible effects on the resonance position. Similarly, Wu and Norlander <sup>(98)</sup> used FDTD modelling to simulate a gold nanoshell on a finite sized dielectric slab to assess at what thickness and distance from the edge of the particle the results become constant. It was found that a thickness equal to the diameter of the particle and a width equal to twice the diameter of the particle is required.

Experimental results support those found in theory and numerical modelling. For instance, Knight *et al.* <sup>(99)</sup> performed dark field spectroscopy of individual nanoparticles on a number of dielectric substrates. They found that the higher permittivity substrates led to a greater red-shift of the plasmon mode, which when large enough, leads to the generation of higher order modes. Additionally, comparing polarisation of the light also shows a greater substrate interaction with p-polarised light resulting in a larger red-shift, as within Figure 2.25. The results of Kadkhodazadeh *et al.* <sup>(93)</sup> also support these findings. Here they performed EELS measurements of gold or silver nanoparticles on varying dielectric substrates, concluding once again, that higher order modes and larger red-shifts occur with the higher permittivity substrates. Additionally they also conclude that these substrate effects are amplified with an increase in the thickness of the substrate.

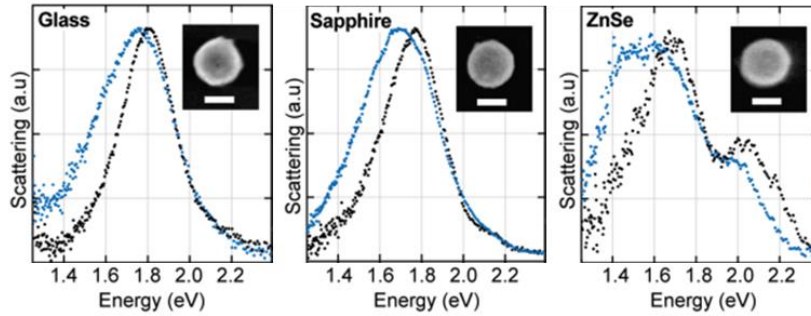


Figure 2.25: Experimental dark field spectroscopy spectra for Au/silica nanoshells on glass ( $n=1.52$ ), sapphire ( $n=1.77$ ) and ZnSe ( $n=2.67$ ). Blue curves represent p-polarised incident light where as black curves represent s-polarised incident light. Adapted from <sup>(99)</sup>.

As already discussed, the presence of a substrate breaks the symmetry of the particles response causing the charge distribution to be anisotropic, whereby it becomes concentrated towards the bottom of the particle. This has potential advantages due to the generation of enhanced fields within this area. For example, Hutter *et al.* <sup>(100)</sup> used FEM to assess the enhancement levels for a particle above a dielectric substrate. As seen in Figure 2.26, the substrate induces a strong localisation of the electric field in the gap with much higher enhancements of the field strength. Plotting the enhancement with distance from the substrate shows an exponential increase in the enhancement with decreasing gap size. It should be noted however, that gaps down to 0.6 nm are simulated, yet despite these small distances, the authors fail to account for non-local effects. As found by Ciraci *et al.* <sup>(101)</sup> non-local effects seen at these separations can drastically limit the enhancement levels, although strong fields are still possible.

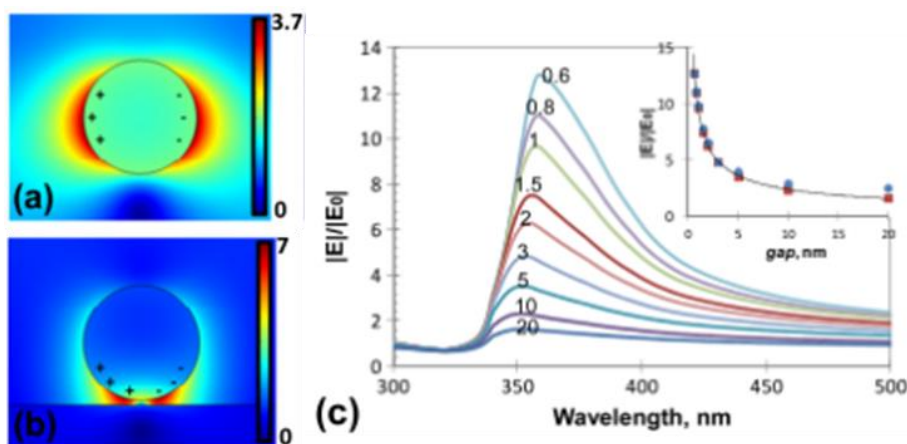
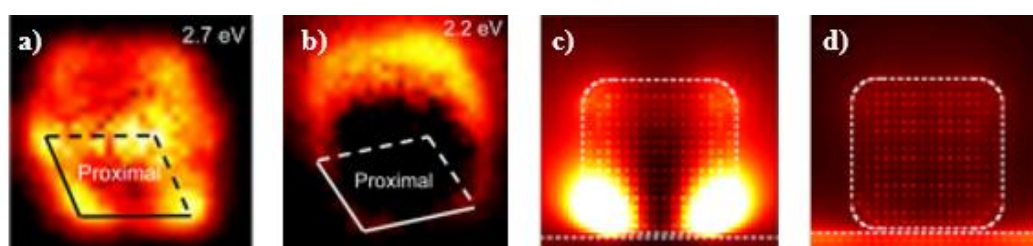


Figure 2.26: E-Field distribution of a Ag nanoparticle of radius 25 nm in a) air and b) 2 nm above a dielectric substrate ( $n=2$ ). c) E-Field enhancements for separations varying from 20 nm to 0.6 nm. The inset represents the maximum field enhancements in the middle of the gap (rectangles) and 0.3 nm below the nanoparticle (circles) <sup>(100)</sup>.

Numerous authors have attempted to utilise these strong electric fields found in the small gap between a particle and substrate. For instance, Linic *et al.* <sup>(102)</sup> placed silver strips on a TiO<sub>2</sub> substrate with small gaps between them governed by the inclusion of an organic spacer layer. They measured the rate enhancement of oxygen evolution with UV illumination for different spacer thicknesses. They found that as the particle was brought closer to the substrate, the rate enhancements increased exponentially due to the increased electric field strength producing more charge carriers in the TiO<sub>2</sub>. The greatest enhancements were seen for a separation of around 2-6 nm, however smaller separations showed a decrease in the enhancement attributed to losses due to Förster resonant energy transfer (FRET) from the semiconductor to the metal.

In addition, plasmonic particles may directly transfer their energy into the substrate via mechanisms known as plasmon-induced resonant energy transfer (PIRET), or direct electron transfer (DET). Li *et al.* <sup>(103)</sup> studied the presence of this energy transfer via EELS of a silver nanocube on both insulating substrates (SiO<sub>2</sub>) and semi-conducting substrates (a-Si and BP). By exciting the substrate localised dipole mode of the nanocube on each substrate they were able to map the EELS probability and effectively probe the energy transfer in each case. As summarised in Figure 2.27, it was found that on the SiO<sub>2</sub> insulating substrate, the dipolar modes of the nanocube were prominent. In contrast, on the semiconductor substrates, these same dipolar corner modes were suppressed. With the support of electron driven DDA simulations this suppression was attributed to PIRET from the particle to the substrate.



**Figure 2.27: a-b) Experimental EELS probability maps for the substrate localised dipole corner mode for the Ag nanocubes supported on a) SiO<sub>2</sub> insulator and b) a-Si semiconductor. c-d) Simulated EELS probability map for the same dipolar mode on a c) insulator and d) semiconductor showing the presence of PIRET. Adapted from <sup>(103)</sup>.**

## 2.7.2 Metallic Substrates

We will now focus the attention on to nanoparticles supported on metallic substrates, however many of the principles addressed with dielectric substrates are also relevant here, such as the applicability of the image charge method. For example, Pinchuk *et al.* <sup>(104)</sup> experimentally

produced 2 nm diameter silver nanoparticles supported on both a semiconductor ( $\text{GeSe}_4$ ) and metallic (Al) substrate. They then also simulated their results using a quasi-electrostatic approximation with the substrate accounted for by the image charge method. Good agreement was found between the simulations and experiments, concluding that the metallic substrate led to a much larger red-shift and an increase in the absorption cross section compared to the dielectric one. This is due to a larger hybridisation between the particle and its substrate image.

This finding is consistent with the results of other literature. For example, Hutter *et al.* <sup>(105)</sup> used FEM to compare the effect of both the real (n) and imaginary (k) part of the substrates refractive index, in addition to comparing this to actual materials. They found that larger red-shifts are seen when a metallic substrate is used over a dielectric one. Additionally, they found increased sensitivity of the red-shift with sphere diameter, and subsequent broadening of the peaks due to the presence of higher order modes from the substrate. In relation to the real and imaginary parts of the refractive index, the highest enhancements were seen for low n and high k substrates, as in the case of low loss metals.

On the other hand, Sobhani *et al.* <sup>(106)</sup> collected single particle scattering spectra in a dark-field microscope of aluminium nanoparticles on both a silica and aluminium substrate. They found the aluminium substrate led to a reduction in the linewidth of the dipole mode and increased its scattering efficiency. This was attributed to the aluminium film being able to hybridise both the dipole and quadrupole modes of the nanoparticle, which consequently reduced the radiative losses and narrowed the dipolar linewidth. This was supported with semi-analytical calculations for an 80 nm aluminium nanoparticle being brought closer to the substrate, as shown in Figure 2.28a. At large distances the spectra has only a single dipolar resonance and is relatively broad, however, as it approaches the metallic substrate a higher energy quadrupole mode is excited and the dipolar resonance consequently narrows. Alternatively, the increase in the scattering efficiency originates from higher reflections of the incident wave and scattered wave off the aluminium surface compared to the silica substrate. This hypothesis was reinforced by experimental and FDTD simulations where the supporting aluminium film thickness was reduced down to levels comparable with its skin depth. At these thicknesses they observe a reduction in the amplitude of the dipole peak, along with a broadening approaching that found in the absence of a film (Figure 2.28b).

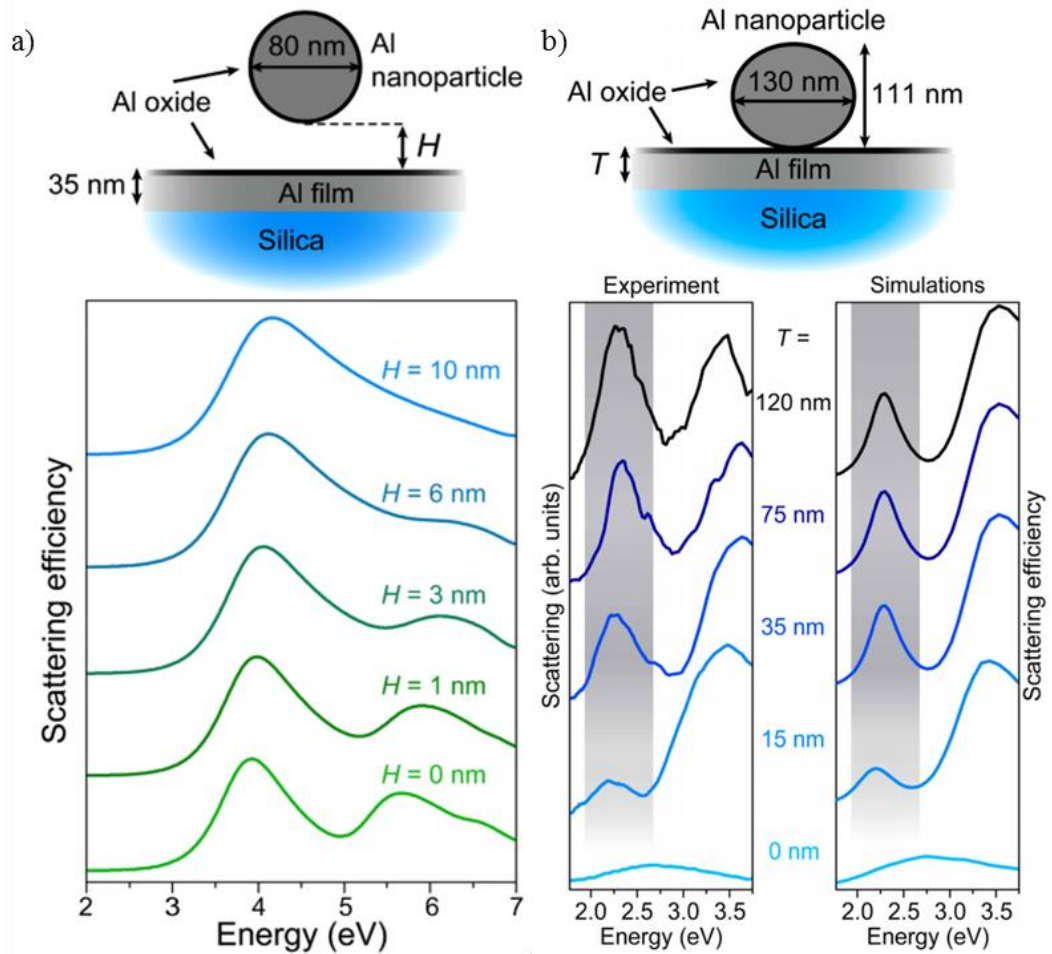


**Figure 2.28:** a) Calculated scattering efficiencies for an aluminium nanoparticle approaching an aluminium film showing the emergence of the higher order modes and a subsequent narrowing of the dipolar linewidth. b) Experimental (left panel) and FDTD simulations (right panel) of an aluminium nanoparticle on an aluminium film of varying thickness. As the film thickness decreases to that of its skin depth, the dipolar linewidth broadens and reduces in amplitude <sup>(106)</sup>.

In contrast, Liu *et al.* <sup>(107)</sup> simulated the induced current density of a single gold sphere, plus that of a gold dimer, supported on a gold substrate. Their results show that with the presence of the substrate, higher enhancements in the electric field are seen, as shown previously. Alternatively, they suggest that these enhancements are due to electrons from the substrate being absorbed into the sphere and contributing to the plasmon resonance. For the dimer scenario, two resonant peaks are seen in the spectra, related to the dipole mode of each individual sphere and additionally a single larger dipole over the dimer. When removing the substrate, the majority of electrons remain in their own spheres leading to relatively weak coupling, however with the addition of the substrate the coupling is much greater, particularly

for the larger dimer dipole mode, attributed to more electrons being able to flow between the particles and contribute to the resonance. This mechanism may therefore provide another physical insight into the increased enhancement levels seen for conducting metallic substrates.

A further consequence of using metallic substrates over dielectric ones is that the substrates themselves may also be able to support plasmonic modes in the form of surface plasmon polaritons (SPP). These propagating plasmons, formed on the interface of a metal and a dielectric have been shown theoretically by Takemori *et al.* <sup>(108)</sup> to be able to couple with the particle, thereby giving high electric field strengths. Expanding on this more, Leveque and Martin <sup>(109)</sup> used full-wave numerical scattering simulations to simulate that of a gold nanocube a small distance above a 50 nm thick gold film that itself is supported on glass. By directing the incident light through the glass at an angle of 45° and under p-polarisation, it experiences total internal reflection, resulting in an evanescent field. The decay of this evanescent field is then able to consequently excite both the LSPR of the particle, and the SPP of the film at the same time (see Figure 2.30a). This occurs for the conditions stated above at a wavelength of 600 nm. In addition to this however, the SPP mode also decays away from the film surface and in doing so couples with that of the nanoparticle.

The results of Leveque and Martin show that when the particle is directly on the gold film, the SPP dominates and is largely unaffected by the presence of the particle. This is due to the film being infinitely larger than the particle and therefore any alterations it has will be minimal. When the particle is lifted small distances above the substrate however (e.g. 5 nm – 50 nm), there becomes strong field enhancements, particularly within the gap, that decreases with increasing separation. This is in line with what we have already discussed regarding particles above substrates. Interestingly, the SPP wavelength is unaffected by this particle-substrate coupling, however as before, the LSPR wavelength of the particle red-shifts for decreasing spacing (see Figure 2.29a). At larger separations (100 nm – 900 nm), the gap acts as a cavity whereby constructive or destructive interference between the particle and the film leads to shifts in the resonance wavelength and fluctuations in the enhancement levels (Figure 2.29b).

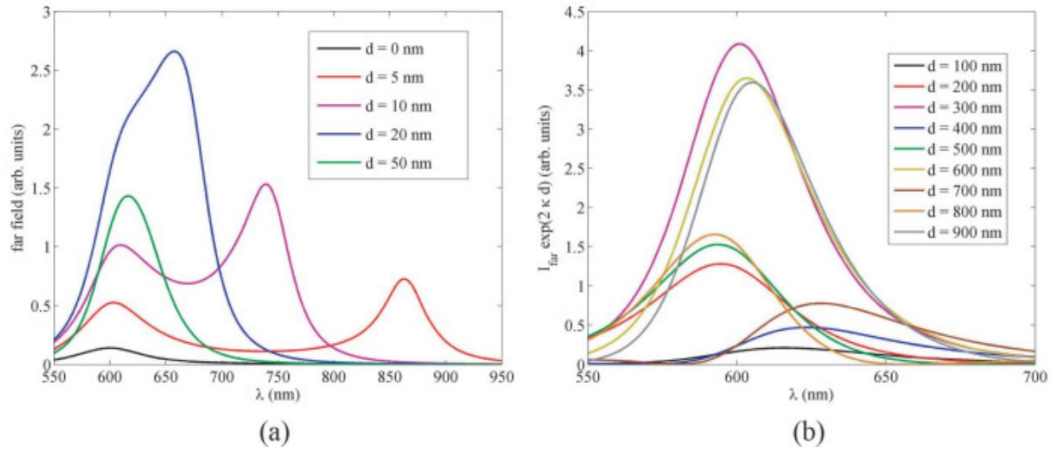


**Figure 2.29: Far-Field spectra for a gold nanoparticle separated by a distance,  $d$  from a gold film with a SPP mode. a) Spectra for distances of 0 nm – 50 nm, b) spectra for distances from 100 nm – 900 nm. Here the intensity has been normalised by the local intensity of the electric field to accurately show comparisons between separation distances <sup>(109)</sup>.**

These numerical results were supported by the experimental work of Mock *et al* <sup>(110)</sup> whereby they acquired the scattering spectra of gold nanoparticles above a gold film using both dark field illumination and total internal reflection illumination. Similar to the above, the total internal reflection method through a glass prism allowed the SPP mode of the gold film to be directly excited in addition to the particles LSPR, as seen in Figure 2.30a. In contrast, the dark field illumination from above only allowed the LSPR of the nanoparticle to be excited due to a mismatch in the in-plane wave vectors (Figure 2.30b). Furthermore, by depositing thin polyelectrolyte layers of varying thickness on the gold film, the spacing of the particle from the film was controlled.

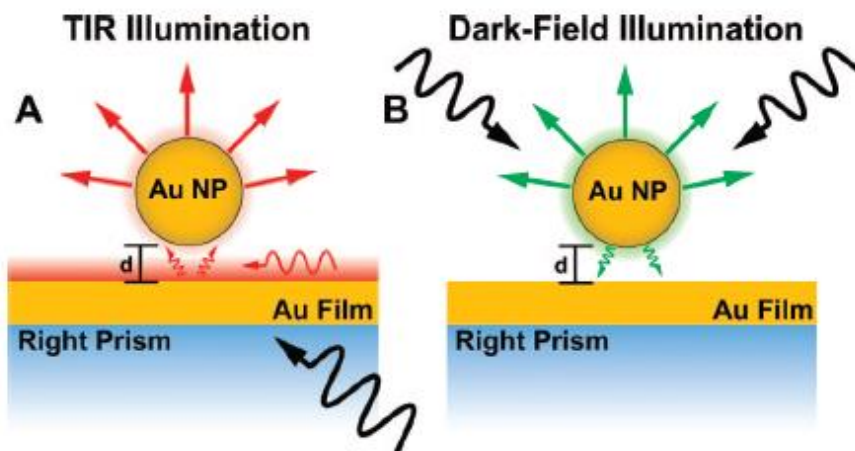


**Figure 2.30: Schematic of a) total internal reflection method and b) dark-field method <sup>(110)</sup>.**

Firstly, using just the dark field illumination, Mock *et al.* found a significant red-shift of over 100 nm for the particle supported on the gold film compared to one simply supported in a dielectric, as seen in Figure 2.31a. As mentioned previously, this is due to the increased hybridisation between the particle and the metallic substrate, compared to its dielectric equivalent. On the other hand, the results when comparing illumination method and separation distance from the film are much more complex due to the intricacies of each and the interaction they have on one another. For example, when the particle is in contact with the substrate, the characteristic dipolar nature of the resonance is found to be normal to the substrate, indicated by a doughnut shape to the point spread function intensity. As it moves away however, the horizontal dipole parallel to the substrate returns, owing to reducing coupling. Interestingly, it was found that this transition occurs slower for the total internal light set-up than for the dark-field illumination, and is also red-shifted in comparison. This difference has its basis in the presence of the SPP mode of the substrate. To elaborate, the transition is slower with the total internal reflection illumination as the SPP mode is excited and decays away from the substrate at a slower rate than that of the evanescent fields, therefore enabling the particle to couple to the substrate at increased distances.

Alternatively, the red-shift seen can be understood better by studying the scattering spectra at different separation distances for each illumination method, as shown in Figure 2.31b-c. With dark field illumination, a similar result is found to that of other literature whereby a gradual red-shift occurs with decreasing separation from the film. When using the total internal reflection method however, this relationship is only found for small separations. At larger distances over around 10 nm, the resonance red-shifts again. They conclude this is due to the slower decaying SPP fields predominately becoming the dominant source of the nanoparticles excitation at the larger separations. This effectively allows the confined SPP mode to scatter to the far field and be detected. As this mode is red-shifted in comparison to that of the particles LSPR, due to the thicker dielectric spacer used having a greater impact on its spectral shift, this therefore explains the red-shift seen.

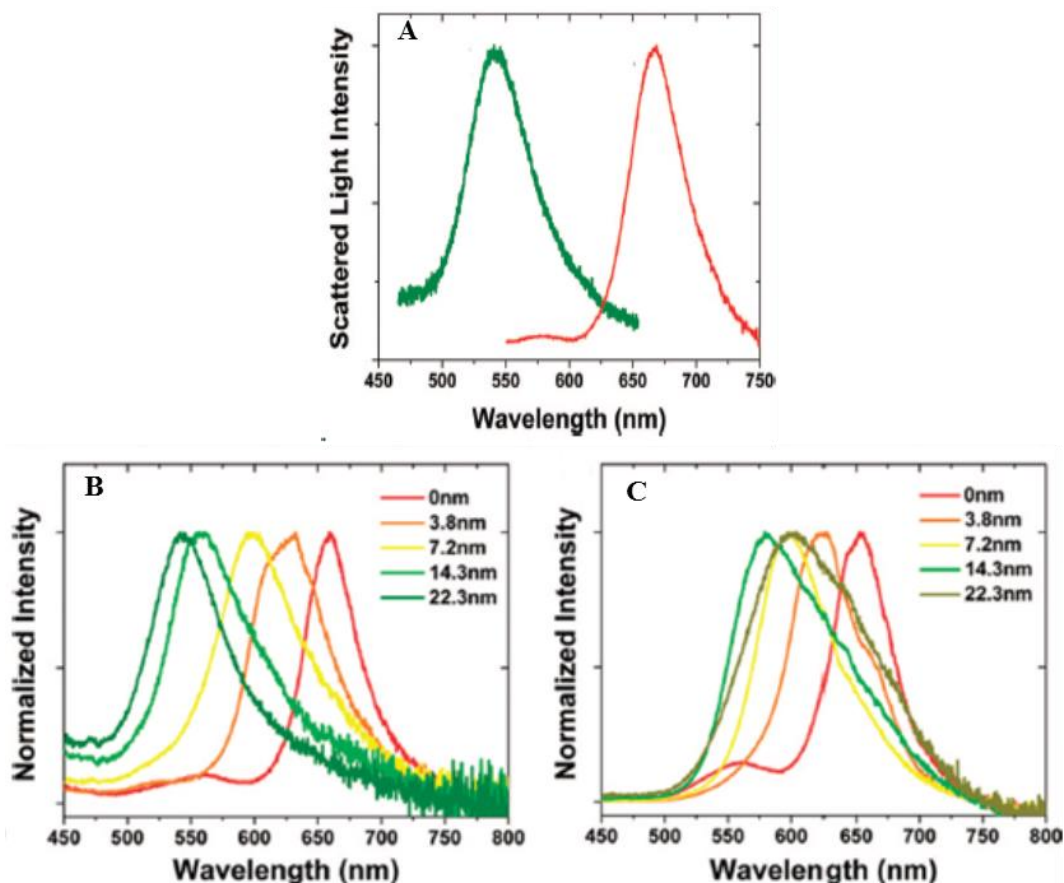
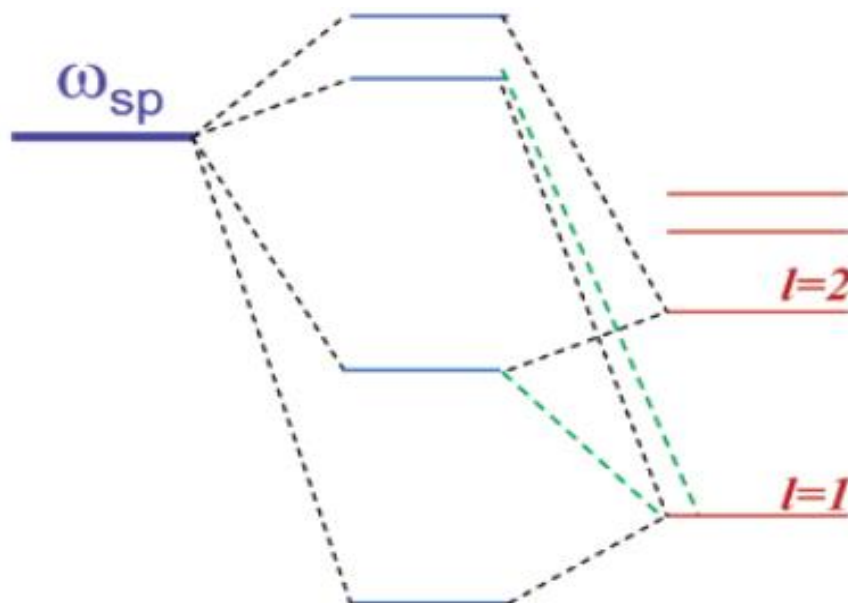


Figure 2.31: Scattering spectra for gold nanoparticles, a) directly supported on a gold film (red curve) compared to a dielectric (green curve), b) using dark-field illumination method with the nanoparticle a distance above the gold substrate, and c) as with b but using the total internal reflection illumination method thereby exciting both LSPR and SPP <sup>(110)</sup>.

From these findings it is clear to see that a metallic substrate's interaction with a nanoparticle is more complex than that of a dielectric due to the enhanced hybridisation and the ability to simultaneously excite both plasmonic modes of the nanoparticle and the substrate. The description of these interactions for various substrate and nanoparticle configurations therefore often requires complicated mathematics or in-depth numerical solutions. Despite this, Norlander and Prodan <sup>(111)</sup> developed a relatively simplistic theory capable of giving insight into these structures, known as the plasmon hybridisation model. This approach is analogous to the widespread molecular orbital theory whereby atomic orbitals hybridise to form molecular orbitals, however, it instead addresses the hybridisation between the plasmonic modes of various nanostructures.

The principle of the plasmon hybridisation models is to deconstruct the plasmonic resonances of complex nanostructures into a series of plasmonic resonances for its much simpler constituent nanoparticles, whereby hybridisation between these describes the overall interaction and the energy at which they occur. To achieve this it is assumed the conduction electrons are treated as a charged incompressible fluid on top of a rigid, uniformly distributed, positive charge, which represents that of the fixed ion cores. The plasmon modes are then self-sustained deformations of this fluid, which due to being incompressible, only leads to the presence of surface charge on the nanoparticle. Furthermore, retardation effects are neglected therefore allowing the dynamics of the charges to be determined via Coulomb interaction. Using this method, the coupling of the individual plasmons can be viewed in the same manner as that for the molecular orbital theory, whereby the structure is comprised of low energy symmetric (bonding) modes and high energy anti-symmetric (anti-bonding) modes.

Initially this theory was applied to multi-layered nanoshells with hybridisation of the plasmons between each shell <sup>(111)</sup>, however since then this has also been expanded to nanoparticles above metallic surfaces <sup>(112)</sup>, as discussed below. Figure 2.32, shows the schematic energy level diagram for a nanoparticle above a metallic substrate. Here  $\omega_{sp}$  relates to the plasmon energy of the flat substrate whereas the opposite nodes are for that of the spheres plasmons of angular momentum  $l$  (higher order modes).



**Figure 2.32: Schematic energy-level diagram showing the plasmon hybridisation principle for a metallic substrate plasmons interacting with the plasmons of a gold sphere. The green lines represent hybridisation between plasmons of different angular momentum  $l$  <sup>(112)</sup>.**

It can be seen that for each angular momentum of the spheres plasmons, an interaction occurs with the substrate with a resultant splitting of the modes into both low energy bonding modes and high energy anti-bonding modes. This indirectly accounts for the coupling between the different plasmonic modes of the sphere.

Norlander and Prodan<sup>(112)</sup>, used this plasmon hybridisation model to investigate how a sphere interacts with a substrate depending on the plasmon energy of the substrate and on the separation distance between the two. For an infinite plasmon energy of the substrate, the results match that exactly of the image charge method whereby the sphere is able to couple with its image and the azimuthal symmetric plasmonic modes of its image. As already seen, this leads to a red-shift with decreasing separation which occurs faster at small distances due to coupling of the higher order modes. This is very similar to the case of a nanoparticle dimer, as discussed in the following section. Alternatively, when the substrate has a plasmon energy only slightly higher than that of the sphere, it was found that this red-shift occurs at a greater separation distance due to the additional hybridisation between the plasmonic modes of the substrate and those of the nanoparticle. Finally, when the substrate has a lower plasmon energy than that of the nanoparticle, as could well be the case with certain metals, the opposite occurs whereby a blue shift in the nanoparticles plasmonic modes is found. These results highlight the complex hybridisations of plasmonic modes that may occur in nanostructures, and signify the importance that a substrate can have on their plasmonic properties.

## 2.8 Effect of Coupling

Focus will now be moved onto the issue of particle-particle coupling. In many respects this shares a lot of the similarities with that of particle-substrate coupling, and therefore it is useful to draw upon theories and relationships from the previous section. The largest difference however is both particles may also support localised plasmon modes that can interact and hybridise with each other. I will begin by discussing the theory behind particle-particle coupling, including that of the plasmon hybridisation theory, before comparing this with experimental findings and examining the near field enhancements. Lastly, the effect of combining these couplings using arrays of particles will be examined, with particular attention given to the case of periodic nanorod arrays, as in the focus of this thesis.

## 2.8.1 Coupling in Nanoparticle Dimers

The simplest case of plasmonic coupling is that of a sphere dimer. Theoretically, this can once again be described using the plasmon hybridisation theory, as achieved by Norlander *et al.* <sup>(113)</sup> and seen within Figure 2.33a. Each nanoparticle is deconstructed into its individual modes of different angular momentum  $l$ , and hybridise with the other nanoparticles plasmonic modes to form both a low energy “bonding” mode and a high energy “anti-bonding” mode. For the case of the dipole mode ( $l=1$ ), in the bonding scenario each nanoparticle has its dipole aligned in the same direction thereby resulting in an overall large induced dipole over the dimer. This dipole would radiate strongly to the far-field leading to it easily being detected and to it therefore being described as a bright mode. On the other hand, the anti-bonding mode has the dipoles of each nanoparticle being aligned in opposite directions, cancelling each other out, and leading to no net dipole over the dimer. This mode would therefore be unable to radiate to the far-field leading to it being labelled as the dark mode <sup>(114)</sup>, as shown in Figure 2.33b..

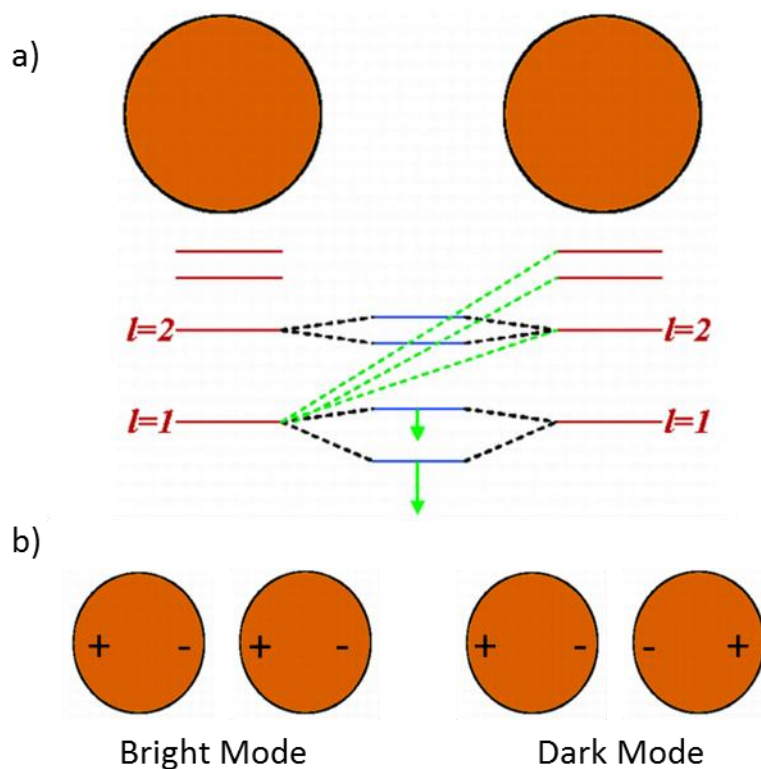


**Figure 2.33:** a) Schematic of the plasmon hybridisation theory for a nanoparticle dimer whereby the plasmonic modes of each nanoparticle are shown to hybridise with the others giving rise to bonding and anti-bonding modes. At small separations, mixing between modes of different angular momentum will also occur (green lines), as shown here for the dipole mode ( $l=1$ ) interacting with those of higher order, leading to a greater shift in energy <sup>(113)</sup>. b) Schematic representation of the  $l=1$  bright and dark modes for a sphere dimer.

In addition, when the nanoparticles of the dimer are in very close proximity there also arises coupling between the modes of different angular momentum. This results in different degrees of shifts in the energy of plasmonic modes, as represented by the green lines and arrows in Figure 2.33. Norlander *et al* <sup>(113)</sup> observed that these shifts are not symmetric, as found with larger separations, but instead the bonding mode develops a greater shift to lower energies (red-shift), whereas the anti-bonding modes blue-shift is somewhat reduced.

Lastly, a comparison between the polarisation direction of the light shows that when the light is polarised along the inter-particle axis, the results and configurations as described above occur. On the other hand, when the light is polarised perpendicular to the inter-particle axis, the dipoles are ordered in the opposite way to that previously described. This means that the bright plasmon mode, whereby the dipoles are aligned symmetrically, is instead allocated to the anti-bonding coupling mode (similar to a  $\pi^*$  bond in molecular orbital theory) and therefore blue shifts with decreasing separation <sup>(113)</sup>. Alternatively, this red or blue-shift with polarisation can be predicted by studying the induced local field for each scenario, as seen in Figure 2.34. For example, when the polarisation is along the inter-particle axis, the induced field occurs in the same direction therefore acting against the restoring field and red-shifting the resonance. On the other hand, when the polarisation is perpendicular to the inter-particle axis, the induced field acts in the opposite direction and therefore supports the restoring forces giving rise to a blue shift <sup>(92)</sup>.

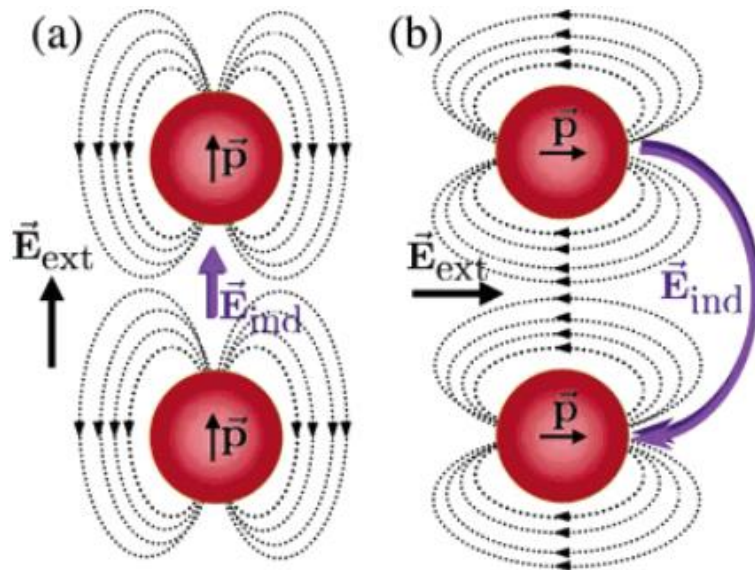


**Figure 2.34: Induced field model for a dimer of nanoparticles with polarisation a) parallel to the inter-particle axis, and b) perpendicular to the inter-particle axis <sup>(92)</sup>.**

Aside from the plasmon hybridisation theory, Jain *et al.* <sup>(115)</sup> highlights another similar theory capable of explaining the interactions in a nanoparticle dimer is that of the exciton coupling theory, whereby plasmons are represented as excitons <sup>(116)</sup>. This theory was initially developed to describe the effects seen when molecules agglomerate or dimerise, with associated strong energy shifts and splitting of the absorption bands into lower energy and higher energy levels compared to that of a monomer. The degree of this energy shift,  $J$ , is then determined from the interaction energy between the dimer chromophores, approximated by Coulombic interaction between each particle's transition dipole moments <sup>(115)</sup>:

$$J = \frac{1}{4\pi\epsilon_0} \frac{|\mu|^2}{n_a^2 R_{12}^3} \kappa \quad (67)$$

where  $\mu$  is the transition dipole moment,  $n_a$  is the refractive index of the medium,  $R_{12}$  is the distance between the dipole centres, and  $\kappa$  is the orientation factor given by  $\kappa = \cos\theta_{12} - 3\cos\theta_{1R}\cos\theta_{2R}$ . Here  $\theta_{12}$  represents the angle between the two nanoparticle dipoles, whereas  $\theta_{1R}$  and  $\theta_{2R}$  represent the angle between the respective nanoparticle dipole and the inter-particle axis.

The similarities between this method and the plasmon hybridisation model are clear to see, and the associated results match qualitatively very well. For instance when the light is polarised along the inter-particle axis of a symmetric dimer, the interaction energy is negative (as  $\kappa=-2$ ), therefore stating the dipoles are attractive, and an associated red-shift is seen. Alternatively, for light polarised perpendicular to the inter-particle axis, the interaction energy is positive ( $\kappa=1$ ), and therefore the dipoles are repulsive with a blue-shift predicted. The main difference however between these two models, as explained by Jain and El-Sayed <sup>(117)</sup>, is that the exciton coupling model only treats the dipolar modes and ignores those of higher order. As we have already discussed, at small separations the coupling between modes of different order become increasingly important. This results in a faster shift in energy predicted with the hybridisation model than with that of the exciton coupling model, and an improved agreement with numerical simulations <sup>(117)</sup>.

Now considering the case of nanorods instead of spheres, both the plasmon hybridisation theory and exciton coupling theory once again allow us to predict the associated energy shifts from coupling. In this scenario, due to the reduced symmetry in nanorods, orientation is

particularly important. Although many different orientations of a nanorod dimer is possible, each at varying angles to the other, here for conciseness only the two main configurations are discussed, namely end to end nanorods and side by side (parallel) nanorods. Each of these however also has its two polarisation dependent modes, namely the previously described transverse and longitudinal modes.

Firstly, for end to end nanorods, the scenario is similar to that for spherical dimers. When the light is polarised along the nanorods length, thereby exciting the longitudinal mode, the bonding mode ( $\sigma$ ) is the bright mode with symmetrical orientation of the nanorods dipoles, and is consequently red-shifted compared to that of an isolated rod. Alternatively, the anti-bonding mode ( $\sigma^*$ ) is the dark mode, and occurs blue shifted from that of the isolated rod. On the other hand, for a side by side arrangement, again using light polarised so that it excites the longitudinal modes, the opposite is true. Here the bonding mode ( $\pi$ ) with anti-symmetric dipoles is the red-shifted dark mode, whereas the anti-bonding mode ( $\pi^*$ ) is the blue shifted bright mode <sup>(118)</sup>. This can be seen clearer in Figure 2.35 below.

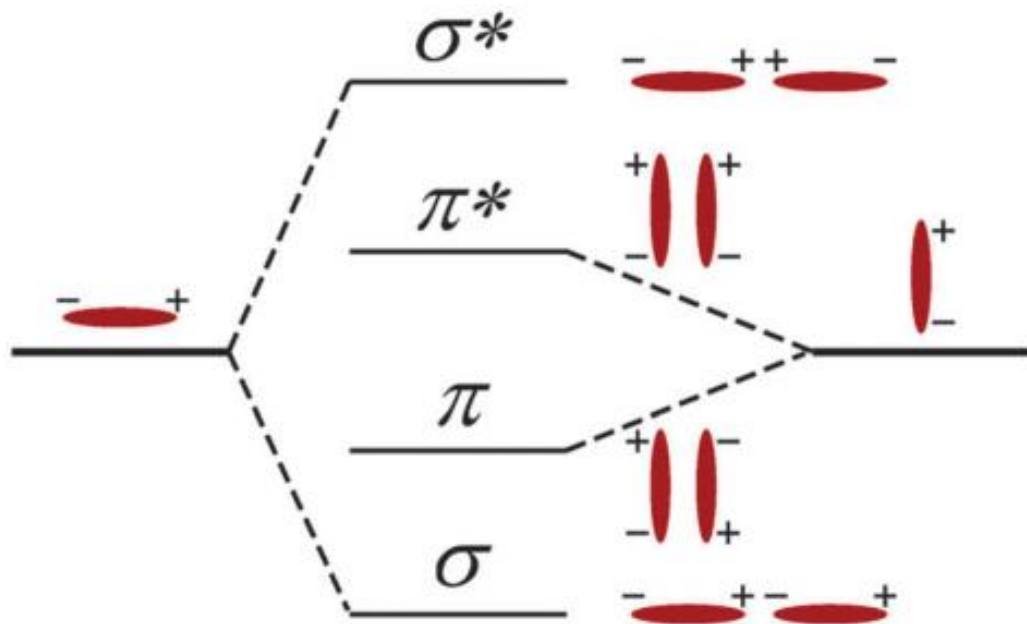


**Figure 2.35: Exciton coupling diagram showing the coupling of the a nanorod dimers longitudinal modes for both an end to end and side by side orientation <sup>(115)</sup>.**

Considering the same orientations, but now with the polarisation of the light across the nanorods width (transverse mode excitation), different trends arise. For an end to end arrangement, Willingham *et al* <sup>(119)</sup> explains the dipole modes hybridise with modes of higher

order leading to a blue shift. This however is significantly weaker than for the longitudinal polarisation. Similarly, for a side by side arrangement, the transverse dipole mode will also hybridise with other modes, but this time leading to a red-shift. This is stronger than in the previous case due to a larger area for the plasmon modes to couple over, however, is still weaker than that seen for longitudinal polarisation.

Although the above theoretical models are able to approximate the energy shifts of various coupled nanostructures fairly well, numerical simulations and experimental work studying the particle-particle coupling is also crucial. Jain *et al.* <sup>(115)</sup> used DDA simulations to model nanorod dimers in a side by side and end to end arrangement under both longitudinal and transverse polarisation, as seen in Figure 2.36.

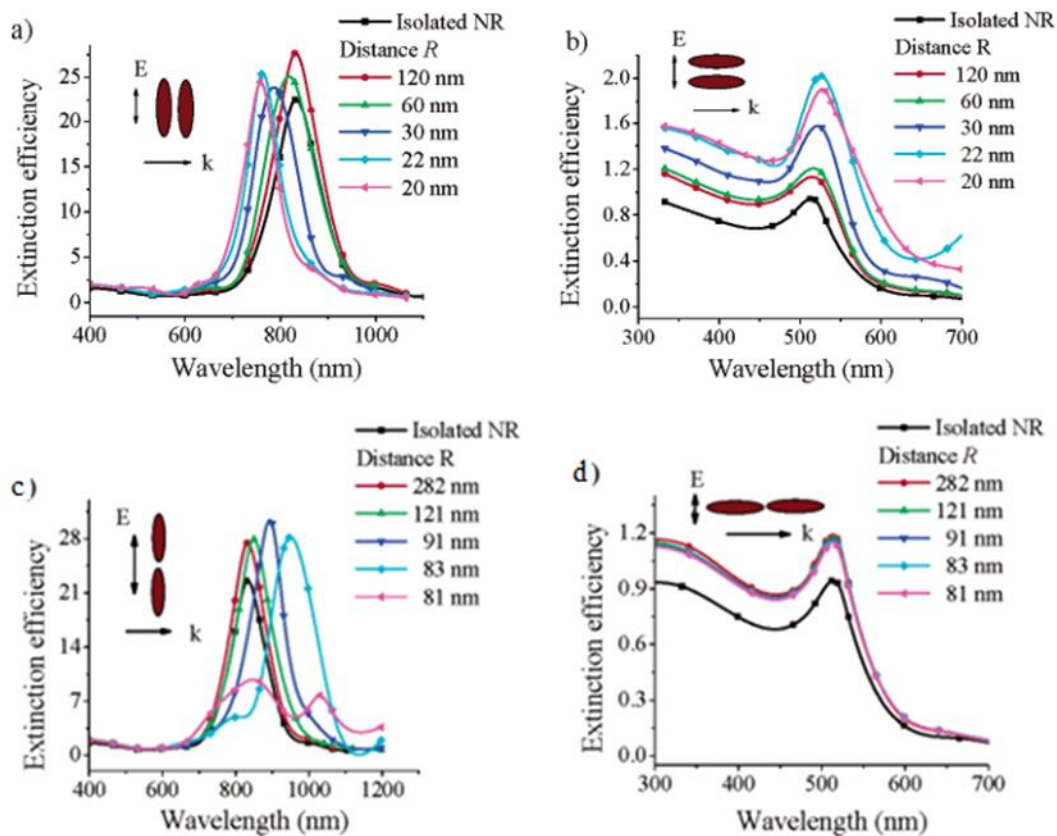
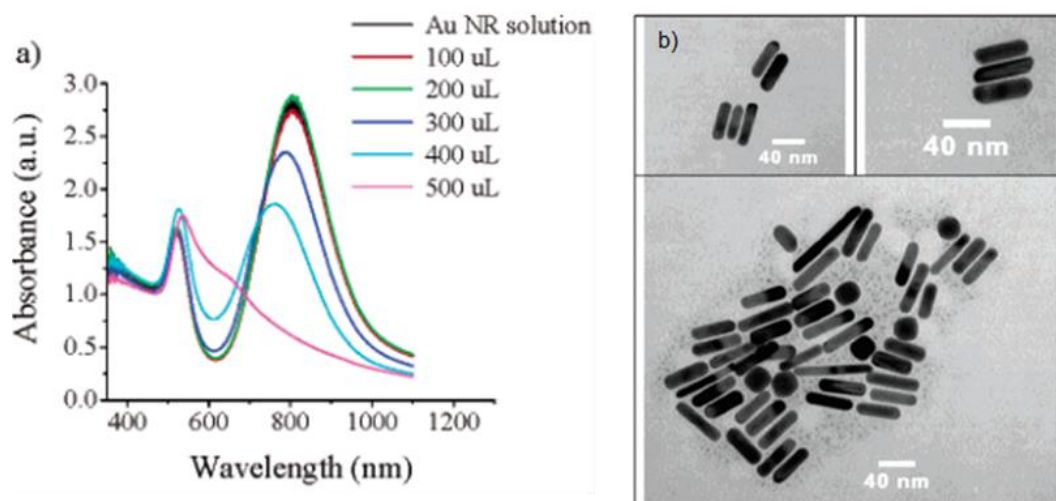


Figure 2.36: DDA simulations of AR=4 nanorod dimers showing the extinction efficiency for a side by side arrangement with a) longitudinal mode excitation and b) transverse mode excitation. Alternatively for an end to end arrangement with c) longitudinal mode excitation and d) transverse mode excitation <sup>(115)</sup>.

Starting with the side by side arrangement, it can be seen that as predicted in the theoretical models, a decreasing separation of the nanorods leads to a fairly large blue shift for the longitudinal mode and a small red-shift for the transverse mode. This shift occurs quicker at smaller separations due to stronger coupling between the rods. Alternatively for the end to end configuration, a good match with theory is once again found. The longitudinal plasmon is red-shifted with decreasing separation, whereas the transverse mode has perhaps a slight blue shift, however this is very weak due to the large separation of the dipoles. Furthermore, when the individual rods in a dimer are of different aspect ratios, it was found that with both orientations the dark mode no longer has a zero net dipole and therefore it becomes visible, albeit as a weak peak in the spectra.

One possible result that casts doubt on these DDA simulations is that the amplitudes of the extinction efficiency for longitudinal polarisation remain fairly constant at different separation distances. It was found in their own experimental work <sup>(115)</sup> however, that adding sodium citrate to a gold nanorod solution predominantly results in aggregation of the nanorods in a side by side arrangement. Consequently, they note a blue shift in the UV-Vis longitudinal mode and a decrease in the absorbance with increasing concentrations of sodium citrate. Additionally, a slight red-shift and increase in the transverse mode is found, as seen in Figure 2.37.



**Figure 2.37: a) UV-VIS of gold nanorods with different sodium citrate concentrations leading to aggregation in a side by side manner as shown in the TEM images in b) <sup>(115)</sup>.**

The results of Lee *et al.* <sup>(120)</sup> support this finding of a decrease and blue-shift in the absorption of the longitudinal mode and an increase and red-shift for the transverse mode when in side by side orientation. Using FDTD simulations they showed that this decrease in the amplitude is amplified with the addition of more interacting nanorods, and therefore an increased coupling strength (Figure 2.38a). Additionally, they concluded the side by side arrangement led to cancellation of the radial component of the electric fields due to destructive interference between the rods therefore causing no hot-spot to be found in the gap (Figure 2.38b-d).

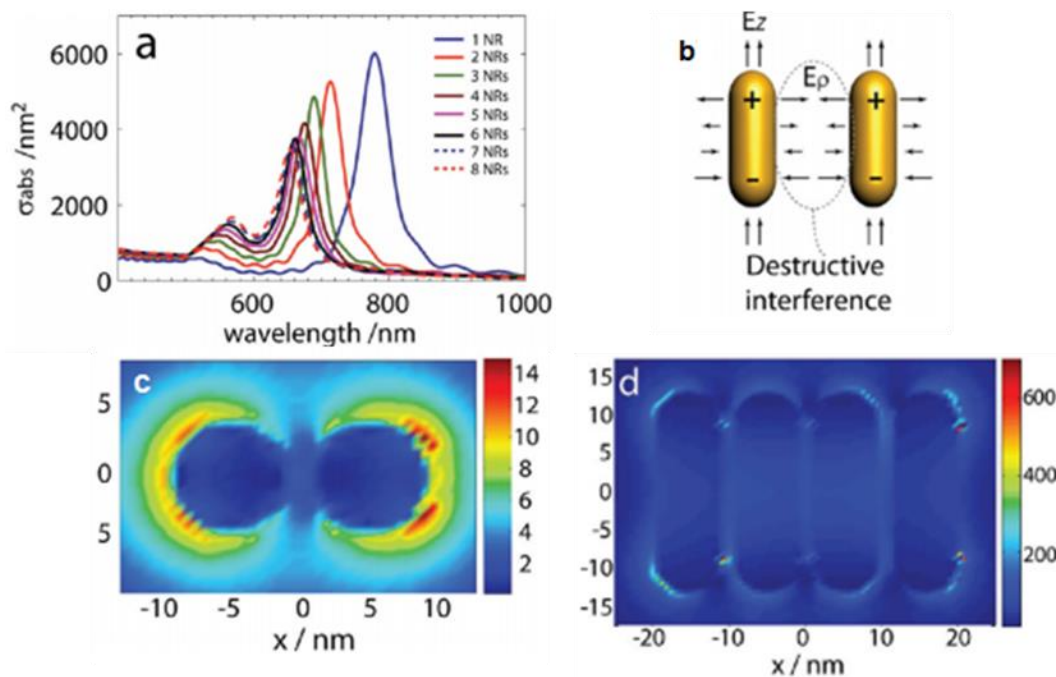


**Figure 2.38:** a) FDTD simulations of gold nanorods of varying number interacting in a side by side arrangement leading to a blue-shift and decrease in amplitude with increasing number of rods. b) Schematic of destructive interference between the radial E-Field components of two side by side rods with accompanying electric field intensity profiles from c) above for two rods and d) side on for four rods <sup>(120)</sup>.

In contrast, for an end to end arrangement of the nanorods, Funston *et al.* <sup>(74)</sup> showed the opposite to be true. Using DDA simulations, a red-shift and increase in the extinction efficiency was found for nanorod dimers with decreasing separation. They also compared these with experimentally derived scattering spectra using a dark-field microscope at very close separations where the nanorods are almost touching (~1 nm). They found that the DDA simulations failed to give accurate results at the very small separations, attributed to the array of point dipoles having a spacing of 1-2 nm, and therefore not being able to resolve these

separations accurately. Additionally, they concluded that the associated shifts with spacing can only be fitted accurately with an exponential decay function when the spacing to rod length ratio is greater than 0.09. At ratios less than this, it is believed that the higher order modes interacting with each other led to greater shifts, as predicted by the previously described plasmon hybridisation theory.

The importance of the orientation and spacing of nanorods is not just related to the spectral shifts but also due to the ability to generate greatly enhanced electric field strengths within the gaps. N’Gom *et al.* <sup>(121)</sup> performed EELS along with energy-filtered transmission electron microscopy (EFTEM) to map the coupling between two gold nanorods in a configuration close to an end to end arrangement. Additionally, this was compared with DDA simulations and the results for isolated particles, as seen in Figure 2.39. An increase in the intensity of the longitudinal peak was seen for the coupled rods, with the greatest EELS intensity arising from within the inter-particle gap. Furthermore, by comparing the decay of both the EELS intensity and the electric field within the DDA simulations, a good agreement between the two was noted, therefore allowing the authors to conclude that EELS is capable of imaging the electric field enhancements of plasmonic nanoparticles with improved spatial resolution. It is important to note however, that differences may occur when exciting coupled nanoparticles with an electron beam, as in EELS, compared to that with light excitation. This is due to light excitation being uniform across the structure therefore allowing the charge distributions to move freely. On the other hand, in EELS, when the beam is located within the gap for instance, it may cause alterations to the coupled nanorods charge distribution by repelling negative charges. This has been shown to result in a slightly blue-shifted mode compared to that with optical excitation <sup>(122)</sup>.

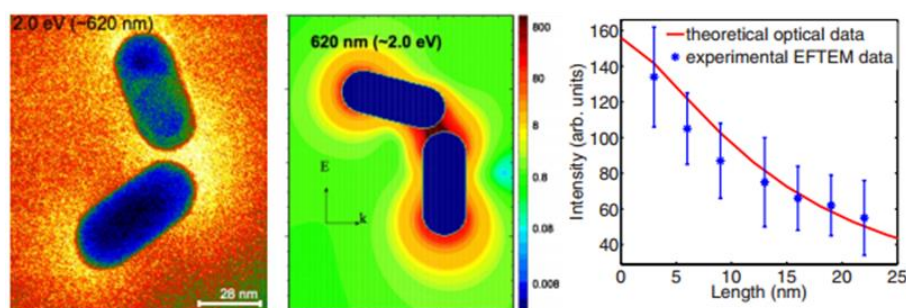


**Figure 2.39: EFTEM image of coupling for the longitudinal mode in an end to end nanorod dimer with a 5 nm gap (left). DDA simulation for the same geometry showing the enhanced E-Fields (middle). Comparison of the plasmon decay between the experimental EFTEM data and the DDA results for the longitudinal mode of a single Au nanorod (right) <sup>(121)</sup>.**

These strong electric field enhancements between the gaps of end to end coupled nanorods have also been found within other works. For instance, Cheng *et al.* <sup>(123)</sup> produced an array of end to end gold nanorods, with a small gap of  $\sim 1.3$  nm between them, by depositing within a porous alumina template. The gaps were filled with 1,4-benzenedithiol molecules, allowing SERS measurements to be taken. The strong coupling between the nanorods led to SERS enhancements of 30 times compared to that for a single rod, with the highest enhancements seen when the length of the two rods are the same. Additionally, Liu *et al.* <sup>(124)</sup> performed FEM simulations to model the coupling of two short nanorods on a quartz substrate with varying gap size. It was found that at large gap sizes the particles acted like individual nanoparticles, however, as the distance decreased the field strength drastically increased leading to enhancements of over 80 times. In fact they concluded that the field enhancement is roughly inversely proportional to the gap size, therefore the most efficient way to increase the electric field enhancement is to decrease the particle spacing.

Despite the prediction of these very strong enhancements at small gap sizes, once again care must be taken to include the effects of non-locality, which were not considered in the examples above. For instance, Wiener *et al.* <sup>(125)</sup> developed a 3D EELS FEM simulation of two gold nanoprisms joined by a thin 0.5 nm wide section. Under local conditions there is the presence of an enhanced electric field around this bridge (Figure 2.40b), however when taking non-local conditions into account, this field strength is reduced by a factor of two (Figure 2.40c).

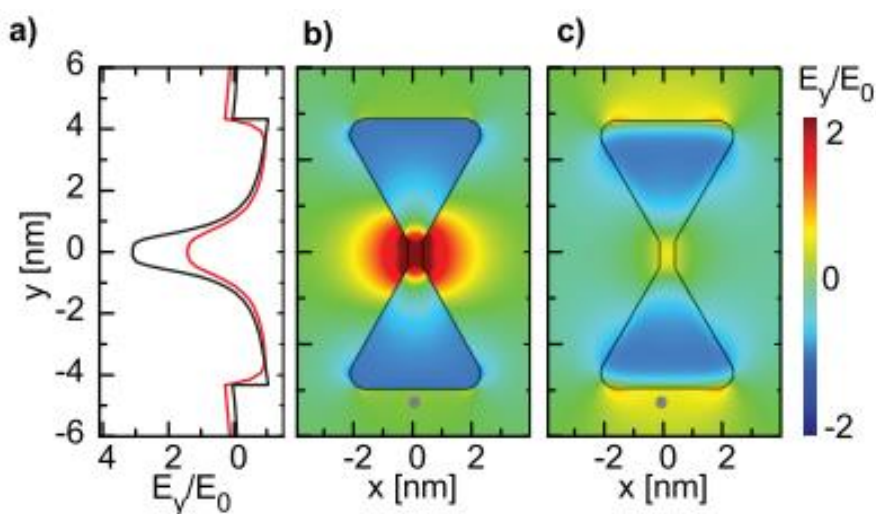


**Figure 2.40: Simulated electric field profiles for the connected gold nanoprisms using local (black) and non-local (red) conditions. b) Electric field maps using local conditions and c) non-local conditions clearly showing the reduction in field strength at the small bridge <sup>(125)</sup>.**

As already mentioned within this section, the addition of more closely spaced nanoparticles leads to an increase in the coupling strength. With this in mind, the plasmonic properties of arrays have become increasingly important due to the high degree of coupling that can be achieved. Additionally, if produced in a regular nature, the arrays allow tuning of the plasmonic properties with potentially excellent control and reproducibility. The plasmonic properties of these arrays and more specifically nanorod arrays will now be discussed.

### 2.8.2 Coupling in Nanoparticle Arrays

Firstly, a regular nanoparticle array where the spacing between the particles is so large that near-field coupling cannot occur may still undergo alterations to its optical properties due to its periodic structure. This comes from coherent scattering between the particles over a long range. For instance, Haynes *et al.* <sup>(126)</sup> fabricated periodic arrays of gold and silver nanoparticles of 200 nm in diameter, and varied the centre to centre inter-particle spacing between 230 nm and 500 nm. They found blue-shifts in the extinction as the spacing was reduced with the largest shift seen at a spacing similar to around half the resonant wavelength, attributed to radiative dipolar coupling. Similarly, Smythe *et al.* <sup>(127)</sup> fabricated horizontally aligned arrays of nanorods with varying control over both the end to end gap and the side by side gap. They found that the fields radiating from neighbouring nanoparticles were capable of coupling either constructively or destructively depending on the spacing and orientation. For the end to end spacing, a constructive interference led to a blue-shift in the resonant wavelength whereas a destructive interference led to a red-shift. On the other hand, the opposite was found for a side by side orientation.

Despite these long range effects, the most interesting features of nanoparticle arrays occurs when the spacing is small enough so that the particles near-fields may couple. In this scenario the plasmonic modes of the individual nanoparticles are capable of combining into a collective coupled mode with unique properties. One example of this is with the longitudinal mode of vertically aligned nanorod arrays, as in the focus of this work, and discussed hereafter. It is noteworthy to mention that the fabrication of these arrays is similar for all the following works, and is typically achieved via electrodeposition of metals into either bulk or thin-film porous alumina. This process can read about in more detail in Chapter 3, however it should be noted that good control over the spacing, aspect ratio, and diameter of the nanorods is achievable, thereby probing the specific coupling interactions.

One of the first works examining the optical properties of these vertically aligned nanorod arrays is that by Foss *et al.* <sup>(128)</sup>. They showed that transmission through the array was possible by depositing gold into the alumina pores and onto a silver backing. This silver was then selectively etched resulting in a gold nanorod/alumina composite material that was transparent in the visible and UV regions, as seen in the TEM image of Figure 2.41. They showed that performing UV-Vis spectroscopy on this composite, with normally incident light and for nanorods with aspect ratios of one and six, resulted in the plasmon peak being found at a wavelength of  $\sim 560$  nm, therefore relating to that of the transverse peak. No longitudinal mode is seen due to normally incident light being used, therefore the electric field cannot excite over the long axis of the rods. In this work, and in follow up papers by the same authors <sup>(129, 130)</sup>, the effects of both the nanorods AR and diameter were studied. As the AR of the rods increases, the mode blue-shifted slightly, whereas increasing the diameter leads to a red-shift. Although these findings fit qualitatively well with the theory for isolated nanorods, the densely packed nature of the particle array led the authors to instead use an effective medium theory whereby particles did not have to be treated as isolated, known as the Maxwell-Garnett theory <sup>(131)</sup>.

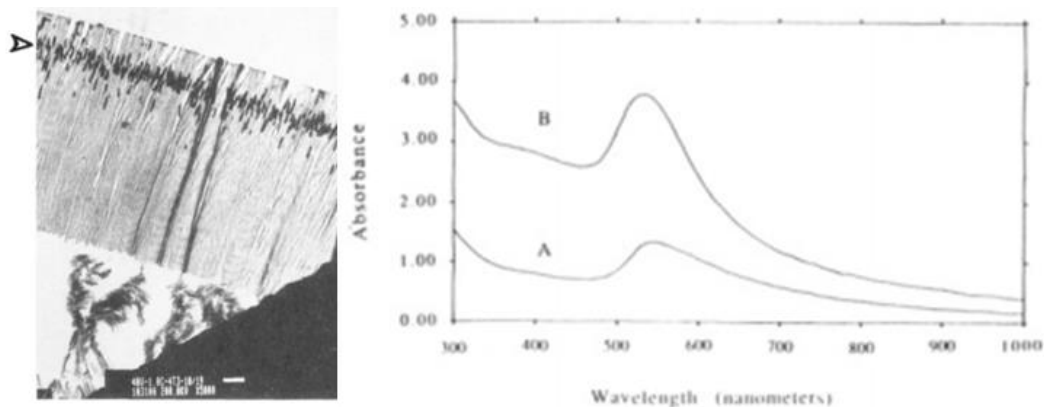


**Figure 2.41: (Left) TEM image of the nanorod / alumina composite material, where the arrow highlights the embedded gold nanorods. (Right) Absorbance spectra taken at normal incidence for gold nanorod/ alumina composite with (A) AR of 1, (B) AR of 6 <sup>(128)</sup>.**

The Maxwell-Garnett theory is based around the assumption that a composite material, such as the gold nanorods embedded in an alumina matrix, may be described by a complex effective dielectric constant  $\tilde{\epsilon}_c$ . This is calculated from the complex dielectric constants of the embedded metal nanoparticles,  $\tilde{\epsilon}_m$  and that of the surrounding material  $\tilde{\epsilon}_0$ , as seen in equation (68).

$$\left(\frac{\tilde{\epsilon}_c - \tilde{\epsilon}_0}{\tilde{\epsilon}_c + 2\tilde{\epsilon}_0}\right) = f_m \left(\frac{\tilde{\epsilon}_m - \tilde{\epsilon}_0}{\tilde{\epsilon}_m + 2\tilde{\epsilon}_0}\right) \quad (68)$$

Where  $f_m$  is the volume fraction of the metal in the composite material and must be significantly smaller than that of the host material <sup>(130)</sup>. Additionally, the factor 2 in the denominator of the above equation is known as the screening parameter, and is geometrically dependent. For a spherical geometry of the particles, this is given the value of 2, however for the case of vertically aligned nanorods with their long axis parallel to the incident light this is typically altered to 1 <sup>(129)</sup>. It is noted here however that the Maxwell-Garnett theory is a quasi-static approach where the nanoparticles are assumed infinitesimally small compared to the wavelength of the incident light. To account for this assumption and apply the theory to relatively larger particles, Foss *et al.* <sup>(129)</sup> adapted the screening parameter to become a complex wavelength dependent term that encompasses the increased scattering from larger particles.

Following this, the calculated complex dielectric constant of the composite material may then be converted to the refractive index ( $n_c$ ) and extinction coefficient ( $k$ ), and used to determine the total transmittance of the material using:

$$T_{\text{tot}} = \left[1 - \frac{(n_c - 1)^2 + k_c^2}{(n_c + 1)^2 + k_c^2}\right]^2 \exp(-4\pi k_c d/\lambda) \quad (69)$$

where  $d$  is the film thickness and  $\lambda$  is the wavelength. Using this approach, good agreement was found between the experimental and calculated results, particularly for smaller radius particles whereby the quasi-static validity of the theory was better achieved <sup>(130)</sup>. Despite this, by using only normally incident light, the above work failed to probe the particularly interesting features related to the longitudinal mode of the nanorods. This was corrected in the work of Atkinson *et al.* <sup>(132)</sup> whereby using a thin film alumina approach, gold nanorods supported on a 5 nm thick gold substrate, followed by a 7 nm Ta<sub>2</sub>O<sub>5</sub> adhesion layer and finally a glass slide were fabricated, as seen in Figure 2.42. Transmission measurements were then taken at varying angle of incidence and light polarisation.

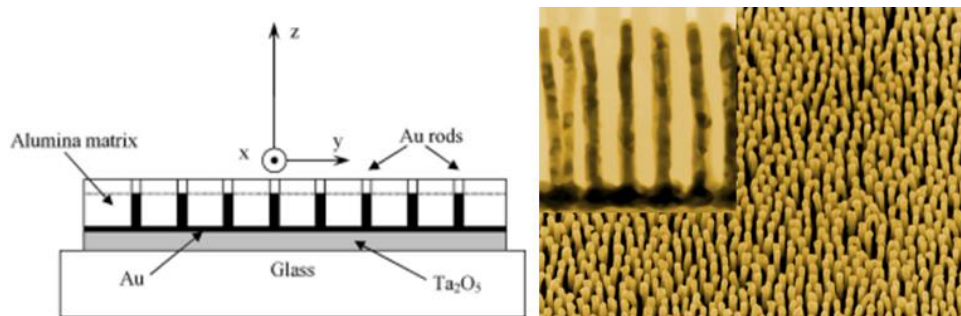


Figure 2.42: (Left) Schematic diagram of nanorod array in alumina <sup>(132)</sup>, (right) SEM image of gold nanorods after removal of alumina template, inset is a TEM cross section of the arrays in the alumina <sup>(133)</sup>.

Firstly, for nanorods of 20 nm diameter, a spacing of 40 nm and a length of 330 nm (AR=16.5), it can be seen that under s-polarised light at varying angles of incidence, the results matched those of Foss *et al.* reasonably well in that a single peak is observed around 520 nm relating to that of the transverse mode (Figure 2.43a). In contrast, for p-polarised light, a second peak appears at a wavelength of around 700 nm that increases in strength at higher angles of incidence (Figure 2.43b). At normal incidence however, this peak vanishes, therefore alluding that the nature of the peak is related to the longitudinal mode due to it requiring a degree of polarisation over its long-axis. The peak therefore also isn't seen with s-polarised light at any angle of incidence, as the polarisation of the light remains normal to the long-axis. Furthermore, this peak at longer wavelengths can also be seen to blue shift slightly with increasing angle of incidence.

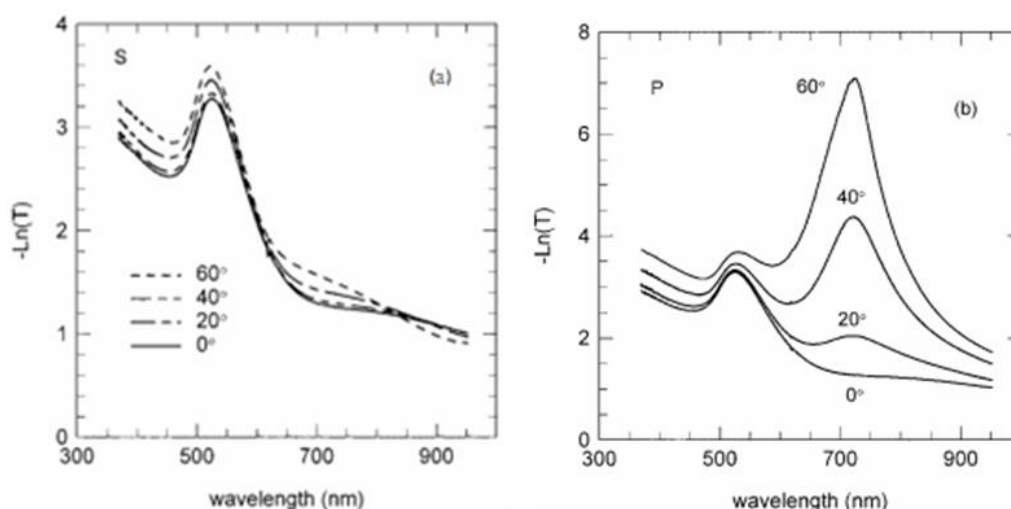
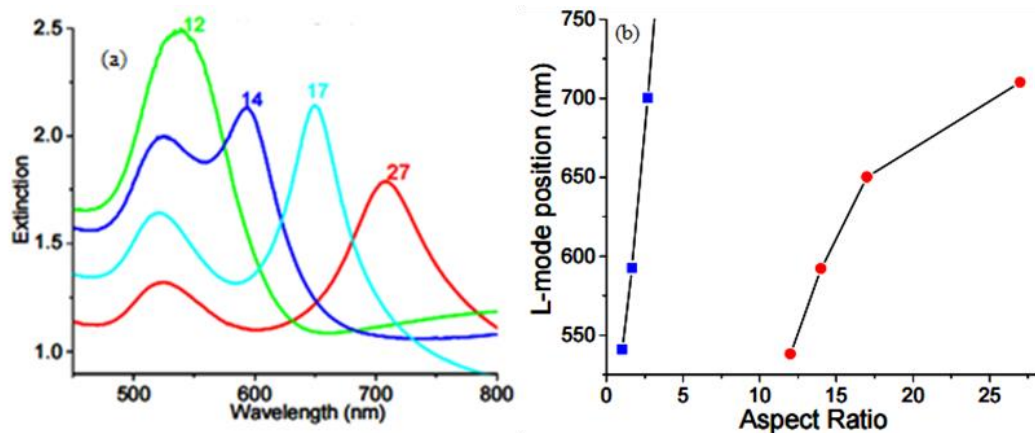


Figure 2.43: Transmission data for a gold nanorod array of AR=16.5 at varying angle of incidence with (a) s-polarised light, and (b) p-polarised light <sup>(132)</sup>.

The first behaviour is consistent with the theory of an isolated nanorods longitudinal mode, however, its variability with angle of incidence is in contrast. A later paper by Wurtz *et al.* <sup>(133)</sup> investigated this in more detail and found that the angular dispersion of the arrays depends on the effective inter-rod distance, defined as  $\bar{n}d$ , where  $\bar{n}$  is the average refractive index of the host medium and  $d$  is the particle separation. As the effective inter-rod coupling distance decreases, the coupling strength increases and a higher angular dispersion is found.

In addition to this, the arrays dependence on AR was studied due to the well-known feature that an isolated nanorods longitudinal mode shifts to higher wavelengths with increasing AR. Atkinson *et al.* <sup>(132)</sup> and Evans *et al.* <sup>(134)</sup> studied this effect with the results summarised in Figure 2.44.



**Figure 2.44:** a) Extinction spectra for gold nanorod arrays with varying AR embedded in alumina. The incident light is p-polarised at  $40^\circ$  angle of incidence and the centre to centre inter-rod spacing is about 100 nm <sup>(134)</sup>. b) Resonant wavelength of the longitudinal mode with AR for both isolated rods (blue) and nanorod arrays (red) <sup>(133)</sup>.

Both works found that as the aspect ratio increased, a red-shift of the longitudinal peak was seen, therefore fitting with the theory of an isolated rod. In the paper by Atkinson *et al.*, nanorods of varying lengths were grown and the presence of this peak can be seen even at aspect ratios of around 3.75 (*not shown*). They state however that as the nanorod length decreases, the mode blue-shifts and overlaps with that of the transverse mode. Similarly, Evans *et al.* in the later paper kept the nanorod length the same, however varied the diameter and therefore its aspect ratio. They found that at aspect ratios of 12 and less, only one peak was present in the spectra due the mode overlapping with transverse peak. As the AR of the nanorod increased however, the mode red-shifted, moving it away from the transverse peak.

The degree of this shift can be seen in Figure 2.44b for both an isolated nanorod (blue) and that of the nanorod array (red). The most striking feature of this graph is that the resonant wavelength of the nanorod arrays longitudinal mode is significantly altered from that of an isolated rod. With increasing aspect ratio, the longitudinal mode of the isolated rod is seen to quickly red-shift in a linear manner, so much so that by an aspect ratio of 4 it is already moving into the NIR wavelengths. Alternatively, for the nanorod array, only above aspect ratios of 12 does the longitudinal mode appear as a distinct peak. Although this also red-shifts with increasing AR, it occurs at a much slower rate. For example, for an aspect ratio of 27, the mode is still in the visible region with a resonant wavelength around 700 nm. Additionally, this red-shift is seen not to be linear but plateaus towards the higher aspect ratios.

Considering the strong dependence that this mode has on the incident angle, aspect ratio and inter-particle coupling strength, it was concluded that the mode must be somehow related to the longitudinal mode, however, elucidating the exact dependence on the longitudinal mode would require more complex analysis. To aid their interpretation, Atkinson *et al.* <sup>(132)</sup> used the previously described Maxwell-Garnett theory with the added adaption of accounting for the optically anisotropic nature of the nanorod composite by applying it in tensor form. By determining the effective dielectric constants for the principle axes, and consequently converting these to the effective refractive indices ( $n_x$ ,  $n_z$ ), the overall effective refractive index for the array may be found for each polarisation of light ( $n_s$ ,  $n_p$ ). For the case of s-polarised light, which has its electric field always parallel to the inter-particle axis, only the x-component is present, therefore  $n_s = n_x$ . For p-polarised light however, a combination of both the x and the z-components of the effective refractive indices is required for a given angle of incidence ( $\theta$ ), calculated using equation (70). These are then used to determine the transmittance, absorption and reflection of the composite material.

$$n_p = \sqrt{n_x^2 + n_0^2 \sin^2 \theta \left(1 - \frac{n_x^2}{n_z^2}\right)} \quad (70)$$

These calculations resulted in a very good agreement with the experimental data both in terms of the resonance wavelength with AR, and the blue-shift with angle of incidence. Greater insight into this result is found however by plotting the calculated complex refractive index for the nanorod array, as seen in Figure 2.45.

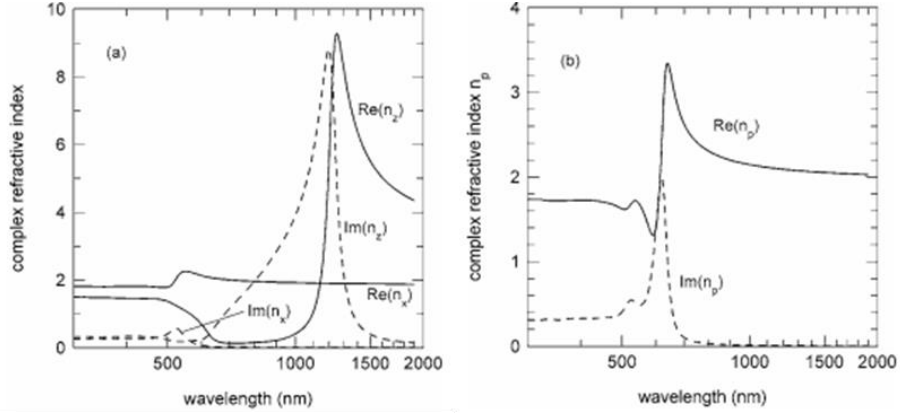


**Figure 2.45: a) Calculated refractive indices for the principal axes x and z for the composite material with 75nm long gold nanorods. b) Effective refractive index for the p-polarised wave within the nanorod array. Both calculations are performed assuming an angle of  $60^\circ$  <sup>(132)</sup>.**

The authors reported <sup>(132)</sup> that the above graphs show a number of distinct features that allow an explanation of the experimental data found. Firstly, studying Figure 2.45a, it can be seen that for the complex refractive indices in the x-direction, a peak is seen around 525 nm. This relates to the transverse mode of the nanorods. A similar peak however is not found around 620 nm, which is the wavelength that the longitudinal mode is seen within the experiments for these 75 nm long nanorods. Instead, at this wavelength the real and imaginary parts of the complex refractive index are seen to be equal, each with comparably low values. As the permittivity is related to the complex refractive index by  $\epsilon_r = n^2 - k^2$  this therefore results in  $\epsilon'_z \approx 0$ . Additionally, considering equation (70), as the values of  $n_z$  are low in comparison to  $n_x$ , this result in a large  $n_p$  value that accounts for the experimental peak (Figure 2.45b).

On the other hand, it is also noted that the real and imaginary z-components are seen to be equal at around 1350 nm, however this time with larger values than that of the x-component. This results in the opposite effect whereby the imaginary component, ( $n_p''$ ), is relatively small and therefore is not seen as a peak in the experimental spectra. Additionally, for wavelengths in-between these two discussed points, the permittivity of the array becomes negative.

The presence of these two modes whereby  $(n'_z) \approx (n''_z)$ , was explained by inter-rod coupling within the array resulting in the creation of a collective plasmonic resonance. This coupled mode has one component at lower wavelengths that is bright with symmetrically aligned dipoles, and a higher wavelength dark mode with anti-symmetric dipoles that cannot be excited by light. This is as predicted by the previously described plasmon hybridisation

theory or the exciton coupling theory, as seen in Figure 2.46. As more nanorods interact, a band of plasmonic states is formed within the nanorod array <sup>(133)</sup>.

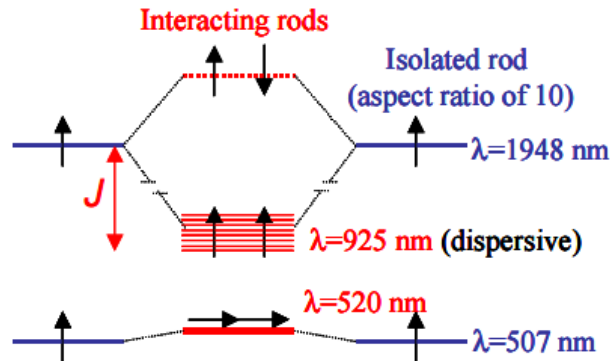


Figure 2.46: Schematic diagram for the plasmonic resonance energy levels of a nanorod array compared to its isolated modes. The top diagram refers to the longitudinal mode which under a strong coupling strength ( $J$ ) splits to form a low and high energy mode. The bottom schematic represents that of the transverse mode coupling <sup>(133)</sup>.

The electric field distribution of this coupled mode will now be addressed. Wurtz *et al.* <sup>(133)</sup> performed FEM simulation of a nanorod array (30 nm by 300 nm), supported on a glass substrate and embedded in alumina. P-polarised light was incident through the bottom glass surface at an angle of  $45^\circ$  and periodic conditions were used on the boundary so as to represent an infinite square array of nanorods. The inter-rod distance was then varied from 500nm to 100nm and the normalised electric field  $\sqrt{\vec{E}^* \cdot \vec{E}}$  and power flow (directional energy flux of the electromagnetic field) plotted, as seen in Figure 2.47.

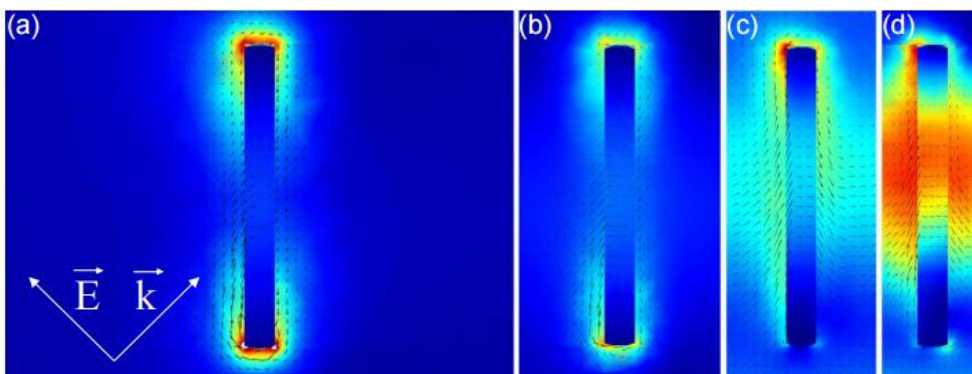
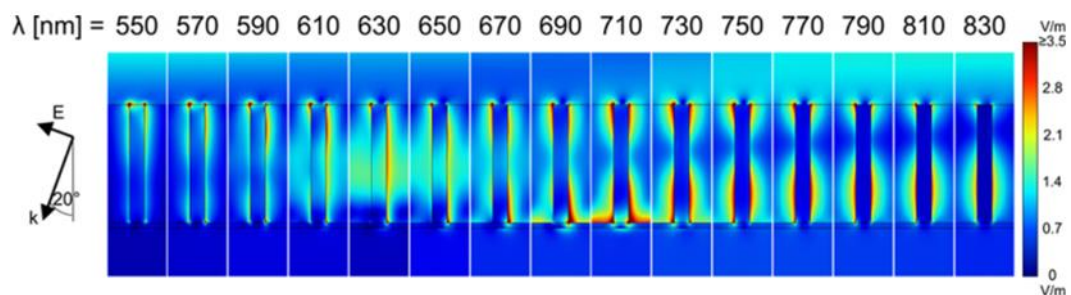


Figure 2.47: Electric field distribution and power flow vectors for the longitudinal mode of a nanorod array (30 nm x 300 nm), at an inter-rod spacing of a) 500 nm, b) 200 nm, c) 150 nm, d) 100 nm. A shift in the electric field spatial distribution occurred with decreasing separation between rods, from being localised at the rod ends to localisation in the middle of the rods.

As the inter-rod distance is reduced, it can be seen that the electric field distribution changes from being localised at the rod ends, as is typical for a longitudinal mode, to being predominantly towards the centre of the rod. This dramatic shift coincides with the power flow altering from being localised at the rod ends for large separations, to a more central distribution with the net energy flux travelling perpendicular to the nanorods long axis. These findings are supported by additional experimental work by Evans *et al.* <sup>(135)</sup> where they found a lack of sensitivity of the nanorod array to a change in refractive index at the nanorod ends.

Fiehler *et al.* <sup>(136)</sup> also performed FEM simulations of a nanorod array in alumina, however, this time for a hexagonal array supported on a 10 nm gold substrate, as in their experiments. The transmission and reflection of the array was determined and compared to experimental results. The authors work further supported the findings described above whereby a mode was found at much shorter wavelengths than one would expect for that of an isolated rod, relating to the presence of this blue-shifted coupled mode. This mode was also seen to further blue-shift as the angle of incidence was increased. Plotting the electric field at this wavelength (630 nm) shows a similar result to the previous simulations in that a mode in the middle of the nanorod is created that is coupled with its neighbouring rods, as seen in Figure 2.48. Additionally however, the authors also report the presence of other modes not previously mentioned. For example, modes between around 600 nm and 700 nm were found to relate to thin-film interference effects, whereas a mode at 710 nm in the simulations is attributed to the transverse mode of the substrate. Further simulations of this substrate mode show that with increasing thickness a large blue-shift is seen. This result is interesting as typically an increase in the thickness would lead to a red-shift of the transverse mode. For this reason I instead believe this mode isn't simply the transverse mode of the substrate but instead is a mode arising from coupling between the nanorods and the substrate, therefore giving it a more complex behaviour.



**Figure 2.48: Simulations of a hexagonally periodic gold nanorod array in alumina showing the electric field plots at varying wavelengths. All plots shown are for p-polarised light at 20° <sup>(136)</sup>.**

Although these works highlight a lot of the optical features of nanorod arrays, a number of omissions are present. For instance, the transmittance of the film was measured and expressed as the extinction so as to compare results. This extinction includes contributions from all the radiation that was absorbed, scattered, or reflected from the structure, and therefore any peaks seen in the spectra cannot solely be attributed to absorption for instance. Additionally, reflection losses in these thin film system can be very high, therefore it is likely the peaks seen also include contributions from these <sup>(132)</sup>. Fiehler *et. al.* <sup>(136)</sup> tried to address this shortcoming by also measuring the transmittance and reflection from nanorod array thin film structure, relating this to the absorption. Although differences between this absorption spectra and the extinction spectra were noted, attributed to accounting for the thin film reflection, once again the diffuse scattering from the array was neglected. This scattering can be particularly high for plasmonic structures, and therefore solely allocating the peaks to absorption may be incorrect. As applications such as that for photocatalysis would benefit from large absorption by the array, this is therefore an important factor to consider.

Furthermore, the studies to present have almost exclusively focused on the bright blue-shifted mode of the nanorod array. This is due to the ease at which optical data on this mode may be obtained using standard UV-Vis equipment. The dark mode however has received little attention in comparison, yet may provide interesting information and confirm the splitting of the modes as predicted by theory. As this cannot be excited by light however, other techniques such as EELS would be required.

Lastly, the bulk of research analysing the optical properties of these nanorod arrays has used a thin film production technique. As discussed in more detail in the following chapter, although this allows relatively easy analysis of the array, the technique suffers from the drawback of having more unordered rods that may not be in a well-defined hexagonal arrangement. Additionally, this technique also limits the system to having a very thin gold substrate in order for the light to be transmitted through it. Typically this gold substrate has a thickness of around 5-10 nm and is attached to the glass slide via a tantalum oxide adhesion layer of comparable thickness. As mentioned within this chapter, the substrate can couple strongly with plasmonic nanoparticles, particularly when of a small thickness. This can give rise to complex behaviours, as seen with the substrate mode in the work of Fiehler *et al.* <sup>(136)</sup>, whereas the presence of the nearby adhesion layer may also alter the optical properties.

The importance of understanding the optical properties of these nanorod arrays arises from the large number of potential applications they may be used in. For instance, coupling within the nanorod array allows the incident electric field to alter direction and travel perpendicular to the nanorods long-axis, therefore essentially propagating the energy through the array. This shows promise in waveguide applications. For example, Wurtz *et al.* <sup>(133)</sup> calculated the group velocity and propagation length of this guided mode as a function of inter-rod spacing. It was found that although group velocities varied considerably with spacing, the highest levels were seen at a relatively large spacing of around 155 nm, giving comparable levels to other plasmonic waveguides. In addition, the propagation lengths seen were from between around 2.7  $\mu\text{m}$  to 1.66  $\mu\text{m}$ , again varying with spacing. This dependence on the nanorod arrays geometry allows control and potential optimisation of the wave-guiding abilities <sup>(137)</sup>.

Similarly, many other applications may arise from the use of nanorod arrays due to the ability to accurately control the resonance position and therefore optimise optical or optoelectronic properties. For example, nanorod arrays have been shown to be excellent refractive index sensors, whereby a small surrounding layer of the alumina is etched creating core-shell particles. A change in resonance position is then only observed when the refractive index of this shell layer is altered and not with the superstrate, due to the field being localised in the centre of the rods <sup>(135, 137)</sup>. Lastly, the unique properties and negative permittivity of these arrays has been shown to be important in other applications and areas of interest, ranging from meta-material development <sup>(138, 139)</sup>, SERS <sup>(140-142)</sup>, plasmon-exciton coupling <sup>(143, 144)</sup>, and photocatalysis <sup>(145, 146)</sup>.

# 3 FABRICATION METHODOLOGY

Although many synthesis methods exist for the production of nanorods, such as that of seeded growth <sup>(147, 148)</sup>, and lithography <sup>(149)</sup>, each has their own drawback that hinders their potential use in the development of photocatalytic nanorod arrays. For example, the seeded growth method for gold nanorod synthesis is a wet-chemical method whereby small nuclei are first produced, and subsequently grown in a solution by reduction of gold salt using a weak reducing agent. These are stabilised with a surfactant to favour anisotropic growth <sup>(150)</sup>. Whilst this method is capable of producing high yields of nanorods with uniform sizes, the nanorods are generally of short aspect ratio and would require difficult and time consuming approaches to self-assemble the rods into a regular array <sup>(151)</sup>. The lithography techniques on the other hand allows the precise control and arrangement of the nanorods that is difficult to achieve with other methods. Unfortunately, depending on the specific method used, it can be very costly to perform, takes long times, has limited resolutions, and is generally not preferable for fabrication of large areas <sup>(152)</sup>. In contrast, as will be discussed in the following section, the templated growth method allows nanorod arrays to be produced over large areas, with good control over the size and spacing in the array, using relatively cheap and accessible equipment.

This chapter will begin by reviewing the templated method for the synthesis of nanorod arrays. Following this, a detailed methodology is included for the production of nanorods in this work, including the initial preparation of AAO templates, and the subsequent electrodeposition within them. Finally, the methodologies regarding how these nanorod

arrays are converted into a TEM format for EELS analysis, plus how a TiO<sub>2</sub> coating is added, are then discussed. The procedures undertaken for the EELS analysis and photocatalytic experiments are omitted from this fabrication section, and instead outlined within their own chapters.

### 3.1 Production of Nanorod Arrays by Template Electrochemical Deposition

Templated growth methods refer to those where the geometry of a nanoparticle is governed by growth, typically by electrodeposition, within a restrictive template. This was initially introduced for nanorod growth in 1970 by Possin<sup>(153)</sup> using the etched nuclear damage tracks in mica, resulting in rods as small as 40 nm in diameter being created. Williams and Giordano<sup>(154)</sup> later optimised the process, creating 8 nm diameter nanorods. Unfortunately, the uptake of the track-etched template method was hindered by a number of disadvantages such as having pores that although uniform in size, were randomly orientated. Additionally, large deviations in direction of the pores occurred meaning they often intersected each other<sup>(155)</sup>. The pores were also not uniform throughout their length but tended to widen in the middle giving rise to so called cigar shapes, as found by Schönenberger *et al.*<sup>(156)</sup>.

In the early 1990's the template-based technique had a resurgence largely led by the work of Charles Martin's research group<sup>(128, 129, 157-159)</sup> and their electrodeposition within porous anodic aluminium oxide (AAO) templates. These templates had the advantage of having hexagonally arranged pores which were of uniform diameter both in respect to each other and throughout their length. Additionally, the AAO templates benefitted from the fact that they could be made relatively simply within a laboratory, and that the size of the pores could be controlled, giving diameters ranging anywhere between 5 nm to hundreds of nanometres. In contrast to the track-etched templates, the pores of the AAO also run very normal to the surface therefore reducing the chance of intersection of pores.

The principles and theory behind the production of these porous AAO templates is outlined in depth by Lee and Park<sup>(160)</sup>, however here only the main points will be summarised. When aluminium is electrochemically oxidised (anodised) within an acidic electrolyte, an initial thin oxide layer, known as the barrier layer, starts to be produced on the surface of the aluminium that increases in thickness with time. As this layer thickens, the resistance of the system increases due to the insulating nature of the oxide and a large decrease in the current occurs down to its minimum value, as seen in Figure 3.1, stage I.

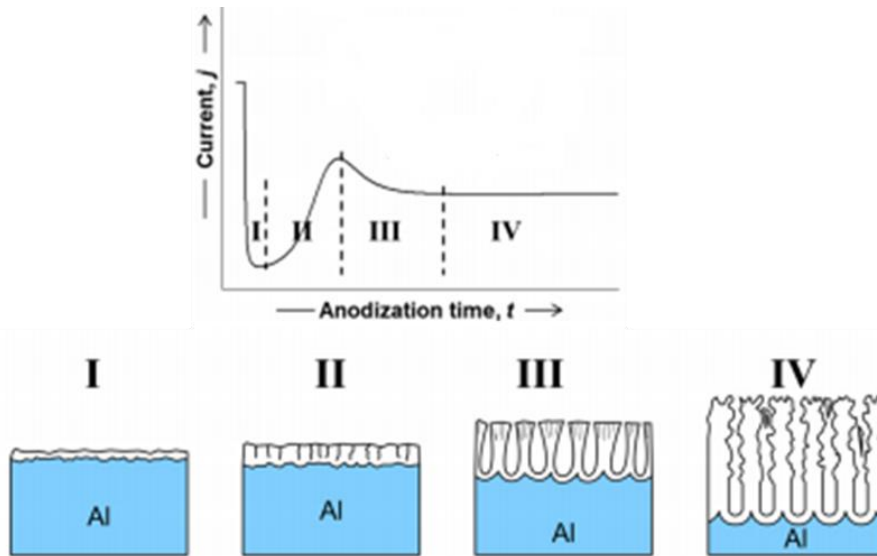


**Figure 3.1:** Current-time curve showing the different stages of anodisation, along with schematic diagrams representing each. Adapted from <sup>(161)</sup>.

During the next stage, pores within the oxide begin to form. The reasoning behind this is under debate, however it is typically attributed to one of two driving forces: either electric field assisted growth from the presence of defects <sup>(162)</sup> or mechanical stress assisted growth due to volume expansion <sup>(163)</sup>. In either case, it is observed that pores are formed with a random distribution on the surface that are disordered and have no relationship to the anodising voltage <sup>(161)</sup> (Figure 3.1, II).

As the oxide thickness is initially at its thinnest at the very bottom tip of the pore, the oxide layer in this area grows quickest. This gives rise to a hemispherical shape both at the pore bottom and at the metal/oxide interface <sup>(164)</sup>. This shape leads to a higher electric field concentration towards the base of the pore which enables further ion migration across the barrier layer, therefore lowering the resistance, and leading to a steady increase in the current up to a local maximum. As the anodisation continues, the stable hemispherical shape essentially propagates down through the aluminium leaving behind a cylindrical pore. The expansion of the pores occurs not only downwards, but also horizontally and at different rates between the pores. This causes the pores to either join with those adjacent, or cut them off restricting their growth, thereby reducing the pore density and leading to a steady decrease in the current <sup>(161)</sup>, (Figure 3.1, III). During this phase, the applied potential is seen to directly control the thickness of the barrier layer at the bottom of the pores. As the pores continue to propagate downwards and enlarge horizontally, they begin to compete with those nearby,

essentially being repulsed by each other and limiting the pore diameter<sup>(164)</sup>. Given sufficient anodisation time, this leads the self-ordering of equal size pores into a close-packed hexagonally ordered structure that continues to propagate down through the aluminium, converting it to an oxide as it goes. This self-ordering process typically take many hours to achieve, during which the current remains relatively stable and the oxide layer grows proportionally with charge passed (Figure 3.1, IV).

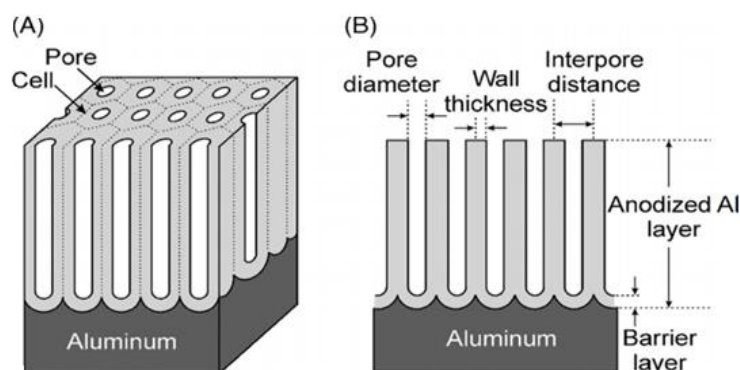


**Figure 3.2: Schematic diagram of the a) arrangement of pores, b) structural parameters<sup>(165)</sup>.**

The structure of this ordered AAO template can be defined by a number of parameters, as seen in Figure 3.2. As previously discussed, the potential used during anodisation directly controls the size of the barrier layer at the base of the pores. Additionally however, it has also been shown the other parameters such as pore diameter, wall thickness and interpore distance, also crucially depend on the potential with a linear relationship<sup>(160)</sup>. These relationships are summarised in the empirical equations below, where  $U$  is the applied potential in volts:

$$\text{Barrier Layer Thickness (nm)} = 1.2 \times U \quad (71)$$

$$\text{Pore Diameter (nm)} = 1.29 \times U \quad (72)$$

$$\text{Interpore Distance (nm)} = 2.5 \times U \quad (73)$$

In addition to the above, there are a number of other factors that are also important to control. For example, it has been shown that the best self-ordering occurs when the voltage applied is just below a factor known as the breakdown potential<sup>(166)</sup>. This relates to the potential at which the oxide begins to crack and burn due to too high current densities. As the breakdown potential is dependent on the electrolyte being used and its concentration, certain

combinations are typically preferred so as to achieve the best results. Additionally, the temperature of the electrolyte has also been known to affect the anodisation, whereby in general lower temperatures are shown to reduce the pore diameters <sup>(162)</sup>.

In industry, when growing a protective oxide layer by anodisation, typically large voltages above the breakdown potential are used as they achieve much quicker growth rates and the quality of the film is generally not important <sup>(167)</sup>. This is known as hard anodisation and usually requires specialist equipment to maintain the operating conditions <sup>(168)</sup>. When creating AAO templates for nanorod growth however, much lower potentials are preferred due to the ability to grow high quality pores. This is instead called mild anodisation. Unfortunately, mild anodisation suffers the drawback that it takes several hours to achieve highly ordered pores, therefore the top of the oxides are generally disordered, whereas the bottom becomes more ordered <sup>(167)</sup>. Masuda and Satoh <sup>(169)</sup> overcame this by performing a two-step anodisation. Here the aluminium was initially anodised until the pores became ordered, before then selectively etching away this initial oxide layer using a phosphoric acid and chromium oxide solution. The remaining aluminium is left textured with dimples on its surface in the hexagonally ordered form which then act as pore initiation site for the subsequent second anodisation. This results in straight ordered pores that run throughout the oxide layer as seen in Figure 3.3.

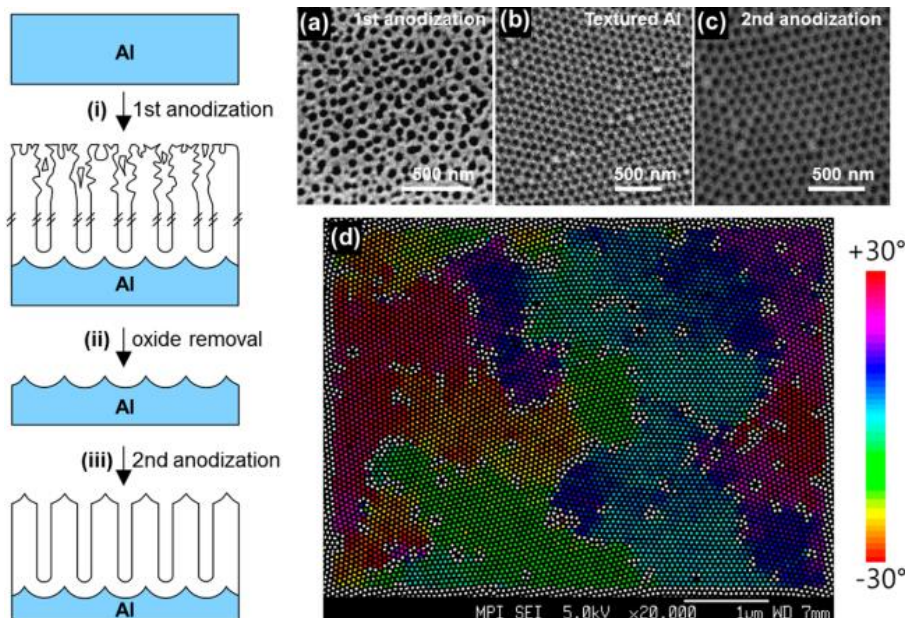


**Figure 3.3:** (Left) Schematic diagram showing the two-step mild anodisation process. a-c) SEM images relating to schematic diagram steps i-iii respectively. d) A colour coded SEM image of the 2-step AAO showing the distribution of domains. Here white resembles defect pores, whereas the colours indicate the average angle to their six nearest neighbours <sup>(160)</sup>.

For reference, an alternate thin film process for the production of AAO has also been developed <sup>(170)</sup>. This involves sputtering a glass slide with a thin 5 nm conductive layer of gold (with 10 nm of tantalum pentoxide as an adhesion layer), followed by magnetron sputtering a few microns of aluminium. Anodisation is then performed as above, however, generally only a single anodisation is possible due to the thin thickness. Although this leads to more disordered pores, greater stability is obtained, plus if using a thin conductive layer, the structure becomes transparent allowing characterisation of the optical properties by transmission measurements <sup>(134)</sup>.

In either case, the pores of the AAO are ideal for use as templates in the growth of nanorods. There are a number of techniques used to achieve this depending on the material required. As outlined by Hulteen and Martin <sup>(155)</sup>, these include electrochemical deposition, electroless deposition, chemical polymerisation, sol-gel deposition, and chemical vapour deposition. In addition, more recently atomic layer deposition (ALD) within AAO templates has also been demonstrated <sup>(171)</sup>.

By far the most popular of these techniques is that of electrochemical deposition. Unfortunately however, it suffers from an additional complication in that the boundary layer at the bottom of the pores acts as an insulating layer, therefore prohibiting electrodeposition. To overcome this, the templates are typically soaked in phosphoric acid for a set period of time to etch this layer. A further consequence of this etching process however is that the pores themselves are also etched becoming wider and more rounded. By carefully selecting the etching time, this can allow for a further degree of control over the pore size and therefore the diameter of the nanorods. On the other hand, care must be taken not to over-widen the pores to the point where neighbouring pores join as this will lead to a breakdown of the periodic structure and severely weaken the template. The appropriate etching times for removal of the barrier layer depends not only on the temperature and concentration of the phosphoric acid, but also on the electrolyte and voltage used during the AAO formation, as this determines the initial size of the barrier layer.

Following this pore widening process, the unreacted aluminium is typically removed via selective etching and replaced by a thin metal film either by thermal evaporation or ion sputtering, <sup>(155)</sup>. This must be done in a manner that it completely covers the pores, and therefore is able to act as the cathode for subsequent electrodeposition. This electrodeposition

process is performed in a three electrode system whereby the working electrode is the cathode, the counter electrode is typically a platinum wire, and a reference electrode allows the open circuit potential (OCP) to be determined by providing a stable potential (see Figure 3.4a). The electrodeposition is typically performed by a potentiostat method, whereby applying a potential more negative than the OCP, allows the electrodeposition to commence <sup>(172)</sup>.

When this potential is applied to the system, the positively charged metal ions in the solution migrate to the cathode whereby they are reduced and deposit on the surface. As a deposited layer builds up on the cathode, subsequent deposition only occurs if this layer is also conductive, thereby allowing the process to continue. For this reason, electrodeposition is typically only viable for metals, semiconductors, or conductive polymers <sup>(173)</sup>. As the electrodeposition continues, the material fills the pores of the AAO template from the bottom until eventually, given sufficient time, the wires grow out of the end of the template and merge to give a continuous layer. The current, time plot for this deposition process is seen in Figure 3.4b. After an initial sharp peak in the current due to the double-layer capacitance charging, nucleation of the metal occurs at the bottom of the pores. As the pores slowly become filled the current remains relatively stable, followed by a large increase as the material emerges from the template and the working electrode size increases. Once these join to form a continuous film, the current remains constant <sup>(174)</sup>.

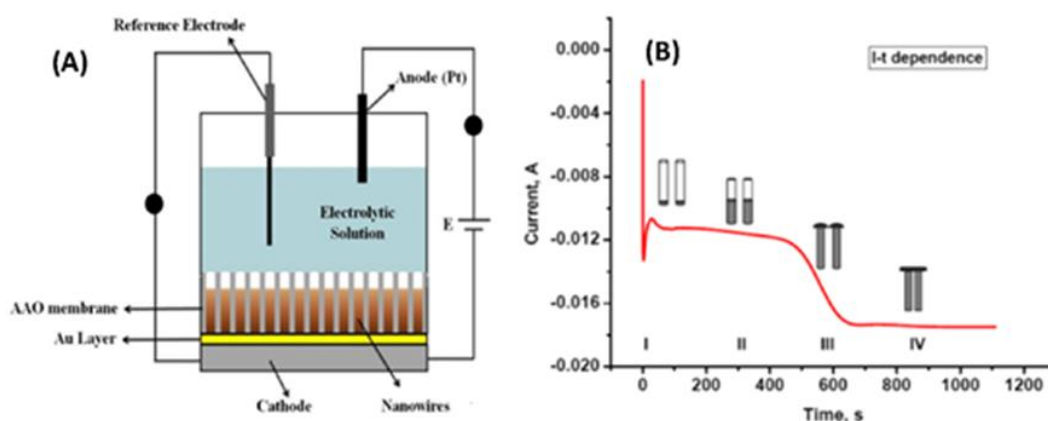


**Figure 3.4:** a) Schematic of the three electrode system used for electrodeposition within AAO templates, b) Current-time curve of electrodeposition in AAO templates <sup>(174)</sup>.

Although the above graph can give an insight into the level of pore filling, in general it is preferential to stop the electrodeposition before the rods emerge from the template. Instead, to determine the length of the nanorods, the mass of material deposited during

electrodeposition can be calculated by monitoring the charge passed and applying Faraday's equation of electrolysis, as seen in equation (74).

$$m = \left(\frac{Q}{F}\right) \left(\frac{M}{z}\right) \quad (74)$$

Here  $m$  is the mass of material in grams,  $Q$  is the charge passed in coulombs,  $F$  is the Faraday constant,  $M$  is the molar mass of the material, and  $z$  is the valency number. By approximating certain factors of the AAO template such as the pore density, pore diameter, and membrane diameter, the effective surface area for the deposition can be determined. The density of the material can then be used to estimate the size of the nanorods produced compared to the level of charge passed. Following this deposition, the last step in the fabrication of nanorod arrays then usually involves removing the AAO template by means of soaking in sodium hydroxide.

### 3.2 Methodology for Fabrication of AAO Templates

The AAO templates used in this work are produced using the following methodology. Firstly, high purity (99.9999%) 0.5 mm thick, annealed aluminium foil supplied by Alfa Aesar is cut into 15 mm diameter sections. These are then ultrasonically cleaned and degreased in acetone for 10 minutes, followed by placing in 0.5 M sodium hydroxide for 5 minutes, before finally ultrasonically cleaning in ultra-pure water for a further 10 minutes.

The next stage of the process involves reducing the surface roughness of the sample surface by polishing. This smooth surface aids in the self-ordering of the pores, leading to higher quality templates produced <sup>(175)</sup>. Typically, other work has achieved this by electropolishing in a perchloric acid and ethanol mixture using relatively high current densities <sup>(176)</sup>, however, a chemical polishing solution was preferred here as it is safer and is capable of achieving equal levels of surface roughness as shown in the work of Alam *et. al.* <sup>(175)</sup>. This involves adding the cleaned aluminium to a solution of 15 parts of 68% nitric acid and 85 parts of 85% phosphoric acid at 85°C for 5 minutes whilst being stirred rapidly. The acid is then neutralised by soaking in 1M sodium hydroxide for 20 minutes, before finally being rinsed in ultra-pure water.

The sample is then secured in a homemade PTFE chamber containing the electrolyte of choice, as shown in the schematic in Figure 3.5. O-rings are used to seal the sample and ensure

only one surface of the aluminium is exposed to the electrolyte. The opposite side of the aluminium is then placed against a copper washer with a wire attached to provide an electrically conductive contact, thereby forming the working electrode. The PTFE chamber is placed within a 5 wt% water-methanol cooling bath which is subsequently cooled to 0° by means of a Cole-Palmer recirculating chiller. A hole in the lid of the PTFE chamber allows the insertion of a thermometer into the electrolyte to monitor the temperature and ensure this too reaches 0°. Additionally, an aluminium counter electrode (10 cm × 2 cm × 0.5 mm) is positioned through the lid of the PTFE chamber and into the electrolyte. This is positioned so that it is separated from the sample by a distance of 1 cm. A TTi QL355TP DC Power Supply then provides a controlled voltage to the aluminium counter and working electrodes. As mentioned in the previous section, the size of the pores created depends not only on the electrolyte used but also on the anodisation voltage supplied. It was found a voltage of 25 V is optimum when using 0.3 M sulphuric acid as the electrolyte, whereas 40 V is preferential for a 0.3 M oxalic acid solution. On the other hand, if larger pore diameters are required, a 0.1 M phosphoric acid may be used as the electrolyte with voltages of either 140 V or 195 V, this however requires extra cooling to keep the temperatures low.

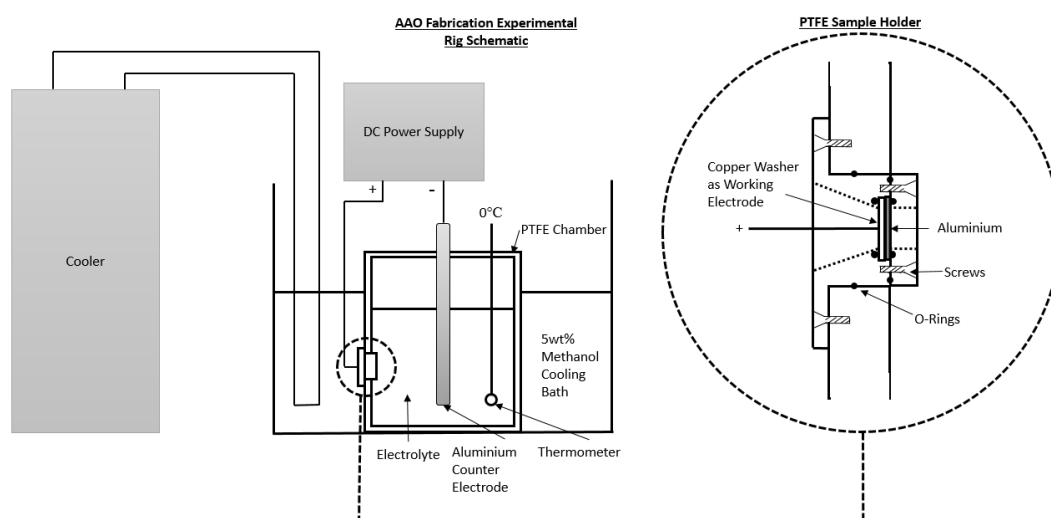


**Figure 3.5 Schematic diagram of experimental rig used in production of AAO templates.**

A two-step anodisation was performed so as to produce the highest levels of order and ensure the pores run perfectly vertical through the alumina. A sufficient length of time was required for this process to achieve satisfactory levels of order, therefore the first anodisation was run overnight for approximately 18 hours. Although this achieved a reasonable degree of order towards the bottom of the pores, the top of the pores were relatively disordered and as such would lead to poor quality nanostructures. To overcome this, the AAO layer produced was

selectively etched using a solution of 6 wt% phosphoric acid and 1.5 wt% chromium (VI) oxide solution at a temperature of 65°C for 2 hours. The etch rate of this AAO layer was monitored by measuring the mass loss of the sample with time as seen in Figure 3.6. Although the mass remained constant after around 30 minutes, signifying the layer is removed, this is typically extended to around 2 hours to ensure complete removal.

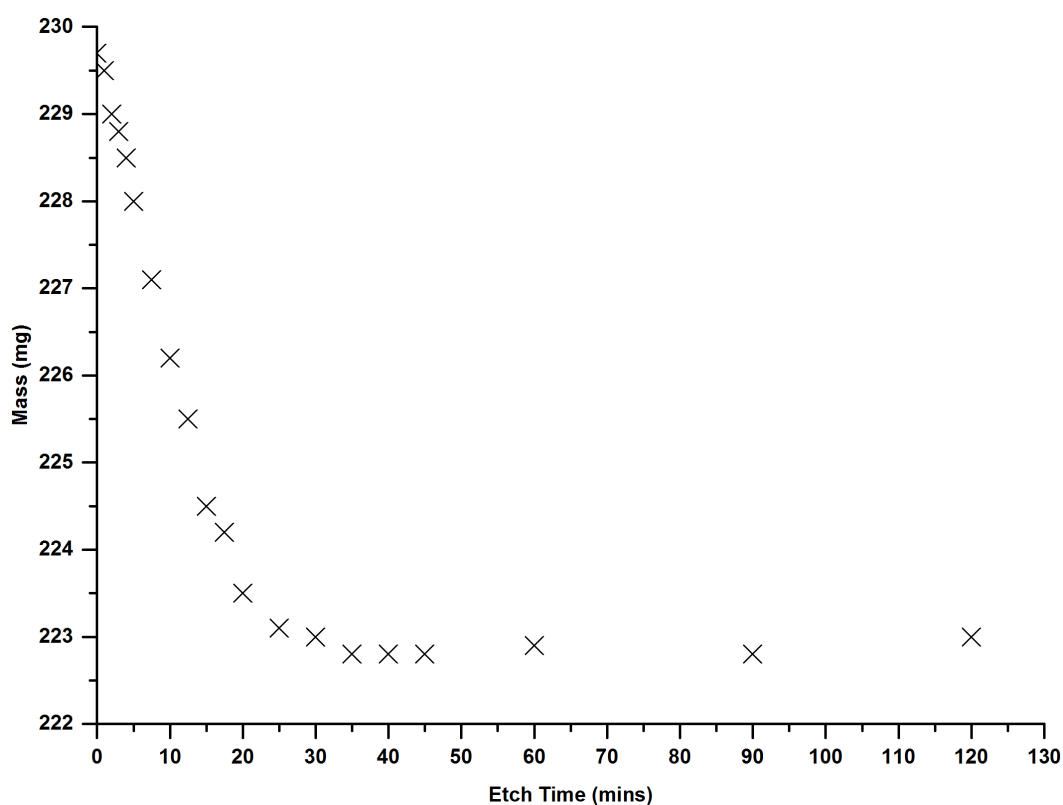


**Figure 3.6: Mass loss with time of the first anodisation AAO layer showing complete removal of the layer by 120 minutes.**

The selective etching of the AAO layer once completely removed leaves an ordered array of dimples due to the bottom of the pores extending further down into the aluminium than its bulk oxide layer. If a second anodisation is performed, these dimples provide a preferential site for pore growth and therefore a well ordered growth is achieved from the start. The second anodisation was implemented identically to the first except for a longer anodisation time of approximately 24 hours. This was due to the AAO layer being very brittle and therefore a thicker AAO layer provides increased strength for subsequent procedures.

Following the second anodisation, the AAO must be prepared for use as a template. This involved removing any residual aluminium and opening up the insulating barrier layer. The

first was achieved by using a solution of 0.1 M copper (II) chloride and 6 M hydrochloric acid, to selectively etch the unconverted aluminium. This process was undertaken by first securing the sample in the PTFE sample holder as seen in Figure 3.5 before slowly pipetting the etching solution on to the aluminium layer until completely removed, which was recognised by the sample turning transparent. The PTFE sample holder restricted the etching solution to the centre of the sample and left a ring of thick aluminium surrounding the fragile AAO to both act as a support and provide a strong area that the O-rings could press upon to secure the sample into its holder during the electrodeposition phase.

The opening of the barrier layer was achieved by using a 5 wt% phosphoric acid solution heated to 30°C. The AAO templates were placed within this solution for a specified time until the insulating barrier layer had been removed and the pores were widened to the required diameter. The time required for this depended on the electrolyte and anodisation voltage used during its production and therefore tests were carried out to determine the optimum conditions for each, as shown in the following chapter. In summary however, AAO templates produced using sulphuric acid were widened for between 15-20 minutes, whereas for oxalic acid, longer times of between 30-50 minutes were needed, depending on the diameter of the pore required.

Lastly, a 150 nm working electrode of gold or silver was added to the pore widened side of the AAO templates by thermal evaporation (*Edwards Auto 306*). A rate of around 0.1-0.2 nm per second gave high quality films that covered the holes of the AAO. A gold substrate was generally preferred due to its stability, however, if removal of the substrate was required after nanorod growth, silver was occasionally used instead due to the ability to selectively etch it relative to the gold nanorods. In both cases, high purity wire of at least 99.95% was used as obtained from Goodfellow. Following evaporation of the working electrode, the templates were ready for growth of the nanorods as discussed in the following section. A summary of the process performed in the fabrication of the AAO templates are shown in Figure 3.7.

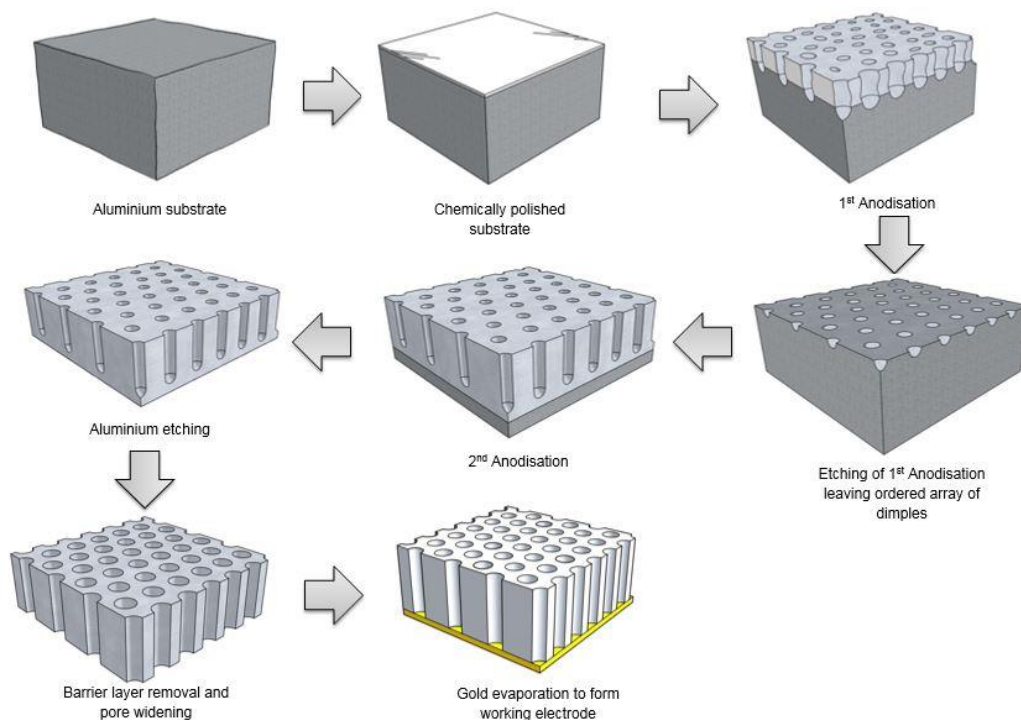


**Figure 3.7: Production steps in fabrication of AAO templates for nanoparticle growth.**

### 3.3 Methodology for Electrodeposition of Nanorod Arrays

The fabrication of the nanorod arrays using the AAO templates was based upon the methodology outlined by Banholzer *et al.* <sup>(177)</sup> for deposition into commercial Whatman AAO templates. A number of modifications and additional steps were required however in order to get high quality deposition in to the homemade AAO templates, as summarised below.

Firstly, as previously mentioned, the templates were left with a ring of unreacted aluminium around the edge so as to give it extra stability and provide an area at which the O-rings may press against to firmly secure it the rig and stop any leaking. Without this strong and relatively thick aluminium ring surrounding the AAO, it was found the pressure needed to secure the sample in the electrodeposition rig often led to the brittle AAO templates cracking. Unfortunately, a disadvantage of having this aluminium ring was that it required to be insulated from the electrolyte so as to avoid deposition of the metal onto its surface. This was achieved by coating the top of the ring in a layer of nail varnish ensuring complete coverage of all the conductive aluminium was achieved and only the AAO template remained exposed. This layer can easily be removed by rinsing in acetone after the electrodeposition stage was complete. The underside of the aluminium ring does not require the insulating nail varnish and should be left free so as to provide a conductive contact for the working electrode. After

this has sufficiently dried, the sample was then secured in a homemade electrodeposition rig, as seen in Figure 3.8.

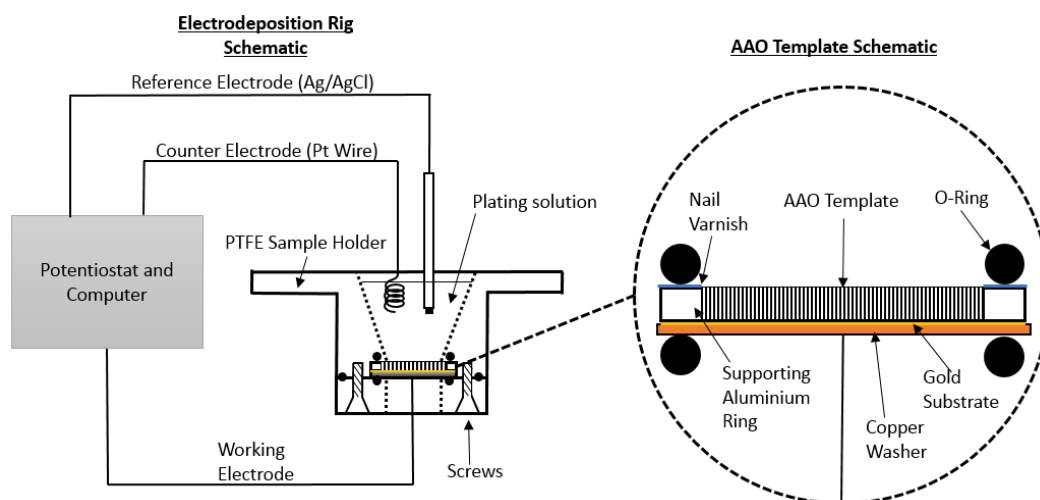


**Figure 3.8: Schematic diagram of electrodeposition setup including close up of how the AAO template is secured.**

The electrodeposition rig also used the same sample holder that was initially used in the fabrication of the AAO template. In contrast however, this was positioned the opposite way around so that the large opening was facing up and could therefore hold the plating solution. The template was secured in the same manner as before, making sure that the porous side faced up whereas the side with the evaporated metal on, was at the bottom placed against the copper washer. A platinum wire counter electrode and a Ag/AgCl reference electrode were positioned within the plating solution opening so that they were at a distance of around 0.5 cm from the template. The wires of these were then attached, along with the working electrode, to the potentiostat (*Metrohm Autolab PGSTAT30*) and operating computer.

Initially ultra-pure water was added to the electrodeposition rig and left for around 30 minutes before being removed. This was to wet the pores of AAO template which in turn enabled the plating solutions to penetrate the pores more easily when added. This wetting of the pores encouraged growth in all the pores simultaneously, therefore allowing much larger and uniform areas of deposition<sup>(156, 178)</sup>. Following this, the plating solution was added and electrodeposition performed. In this work, both self-made Au thiosulphate-sulphite<sup>(179)</sup>, and commercial Au and Ag potassium cyanide, plating solutions were tested. Although the self-made solution had the advantage of being relatively non-toxic compared with the cyanide

based commercial ones, the growths were significantly poorer and the solution more unstable. For this reason, commercially produced plating solutions from Technic Inc. were preferred, with the subsequent electrodeposition conditions shown in Table 1:

**Table 1: Electrodeposition conditions for nanorod growth.**

<b>Material</b>	<b>Plating Solution (from Technic Inc)</b>	<b>Dilution from Stock</b>	<b>Applied Potential (vs. Ag/AgCl)</b>
Au	Orotemp 24 RTU	0	-0.92 V
Ag	Techni Silver 1025	1:5	-1.1 V

Due to the dangers of cyanide-based plating solutions, the electrodeposition had to be performed with appropriate protective equipment and thoroughly rinsed with ultra-pure water afterwards. The potentiostat and operating software (*GPES*) were used to both control and monitor the deposition. The settings were set to Amperometric thereby allowing a constant potential to be applied and the current to vary. The potentials used for each plating solution are shown in Table 1 above, as obtained from literature <sup>(177)</sup>, and supported by our own cyclic voltammetry tests. By monitoring the charge passed during deposition, an approximation of the length of the rods could be made. This control allowed rods of many different AR to be produced with the only limit being the length of the pores. Additionally, by alternating the metal you deposit, layered Au/Ag nanorods could be fabricated. These require rinsing with water, typically around five times, after each deposition to ensure the previous plating solution was completely removed and guarantee a sharp boundary between the two metals. This process can be repeated as many times as needed to grow the required multi-layered nanorods.

If silver was evaporated as the working electrode followed by gold being electrodeposited within the pores, selective etching of the silver substrate was possible. This was performed by soaking the AAO template in a nitric acid solution for a few minutes until the substrate had visibly been removed, followed by rinsing in ultra-pure water. This resulted in an AAO/nanorod composite material whereby the rods were supported within the template but were not on a substrate. By removing the opaque substrate, the composite material transmitted light and therefore allowed UV-Vis transmission measurements to be recorded for the aligned nanorod array. Alternatively, it was found that if gold was used as the

evaporated substrate, a sharp scalpel was capable of scratching off the substrate leaving behind the nanorods supported in the AAO, which again showed transmission of light.

On the other hand, if the nanorods were to be removed from the AAO template, the following steps were taken. Firstly, the sample was carefully cut from the aluminium supporting ring using a sharp scalpel, and stuck onto a section of high purity adhesive copper tape, as typically used for SEM. This was performed before the removal of the thick AAO template as if attempted after, the thin substrate and nanorod sample lost its rigidity and curled in on itself. Alternate supports other than copper could be used by adhering the sample with epoxy resin, however care had to be taken that they were compatible with the sodium hydroxide etching solution, including any surface oxide layer they may have had. In this work, copper tape was the preferred support due to its compatibility with low concentration NaOH and its high conductivity, therefore allowing ease of SEM imaging and providing a potentially large conductive contact point for any later photocatalytic experiments.

The secured sample was then added to a 0.5 M NaOH solution for 10-12 hours so as to selectively etch the AAO template and ensure the alumina was completely removed. After rinsing several times with ultra-pure water, the nanorod array could then be imaged by SEM, or alternatively have additional procedures performed such as coating with TiO<sub>2</sub>. A summary of the fabrication process for the production of nanorod arrays is shown in Figure 3.9.

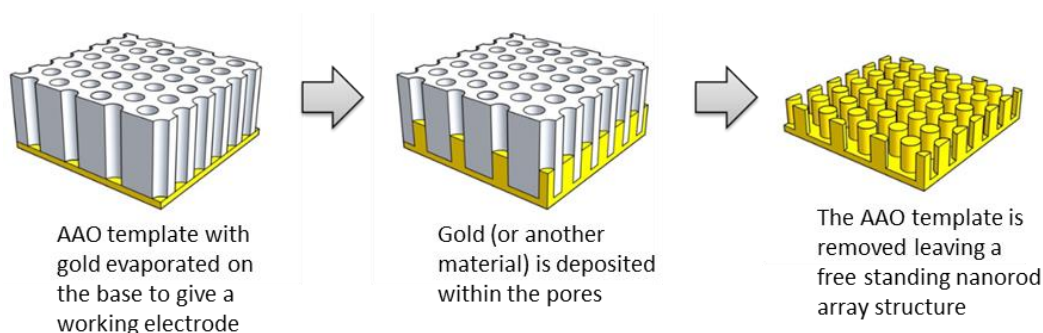


**Figure 3.9: Schematic diagram of fabrication steps for electrodeposition within AAO templates**

### 3.4 Methodology for Preparation of TEM Cross Section

To perform EELS and probe the plasmonic properties of the nanorod arrays, TEM cross sections with thin thicknesses ( $<100$  nm) had to be constructed from the larger nanorod array. Ideally, it was required that the nanorods were free from the AAO so as to assess the nanorods themselves rather than the nanorods embedded in the porous anisotropic alumina. The difficulty with this however was that the template provided a lot of support for the nanorods when creating such thin sections, and therefore without this they were liable to break.

Initially, focussed ion beam (FIB) milling was used and a lift-out technique applied so as to remove a small section of the nanorod array after the AAO template had been etched. Although it was found this method largely worked, it suffered from a number of disadvantages. Firstly, a layer of platinum was required to be deposited on to the nanorods to provide protection during the FIB milling process. This platinum significantly altered the environment of the nanorods possibly leading to changes in the plasmonic properties. Additionally it was found the sample lost a lot of its strength as the FIB lamella reached thinner thicknesses, resulting in the rods and the gold substrate often breaking apart. To avoid these effects, the rods were preferably left in the alumina template during FIB milling, and then potentially selectively etched away later. Unfortunately however, in contrast to the thin film alumina samples in other works, the large thickness of the alumina ( $\sim 40$ - $50$   $\mu\text{m}$ ) prohibited FIB milling of these samples.

To overcome these difficulties, a conventional bulk TEM preparation technique was preferred. This is where initially the sample was secured onto a silicon wafer using epoxy, and a small section of a few millimetres cut away using an ultrasonic disk cutter (*Gatan Model 601*). This was then secured between additional silicon wafers by means of epoxy so two sets of nanorods faced inwards. Following this, a 2.3 mm cylinder was removed from the silicon block, again using the ultrasonic cutter, and glued within a metal supporting tube. A diamond saw was then used to cut thin sections from this cylinder to give 3 mm diameter slices. Following this, the thickness of this slice was slowly reduced, initially by means of polishing to  $\sim 80$   $\mu\text{m}$  (*Gatan Model 623*). A dimple grinder (*Gatan Model 656*) was then used to preferentially thin the centre of the disk to around 5  $\mu\text{m}$ . Lastly, a precision ion polishing system (*Gatan Model 691*) was used to slowly thin the centre of the dimple at varying angles until a hole was formed within the middle. At the edges of this hole the nanorod array was thin enough to perform TEM (i.e.  $<100$  nm).

Similar to the FIB technique, using a sample whereby the AAO had been removed beforehand led to the nanorod array breaking during thinning. On the other hand, retaining the alumina template during thinning, enabled the nanorod arrays to maintain their structure. Although this led to the nanorod arrays being encapsulated in AAO, by quickly etching in a 0.5 M NaOH solution for 4 minutes, the alumina was etched in a number of areas allowing both “in AAO” and “without AAO” measurements to be taken by TEM.

### 3.5 Methodology for Coating in Titanium Dioxide

To allow the nanorod array to act as a photocatalytic plasmonic platform, a semiconductor was added onto its surface. Titanium dioxide was chosen in this regard due to its widespread use and availability. Additionally, although the large band-gap of 3.2 eV for anatase or 3.0 eV for rutile, limits its applicability in the abundant visible region, it has been shown plasmonic nanoparticles may alleviate this <sup>(180, 181)</sup>. A TiO<sub>2</sub> coating on the nanorod array therefore allows assessment of its photocatalytic abilities, including its potential for enhancement via visible light excitation. A more in-depth discussion of these photocatalytic aspects is given within Chapter 7, whereas only the methodology is discussed here.

Ideally, it is required that the TiO<sub>2</sub> deposition has both a high surface coverage and gives a homogeneous layer where the thickness may be accurately controlled. Unfortunately, the high surface area and anisotropic geometry of the nanorod array makes this challenging for many techniques. On the other hand, atomic layer deposition (ALD) has shown excellent ability to coat large surface areas whilst providing a homogeneous coating with accurate control over the thickness <sup>(182)</sup>. The principle behind ALD is that two or more precursor gases are sequentially pulsed over the sample so they react on the surface. This occurs in a self-limiting manner whereby saturation occurs very quickly and growth is restricted to just a single atomic layer for each of the different precursor pulses, as seen in Figure 3.10. The unreacted precursor gases never come in contact with the other species due to purging with an inert gas between each pulse for a set length of time. By repeatedly cycling this process, multiple layers can be built up forming thin films <sup>(183)</sup>. Traditionally, high temperatures have been required to ensure the precursors react quickly and completely, however, the addition of a plasma allows much lower temperatures to be used alongside quicker purge rates. This is known as plasma enhanced atomic layer deposition (PE-ALD) <sup>(184)</sup>. A more thorough description of the complexities of the ALD process is addressed in a number of review papers <sup>(182-184)</sup>.

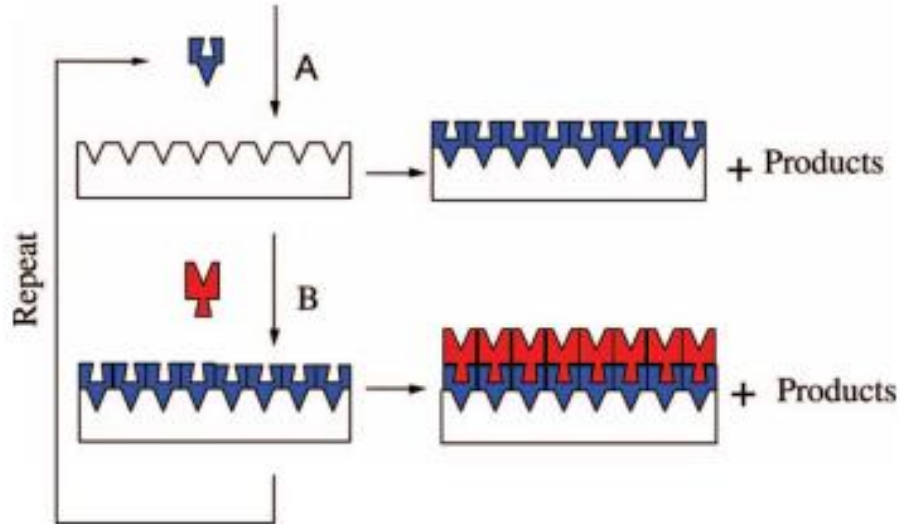


**Figure 3.10: Schematic diagram of a single ALD deposition cycle with precursors A and B. The shapes of the reactants highlight the self-limiting surface chemistry** <sup>(182, 185)</sup>.

The methodology for the deposition of TiO<sub>2</sub> by PE-ALD was as follows. Firstly, the samples were cleaned by rinsing in acetone, then isopropanol, followed by plasma cleaning in an O<sub>2</sub> Asher (*Emitech K1050X RF Plasma Cleaner*) for 15 minutes at 50 W (30 mm O<sub>2</sub>). The PE-ALD was then performed in a Cambridge nanotech/Ultratech Fiji 200, operated with a plasma power of 300 W (13.56 MHz RF) and a chuck temperature of 150°C. After an initial in situ O<sub>2</sub> clean, the deposition of the TiO<sub>2</sub> was performed using Tetrakis(dimethylamido)titanium (TDMAT) and H<sub>2</sub>O as the precursors. A constant 60 sccm flow of argon was used as the precursor carrier, whilst the argon plasma carrier had a flow rate of 200 sccm. A typical cycle consisted of an initial 60 ms H<sub>2</sub>O pulse, then a 30 second wait, followed by a 100 ms pulse of TDMAT, again with a 30 second wait. In total 200 cycles were performed before cooling under vacuum conditions.

Deposition of the TiO<sub>2</sub> was confirmed using X-ray photoelectron spectroscopy (XPS), as seen within the results in Chapter 7. It should be noted however that difficulties arose initially with high carbon contamination on the surface of the rods following the TiO<sub>2</sub> ALD deposition. This was believed to be due to the adhesive layer of the copper tape contaminating the sample when exposed to the ALD operating conditions. To solve this, the adhesive layer around the sample was removed prior to TiO<sub>2</sub> deposition by washing repeatedly in acetone until visibly gone. The sample was then washed in isopropanol, followed by ultra-pure water.

These methodologies allowed the fabrication of well-ordered, high quality nanorod arrays over a large area. Additionally, it provides a level of control over the diameter, length and spacing of the nanorods by altering the AAO template. These regular spacing's and the potential for large aspect ratio rods are features that other techniques such as the seeded growth method find challenging. As shown within the following chapter, these large aspect ratios and the strong coupling due to the regular spacing in the array provides unique and interesting optical properties. Furthermore, by also using ALD to coat the nanorods in a semiconductor, the nanorod arrays may be transformed into a potential photocatalytic structure, as in the focus of this work.

# 4 CHARACTERISATION AND OPTICAL PROPERTIES

This chapter will focus on the characterisation of the fabricated structures, including both the AAO templates produced, and the subsequent nanorod arrays. The structures produced are mainly investigated by means of SEM imaging, however, additional image analysis using the MATLAB code *Pore Image Processor*<sup>(186)</sup> and *Image J*<sup>(187)</sup> software provides quantitative results. Following this, the optical properties of the nanorod arrays are investigated by UV-Vis spectroscopy. Although further analysis of the arrays is achieved using modelling and electron energy loss spectroscopy, these results will instead be included within their own relevant chapters.

## 4.1 Characterisation of AAO Templates

In the initial attempts at the production of nanorod arrays, commercial AAO templates were used in the hope they would allow rapid development of the arrays. The commercialisation of the templates is by GE Healthcare under a brand called Whatman®, whereby primarily the templates are produced for filter applications. Although quoted pore diameters are as small as 20 nm, distributed on relatively large membranes up to 47 mm in diameter, the commercial templates have a number of drawbacks mainly relating to the size and ordering of the supplied product. For instance, although quoted as having pore diameters as low as 20 nm, SEM images revealed this was only the case for the very bottom of the pores and the diameter increased to much larger values (~190 nm) at greater heights, as seen in Figure 4.1.

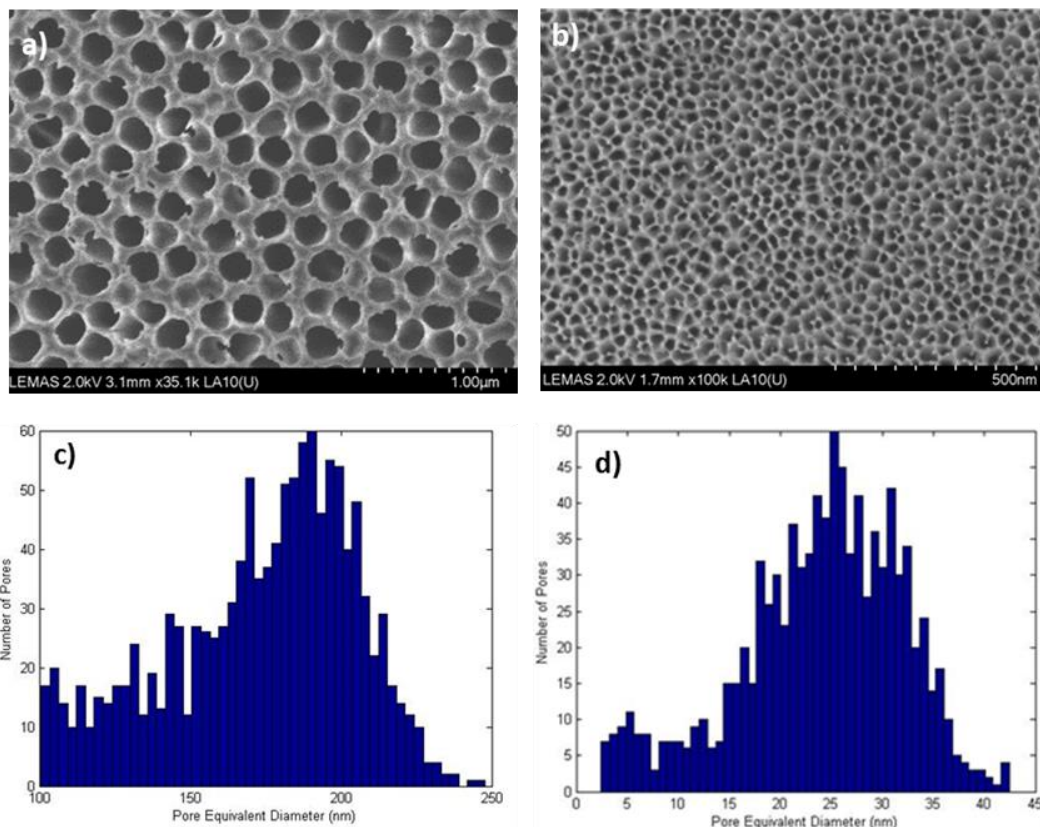


**Figure 4.1: SEM images of a commercial Whatman AAO with quoted pore diameter of 20 nm for a) top and b) bottom surface and their respective pore diameter histograms (c,d) determined using image processing software.**

This variation in the pore diameter along its length is acceptable for use in their primary application as filters, where only the minimum pore diameter controls the filter size. When used as a template for nanorod growth however, this variation has consequences on the morphology of the nanorods produced, as seen in the following section. Furthermore it is seen that the ordering of the nanorods is relatively low, with poor roundness and a large variation in diameter.

Following these results, it was established that the commercial AAO templates were unsatisfactory and therefore the production of self-made AAO templates was required, the methodology of which has been outlined previously. Not only did this allow higher quality templates to be produced with pore diameters that remained constant throughout the AAO, but it also allowed customisation so as to achieve the desired pore diameters and inter-pore spacing.

This customisation of the AAO templates arises from the ability to control the anodisation voltage, temperature, electrolyte, and concentration. Figure 4.2 shows the plan view and cross-sectional SEM images for two different two-step mild anodisation (MA) configurations, namely that of 0.3 M sulphuric acid at 25 V, and 0.3 M oxalic acid at 40V. These results were obtained in collaboration with the University of Siegen, Germany.

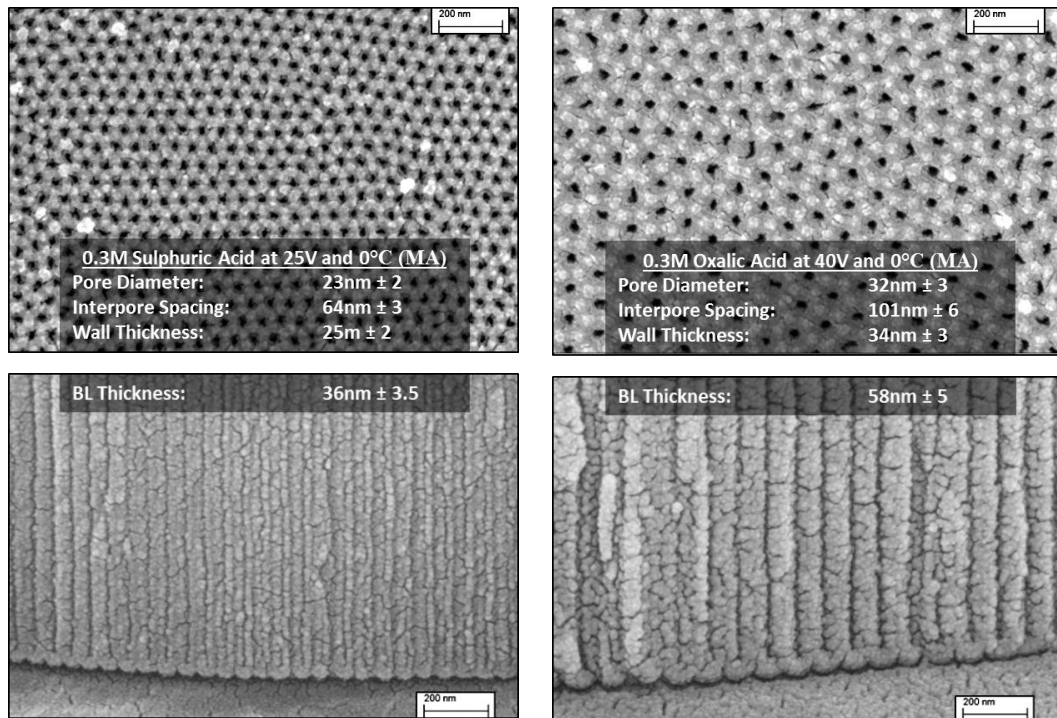


**Figure 4.2: SEM images and pore measurements for left: 0.3 M sulphuric acid at 25 V, and right: 0.3 M oxalic acid at 40 V. The images at the top are for a plan view whereas the bottom images are cross-sectional views showing the barrier layer. All images are without any pore widening.**

The above results showed that pore sizes between 23 nm and 32 nm could be produced using relatively low voltages. By increasing the voltage, much larger pores could also be fabricated. In this scenario however, forced cooling by means of a pump was required to ensure the temperatures remained low. To illustrate the effects of higher voltages, the results from a hard anodisation (HA) run using 0.3 M oxalic acid at 140 V are shown in Figure 4.3.

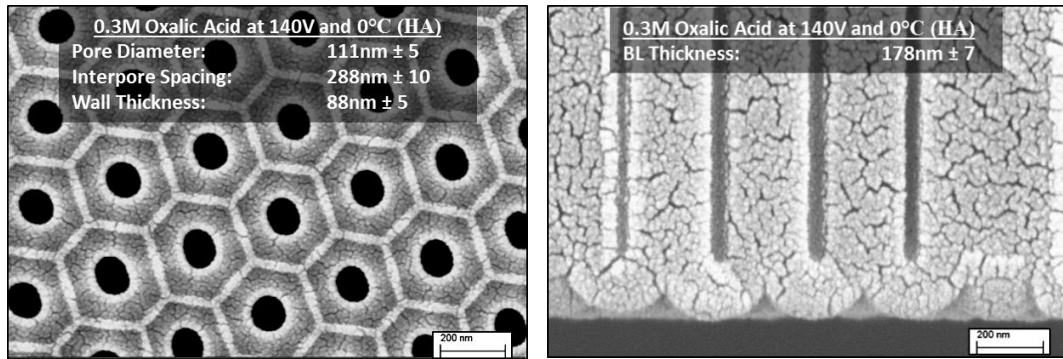


**Figure 4.3: SEM images and pore measurements for a hard anodisation using 0.3 M oxalic acid at 145 V. The left-hand image is the plan view of the pores whereas the right-hand image is a cross-sectional view of the barrier layer. All images are without any pore widening.**

Comparing these results to theory and the empirical equations outlined in the previous chapter, shows that good agreement is found. For instance, an increase in the anodisation voltage in general led to a linear increase in the pore diameter, interpore spacing, and wall thickness. The interpore distances in particular matched the calculated values extremely well, and were typically within a few nanometres of that expected. This was only the case for the mild anodisation runs however, whereas for the hard anodisation run, the distance was less than that predicted. Lee *et al* <sup>(188)</sup> also found the same to be true in their work and instead proposed a 2 nm per volt relationship for interpore spacing under hard anodisation conditions, therefore in good agreement with my findings.

Alternatively, in terms of the pore diameter, although an increase in potential led to larger pores, there were some discrepancies compared to the values predicted by the empirical equations, in that the actual values were somewhat smaller. This was also found in the work of Nielsch *et al.* <sup>(189)</sup> who concluded that self-ordered pores, such as the ones shown produced in this work, instead have their pore diameter related to the anodising voltage by a factor of 0.83 nm per volt <sup>(160)</sup>. Applying this factor to the experimental data instead of the previous value of 1.29 nm per volt (see equation (72)), gave much better agreement.

Lastly, the barrier layer measurements again followed the correct trend for increasing in size with potential. On the other hand, although they showed a reasonable agreement with the empirical equations, they were often slightly larger than predicted, possibly due to the specifics of the anodisation procedure such as the temperature, anodisation time, and acid concentration. This had consequences for the pore widening process as slightly longer times

than that quoted in literature were required to remove the barrier layer. This removal of the barrier layer was integral to the production of nanorod arrays via electrodeposition as it allowed the open pores to be attached the conductive working electrode, plus it allowed further control over the pore diameter as the pore walls were also simultaneously etched. For example, Figure 4.4 below shows the results for a mild anodisation using a 0.1 M phosphoric acid electrolyte at 195 V following pore widening for 90 minutes at 37°C in 5 wt% phosphoric acid. Initially these settings gave pore diameters of 160 nm, however, after pore widening this increased to 370 nm. This result, plus those shown previously, highlights the ability to create pores from as small as 23 nm such as when using sulphuric acid, up to nearly 400 nm when using 0.1 M phosphoric acid at 195 V with a subsequent pore widening step.

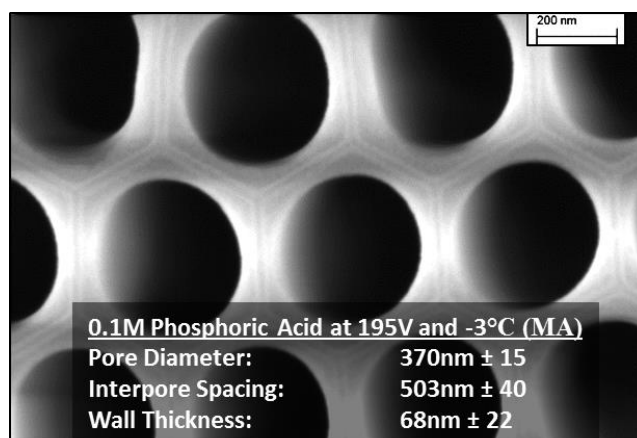


**Figure 4.4:** SEM image of the top of an AAO template created using 0.1 M phosphoric acid electrolyte at 195 V and subsequently widened in 5 wt% phosphoric acid at 37°C for 90 minutes.

Despite the ability to create large pore diameters, this work was focussed on much smaller dimensions so that the nanorod arrays could sustain a plasmonic response. Hence, the focus was solely addressed to the sulphuric and oxalic acid electrolytes which were capable of producing pores less than 100 nm in diameter.

To determine the appropriate length of time required to remove the barrier layer and widen the pores to the required level, multiple experiments were conducted whereby AAO templates were left in the pore widening solution for varying etching times. The resulting SEM images of the barrier layer side using sulphuric acid as the electrolyte at 25 V can be seen in Figure 4.5 for four different etching times.

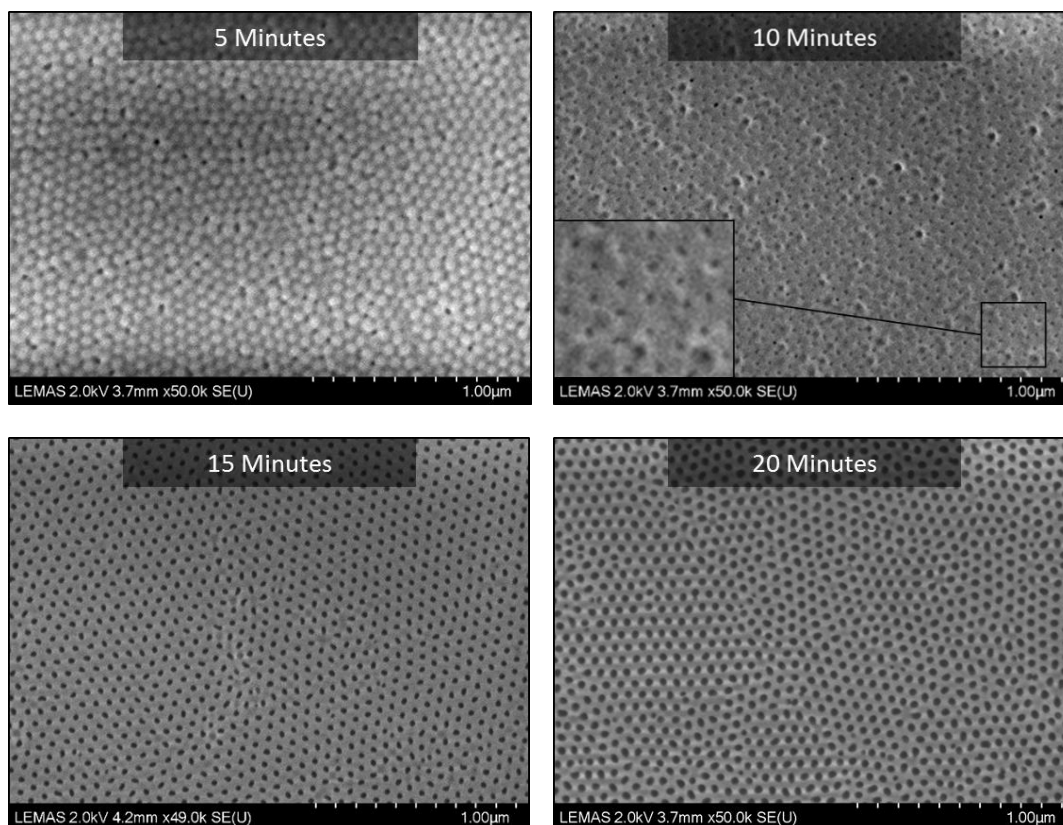


**Figure 4.5:** SEM images for the barrier layer side of an AAO template produced using 0.3 M sulphuric acid at 25 V and widened in 5 wt% phosphoric at 35°C for varying times. The inset in the 10 minutes image shows a magnified view of the small pores just after the barrier layer is removed.

It can be seen that after 5 minutes of etching, the barrier layer was not removed and instead the surface largely still resembled the typical hemispherical capped geometry of the barrier layer. It is noted however that some pores were visible in a number of locations. By analysing their positions with respect to the hemispherical caps it is found that they usually occur within the centre of a hexagonal arrangement, therefore it is believed that these were indeed the first few pores to have their barrier layer removed. In other cases however, the pores were seen to occur not in a hexagonal arrangement, but in lines in between the hemispherical caps. These were instead most likely due to defects in the film that are most prominent along grain boundaries.

Following 10 minutes of etching the results changed considerably. Here it was found that all of the pores have had their barrier layer removed and remained fairly small in diameter. This removal of the barrier layer would allow electrodeposition through the pores at this stage and

therefore 10 minutes was around the minimum length of time that pore widening needed to be performed for the sulphuric acid AAO templates. Despite this, it can also be seen that there is a large variance in the pore diameters, with certain pores significantly larger. These are most likely the pores that had their barrier layer removed after 5 minutes and subsequently carried on growing. On the other hand, after 15 minutes the pore diameters were much more even in size suggesting that the pore widening rate slowed slightly following removal of the barrier layer. In addition, the pores are now all clearly visible and well-ordered. Considering this result, 15 minutes represents a preferential etching time to achieve homogeneous growth of nanorods. Extending this to 20 minutes once again widened the pore diameters in a relatively even manner, therefore providing the option to have larger diameters if required. With continued etching however, the pores would eventually intersect and the stability and ordered arrangement may be lost.

The SEM images of the barrier layer side, as shown in Figure 4.5, were analysed by means of Image J and the Matlab Pore Image Processor software<sup>(186)</sup>. Additionally, the top side of the AAO template was also imaged and analysed in the same manner. This allowed quantitative results to be obtained, as plotted in Figure 4.6.

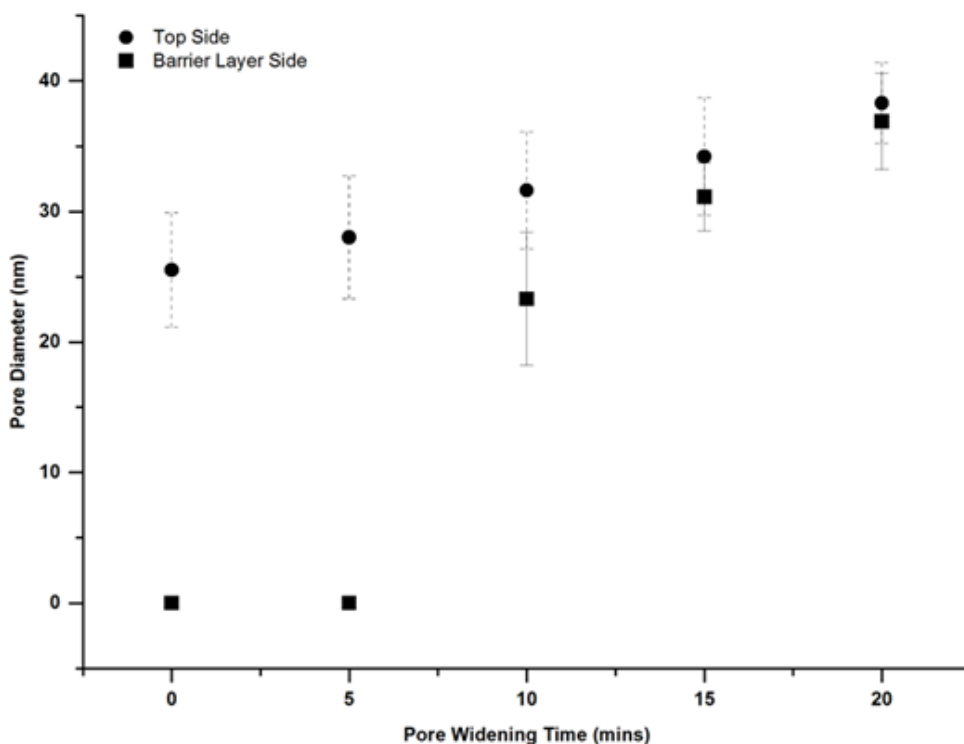


**Figure 4.6: AAO pore diameters for both the top and barrier layer side with pore widening etching time. The AAO was produced using a 0.3 M sulphuric acid electrolyte at 25 V.**

Figure 4.6 shows a number of trends. As expected, with increasing etching time the diameter of the pores also increases. For the top side of the AAO template this widening occurred in a linear manner, giving diameters from 25 nm for 0 minutes, up to 38 nm for 20 minutes. In contrast for the bottom side, the barrier layer was not fully removed until around 10 minutes of etching. At this point the pore diameters averaged around 23 nm, therefore being very similar to the values seen prior to etching. This may signify that the pores had in general only just opened and further widening was yet to commence. In contrast, the pores at the top of the film had widened by around 6 nm at this point, and therefore it may be expected that this increase should have occurred over the entire length of the pore. The reasoning behind this difference is twofold. Firstly, it is noted that during the production of the AAO template, the top of the film may have become slightly wider than that at the bottom due to it being in contact with the acid electrolyte for long periods of time and therefore undergoing dissolution<sup>(160)</sup>. Additionally, for pore widening, the templates are placed in the phosphoric acid solution with their top surface face down so that the barrier layer was completely exposed to the etchant. This may mean that air that was within the pores was unable to escape until the barrier layer was removed, therefore inhibiting the region further down the pores to be widened at the same rate. Despite this, it was noted that with further pore widening the diameter of the pores at the top and bottom of the film increasingly became similar in magnitude.

The above experiments were for the case of using sulphuric acid in the anodisation procedure. For templates made with oxalic acid, similar trends were observed, although longer times of around 30 minutes were required to ensure complete removal of the barrier layer and achieve relatively homogeneous pores. This is expected as the higher potential of 40 V used for the oxalic acid anodisation makes the barrier layer proportionally thicker. Etching the oxalic acid templates for 30 minutes led to pores around 60 nm in diameter, however, larger sizes could be produced if necessary. For example, by carefully controlling the pore widening time, templates with pores as high as 80 nm were fabricated using oxalic acid templates, as seen in Figure 4.7. Alternatively sulphuric acid templates were successfully widened for 40 minutes to give pores around 50 nm in size.

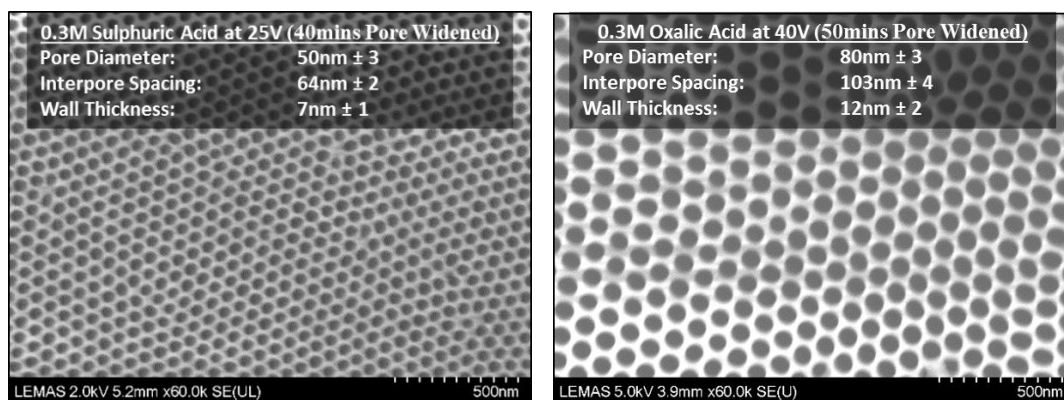


**Figure 4.7: SEM images for the top surface of AAO templates using various electrolytes, voltages and pore widening times.**

These results highlight that the AAO templates produced are capable of being customised to give a large variety of diameters that would be suitable for growing a plasmonic nanorod array. In addition however, it should be noted that the pore widening process not only allows control over the diameter, but also dictates the wall thickness of the pores. This is crucial as the spacing between the nanorods (edge to edge) will be directly equal to twice the wall thickness, and therefore this will determine the degree of coupling. For example, in the pre-widened templates shown previously in Figure 4.2, the spacing would be 50 nm and 68 nm for sulphuric and oxalic acid electrolytes respectively. Alternatively, after significant widening such as those in Figure 4.7, these spacing are reduced down to 14 nm and 24 nm respectively, therefore allowing the inter-rod coupling strength to be controlled.

## 4.2 Characterisation of Nanorod Arrays

The fabricated AAO membranes shown in the previous section were used as templates during electrodeposition to grow ordered nanorod arrays. The aim was that the nanorods grown should have a high quality whereby they are well ordered, have equal dimensions in terms of their aspect ratio, diameter and spacing, and lastly that they are grown in all of the pores of the template thereby providing a large deposition area that may be used for subsequent experiments. Within the following section, it will be shown that the following criteria were met and that high quality nanorods were produced. All nanorods and substrates shown were produced from gold and had the AAO template removed unless stated otherwise.

In addition to the above, to further understand the plasmonic properties of the arrays, it was required that certain elements of the array be varied such as the aspect ratio, spacing, and diameter. This allowed the ability to assess how these parameters affected the plasmonic

properties of the array, and therefore determine configurations that may be suitable for taking forward into photocatalytic experiments. This section will outline the nanorod arrays produced, showing that excellent control over the geometry was achieved as determined via analysis using a combination of SEM, Pore Image Processor software <sup>(186)</sup>, and Image J <sup>(187)</sup>. The optical properties of the arrays are then also outlined, obtained via UV-Vis spectroscopy with an integrating sphere. As explained later, this allows specific determination of the absorption and scattering from the arrays, therefore probing the optical properties in detail.

#### 4.2.1 SEM Analysis of Nanorod Arrays

Firstly, the nanorod arrays that were initially grown in the commercial Whatman templates were analysed, as seen in Figure 4.8. Here the images on the left refer to nanorods produced using the Whatman templates that were quoted as having a pore diameter of 200 nm, whereas the images on the right are for nanorods produced using the Whatman templates quoted as having a pore diameters of 20 nm. Both of the images at the bottom of Figure 4.8 were taken with the sample tilted so as to better see the long axis of the rods.

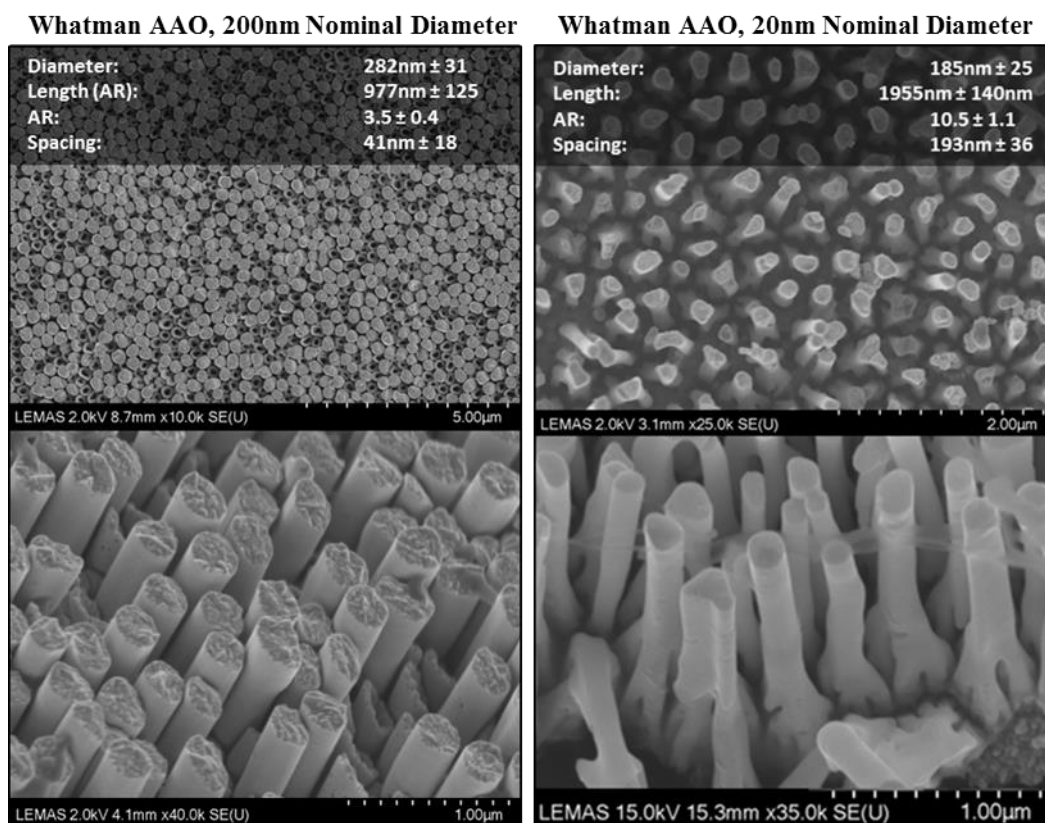


Figure 4.8: SEM images of the nanorod arrays produced using Whatman AAO templates.

Studying the above images it can be seen that for both AAO templates, nanorods were successfully produced. For the 200 nm nominal diameter templates, although the bulk of the nanorods formed were solid, there are many that appeared hollow towards the centre and therefore represented nanotubes. These nanotubes typically form in pores when nucleation on the walls is encouraged, such as with a conductive layer. With further deposition, the walls of the nanotubes typically grow until eventually they join and form solid nanorods <sup>(190)</sup>. One possible explanation why both nanorods and nanotubes are formed when using the large diameter Whatman template is that during evaporation of the gold substrate, the gold is unable to fully cover the open pores and instead goes inside the pores coating the walls. This method has in fact been shown as a potential method to fabricate nanotubes without subsequent electrodeposition, as seen in the work of Dickey *et al.* <sup>(191)</sup>. On the other hand, the nanorods formed were therefore located either in pores that have had their bottom completely covered during the evaporation procedure, or where the walls have grown sufficiently to give solid rods. This hypothesis for the production of nanotubes was further supported when analysing the dimensions of the nanorods. It was seen that although a 200 nm nominal diameter is given, in fact the nanorods were much larger than this, equalling nearly 300 nm. This would therefore have further encouraged the evaporated gold to go inside the pore walls and promote formation of nanotubes. Additionally, it can be seen that although these nanorods have large diameters, the spacing between them was relatively small at ~40 nm. The nanorods also appear to have smooth surfaces and are well distributed, with deposition occurring in all pores. This is encouraging as it shows that high quality nanorods were produced. Despite this, the large diameters of 300 nm are far from ideal for plasmonic applications and therefore much smaller diameter nanorods needed to be produced.

As a result of this, the 20 nm nominal diameter Whatman AAO templates were also initially employed, as seen in Figure 4.8. As discussed in the previous section, the pores of these templates varied greatly along its length from around 20nm towards the bottom of the templates, to 190 nm at the top. This change in morphology was therefore also reflected in the nanorods produced whereby they had relatively large diameters averaging 185 nm, which break down towards the bottom into a root-like structure with diameters typically less than 60 nm. This feature greatly disordered the array and gave an undesired inhomogeneity to the rods. Furthermore, the spacing seen between the nanorods, calculated between the more prominent larger diameter sections, was relatively high at nearly 200 nm. At these distances it was unlikely that any strong inter-rod coupling would occur, and this therefore would hinder its plasmonic properties. On the other hand, once again the majority of the pores in the

template were filled and the lengths of the rods were relatively similar. Despite this, it is apparent that the commercial Whatman templates were, as suspected, unsuitable for producing plasmonic nanorod arrays and instead homemade AAO templates were required.

As previously stated, it is important that the deposition within the AAO templates covers large regions (several mm<sup>2</sup>) so that subsequent experiments could be performed such as the photocatalytic ones described in Chapter 7. It was found that this was capable of being achieved in the homemade AAO templates shown in Figure 4.9. Here the inset shows a template before and after deposition of gold with the deposited area clearly turning red due to the plasmonic properties of the nanorods.

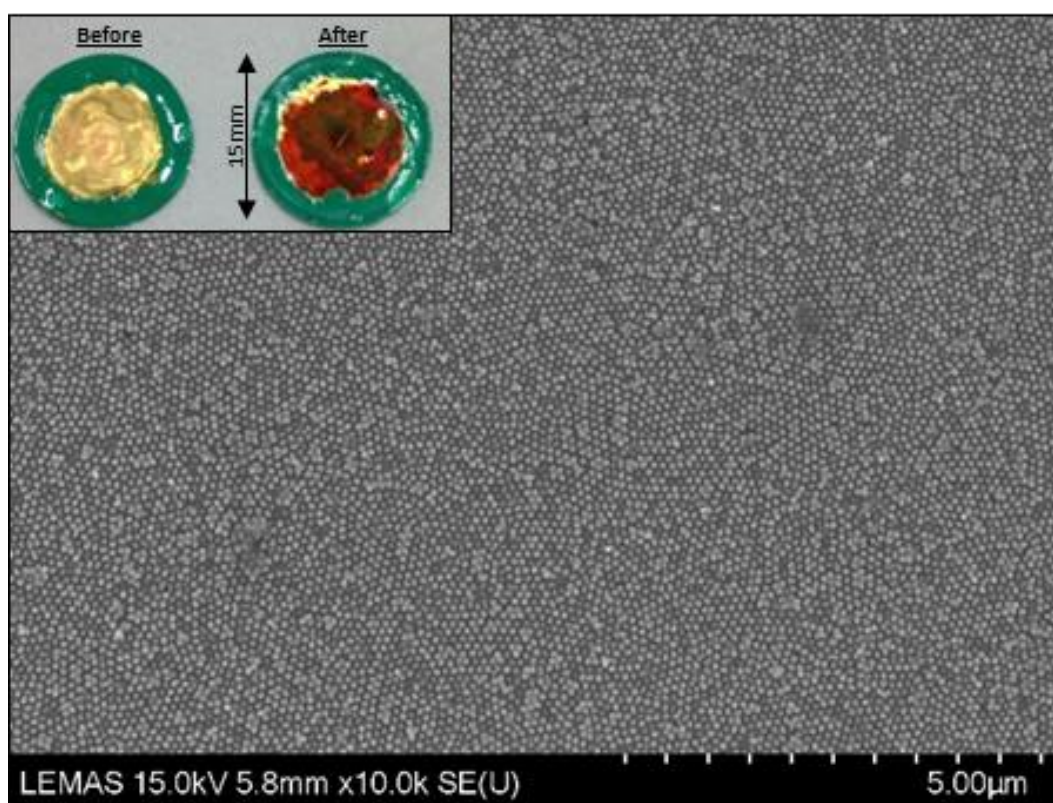
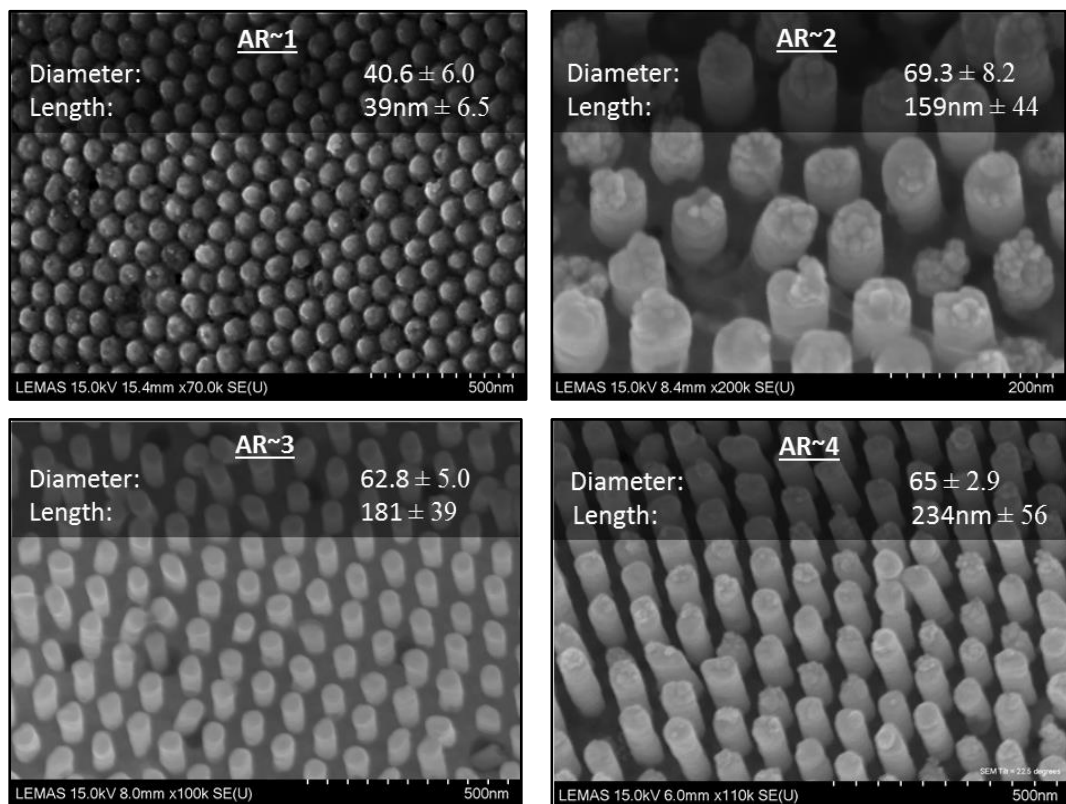


**Figure 4.9:** SEM image showing widespread deposition in pores of homemade AAO template over large areas. The inset shows a picture of typical templates before and after deposition where the colour changes from gold to red due to the plasmonic properties of the gold. The green around the outside is the nail varnish used to insulate the aluminium supporting ring.

This high degree of deposition, whereby the vast majority of pores were filled, was achieved by wetting the pores before deposition, as outlined in Chapter 3. It was further found however, that in addition to this, the best depositions occurred in templates that had a high quality

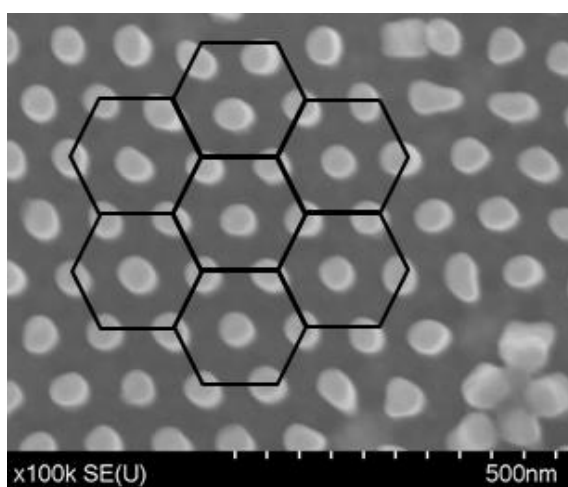
substrate evaporated on to them at a slow rate (0.1-0.2 nm/sec), and those that had their barrier layers evenly etched. Additionally, it was also found that more homogeneous growth occurred if the electrolyte was allowed to sit for a minute in the template before deposition, and when the open circuit potential remained constant (typically at around -0.07 V) , indicating no leaks or exposed aluminium was present.

The homogeneous growth mentioned above was crucial when growing short nanorods. This is because the deposition was performed for only a small time period, and therefore if nucleation did not occur in all pores simultaneously, certain pores may be left without any growth. This would result in them appearing as gaps in the array and disrupt its periodicity. Similarly, if nucleation occurred but the growth rate varied between pores, this would result in nanorods that are not of uniform length. The difference in the length of the rods was much more significant compared to the total length of the rods when aspect ratio was small, leading to relatively larger variance. Despite these difficulties, homogeneous growth of short nanorods was achieved over large areas with only occasional defects. This is summarised by the SEM images in Figure 4.10 for nanorods with AR's produced between one and four.



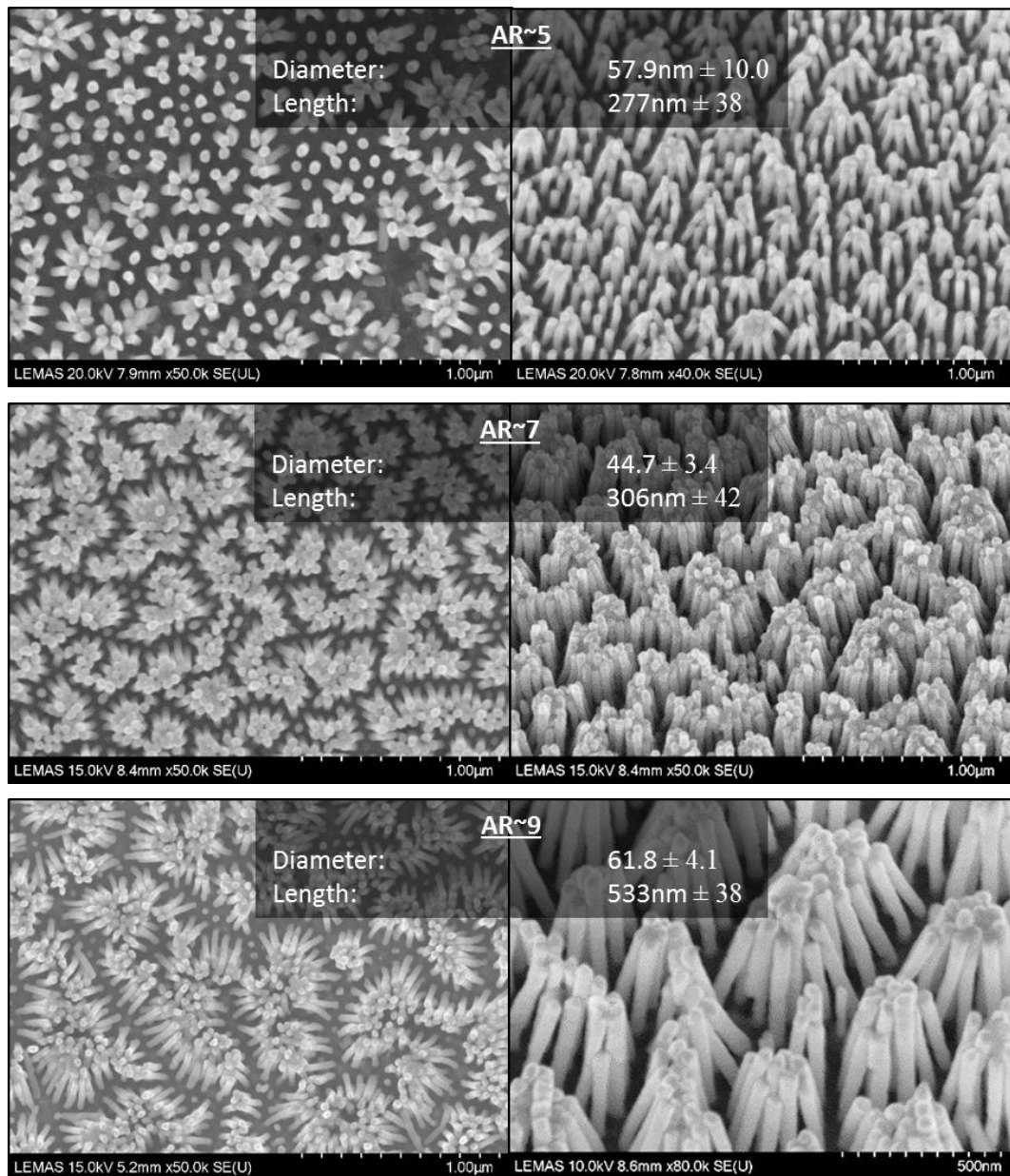
**Figure 4.10: SEM images for short nanorod arrays with aspect ratios between 1 and 4.**

Figure 4.10 shows that good control was achieved over the size of the nanorods produced, allowing aspect ratios as small as one to be fabricated. In all cases, the lengths of the nanorods were reasonably uniform with lengths deviating in general by no more than 25% of the total length. Although it was apparent that some pores did not have growth within them, as clearly seen in the images of aspect ratio of one and two, the vast majority of pores have been utilised. In contrast to the previously shown depositions within commercial templates, the nanorods produced in the homemade AAO templates had much smaller diameters and remained even throughout their length. Additionally, a high degree of order is apparent, with a hexagonal arrangement recognisable, as represented in Figure 4.11 for a plan view image of the array.



**Figure 4.11: SEM image for a nanorod array with the hexagonal ordered arrangement highlighted by the drawn lines.**

One of the benefits of using templated electrochemical deposition is that much longer aspect ratios can be produced compared to other fabrication techniques, such as the seeded growth method. This gives the ability to have much greater control over the resonance position due to its strong dependence on the aspect ratio. In addition to the above short nanorod arrays ( $AR < 5$ ), arrays with longer lengths were produced ( $AR 5-10$ ). This was simply achieved by allowing the deposition to run for longer time periods, and therefore, more charge to pass. These arrays for aspect ratios of 5, 7 and 9 can be seen in Figure 4.12 whereby the left-hand image is in plan view and the right-hand image is with the sample tilted. It can be seen that a major difference occurred for these longer nanorods than for the shorter rods previously shown, whereby the top end of the nanorods appeared to coalesce. As the base of the rods is fixed, this resulted in many of the nanorods being no longer vertical but instead being bent towards each other. This effect was due to surface tension (capillary forces) during drying following removal of the template by wet-chemical etching <sup>(134, 192, 193)</sup>.



**Figure 4.12: SEM images of nanorod arrays produced with aspect ratios of 5, 7 and 9. The left-hand images show the plan view whereas the right-hand images are with the sample tilted.**

Discussing the aggregation of the nanorods in more detail, Hill *et al.* <sup>(193)</sup> explained that this occurs when the water level during drying drops to levels below the tips of the nanorods. At this moment, the meniscus between two nanorods either has an attractive force, or a repellent force, that causes the nanorods to bend towards those adjacent. This only occurs however when this force is greater than the tensile strength of the rod, which is why no agglomeration was seen for the larger 185 nm diameter nanorods with an aspect ratio of ten, as shown previously in Figure 4.8. On the other hand, if the diameter and spacing is small enough, or the AR is sufficiently large, the surface tension forces will act to plastically deform the

nanorods together. Additionally, if this was done to the point whereby the nanorod ends touch, further van der Waals or surface energy forces act to keep them together following drying.

As can be seen in Figure 4.12, the onset of the agglomeration for the nanorod diameters and spacing's typically used within this work, was around an aspect ratio of five. At this point, some of the slightly shorter nanorods were free standing, however, the longer nanorods agglomerated. As the aspect ratio was increased, such as in the AR=7 and AR=9 images, the agglomeration became more apparent and very few nanorods were left free standing. This has negative consequences as it reduces the periodic nature of the array and creates an uneven spacing between the rods. Although a number of techniques have been shown to be able to stop this agglomeration, such as that of drying within an electric field <sup>(193)</sup> or supercritical fluid drying <sup>(192)</sup>, the scope of these methods was beyond this work.

It should be noted that the agglomeration was only prominent following the removal of the AAO template. In contrast, before etching of the template the nanorods stayed evenly spaced including those with high aspect ratios. This is beneficial as it allowed determination of the optical properties for non-agglomerated nanorods, therefore allowing better comparison both with smaller aspect ratio nanorods, and with other high aspect ratio rods. This distribution of the nanorods in the AAO could be seen by taking a flake of the sample and mounting it vertically in the SEM, as seen in Figure 4.13. This allowed the nanorods, substrate, and the supporting AAO to be viewed simultaneously, whereby it could be seen that the pore channels and subsequent nanorods grown within them were straight and separated only by the thickness of the AAO wall. Incidentally, this method also allowed the accurate determination of the height of the rods, and was therefore used throughout this work to measure the lengths.

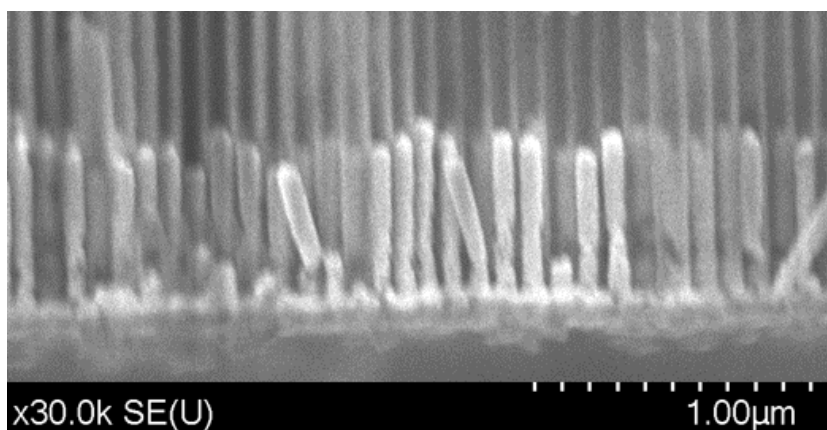
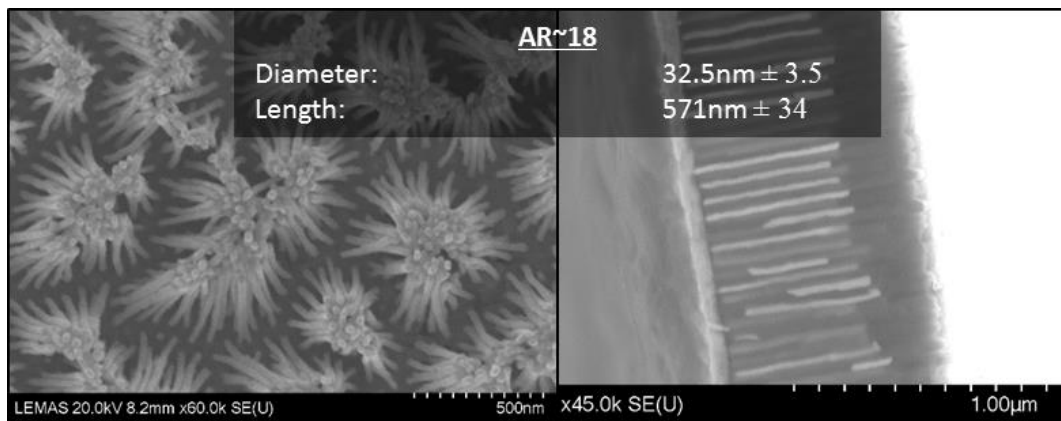


Figure 4.13: Cross-Sectional SEM image of nanorods supported in AAO template.

As discussed in Chapter 2, nanorod arrays with strong inter-rod coupling often have unique optical properties, such as a coupled mode, that only becomes apparent for very long nanorods. For this reason, nanorods with aspect ratios greater than 10 were also fabricated, such as that seen in Figure 4.14. Here the aspect ratio of the rods was around eighteen with a gap size, measured between the walls of adjacent rods, of  $44 \text{ nm} \pm 4.8$ . Once again it can be seen that without the AAO, the rods agglomerated together, however within the template they were well separated.



**Figure 4.14: SEM images showing long nanorods with AR=18 including a cross sectional view to enable accurate measurement of the lengths.**

So far the bulk of the results have focussed on the high degree of control that may be achieved on the aspect ratio, achieved by performing electrodeposition for varying lengths of time. In addition to this however, the spacing between the rods was also a critical feature and may too be controlled by careful adjustment of the template. For instance, Figure 4.15 shows a number of nanorod arrays with the spacing varied from fifty nanometres down to ten. This was achieved by pore widening the AAO templates for different time periods.

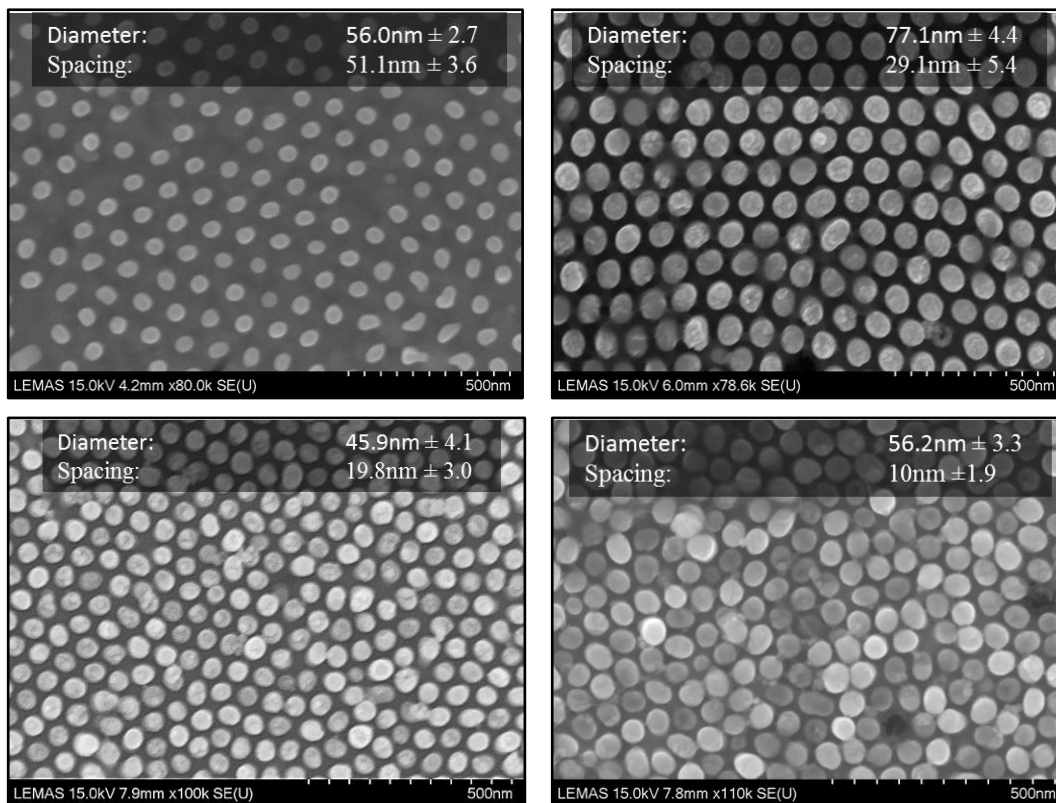


**Figure 4.15: SEM images showing the ability to control the spacing of the nanorod arrays.**

Lastly, in addition to the geometrical factors already outlined, the material deposited may also be altered. The above has so far focussed on the deposition of gold due to its stability and resistance to oxidation, however, other metals such as silver can readily be deposited. This can be done either singularly, or the electrolyte may be periodically alternated to grow multi-material nanostructures, aptly named barcode nanorods due to the difference in contrast seen between the metals in SEM images. An example of one of these multi-material nanorod arrays is shown in Figure 4.16 whereby a 20 nm Whatman AAO template was used with gold deposited first, followed by silver. The distinct boundary between the metals was apparent, and by performing EDX, the presence of the two metals was confirmed.

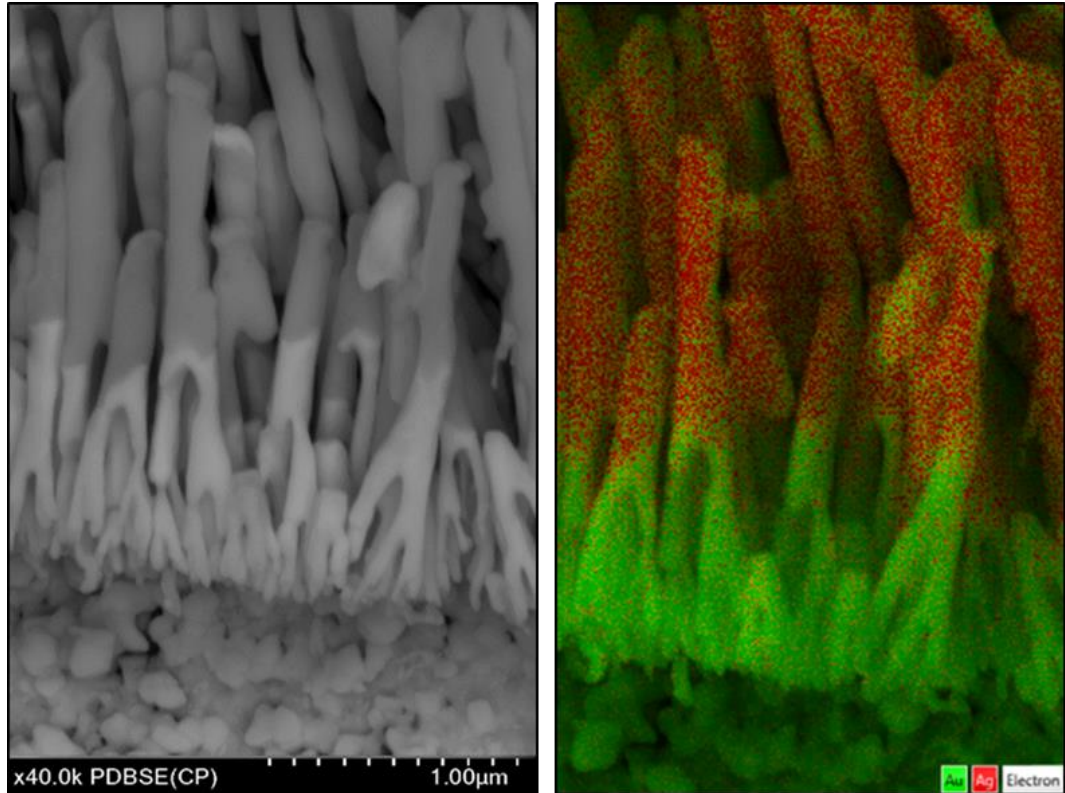


**Figure 4.16: SEM image of Au-Ag multi-material nanorod array grown in a Whatman 20 nm commercial template (left), and accompanying SEM-EDX layered image highlighting the two materials (right).**

#### 4.2.2 Optical Properties of Nanorod Arrays

The optical properties of the nanorod arrays were investigated by means of UV-Vis spectroscopy using an additional integrating sphere module. The integrating sphere is a versatile tool that is particularly useful for highly scattering or reflective samples. In previous work<sup>(132, 134, 194)</sup>, the optical properties of nanorod arrays has been collected from transmittance data and expressed as the optical extinction. Due to the high reflectance and diffuse scattering from the samples however, the reduction in transmission measurements could not be solely attributed to absorption by the array. Within this work, the use of the integrating sphere in a number of different configurations allowed the determination of the nanorod arrays optical properties, including the absorption. The principle behind the integrating sphere along with an outline of the possible configurations is shown within Figure 4.17.

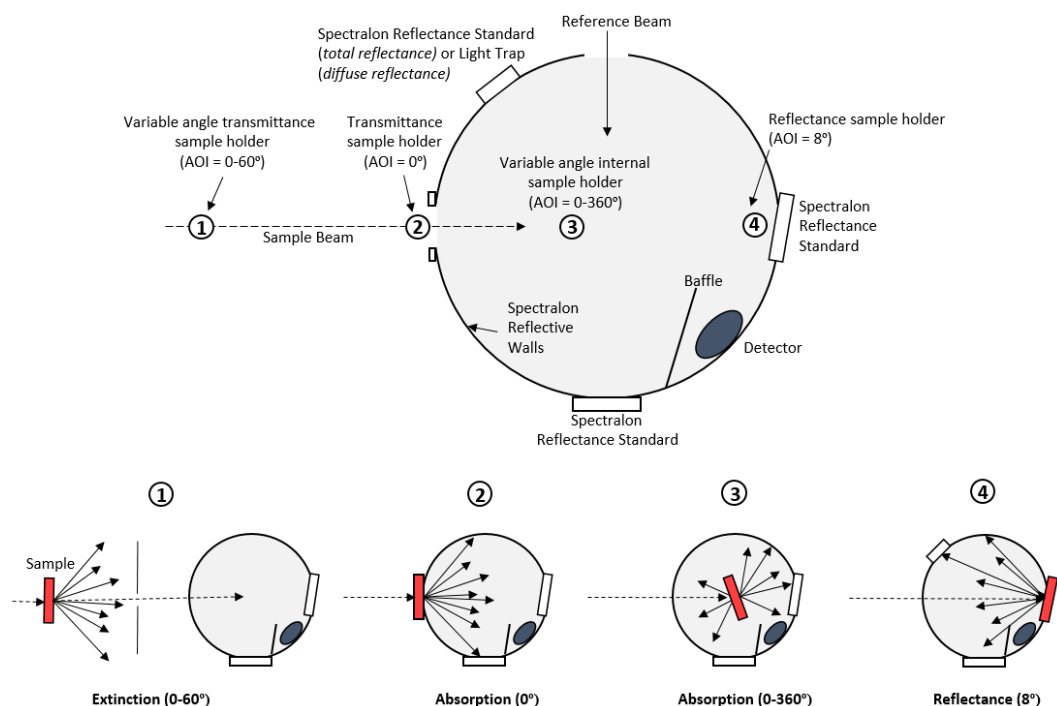


**Figure 4.17: Schematic diagram of the 150 mm integrating sphere. The numbers 1-4 represent possible positions the sample may be placed and the resultant optical properties they probe, as discussed within the text.**

An integrating sphere consists of a highly reflective hollow sphere with a number of ports to allow light to enter or exit. The light inside the sphere undergoes multiple reflections off the walls so that a constant radiance (radiant flux density per unit solid angle) is achieved. A detector is also placed within the sphere, however a reflective baffle restricts it so that it is not directly illuminated from the primary light but only from the reflections. The homogeneous radiance within the sphere then dictates the total flux that is incident upon the detector. This in turn can then be related to the total radiance over the sphere surface by accounting for factors such as the diameter of the sphere and the fraction of the surface occupied by ports.

The accuracy of an integrating sphere is reliant on the ability of the surface coating to be reflective over all the experimental wavelengths. For this reason, Spectralon® is typically used which shows exceptional reflectance over the wavelength range 200-2500 nm. Additionally, the sphere size must be large enough so that the ports do not occupy too much of the sphere's surface area. Both of these factors were accounted for within these experiments by using a Perkin Elmer Lambda 1050 UV-Vis equipped with a large 150 mm integrating sphere.

The benefit of using an integrating sphere for optical measurements is due to its versatility in measuring various properties of the sample by altering the configuration used, as shown in Figure 4.17. For example, if the sample transmits light, transmission measurements may be performed. In configuration one, the sample is placed a large distance from the integrating sphere, or within this specific case even a standard detector, meaning the scattered light from the sample does not reach the detector, and instead only the directly transmitted light is measured. This results in the attenuation of the signal being related to both the absorption and scattering of the sample, therefore giving the optical extinction. Under this setup, a Perkin Elmer Solid Sample Variable Angle Holder (*P/N B0152471*) was utilised allowing accurate control of the sample angle between 0 and 60° with respect to the incident beam.

On the other hand, by placing the sample in the in-built transmission sample holder at the sample beam entrance port, as in configuration two, the absorption of the sample may be measured. This is due to the scattered light being directed into the integrating sphere, and therefore contributing to the radiant flux on the detector. Unfortunately, this configuration is only applicable to samples placed normal to the incident beam as it must be ensured that all scattered radiation enters the sphere. A solution to this problem is to mount the sample inside the integrating sphere using the Perkin Elmer Centre Mount Sample Holder (*P/N PELA9039*). Under this third configuration, all the scattered and transmitted light is collected by the sphere and therefore the attenuation of the signal can directly be related to the absorption of the sample at varying angles of incidence.

Lastly, if the samples are opaque, the integrating sphere may also be used in reflectance mode, as represented by configuration four. By replacing the Spectralon reflectance standard with the sample, light that is reflected from the sample is gathered by the sphere and contributes to the radiant flux on the detector. Additionally, this rear sample holder is positioned at an angle of 8° with respect to the incident beam, thereby directing the specular reflected light on to either a light trap or a Spectralon reflectance standard. In the first case, the specular component of the reflected light is captured therefore eliminating any back reflection and resulting in only the diffuse reflectance being measured. On the other hand, in the second case, all the reflected light is re-radiated thereby measuring the total reflectance of the sample.

In the analysis of the nanorod arrays, the above configurations were used to identify their optical properties, the results of which are outlined below. Firstly, the extinction of the

nanorod arrays was investigated for three different aspect ratios, namely short nanorods (AR=3), medium nanorods (AR=7), and long nanorods (AR=18) using unpolarised light at both 0° and 20° angle of incidence. In these experiments the nanorods were left within the AAO template so as to prevent agglomeration of the rods, however the opaque backing was removed thereby allowing transmission of light. With regards to the dimensions of the arrays, both the long and medium aspect ratio nanorods were produced in sulphuric acid AAO templates, however they were pore widened for varying lengths of time. In contrast the short aspect ratio nanorods were produced in an oxalic acid AAO template. The diameters and spacing for each of these nanorod arrays are summarised in Table 2 below, whereas the respective extinction spectra are shown in Figure 4.18.

**Table 2: Diameter and spacing of the arrays analysed by UV-Vis spectroscopy**

Name	AR	Diameter	Spacing
Short Nanorods	3	62 nm	40 nm
Medium Nanorods	7	46 nm	22 nm
Long Nanorods	18	32 nm	44 nm

The results in Figure 4.18 show a number of interesting points. Firstly, for all aspect ratios, a peak is seen both at 480 nm and 540 nm. The peak at 540 nm is due to the transverse mode of the nanorods, and appears at both 0° and 20°. Furthermore, although difficult to visualise within the spectra, it is noted that with increasing diameter the peak red-shifts slightly from approximately 537 nm to 542 nm and appears to broaden. These observations fit with those found within the literature review for nanoparticles with increasing diameter <sup>(58)</sup>. Similarly, this slight shift in the transverse wavelength may also be due to the theoretical small blue-shift seen as the aspect ratio of the nanorods increases <sup>(59)</sup>.

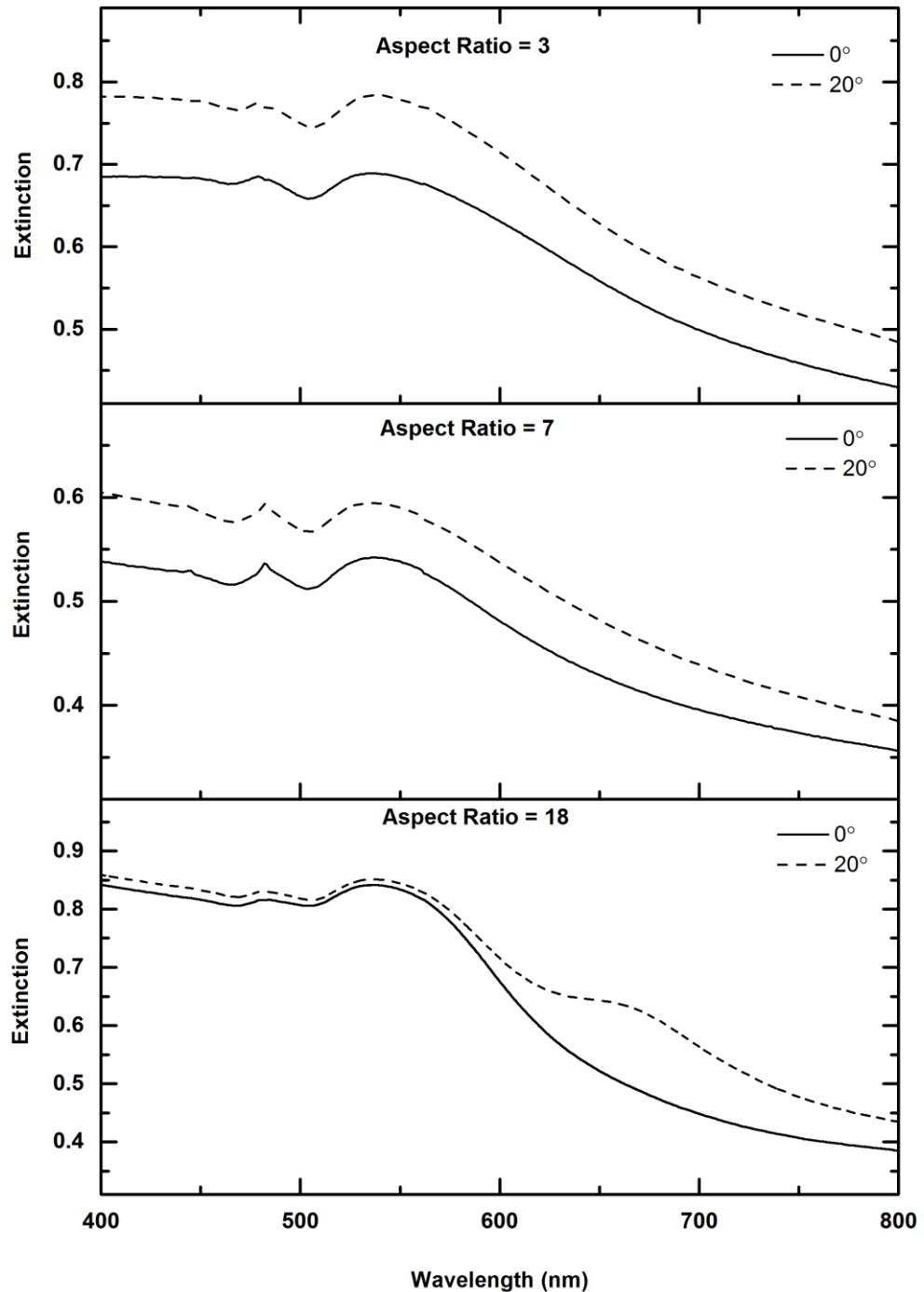


**Figure 4.18: Extinction data for nanorod arrays in AAO with varying aspect ratios and at 0° and 20° angle of incidence. Unpolarised light was used for all measurements shown.**

In contrast, the origin of the peak seen at 480 nm is difficult to explain as it occurred at around the same position for all angles of incidence tested. Although initially believed to be due to interference effects from the thick AAO template, subsequent analysis later on suggested that this is not the case. This is discussed in more detail later within this section.

Another prominent result from Figure 4.18 is the lack of a longitudinal peak at higher wavelength than that of the transverse mode for all conditions except the AR=18 nanorod at 20°. This was confirmed by performing additional scans up to a wavelength of 2000 nm and noting that no discernible peak was observed. Based upon an isolated rod, it would be expected that a longitudinal peak occurs for all non-zero angles of incidence, which for the AR=3 rods would occur within the visible spectrum, and for the longer aspect ratios, would red-shift into the infra-red. The reasoning why no longitudinal peak was seen however for both the AR=3 and the AR=7 nanorod arrays is due to their unique optical properties.

As discussed within Chapter 2, the longitudinal mode for an isolated nanorod red-shifts linearly with increasing aspect ratio. When arranged in a side by side array however, this longitudinal mode splits into both a blue-shifted bright mode and a red-shifted dark mode, the degree of which is dependent on the inter-rod coupling strength. As previously discussed, this coupling strength increases for a decreasing particle separation and lower refractive index of the surrounding medium. Within these experiments, the relatively small spacing resulted in a strong inter-rod coupling strength. For both the small and medium aspect ratio nanorods this was strong enough to blue-shift this coupled mode into that of the transverse mode, meaning only one peak was apparent in the spectra. Alternatively, at an aspect ratio of 18, although it is also blue-shifted significantly from the position of the isolated longitudinal mode wavelength, the longer aspect ratio sufficiently red-shifts the coupled mode away from the transverse mode, to instead give a separate peak within the visible region.

To confirm the higher wavelength peak seen for the aspect ratio of 18 nanorods is indeed the blue shifted coupled mode, a number of further investigations were carried out. For example, theory predicts that the coupled mode may only be excited at an angle of incidence greater than zero using p-polarised, and not s-polarised light. This is due to its origin being from that of the longitudinal mode, therefore requiring an E-field component along its long axis. As seen previously in Figure 4.18, using unpolarised light, which included contributions from all polarisations, the mode was only excited for the 20° angle of incidence and not for 0°, therefore supporting the conclusion that this was indeed the coupled mode. Additionally, by using a Glan-Thompson polariser supplied from Perkin Elmer (*P/N B050-5284*), the polarisation of the incident light could also be controlled. As seen in Figure 4.19, using an angle of incidence of 20°, but varying the polarisation, results in the coupled mode being excited only for p-polarised light. Once again this supports theory and gives increased confidence to the origin of this mode.

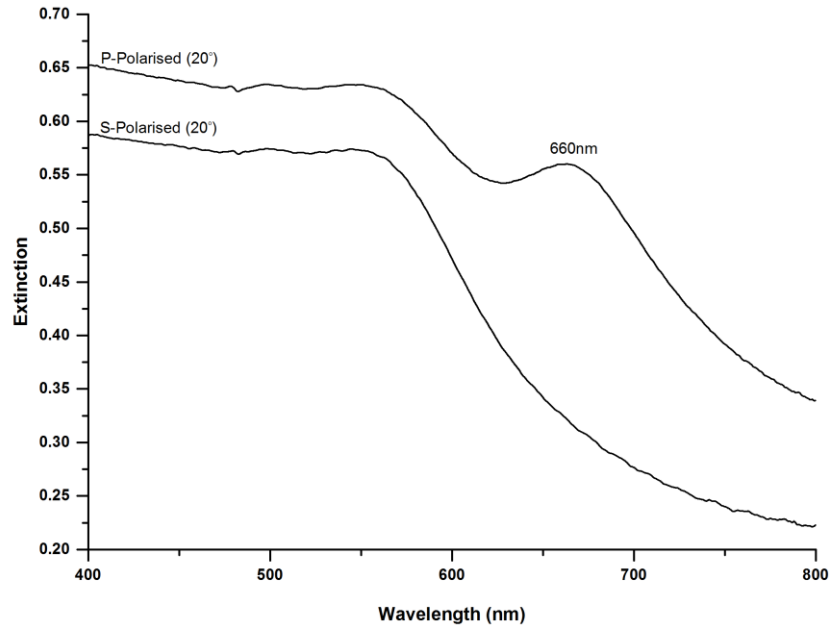


**Figure 4.19: Extinction data for a nanorod array with AR=18 at 20° angle of incidence for S and P polarised light.**

This polarisation dependence can also be viewed in greater detail by performing a polarisation scan whereby the wavelength is kept constant and the polarisation angle is varied between 10° and 330°. Here a polarisation of 0° and 180° represents s-polarised light, whereas 90° and 270° is for p-polarisation. The results of this can be seen in Figure 4.20 using a constant wavelength and angle of incidence of 660 nm and 20° respectively.

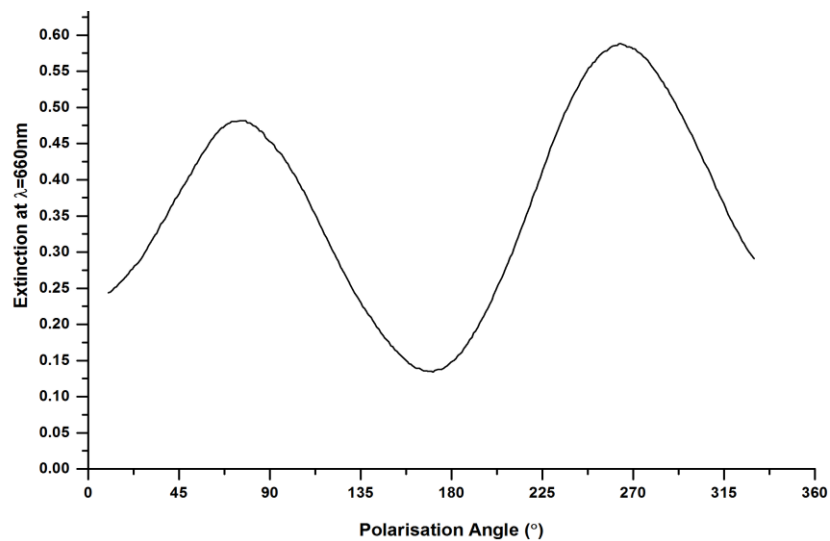


**Figure 4.20: Polarisation scan of nanorod array with AR=18 at a wavelength of 660 nm and angle of incidence of 20°. In this figure, 0° and 180° represent the light being completely s-polarised, whereas 90° and 270° represents the light being completely p-polarised.**

As with the previous results, Figure 4.20 shows the dependence of the coupled modes on the polarisation of the incident light. At both  $90^\circ$  and  $270^\circ$  the incident lights polarisation was completely p-polarised and consequently a maximum in the extinction of the coupled mode was seen. On the other hand, as the polarisation angle shifts towards either  $0^\circ$  or  $180^\circ$ , it increasingly had more s-polarised components resulting in a decrease in the extinction.

In addition to the above, the dependence of the coupled mode on the angle of incidence using p-polarised light was also studied, as summarised in Figure 4.21. It was seen that as the angle of incidence increases from  $0^\circ$  to  $10^\circ$ , the coupled mode began to appear as a shoulder on the side of the transverse peak. At  $20^\circ$  this had developed into a standalone peak with a maximum at approximately 660 nm. Beyond this angle of incidence however the coupled mode appeared to significantly broaden. This broadening above a certain angle of incidence was also found by Kullock *et al.* <sup>(195)</sup> in their retarded dipolar interaction model (DIM). On the other hand, in works <sup>(132, 134, 194)</sup> that have measured the nanorod array extinction with angle of incidence using thin film AAO templates ( $<1 \mu\text{m}$ ), this broadening was not as apparent. The thick (approximately  $40 \mu\text{m}$ ) AAO templates used throughout this work therefore may also have contributed to the broadening of the peaks. Due to this broadening, it is difficult to determine if the resonant wavelength of the peak shifted with angle of incidence, as found by Atkinson *et al.* <sup>(132)</sup> for similar arrays.

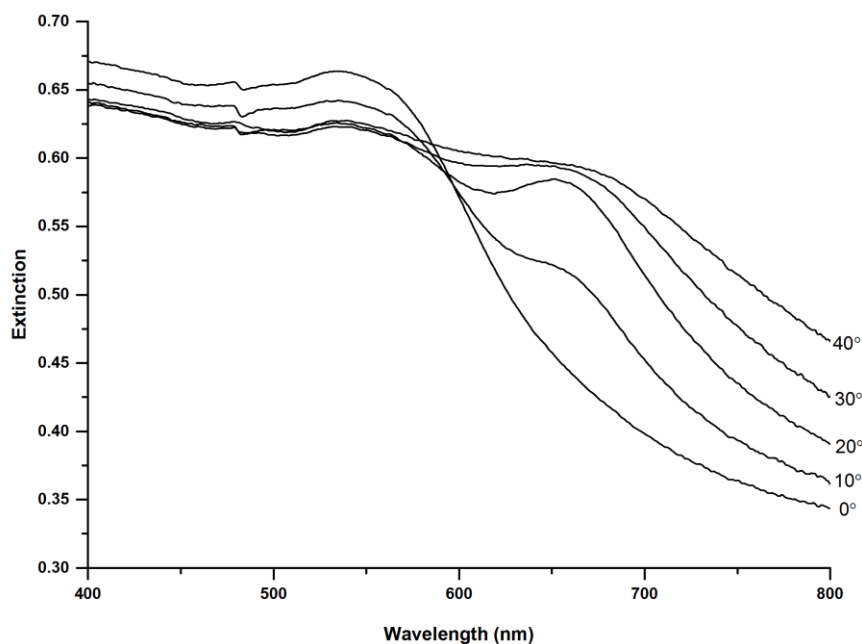


**Figure 4.21: Extinction data for a nanorod array with aspect ratio of 18 using p-polarised light at varying angles of incidence.**

So far the analysis of the nanorod arrays has focussed on the optical extinction, however, as described previously, the use of an integrating sphere also allows the absorption of the arrays to be determined. Here, the samples were placed within the integrating sphere using a centre mount accessory, as in configuration three of Figure 4.17. The absorption by the long nanorods of aspect ratio 18 at varying angles of incidence and using p-polarised light is shown in Figure 4.22.

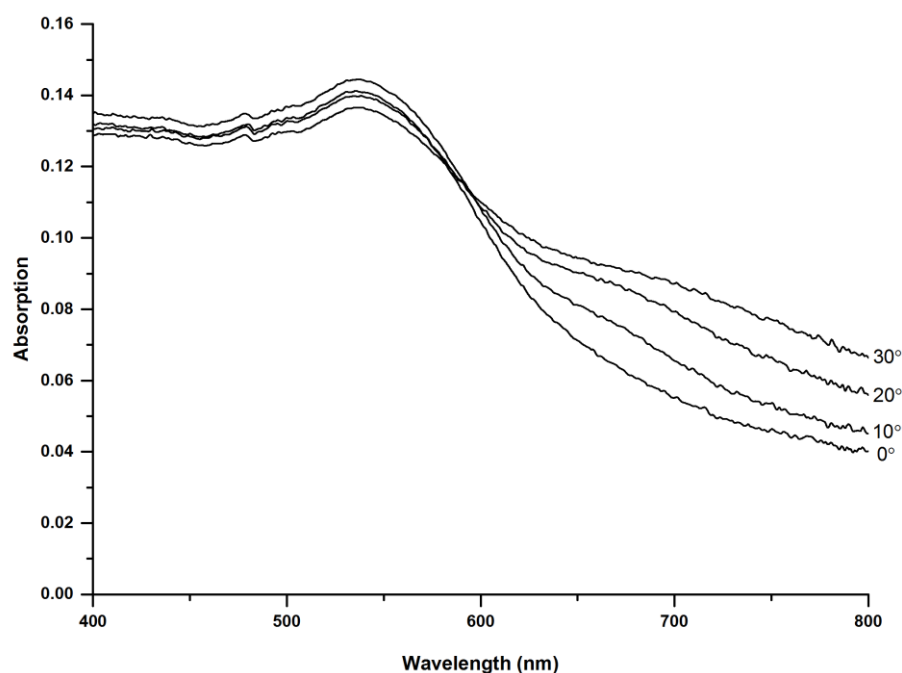


**Figure 4.22: Absorption data for a nanorod array with aspect ratio of 18 using p-polarised light at varying angles of incidence.**

Although a direct quantitative comparison of the extinction and absorption values was not possible due to the sample being positioned in a different location, the upmost effort was taken to ensure the same sample area was illuminated in both configurations. This therefore allowed a qualitative comparison and a general assessment of how the peaks varied. From Figure 4.22 it is immediately clear that the absorption values were significantly less than the extinction values shown in Figure 4.21. This suggests that, at least for the geometrical parameters of this nanorod array, scattering dominates over absorption. Additionally, the transverse mode has a relatively sharp peak relating to strong absorption whereas the coupled mode is weak and broader in comparison. Modelling results shown in the following chapter support this finding that scattering is dominant for the coupled mode, however, this was only true for long aspect ratio arrays. Interestingly, the peak at 480 nm was also evident within the spectra therefore signifying that this is not due to scattering or reflection from AAO template.

The optical data presented so far focusses exclusively on nanorod arrays that are still embedded within the AAO template and which have had their substrate removed so as to perform transmission measurements. Despite this, it is also worthwhile to study the typical optical properties of the arrays themselves that may be taken forward into photocatalytic experiments, whereby a 150 nm substrate was present and the templates are removed. As these samples are opaque, transmission measurements could not be performed and instead the optical properties were derived by reflectance measurements. This is shown in Figure 4.23 for a gold nanorod array (AR=9) at 8° as compared to a blank gold substrate using a total reflectance configuration. As can be seen, the nanorod array showed distinct differences from that of the bare gold substrate, with in particular a substantial reduction in reflectance seen around 540 nm relating to that of the transverse mode. In contrast, the coupled mode was not visible, possibly due to it either being blue-shifted into the transverse peak, or alternatively it having been too weakly excited at the 8° angle of incidence used. Additionally, it is also interesting to note that the minimum in reflectance of the gold substrate was at 480 nm, therefore matching that of the unknown peak seen in the transmission data. As primarily the substrates were removed from the samples via scratching with a sharp scalpel, it was possible that small fragments were not completely removed and instead contributed to the peaks observed.

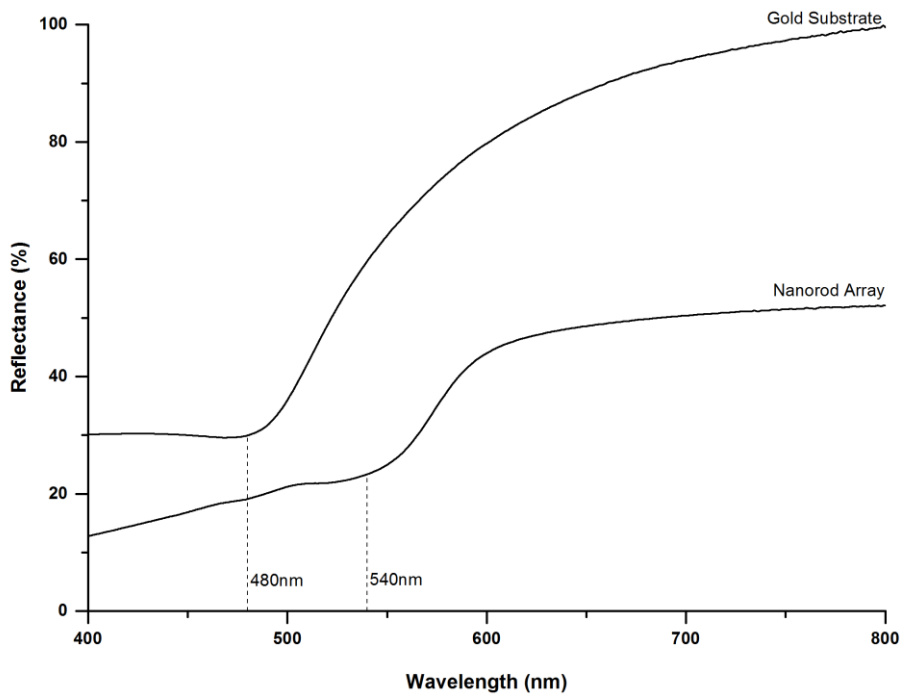


**Figure 4.23: Reflectance data for a bare gold substrate and a supported gold nanorod array at 8° angle of incidence using unpolarised light.**

Lastly, by replacing the Spectralon® reflectance with a light trap, the diffuse reflectance may also be examined. This is shown below in Figure 4.24 for a supported nanorod array of 69 nm in diameter with an aspect ratio 2.3. It can be seen that the diffuse reflectance accounts for the majority of the reflection from the array and that in turn, the specular reflectance is very low.

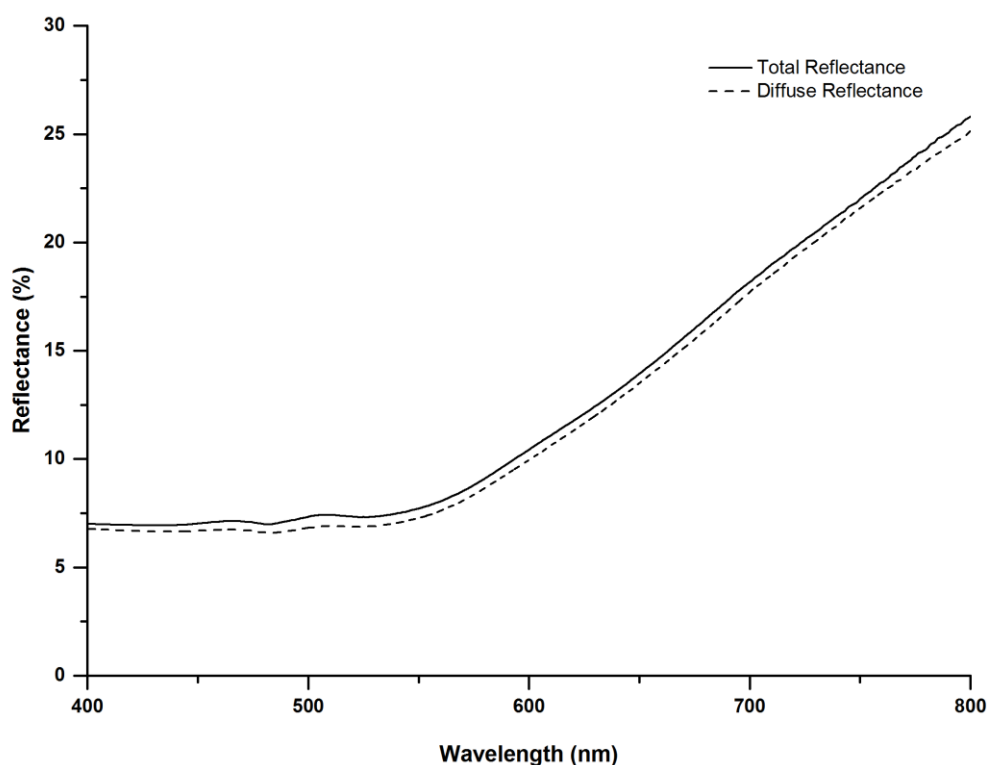


**Figure 4.24: Reflectance data for a supported gold nanorod array at 8° angle of incidence using unpolarised light considering both diffuse reflection and total (diffuse + specular) reflection.**

### 4.3 Summary of Results

In summary, a number of the aims and objectives as outlined within Chapter 1 were successfully met. Firstly, it has been shown that high quality porous alumina membranes have been produced. This was achieved with good control over their size, separation and arrangement, therefore allowing them to be used as templates in the growth of nanorod arrays. In respect to this, it has also been shown that nanorod arrays can be produced over large areas within these templates whereby the diameter and spacing is controlled accordingly. Additionally, by varying the electrodeposition time, the aspect ratio of the nanorods was further controlled. This has allowed nanorod arrays to be produced with a large range in the aspect ratio, limited only by the size of the template. Finally, the far-field optical properties of the nanorod arrays have been determined by using UV-Vis spectroscopy, including

information on the extinction, absorption and reflection, derived via the use of an integrating sphere. This led to interesting optical properties of the nanorod arrays being determined whereby strong coupling between the nanorods leads to the longitudinal mode splitting into a blue-shifted mode. At short aspect ratios this is generally overlapped with the transverse mode, however it has also been shown that at longer aspect ratios, this red-shifts away to form a stand-alone mode within the visible spectrum. Further analysis of these interesting optical properties is covered within the following modelling and EELS chapters in the hope of gaining a greater insight.

# 5 MODELLING OF PLASMONIC RESONANCES

## 5.1 Aims of Modelling

The fabrication of the nanorod arrays studied in this thesis can be a very difficult and time consuming process, furthermore their subsequent characterisation can also prove to be challenging. To aid understanding and provide a means of analysing the plasmonic resonances, modelling techniques can prove to be very useful. For instance, modelling offers the ability to quickly experiment with variables in a system and produce both qualitative and quantitative data on the influence of its parameters. In addition, modelling allows you to test idealised and simplified systems that would otherwise be impossible to fabricate, and therefore probe the underlying fundamental physics. Specifically for this research, the main modelling objectives can be split into three distinct sections:

- 1) Firstly, a simplified system is addressed, consisting of isolated nanospheres or nanorods in a homogeneous medium. As the plasmonic response of nanospheres has a rigorous solution via Mie Theory, the modelling of these systems allows a comparison of the solutions and hence aims to validate the model. Additionally, the modelling of nanorods in a homogeneous environment provides an understanding of how the optical properties are affected by certain variables such as their size, geometry and environment. This fundamental knowledge assists in the analysis of the work in this thesis, and provides objectives during the fabrication of nanorods in order to optimise the plasmonic response.

2) Following on from the initial validation of the model and the subsequent analysis of basic plasmonic systems, the modelling of more interesting plasmonic properties is covered. Specifically this focusses on the affect that coupling has on the plasmonic resonances. This coupling is concerned with both particle-particle interactions and particle-substrate interactions, with the aim of analysing how the presence of each can alter the plasmonic properties of nanorods in a supported array.

Beginning with particle-substrate coupling, the interactions of a sphere with a dielectric and metallic substrate is analysed, before expanding into the more relevant but complex nanorod geometry. The nanorods are placed vertically on the substrate so as to compare with the electrodeposited nanorods fabricated within this work. The modelling is then directed towards coupling between multiple nanorods. This also aims to match the electrodeposited nanorods fabricated, and therefore focusses on nanorods stood in a side-by-side orientation whereby the long-axis of the rods are parallel to each other. Although initial modelling is performed for finite arrays of nanorods, this is expanded into infinite periodic arrays so as to truly represent the coupling that occurs over a large scale. This concludes with the analysis of nanorods that are both in an array and on a substrate. The inclusion of both types of coupling aims to give a direct representation of the fabricated plasmonic arrays produced in this work with the hope of understanding and optimising the interactions that occur.

3) Lastly, I develop a model to simulate electron energy loss spectroscopy (EELS) experiments with the aim to help support the characterisation of the nanoparticles studied in this work. Furthermore, I hope the model will prove useful in analysing other fabricated nanoparticles and provide a means to test plasmonic responses at a fraction of the time and cost of EELS experiments. In addition, due to an electron beam being used within these EELS experiments to excite the plasmons, the point source means that it is possible to excite dark modes of the nanorod arrays that cannot be excited using the more typical plane wave approach. It is hoped this will provide a better understanding of the EELS experiments and aid in the data analysis. As this specific model is in conjunction with the EELS experimental data however, this is not outlined here, but is instead included within the following chapter.

## 5.2 Review of Plasmonic Modelling Techniques

In plasmonics research, the ability to determine the resonant position and strength, plus analyse under what conditions it can be enhanced, is of vital importance. As discussed in Chapter 2, the first widespread means of achieving this was performed by Gustav Mie in 1908

whereby he proposed a general solution to Maxwell's equations to give the absorption and scattering from particles <sup>(196)</sup>. Now referred to as Mie Theory, for the first time this provided a means to produce theoretical spectra for different sized colloidal gold nanoparticles and compare these to experimentally derived ones thereby allowing a rough approximation of the nanoparticle size, well before the existence of electron microscopes <sup>(48)</sup>. Unfortunately, several limitations with this method exist, for instance Mie theory can only deal with spherical particles and requires a homogeneous non-absorbing surrounding medium. Various analytical extensions have been proposed which estimate the results with supporting substrates <sup>(88)</sup> and coatings <sup>(38)</sup> for instance, however Mie theory is still primarily only applicable for spherical particles or its close equivalents in spheroids and ellipsoids <sup>(37)</sup>.

To simulate more complex geometries and environments, it is necessary to move away from analytical solutions towards approximated numerical solutions instead. Since the rise of computing power, numerical solutions have increased in popularity to become a staple amongst engineering and physical science disciplines. With regards to numerical methods for plasmonics, there are a variety of applicable techniques as will be discussed below, each with their own advantages and disadvantages. Here I give just a brief overview of the methods, however for a more indepth discussion I advise the reader to study the following reviews <sup>(197, 198)</sup>.

### 5.2.1 Discrete Dipole Approximation (DDA)

The principle of DDA modelling is based upon representing a target nanoparticle as a finite cubic array of polarisable point dipoles with the spacing between each dipole small compared to the wavelength. The occupied sites of this cubic array may be controlled so as to represent more complex geometries or even multiple interacting particles <sup>(45)</sup>. In the presence of an incident electromagnetic field the polarisability of each point is calculated as a contribution from its interaction with this incident field and with its neighbouring dipoles. Considering an array of dipoles, the solution may be solved exactly to give the scattering and absorption cross sections, meaning the only errors incurred are those derived from the assumption of representing a particle by an array of finite point dipoles <sup>(199)</sup>.

Although, this numerical method takes considerably longer to solve than the analytical solutions, in comparison to other numerical methods it is relatively quick <sup>(198)</sup>. The DDA method also has the advantage of being able to represent geometries of arbitrary shape, composition, and even multiple objects, including for instance, the presence of a substrate <sup>(45)</sup>.

Unfortunately, there are also a number of drawbacks to DDA. When simulating multiple particles such as those in arrays, the memory requirements may grow very rapidly due to the need to assign dipoles to each particle <sup>(198)</sup>. In addition, in order to converge, it cannot simulate high aspect ratio nanoparticles or ones having a particularly large refractive index <sup>(198)</sup>. The accuracy of the technique is also questionable with Draine and Flatau <sup>(199)</sup> reporting typical errors of between 2-5% for the simulation of spheres, however others have reported this to be up to 10% for metallic particles <sup>(45)</sup>.

### 5.2.2 Finite Element Modelling (FEM)

Another numerical method that is particularly suited to simulating complex geometries and environments is that of finite element modelling (FEM). Perhaps the most widely used simulation technique, particularly in the field of engineering, its principle involves discretisation whereby it splits a geometry into a finite number of elements. These discretisation, known as meshing, typically employs tetrahedral elements for 3D structures allowing complex shapes and curves to be represented providing a sufficiently small element size is used, as shown in Figure 5.1.

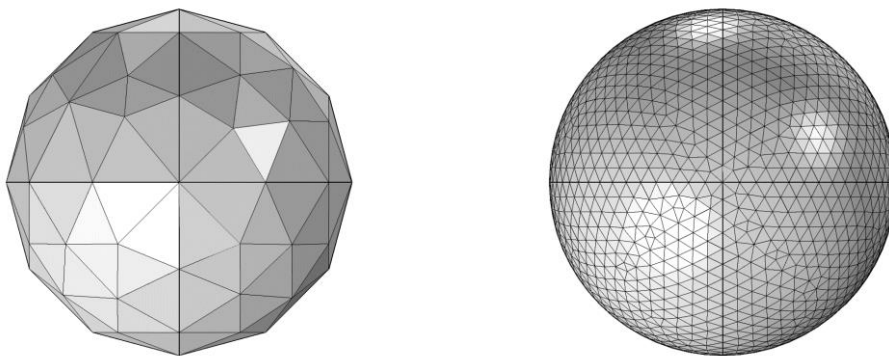


**Figure 5.1: Comparison between course (left) and fine (right) meshing of a sphere showing sufficiently small elements are needed to accurately represent geometries.**

A solution to the simulation is determined by assigning partial differential equations to the element nodes that may be solved or approximated by iterative means to satisfy the boundary conditions. The solutions from each element are then combined to give the overall solution <sup>(200)</sup>. This technique allows a whole variety of problems to be solved in many disciplines, including analysing how nanoparticles interact with electromagnetic waves as is the focus of this work.

The accuracy of the FEM method relies on the ability to create sufficiently small elements, particularly in the areas of interest or where there is a large change in the variables. On the other hand, a trade-off needs to be made with the solution time and computational requirements, as finer meshes drastically increase the time taken to solve and the RAM required. Unfortunately, even with appropriate meshing techniques utilised, FEM still tends to have high computational requirements and solution times, especially for 3D modelling, meaning high-performance PC's with lots of RAM are often needed. On the other hand, it is a very flexible technique that may provide accurate results. For instance, Parsons et. al. <sup>(198)</sup>, found that for a 80 nm gold sphere in a vacuum, FEM results varied from the exact Mie solution by only 0.4% whereas DDA varied by 1.6%.

Despite having high computational requirements and solution times, FEM modelling is incredibly popular due to its versatility and ability to solve a variety of problems, including in multi-physics applications. For example FEM multi-physics models have been used to simulate nanoscale fluid flow from the heating of nanoparticles by lasers <sup>(201)</sup>, thereby combining fluid flow, heat transfer and electromagnetic physics into one model. Furthermore, FEM models are particularly well suited to solving electromagnetic simulations involving arrays of nanoparticles. Unlike DDA which has to represent each individual nanoparticle, FEM models can utilise periodic boundary conditions (PBCs) to vastly reduce the computational domain size. The PBCs are applied in parallel to the sides of the simulation cell and calculate the electric and magnetic field vectors at this interface. The fields at one edge are then matched with those at the opposite edge and solved, resulting in the representation of an infinite array of nanoparticles <sup>(198)</sup>.

### 5.2.3 Finite Difference Time Domain (FDTD)

The Finite Difference Time Domain technique is used for determining approximate solutions to electromagnetic problems within the time domain by solving Maxwell's curl equations by a finite difference method. It operates by splitting the domain into a number of regular box shaped cells that are much smaller than the wavelength of light thereby creating a discretisation of space. These cells also quantize time, whereby the time taken for the fields to travel between the adjacent cells is the step size. Each cell is assigned the electric field along its edges and the magnetic field to the centre of its faces, so that they are half an interval apart. The fields can then be calculated using a leapfrog method where for instance the electric field is solved first and then used to solve the magnetic field, which in turn is then used to solve the electric field at the next time interval <sup>(202)</sup>.

The main advantage of this method is that it allows you to visualise the propagation of a wave with time and how it interacts with a target. It is therefore very useful to use for transient problems. In addition to this, FDTD is also preferable for large simulations as the numerical complexity scales linearly instead of exponentially as with other techniques <sup>(202)</sup>. Furthermore, unlike FEM which requires complex coding and professional software, the simplicity of FDTD means basic problems can be solved by self-written code with less than 100 lines <sup>(203)</sup>. On the other hand, there are a number of significant drawbacks to this approach. For instance, as the model is solved in the time domain, the material properties must be stated for a large range of frequencies. In contrast, other models such as FEM may use readily available experimental data over just the frequencies of interest. This requirement for a large frequency range for FDTD can be mitigated somewhat by using theoretical models to predict the optical data, as with the Drude-Lorentz model for metals, however this may prove difficult for novel materials <sup>(198)</sup>. Additionally, the FDTD method also suffers from disadvantages due to its need for discretisation of the geometry into a cubic lattice. This is due to the difficulty in accurately representing complex shapes, particularly ones which have curved surfaces using cubes. Following on from this, the regular grid structure also may cause problems with regards to the time it takes to solve. As the grid spacing controls the time step, a small step size may be required, however for models with large changes in scale this will likely drastically increase the solution time <sup>(203)</sup>.

#### 5.2.4 Boundary Element Method (BEM)

The Boundary Element Method although very similar to the FEM technique, has offered an alternate option for modelling the nanoparticles, with a number of improvements. The largest of these being that the dimension of the problem is reduced by one so that only the solutions at the boundaries of the surfaces must be determined, rather than the entire volume. This means the meshing is applied only to the surfaces making its implementation much simpler, plus this reduced dimension greatly decreases both the solution time and computational requirements <sup>(204, 205)</sup>. In addition, as only the boundaries are meshed, the surrounding medium of the particle needn't be, and is instead represented to infinity. This offers a benefit when large domains are present and makes the process much more efficient as generally, the solution at the boundaries is what is of interest <sup>(205)</sup>.

The principle underlying BEM is that the solution on a boundary may be approximated by numerical methods by solving boundary integral equations on the surface mesh. This boundary solution is then an exact solution of the differential equation within the interior of

the domain <sup>(204)</sup>. For instance, from an electromagnetics standpoint, the electromagnetic fields scattered from a nanoparticle can be represented by both the surface currents and charges. By applying the boundary condition of continuity of the parallel components of the magnetic and electric fields, a set of surface integral equations can be formed. By meshing the surface these integral equations can be split up into a finite number of linear equations that may be solved numerically <sup>(30)</sup>. For a more detailed mathematical description, we refer the reader to the following work <sup>(206)</sup>.

The drawbacks to this method are that inhomogeneity and non-linear partial differential equations are generally not applicable with BEM. If the inhomogeneity is restricted to certain regions, a combination of FEM and BEM may be used to solve this, however this gives a degree of added complexity <sup>(204)</sup>. In contrast, FEM is a valid for a wider range of problems. Furthermore, the mathematics behind BEM can be unfamiliar and this can hinder its uptake, especially compared to the well understood and validated FEM approach that has been thoroughly developed and can be accessed via professional software.

### 5.3 Modelling Methodology and Validation

As outlined in section 5.2 there are many types of modelling that allow the prediction of the plasmonic response of a nanoparticle. Each of these techniques has its own advantages, drawbacks, and assumptions that need to be considered in order to select an appropriate model for the task. After careful analysis it was decided that FEM modelling was best suited to the purpose of this thesis, owing to its ability to represent accurately complex structures including curved surfaces, as in the case of the nanorods studied here. Furthermore, its ability to greatly simplify arrays of nanoparticles by the use of PBCs is highly advantageous for this work.

The FEM program used throughout this work is Comsol Multiphysics 5.2a in combination with the additional RF module that allows the simulation of electromagnetic waves within the frequency domain. A 3D approach is preferred despite the higher memory requirements due to the anisotropic nature of some of the models. Unlike other modelling techniques whereby geometries can be difficult to define, Comsol allows complicated geometries to be designed simply using its inbuilt geometry tools, or via importation from external CAD software.

A number of different models have been used throughout this work in order to build progressive understanding. In this section I describe the methodology of each model,

beginning with the most basic example of a nanoparticle in a homogeneous environment irradiated by a plane wave. Many of the principles however remain the same between each model and therefore for the more advanced models, only the differences are discussed. To aid in the description of the modelling methodology, the names of definitions, functions and input parameters as termed within Comsol Multiphysics are given in italics.

### 5.3.1 Nanoparticle in a Homogeneous Medium Model

Firstly, a square block representing the medium was constructed in which the electromagnetic wave can propagate. This medium was truncated by the use of *Perfectly Matched Layers* (PMLs) set to absorb all outgoing radiation and stop reflections from the external boundaries interfering with nanoparticle. Comsol advised that the size of the medium should be at least the distance of half the wavelength from the nanoparticle to the PML <sup>(207)</sup>. An incident plane wave travelling in the  $-z$ -direction and polarised in the  $y$ -direction was then defined by setting the *Electromagnetic Waves, Frequency Domain* to solve for the *scattered field*. This allows the input of a background field whereby the results generated are a perturbation of this field caused by the presence of a nanoparticle. The plane wave specified is then:

$$\begin{aligned} X & 0 \\ Y & E_0 \cdot \exp(-i \cdot (\text{emw.k0} \cdot n_a) \cdot z) \\ Z & 0 \end{aligned} \tag{75}$$

Where  $E_0$  is the incident electric field strength (V/m) set as 1 for all simulations,  $\text{emw.k0}$  is the wavenumber in free space and  $n_a$  is the refractive index of the medium. Both  $E_0$  and  $n_a$  were set within the *parameters* node, whereas  $\text{emw.k0}$  is a built in Comsol function. To excite different modes of a nanoparticle the polarisation can be altered by modifying the above equation, alternatively however, as the nanoparticle is in a homogeneous medium it may be simpler to simply rotate the nanoparticle with respect to a constant polarisation.

The geometries under consideration were created and placed within the centre of the medium, making sure there was a sufficient gap between the PML and the nanoparticle. Material properties were then assigned to each region. For a simple medium such as a vacuum, this was achieved by creating a blank material and setting the relative permittivity to 1. For complex valued optical data which varies within the studied frequency range, such as gold for instance, a linear interpolation function of both the real and imaginary parts with respect to

frequency was created, and assigned to the material instead. Alternatively, Comsol has some predefined material properties within its material library that can be used instead if available. For gold and silver, experimental data from Johnson and Christy<sup>(208)</sup> was used throughout this work. The model was then set to solve using the selected material property such as complex relative permittivity or complex refractive index by altering the *Solve For* option under the *Wave Equation, Electric* node.

To gain qualitative results, the optical cross sections were determined. This was performed by creating a new *variables* node with the following equations:

**Table 3: Definitions for the calculation of the optical cross sections**

Relative Normal Poynting Flux (nrelPoav)	$nx*emw.relPoavx + ny*emw.relPoavy + nz*emw.relPoavz$	(76)
Absorption Cross Section	$vol\_int(emw.Qh)/I_0$	(77)
Scattering Cross Section	$surf\_int(nrelPoav)/I_0$	(78)
Extinction Cross Section	Absorption Cross Section + Scattering Cross Section	(79)

Here  $n_x$ ,  $n_y$  and  $n_z$  refer to the normal vectors from the nanoparticle surface, whereas  $emw.relPoav(x,y,z)$  is the scattered Poynting vector (directional energy flux of an electromagnetic field). For the cross sections,  $emw.Qh$  represents the power loss density in the nanoparticle and  $I_0$  is incident intensity ( $W/m^2$ ), calculated from the incident electric field strength ( $E_0$ ) as seen in equation (80), where  $Z_0\_const$  is the Comsol constant for the impedance of free space. The volume ( $vol\_int$ ) and surface ( $surf\_int$ ) integrals for the absorption and scattering cross sections respectively were then established by creating an *integration* function under the *definitions* node and selecting the appropriate boundaries.

$$I_0 = (E_0^2 \times na)/(2 \times Z_0\_const) \quad (80)$$

The last steps were then to mesh the geometry and assign solver settings. With regards to the meshing, around five to six elements deep in the PML was usually sufficient to absorb all the incident waves. Alternatively the medium should use an element size no larger than the 0.2

times the wavelengths in free space, whereas the particle should have a maximum element size around half of the minimum skin depth<sup>(207)</sup>. For visible frequencies this equates to around 14 nm. In addition however, mesh independence tests were also conducted. This is where the mesh size is reduced until the results no longer vary, as shown in section 5.4.1.

A direct solver was used for the model with the Parallel Sparse Direct Solver (*PARDISO*) showing the best convergence compared to time and computational requirements. A direct solver was chosen over an iterative one when the RAM requirements could be met, however as the model became more complicated, a switch to an iterative method was often required as this greatly reduced the amount of RAM needed. At this point the model was solved. As previously mentioned, the model operates within the frequency domain meaning a solution was determined for only a single frequency. To build up a spectral solution, the frequency was stepped over the required range. This was done by creating a *parametric sweep* and allocating a range of frequencies.

### 5.3.2 Nanoparticle on a Substrate Model

The principle of modelling nanoparticles on a substrate involved firstly solving the interaction of an incident wave on a bare substrate that was infinitely wide in the absence of a nanoparticle. This solution was then used as the background field with the nanoparticle present. This two-step process was useful as it allowed the substrate to be regarded infinite, yet with only a single nanoparticle supported on it. Additionally, it also separated the nanoparticle solution from the substrate solution therefore allowing the intrinsic plasmonic response to be clearly identified.

To perform this simulation, a number of changes to the previously described model were made. Firstly, a geometry was constructed in the same manner as before however now a second medium was added below to represent the substrate with equal width as the homogeneous medium domain, but of a height equal to that of the substrate. Both of these domains were again enclosed within an encapsulating PML layer.

The *Electromagnetic Waves, Frequency Domain (emw)* was also altered to *solve for the Full field*. This differs from the *scattered field* which was solved for in the case of the homogeneous medium model by including both the incident field and the scattered field. It was solved in this manner as the full field solution represents both the transmitted proportion

of the incident wave through a substrate, and the superposition of the incident and reflected wave above the substrate, thereby giving a correct background field. This full field solution however was only allocated to the physical domains, thereby excluding the PML layer. The reasoning behind this was that the substrate was modelled as infinite in the x-y plane by using relevant boundary conditions on the domain walls. These boundary conditions negated the need to absorb outgoing radiation, and therefore the PML was redundant at this stage.

The boundary conditions in question include both *ports* and Floquet boundaries, which define the incident wave and create periodic conditions respectively. Focusing on ports initially, these were used to both launch and absorb electromagnetic waves, with one defined at the top of the medium and the other located at the base of the substrate respectively. The port above the medium had its *type* set to *user defined* and *Wave excitation at this port* set to *on*. Its *input power* was then defined as seen in equation (81) where  $I_0$  was the incident intensity from equation (80),  $w$  is the width of the domain and  $\theta$  was the angle of incidence:

$$I_0 \times w^2 \times \cos \theta \tag{81}$$

The local wave field vectors and propagation constant are also needed to define the wave. Assuming the following coordinate system for the wave incident on the substrate:

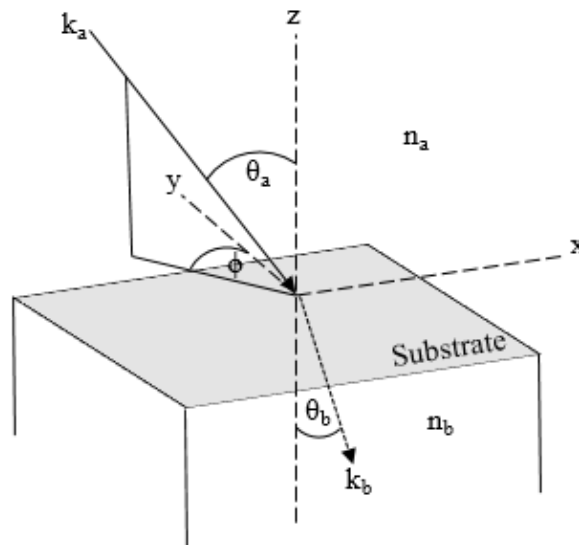


**Figure 5.2 – Coordinate system for a wave in a medium of refractive index  $n_a$  incident on a substrate with refractive index  $n_b$  at an angle of incidence  $\theta_a$ , angle of refraction  $\theta_b$ , and azimuthal angle  $\phi$ .  $k_a$  and  $k_b$  refer to the wavenumber above and in the substrate respectively.**

The wave vectors were set in the *definitions* node for the medium and substrate domains respectively as:

$$\mathbf{k}_a = (k_{ax}, k_{ay}, k_{az}) = \mathbf{k}_a(\cos\phi \sin\theta_a, \sin\phi \sin\theta_a, -\cos\theta_a) \quad (82)$$

$$\mathbf{k}_b = (k_{bx}, k_{by}, k_{bz}) = \mathbf{k}_b(\cos\phi \sin\theta_b, \sin\phi \sin\theta_b, -\cos\theta_b) \quad (83)$$

$$\text{where: } \theta_b = \sin^{-1}(n_a/n_b \times \sin\theta_a) \quad (84)$$

Here  $\mathbf{k}_a$  and  $\mathbf{k}_b$  are the wavenumbers in the medium and substrate respectively, defined as the wavenumber in free space multiplied by the refractive index of the material. When gold was used as the substrate, this refractive index was obtained by converting the frequency dependent complex relative permittivity into the refractive index, as shown below:

$$n = \sqrt{\frac{\sqrt{\varepsilon' + \varepsilon''} + \varepsilon'}{2}} \quad (85)$$

These wave vectors were then assigned to the ports by expressing them as the tangentially polarised field vectors at each plane under the *Electric field* inputs.

$$\text{At input port} \quad E_0 \exp\left(-i(\mathbf{k}_{ax}x + \mathbf{k}_{ay}y)\right) (-\sin\phi_a, \cos\phi_a, 0) \quad (86)$$

$$\text{At output port} \quad E_0 \exp\left(-i(\mathbf{k}_{bx}x + \mathbf{k}_{by}y)\right) (-\sin\phi_b, \cos\phi_b, 0) \quad (87)$$

The z-components from equation (82) were then entered into the *Propagation constant* input as absolute values to finish defining the ports.

In the previously described homogenous medium model, different plasmonic modes of the nanoparticles were excited by simply keeping the polarisation of the light the same but rotating the nanoparticle with respect to it. This is acceptable due to its homogeneous surroundings. In contrast however, when the nanoparticle was modelled on an infinitely wide

substrate, the surroundings are no longer homogeneous and therefore the polarisation of the incident wave had to be altered with respect to the substrate.

Following the above described methodology leads to the propagation of an s-polarised wave with incident angle  $\theta$  and azimuthal angle  $\phi$ . This however will only excite transverse modes of the nanoparticle, whereas p-polarised light is needed with an angle of incidence greater than zero to excite longitudinal modes of nanorods. The easiest way to achieve this is to alter the *Input quantity* to solve for the *Magnetic field* instead of the *Electric field*. As the magnetic field is perpendicular to the electric field, this therefore resulted in the propagation of a p-polarised wave.

Now moving on to the boundary conditions at the side walls, periodic conditions were applied to simulate a substrate that is infinite in the x-y plane. As discussed previously, periodic conditions operate by matching the field at one boundary to the field at an opposite boundary of equal size. If the incident wave has normal incidence, therefore has electric and magnetic fields that are perpendicular and parallel to the side walls, both *Perfect Electric Conductors* (PECs) and *Perfect Magnetic Conductors* (PMCs) can be used as the boundary condition. The PEC effectively applies symmetry to a magnetic field whereas the PMC applies symmetry to the electric field. Considering this, the PEC was therefore allocated to the boundary perpendicular to the E-Field as opposed to the PMC which was applied parallel to the E-Field.

For oblique angles of incidence, the use of both PECs and PMCs was not applicable and instead Floquet boundary conditions were used. Floquet boundary conditions are a more general case of periodicity whereby it states the solution at one boundary is equal to the solution at the other boundary multiplied by a complex valued phase factor. Although they are more applicable to different situations, they also take longer to solve.

If the azimuthal angle ( $\phi$ ) was greater than zero, Floquet boundaries must be added on all side walls, however if the azimuthal angle was equal to zero, as was often the case, a compromise was made whereby only two of the boundaries have Floquet conditions, with the others having either PECs or PMC's depending on the polarisation. For instance, considering an s-polarised wave travelling in the  $-z$  direction and polarised in the y-direction, even with an oblique angle of incidence, it only has E-Field components in the y-direction. This means a PEC condition could have been added to the boundaries perpendicular to the E-Field polarisation whereas

Floquet conditions were applied to those parallel to it. Alternatively solving for the magnetic field instead makes the E-Field only have components in the x and z-direction with the E-Field in the y-direction being zero. Floquet conditions in this case would therefore be assigned to the boundaries parallel to the H-Field, with PMC conditions on those boundaries perpendicular to it. This allocation of the boundary conditions is shown in Figure 5.3 for cases when the azimuthal angle is both greater than zero and equal to zero, and for both s and p-polarisation:

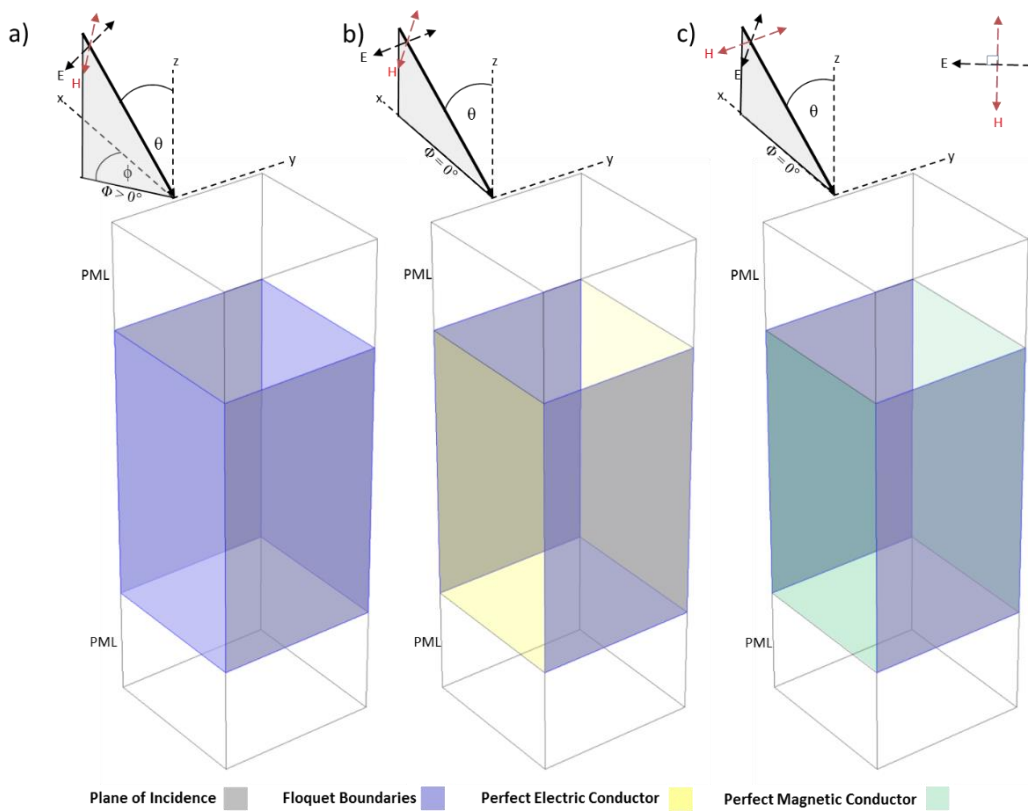


**Figure 5.3: Schematic diagram showing the allocation of periodic boundary conditions under various incident conditions. a) s-polarised light with both  $\theta$  and  $\phi > 0$ , b) s-polarised light with  $\phi = 0$  and  $\theta > 0$ , c) p-polarised light with  $\phi = 0$  and  $\theta > 0$ .**

This previous description completes the allocation of boundary conditions, however to make this initial full field solution the background field, the effects of the nanoparticle had to be removed. This was achieved by creating a new *Wave Equation* under *Electromagnetic Waves, Frequency Domain 1 (emw)* and assigning it to the nanoparticle. The refractive index of this domain was then altered to the same as the surrounding medium, therefore essentially erasing the nanoparticle. The solution of this frequency domain now gave that of an incident plane wave with controllable angle of incidence and polarisation impinging on an infinitely large,

bare substrate. To apply this solution as the background field with the presence of a nanoparticle, a further frequency domain had to be solved for.

This second frequency domain was added by selecting *Add Physics* followed by *Electromagnetic Waves, Frequency Domain*. The new frequency domain had the tag (*emw2*), instead of the previously used (*emw*), and therefore any equation with this suffix referred to the second frequency domain. This new frequency domain was then altered to *solve for* the *scattered field* as in the homogeneous medium model, with the background field input defined as the solution to the first frequency domain.

The other settings in this frequency domain were kept the same as those in the homogeneous medium model, whereby the *wave equation, Electric 1*, was allocated to use the material property of choice such as the relative permittivity or refractive index. No ports or additional boundary conditions were needed in this second step, however, the PML under *definitions* was altered so as to only apply to this second frequency domain. In addition, the cross section equations had to be altered so that they use the solutions calculated for the scattered field in the second step. This was done by altering the equation listed in Table 3 to use the tag *emw2* instead of *emw*. The final step in this nanoparticle on a substrate model then required two frequency domains to be created under *Study 1* so that each step may be solved sequentially instead of simultaneously to save on processing power. The outcome of this model therefore represents a single nanoparticle on an infinite substrate. If a periodic array of nanoparticles was required, the steps in section 5.3.3 were used instead.

### 5.3.3 Nanoparticle Array Model

The methodology for the modelling of an infinite array of nanoparticles was very similar to that described for previous models. Once again a two-step method was used whereby the first frequency step calculated an infinite background field without the presence of the nanoparticle. The second frequency domain then used this background field to derive the scattered field from the nanoparticle when represented as an infinite array, again achieved by harnessing periodic boundary conditions. These were allocated in the same manner as that shown in Figure 5.3.

In contrast to the homogeneous medium model which directly solved for a scattered field, this two-step process was also required even when not using a substrate. This was because the nanostructure in this model represented an array, which possessed a directional dependence relative to its periodic boundary. This meant that, unlike the homogeneous medium model where the nanoparticle could be rotated relative to a fixed incident field, the nanoparticle had to remain fixed and the incident field varied instead. For exciting p-polarised light with oblique angles of incidence, this was most easily achieved by using port conditions. Here a background scattered field was not entered, but a full field solution was used in its place. The method to derive the background field was then identical to that of the nanoparticle on a substrate model for both substrate and without substrate cases.

Despite the same method being used as that for a nanoparticle on a substrate model, an alteration to the simulation domain was required due to the sides of the model no longer requiring the use of a PML layer. This was due to the nanoparticle now also being periodic and therefore the outgoing radiation did not need to be absorbed by a PML. Instead the side boundaries were made periodic for both frequency steps. The top and bottom PML layer was still kept however as the array was periodic in only one plane. This use of PMLs at the top and bottom also has the advantage that it allows the far-field properties to be determined, such as the scattering cross section.

## 5.4 Validation of Model

### 5.4.1 Mesh Independence

To ensure the validity of the models a number of initial assessments were performed. Firstly a mesh independence test consisting of repeating simulations with a varying mesh size from course to fine was undertaken. The size at which further refinement of the mesh did not significantly alter the result was deemed to be the optimum size. Only the mesh in the nanoparticle was adjusted as this is the area of interest, however, the mesh in the other domains was governed by the global definition of at least five elements per wavelength. As the skin depth of gold in the visible frequencies is around 14 nm, the mesh size of the nanoparticle should be no more than 7 nm<sup>(207)</sup>. To illustrate the importance of having an appropriate mesh, the mesh independence tests were started at the same value as the skin depth and reduced down to a maximum size of 2 nm. The results shown in Figure 5.4 are for a 40 nm gold sphere at a wavelength of 510 nm in a vacuum.

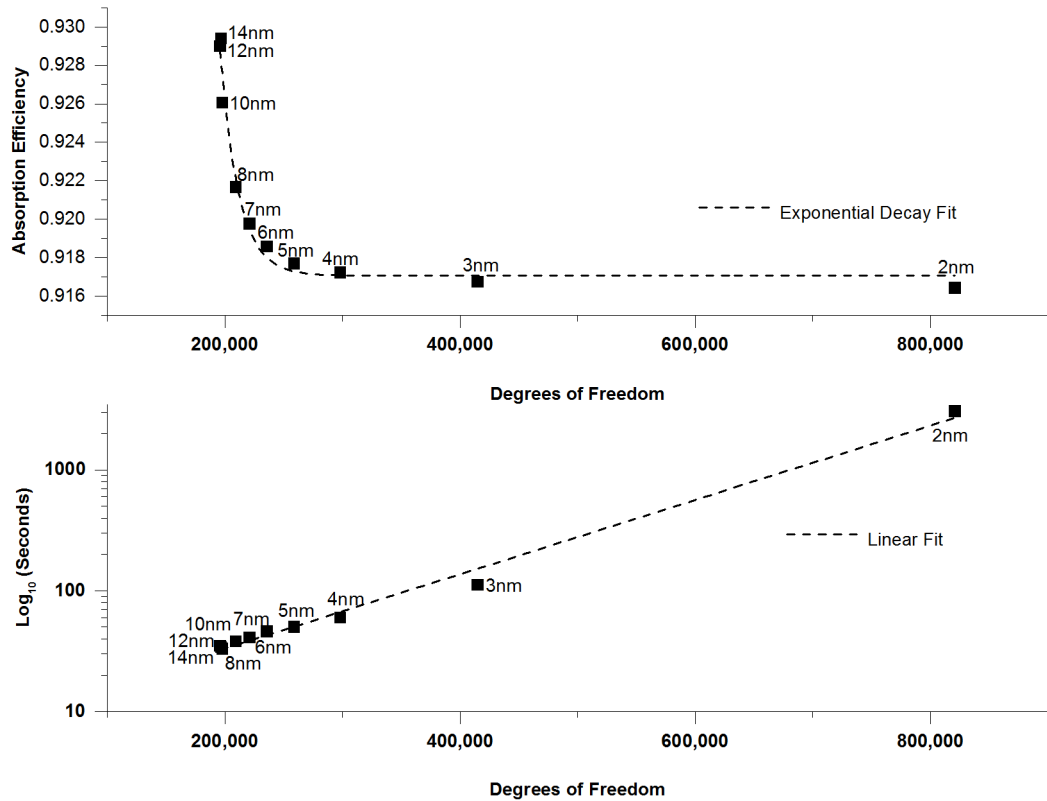


**Figure 5.4: Mesh independence test for a 40nm gold sphere in a vacuum at a wavelength of 510nm. a) Comparison of absorption efficiency with mesh size and degrees of freedom, b) time taken to solve for each mesh size and with the number of degrees of freedom.**

The results shown in Figure 5.4 show that with refinement of the mesh the number of degrees of freedom increase rapidly, particularly for small mesh sizes. This refinement of the mesh also caused a decrease in the absorption efficiency until around a mesh size of 4 nm, after which the solution stayed relatively constant. In contrast, the time to solve the simulation increased exponentially with the number of degrees of freedom, taking typically less than a minute for mesh sizes greater than 4 nm, however, increasing up to 50 minutes per wavelength for a mesh size of 2 nm. The required RAM for the 2 nm mesh size also increased rapidly using 18.49 GB compared to 5.57 GB for the 4 nm mesh. Finally calculating the error with respect to Mie theory at the same wavelength gives a percentage error of 3.32% for a course mesh of 14nm compared with an error of 2.01% for a 4nm mesh, 1.96% for a 3 nm mesh and 1.93% for a 2 nm mesh. Considering this, the 4nm or 3nm mesh size would be chosen to use for the full simulation as this gives a good balance between solution time, accuracy, and RAM requirements. As this result is geometry dependent, this process was repeated for each new simulation.

### 5.4.2 Comparison to Mie Data

As discussed within the modelling aims, a single sphere within a homogeneous medium was modelled in order to validate the FEM model. As Mie Theory also provides a rigorous solution to this problem, it therefore allows a direct comparison to be made. The results of this can be seen within Figure 5.5 whereby a 40 nm gold nanosphere was simulated in a homogeneous medium with permittivity  $\epsilon_m = 5$ . The Mie solution for comparison was instead generated using the freely available software MiePlot version 4.6 <sup>(57)</sup>. The absorption and scattering cross sections for each solution are compared and excellent agreement is seen. Indeed, the results match so accurately that it is often difficult to distinguish between each set of results.

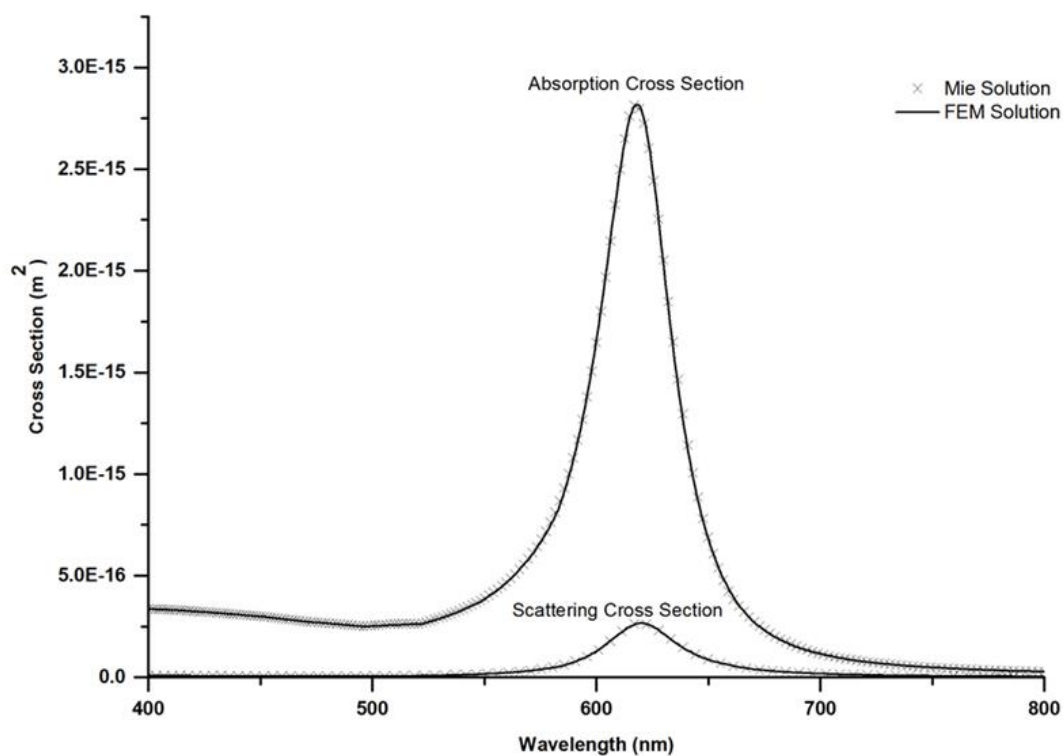


**Figure 5.5: Comparison of absorption and scattering cross section for both Mie Theory and the FEM solution for a 40 nm gold nanosphere in a homogeneous medium ( $\epsilon_m = 5$ ).**

Although the excellent agreement validates the model when using a medium permittivity of five, it is also necessary to determine if this agreement continues for other media. For this, both the absorption and scattering cross sections were modelled for a 40 nm gold spheres in a homogeneous medium with a variable permittivity of between one and eight ( $\epsilon_m = 1-8$ ). The peak resonance wavelength ( $\lambda_{\max}$ ) of the absorption cross section was then also compared for both FEM simulations and Mie theory. The results are shown in Figure 5.6 whereby both a red-shift and increase in amplitude of the cross sections is seen as the medium permittivity

increases. This matches the theory outlined in Chapter 2 whereby an increase in the optical contrast between that of the particle and the medium results in both an increasing amplitude and a linear red-shift of the resonance wavelength. This linear red-shift is confirmed in Figure 5.6c, and once again shows excellent agreement between both FEM and Mie solutions, with the peak wavelength position typically only differing by 1nm. This agreement shows that the model is validated in terms of calculating the far-field optical cross sections.

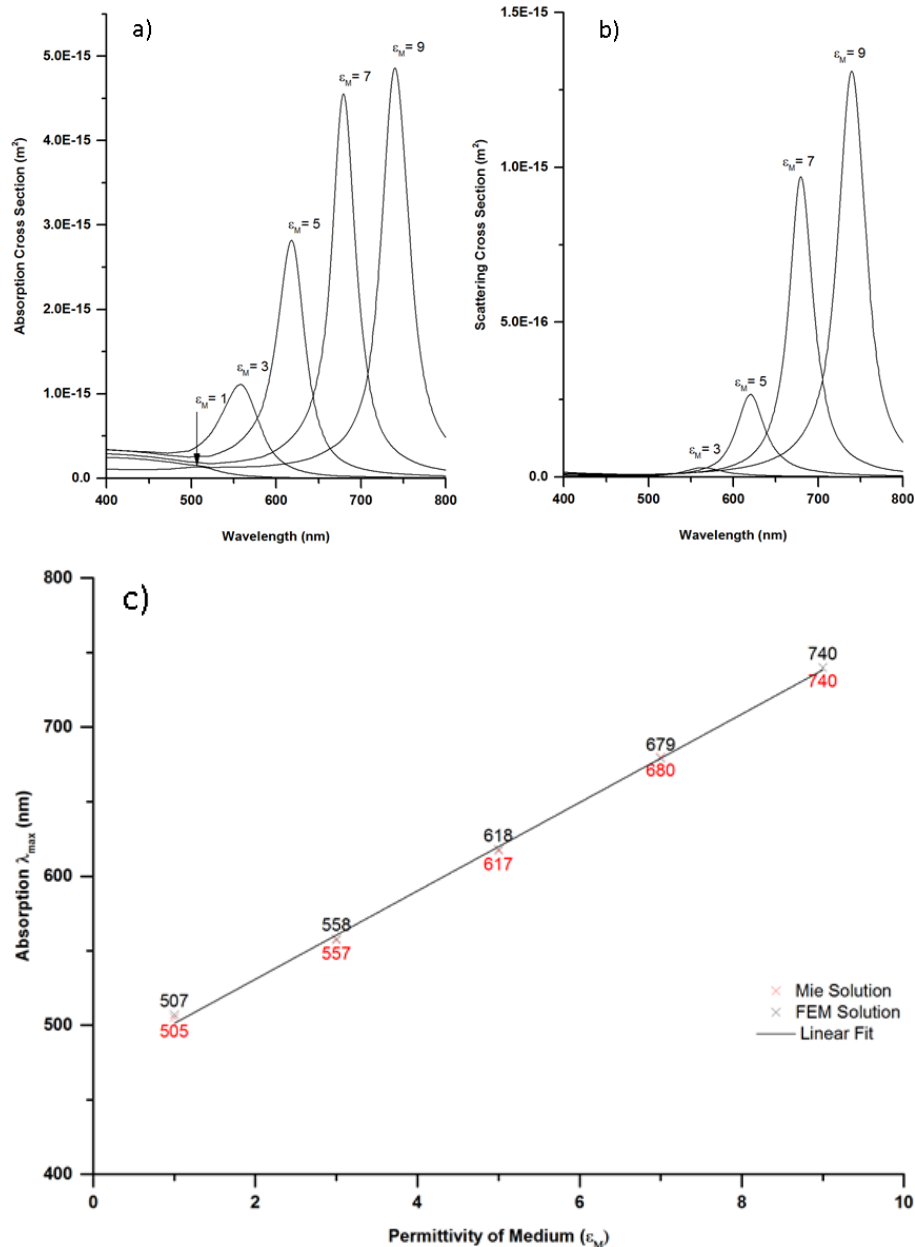


**Figure 5.6:** a) The absorption and b) scattering cross section FEM solution for a 40nm gold nanosphere in a homogeneous medium with changing permittivity from  $\epsilon_m = 1$  to 8. c) A comparison of the absorption resonant wavelength ( $\lambda_{max}$ ) with Mie theory.

### 5.4.3 Near Field Validation

Although the comparison of cross sections to Mie theory in the previous section provides a validation of the far-field results, the near field must also be validated. This was achieved by producing a map of the electric field distribution (normalised E-field amplitude) at the resonance wavelength of 508 nm. Additionally, by plotting the normalised electric field amplitude with distance from the surface of the nanoparticle, the decay of the surface plasmon may be analysed, as seen in Figure 5.7.

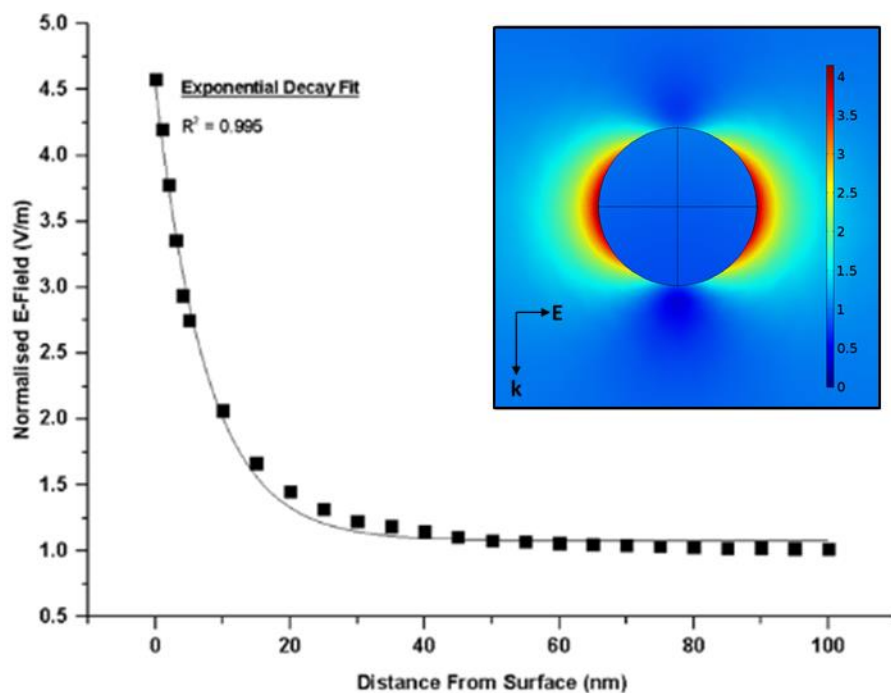


**Figure 5.7: Normalised electric field with distance from the surface of a 40 nm sphere in vacuum at a wavelength of 508 nm. The inset shows the normalised electric field distribution.**

It may be seen from the above graph that the electric field decays approximately exponentially away from surface of the nanoparticle in agreement with theory<sup>(36)</sup>. Additionally, the electric field plot shown in the inset shows the dipolar plasmonic mode, as would be expected for this small sized nanosphere where higher order modes are negligible.

From these results it was concluded that the model is able to accurately model nanoparticles in homogeneous media. This validation allowed other factors that affect the plasmon resonance of both nanospheres and nanorods to be investigated so as to gain a more thorough understanding, as well as to determine features that may allow for the optimisation of their properties.

## 5.5 Modelling of Isolated Nanorods

Following on from the validation of the FEM model, focus is now addressed to the modelling of single nanorods within a homogeneous medium. Analysis of these isolated nanorods aims to give insight into the factors that affect the plasmonic resonance. This is in the hope that it will help with the interpretation of the more complicated coupled structures later on, plus also provide an idea of what conditions optimise the absorption of visible light. As discussed in Chapter 7, although both absorption and scattering have a role to play in enhancing plasmonic photocatalysis, this high absorption in particular is critical in the generation of a successful plasmonic photocatalyst. This is due to the nanoparticles typically being located directly on the semiconductor, with enhancements arising from the high local electric field strength, plasmon resonant energy transfer (PRET) and injection of hot electrons <sup>(21)</sup>.

Initially, an isolated nanorod of diameter 40nm and an aspect ratio of three was modelled in a water with a refractive index of 1.33, as seen in Figure 5.8. The absorption efficiency spectra, defined as the absorption cross section divided by the geometrical cross section, was modelled at an angle of incidence of 45°. This allowed both the transverse mode and the longitudinal mode to be excited with peaks at 511 nm and 743 nm respectively. Both these modes are seen clearly in the electric field maps whereby the transverse mode has an oscillation over the short-axis of the rod and the longitudinal mode has an oscillation over the long-axis. As explained within Chapter 2, the longitudinal mode is red-shifted compared to the transverse mode due to its longer length requiring an increase in the wavelength to effectively excite an electron oscillation over its length.

Next, the effect of the end geometry of the nanorods was studied by comparing a flat ended rod to a spherically capped rod. Additionally, an analytical solution in Gans theory was also used for comparison as this represents a spheroid, and is often used to approximate the resonant position of nanorods. This was normalised to the FEM spectra at a wavelength of 400 nm for easy comparison however, as it was calculated over all orientations unlike the FEM simulations which were calculated for just a longitudinal orientation, its amplitude was correspondingly reduced.

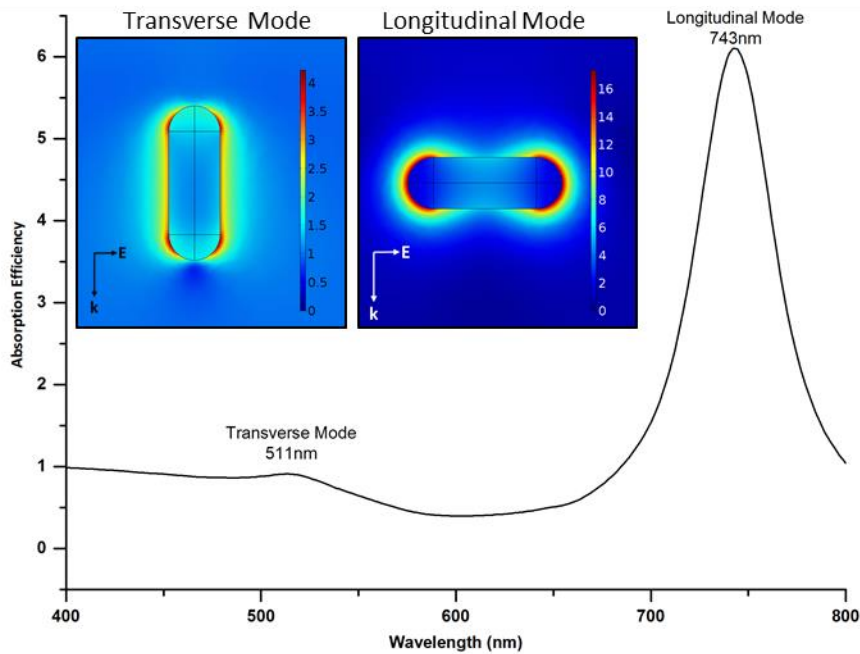


**Figure 5.8: Absorption efficiency spectra for a gold nanorods (40 nm x 120 nm) in water ( $n=1.33$ ) at  $45^\circ$ . The insets show the electric field distribution for the transverse and longitudinal modes.**

The results of the effect of the rod end geometry are seen within Figure 5.9, again including maps of the electric field distribution. Firstly, in terms of the resonant wavelength, it was noted that as the rod end geometry transitions from a spherically capped cylinder to a flat ended cylinder with sharp corners, the resonant wavelength increased. Similarly, a red-shift was also seen for the spherically capped cylinder as compared to that predicted by Gans theory. Interestingly, the wavelength shift seen in the different structures was relatively large at approximately 100 nm and this therefore highlighted the importance of accurately accounting for the rod end geometry.

By studying the electric field distributions, it was found that the flat ended cylinder had electric field strengths over twice that of the spherically capped cylinder. This however is likely to be inaccurate as the cylinder goes to a perfect corner, which is unrealistic in fabricated-structures. Considering this, and by observing that the nanorods produced in this work typically did not have perfectly flat ends, the spherically capped cylinder was deemed to be the most appropriate end geometry for use in this modelling work.

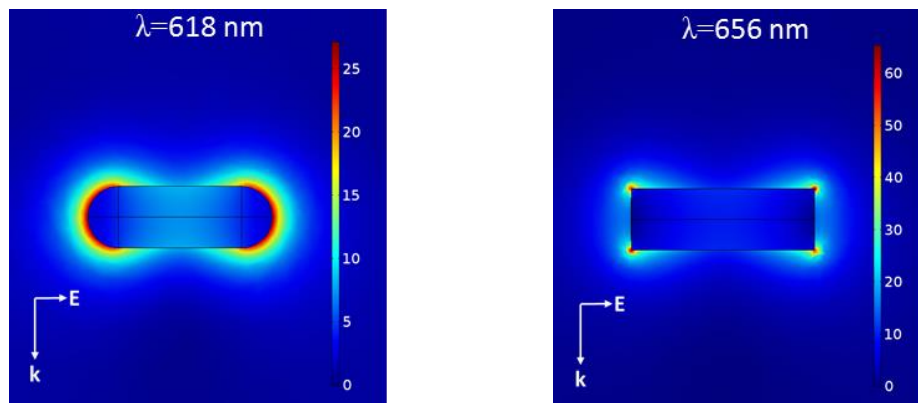
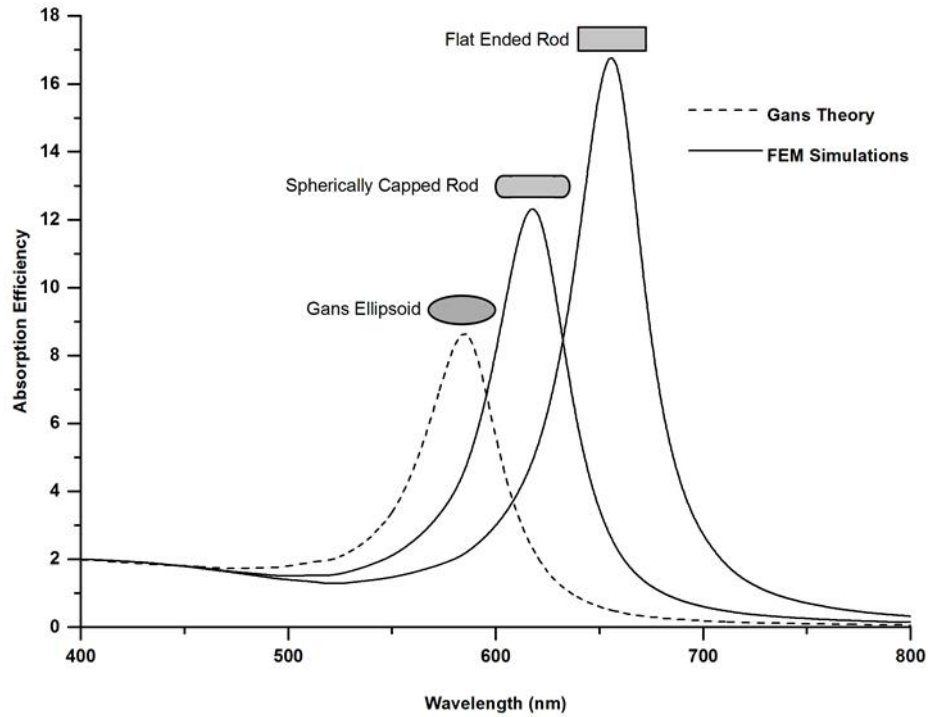


**Figure 5.9: Absorption efficiency spectra for spherically capped gold nanorods and flat-ended nanorods compared to Gans theory. The maps at the bottom show the electric field distribution for each of the rod end geometries (30 nm x 90 nm in vacuum).**

In order to maximise the absorption within the visible region, both the diameter and the aspect ratio of the rod should be optimised. The effect of the nanorod diameter was first investigated in Figure 5.10 for the longitudinal mode of a gold nanorod with a constant aspect ratio of three in a vacuum. Additionally, the transverse modes dependence on diameter is seen in the inset.

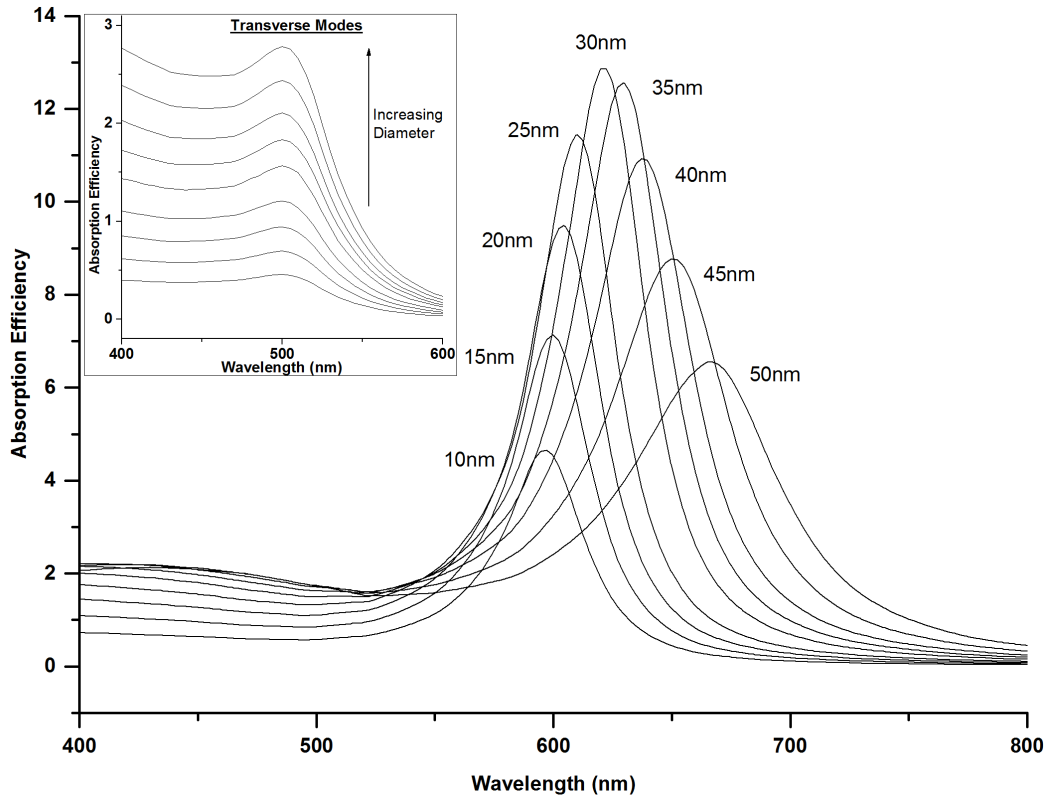


**Figure 5.10: Effect of diameter on the longitudinal modes absorption efficiency for a gold nanorod of AR=3. The inset shows the dependence on diameter for the transverse mode (diameter 10 nm – 50 nm).**

The longitudinal mode showed a relationship with the diameter whereby it red-shifted with increasing diameter of the nanorod. The peak started initially relatively sharp however broadened and decreased in amplitude at the larger diameters. A clear maximum in the absorption efficiency was seen for a diameter of 30 nm, therefore this represents an optimum size to fabricate nanorods. Considering the electrodeposition within AAO templates fabrication route, this could be achieved using 0.3 M sulphuric acid as the electrolyte and anodising at 25 V. In contrast however, the absorption efficiency for the transverse mode showed a steady increase in the absorption efficiency as the diameter increases. This was only performed up to a diameter of 50 nm however, and may be instead expected to broaden and decrease with larger sizes, as seen with spheres at diameters above approximately 100 nm.

On the other hand, when analysing the effect of the nanorod's aspect ratio, a monotonic trend was seen in Figure 5.11 for a gold nanorod with aspect ratio varying from two to ten. As typically reported for isolated nanorods, the longitudinal mode red-shifted linearly with increasing aspect ratio and an increase in the absorption efficiency was also seen. It should be

noted however that this red-shift is so pronounced that by an aspect ratio of five, the resonant wavelength had red-shifted to 801 nm and therefore had moved out of the visible range and into the near infrared. As seen later, this is in contrast to the results found when the longitudinal modes are coupled in a side by side periodic array of nanorods, whereby a much smaller red-shift with aspect ratio was seen.

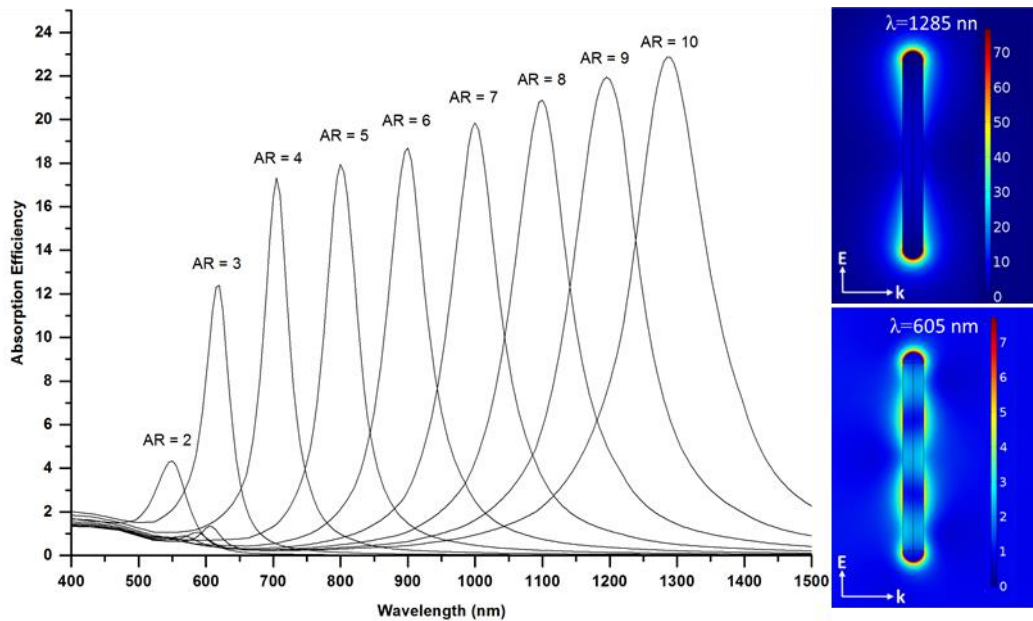


**Figure 5.11: Absorption efficiency with AR for a gold nanorod in a vacuum with diameter of 30nm. The field plots on the right show the electric field distribution for the longitudinal mode ( $\lambda=1285$  nm) and the sextuple mode ( $\lambda=605$  nm) of an AR=10 nanorod.**

Additionally, it was seen in the spectra that smaller peaks around a wavelength of 600 nm become visible. These belong to the longer AR nanorods and represent the presence of higher order modes, which again red-shift with increasing AR. The distribution of the electric fields both for a longitudinal mode and the sextuple higher order mode is seen within the field plots of Figure 5.11. The longitudinal mode has a characteristic dipole distribution whereas the sextuple mode has additional nodes along the nanorods length. The quadrupole mode is not visible within the spectra due to the polarisation being parallel to the long axis of the nanorod, which as shown in Figure 2.16 of the literature review cannot excite the quadrupole mode.

The modelling so far has focused on bare gold nanorods so as to determine how various factors affect their plasmonic resonance. This will now be broadened to include the effect of placing a titanium dioxide shell on the surface, and also assessing multi-material nanorods.

Both of these structures are able to be fabricated as shown within Chapter 3, and therefore it is useful to gain an understanding on how they alter the plasmonic resonances.

Firstly, the effect of a  $\text{TiO}_2$  shell was addressed. This is modelled assuming rutile  $\text{TiO}_2$  using permittivity data taken from the work of DeVore<sup>(209)</sup>. The shell thickness was varied from 2 nm to 10 nm for a longitudinal polarisation, as seen in Figure 5.12.

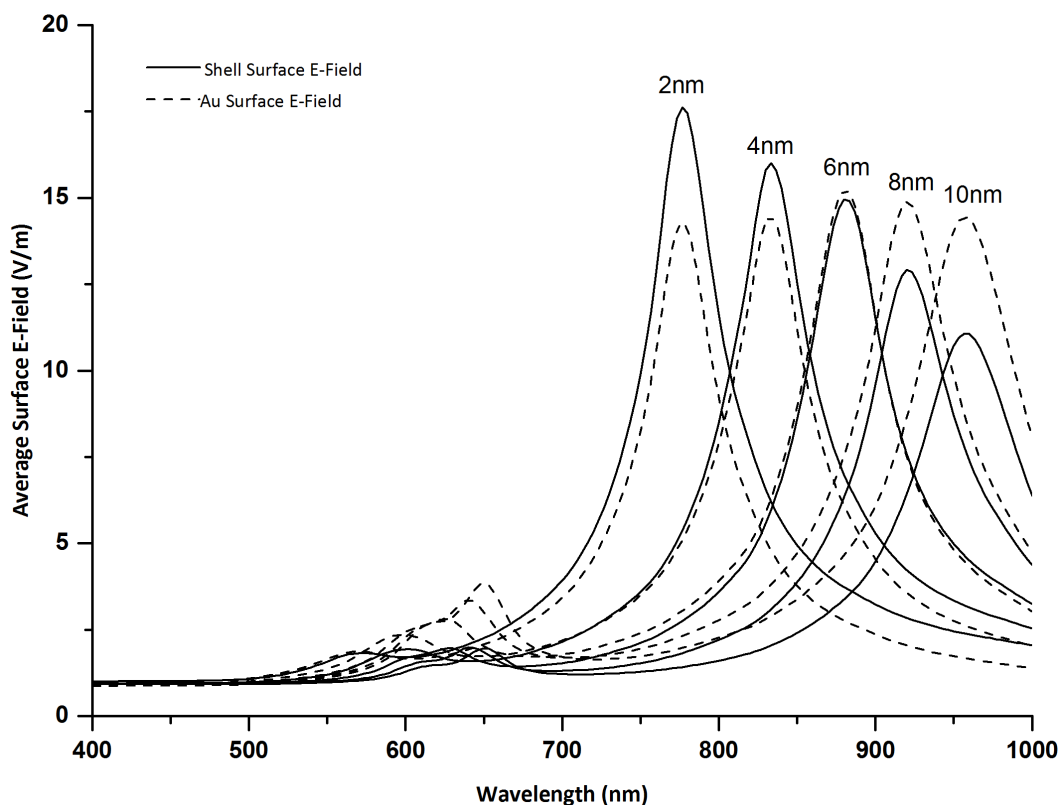


**Figure 5.12: Average surface electric field strengths for a 30 nm x 90 nm gold nanorod with a  $\text{TiO}_2$  shell on its surface varying from 2 nm to 10 nm in thickness.**

In Figure 5.12, the average electric field over the surface of both the gold nanorod and the  $\text{TiO}_2$  shell was calculated separately for comparison. This was plotted instead of the optical cross sections owing to the desire to ascertain at what shell thickness the electric field within the  $\text{TiO}_2$  layer became maximised. This is important as the electron-hole production within the semiconductor is proportional to the electric field intensity  $|E^2|$ <sup>(210)</sup>, which occurs when the electric field on the surface of the gold nanoparticle is at a maximum. In contrast, the electric field on the surface of the  $\text{TiO}_2$  will give high field strengths in the surrounding medium, as in the electric field distribution plots shown in Figure 5.13.

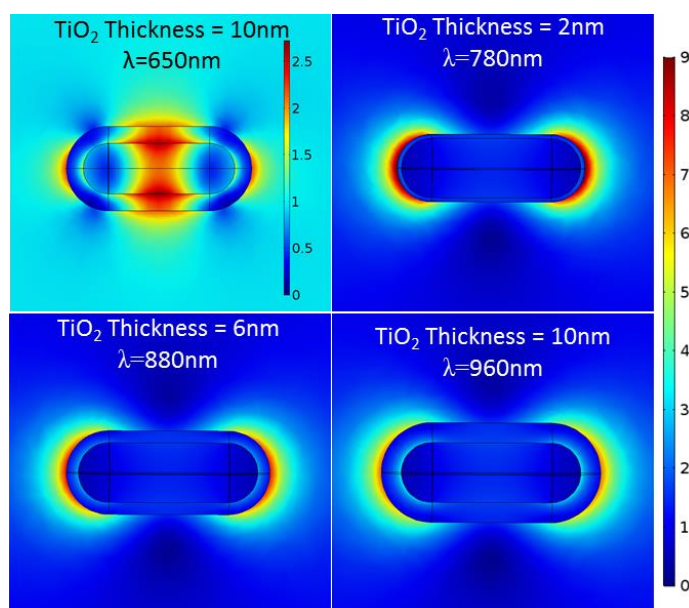


**Figure 5.13: Electric field distributions of 30 nm x 90 nm gold nanorod coated in TiO<sub>2</sub> of varying thickness. The plots are taken at the longitudinal resonance wavelength with a scale of 0-9 V/m apart from the plot at 650 nm which is taken at the peak of a lower wavelength resonance with a scale from 0-3 V/m.**

By studying both these figures it was found that as the TiO<sub>2</sub> layer increased in thickness, a red-shift in the longitudinal position occurred. This is as expected due to the higher refractive index of the TiO<sub>2</sub> ( $n \sim 2.5$ ) compared to that of the medium ( $n=1$ ). As discussed within Chapter 2, as the shell becomes thicker it has a more dominant role on the resonance position, whereby when sufficiently thick it will match that of the particle completely embedded within a medium of equivalent refractive index.

It was also seen that with increasing thickness of the shell, the average surface electric field strengths for both the gold and TiO<sub>2</sub> surface showed different behaviours. The gold surface electric field strength stayed relatively constant although a slight maximum was seen at around 6 nm thickness. The TiO<sub>2</sub> shell surface electric field strength however decreased with increasing shell thickness. In addition, a shorter wavelength peak typically between 600-700 nm was also visible within the spectra. It is believed this relates to a higher order mode that occurs even at this short aspect ratio due to the high refractive index of the surrounding TiO<sub>2</sub>. The electric field map supported this conclusion with a mode visible towards the centre of the nanorod. Additionally, by performing simulations of the nanorod without a shell but in a homogeneous medium of TiO<sub>2</sub>, a similar mode was observed (*not shown*), thereby suggesting this is not a mode relating to just the core-shell geometry.

Based upon these results it was concluded that a TiO<sub>2</sub> layer of around 6 nm may be optimum for photocatalytic experiments. This is because both the electric fields within the TiO<sub>2</sub> layer and on its surface remain high. However, many photocatalytic processes are complex and therefore the maximum in photocatalytic activity may rely on other parameters that would need to be carefully optimised <sup>(211)</sup>.

Moving onto the multi-material nanorods, by sequentially alternating the metal deposited inside the pores of the AAO template, multi-layered structures can be fabricated. These are briefly analysed here in order to show the merits of such a technique, however the application of these multi-layered rods was beyond the scope of this current work. Figure 5.14 shows the transverse orientation results for a two layered nanorod made from gold and silver with varying ratios of each. It was seen that two peaks were present relating to the transverse mode of each metal, with silver at approximately 350 nm and gold at ca. 500 nm. As the relative amount of each metal increased, the amplitude of its transverse peak also increased. The transverse mode relating to the silver segment however was much stronger than that of the gold. This is due to the silver transverse resonance being located at a wavelength that is separated from its bulk interband transition, in contrast to the situation in gold <sup>(212)</sup>.

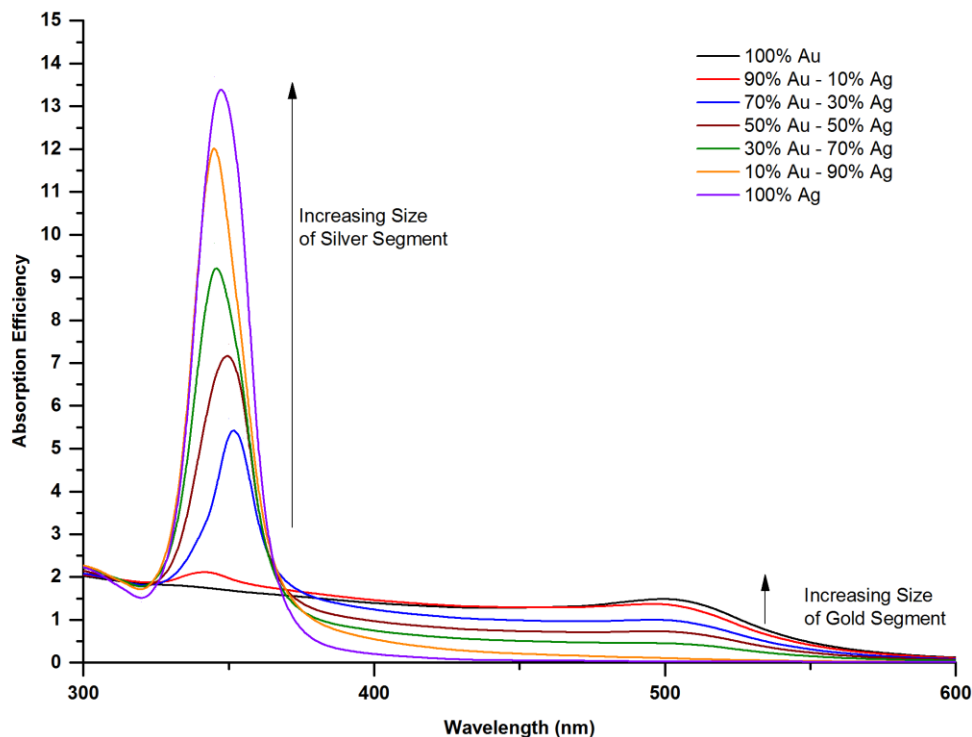


**Figure 5.14: Absorption efficiency for the transverse mode of a Au-Ag bimetallic nanorod with varying size of each material. The nanorod is kept at a constant diameter of 30 nm and AR=3.**

The longitudinal mode of the multi-material nanorods showed a more complex trend, as shown in Figure 5.15. Once again two peaks were noted relating to the longitudinal mode of each material, located at around 610 nm and 510 nm for single material Au and Ag nanorods respectively. Starting from a 100% gold nanorod, it was seen that as this was progressively replaced by silver, the gold longitudinal mode blue-shifted back towards its transverse mode, eventually overlapping with that of the silver longitudinal peak. On the other hand, as the silver segment grew, a peak occurred initially at its transverse resonant wavelength, before then red-shifting as the segment became longer. Based upon these results, layered multi-material nanorods such as the Au-Ag nanorod shown here may be useful for achieving absorption right across the visible spectrum. Additionally, the ability to alter the relative segment sizes to further tune the resonant position may also prove useful as it allows another degree of control.

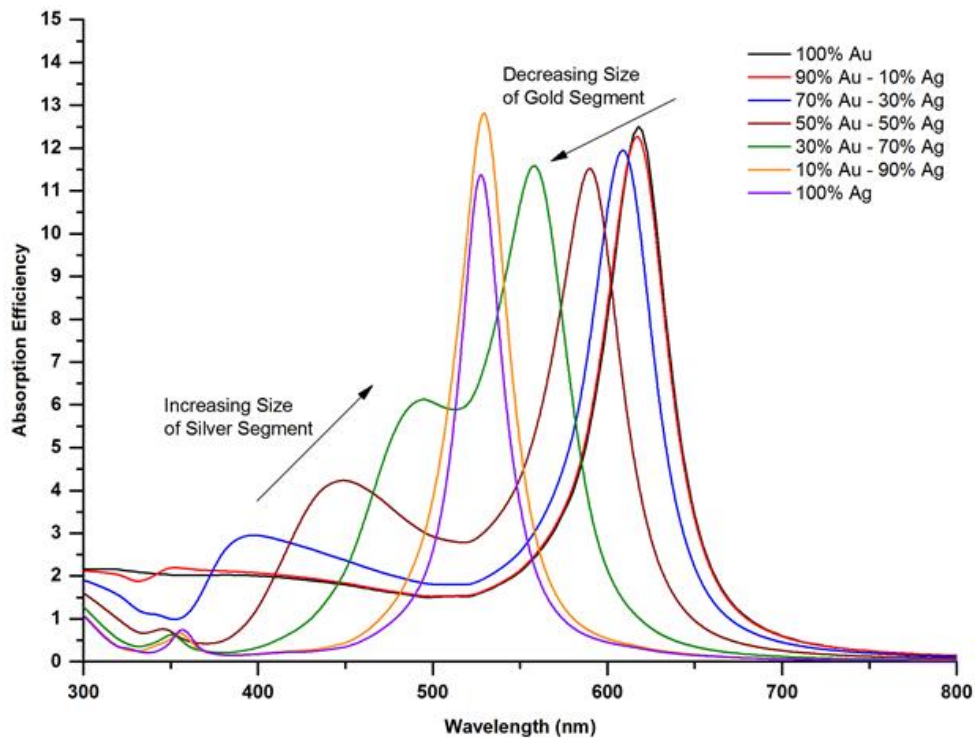


**Figure 5.15: Absorption efficiency for the longitudinal mode of a Au-Ag bimetallic nanorod with varying size of each material. The nanorod is kept at a diameter of 30 nm and AR=3.**

## 5.6 Modelling of Coupled Nanoparticles

Following the analysis of single isolated nanoparticles within the previous section, attention will now be directed towards the consequences of coupling. These coupling effects can lead to dramatic shifts in the optical properties and give extremely high electric field strengths, particularly within small gaps. As the nanorod arrays produced in this work are supported on

a metallic substrate, both interactions with the substrate, and with other nanorods within the array, may alter the optical properties compared to a simpler isolated nanorod. These interactions will be studied separately initially, whereby modelling is first performed to analyse the effect of the substrate with a single isolated rod. Multiple nanorods in an array but within a homogeneous medium will then be addressed, before eventually combining the array and the substrate to give a representative model of the fabricated nanorod arrays.

### 5.6.1 Particle - Substrate Coupling

In regards to particle–substrate interactions, the vast majority of previous work has relied on the modelling of nanospheres directly on, or above a substrate. To validate the *nanoparticle on a substrate* model plus also further analyse the effect of the substrate in a relatively simple model, a sphere was also modelled initially within this work, before then addressing the case of a supported nanorod.

Firstly, modelling was performed to analyse how a dielectric substrate affected the plasmonic response of a gold sphere sat directly on top of it, as compared to that of a gold substrate or a vacuum. The absorption efficiency spectra for this are shown in Figure 5.16 with additional electric field plots of both the background field and the scattered field. Analysing the spectra it can be seen that a red-shift occurred when the nanoparticle was sat on a substrate as compared to one surrounded by a vacuum. This shift was relatively small for a dielectric substrate, shifting by only 2 nm, however, was much more pronounced for the gold substrate giving a red-shift of 10 nm. Furthermore, the absorption efficiency was seen to decrease for the dielectric substrate yet increase for the gold substrate relative to the vacuum resonance. Both of these findings agreed with those cited in the literature review. The red-shift was caused by the nanoparticle coupling with the substrate, such as is described by the image charge approach. A strong coupling occurs for a gold substrate resulting in a large shift whereas a weaker coupling with a dielectric substrate leads to a smaller shift.

On the other hand, the change in the absorption efficiency amplitude is due to the substrate altering the local field intensity around the nanoparticle due to factors such as reflection and the presence of standing waves. This was seen in the background field plots whereby for the gold substrate the wave was unable to penetrate deep into the material, but was instead reflected away. The local field around the nanoparticle was then a superposition of the incident wave and the reflected wave, resulting in a standing wave with a higher field strength. Alternatively with the dielectric substrate, the wave was able to propagate through the

substrate, however with a much reduced amplitude. This resulted in the field strength above the substrate being reduced compared to the vacuum case thereby leading to a drop in the absorption efficiency. Furthermore, although the dielectric substrate case had a plasmonic resonance that is similar in form to the vacuum scenario, this altered significantly for the gold substrate. Here the electric field was a greatly enhanced towards the bottom of the particle, therefore demonstrating the strong coupling that was present.

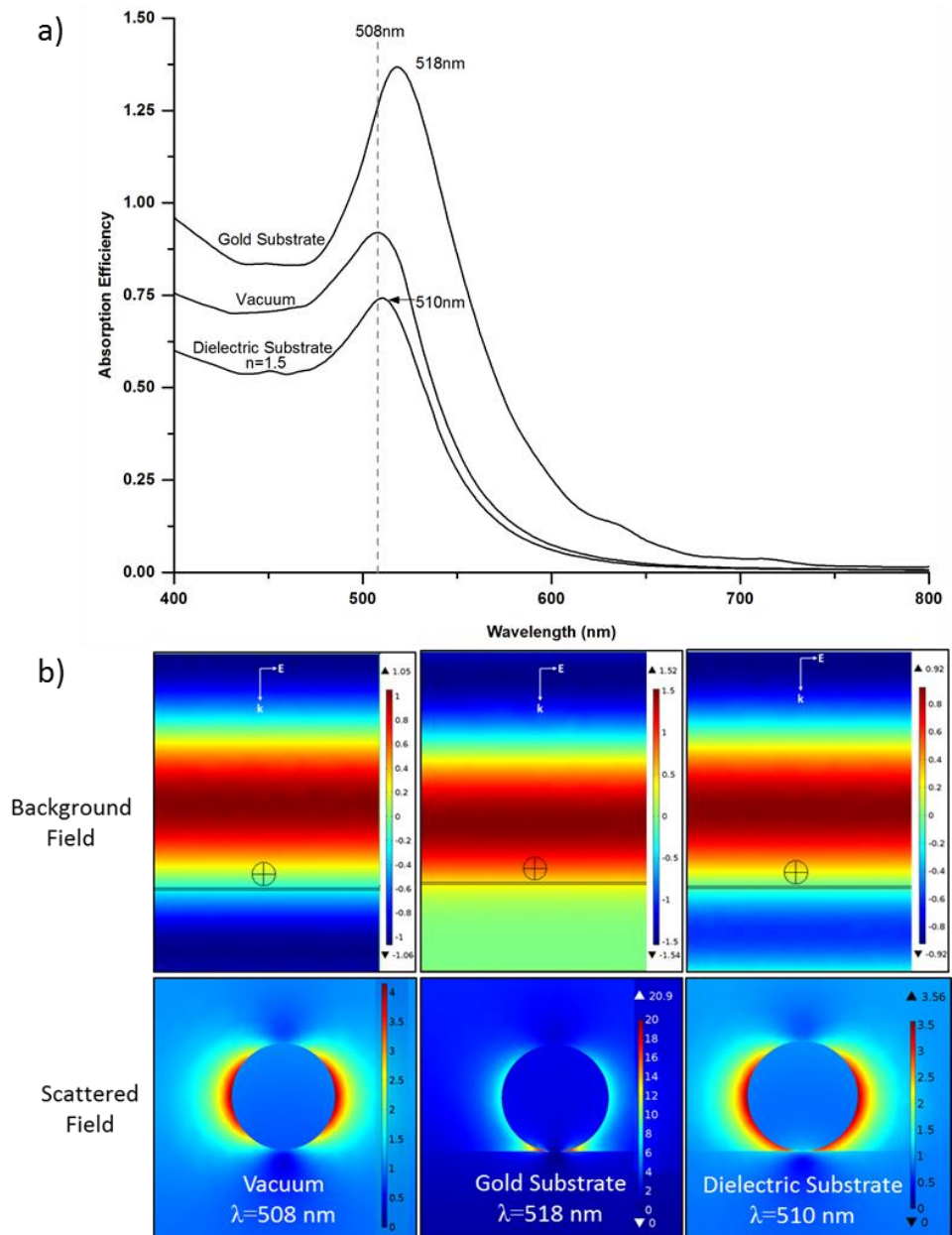


**Figure 5.16:** a) Absorption efficiency spectra of a 40 nm gold sphere on top of a gold substrate, dielectric substrate and within a vacuum. S-polarised light is used incident normal to the substrate. b) Electric field plots for the background field ( $E_y$ ) and the scattered field at  $\lambda_{\max}$  from a side on view.

This particle-substrate coupling was addressed in more detail by studying how a gold nanosphere interacted with a gold substrate as it was brought closer to it. In this setup, the polarisation with respect to the nanoparticle is important and therefore both s and p-polarised light was tested at an angle of incidence of  $45^\circ$ , as seen in Figure 5.17.

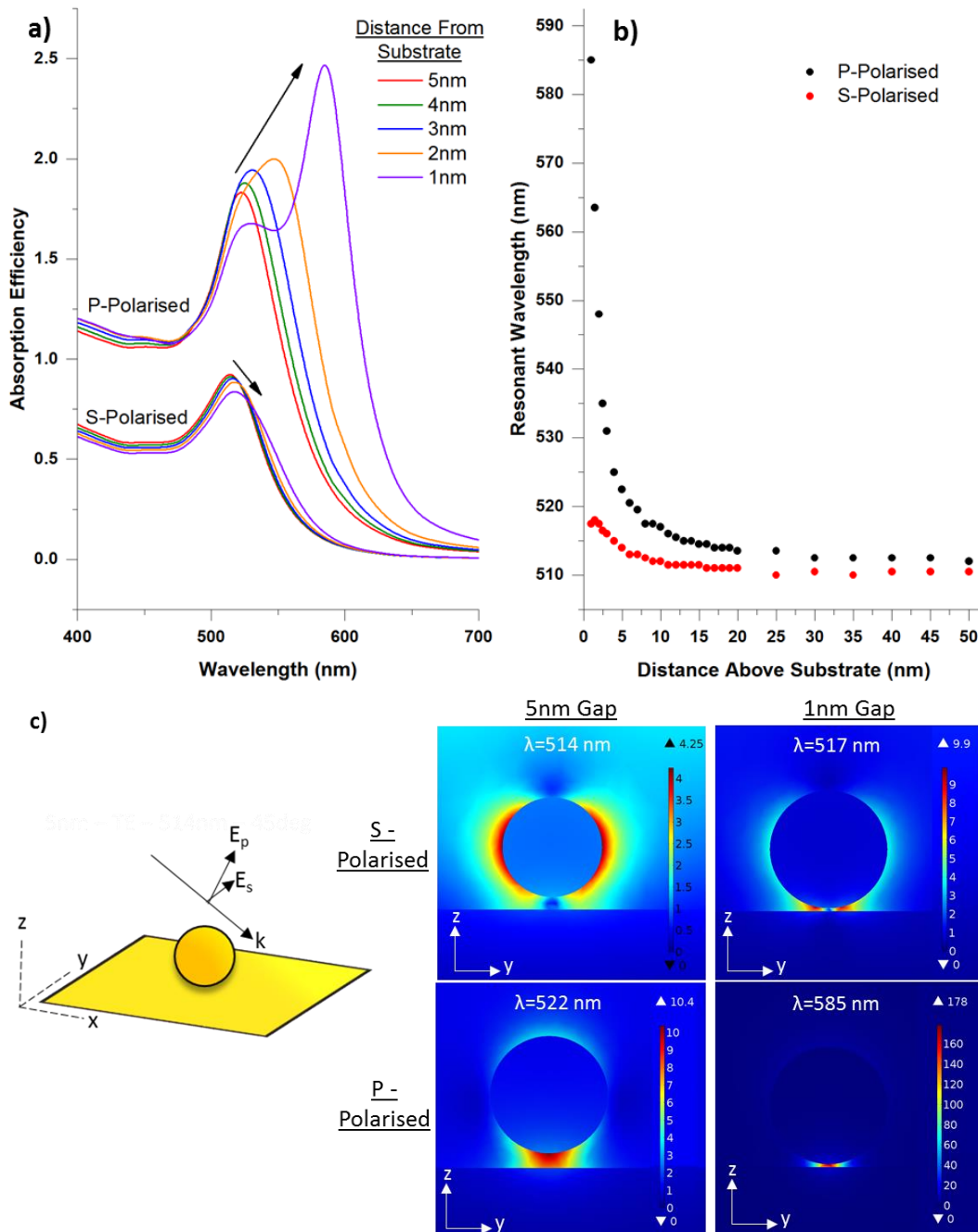
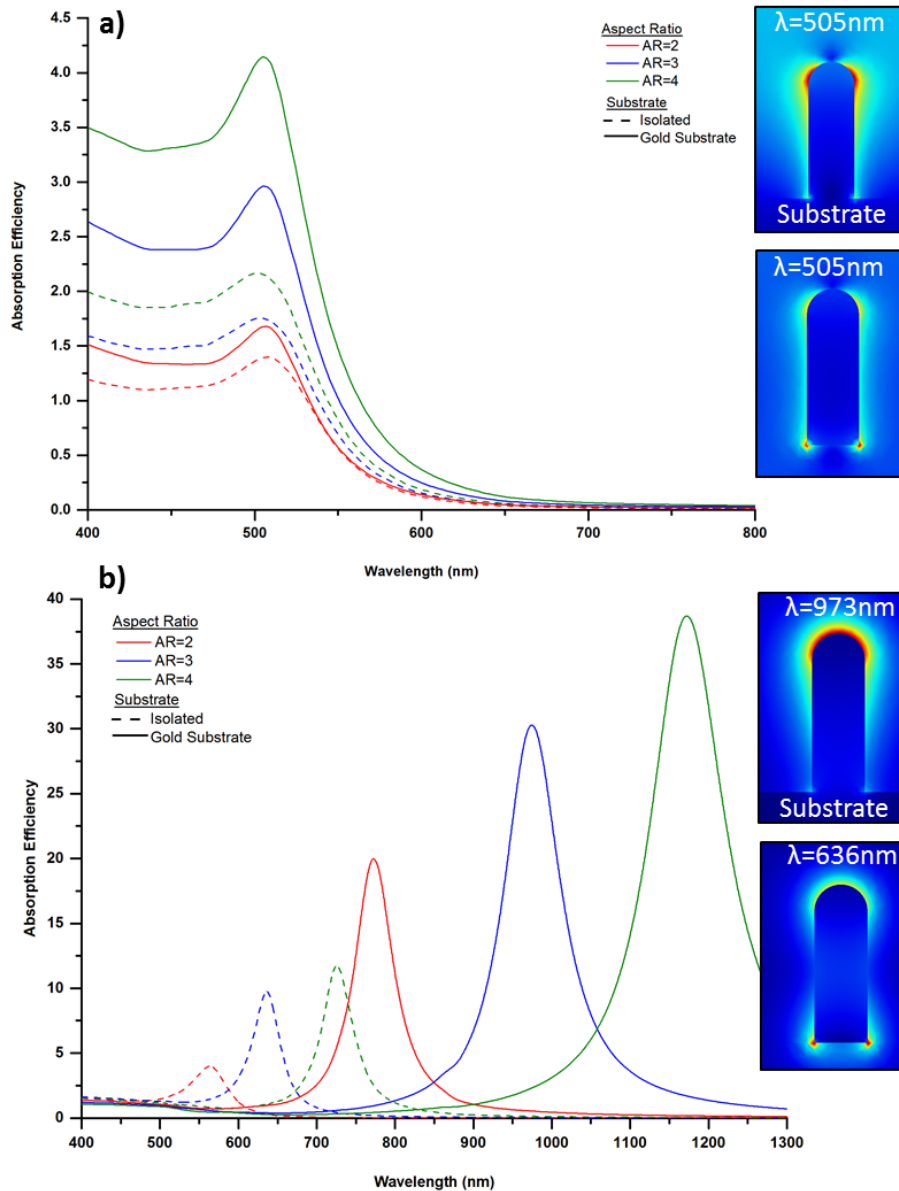


Figure 5.17: a) Absorption efficiency of a 40 nm gold sphere with distance above a 150 nm thick gold substrate for both s and p-polarised light at  $45^\circ$  angle of incidence. b) Resonant wavelength with distance above substrate. c) Electric field plots for both a 5 nm and 1 nm gap from the substrate when using s and p-polarised light at  $45^\circ$ .

Firstly, as seen in Figure 5.17a, both polarisations resulted in a red-shift as the particle approached the substrate. This was small for the s-polarisation however it was much more pronounced for p-polarisation, as seen in Figure 5.17b. Similarly, the s-polarisation underwent a slight reduction in absorption efficiency whereas, in contrast, with p-polarisation, this increased greatly. This polarisation dependence matched that found in the literature review and was the result of the electric field direction under each polarisation as seen in the schematic diagram of Figure 5.17c. For example, in s-polarised light the electric field remains parallel to the substrate regardless of the angle of incidence. When the particle gets in close proximity to the substrate, the resonance is still being excited in the same manner as it was when far away, however, the fields at the bottom of the particle may interact with the substrate and undergo a small degree of coupling. On the other hand, with p-polarised light the electric field has a component perpendicular to the substrate depending on the angle of incidence. Considering this, the plasmon is excited towards the substrate and therefore much stronger coupling can occur even at large distances. This was seen in the electric field plots where for p-polarisation the fields were clearly located towards the base of the particle in the gap between it and the substrate. This strong coupling resulted in the generation of very high electric field strengths and even the generation of higher order modes when at small distances, such as in the 1nm gap size shown. Despite this, it should be stated that the model used in the simulation of these results relies on local approximations which are known to overestimate the field strengths and spectral shifts at very small gap sizes of around 2 nm or less <sup>(63)</sup>. Despite this, field enhancements and shifts in the spectra are still expected.

These results for a sphere above a substrate gave an indication of the trends seen for a relatively simple system. Focus was then directed to the more relevant structure of gold nanorods standing vertically on substrate, as with the nanorods fabricated in this work. Figure 5.18 shows the absorption efficiency of gold nanorods supported on a 150 nm thick gold substrate for both the transverse and longitudinal modes. Here the transverse mode could be excited using s-polarisation at any angle of incidence, whereas the longitudinal mode required p-polarised light with an angle of incidence greater than zero. The electric field plots with and without a substrate are also shown. The same geometry was used in both simulations for an accurate comparison.



**Figure 5.18: Absorption efficiency spectra for 30 nm diameter gold nanorods supported on a 150 nm thick gold substrate with varying aspect ratios. 45° angle of incidence plane waves were used under a) s-polarisation or b) p-polarisation. The field distributions on the right are for both a “with substrate” and “without-substrate” scenario.**

Focussing first on the transverse modes, it was seen that as the AR increased, the nanorods absorption efficiency also increased. This appeared to occur quite systematically for both the “with substrate” and “without substrate” cases. This was due to the nanorod length (at which a plasmon is sustained over) increasing with the aspect ratio, however the geometrical cross section as viewed from above, remained constant. Interestingly, it was also observed that the substrate led to an increase in the absorption efficiency as compared to the same geometry without it. This was likely due to the higher local field intensity above the substrate.

The longitudinal modes, excited using p-polarised light at 45° angle of incidence, showed similar trends. Once again the absorption efficiencies were higher for the nanorods on a gold substrate than for those without it. Additionally however, there was also a remarkable red-shift of the resonance position for the substrate case compared to the without substrate case. For example, it was found that even at an aspect ratio of two, the resonant wavelength had shifted 266 nm and was only just still located within the visible region. Studying these supported nanorods in more detail, it was also noted that the red-shift with aspect ratio has a fairly linear trend whereby it shifts at a rate of around 200 nm per unit aspect ratio. As this red-shift with increasing aspect ratio occurred at a much larger rate than for the nanorods without substrates, the difference between the resonant wavelengths of a substrate and non-substrate nanorod increased dramatically for higher aspect ratio nanorods.

As discussed within the literature review, it is expected that metallic substrates give rise to larger red-shifts than dielectric substrates due to the strong coupling that occurs. For example, red-shifts of approximately 130 nm were reported by Mock *et. al.* <sup>(110)</sup> for gold spherical nanoparticles placed on a gold substrate as compared to a dielectric one (located at a glass-water interface). Considering that a dielectric substrate would also red-shift the resonance with respect to a vacuum scenario, the shift between a gold substrate and vacuum conditions would be expected to be even larger, as was shown by these results. Additionally, as the nanorods in this work stood perpendicular to the substrate, this meant that the relatively strong longitudinal modes excited were directed straight towards the substrate. As shown previously in Figure 5.17, when the plasmonic modes were orientated so that they could effectively couple with the substrate, a greater red-shift was seen. Similarly, Lermé *et. al.* <sup>(91)</sup> also concluded that this coupling with the substrate is principally responsible for the red-shifts in the resonance position. Considering this, it was therefore hypothesised that the much higher resonant wavelengths could be attributed to the longitudinal mode of the nanorod coupling strongly with that of the substrate.

Further modelling also supported this conclusion. For example, in a similar fashion to that done with spheres, the gold nanorods were modelled as they were moved progressively closer to the substrate, as seen in Figure 5.19. Here the nanorods were modelled with their long axis perpendicular to the substrate, eventually joining with it at a gap size of 0 nm. It was seen that with a decreasing gap size, and therefore stronger coupling, the longitudinal mode red-shifted and increased in amplitude. At a gap of 1 nm, higher order modes were seen to be excited however these seemed to disappear when the nanorod joined the substrate. This indicated that

these higher order modes were related to coupling within the gap, with electric field plots supporting this. As a further red-shift was seen in the longitudinal mode when the nanorod joined with the substrate, this also suggested that the substrate coupling seen was not solely related to the gap, but instead continued when the nanorod joined it.

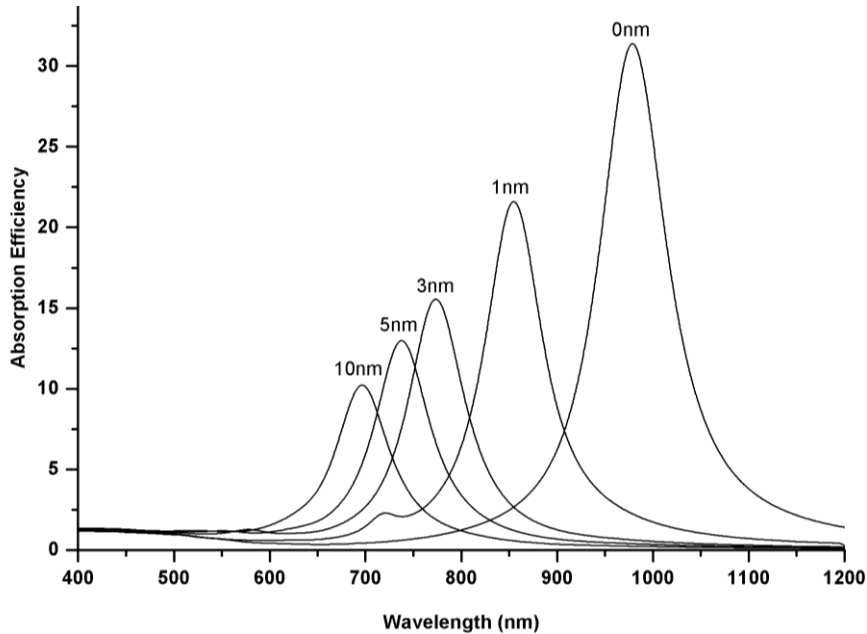


**Figure 5.19: Absorption Efficiency spectra for an AR=3 gold nanorod with its long-axis perpendicular to a 150nm thick gold substrate at various particle-substrate gap sizes.**

Discussing these higher order modes in more detail, although an AR=3 nanorod at a gap size of 0nm did not exhibit these modes, they did appear for higher aspect ratio rods albeit with relatively weak intensity. The onset of these was at an aspect ratio of four to five, with a progressive red-shift and the generation of further modes observed with increasing aspect ratio. This was in contrast to that seen for non-supported nanorods, whereby the same higher order modes only began to appear at an  $AR \geq 6$  and gradually became more prominent after that. This onset of higher order modes at slightly lower aspect ratios for supported rods was as expected based upon the work in the literature review, and the results of Figure 5.19. This was because the substrate enabled strong coupling to occur between itself and the nanorod which in turn led to the hybridisation of the modes and therefore the onset of these higher order modes earlier. The electric field plots for the longitudinal mode and the first two occurring higher order modes are seen in Figure 5.20. An appreciation of the electric field distribution for these modes is required as this helps with the analysis of modes in later sections of this work.

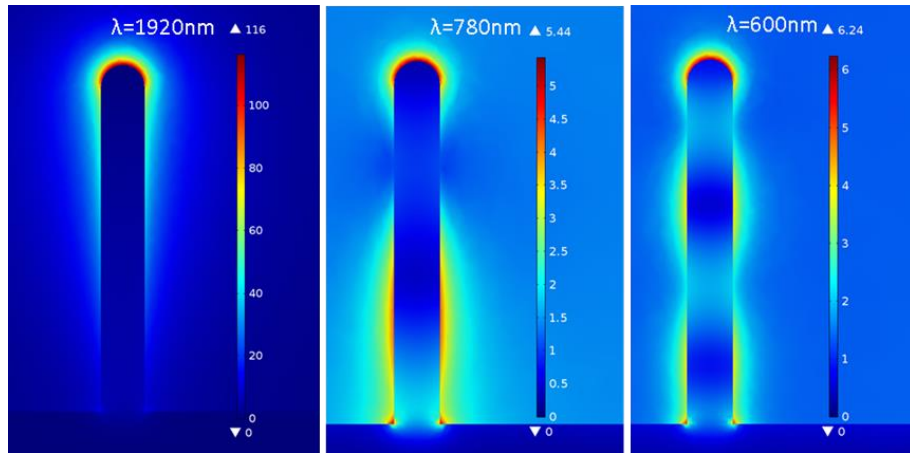


**Figure 5.20: Electric field distribution plots for the longitudinal mode and higher order modes at decreasing wavelengths (left to right). The nanorod is 30 nm diameter with an aspect ratio of 8 and is supported on a 150 nm thick gold substrate.**

Lastly, an assessment of the effect of angle of incidence on a supported single nanorod was undertaken, as shown in Figure 5.21. It was noted that with increasing angle of incidence, the transverse mode decreased in amplitude whereas the longitudinal mode increased. More importantly however was the appreciation that the resonant wavelengths of the modes did not alter with polarisation. Although this may seem a trivial result, it is found to be in contrast to the behaviour found for arrays of nanorods, as described later.

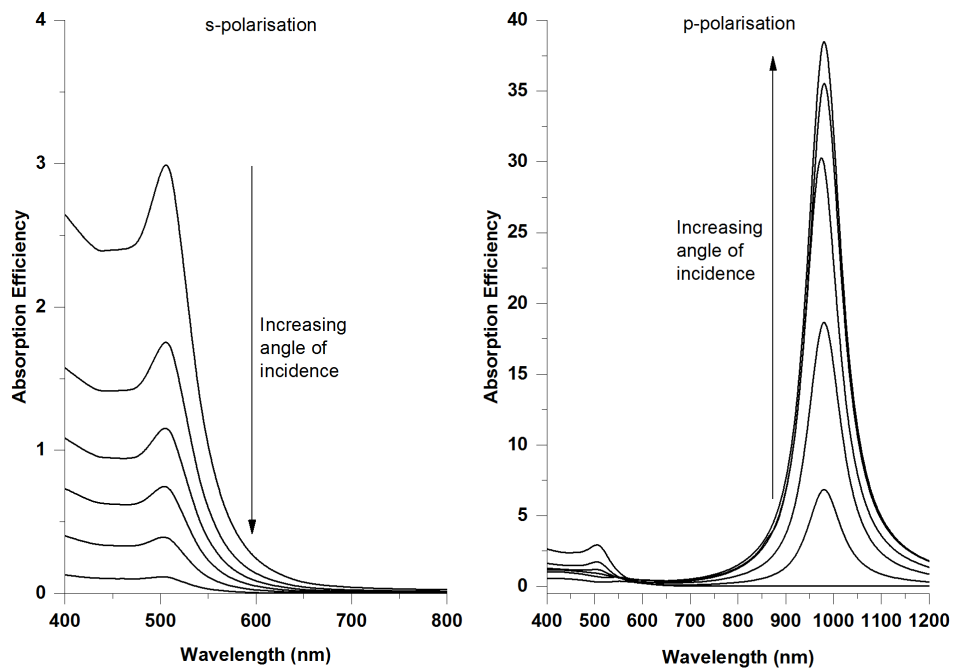


**Figure 5.21: Absorption efficiency for a 30 nm x 90 nm gold nanorod stood vertically on a gold substrate and illuminated by an s or p-polarised plane wave with varying angle of incidences.**

## 5.6.2 Particle - Particle Coupling

Following on from the effect of the interaction of a single nanorod with a substrate, attention was then directed to the coupling experienced between multiple nanorods. A wealth of research has studied these systems for the case of nanoparticle dimers or end to end orientated nanorods, however, relatively little attention has been given towards side by side orientated arrays of nanorods despite the interesting optical properties they possess and the ease at which they can be fabricated. For conciseness, only this side by side orientation is studied here as it matches those fabricated within this work.

Firstly, a trimer of AR=3 nanorods were simulated in a homogeneous medium ( $n=1$ ) with a variable spacing, as shown in Figure 5.22. This spacing was defined from the edge to edge of adjacent nanorods, whereby 0 nm represented touching nanorods. This is in contrast to the inter-particle spacing given elsewhere, which measures between the centres of nanorods, as the former allowed a deeper insight into the particle coupling strength that was irrespective of the nanorod diameter.

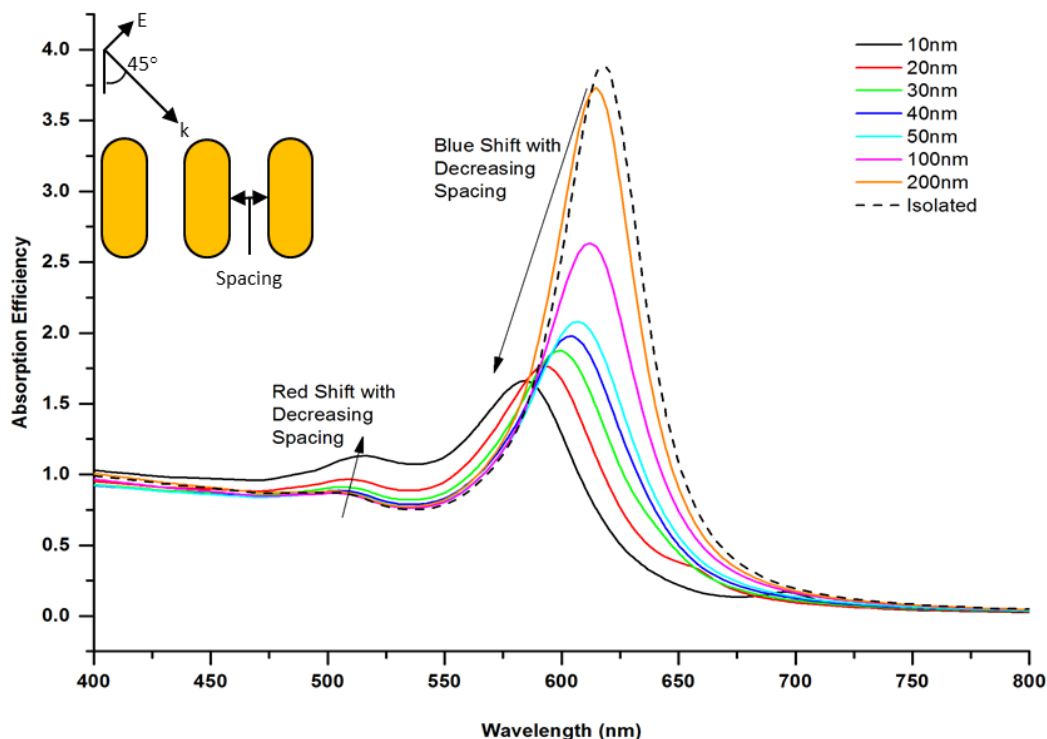


**Figure 5.22: Effect of spacing on the absorption efficiency for a trimer of side-by-side aligned gold nanorods of AR=3 and diameter 30 nm, excited using p-polarised light at 45°. The isolated curve represents that of a single gold nanorod therefore with no inter-particle coupling.**

The above results show that as the trimer of nanorods moved closer together, and therefore the inter-particle coupling strength increased, a blue shift of the longitudinal mode occurred, with it moving from 618 nm to 584 nm. This was also accompanied by a drop in the absorption efficiency. Alternatively a red-shift occurred for the transverse mode from a wavelength of 502 nm to 516 nm, with an additional increase in the absorption efficiency. Both of these relationships match those found in the literature review. For instance, as predicted by the plasmon hybridisation model, parallel aligned nanorods with the electric field polarised along the long-axis have a bright mode (parallel aligned dipoles) that occurs blue-shifted in comparison to that of an isolated nanorods longitudinal mode <sup>(115)</sup>. Alternatively, when the electric field is perpendicular to the nanorods long-axis, a slight red-shift of the transverse mode was predicted <sup>(119)</sup>. On the other hand, in regards the change in absorption efficiency, a similar result was also found by Lee *et. al* <sup>(120)</sup>. The decrease in absorption efficiency of the longitudinal modes with spacing may be attributed to destructive interference of the radial components of the electric field as the nanorods are brought closer together. The opposite was true for the transverse mode whereby the radial components constructively interfere therefore increasing the strength of the plasmon and giving a higher absorption efficiency. This can be seen in the electric field plots of Figure 5.23.

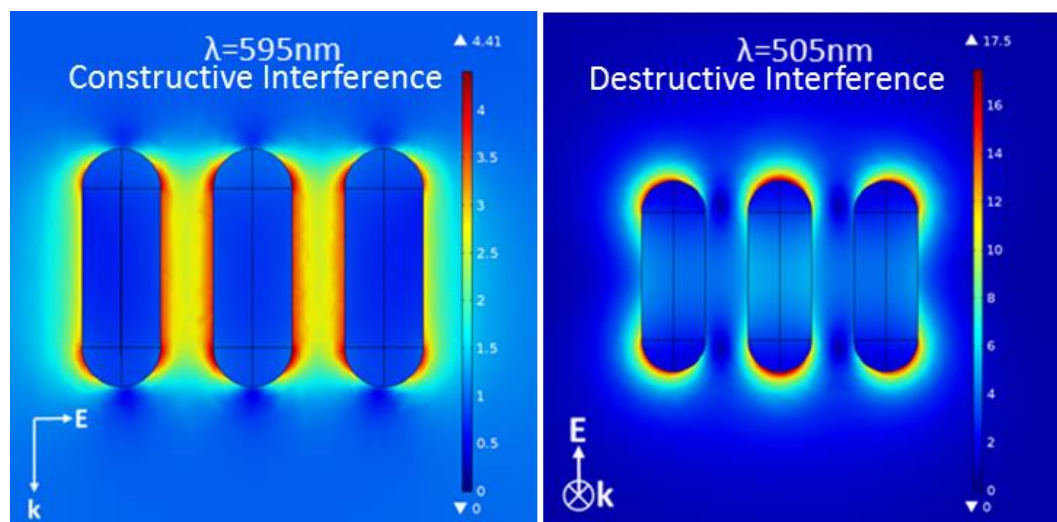


**Figure 5.23: Electric field distribution for a trimer of side-by-side nanorods showing the constructive interference between the transverse modes and destructive interference between the longitudinal modes.**

Referring back to Figure 5.22, the absorption efficiency spectra for a single nanorod is also included within the plot. It appeared as though at a large spacing within the nanorod trimer,

the longitudinal mode regained both the resonance position and strength of that of a single isolated nanorod. In fact, further analysis showed this to be more complex. For instance, the trimer spacing was extended up to large gaps of 3000 nm, as seen in Figure 5.24. The cross section efficiencies actually surpassed that of the isolated nanorod before then decreasing and repeating so that a fluctuating trend was produced. Similarly, although not shown within the figure, the resonance wavelength similarly fluctuated by a few nm either side of the isolated nanorod longitudinal wavelength. These effects can be explained by constructive or destructive interference between the scattered fields of the nanorod array according to Bragg's law, as seen in equation (88).

$$2d \sin \theta = n\lambda \quad (88)$$

Where  $d$  is the periodic distance,  $\theta$  is the angle of the scattered rays,  $n$  is an integer, and  $\lambda$  is the wavelength.

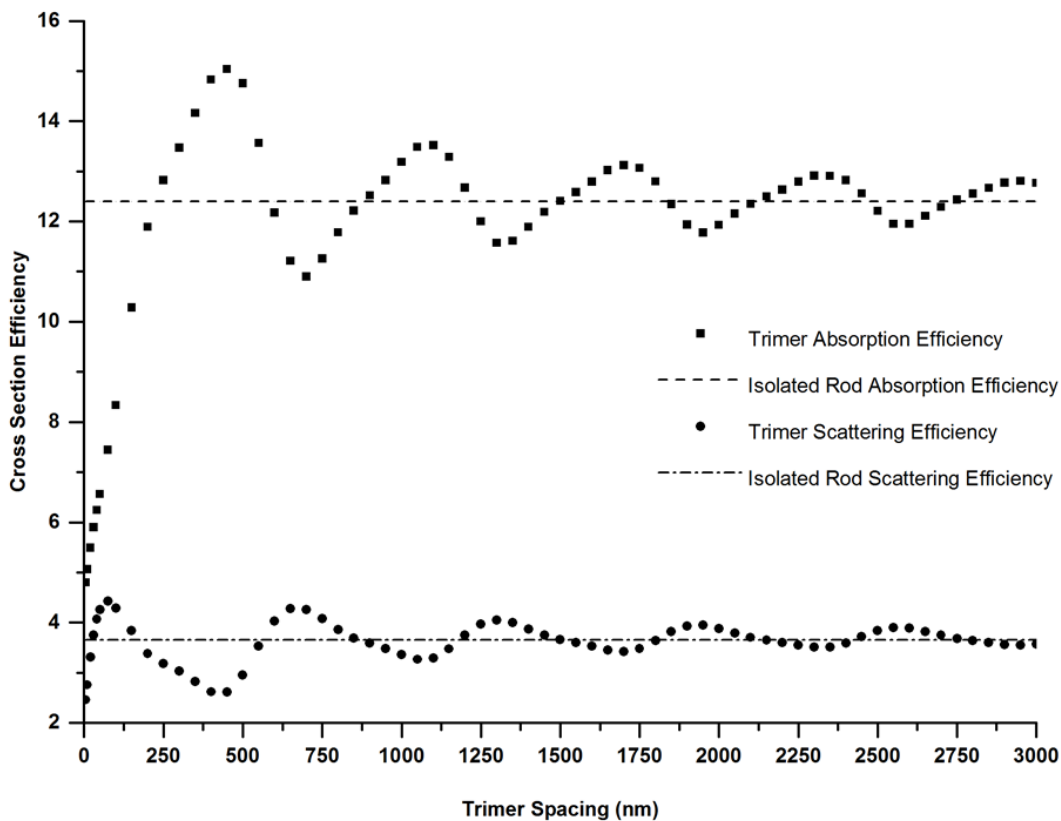
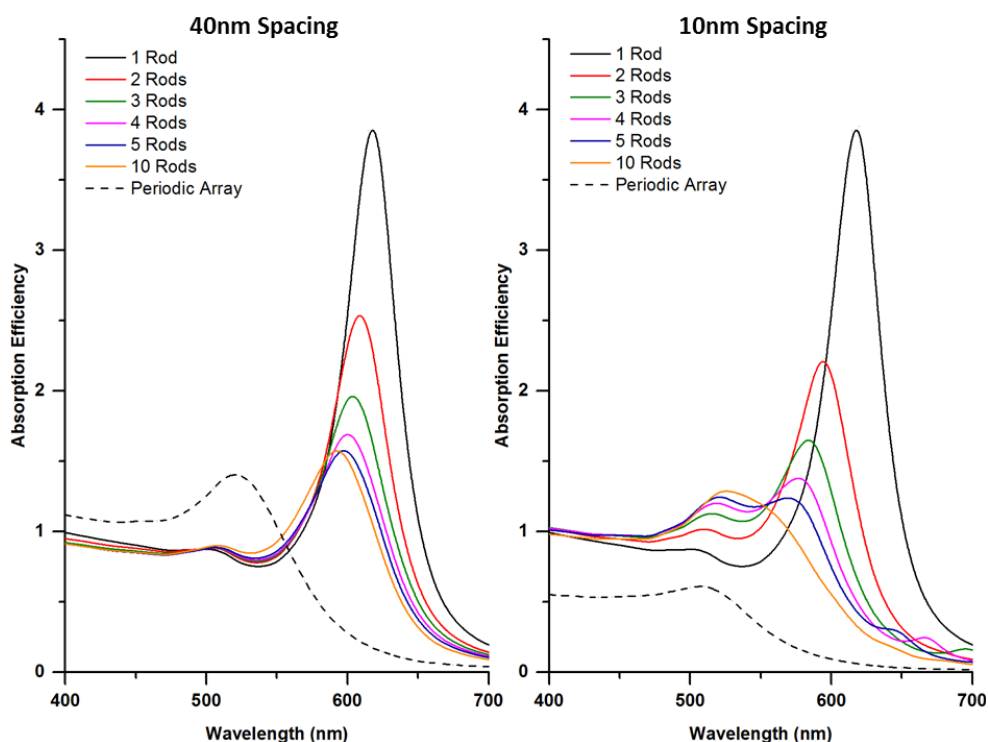


Figure 5.24: Dependence of the longitudinal modes optical cross section efficiencies on the inter-particle spacing for a trimer of gold nanorods (30 nm diameter, AR=3).

The dependence on spacing, and therefore inter-particle coupling strength, for a trimer of nanorods has been addressed so far. The coupling strength however does not depend solely on the separation of the nanorods, but also on the number of nanorods within the array. Considering this, modelling of a nanorod array was also performed whereby the spacing was kept constant at either 10 nm or 40 nm, however, the number of interacting rods was varied. The results of this may be seen in Figure 5.25 including the spectra for a periodic array which represents an infinite number of interacting nanorods. This latter data was simulated using the previously described *nanorod array model* which harnesses the use of periodic boundary conditions.

The results showed that with increasing number of nanorods in the array, once again a blue shift of the longitudinal mode occurred, along with a red-shift of the transverse mode. At a spacing of 40 nm these shifts were relatively small, with the longitudinal mode shifting from a wavelength of 618 nm for a single nanorod, down to 592 nm for ten interacting rods. At a spacing of 10 nm however, the shifts were much more pronounced with the longitudinal mode actually beginning to overlap that of the transverse mode for a ten particle nanorod array.



**Figure 5.25: Effect of number of interacting nanorods on the absorption efficiency for an array of side-by-side aligned gold nanorods of AR=3 and diameter 30 nm, excited using p-polarised light at 45°. The periodic array curve represents that of an infinite array of gold nanorods.**

Figure 5.25 also highlights the effect of going from a finite number of interacting nanorods to an infinite array of nanorods. It was seen that for both spacing's modelled, only a single peak was evident within the periodic array spectra, occurring at the transverse mode resonant wavelength. To confirm the longitudinal mode was not located at a wavelength above that shown, the wavelength modelled was extended in steps up to 3000 nm, with no additional peaks being noted. Although theoretically there should be a peak at higher wavelength attributed to the dark mode (anti-symmetric alignment of dipole moments), this is unable to be excited by linearly polarised light and therefore cannot be seen in these simulations <sup>(213)</sup>. Based upon these results, it was therefore concluded that the longitudinal mode had blue-shifted completely into the transverse mode. This large shift between the results of ten rods and a periodic array of rods, particularly for the 40 nm spaced nanorods, suggested that both the inter-particle coupling and the number of interacting rods were crucial towards the resonant wavelengths of the modes and therefore the coupling strength.

The single peak seen within these simulations when using a periodic array of nanorods is similar to that seen in the UV-Vis results of Chapter 4 for short nanorods (Figure 4.18). In fact, a good comparison can be made as these also were measured to have an aspect ratio of three and spacing of 40 nm. Considering this, it would be expected to also match the UV-Vis result found for the larger aspect ratio nanorods (AR=18), which also had a spacing of around 40nm. In this longer nanorod array the longitudinal mode red-shifted away from the transverse mode and occurred within the visible spectrum at approximately 660 nm. To verify this, further modelling was performed for increasing nanorod aspect ratios, however this time using only periodic nanorods and once again keeping the spacing constant at 40nm. The results of this can be seen in Figure 5.26.

The extinction cross section was plotted rather than the absorption efficiency due to scattering being dominant in the larger aspect ratio nanorods, as shown later. Additionally the cross section was not given in terms of its efficiency as it allows the development of the individual modes to be better visualised. Taking the efficiency instead however shows a maximum in the longitudinal mode extinction efficiency at an aspect ratio of approximately 13, followed by a gradual reduced at higher AR's.

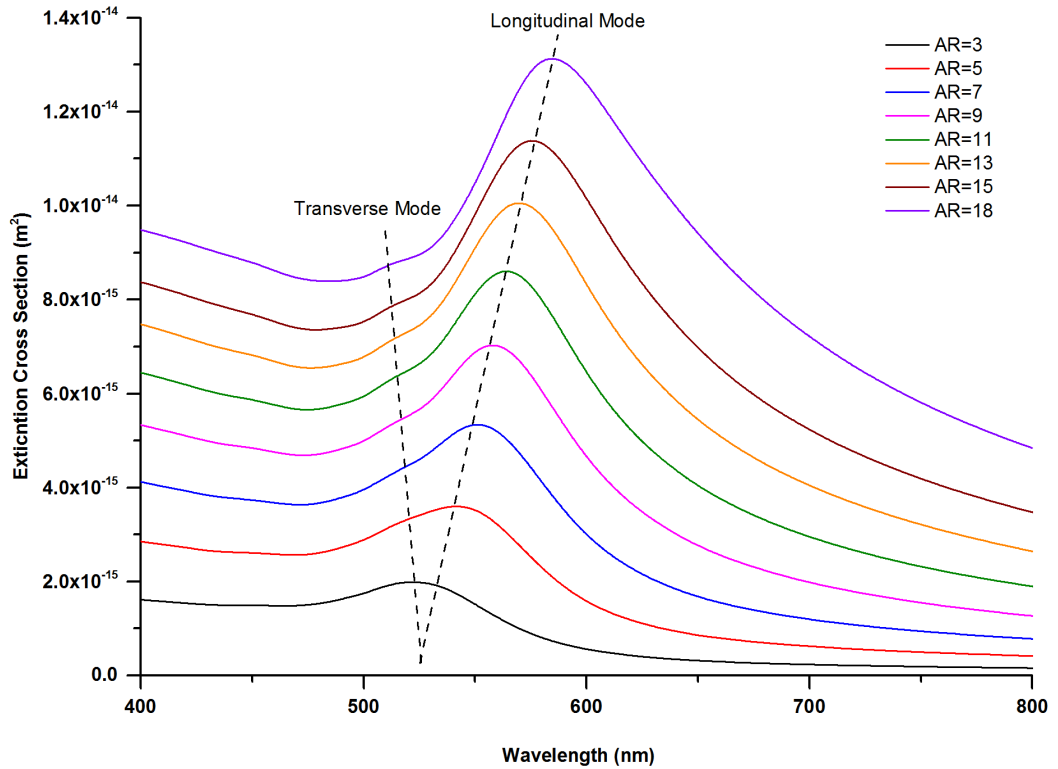


**Figure 5.26:** Extinction cross sections for a 30 nm diameter nanorod array with a spacing of 40nm and varying aspect ratio. The array is excited by p-polarised light at an angle of incidence of 20° in a vacuum.

The results in Figure 5.26 showed that at an aspect ratio of three, once again only a single peak in the spectrum occurs, with the longitudinal mode therefore completely overlapped with that of the transverse mode. As the aspect ratio was increased however, the longitudinal mode was seen to emerge from the transverse peak at a slightly higher wavelength. This then red-shifted with increasing aspect ratio of the nanorods, whereas conversely the transverse mode blue shifted. These shifts with respect to the aspect ratio agree with those found for an isolated rod of increasing length, as shown previously and as predicted by Gans theory <sup>(37)</sup>. The largest difference however is in the rate at which this red-shift of the longitudinal mode occurred. For instance, referring back to Figure 5.11 which shows the results for an isolated nanorod with aspect ratio, the red-shift was very quick. In fact by an aspect ratio of five it had already begun to shift away from the visible spectrum. In contrast, in the periodic array of nanorods the rate of red-shift with increasing aspect ratio was much reduced so that even by an aspect ratio of 18, the longitudinal peak is still only located around 600 nm.

This finding is in good agreement with that found in other work such as that of Evans *et. al.*<sup>(134)</sup>. Similarly, it also fits with the trend shown in the experimental results of this work, whereby the longitudinal mode was red-shifted out of the transverse mode. Despite this agreement, there are some discrepancies in the absolute values. For example, the long nanorods of aspect ratio 18 shown in Chapter 4 were found to have a longitudinal mode located at approximately 660 nm. In the simulations however, this was shown to be at a slightly shorter wavelength of approximately 585 nm. This difference can be explained by the experimentally derived results being measured for nanorods embedded in the higher refractive index of alumina as compared to a vacuum in the simulations. The higher refractive index not only leads to an intrinsic red-shift in the resonance position, but it results in a reduced coupling strength that in turn would also red-shift the results. Indeed, if the media in the modelling is altered to have a refractive index of 1.6, as is assumed in other works studying AAO templates<sup>(214, 215)</sup>, a closer match in resonance wavelength occurs at approximately 720 nm (*not shown*). This slight overestimation of the red-shift is possibly a result of variation in the actual lengths of the nanorod samples, possibly making them on average shorter than expected. Alternatively it may also be due to the refractive index of the AAO actually being less than the estimated  $n=1.6$  value. For instance Gong *et. al.*<sup>(216)</sup> showed the refractive index of AAO membranes decreases with increasing pore size and thickness of the template. As this work did not use thin-film AAO, a reduction in the refractive index is therefore potentially likely to occur.

Due to the good agreement of the model with the trends observed in the experimental UV-Vis results, further features of the nanorod arrays could be simulated so as to provide more in-depth analysis and determine methods to optimise the plasmonic response of arrays. For example, the effect of spacing on periodic nanorod arrays with an aspect ratio of either three or seven was addressed, as seen in Figure 5.27 and Figure 5.28 respectively.

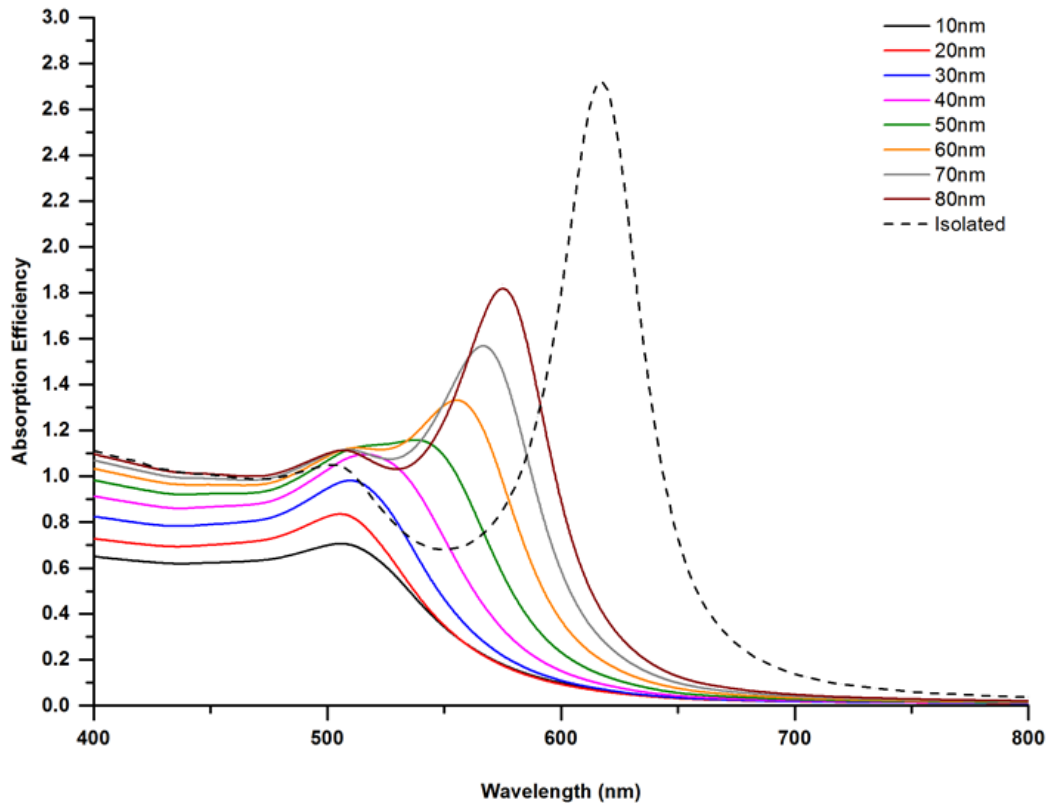


**Figure 5.27: Effect of spacing on the absorption efficiency of a periodic array of nanorods with aspect ratio three in a vacuum (diameter of 30 nm).**

Focussing initially on the AR=3 periodic nanorod array, a result similar to that shown for a finite number of nanorods interacting was found. With decreasing spacing and therefore increasing coupling strength, the longitudinal mode was blue shifted towards that of the transverse mode whereby it eventually overlapped around a spacing of 40 nm to give a single peak. Additionally, a decrease in the absorption efficiency as the spacing is reduced is again also noted, attributed to the destructive interference between the modes of adjacent nanorods. The difference for this periodic array of nanorods however, was that a greater red-shift with spacing occurred compared to for instance, the nanorod trimer results shown previously in Figure 5.22. This spacing was easy to control using the AAO template fabrication method and therefore it allowed the fine tuning of the longitudinal resonance position. Although this was also possible by controlling the aspect ratio of isolated rods, these are typically made within solution and therefore have random orientations and spacing. In contrast, with the nanorod arrays there is complete control over the diameter, spacing, aspect ratio, and orientation of the nanorods therefore allowing these features to be optimised for specific applications.

The results for an AR=3 nanorod showed that by controlling the features of the array, the longitudinal resonant wavelength may be precisely tuned to occur up to a wavelength of around 600 nm. By harnessing longer aspect ratio rods however, this may be extended to cover the whole visible spectrum, as seen in Figure 5.28.

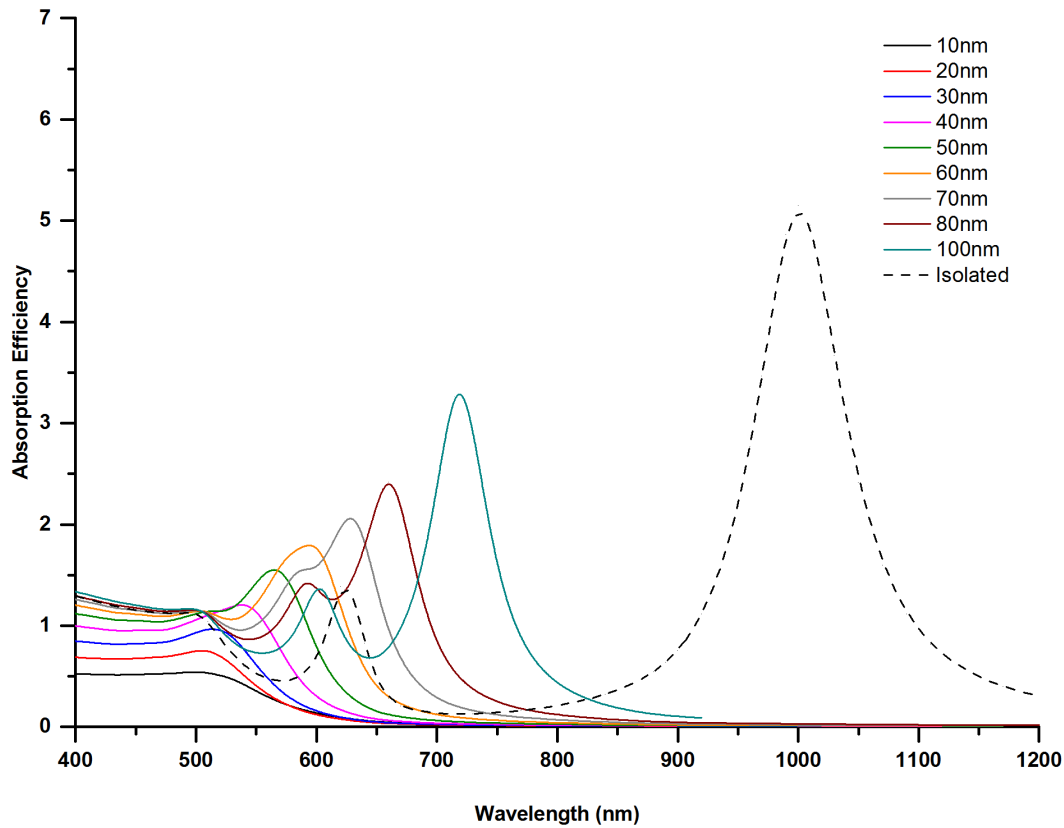


**Figure 5.28: Effect of spacing on the absorption efficiency of a periodic array of nanorods with aspect ratio seven in a vacuum (diameter of 30 nm).**

Studying these results showed that the same trends were seen to that of the aspect ratio three nanorod, whereby a decreasing spacing blue-shifts the longitudinal modes resonance position. Additionally however, further features were also present. For example, a mode in-between that of the transverse mode and the longitudinal mode was evident for the isolated nanorod or when the spacing was above around 70 nm. This was related to a higher order mode of the nanorod due to its increased length compared to the aspect ratio three nanorod. At smaller separations the longitudinal mode and the higher order mode overlapped, before then blue-shifting into the transverse mode.

An additional benefit of modelling is the ease at which the absorption and the scattering efficiencies for the nanorod array could be calculated. As found within the experimental UV-Vis measurements, when just the absorption by the array was determined, the longitudinal mode for high aspect ratio nanorods was relatively weak. This result is supported by the simulations. For instance, the absorption, scattering, and extinction efficiency for a number of periodic nanorod arrays with aspect ratios ranging from 3 to 15 were modelled, as seen in Figure 5.29. It was seen that at the shorter aspect ratios, absorption dominated and provided the largest contribution towards the extinction efficiency. On the other hand, as the aspect ratio increased, the absorption efficiency stayed relatively constant, however, the scattering became more prominent eventually becoming the major influence on the extinction efficiency. This result highlighted that the extinction of the nanorod samples, as typically given within works that study the optical properties, cannot be simply attributed to absorption by the sample, but instead has a more complex behaviour that is dependent on the geometry of the nanorods within the array.

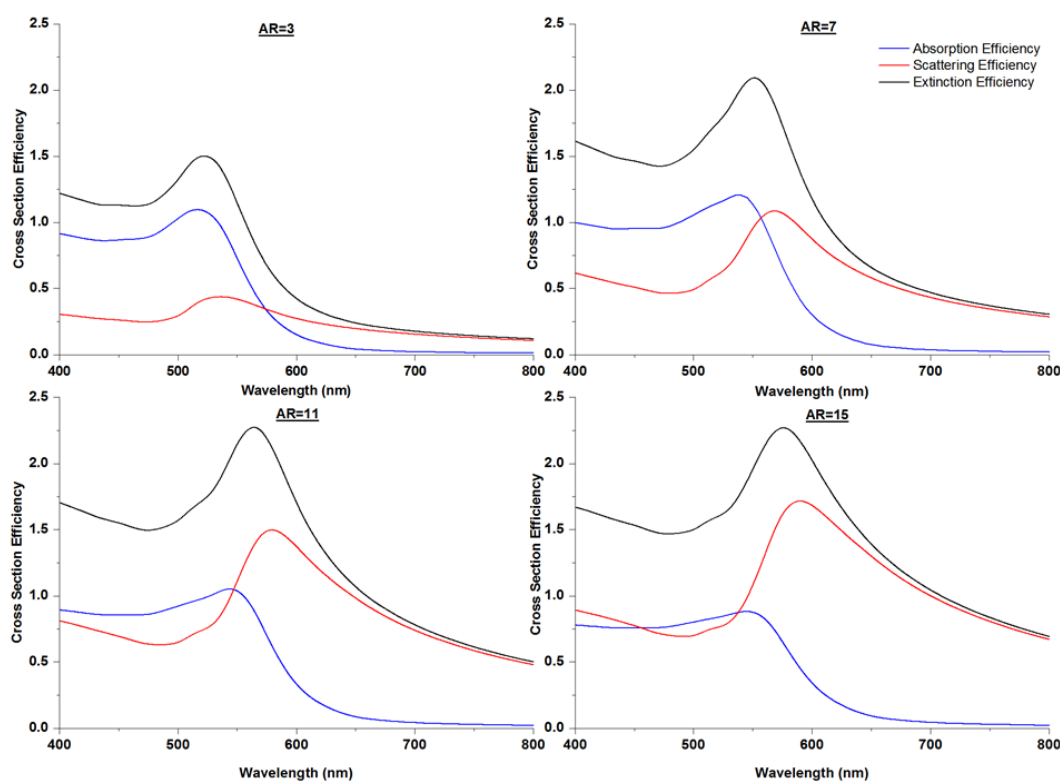


**Figure 5.29: Optical cross section efficiencies for gold nanorod arrays of aspect ratio 3,7,11 and 15. The diameter of the nanorods is 30 nm with 40 nm spacing and embedded in a vacuum. 20° angle of incidence p-polarised light is used to excite the plasmonic modes.**

In addition to the above results, the effect of the angle of the incident light with respect to the resonant wavelength of the longitudinal mode in a periodic array was modelled, as seen in Figure 5.30. An interesting result is shown whereby in contrast to that previously described for isolated nanorods in Figure 5.21, the resonant wavelength of the longitudinal mode was dependent on the angle of incidence. For instance, as the angle of incidence was increased, a blue-shift in the longitudinal resonant wavelength occurred. This was fairly gradual at low angles, however increased significantly for the higher angles of incidence.

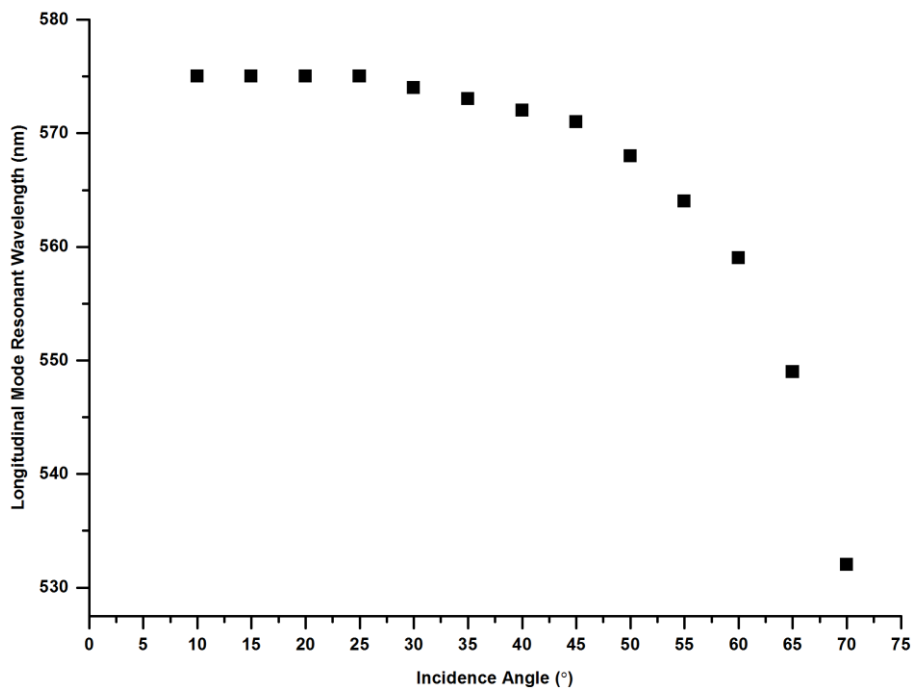


**Figure 5.30: Resonant wavelength of the longitudinal mode with angle of incidence for an aspect ratio 3 nanorod array using p-polarised light. The nanorod diameter is 30 nm and the spacing is 80 nm.**

This angular dispersion supported that found in other work for parallel aligned nanorod arrays (134, 194, 217) as does that of the dependence they have on spacing and aspect ratio. These properties may be explained by the concept that the longitudinal mode does not follow the same relationship as it does for individual nanorods, but instead that it forms a collective coupled mode based around the individual nanorods interacting with those adjacent. This coupling within the array is reliant on the inter-particle coupling strength, whereby stronger interactions between the nanorods enhances the generation of the collective mode. As previously discussed, this collective mode of the array is different from that of an isolated nanorod as, according to the plasmon hybridisation theory, it splits into a blue-shifted bright mode with symmetric dipole moments and a red-shifted dark mode with anti-symmetric

dipole moments. Additionally, as predicted in simulations by Wurtz *et. al.* <sup>(133)</sup> and Fiehler *et. al.* <sup>(136)</sup>, the electric field distribution for the blue-shifted coupled mode changes significantly compared to that for an isolated nanorods longitudinal mode in that it is no longer restricted to the nanorod ends. Instead the electric field was found to concentrate at the centre of the nanorod, with the fields extending away perpendicularly from the nanorod edge, as well as also being prominent within the nanorod itself. Based upon this, it was concluded by the authors of each work that the mode simulated is propagating along the array.

To verify this result, the electric field distributions for the periodic nanorod arrays simulated within this work were plotted at varying inter-particle spacing, as shown in Figure 5.31. It should be remembered at this point that the periodic arrays modelled within this work use Floquet boundary conditions on the side walls to represent an infinite array. In this regard, the images shown are for a unit cell that include just a single nanorod for each spacing. These however represent a single nanorod within an infinite array of parallel nanorods and therefore may be tessellated horizontally infinitely.

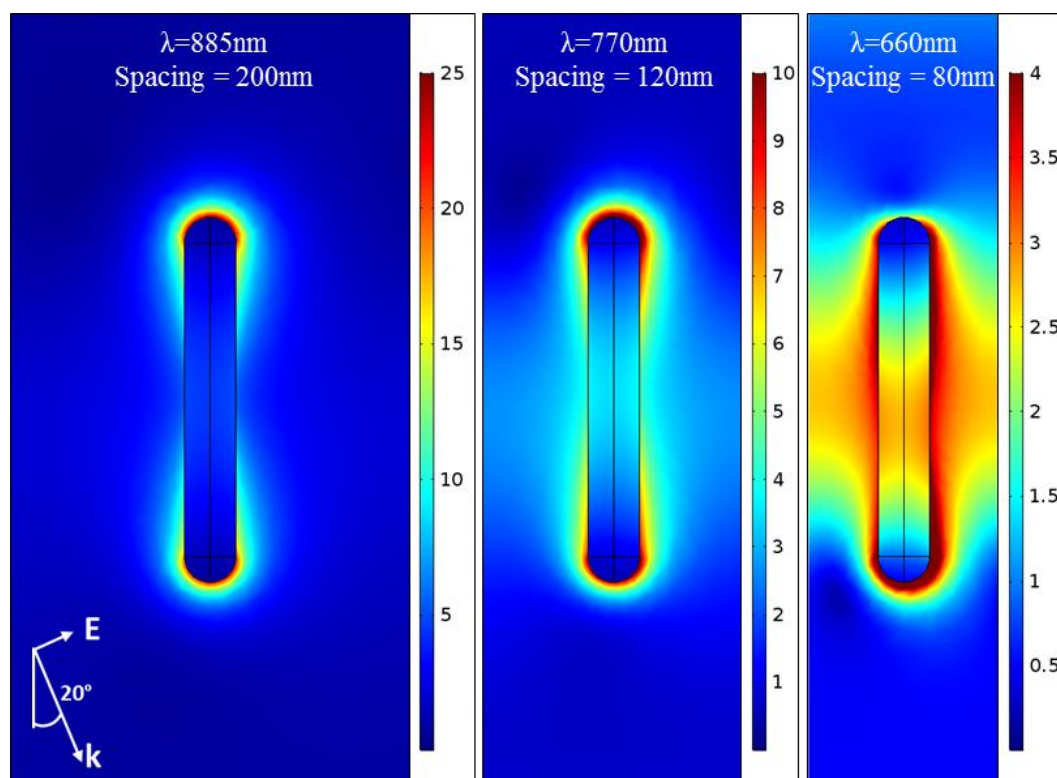


**Figure 5.31:** Electric field distributions for the longitudinal mode of periodic gold nanorod arrays with spacing. The nanorods are 30 nm in diameter and AR=7. The incident light is p-polarised at 20°.

The wavelengths used in the above plots refer to the resonant wavelength of the longitudinal mode and are not to be confused with higher order modes. As demonstrated previously, as the spacing was reduced, the resonant wavelength blue-shifted due to the stronger inter-particle coupling strength. At large separations the distribution of the electric field matched that of the longitudinal mode seen in isolated nanorods with a dipolar characteristic. As the spacing was reduced however, a dramatic change to the electric field distribution occurred where it shifted towards the centre of the nanorod and propagated towards the simulation side boundaries. As the fields were seen to extend right up to the boundary of the simulation this would therefore represent an electric field that is coupled to the nanorods adjacent to it.

Alternatively, by plotting the Poynting vector, the energy flow within the array may be visualised. This is shown within Figure 5.32 for both an isolated nanorod (a) and a periodic nanorod (b) so as to compare the difference. The unit cell of the periodic array has been repeated four times so as to better analyse how the electromagnetic energy flows between the nanorods and visualise the coupling.

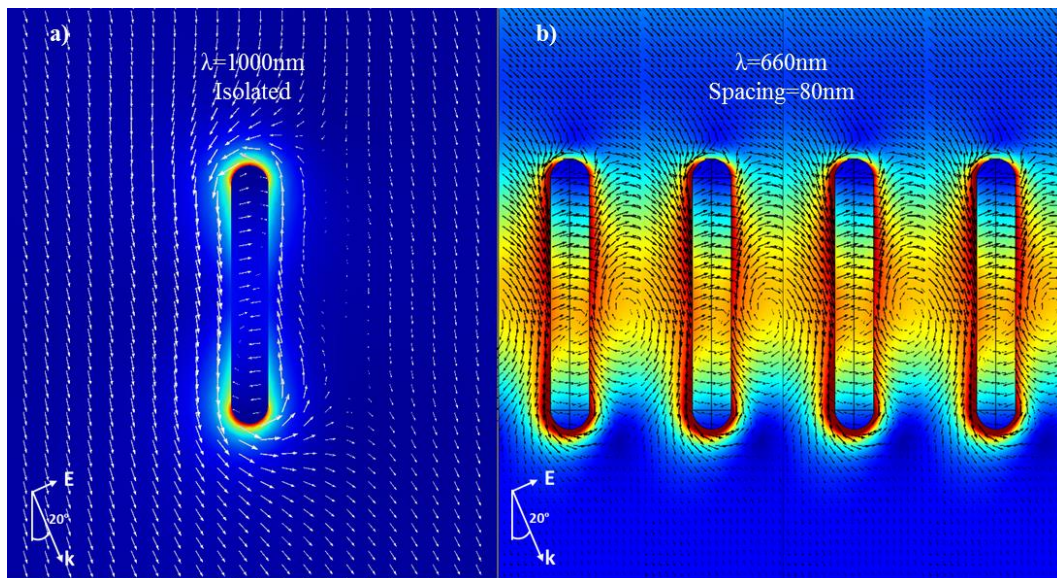


**Figure 5.32: Electric field distribution (colour plot) and Poynting vector (arrows) for an a) isolated and b) periodic array of nanorods of aspect ratio 7. The diameter of the nanorods is 30 nm and the incident light is p-polarised at an angle of  $20^\circ$ .**

Studying the arrows within Figure 5.32 which represent the electromagnetic energy flow, it was clear to see a large difference occurred when placing the nanorods within an array as compared to when they are isolated. For instance, in an isolated nanorod the energy flow

travelled predominantly parallel to the nanorod, along its length. On the other hand, for the nanorod array the electromagnetic energy was seen to convert towards a direction that is perpendicular to the long axis of the nanorods. In this scenario, the electromagnetic energy is capable of travelling between each of the nanorods in the array and therefore to propagate along it. This result supports that found by Wurtz *et al.* <sup>(133)</sup> and has important implications for potential applications such as in the development of waveguides. Additionally, it signified that the optical properties of nanorod arrays are much more complex than those found for just single isolated nanoparticles, and that by controlling the coupling strength, a degree of control over both the spectral position of the resonances and the spatial location of the electric field may be achieved.

### 5.6.3 Plasmonic Nanorod Arrays on Gold Substrates

So far the optical properties of isolated nanorods have been studied and compared to those where coupling with either a substrate or other particles is prominent. These different coupling types were separated initially so as to effectively analyse the individual effects of each, however, they are now addressed together. This aimed to represent a plasmonic nanorod array that is supported upon a gold substrate as in those fabricated within this work.

Firstly, a nanorod array stood vertically on a 150 nm gold substrate was simulated, as in Figure 5.33. This was compared to the results previously found for an unsupported nanorod array, and that of a supported and unsupported isolated nanorod of the same dimensions. It may be seen that the nanorod array supported on the gold substrate was red-shifted in comparison to that of the nanorod array without a substrate. This therefore followed the same trend as that seen within section 5.6.1 where it was found that gold nanoparticles placed on a gold substrate underwent strong coupling that significantly red-shifted the resonant wavelength. On the other hand, the red-shift observed was much smaller than that seen for single supported nanorods, with the longitudinal resonance occurring at around 690 nm compared to approximately 980 nm. This was due to the previously described blue-shifts associated with coupling between side-by-side orientated nanorods.

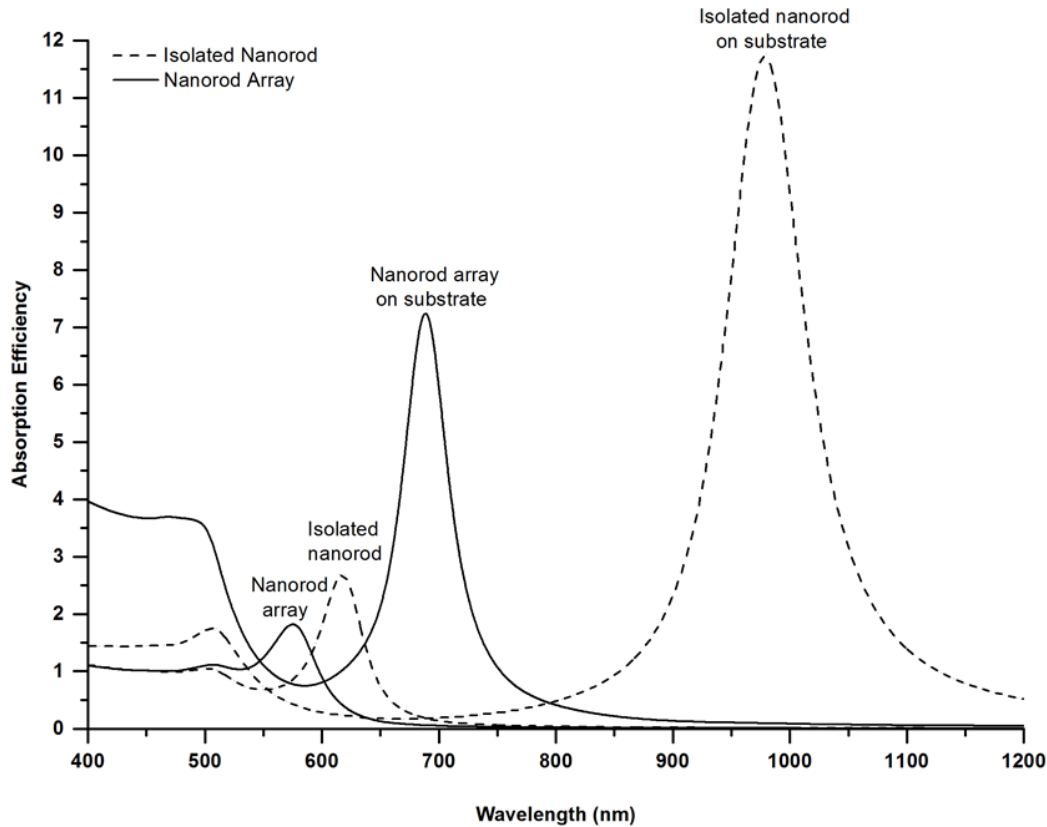


**Figure 5.33: Comparison of absorption efficiency for a periodic array of nanorods (solid lines), both in a homogeneous medium ( $n=1$ ) and supported on a 150 nm thick gold substrate. Additional dashed lines represent single nanorods not in an array, again in a homogeneous medium and supported on a gold substrate. P-polarised light at an angle of incidence of  $20^\circ$  was used in all these simulations. The nanorods in the arrays had a spacing of 80 nm.**

If the absorption efficiency instead of the resonant wavelength was analysed, a similar observation was made. For instance, the nanorod array on the gold substrate was also predicted to have an increased longitudinal absorption efficiency compared to that of an unsupported nanorod array. Once again this is as expected based upon the results in section 5.6.1 for substrate-particle coupling effects. This increase however was again not as great as that seen when comparing a single isolated nanorod to one placed upon a gold substrate. This is due to the nanorods within the array coupling together, resulting in either the destructive interference of the longitudinal modes, or potentially the redistribution of the electric field away from a strong dipolar mode towards the centre of the nanorods.

Considering these results in more detail, it was therefore hypothesised that when a nanorod array is placed upon a gold substrate, both particle to particle, and substrate to particle coupling occurs. In the first scenario, the nanorods are aligned in a side-by-side manner, which

as predicted by the plasmon hybridisation theory, gives rise to a blue-shift in the longitudinal mode depending on the coupling strength (bright-mode only). Alternatively, the nanorods on a substrate can also be thought of as coupling with their substrate images. This would represent an end-to-end orientation of the nanorods, which again according to the plasmon hybridisation model, would result in a red-shift of the bright longitudinal mode the degree of which is related to the coupling strength. In the current system, where both these coupling types occur, there is therefore a trade-off between the contrasting coupling effects. In this situation, the spectral shift or alternatively the change in absorption efficiency, is then dependent on the relative coupling strengths of each interaction.

This finding is believed to have beneficial implications with regard to achieving a high absorption over the visible wavelength range when using gold nanorods. For example, by placing the nanorods on top of the gold substrate, a large enhancement in the absorption efficiency may be achieved. Unfortunately this also results in an undesired red-shift away from the visible region, even for small aspect ratio nanorods. To counteract this, the nanorods may be coupled together in a side-by-side array. This has the effect of blue-shifting the resonance back into the visible spectrum, albeit with a degree of reduction in the absorption efficiency. It is therefore proposed that with careful control over the coupling strength in the array, the resonant wavelength may be tuned throughout the visible spectrum whilst still partially benefitting from the enhanced absorption efficiencies.

This principle is demonstrated in Figure 5.34 for an aspect ratio three nanorod array with varying spacing, supported on a gold substrate. For comparison, single unsupported nanorods of aspect ratio three and four are also included as represented by the dashed and dotted lines respectively. It may be seen that by controlling the spacing of the supported nanorod array, the resonant wavelength of the longitudinal mode could be tuned throughout the visible spectrum. Additionally, although a large decrease in the peak absorption efficiency occurred as the spacing was reduced, the levels achieved are still greater than those found for isolated rods without a substrate. This was particularly evident towards the shorter wavelengths, around that of the transverse mode and below. It is believed this is due to the coupling between the transverse modes being enhanced due to the stronger local field strengths above the substrate. As the transverse mode coupling is constructive rather than destructive as in the case of the longitudinal modes, this leads to the high absorption efficiencies.

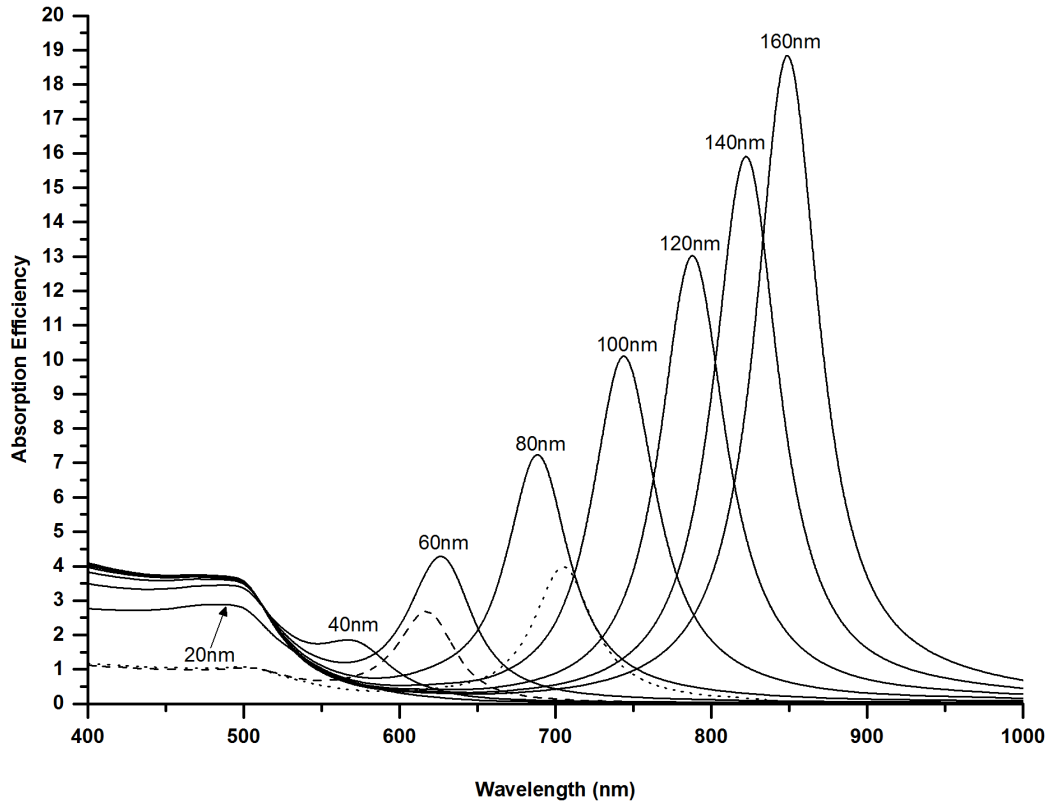


**Figure 5.34: Absorption efficiency for a gold nanorod array stood vertically on a gold substrate at varying spacing. Here the aspect ratio of the nanorods is three and the substrate thickness is 150 nm. The dashed and dotted line represent isolated unsupported nanorods of aspect ratio three and four respectively.**

In addition to the above results, once again the electric field distribution was analysed. This is shown for an AR of seven nanorod so as to compare with the unsupported nanorod arrays shown previously. As before, the mode at the highest wavelength is plotted, this being that of the longitudinal mode, as a functions of decreasing spacing. This is shown in Figure 5.35.

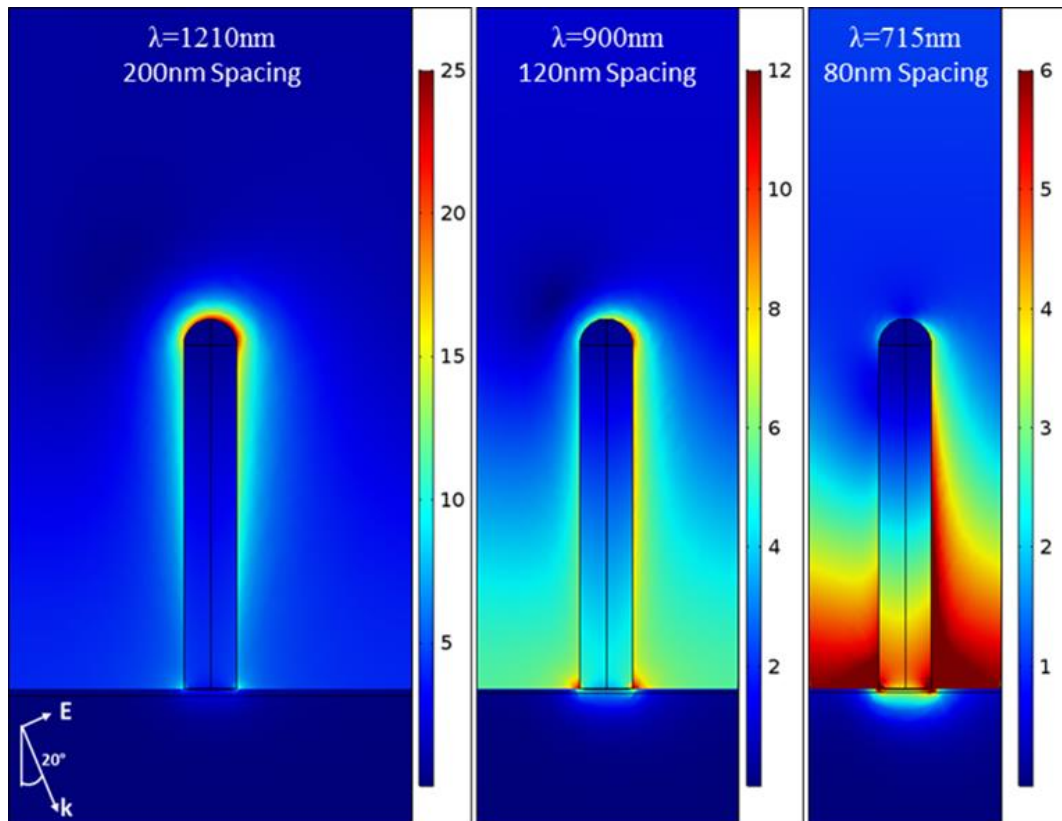


**Figure 5.35: Electric field distributions for the longitudinal mode of periodic gold nanorod arrays stood vertically on a 150 nm thick gold substrate with spacing. The nanorods are 30 nm in diameter and AR=7. The incident light is p-polarised at an angle of 20°. Each plot is taken at the resonant wavelength of the lowest energy peak, therefore representing the longitudinal mode.**

The electric field distribution of the supported nanorod array at a larger spacing of 200 nm was seen to very similar to that seen previously for a single supported nanorod. The electric field was concentrated primarily at the top end of the nanorod. As the spacing was reduced however, a change in the electric field distribution was seen to occur whereby the field was no longer strongest at the nanorod end, but instead spanned down the length of the nanorod before expanding to give particularly high field strengths along the surface of the substrate. As these fields were seen to spread to the side boundaries of the simulation they would therefore couple to the adjacent rods in the array.

This coupling can be visualised by once again plotting the Poynting vector, as shown in Figure 5.36 for a single supported nanorod, as well as the periodic array of supported nanorods.

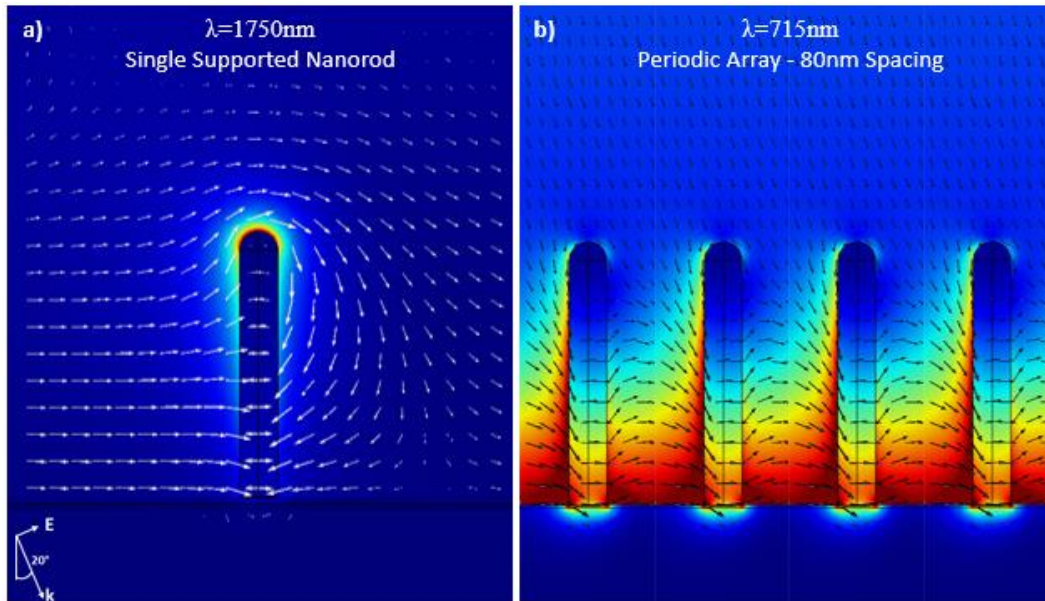


**Figure 5.36: Electric field distribution for a) a single supported nanorod, b) a periodic array of supported nanorods, both at their longitudinal resonant wavelengths. The arrows represent the Poynting vector for each scenario. P-polarised light is incident at 20° angle of incidence. All nanorods are 30 nm in diameter and AR=7.**

Firstly, the power flow and electric field distribution related to the single supported nanorod showed that, as expected, the field was strongest at the end of the nanorod. The power flow then circulates around this end before flowing back in towards the nanorod. In contrast, the periodic array of nanorods did not have the electric field localised towards the top of the nanorod, but as mentioned previously, it concentrated towards the base of the nanorod and along substrate surface. This results in the power flow also being markedly different whereby it radiated out from the nanorod base into the embedding media. This began to once again circulate back round, however at this point it was seen to interact with the adjacent nanorod and the process is repeated. This therefore again caused the power to flow between the adjacent nanorods of the array and in doing so, propagate along it. This matches the result found for the unsupported nanorod array, although the breaking of symmetry caused by the substrate stops the power flow being restricted to the centre of the array.

## 5.7 Summary of Results

In conclusion, the modelling performed in this thesis has allowed the analysis of plasmonic nanorods and in particular has addressed the effect that coupling has, both with a substrate, and with other nanorods within an array. For example, after initial validation of the model against Mie theory, the scope was expanded to simulate single isolated nanorods with regards

to effects of size, environment, and material. It was found that a diameter of around 30 nm typically gives the highest absorption efficiencies, and that by controlling the aspect ratio and material, the absorption may be tuned throughout the visible spectrum. Furthermore, if the nanorods are to be coated in a TiO<sub>2</sub> shell for photocatalytic purposes, a thickness of around 6 nm is predicted to be optimum.

Alternatively, in regards to coupling with a substrate, it was found that a metallic substrate leads to both a red-shift and an increase in the absorption efficiency compared to nanoparticles in either a vacuum or on a dielectric substrate. These coupling effects were amplified as the nanoparticle was brought closer to the substrate, as long as p-polarised light is used for excitation. With gold nanorods stood vertically on a gold substrate for instance, the red-shift and increase in absorption efficiency observed was very large. This was attributed to the nanorods longitudinal mode coupling with the substrate, analogous to nanorods in an end to end configuration. This configuration may therefore prove useful in systems that require large absorption of light, such as in plasmonic photocatalysis.

The modelling performed on arrays of side-by-side orientated nanorods showed that coupling of the longitudinal modes results in the opposite effect in that a blue shift in the resonant wavelength occurs along with a decrease in the absorption efficiency. It was also shown that the degree of these effects are dependent on the strength of the inter-particle coupling, which increases with decreasing separation distance and reduced refractive index of the surrounding environment. This therefore allows a further mechanism to control the resonant wavelength of the arrays instead of relying solely on the aspect ratio. For instance, even very long aspect ratio nanorods (AR=18) were found to be able to support a longitudinal mode in the visible spectrum under the right coupling conditions.

Interestingly, these nanorod arrays also showed additional effects whereby the longitudinal resonant wavelength was found to vary with the angle of the incident light. Additionally, electric field plots revealed that a drastic change in the electric field distribution occurs when under strong coupling. This is that the fields move from being localised at the end of the nanorods, as typical for the longitudinal mode, to being concentrated within the centre of the array. This is also matched by the power flow altering so that it travels between adjacent nanorods and essentially propagates along the nanorod array.

Lastly, the knowledge gained from modelling the substrate-particle coupling and particle-particle coupling was applied to analyse a nanorod array stood vertically on a gold substrate, therefore representing those fabricated in this work. It was found that in this scenario, coupling with both the substrate and the other particles in the array occurs. This results in a trade-off between the opposing coupling effects that is dependent on the relative coupling strengths of each. This was shown to again provide a controlled means to tune the resonant wavelength throughout the visible region, plus was also seen to give an enhancement over that found for isolated non-coupled nanorods. Finally, the electric field and Poynting vector was also plotted for these supported nanorod arrays. Once again a redistribution of the electric field is seen so that it localises towards the base of the nanorod, with the power flow again showing that light is able to propagate parallel to the inter-particle axis along the array.

# 6 ELECTRON ENERGY LOSS SPECTROSCOPY

So far the work in this thesis has focused on the optical characterisation of the plasmonic nanorods via excitation with light. For example, UV-Vis measurements were performed on the fabricated arrays in Chapter 4, and FEM modelling using plane waves was shown in Chapter 5. Although this characterisation using optical spectroscopy is practical due to the plasmonic resonances studied typically lying within the visible or near infrared region, there are a number of drawbacks that inhibit a full characterisation of the nanorod arrays. Firstly, as previously mentioned, the dark modes of the nanorod arrays that are predicted in theory by the plasmon hybridisation model cannot be excited by light. This is due to the dark mode representing an anti-symmetric configuration of the individual nanorods dipole moments, therefore meaning the excitation must also be anti-symmetric, such as a point source. As will be shown in this chapter however, by using an electron beam as the excitation source both the blue-shifted bright mode (high energy) and the red-shifted dark modes (low energy) may be excited and characterised by electron energy loss spectroscopy (EELS).

This complete characterisation of the plasmonic resonances in nanorod arrays is important not just from a fundamental point of view in understanding the hybridisation and coupling between nanoparticles, but may also be crucial in practical applications. For example, dark plasmonic modes are known to be able to store electromagnetic energy more efficiently than the bright modes due to a reduction in their radiative losses <sup>(213)</sup>. This gives them great potential in low-loss waveguides <sup>(218)</sup>. In addition, the reduced losses leads to the dark modes

having a reduced spectral linewidth which may prove particularly useful in sensing applications <sup>(219)</sup>.

Characterisation using electron microscopy is also useful in characterising the near-field properties of plasmonic nanoparticles. Although the simulations shown in the previous chapter may predict this near-field response, obtaining experimentally derived analysis in fabricated samples by optical methods remains challenging. This is due to the inherent disadvantage that the spatial resolution is limited by the diffraction limit, which in this context is typically hundreds of nanometres. On the other hand, by using a scanning transmission electron microscope (STEM) sub-nm resolution is achievable, which by rastering the electron beam, can build up information over a larger area. Additionally, by collecting and analysing the signals produced by interaction of the electron beam with the sample, detailed information may be acquired. One particular signal is that of electron energy loss (EEL). As discussed in more detail later, this allows the analysis of plasmonic modes in addition to information on elemental composition and electronic structure <sup>(220)</sup>.

This chapter will begin by giving a brief overview of the experimental methods used within this chapter. This will include an introduction to STEM followed by an explanation of the EELS technique. In this section, particular emphasis is given to how EELS may be used to characterise the plasmonic resonances of nanoparticles, in addition to an explanation of the post processing that is required to analyse the data. This then leads on to an additional explanation of the methods used in the production of an FEM model that in contrast to the previous chapter, uses electrons as the excitation and measures the electron loss probability. This is used to model and interpret the experimental work outlined in this chapter. Lastly, the results from the EELS modelling and EELS experiments is presented. This includes analysis and visualisation of the dark mode formed by coupling within a side-by-side nanorod array, which is believed to be an original finding. The sample fabrication and subsequent conversion into a cross-sectional, thin TEM sample for these experiments has been shown previously in Chapter 3, and therefore is not repeated here.

## 6.1 Overview of Transmission Electron Microscopy

### 6.1.1 Basics of TEM and STEM

Transmission electron microscopy (TEM) is a thoroughly established technique that has been extensively covered before in many books <sup>(221)</sup>. In this sense, only a brief description of the underlying principles is addressed here.

TEM is a technique where electrons are transmitted through a sample. In doing so the electrons undergo an interaction with the material, which in turn may be detected and used for analysis. These electrons are typically produced via applying a high voltage to either a tungsten filament or a lanthanum hexaboride crystal (LaB<sub>6</sub>), before focussing them into an electron beam by means of a Wehnelt cylinder <sup>(221)</sup>. This electron beam is then accelerated towards the sample and focussed upon an area by means electromagnetic condenser lenses. In conventional TEM (CTEM), the area covered by this beam of electrons addresses the entire region of interest simultaneously. On the other hand, in a variation of this technique known as scanning transmission electron microscopy (STEM), the electron beam is focussed into an extremely small probe, and scanned in a serial raster pattern across the sample. The interaction at each point is then monitored and recorded to build up an image over a larger area <sup>(222)</sup>.

Before outlining the specific operation of each case, an overview of the how an electron beam interacts with a thin sample will be given, as shown in Figure 6.1. Firstly, for a high energy electron beam impinging on a thin (<100 nm) sample, a number of the electrons will be able to penetrate the sample and emerge the other side. These electrons will have either passed through the sample without interacting with any of the material, or alternatively, will have been scattered. This scattering occurs in two ways, namely elastically where the energy of the electron does not change, or inelastically whereby a proportion of the energy is lost. Focussing firstly on elastically scattered electrons, although the energy of the electron remains unaffected, the direction of the scattering may vary significantly. For instance, if an electron passes close to the nucleus of an atom, columbic interaction may cause the electron to scatter over large angles (>5°), known as Rutherford scattering. If however, the electron passes far away from the nucleus and therefore only interacts with an electron cloud, the scattering angle is much less. Alternatively, electrons that undergo inelastic scattering generally only have a low scattering angle. The inelastic reduction in energy is then caused by a number of interaction processes that occur with the sample. These include phonon excitation based around atomic vibrations, single electron excitation related to ionisation of an atom, radiation

losses with regards to the emission of photons, or lastly resonant collective oscillations of either bulk or surface valence electrons (plasmon excitations), as in the basis of this work <sup>(220)</sup>.

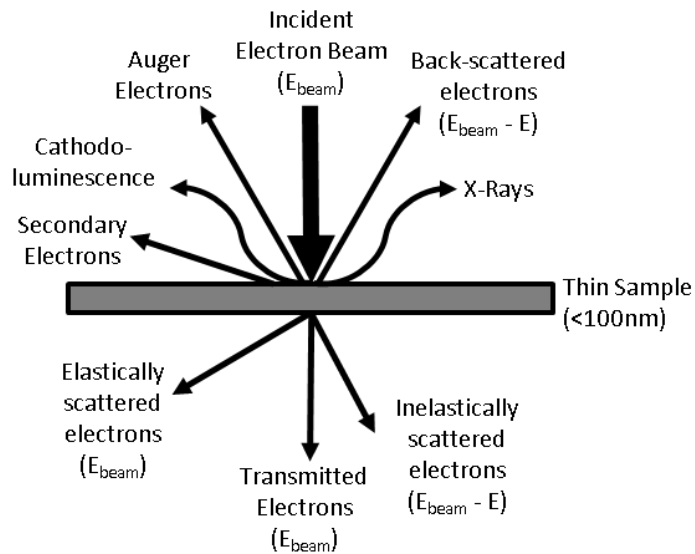


**Figure 6.1: Schematic diagram of an electron beam interacting with a thin sample.  $E_{\text{beam}}$  is the energy of the incident beam, whereas  $E$  is the energy lost during an interaction.**

Focusing once again on the operation, a schematic diagram of the instrumentation used in both CTEM and STEM, along with a representation of the electron beams in each is shown in Figure 6.2. As previously mentioned, both systems first use electromagnetic condenser lenses (also called probe-forming lenses or objective lens in STEM), to initially focus the beam on the sample. This is generally done from the bottom of the column in a dedicated STEM as opposed to from the top of the column in CTEM, however the principle remains the same. The electrons are then subsequently transmitted through the thin sample whereby they may go through some interaction as already discussed. In CTEM these transmitted electrons are collected by an objective lens (not to be confused with that in STEM), where they are focussed onto an objective lens image plane. A series of additional intermediate and projector lenses then further magnifies this image on to either an electron fluorescent screen or TV camera. Alternatively, the electrons may be sent into an EELS spectrometer for analysis, as covered within section 6.2 of this chapter.

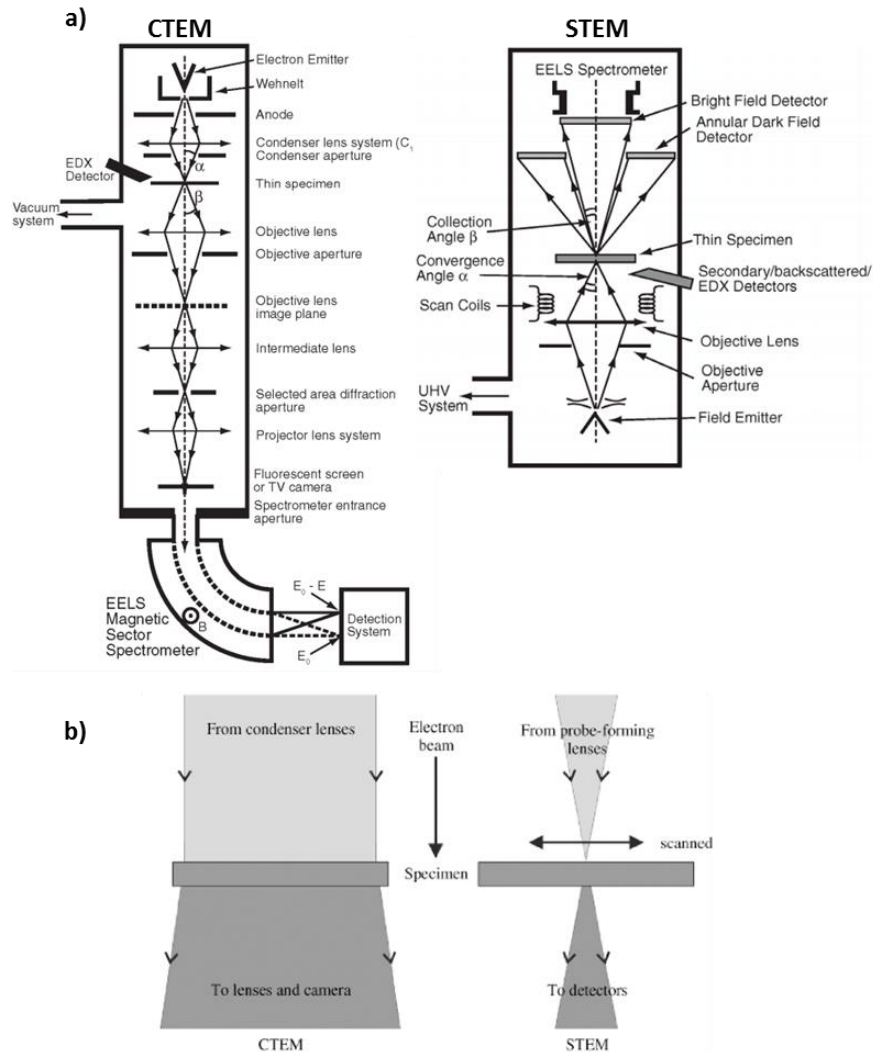


**Figure 6.2: a) Schematic diagram of the components in a CTEM and STEM <sup>(223)</sup>, b) Schematic representation of the electron beam in both a CTEM and STEM instrument <sup>(222)</sup>.**

In a STEM instrument on the other hand, the transmitted electrons are not focused by any electromagnetic lens after the sample, but instead collected by a number of detectors that record the intensity. As the scan coils move the beam over the sample in a raster scan, the transmitted intensity over a certain angular range of scattering at each location is measured, and subsequently combined to give an overall image. Once again, the electrons may also be directed into an EELS spectrometer. One particular benefit of this STEM technique over CTEM is the reduced reliance on electromagnetic lenses, with in principle only the probe-forming lens required. As each lens naturally has a degree of aberration, whereby the image is not focussed on a single image plane but deviates slightly, this leads to improved resolution, as covered within the following section.

## 6.1.2 Improving Resolution

### 6.1.2.1 Spatial Resolution

The spatial resolution using a STEM setup is governed primarily by the electron probe size on the sample after being focused by the probe-forming lens. This in general may be reduced down to diameters of between 0.2-0.5 nm, however it is limited by the lens aberration <sup>(224)</sup>. These lens aberrations must therefore be corrected in order to improve the spatial resolution.

With regards to the aberrations, these may be split into two categories, namely monochromatic aberrations and chromatic aberrations. Monochromatic aberrations refer to aberrations that are still present even when using a monochromated electron source, and are instead as a result of the lens geometry. Chromatic aberrations on the other hand are as a result of electrons with varying wavelengths naturally being focussed on different points according to their wavelength. The monochromatic aberrations can again be divided up into spherical aberration, astigmatism, coma, field curvature, and distortion <sup>(222)</sup>. Of these, spherical aberration is of particular importance. Despite this, recent advancements have allowed the spherical aberrations to be corrected for by the use of what is known as a quadrupole-octupole corrector <sup>(225)</sup>. This works by applying negative spherical aberration to cancel out the positive spherical aberration of the probe forming lens which in turn can lead to significantly improved resolution, with even sub-angstrom levels now achievable <sup>(226)</sup>.

### 6.1.2.2 Energy Resolution

In line with the spherical aberration correction, chromatic aberration must also be addressed so as not to be the limiting factor. This may be achieved by ensuring the electron source has a low energy spread, with typically less than 0.3 eV spread being required <sup>(226)</sup>. In order to achieve this a cold field emission tip is generally used <sup>(222)</sup>. As will be shown later, this low energy spread is useful not just in terms of limiting aberrations, but also for the energy resolution in EEL spectroscopy (EELS). In this sense, a monochromator further allows a reduction in the energy spread, with less than 20 meV now possible <sup>(227)</sup>.

## 6.1.3 Imaging

In a CTEM the transmitted electrons are directly focused via an objective lens through an objective aperture onto the florescent screen. If only the direct beam is allowed through the aperture, the areas of the sample with high mass or thickness show up as dark due to partially blocking (absorbing or high angle scattering) of the electrons. As areas with no sample do not affect the beam however, this gives a bright background and is therefore known as bright field

imaging. Alternatively, if the aperture is aligned to only allow through the scattered electrons, areas where the electrons have had strong interaction with the sample appear brighter. This is instead called dark field imaging due to its dark background in the absence of matter <sup>(228)</sup>.

For STEM on the other hand, the lack of a lens or aperture after the sample means this approach may not be used. Instead the images are formed by having detectors at varying angles with respect to the sample. A bright field detector for instance is placed in line with the optical axis of the beam and therefore once again shows the particles as darker regions upon a bright background. This is particularly useful for identifying fine detail and is more affected by lighter elements. Alternatively, detectors may be placed at an angle away from that of the main beam. The most common of these is the high angle annular dark field (HAADF) detector. This is placed at a large angle so that only the electrons that have undergone elastic scattering with large deviations in direction (Rutherford scattering from atomic nuclei) are collected. At these large angles, the signal intensity can be directly related to the thickness of the sample or its atomic number <sup>(229)</sup>. The high angle also results in none of the Bragg diffracted electrons being collected which allows improved resolution due to elimination of diffraction contrast <sup>(229)</sup>. Furthermore, as seen in Figure 6.3, the lack of an aperture means the HAADF images may be collected simultaneously with other signals such as energy-dispersive x-ray spectroscopy (EDX), medium angle annular dark field (MAADF), low angle annular dark field (LAADF) and bright field (BF) <sup>(230)</sup>. Alternatively, the bright field detector may be removed completely so as to allow the inelastically scattered electrons to enter the EELS spectrometer, as discussed within the following section.

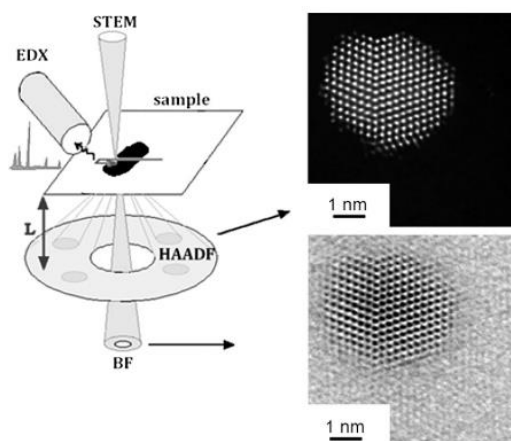


**Figure 6.3: Schematic diagram highlighting the parallel imaging capabilities of STEM along with examples of BF and HAADF images. L represents the camera length which is the distance or magnification between the sample and detector <sup>(230)</sup>.**

## 6.2 Overview of Electron Energy Loss Spectroscopy (EELS)

### 6.2.1 Introduction to EELS

Electron Energy Loss Spectroscopy is an incredibly versatile and information rich technique that is particularly useful for analysing the structural, electrical, and chemical properties with excellent spatial and energy resolution unrivalled by other techniques <sup>(231)</sup>. For example, the electronic properties in the form of localised surface plasmon resonances may be studied as is the subject of this thesis.

The technique works by analysing the inelastically scattered electrons in terms of the energy lost during interaction with the sample. This energy loss may be represented by a spectra, as well as being filtered over energy ranges and recombined to give spectroscopic imaging (SI) maps <sup>(220)</sup>. As the energy lost during an interaction is directly dependent on both the chemical and electronic properties at that specific location, this information may be analysed to reveal the local properties such as the elemental composition or formation of plasmonic resonances. Additionally, when combined with STEM (STEM-EELS), particularly on monochromated aberration-corrected electron microscopes, this may be achieved with sub-Angstrom resolution therefore meaning probing single atoms becomes a possibility <sup>(231, 232)</sup>.

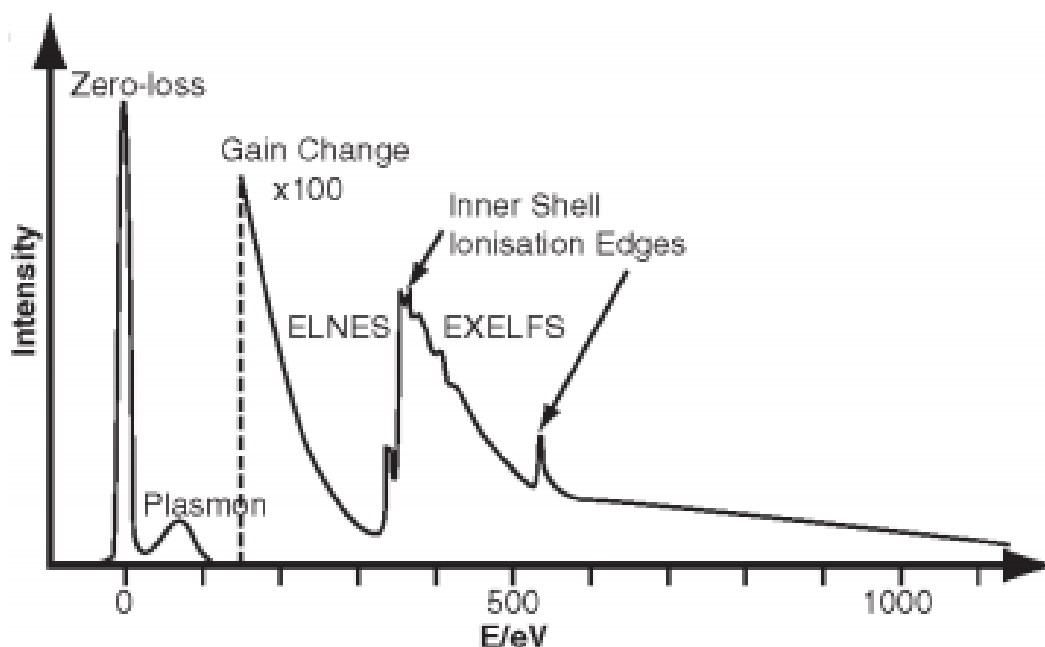


**Figure 6.4: Typical EELS spectrum with linear intensity showing the zero-loss peak (ZLP), plasmonic modes of the low loss region, and ionisation edges of the atoms in the higher energy core loss region <sup>(223)</sup>.**

A typical EELS spectra is shown within Figure 6.4. The x-axis represents the energy loss of the incident electron in eV, whereas the y-axis shows the intensity of the signal which is in arbitrary units and relates to the count of electrons. The intensity shown has a linear scale, although a gain change of 100 times is shown schematically at approximately 150 eV.

The first peak with the highest intensity, is apparent at 0 eV and is known as the zero loss peak (ZLP). This peak is formed due to the contribution of unscattered or elastically scattered electrons which do not undergo an energy change on interaction with the sample. Considering this, the ZLP width is therefore dependent on the energy spread of the electron source, which as previously mentioned may be reduced down to 0.3 eV using a cold field emission gun (FEG) electron source <sup>(226)</sup>. The energy resolution of the instrument is then defined based around the full width at half maximum (FWHM) of the ZLP. Despite the cold FEG emission source giving a reduced energy spread compared to other emission sources, this may still be unsatisfactory in certain cases to probe the very low-energy loss interactions. For example, the excitation of phonons typically occurs in the energy range of 10-100 meV <sup>(220)</sup>. These would therefore contribute to the ZLP making these interactions indistinguishable. Similarly, as seen within this work, the plasmonic resonances of certain nanoparticles may lie within the visible to infrared region and also be characterised by relatively sharp peaks. This is the case for the dark modes of gold plasmonic arrays which are significantly red-shifted and therefore occur at relatively low energies. To identify these peaks and accurately resolve the plasmonic modes, in recent years the inclusion of a monochromator has been used to improve the energy resolution to less than 20 meV <sup>(227)</sup>. This is generally at the expense of probe current, however, leading to a deterioration in the signal-to-noise ratio <sup>(223, 233)</sup>. Despite this, the improved energy resolution, coupled with the excellent spatial resolution achieved in STEM, means analysis of complex plasmonic nanostructures may be achieved.

The above interactions occur in what is known as the low-loss region which typically extends to around 50 eV. Beyond this is the high-loss region which instead extends up over a thousand eV. In this region, the energy losses are in general as a consequence of excitation of the inner shell “core” electrons of an atom. These ionisation events are characteristic of the atom being probed and result in the formation of steps in the EELS spectra, known as ionisation edges. The energy, intensity, and shape of these ionisation edges may then be used to identify the chemical element amongst other information. The electron energy loss near edge structure (ELNES) on the ionisation edge gives information on the bonding and local structure, whereas the extended electron energy loss fine structure (EXELFS) at higher energies gives

information on the bond lengths and coordination number <sup>(220)</sup>. This analysis in the high-loss region is generally referred to as core-loss and may be recorded simultaneously with the low-loss spectra, HAADF imaging, and EDX spectra to provide a thorough analysis of the sample characteristics <sup>(234)</sup>.

## 6.2.2 Measuring Plasmons with EELS

Although the previous section outlines the versatility of the EELS technique, from now on the focus will only be addressed to the low-loss region between typically 0-3 eV where plasmonic resonances of gold nanoparticles dominate. Unfortunately, this low energy region (and in particular for energies below 1 eV), is susceptible to interference with the tail of the ZLP and therefore state of the art equipment is required to reduce the energy resolution and accurately resolve the plasmonic modes, as achieved in this work. The specific equipment used for data collection in this work is outlined in section 6.3.1, however, here the concept relating to how plasmons may be excited by an electron beam is discussed.

Firstly, considering the electron beam within the TEM/STEM, this may be considered to be the same as a current carrying wire whereby an electric field is formed that radiates radially away <sup>(235)</sup>. This electric field then excites the LSPR of the nanoparticle. This is best achieved when the electron beam is located adjacent to the nanoparticle and has its incident field normal to the surface of the nanoparticle <sup>(233)</sup>. Once a plasmonic resonance of the nanoparticle is excited, the oscillating electrons associated with the plasmon induce an electric field themselves. This induced field is both spatially and energy dependent, as shown for instance in the other sections of this work, and acts back on the incident electric field of the electron beam. The electrons in the beam then lose a degree of energy as they encounter this induced field, which may be detected by the EELS spectrometer to produce a spectra <sup>(233)</sup>. Under a STEM setup the EELS spectrum at each probe location may be stored and mapped depending on a chosen energy range whereby contrast is formed based on the intensity of the selected EELS signal <sup>(236)</sup>. This method is known as spectrum imaging (SI) and therefore allows the visualisation of the plasmonic resonances of a sample. A more detailed description of the method behind SI maps is given within section 6.2.4.

In contrast to excitation by light, the electric field incident on the nanoparticle from the electron beam is also able to excite dark plasmonic modes <sup>(237)</sup>. This therefore allows EELS to characterise both the plasmonic bright and dark modes of nanoparticles as seen within other works <sup>(237-239)</sup> and as will be demonstrated later.

### 6.2.3 Operating Concept

Following on from the description of the EELS technique and how it may be used to measure plasmons, a brief explanation of the operating concept will be given. As already explained, EELS works by detecting the energy loss of inelastically scattered electrons after interacting with the sample. This energy loss is detected by allowing the electrons to pass through an aperture and into an EELS spectrometer. The aperture acts to limit the effect of aberrations in the spectrometer and restrict the electrons to those which have been scattered up to a certain scattering angle<sup>(220, 240)</sup>. The spectrometer most commonly used is that of a magnetic prism spectrometer. This operates in general by separating the electrons based upon their velocity, and therefore kinetic energy, with a magnetic field according to the Lorentz force<sup>(240)</sup>. This resultant spatial dispersion of the electrons by their energy loss is then focused on a scintillator and CCD camera, whereby the electrons are measured according to their displacement and used to form a spectrum. In STEM, the serial nature of the scanning builds up a spectrum for each location probed with the spatial resolution dependent on the electron probe size. The energy resolution of the spectra is a function of the spread of the electron source, the resolution of the spectrometer, and the resolution of the EELS detector<sup>(220)</sup>. This process is summarised in Figure 6.5.

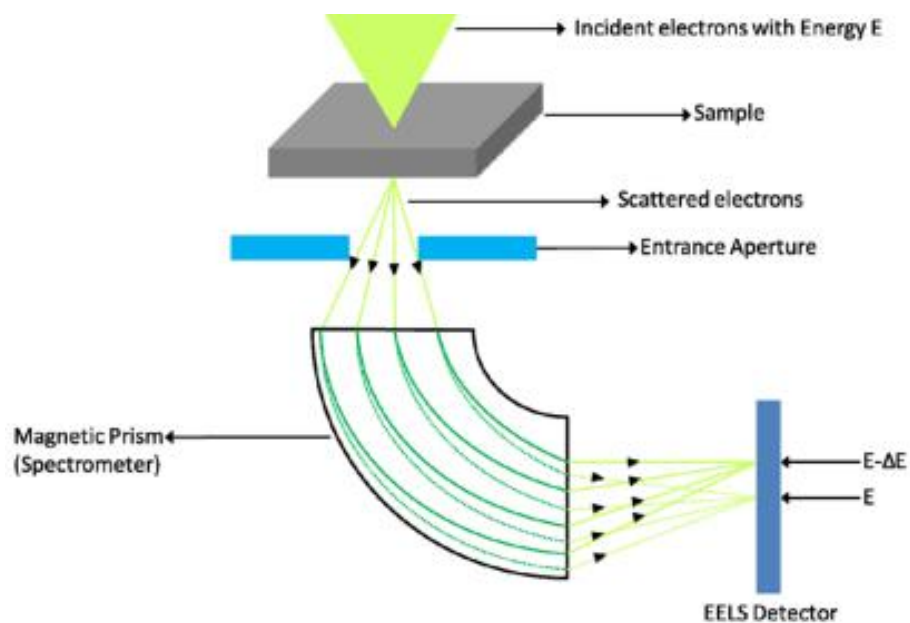


**Figure 6.5: Schematic representation of a STEM-EELS instrument highlighting the operating principle of the spectrometer and EELS detector<sup>(241)</sup>.**

## 6.2.4 Data Analysis

As shown, the EELS technique is incredibly information rich. In this sense data analysis is often required in order to process the information and successfully analyse the interactions that are occurring. This section will focus upon the data analysis methods used throughout this work. It should also be noted that the EELS measurements were performed in STEM mode and analysed using the software Digital Micrograph by Gatan Inc. <sup>(242)</sup>. Additionally, only the low-loss region is discussed as relevant to the plasmonic interactions.

As previously mentioned, the raw data consists of an EELS spectra for every location that is scanned. These are combined into a three-dimensional image, known as a spectrum image (SI) map, whereby for example the x-y pixels contains the spatial information and the z-pixels contain the EELS spectra. By selecting an energy range within the EELS spectra, an SI map can be produced whereby each pixel of the image has contrast according to the integral of signal intensity over the selected energy range. This allows a spatial visualisation of where a certain energy loss occurred and therefore allows the induced electric fields associated with the plasmonic resonances to be visualised. This concept is summarised in Figure 6.6 for the example of a nanorod whereby the SI map is formed over the longitudinal mode energies.

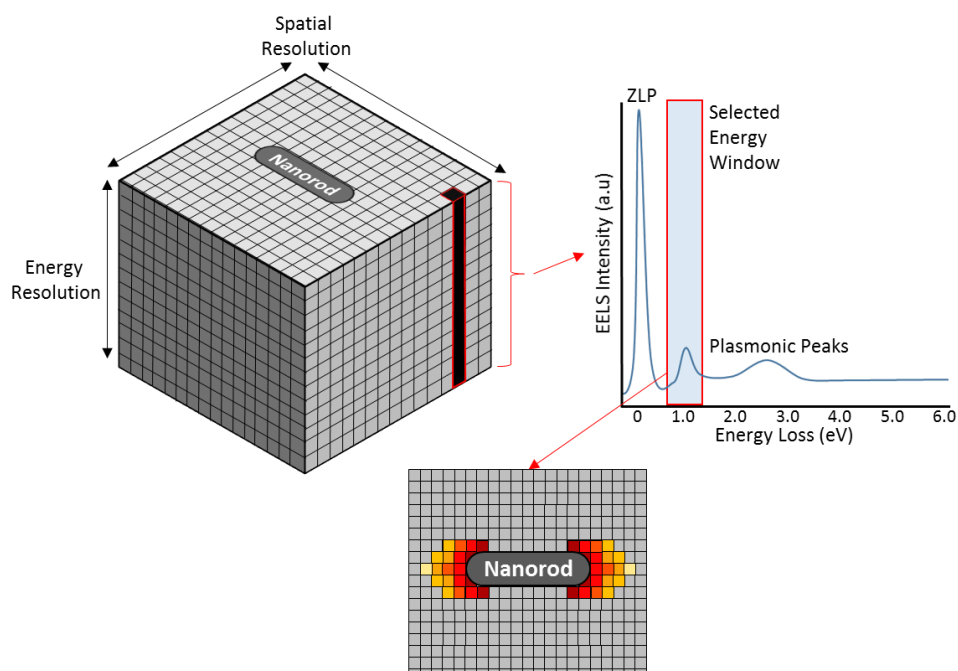


**Figure 6.6: Illustration of the concept behind the SI mapping of plasmon resonances acquired using a STEM-EELS technique. A gold nanorod is used as the example where the energies relating to the longitudinal mode are mapped.**

The spatial resolution shown in Figure 6.6 is theoretically only limited by the size of the electron probe. Realistically however, other factors must be taken into account. For example, there is a degree of time taken to acquire a spectra at each pixel, which is then multiplied by the image size to get an overall acquisition time. Consideration therefore needs to be given in regards to the available time to run the experiment, as well as factors such as hydrocarbon contamination, sample damage and spatial drift if the acquisition time is too long <sup>(233)</sup>. On the other hand, the spectra needs to be acquired over a sufficient time such that a quantifiable low noise signal is produced <sup>(243)</sup>.

In addition to the SI maps, it is also useful to analyse how the EELS spectra vary spatially. This is performed by creating a region of interest (ROI) in digital micrograph that encompasses a number of x-y pixels. The spectra from each of these pixels is then summed together to show a composite spectrum for that region. This not only reduces noise in spectra, but also allows the identification of peaks at different locations and may also help with the selection of energy windows for SI mapping. Unfortunately, as previously discussed the peaks arising from plasmonic resonances are often hard to distinguish due to them overlapping with the tail of the ZLP. To improve this, a background removal is often required on these spectra whereby the ZLP is extrapolated and removed. Alternatively, the use of cold FEG emission sources and a monochromator also gives the ability to drastically reduce the energy resolution and tail of the ZLP, making these interferences less likely <sup>(241)</sup>. For this reason, ZLP removal was generally not necessary in this work.

Lastly I will discuss two data analysis techniques used specifically in this work, namely the normalisation of SI maps with respect to the background, and the generation of large scale SI maps. The normalisation of the SI maps was performed in certain locations where the background to the nanorods consisted of areas of both alumina template and vacuum. When this was the case, the SI maps produced show significantly weaker modes in the alumina due to its thickness giving a much reduced EELS intensity signal compared to a vacuum background. This has consequences in that the plasmonic resonances that occur within the alumina are difficult to see compared to those in the vacuum, leading to SI maps that do not accurately show the true distribution of plasmons. To rectify this the SI maps can be normalised with respect to the overall number of electron counts at each pixel. This was achieved by first creating an image whereby the contrast of its pixels is represented by the total electron counts over all the acquired energy range. An SI map over the desired energy range is then divided by this image using the *simple math* option in Digital Micrograph to

produce a normalised SI map. Although this allows the distribution of the plasmonic modes to be visualised more accurately, it has the drawback of also producing much noisier images. For this reason the normalisation was generally only performed for SI maps that had large areas of both vacuum and AAO background, and is typically presented in conjunction with non-normalised SI maps.

In addition to the normalised maps, it was also necessary in certain cases to perform SI maps over large micrometre length scales. Unfortunately, this was not possible to perform in a single SI map due to the microscope being unable to acquire spectra at such a low magnification. Instead, this was achieved by acquiring spectra at multiple locations ensuring a degree of overlap and that the same operating conditions were used. An SI map for each location was then produced with the same energy range used throughout. By setting the *Low* and *High* contrast levels the same in each of these SI maps, the images were comparable and able to be stitched together therefore allowing the plasmonic modes to be visualised over large areas.

## 6.3 Electron Energy Loss Spectroscopy Methodology

### 6.3.1 Experimental Methodology

With regards to this thesis, all data was collected at the SuperSTEM laboratory in Daresbury, UK on the SuperSTEM 3 microscope (Nion UltraSTEM 100MC “Hermes”). This is an aberration-corrected STEM-EELS electron microscope with a monochromated electron source. The Nion QO aberration corrector allows sub-angstrom spatial resolution to be achieved, whereas the monochromator gives extremely high energy resolutions of the order of 15 meV<sup>(244)</sup>. Unless otherwise stated, the operating conditions were an accelerating voltage of 60 kV and an energy dispersion of 0.01 eV. All post-collection data processing was achieved using the software Digital Micrograph<sup>(242)</sup> by Gatan Inc.

The nanorod arrays samples were prepared as TEM cross-sections by the method described in Chapter 3. Alternatively, the single gold nanorods shown in the results were produced in-house by the seeded growth method, with thanks to Dr Sunjie Ye. These were drop cast onto SiMPore pure silicon TEM windows of 5 nm thickness<sup>(245)</sup>.

### 6.3.2 Modelling Methodology

The experimental EELS data shown in this thesis are complimented by EELS simulations produced using Comsol Multiphysics version 5.2a. This aimed to help with the analysis of the experimental EELS results by testing simplified systems, or geometries that would be difficult to otherwise fabricate. It was hoped this not only allowed validation of the results, but also provided a means to model EELS experiments at a fraction of the time and cost. Additionally, as previously mentioned, the EELS modelling has the benefit over those in Chapter 5 that used plane-wave excitation, in that the dark modes may also be excited <sup>(238)</sup>.

The methodology for the modelling of EELS was based upon the theory as outlined by Garcia de Abajo and Kociak <sup>(246)</sup> and implemented in the manner described by Wiener *et al.* <sup>(125)</sup> and Raza *et al.* <sup>(247)</sup>. As many of the more basic modelling details are similar to those outlined in the modelling within Chapter 5, only the alterations will be discussed here. This includes how to excite the plasmonic resonances with an electron beam instead of a plane wave, as well as the means to measure the energy loss probability as opposed to the optical cross sections.

Firstly, it was assumed that the electron beam was represented by a current carrying wire. This wire was defined to have a relativistic electron velocity as follows:

$$v = c \sqrt{1 - \frac{1}{\left(1 + \frac{eU}{mc^2}\right)^2}} \quad (89)$$

Where  $v$  is the electron velocity,  $c$  is the speed of light,  $e$  is the electron charge,  $U$  is the accelerating voltage (typically 60 kV), and  $m$  is the electron mass. This wire was drawn as a line in the model that traverses the  $z$ -direction between the PML layers. In contrast to the EELS experiment, this line was kept stationary and instead the nanoparticle moved in order to obtain spectra at different locations. The wire was then allocated a current density as:

$$j(z, \omega) = -e\hat{z}\delta(R - R_0)e^{i\omega z/v} \quad (90)$$

Here  $j$  represents the current density in the  $z$ -direction,  $\omega$  is the angular frequency and  $R_0$  is the impact parameter of the electron beam in the  $x$ - $y$  plane, positioned 5 nm from nanoparticle

edge for all simulations. As with the electron beam in the EELS experiments, this current carrying wire produced a background electric field,  $E_0(z,\omega)$  that interacted with the nanoparticle and excited plasmonic modes. These plasmonic modes had an associated induced electric field,  $E^{ind}(z,\omega)$  that acts against the background field causing a degree of energy loss in the moving electron. This energy loss may be expressed in terms of the energy loss probability ( $\Gamma_{EELS}(\omega)$ ), which is directly proportional to the EELS intensity signal seen within the EELS experiments <sup>(247)</sup>. The energy loss probability was then calculated in the frequency domain using the following equation:

$$\Gamma_{EELS}(\omega) = \frac{ve}{2\pi\hbar\omega} \int dz \text{Re} \left( e^{-i\omega z/v} E_z^{ind}(z, \omega) \right) \quad (91)$$

Where  $\hbar$  is the reduced Plank constant, and the integral was taken in the z-direction over the electron beam path. The induced field ( $E_z^{ind}$ ) was then calculated by subtracting the background field  $E_0(z,\omega)$ , without the nanoparticle present, from that of the full solution with the nanoparticle present,  $E(z,\omega)$  <sup>(125)</sup>:

$$E_z^{ind}(z, \omega) = E(z, \omega) - E_0(z, \omega) \quad (92)$$

This was achieved by operating two frequency domains, both with the electron beam active. In the first frequency domain (*emw*) the electron beam without the presence of a nanoparticle was modelled. This was done in the similar manner to the plane wave models whereby the nanoparticles refractive index was set to equal that of the background. The second frequency domain (*emw2*) then calculated the full solution with the nanoparticle present.

In addition to the energy loss probability spectra, the induced electric field was plotted at certain energies in a similar manner to SI maps. This showed both the positive and negative electric fields therefore allowing assessment of whether the modes were aligned symmetrically (bright) or anti-symmetrically (dark). Similarly, for comparison with the experimental EELS maps, the modulus of induced electric field was taken as follows, where  $\bar{E}_z^{ind}$  is the complex conjugate of the induced electric field:

$$\left| E_z^{ind} \right| = \sqrt{E_z^{ind} \times \bar{E}_z^{ind}} \quad (93)$$

## 6.4 EELS Results

The results in this chapter are a combination of both experimental results obtained from the SuperSTEM facility, as well as those obtained from FEM modelling using electron beam excitation. These are shown in order of increasing complexity, starting with a simple isolated nanorod, before moving on to unsupported arrays of nanorods, supported dimers, and finally supported arrays consisting of multiple nanorods.

### 6.4.1 Isolated Nanorods

Analysis of the gold nanorods produced by the seeded-growth method found that they had an average AR of 2.49. Due to the nature of growth, these nanorods also had a Cetrimonium bromide (CTAB) surfactant on their surface, estimated in the literature to be around 3.2 nm thick<sup>(248)</sup>. UV-vis measurements (*not shown*) found the longitudinal mode to be located at ca. 640 nm whilst the transverse mode was located at ca. 520 nm. Following the drop casting of the nanorod solution onto the 5 nm silicon TEM support grids, EELS measurements on a single nanorod were performed, as shown in Figure 6.7. The nanorod had a diameter of 27.4 nm, a length of 60.3 nm and an aspect ratio of 2.2.

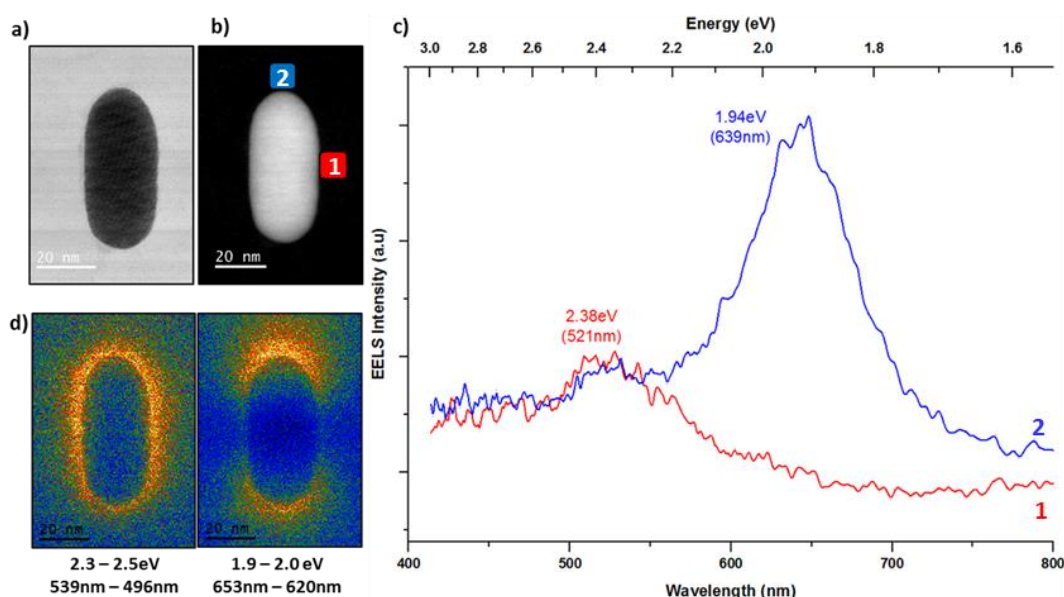


**Figure 6.7:** a) Bright field image of the nanorod also showing the silicon substrate. b) HAADF image of the nanorod where the coloured boxes represent the two locations the spectra was integrated over. c) EELS spectra with colours relating to the electron probe locations shown in the HAADF image. The text refers to the peak positions, found by applying a Gaussian fit to the curves. d) SI maps over the stated energy ranges showing both plasmonic modes.

The EELS spectra in Figure 6.7c showed that when the EELS signal is integrated over a ROI at the end of the nanorod, a peak occurred at higher wavelengths, estimated to be 639 nm by performing a Gaussian fit. Alternatively, when placed alongside the nanorod, the peak occurred at a shorter wavelength of 521 nm. These peaks relate to the longitudinal and transverse modes respectively. It should be noted however, that in contrast to excitation with plane waves, whereby the polarisation across the nanoparticle is homogeneous, the incident electric field from the electron beam will give a radial polarisation that depends on the relative position of the beam <sup>(249)</sup>. This means that both modes may be simultaneously excited depending on the beam location <sup>(233)</sup>. This was seen for the ROI at the end of the nanorod (blue line), where a peak for both the longitudinal and transverse oscillation occurred in the spectrum in Figure 6.7c. Similarly, the ROI at the side of the nanorod (red line) would also excite both modes, however its greater distance from the nanorod ends means the oscillation over the long-axis (longitudinal mode) is very weak and therefore difficult to resolve.

The transverse and longitudinal plasmonic modes were also represented in SI maps over the energy range 2.3-2.5 eV and 1.9-2.0 eV respectively. The longitudinal mode was seen to have a dipolar distribution over the nanorod length, whereas with the transverse mode, the field surrounded the entire surface of the particle. In general these distributions match those found with FEM modelling in the previous section. Perhaps a slight deviation however is that the transverse mode is not as distinctly dipolar as that seen in the modelling, but instead was seen to be distributed over all the surface, including the nanorod ends. This may be attributed to either the radial polarisation of the incident electric spreading the transverse resonance over many directions, or alternatively, may include contributions from the tail of the longitudinal mode. In either case these distributions support the results found in other work <sup>(121, 249, 250)</sup> and highlight the ability of the EELS to visualise the spatial distribution of surface plasmons.

Comparing the EELS spectra to the UV-Vis results performed on a dispersion of nanorods (*not shown*) revealed that the position of the modes matched almost exactly. As the UV-Vis measurements were acquired with the nanorods in water, whereas the EELS measurements were performed in vacuum, a red-shift shift of several nm would be expected for the UV-Vis results, as found in Chapter 5. Similarly, the average aspect ratio of the rods in solution was 2.49 compared to 2.2 for the nanorod tested with EELS, therefore also expecting to red-shift the UV-Vis spectra compared to EELS. To investigate this, the nanorod measured by EELS was modelled using the EELS Comsol model. The results of this are shown in Figure 6.8 whereby the effect of a substrate and CTAB layer was also investigated.

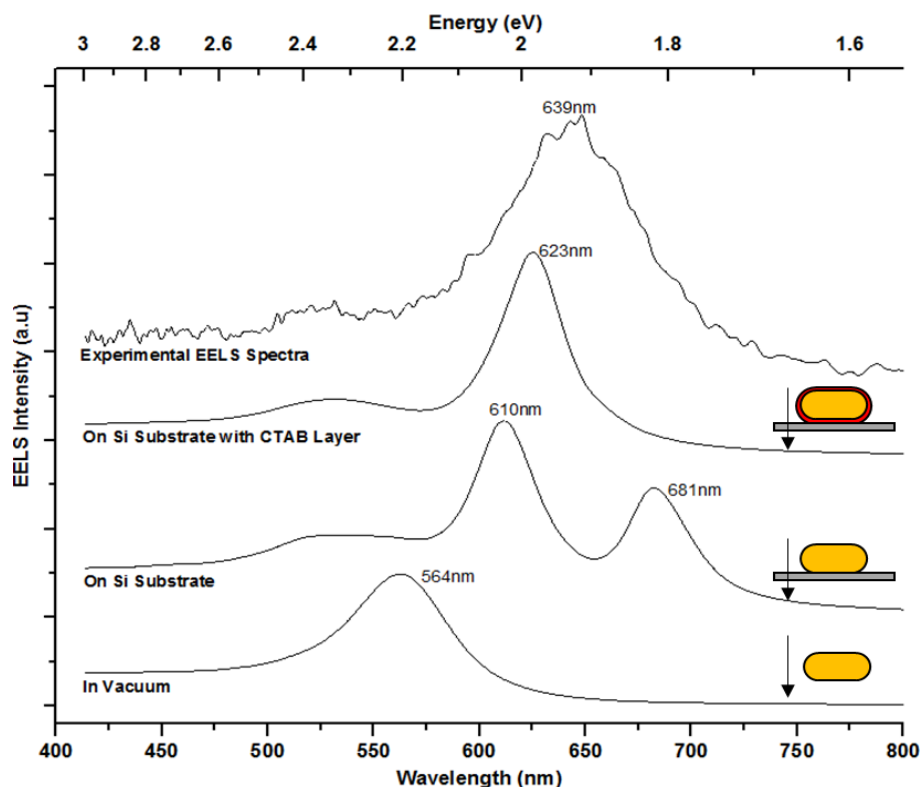


**Figure 6.8:** Comparison between experimental EELS spectra to that of modelled EELS spectra where the gold nanorod is either in vacuum, supported horizontally on a 5 nm thick Si substrate, or supported horizontally on a 5 nm thick Si substrate with a 3.2 nm CTAB layer on the nanorod surface. The nanorod has a diameter of 27.4 nm and length of 60.3 nm (AR=2.2). The arrows in the schematic diagram insets represent the position and direction of the electron beam in the simulations. In all cases this was placed 5 nm from the edge of the nanorod. The experimental EELS spectra is the same data as shown in Figure 6.7c (blue line).

Initially, the nanorod was modelled completely surrounded by a vacuum, with the resultant longitudinal mode seen at 564 nm. This is considerably less than the 639 nm resonance wavelength seen in the experimental EELS spectra, and therefore shows that for the aspect ratio nanorod tested, one would expect the resonance to occur at a lower wavelength than that found. To assess if the red-shift seen in the resonance position for the experimental spectra was due to the nanorod laying horizontally on a 5 nm thick supporting amorphous silicon TEM grid, this was also included in the modelling. The refractive index of the silicon substrate was taken from data derived by Aspnes and Studna<sup>(251)</sup>. Interestingly the modelling of this setup led to two higher wavelength peaks being formed. The first of these occurred at a wavelength of 610 nm and corresponded to the longitudinal mode of the nanorod. This therefore red-shifted the resonance slightly closer to that seen in the experiment. The second peak at 681 nm however was found to be due to the interaction between the nanorod and the

substrate. Namely, as the nanorod is modelled as lying flat on the silicon surface, its curved edge meets the substrate with a perfect tangent. This creates infinitesimally small gaps between the nanorod and substrate that results in the formation of another mode at higher wavelength. Unfortunately, this mode is believed not to be real and is instead a result of the model being based around local approximations. This local approximation predicts fields and enhancements that do not match with real experiments for very small gaps (typically less than a couple of nanometres), as found by several authors<sup>(64, 247, 252)</sup>. In a real life scenario however, the nanorod would not form a perfect tangent with the substrate. Furthermore, the strong coupling seen would likely be significantly damped due to non-locality as discussed previously. This therefore highlights one of the drawbacks of FEM modelling using local approximations.

Neglecting the peak at 681 nm, the longitudinal mode was still found to occur at a lower wavelength (610 nm) compared to that in the experiment (639 nm). This discrepancy may also be due to the model not accounting for the CTAB surfactant layer that exists on the surface of the nanorod from its fabrication. This is estimated to be around 3.2 nm thick<sup>(248)</sup> and have a refractive index of 1.435<sup>(253)</sup>. It was found that by including this layer on the surface of the nanoparticle, the longitudinal mode red-shifted to a wavelength of 623 nm and therefore matched that found in the experiment reasonably well, only deviating by 16 nm. This small difference may be attributed to potential differences between the modelled and experimental setup, such as slight variations in size, surface roughness, or actual CTAB refractive index and thickness.

Additionally, by including the CTAB layer on the surface of the nanorod it was lifted off the silicon surface by a few nanometres. This meant that the issue regarding the metal rod forming a tangent with the substrate no longer occurred, and therefore the artefact peak at higher wavelength disappeared. Despite this good agreement, it should be noted that a model that accounts for non-local effects would be useful for future work in order to accurately model nanoparticles placed directly on a substrate, or with small features and gaps. To this end, myself and Dr Patricia Abellan at SuperSTEM have made significant progress in producing a three-dimensional non-local FEM model that is capable of achieving this, similar to that in the work of Wiener *et al.*<sup>(125)</sup>. Unfortunately, the computer requirements required for this scenario have so far limited us to only a two-dimensional model. Despite this, excellent agreement with other non-local works has been achieved<sup>(252)</sup>. It is hoped that with increased computer resources the three-dimensional non-local model may also be realised in the future.

## 6.4.2 Unsupported Nanorod Arrays

Before the EELS experimental results are shown, modelled using the EELS model will be discussed. This aimed to assess the impact of going from a single nanorod to an array when excited with an electron beam. Unfortunately, unlike with the plane wave models, the point source of the electron beam meant that Floquet boundary conditions could not be applied as this would also incorrectly apply periodicity to the electron beam. Instead finite arrays of nanorods were used. Additionally, as will be discussed later, a direct identification of bright and dark modes from experimental EELS data is challenging. Modelling arrays of perfect nanorods (starting with a dimer) where symmetry considerations apply, simplifies the analysis and helps identify tests for the subsequent interpretation of experimental results.

Modelling was initially performed at varying inter-rod spacing for a nanorod dimer in vacuum, and compared to an isolated nanorod (Figure 6.9). As with the previous modelling, the spacing is defined from the edges of adjacent nanorods. Additionally, the same modelling was also performed for a nanorod dimer embedded in AAO, as shown in Appendix 1.

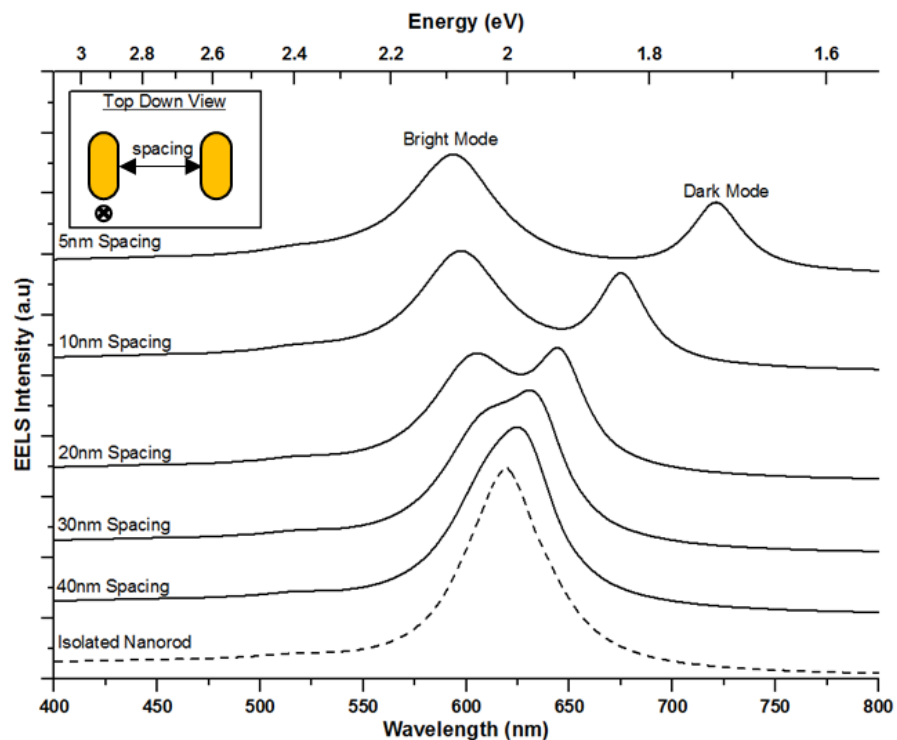


**Figure 6.9:** Modelled EELS intensity for a dimer of side-by-side aligned gold nanorods (30 nm x 90 nm) at varying spacing compared to an isolated nanorod. The nanorods are modelled within a vacuum with the electron beam aligned 5 nm above the left nanorod as demonstrated by the cross in the inset. Each curve has been offset in the y-direction.

Starting with the isolated nanorod, this was predicted to have a single longitudinal peak at a wavelength of 620 nm, in agreement with the modelling when using plane-waves for the same size nanorod. It was seen however, that for a dimer of nanorods the longitudinal mode splits into two peaks, one at higher energy and the other at lower energy relative to the isolated nanorod. As the spacing between the nanorods was reduced and therefore the coupling strength increased, these modes were seen to split further apart. This splitting is asymmetric at smaller separations with the low energy mode red-shifting at a quicker rate than that of the blue-shift of the higher energy mode. This is also seen within the plasmon hybridisation model<sup>(113, 119)</sup> and is due to the hybridisation between multiple modes of different order. As these trends match those predicted by the plasmon hybridisation model very closely, it was therefore hypothesised that the low energy peak seen was the bonding (dark) mode, whereas the high energy peak was the anti-bonding (bright) mode of a side-by-side nanorod array.

To test this hypothesis a number of investigations were performed. Firstly, the induced electric field ( $\vec{E}_z^{\text{ind}}$ ) and surface charge distribution for the nanorod dimer at a spacing of 5 nm was plotted, as seen in Figure 6.10.

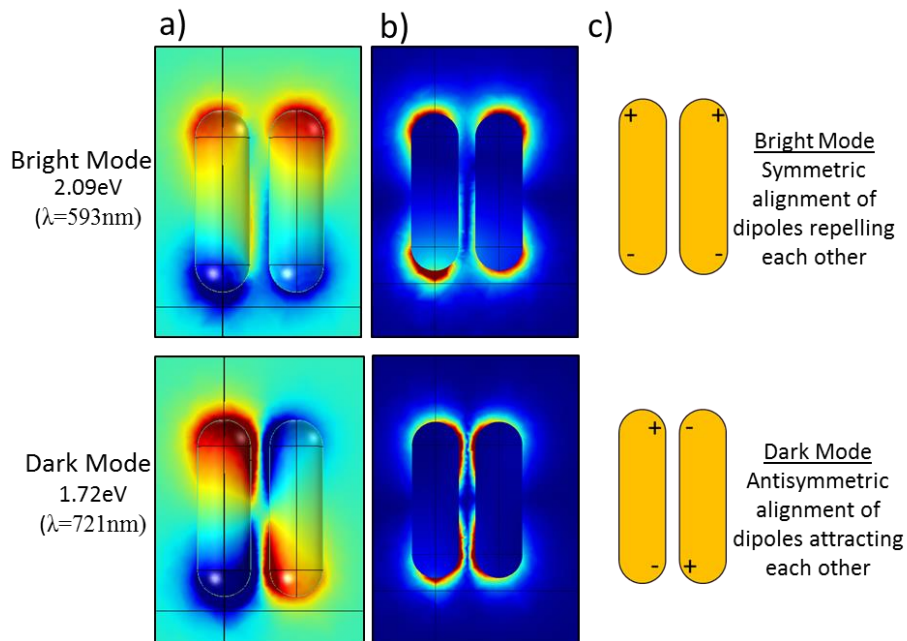


**Figure 6.10:** a) Induced electric field plots for a gold nanorod dimer spaced 5nm based upon the data from Figure 6.9. The plots on the nanorod surface shows the surface charge distribution. b) Plots of the induced electric field modulus ( $|\vec{E}_z^{\text{ind}}| = \sqrt{\vec{E}_z^{\text{ind}} \times \vec{E}_z^{\text{ind}}}$ ), where  $\vec{E}_z^{\text{ind}}$  is the complex conjugate of the induced electric field. c) Schematic representation of the surface charge distribution based upon the results from (a).

It was seen that the induced electric fields and surface charge distribution for both the low and high energy modes differed considerably. With the higher energy mode, the polarity of the nanorods were symmetrically aligned between each nanorod, whereas with the lower energy mode the polarity was antisymmetric for each nanorod. Furthermore, in the higher energy mode the induced fields appeared to repel each other thereby being most prominent on the outside of the dimer. In contrast, the lower energy mode had the induced electric fields located predominantly in the gap between each nanorod, thereby appearing attractive. This is as expected for bright and dark modes respectively based on the Coulombic interaction of their dipole moments. Additionally, this splitting of the longitudinal mode based upon the interaction of the individual nanorods dipole moments agrees with theory, such as in the plasmon hybridisation model <sup>(113)</sup> or exciton coupling theory <sup>(115)</sup>.

Lastly, proof that these modes are indeed the bright and dark modes can be provided by exciting the dimer with the electron beam in different locations and monitoring the changes in the spectra modelled. For example it has been shown by Chu *et. al.* <sup>(237)</sup> that when exciting end to end nanorod dimers with the electron beam placed within the dimer gap, only the dark mode could be excited, whereas the bright mode was forbidden due to charge symmetry. This is due to the requirement that if both nanoparticles are at an equal distance away from the electron beam, they will both feel the presence of the electron beam to the same degree and therefore must have equal charges. Alternatively, if the electron beam is placed over either of the nanoparticles the symmetry is broken and both the bright and dark modes can be excited. This result was also confirmed by the work of Barrow *et. al.* <sup>(238)</sup> for gold nanoparticles and is summarised in the schematics of Figure 6.11. In contrast, for side by side nanorods the same charge symmetry applies however this time when the electron beam is placed in the dimer gap, only the bright mode may be excited whereas the dark mode is instead symmetry forbidden. This is also summarised in Figure 6.11 with modelling confirming the result for the side by side alignment.

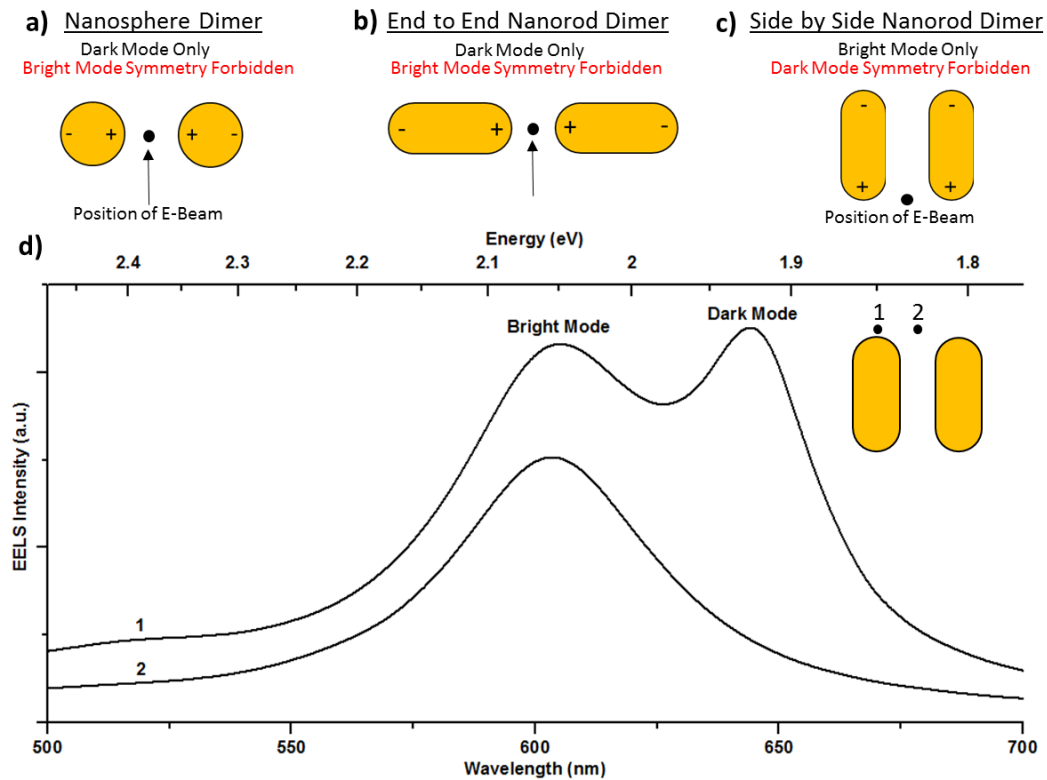


**Figure 6.11: Schematic illustrations showing which modes may be excited when the electron beam is located in the dimer gap for a) nanosphere dimer, b) end to end nanorod dimer, and c) side by side nanorod dimer. d) Modelling results for a side by side nanorod dimer (AR=3, 20 nm gap) with the electron beam located above a nanorod and in centre of the dimer gap.**

As can be seen in Figure 6.11d, when the electron beam is located within the centre of the dimer the low energy mode disappears. This is due to the symmetry of the system requiring both charges to be the same and therefore acts as the final proof that the modes simulated are indeed the bright and dark modes of the array.

When analysing experimental EELS data these relationships may be used to determine whether the modes seen are bright or dark in nature. Unfortunately, this is made more difficult due to a number of reasons. Firstly, when the nanorods in a dimer are of different size, then the symmetry is once again broken, potentially allowing a dark mode to be excited within the gap. This will be discussed in greater detail later. In addition, analysing experimental EELS spectra is also more difficult than that of the modelling results as the EELS method is insensitive to the polarity of the charge. This results in the EELS maps produced resembling maps of the electric field modulus (such as seen in Figure 6.10b), and therefore it cannot be ascertained for certain whether the charges are symmetrically or anti-symmetrically aligned.

On the other hand, the distribution of the energy loss may instead help with the analysis. For example, as stated previously, the dark modes are seen to attract one another whereas the bright modes repel. This however is only the case for the modelling results when excited in a single position. In the EELS experiments the electron beam is scanned over multiple locations with the energy loss recorded at each position. When this transfers over to a SI map, the areas at which high energy loss occurred (at a specific energy) appear intense, whereas the areas where the energy loss wasn't as prominent appear weaker. This therefore leads to the opposite effect to that seen in the modelling whereby the bright mode looks attractive due to it being able to be excited both above each nanorod and in the gap. Alternatively, as the dark mode is only excited strongly above each nanorod, the SI map shows the energy loss only in this area with it being much weaker within the dimer gap.

Finally, a further technique to analyse whether experimental EELS peaks are bright or dark in nature is to study the spectral linewidths. This is based on the premise that dark modes do not have radiative losses and therefore their spectral linewidths are characteristically sharp and narrow <sup>(197, 254, 255)</sup>. In contrast, bright radiative modes have broader spectral linewidths. This can be seen in the results of Figure 6.11 whereby the bright mode was found to have a linewidth (FWHM) of 0.139 eV, compared to the slightly narrower linewidth of 0.115 eV for the dark mode, as measured by applying a Gaussian fit.

Following the proof that the splitting of the modes seen in the modelling work is due the generation of bright and dark modes, the effect of the nanorod aspect ratio on the degree of splitting was studied, as shown in Figure 6.12.

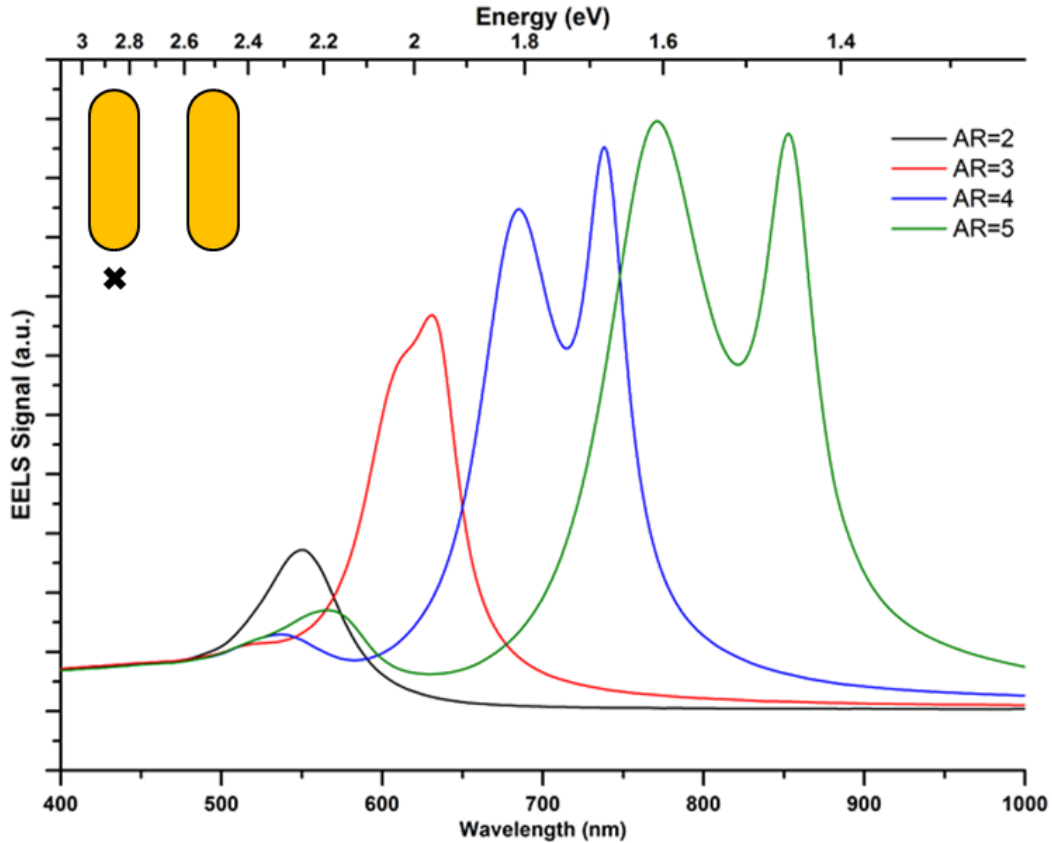


**Figure 6.12: Modelled EELS intensity for a dimer of side-by-side nanorods of diameter 30 nm and with varying aspect ratios. The spacing within the array was kept constant at 30 nm. The array was excited with the electron beam located 5 nm below the left nanorod.**

It was seen that with increasing aspect ratio, both the bright and dark modes of the nanorod dimer red-shifted monotonically, similar to that for an isolated nanorod. In addition, the degree of splitting of the modes was found to vary, with an increase in the aspect ratio leading to a larger splitting. For instance, at an aspect ratio of two, the longitudinal mode does not appear to be split into its bright and dark components. However, by an aspect ratio of five, there is a relatively large separation of the modes of approximately 80 nm. This was attributed to the dipolar modes being stronger for the longer aspect ratio nanorods, therefore leading to a stronger Coulombic interaction and a larger degree of coupling. Additionally, the longer aspect ratio nanorods (AR=5) are also seen to generate higher order modes, such as the quadrupole mode seen at a wavelength of 570 nm.

Now the expected trends of nanorod dimers have been modelled, the experimentally derived EELS data for side-by-side nanorod arrays is shown. For this the gold nanorods produced via growth in the AAO templates were used. As explained in Chapter 3, these arrays were

converted into a TEM thin cross section by using a conventional bulk TEM preparation technique with the AAO template intact, before then being quickly etched for 4 minutes in a 0.5M NaOH solution. This caused areas where the nanorods were both embedded in AAO and where the AAO was removed. Additionally, the etching also caused the gold substrate to be removed in certain areas. This section will therefore focus first on the relatively simple area where the nanorods were embedded partially in the AAO template, but the substrate had been removed, therefore allowing comparison with the previous simulations.

To begin with, the data for a nanorod dimer will be shown. The left hand rod was found to have a diameter of 26.2 nm with an aspect ratio of 3.0, whereas the nanorod on the right had a diameter of 22.9 nm and an aspect ratio of 3.25. These were spaced 37 nm apart and were supported by means of a section of their length being embedded in the AAO template. This can be seen in the HAADF image in Figure 6.13, along with the EELS spectra, SI maps, and a comparison using simulations based on the same dimensions and environment.

The results from Figure 6.13 highlight a number of points. Firstly, the coupling strength in the dimer is not strong enough to lead to a splitting of the modes. Instead the spectra resemble that of isolated nanorods. The simulations in Figure 6.13b confirm this by also predicting the longitudinal mode for each nanorod to be intact. Although the peaks do have shoulders, most noticeably for the spectra within the alumina, these instead relate to the electron beam exciting the longitudinal mode of the other nanorod slightly and are therefore not due to splitting of the mode as result of coupling. This is instead seen as a broadening of the modes in the experimental data due to imperfections in the sample and energy spread of the electron beam. Despite this, excellent agreement is found between the simulations and experiments with regards to both the peak positions and the damping of the signal if located within the AAO template. This damping of the signal for the spectra acquired in the AAO is due to the template causing fewer electrons to reach the EELS detector as compared to the regions in vacuum. This has the effect that it makes the SI maps appear as if the longitudinal mode is not dipolar as the signal is much stronger in the vacuum regions. As previously discussed, to resolve this the SI maps are normalised by the total number of electron counts at each pixel. These normalised maps then give a better indication of the true dipolar nature by better accounting for the effect of local thickness variation at each pixel, albeit suffering from increased noise, as seen in Figure 6.13c.

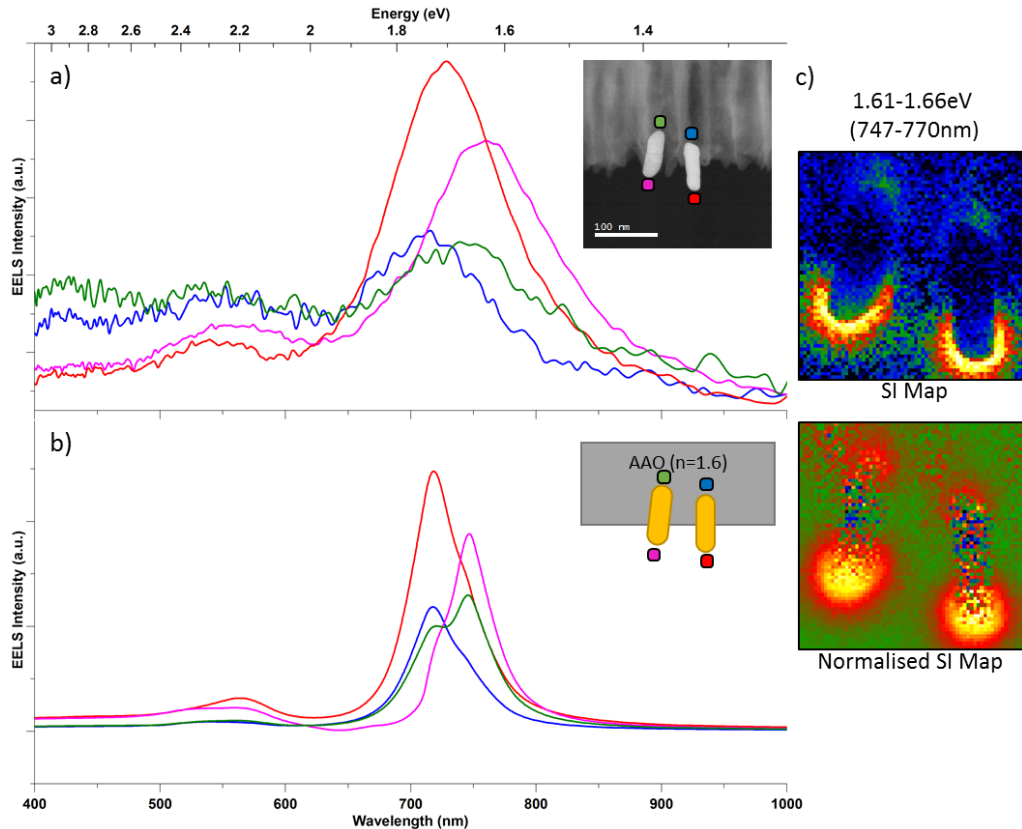


**Figure 6.13: a) Experimental EELS spectra for a dimer of nanorods half in AAO, compared to b) Simulated EELS spectra for the same dimer. The coloured blocks relate to the area integrated for the various spectra, and therefore the position of the electron beam c) SI and normalised SI map over the energy range 1.61-1.66 eV showing the nanorods dipole modes.**

Based upon this result the question should be asked why coupling was not seen within this dimer, however for nanorod arrays with the same spacing, UV-Vis measurements showed the coupling was strong enough to blue-shift the longitudinal mode over that of the transverse mode. One explanation of this is that in the UV-Vis experiments the incident light excites all of the nanorods simultaneously leading to many nanorods interacting. Within this EELS experiment however, the excitation is spatially dependent on the location of the electron beam as it is scanned over just two nanorods. This results in the incident field being considerably weaker as the distance from the electron beam increases, and therefore a potentially much reduced coupling strength for the rods further away. Additionally, when light is incident on the nanorods, the charge density distribution in each nanorod is equally affected thereby forcing them to all align coherently. Although this prohibits the formation of dark modes, it results in a strong bright mode with contributions from many nanorods. On the other hand, the spatial localisation and intensity of the electron beam is known to result in charge displacement in nearby nanorods <sup>(121)</sup>. For instance, when the electron beam passes near a

nanoparticle its surface charge distribution will be altered due to the electrostatic interaction with the electron beam. Adjacent nanorods will then also alter their charge distribution based upon both the charges in the neighbouring nanorods and on the intensity of any incident field. This competing secondary process may therefore also weaken any coupling.

As the coupling strength is related to both the number of interacting nanorods, and the spacing, an area that included four aligned nanorods was also studied, again supported by around half their length being embedded in the AAO template, as shown in the bright field image in Figure 6.14. The spacing was found to be smaller on average than for the previous dimer scenario, and therefore it would be expected to have a greater coupling strength that may lead to the splitting of the longitudinal mode. For instance, the two nanorods on the right are spaced on average  $\sim 28$  nm apart, whereas the centre two nanorods are almost touching at one point.

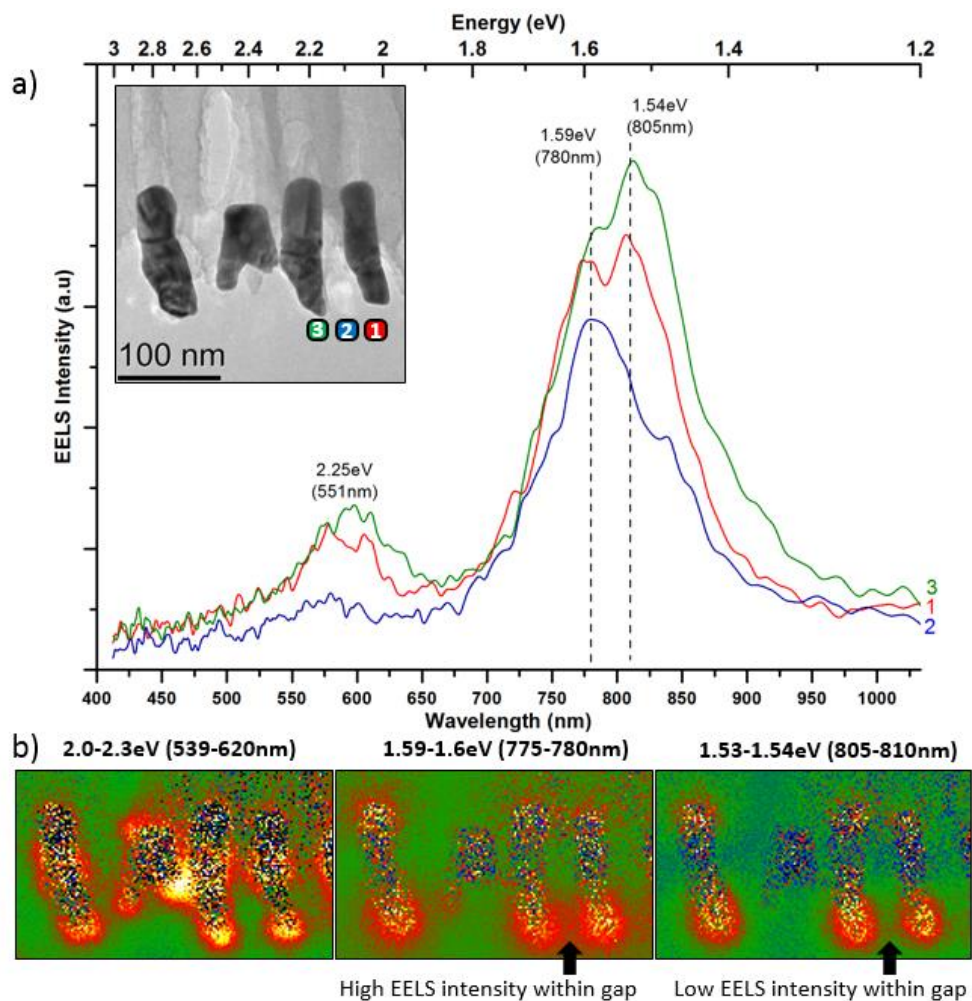


**Figure 6.14:** a) EELS spectra and corresponding bright field image showing the locations the spectra was integrated over. b) Normalised SI maps according to the energy range stated.

By studying the EELS spectra in Figure 6.14 it appears as though in general three peaks are resolved when the electron beam is located beneath either of the right hand nanorods. One of these peaks is at lower wavelength and will be discussed later, whereas the other two peaks are relatively close together and occur at higher wavelength. Although these peaks are only separated by around 25 nm and as such are seen to overlap, the use of an energy dispersion of 0.01 eV allows their distinction. This is particularly evident for location one whereby each peak is clearly resolved.

To determine whether coupling is occurring between the nanorods, a number of techniques can be harnessed. For instance, if the two peaks occur due to the electron beam simultaneously exciting each nanorod, as was the case with the previously shown dimer (Figure 6.13), it would be expected that as the electron beam was positioned further away from one of the nanorods, the amplitude of its respective peak would decrease. This however is not seen in the spectra of Figure 6.14. For example, in location three, the largest peak is seen at a wavelength of 805 nm. It would therefore be assumed that this is the longitudinal peak of the nanorod located directly above this location. If the nanorod was not coupled you would expect to see a decrease in the amplitude with increasing distance. Instead it is seen that the amplitude of this peak decreases at position two, then increases again further away at position one. It is proposed this relationship is therefore due to coupling between the two nanorods.

Further proof is obtained by noting that at position two (in the gap between the particles), the higher wavelength peak seems to disappear to an extent, as would be expected for the dark mode of two similarly sized nanorods due to charge symmetry. The lower energy (bright) mode however remains as a distinct peak. This may also be seen in the corresponding normalised SI maps shown in Figure 6.14b whereby for the higher wavelength mode (dark mode) there is a lack of intensity in the gap region. In contrast the slightly lower wavelength mode (bright mode) appears to have a higher intensity within the gap. As previously discussed, this distribution of the energy loss may be used to assess whether the mode is bright or dark due to the premise that the dark mode of side by side aligned nanorods may not be excited within the inter-particle gap whereas the bright mode can be. This affects the distribution of the energy loss in an SI map (at a specific energy) by making the gap region appear to have a low intensity for dark modes and a higher intensity for bright modes. As this matches that shown in Figure 6.14b, it therefore supports the theory that the modes are coupled.

Finally, additional proof of the presence of coupling was acquired by modelling the degree of splitting with spacing for a nanorod dimer embedded in AAO (see Appendix 1). It was found that the spacing required to achieve splitting of the longitudinal mode for AR=3 nanorods was approximately 30 nm. This is therefore slightly larger than the spacing of the two nanorods on the right in Figure 6.14, and therefore based upon this a small degree of splitting due to coupling would be expected.

Turning our attention now towards the other two nanorods within this segment of the array, it was found that unlike the nanorods on the right, the longitudinal modes did not show a clear splitting in the spectra (*not shown*). This is believed to be due to one of the nanorods being significantly shorter than the others, and also due to the spacing between the two left nanorods being relatively large at approximately 48 nm. This therefore shows that a degree of disorder in the array may act to disrupt near field coupling. On the other hand, the smaller nanorod is seen to come within close contact of the nanorod adjacent on its right, leading to a very high EELS signal at a wavelength of around 550 nm. This may be seen in the corresponding normalised SI map of Figure 6.14b. Despite this coupling, once again a splitting of the longitudinal mode was not apparent, likely due to the nanorods having significantly different geometries. Lastly, the normalised SI map of the lower wavelength mode (2.0-2.3 eV) also reveals a small enhancement in the energy loss towards the centre of the rods. This is believed to be due the higher order quadrupole mode being excited based upon its energy and distribution.

To summarise, it has been shown that FEM modelling that uses an electron beam to excite the plasmons is capable of probing both the bright and dark modes of a nanorod array. These simulations found that the degree of splitting of the longitudinal mode depends on both the aspect ratio of the nanorods, the inter-particle spacing, and lastly the location of the electron beam. In addition to this, a comparison between the simulations and experimental EELS data showed excellent agreement therefore supporting its use in the analysis of the following more complicated geometries. For the experimental EELS measurements on a nanorod dimer it was found that the spacing was too great to achieve coupling, and instead the nanorods behaved in an isolated manner. In contrast however, for nanorods whereby the spacing was reduced and a greater number of rods interacted, it was found that coupling occurred and led to the generation of both bright and dark modes. This was confirmed by studying the EELS spectra at different locations, analysing the SI maps, and performing modelling.

### 6.4.3 Supported Nanorod Dimers

The nanorod arrays fabricated in this work were grown by means of electrodeposition through the pores of an AAO template on to a gold substrate which acts as a working electrode. Due to this, the nanorod arrays were typically supported on a 150 nm thick gold substrate. In the previous modelling chapter it was predicted that the nanorods couple with their substrate image, thereby resembling end-to-end orientated nanorods, which gave rise to larger red-shifts of the longitudinal mode, as well as stronger enhancements in the electric field strengths. It was also found that this phenomenon was counteracted by side-by-side coupling effects which blue-shifted and weakened the modes. By means of the EELS technique, these effects may be analysed in real structures whilst also probing both the bright and dark modes.

Firstly, a side-by-side nanorod dimer supported on a 150 nm gold substrate was modelled, with the spacing between the dimer varied between 5 nm and 80 nm, as seen in Figure 6.15. The AR of both the nanorods was set to be 3, and therefore a comparison was able to be made with that of the previously shown unsupported nanorod dimer simulations (Figure 6.9).

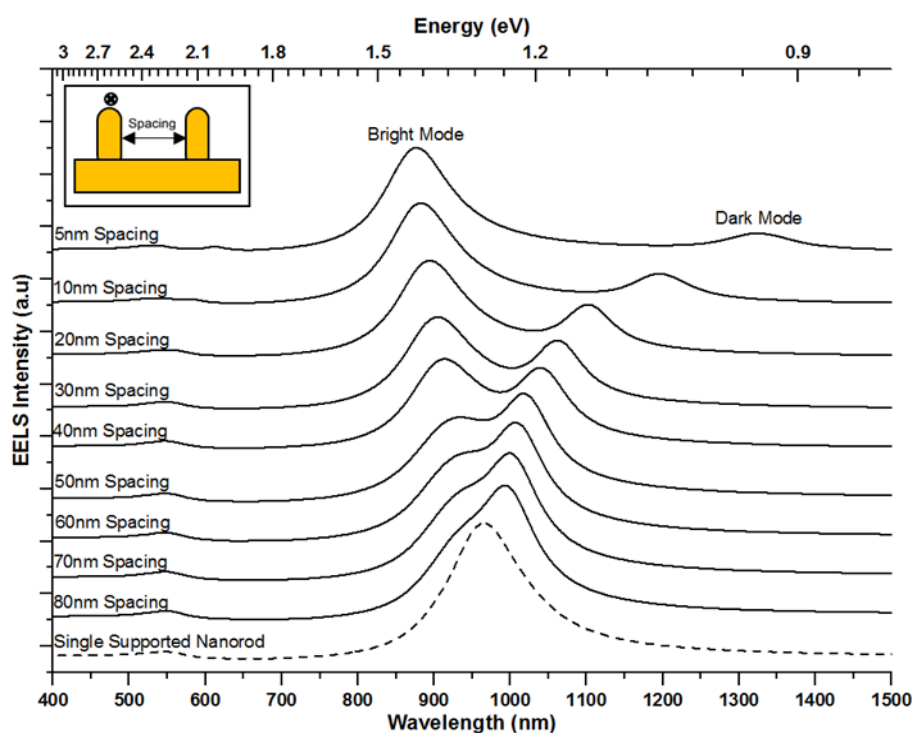


**Figure 6.15: Modelled EELS intensity for a dimer of side-by-side aligned gold nanorods (30 nm x 90 nm) supported on a 150 nm thick gold substrate at varying spacing and compared to an isolated nanorod. The nanorods are modelled within a vacuum with the electron beam positioned 5 nm above the left nanorod as demonstrated by the cross in the inset. Each curve has been offset in the y-direction to highlight the development of the modes.**

Firstly, it was noticed that the longitudinal peak of the single supported nanorod was significantly red-shifted compared to that found for the previous unsupported nanorod. As shown in the modelling of Chapter 5, this is typical for a gold nanorod aligned vertically on a gold substrate and was attributed to the nanorod coupling to its substrate image. This therefore shows that both the EELS model and plane wave models are capable of reproducing the coupling effects expected with substrates.

With regards to the dependence of the EELS intensity on the spacing of the dimer, a similar result was seen to that of the unsupported nanorod dimers (see Figure 6.9). For example, at large spacing the longitudinal modes were seen to resemble that of the single nanorods, however, as the spacing was reduced and coupling strength increased, the modes were split into both bright and dark modes. Although this qualitatively matched the previous unsupported dimer results, a discrepancy was seen with respect to the value of the spacing required to cause a splitting of the mode. For instance, in the unsupported nanorod dimer, the longitudinal mode began to split at an inter-rod spacing of ca. 30 nm and had red-shifted the dark mode to a wavelength of 721 nm when spaced 5 nm apart. Alternatively, in the supported nanorod dimer the splitting was seen to be apparent at a much larger spacing of 80 nm. The dark mode also red-shifted considerably more, moving to a wavelength of 1320 nm when spaced 5 nm apart. This is due to the strength of the dipole mode increasing considerably for the supported nanorods due to their coupling with the substrate. This increased dipole strength then allows the nanorods to interact with those adjacent more effectively, thereby increasing the nanorod to nanorod coupling <sup>(115)</sup>. This interdependence between the substrate coupling and the particle to particle coupling further highlights the complex nature of these supported nanorod arrays.

To investigate the bright and dark modes of these supported arrays in more detail, the induced electric field, surface charge density, and a schematic diagram of the surface charge distribution were plotted, as shown in Figure 6.16. The supported nanorods appear to have a monopole-like charge density distribution with the metallic substrate surface acting as the opposing charge. This is consistent with other works such as that of Malerba *et. al.* <sup>(256)</sup> whereby additionally they also find a blue-shift and reduction in intensity for the bright mode of the arrays, thereby supporting these results.

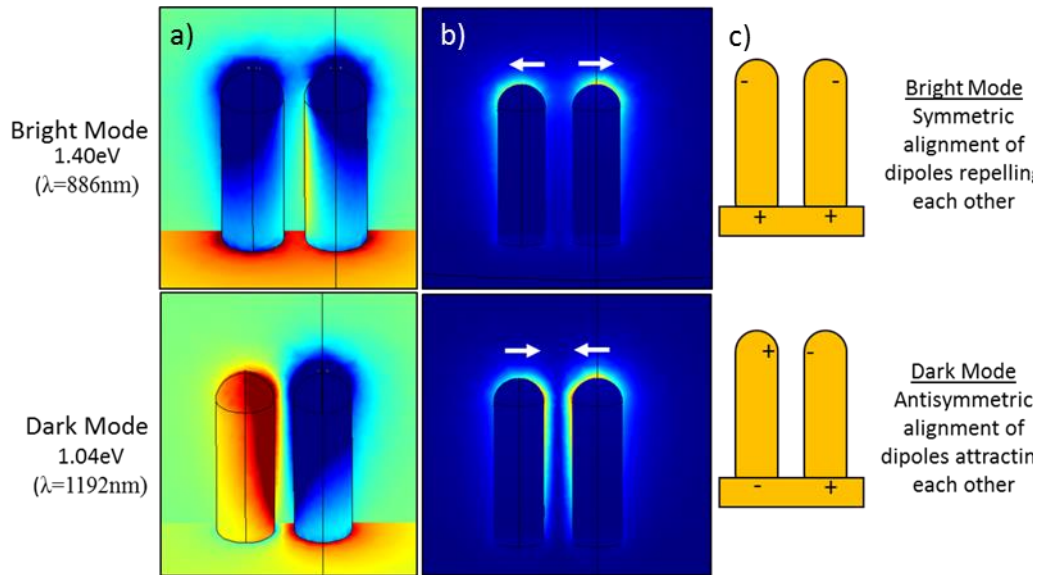


**Figure 6.16:** a) Induced electric field plots for an AR=3 gold nanorod dimer supported on a 150 nm thick gold substrate and spaced 10 nm apart. The plots on the nanorod surface shows the surface charge distribution, however the view is tilted so as to also see the charge distribution on the substrate surface b) Plots of the induced electric field modulus. c) Schematic representation of the surface charge distribution based upon the results from (a).

Additionally, in a similar manner to the unsupported nanorod dimer, the plasmons appear to either repel or attract each other depending on whether the mode is bright or dark. As discussed with the unsupported nanorods however, this may not necessarily be evident in the experimental EELS SI maps, and in fact the bright mode in the experimental data may instead appear to attract based upon it being able to be excited within the dimer gap whereas the dark mode cannot. To test if this was still true for supported nanorods, and to ensure that the presence of the substrate does not remove the symmetry that forbids the dark mode to be excited within the gap, further simulations were performed. These can be seen in Appendix 2, however for reference it was noted that, as with the unsupported dimers, only the bright mode could be excited within a dimer gap. This therefore allows the nature of the modes in the experimental data to once again be assessed by altering the location of the electron beam.

As before the effect of the aspect ratio of the nanorods was also studied, as shown in Figure 6.17. This followed a similar trend to that of the unsupported nanorod arrays, however the modes were substantially more red-shifted. Furthermore, the presence of the substrate acted to excite higher order modes more readily. This is consistent with the results shown when modelling using plane waves and, as outlined in Chapter 5, is due to coupling between the nanorod and the substrate causing increased hybridisation of the plasmonic modes.

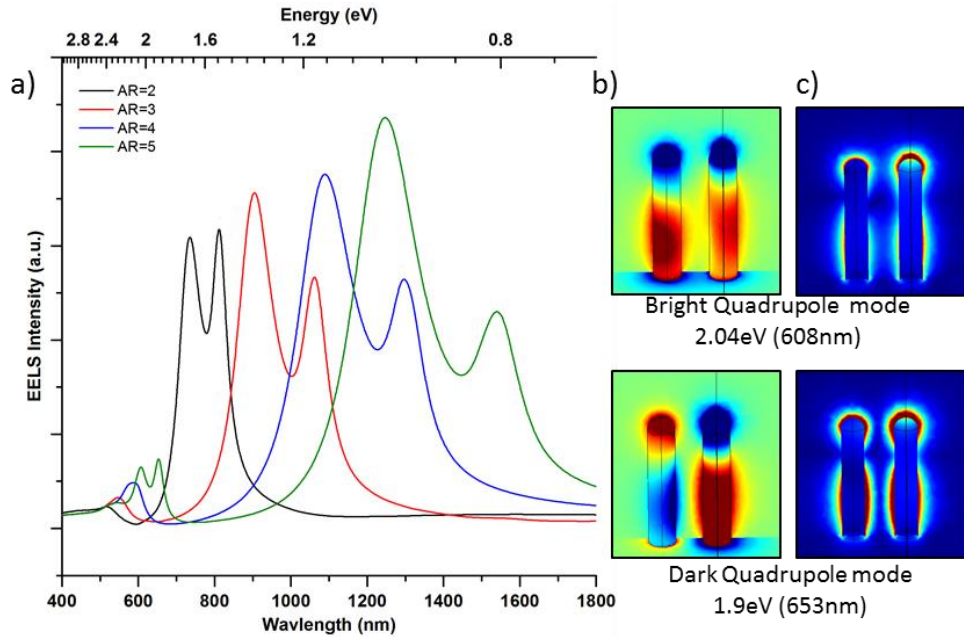


**Figure 6.17:** a) Modelled EELS intensity for a dimer of side-by-side nanorods of diameter 30 nm and with varying aspect ratio. The nanorods are stood vertically on a 150 nm gold substrate with a spacing of 30 nm. The array was excited with the electron beam located 5 nm above the right nanorod. b) Induced electric field plots, c) modulus of induced electric field.

Interestingly, it was seen that the higher order modes that were excited in the supported nanorod dimer also appeared to have been split into both bright and dark components. This splitting did not occur for the higher order modes belonging to lower aspect ratio nanorods due to these being relatively weak, however, by an aspect ratio of five a clear separation of the peaks was seen. To confirm that this was due to the mode splitting and not from the presence of an alternate higher order mode, the induced electric fields were plotted as shown in Figure 6.17b. These showed that both peaks were related to the quadrupole mode of the nanorod, and that as expected both the bright and dark configurations were present. In this quadrupolar mode the electric field was distributed both at the top of the nanorod and at the base. This bottom area in particular is seen to differ between the bright and dark mode with the plasmons repelling and attracting each other respectively.

Now that a basic understanding of what is expected to occur in supported nanorod arrays has been derived, the experimentally obtained results will be addressed. EELS spectra for a supported nanorod dimer is shown in Figure 6.18. The left-hand nanorod was found to have an aspect ratio of 3.0 whereas the right nanorod had an aspect ratio of 2.63. The spacing between the two nanorods averaged 32 nm.

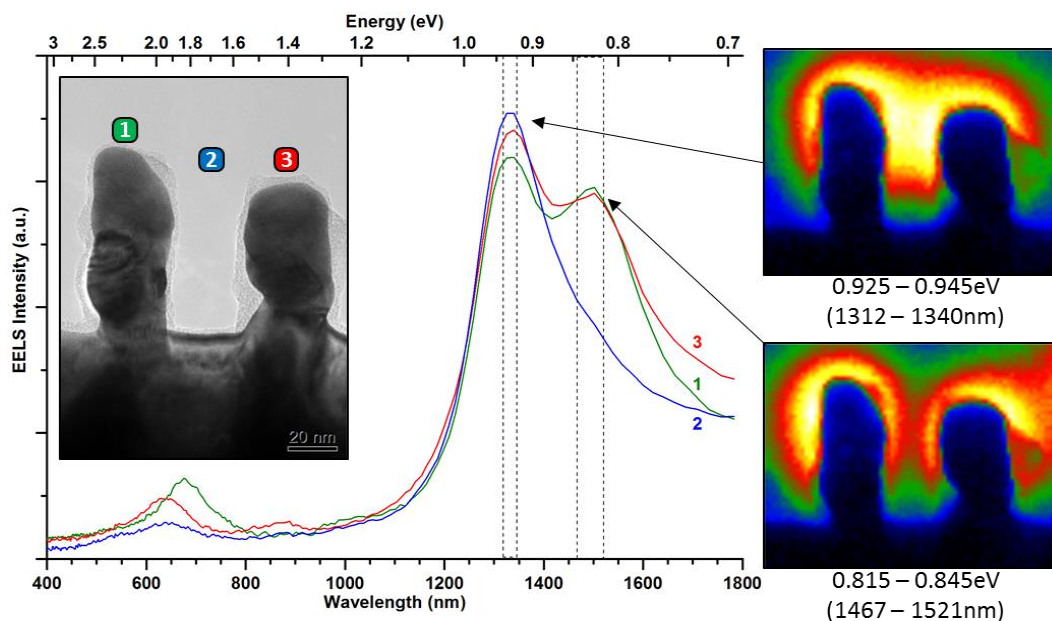


**Figure 6.18: EELS spectra for a supported nanorod dimer. The inset shows a bright field image whereby the coloured squares represent the regions integrated for the spectra shown. The SI maps are taken over the energy window stated and as shown by the dashed boxes.**

The AAO template that was used to grow these nanorods was removed by etching with NaOH to leave the nanorods free standing and exposed to vacuum. Despite this, small fragments of the AAO are visible on the surface of the nanorods, as seen in the bright field image. This is due to the AAO template not being fully etched by the NaOH as a compromise had to be made on the etching time so as to not damage the other components in the TEM cross-section. Despite this, the thin AAO layer may actually prove useful as it gives an indication of how the plasmons distribute when a shell is present on the surface, as would be the case for the nanorods coated in  $\text{TiO}_2$ . It was found that the layer has a limited effect on the plasmons, with the fields appearing to propagate through it. This would therefore signify that strong electric fields would occur within the layer itself leading to possible enhancements to photocatalysis.

With regards to the spectra collected above each nanorod, it was apparent that two strong peaks occurred at relatively high wavelengths of 1335 nm and 1494 nm based upon performing Gaussian fits. The SI maps for this energy range confirm these were related to the longitudinal mode of the nanorods as their fields were localised towards the top of each nanorod. Considering this, these modes were greatly red-shifted in comparison to what would be expected for the longitudinal mode of an unsupported single nanorod of the same size ( $\sim 600$  nm). As previously shown in the simulations and theory, the presence of the substrate causes a dramatic red-shift due to coupling between the nanorods and their substrate image.

It is therefore likely that this was the reason why the peaks occurred at such high wavelength and provides experimental evidence of this substrate coupling to support theory. On the other hand, it has also been shown that particle-particle coupling in a dimer may also lead to the generation of a red-shifted dark mode, and therefore this must also be considered as a possible cause as to why the modes occurred so far red-shifted. Indeed, the spacing (~30 nm) and aspect ratio (~3) of these supported nanorods is predicted to have relatively strong coupling and a splitting of the longitudinal mode into both bright and dark modes based on the previous modelling work (see Figure 6.15 and Figure 6.17). Considering this, particle to particle coupling may also be expected to occur within the experimental data leading to spectral shifts.

To determine whether particle to particle coupling is present, the EELS data was analysed by acquiring EELS spectra both above the nanorods and in the gap. Only the two peaks at the higher wavelengths will be discussed initially, whereas the observed lower wavelength peaks (~600-800 nm) are covered later. It was found that when the electron beam was located above either of the nanorods, both peaks occurred. In contrast, when placed within the dimer gap the higher wavelength peak disappeared, yet the lower wavelength peak remained. This relationship matches that expected for bright and dark modes based upon the requirement for charge symmetry within a gap. It is therefore proposed that the lower wavelength peak seen in Figure 6.18 was that of the bright mode, whereas the higher wavelength peak was the dark mode of the nanorod dimer. This is further supported by analysing the SI maps for both peaks. For example, the lower wavelength bright mode had a strong EELS intensity within the dimer gap and also above each nanorod. This therefore signified that the plasmon resonance at this wavelength may be excited in all these locations, as would be expected for a bright mode. Alternatively, the higher wavelength dark mode was seen to only have a high EELS intensity above each nanorod, whereas on the other hand a very low EELS intensity occurred within the dimer gap. These results therefore confirm that particle-to-particle coupling occurred within the nanorod dimer with both bright and dark modes being formed.

Considering this result, the uncoupled longitudinal modes would be predicted to have a resonance wavelength in-between that of the bright and dark mode at approximately 1400 nm. As this is at much higher wavelength than would be expected for an unsupported nanorod, it is further proposed that the reason for this large red-shift is due to coupling with its substrate image. The nanorod array was therefore believed to be influenced by both particle-to-particle coupling, and particle-to-substrate coupling.

To confirm this theory and investigate the degree to which the substrate coupling had on the nanorods, further simulations were necessary. Firstly, each of the nanorods in Figure 6.18 were simulated individually both unsupported and supported on the substrate. The purpose of this was to determine the likely red-shift experienced from coupling with the substrate only. These simulations also included the presence of the thin alumina layer on the surface of each nanorod, as clearly evident in bright field image in the inset of Figure 6.18. This thin alumina layer was important to include due to its higher refractive index possibly also influencing the red-shift. Following this, the single supported nanorods were then placed in a dimer with a spacing of 32 nm and again modelled. By comparing the spectra it was possible to approximate the red-shift due to the substrate, as well as the red-shift due to any possible coupling with the adjacent particle. The result of this can be seen in Figure 6.19.

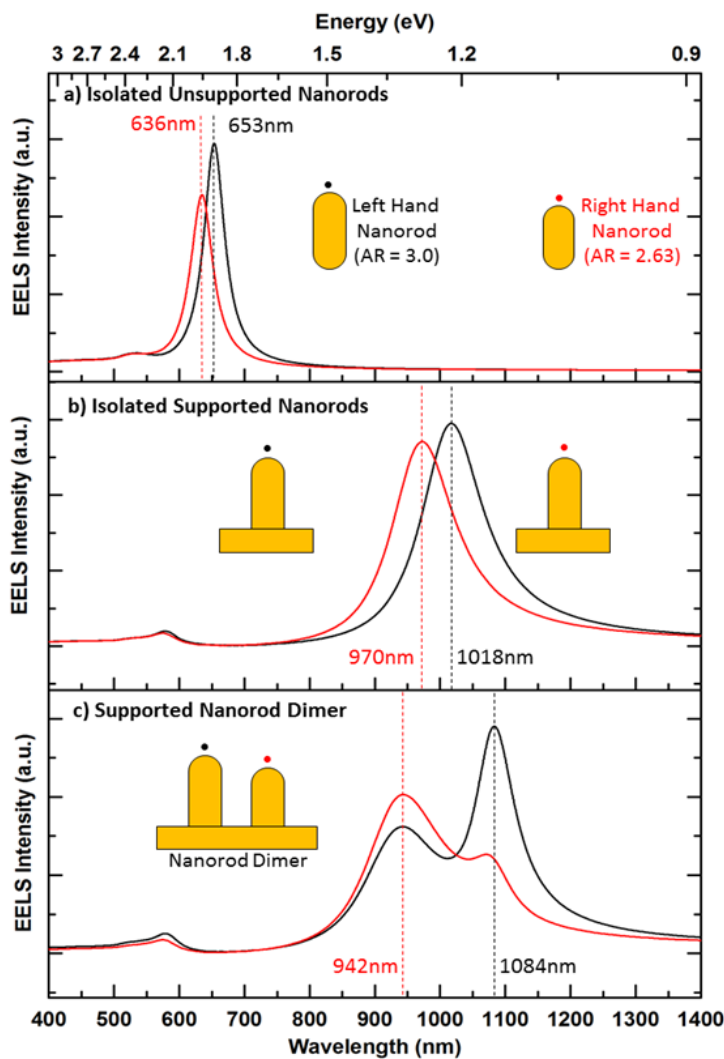


**Figure 6.19: Modelling of the experimental nanorod dimer comparing resonant wavelengths for nanorods that were a) unsupported and isolated, b) supported but isolated, and c) supported and in a dimer separated by 32 nm.**

The supported nanorods were seen to be dramatically red-shifted from those that were unsupported, with the average longitudinal mode predicted to occur at approximately 994 nm. This is significantly red-shifted compared to their unsupported equivalents, whereby the average longitudinal mode was at 645 nm. This therefore suggests that around a 350 nm red-shift would be expected for these gold nanorods stood vertically on the substrate. Alternatively, when the nanorods were placed within a dimer as in the experiments, a further red-shift was seen for the dark mode of approximately 90 nm, thereby taking the resonance to a wavelength of 1084 nm. The particle-to-particle coupling was therefore responsible for a much smaller spectral shift. This is as expected due to the particles having a spacing of 32 nm whereas the substrate is in direct contact with the nanorod therefore leading to much stronger coupling.

Despite these noted red-shifts, the predicted resonances still do not reach the values seen for them in the experimental data whereby wavelengths as high as 1500 nm were observed. This may partly be down to simplifications in the simulations whereby surface roughness and variations in end cap geometry were neglected. Alternatively, although the nanorods were shown as a dimer, they were actually part of a much larger array of nanorods. The presence of these adjacent nanorods may also lead to stronger coupling strengths and therefore shift the modelled data closer to that of the experimental data. This concept will be studied in more detail later.

In addition to the supported nanorod dimer without AAO, further EELS measurements were performed for a nanorod dimer completely embedded in AAO and again supported on the gold substrate, as shown in Figure 6.20. Due to the background being composed of AAO with an inhomogeneous thickness, the EELS spectra had to be normalised to one another. This was achieved by dividing the spectra for a set region of interest by the total electron counts (integrated over all energy ranges including those in the ZLP) for that same region. Additionally, as before the SI maps were also normalised according to the previously reported method.

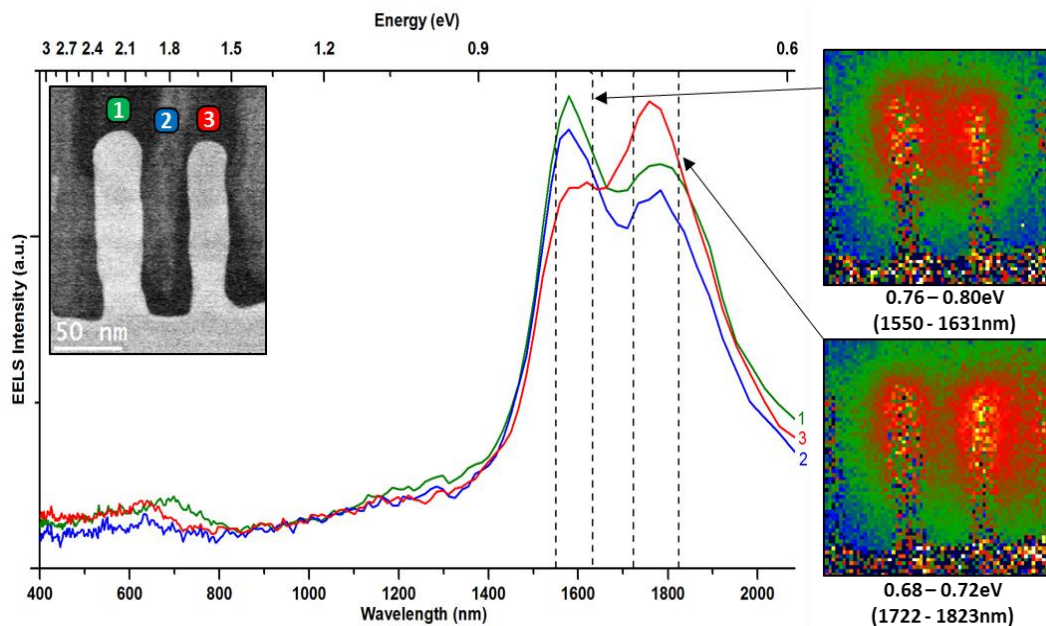


**Figure 6.20: EELS spectra for a supported nanorod dimer in AAO. The inset shows a HAADF image whereby the coloured squares represent the regions integrated for the spectra shown. The SI maps for each peak are taken over the energy window stated and as shown in the spectra by the dashed boxes.**

The diameter and AR of the left-hand nanorod was 32 nm and 4 respectively, whereas the right-hand nanorod had a diameter of 27 nm and an AR of 4.4. The spacing between the two measured from edge to edge was approximately 34nm. Based on the previously shown modelling results for a supported nanorod dimer and how this varies with aspect ratio, these dimensions would therefore once again be likely to also induce a splitting of the longitudinal mode into both bright and dark components. This is still the case when the nanorod dimer is embedded in AAO instead of vacuum, as shown in Appendix 3.

As with the other dimers studied, two main peaks occurred when the electron beam is located above the nanorods. These once again were at relatively high wavelengths of 1590 nm and 1760 nm, therefore they were likely red-shifted due to coupling with the substrate and also due to being embedded in a higher refractive index material. By analysing how the peaks vary with location it was seen that in contrast to the previously shown dimers, the higher wavelength mode is present even when the electron beam is located within the dimer gap. This therefore suggests that no coupling is present between these nanorods and instead that the lower wavelength peak was the longitudinal mode of the AR 4.0 nanorod, whereas the higher wavelength peak was for that of the AR 4.4 nanorod. Alternatively, there are a number of factors that would still suggest coupling may still have occurred within the dimer. For

example, it was seen that the intensity of the higher wavelength peak does not decrease monotonously with increasing distance, as would be expected for non-coupled longitudinal modes, but instead was slightly weaker in the gap than above the further away nanorod. Additionally, the normalised SI map show similar distributions to those seen previously whereby the lower wavelength mode was shown to be intense within the dimer gap, whereas the higher wavelength mode appeared weaker. Considering these discrepancies it was proposed that the modes were in fact bright and dark modes of the dimer, and the reason for the dark mode not disappearing when excited within the gap was due to the different sized nanorods not being symmetric. This lack of symmetry then allows the nanorods to have opposing charges as they do not feel the same incident field from the electron beam. To confirm this theory, a nanorod dimer was modelled whereby the electron beam was placed within the centre of the dimer gap and the aspect ratio or diameter of one of the rods was gradually altered. The results of these systematic tests can be seen in Figure 6.21.

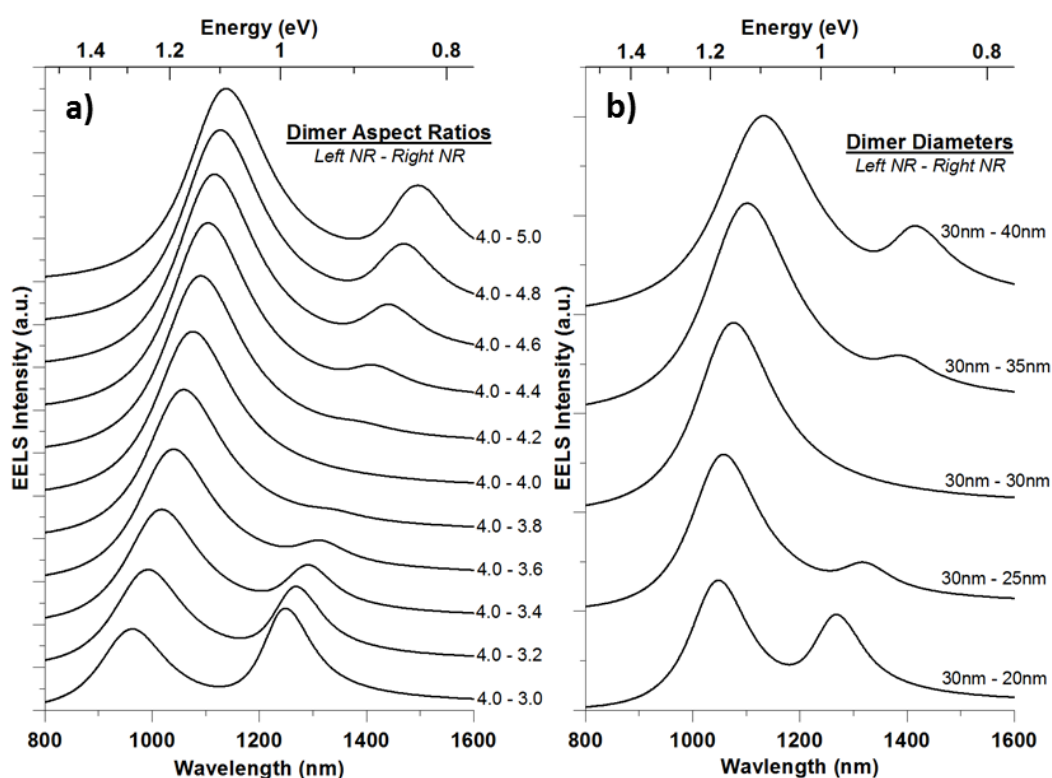


**Figure 6.21: Modelling of a nanorod dimer with a) varying aspect ratio and b) varying diameter. The dimer was excited with an electron beam located in the centre of the dimer gap and has a spacing of 20 nm. Each spectra has been offset so as to assess the change in peak intensities.**

The modelling showed that as the aspect ratio or diameter of one of the nanorods was varied compared to the other nanorod in the dimer, the dark mode was able to be excited. With increasing difference in size between the nanorods, the dark mode also gained a higher intensity. Despite this, even relatively small variations of around 10-20% were seen to be sufficient to break the symmetry and allow the formation of the dark mode. These results therefore confirm the theory that a dissimilar nanorod dimer may still have a dark mode when excited within the dimer gap. As seen in Figure 6.20, the aspect ratios, diameter and perhaps even the inhomogeneous nature of the AAO template, all lead to a breaking of the symmetry and therefore this dark mode within the dimer gap would be expected.

In addition to the formation of a dark mode, the results of Figure 6.21 revealed that the resonance wavelength of the modes was also affected by the varying aspect ratio and diameter. For example, as one of the nanorods in the dimer increased in AR, a red-shift of both the bright and dark modes occurred. Similarly, as one of the nanorods in the dimer decreased in aspect ratio from that of equal values, both modes blue shifted. The resonance positions are therefore seen to depend on the average aspect ratio of the dimer as a whole. This was also found to apply for the nanorods with varying diameter when the aspect ratio of the rods was kept constant at a value of four. The shifts for this scenario however were not as great as that for varying aspect ratios due to the longitudinal modes reduced dependence on the diameter.

#### 6.4.4 Supported Nanorod Arrays

So far within this chapter, analysis by EELS has predominantly focussed on nanorod dimers. These dimers however are actually part of a much larger array of nanorods. It is therefore necessary to assess how the addition of adjacent nanorods may affect the coupling response seen, as covered within this following section. Before the experimental results are presented however, the expected relationships based upon modelling work will be outlined.

Firstly, an unsupported nanorod array of aspect ratio three was simulated whereby the number of nanorods was systematically increased to five interacting nanorods. An unsupported array was chosen over a supported array as the subsequent analysis is clearer. Despite this no differences were found in the trends. The results for the supported nanorod arrays modelling are given in Appendix 4.

The modelling was performed with the electron beam located both above the end nanorod (dashed lines), second from end nanorod (dotted line), and above the centre nanorod (solid lines). For arrays with an even number of nanorods this centre alignment was such that the electron beam was located above either one of the centre most nanorods and not within the gap. This alignment of the electron beam in multiple locations was in order to ensure all modes of the array were visible and not forbidden due to charge symmetry requirements. The results of these simulations can be seen within Figure 6.22 along with additional induced electric field plots for the trimer scenario.

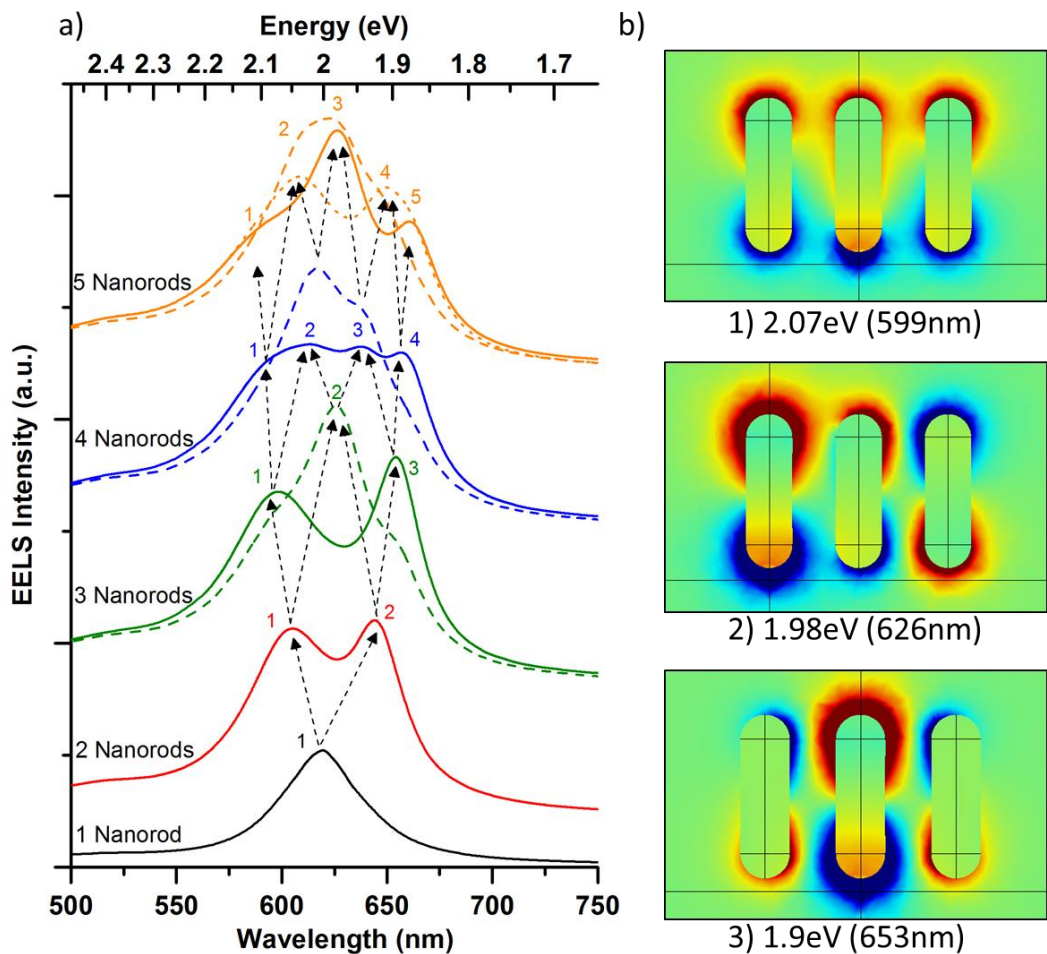
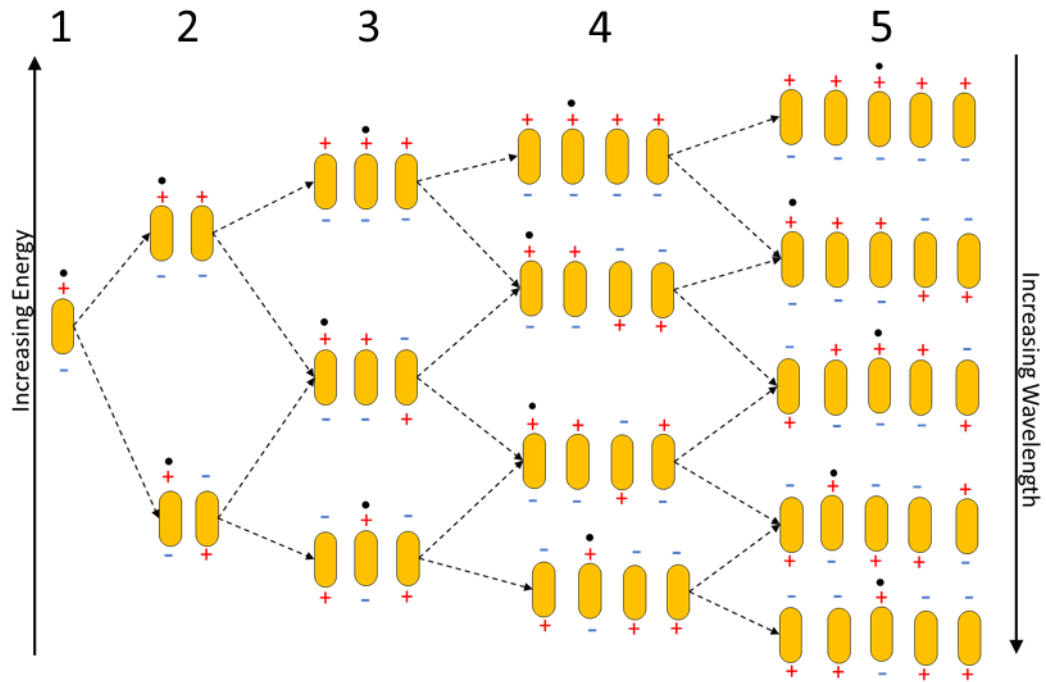


Figure 6.22: a) Modelling of EELS spectra for a nanorod array with increasing number of interacting nanorods. The solid lines were modelled with the electron beam located above the centre most nanorod in the array, the dashed lines were for the electron beam located above the end nanorod, and the dotted line is with the electron beam above the 2<sup>nd</sup> from the end nanorod. The arrows help show the splitting and hybridisation of the modes with increasing number of nanorods, whereas the numbers aim to help identify the peaks. b) Induced electric field plots for each mode of the nanorod trimer. The aspect ratio of the rods used in all these simulations was 3, along with a diameter of 30 nm and a spacing of 20 nm.

It was seen that the number of observable modes excited was directly equal to the number of nanorods within the array, therefore is analogous to the molecular orbital theory. With the dimer for example, two modes exist being namely the bright and dark mode. Alternatively for a trimer these modes still occur however there is also the addition of a further mode with a resonant wavelength in-between that of the other two modes. Studying the induced electric field plots in Figure 6.22b shows that this mode was a hybridisation of both the bright and the dark modes whereby the centre nanorod bonds symmetrically with one nanorod and anti-symmetrically with the other nanorod. Once again due to charge symmetry restrictions, this mode was only evident when the electron beam was placed over one of the end nanorods. Alternatively, for the four nanorod array it was seen that four observable modes existed. The highest and lowest energy modes were again attributed to the bright and dark mode of the array respectively. These were seen to continue to shift in energy, with the dark mode going to lower energy and the bright mode shifting to higher energy. This degree of energy shift however was reduced with it appearing to plateau as more nanorods were added to the array. Alternatively, the two additional modes of the four nanorod array were located in-between the bright and dark mode and once again were hybridised modes consisting of elements with both bright and dark components.

These results are in agreement with other work that has studied the interaction of multiple nanoparticles with a point source excitation method such as EELS. For instance, Barrow *et al.* <sup>(238)</sup> performed EELS on a gold nanoparticle chain of different lengths ranging from one to five. They concluded that the number of experimentally observable modes is at least equal to the number of nanoparticles in the chain, plus the additional transverse mode. They too also found that with increasing chain length, the energy shift of the modes begins to plateau.

The exact configuration of the hybridised bright and dark modes is best assessed by creating a plasmon hybridisation diagram based upon the modelled data, as seen in Figure 6.23. A number of the configurations shown are only active when the electron beam is located away from the centre nanorod due to symmetry requirements. Additionally, for modes that may be excited in multiple locations, the arrangement of the dipoles was seen to vary as the electron beam moved position. This change to the arrangement however did not affect the resonant energy of the mode. The black dots in Figure 6.23 show the location of the electron beam for the configuration depicted. These generally relate to the strongest peaks according to Figure 6.22.



**Figure 6.23: Plasmon hybridisation diagram for a side by side nanorod array with increasing number of nanorods. The aspect ratio of the nanorods was 3 whereas the spacing and diameter of the rods was 20 nm and 30 nm respectively. The relative energy positions of the above modes are located based upon the data from Figure 6.22a. The black dots refer to the location of the electron beam according to the configuration shown.**

To analyse the hybridised modes, the five nanorod array will be discussed going from highest energy to lowest energy. It was seen that the highest energy mode was that of the bright mode whereby all the dipoles were aligned symmetrically. Following this, the next highest energy modes configuration was such that the two nanorods furthest away from the electron beams location aligned anti-symmetrically, therefore forming both bright and dark modes in one array. It is proposed that these furthest away nanorods were the ones to align anti-symmetrically as the incident field and resulting coupling strength between these nanorods was weak, therefore making the bright coupling modes more dominant. Alternatively, in the following configuration the nanorods at both ends of the array align anti-symmetrically. As these dark modes were closer to the electron beam, they were stronger than the previous case and therefore the mode occurred at lower energy. Leading on from this, the next mode had the anti-symmetrically aligned dipoles directly adjacent to the excited nanorod. This therefore occurred at lower energy than the previous mode due to the strong excitation of the dark mode. Finally, the lowest energy mode had its dipoles aligned so that only the nanorod with the electron beam located above it was anti-symmetrically aligned. This therefore results in an

extremely strong dark mode and the resulting shift to lower energy. This final mode may have been expected to have a distribution whereby each dipole alternates in polarity along the chain, similar to that shown for the trimer of rods. Instead however the configuration shown was seen for the lowest energy peak. This is believed to be due to the bright modes at either end of the array repelling each other and causing the plasmons of the penultimate rods to be located closer to the centre nanorod, thereby giving a stronger dark mode. On the other hand, the configuration whereby the dipoles continually alternate is found for lower energies, however it was too weak to show up as an observable peak in the spectra.

To summarise these findings, a nanorod array consisting of  $N$  nanorods and excited from a point source, has  $N$  observable coupled longitudinal modes. The highest energy mode is that of the bright mode where all dipoles are aligned symmetrically. With decreasing energy of the mode however, certain nanorods begin to align anti-symmetrically. This first occurs for nanorods far away from the point source before then affecting the nanorods closer to the point source as lower energy modes are reached. The lowest energy mode is arranged as such that the anti-symmetric dipoles are located adjacent to the nanorod being excited, in a manner that would give the strongest interaction.

Interestingly, both the spectra in Figure 6.22, and those for the supported nanorods in Appendix 4, show that when multiple nanorods are in an array the strongest mode is generally not that of the bright or dark mode as may be expected, but instead occurs for one of the hybridised modes with both bright and dark elements. In fact it was noted that as more nanorods were added to the array, the bright mode drastically reduced in intensity and broadened. Additionally, it was seen that the electric field distribution for this bright mode began to alter with the longitudinal mode moving towards the centre (or base for supported nanorods) of the nanorods, as seen in the induced field plots of Figure 6.24. This result therefore matches that found within the modelling of Chapter 5 whereby for an infinite periodic array of nanorods the symmetrically aligned dipoles destructively interfered to both blue-shift and weaken the bright mode, as well as leading to a redistribution of the electric field whereby a shift towards the centre of the nanorods was observed.

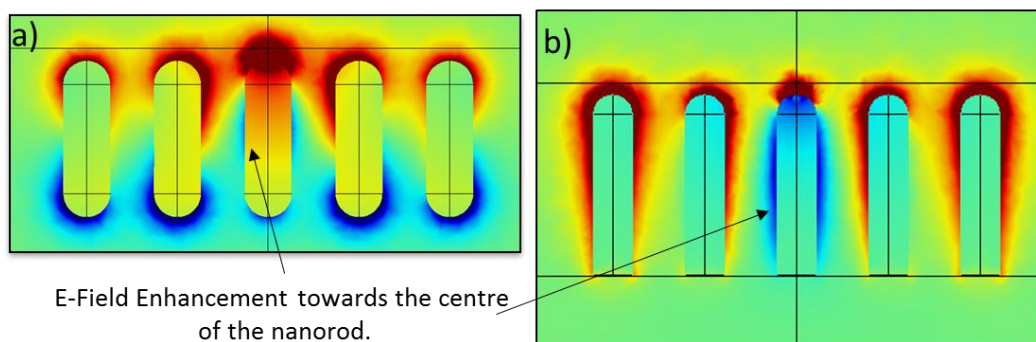


**Figure 6.24: Induced electric field plots of the bright mode for an a) unsupported nanorod array, and b) supported nanorod array showing the electric field distribution altering to the centre or bottom of the nanorod.**

Following the modelling of nanorod arrays, the experimentally derived results will now be discussed. EELS spectra were acquired for a section of the nanorod array whereby the AAO template had been etched as part of the preparation of the TEM sample. The spectra at the corresponding locations and an SI map are shown in Figure 6.25. The HAADF image in the inset shows seven nanorods within the region of interest which were found to have aspect ratios with values ranging typically from approximately two and a half to four ( $AR \sim 2.5-4$ ). Here the nanorods labelled two and three relate to the previously shown nanorod dimer (Figure 6.18). Within this array, the spacing appeared relatively constant at around 30nm, although it should be noted that due to the hexagonal arrangement of the nanorods in the initial array, these may not be represented accurately in 2D form. Despite this, the 30 nm spacing fits well with that found for the bulk array, plus the slight tilt seen in the TEM cross-section HAADF image and relatively equal focus suggests these nanorods were generally in the same plane. One exception to this, is the nanorod in the area described as four in the HAADF image whereby it appeared behind the others and as such was somewhat out of focus. The tilt seen in the HAADF image was corrected for prior to the acquisition of the EELS spectra.

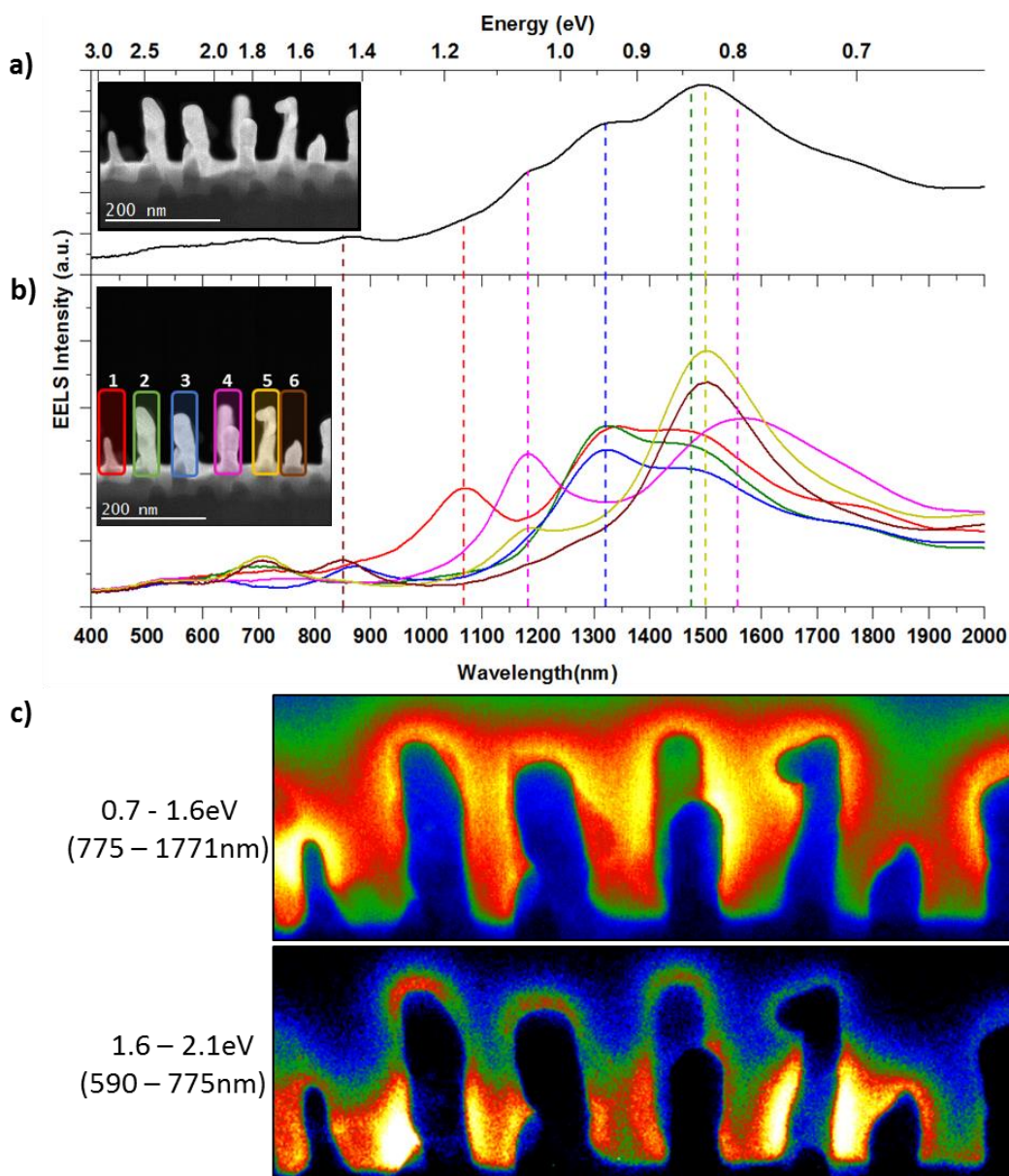


**Figure 6.25:** EELS data for a nanorod array of AR  $\sim 2.5$ -4 on a 150 nm gold substrate. a) EELS spectra obtained from integrating over all pixels in the corresponding SI b) Individual EELS spectra for each nanorod, integrated over a region as represented by the coloured blocks in the HAADF image. The coloured dashed lines represent the dominant mode for the nanorod principally excited in that location c) SI maps for the energy windows 0.7-1.6 eV and 1.6-2.1 eV.

The EELS spectrum in Figure 6.25a, was obtained by integrating over all pixels in the spectral image. It was seen that a broad peak within the near infra-red region occurred, formed due to variations in the geometrical factors such as aspect ratio, leading to shifts in spectral position of each nanorod and resulting in overlapping peaks. Although this peak was not located within the visible region as would be preferred for most photocatalytic applications, it should be

noted that these spectral positions observed when exciting with an electron beam are not directly transferable to optical methods due to the localisation of the excitation source, and the ability to probe both bright and dark modes. Indeed, it has already been shown within Chapter 4 that for a similar nanorod array the longitudinal modes are blue-shifted considerably so that they overlap the transverse mode and that no higher wavelength peaks occur. Instead the results here aim to help interpret any coupling that occurs in the array from a fundamental viewpoint, as well as to relate intensities and distributions of the plasmonic modes to those that may be beneficial in particular applications.

It should be noted that there is a degree of variance in the shape, aspect ratio, and diameter of the nanorods. Considering the previously shown results, it would therefore be expected that if coupling between nanorods occurred, both the bright and the dark mode would likely be visible in many positions. Studying the location dependent spectra in Figure 6.25b, it was seen that a large number of peaks occurred. These peaks are once again at much higher wavelength than would be expected for nanorods of their size, believed to be mainly due to the coupling with the substrate, however particle-particle coupling may also have had an impact in this shift. For each location tested, the resulting spectra typically consisted of two to three peaks between the wavelengths of 800 nm and 1800 nm. These were found to be maximised in intensity towards the top of the nanorods and therefore are likely related to the longitudinal modes. Alternatively, each location was also found to have an additional two peaks at lower wavelength. One of these occurred at a wavelength of 520 nm and is therefore believed to be the transverse modes of the nanorods. On the other hand, a second peak was found within the region from 600 nm to 800 nm. Both of these modes were found to increase in intensity as the electron beam was positioned towards the bottom of the nanorods.

To assess these modes, the energy ranges 0.7-1.6 eV and 1.6-2.1 eV were plotted in SI maps, as seen in Figure 6.25c. For the lower energy range, the electron energy loss predominantly occurred towards the ends of the nanorods and therefore is related to the longitudinal modes as expected. Alternatively, the higher energy modes resulted in an energy loss distribution located at the base of each of the nanorods. It is likely this may be related to the higher order modes of the nanorods, however potential other options for this will be discussed later.

Unfortunately, it is difficult to ascertain for certain whether the nanorods in this array are coupled or not due to the previously used methods not applying. For instance, the dark mode

would not be expected to disappear in the gap between nanorods due to the large variance in aspect ratio, diameter and geometry of the individual rods. Additionally, as shown in the modelling of multiple nanorods, the arrangement of the charges is complex and dependent on the location of the electron beam. The experimental EELS SI maps however show the energy loss for all positions of the electron beam, therefore this may hinder the ability to assess whether the modes are bright or dark based on the SI map alone. Despite these difficulties, I believe there are three possible explanations for the observed spectra and multiple peaks seen in the experimental data, as will be outlined below.

Firstly, it is possible that the strongest peaks in each spectra (as represented by the dashed lines) relate to uncoupled longitudinal mode of the nearest nanorod. The additional peaks in the spectra then arose due to the electron beam exciting other nearby nanorods simultaneously from its location. For this to hold true, it would be expected that a decrease in intensity of a peak would be found with increasing distance from the nanorods end. This was found for a number of the nanorods, for instance those in the regions of 4, 5, and 6, therefore suggesting that these may not be coupled. This lack of coupling may be due to the nanorods having a greater spacing than estimated by the HAADF image due to the 3D nature of the array not transforming accurately into a 2D image. For instance, it is believed nanorod 4 is set some distance back from the other nanorods. Alternatively, the relatively large variation in sizes and shapes of the nanorods may also inhibit coupling between the nanorods.

Secondly, it has already been shown that coupling between certain nanorods in the array was believed to have occurred. For example, the nanorods in regions 2 and 3 relate to the previously shown dimer (Figure 6.18) which clearly showed an interaction based on the intensity of their peaks with location. Similarly, the lower energy dark mode was also seen to disappear within the dimer gap as expected for two similarly sized nanorods. This therefore leads to a second explanation in that only certain nanorods within the studied array are actually coupled. These are likely to be the ones with either a close spacing to a neighbouring nanorod, or a large aspect ratio so that the dipolar modes are able to interact.

The third possible explanation arises based on the analysis of the modelling results. For example, the previously shown modelling work for supported nanorod dimers with different spacing (Figure 6.15) showed that coupling would be expected to occur up to spacing's of at least 80 nm for AR=3 nanorods, resulting in a splitting of the longitudinal mode. For larger

aspect ratio nanorods, as is often the case for this array, this distance would be even greater. It could therefore be assumed that all of the nanorods within this array were coupled with sufficient strength to cause a splitting of the longitudinal modes. The SI map over the energy range 0.7-1.6 eV in Figure 6.25c would also suggest this coupling should have occurred based on the dipole modes clearly coming into contact with each other.

Considering the last explanation to be true, the spectra in Figure 6.25 would then be expected to follow the trends seen for the modelling of multiple nanorods when using a point source excitation. Namely, for each location of the electron beam, the nanorods within the array would couple together producing combinations of both bright and dark modes depending on the excited nanorods relative position within the array. The multiple peaks within the spectra of Figure 6.25 may therefore relate to these modes.

Unfortunately, as previously stated, the SI maps cannot show the energy loss distribution for one location of the electron beam as the modelling does, but instead shows the energy loss distribution for the electron beam over all pixels. This therefore means the SI maps are incapable of showing the individual configurations of bright and dark modes, but instead essentially show the accumulation of all configurations. Despite this, the spectra are location dependent and therefore may give clues as to whether bright and dark configurations existed. This is due to the principle that some modes cannot be excited when the electron beam is located in certain positions, as shown in the modelled spectra of Figure 6.22. For example, in the trimer scenario, the mode at approximately 2 eV could not be excited over the centre nanorod due to restrictions based on charge symmetry, but could be excited on the adjacent nanorod. Considering this, the following would be expected. If coupling was not occurring, each spectra would have a dominant peak relating to the longitudinal mode of the nearest rod, with then significantly weaker peaks relating to the longitudinal modes of directly adjacent but further away nanorods. Alternatively, if coupling was occurring in the array, the peaks in each spectra would likely have more equal intensities, plus it would be expected that some peaks would be absent from spectra even when the electron beam is placed over an adjacent nanorod.

Reviewing the spectra of Figure 6.25 once again, it can be seen that for most spectra the peaks tend to be of a similar intensity. Additionally, there are also locations whereby an adjacent nanorod is not excited. For example, in location 4 the longitudinal modes of nanorod 3 and 5

should also have been excited if coupling was not occurring. Although this may have occurred for nanorod 5, there is a distinct lack of a peak where you would expect the longitudinal mode of nanorod 3 to occur (as represented by the blue dashed line). Similarly, when the electron beam was placed in location 2, it did not excite the nanorod in location 1, however the opposite is true in that location 1 could strongly excite the nanorod in location 2. These relationships therefore suggest that coupling may be occurring within the array.

On the other hand, a possible factor that may go against this theory is that the bright mode should have been excited in all locations. A peak at lower wavelength would therefore have been expected to occur in the spectra regardless of location. Although there wasn't a longitudinal related mode seen within the spectra that fulfils this, it was possible that the modes seen at a wavelength of between 600 nm and 800 nm were that of the bright mode. As shown in the SI map of Figure 6.25c, the energy loss distribution of these modes is one whereby it was primarily confined to the base of the nanorod, suggesting an oscillation over the width of the nanorod. This therefore matches that predicted by the modelling both within Chapter 5 for infinite supported arrays, and within this chapter for finite arrays. Additionally, although this mode was originally proposed to be that of a higher order mode, interestingly it appears as though all of the nanorods within the array, except that of the very short nanorod in location 6, were able to sustain it. As higher order modes generally only become prominent for larger aspect ratio nanorods, and many of these nanorods have an aspect ratio of 3 or less, this therefore suggests that this mode may not be related to a higher order mode as previously thought, but instead related to the bright coupled mode of the array.

These findings were further compared to other areas of the array to see if similar results occurred. For example, a section of the nanorod array embedded in the AAO template was studied, as shown in Figure 6.26.

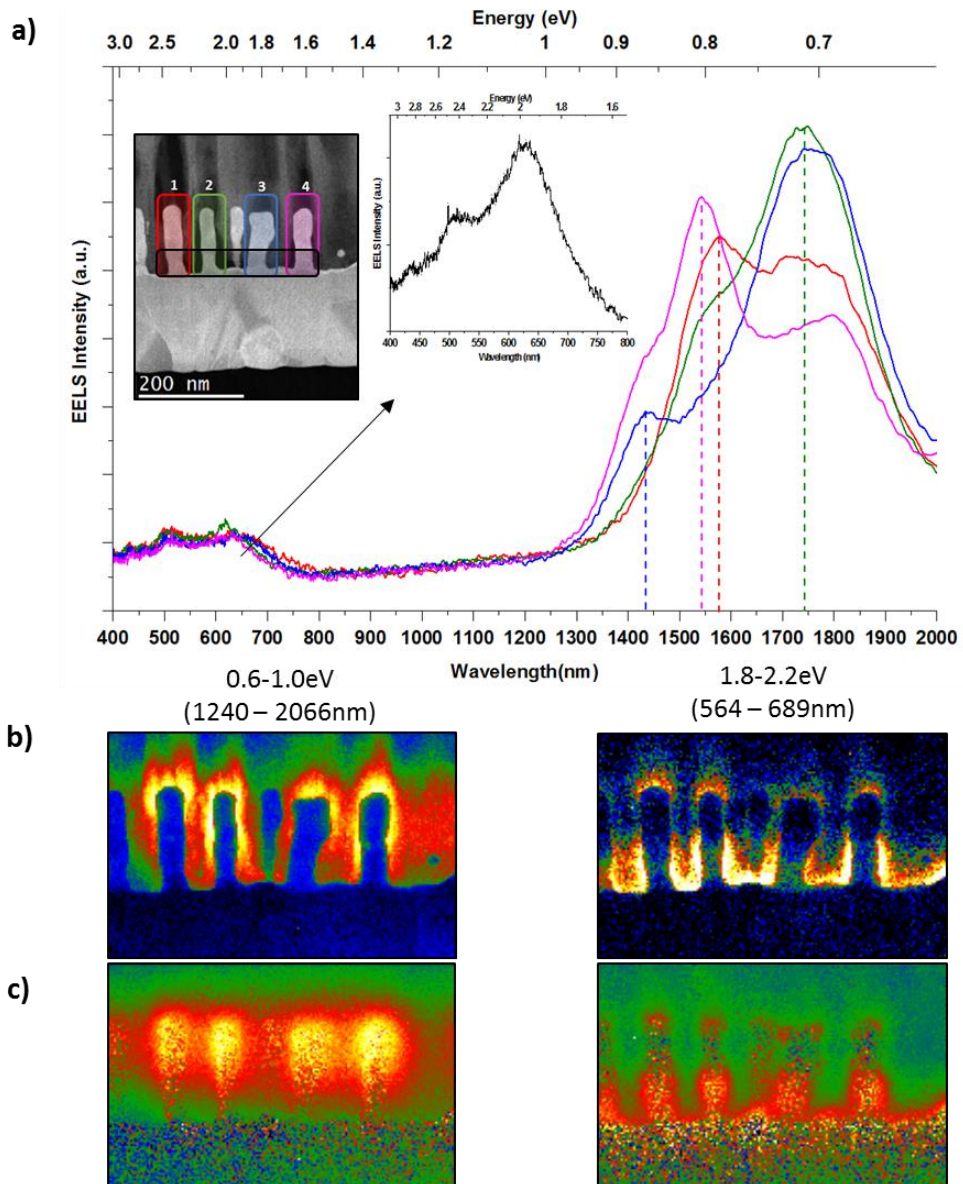


**Figure 6.26:** Normalised EELS measurements for a gold nanorod array embedded in AAO. a) Normalised EELS spectra for each nanorod, integrated over a region as represented by the coloured blocks in the HAADF image. The coloured dashed lines represent the dominant mode for the nanorod principally excited in that location. The inset shows the lower wavelengths peaks based on integrating a region spanning the bottom of all the nanorods (black box). b) SI maps over the energy windows 0.6-1.0 eV and 1.8-2.2 eV, and c) their normalised equivalents.

It may be seen that the array in the AAO followed the same trends as that for the previous uncoated array. For example, each location was seen to result in a number of peaks in the spectra with fairly equal intensities. Additionally, when the electron beam was located in certain positions, it was seen to not excite the nanorods in a way that would be expected for uncoupled nanorods. For example, when in location 3 the peak believed to relate to nanorod

2 was strongly excited, however, the mode of the closer nanorod 4 was not. Similarly, in location 4, the peak of nanorod 3 was only weakly present, whereas the mode for the further away nanorod 2 was much stronger. Furthermore, once again a distinct peak at lower wavelength was found, as clearly evidenced by the plot in the inset of Figure 6.26. The SI maps for this energy range show that as before, the energy loss distribution was located around the base of all the nanorods in the array, therefore potentially relating to the bright mode. These factors therefore once again suggest that the nanorods in the array may have coupled together to give combinations of bright and dark modes.

Finally, the EELS results so far have focused upon the visible and NIR region up to a wavelength of approximately 2000 nm. Beyond this wavelength it is believed that the nanorods no longer have any plasmonic modes. Despite this, it should be noted that several significantly more intense peaks were observed in the EELS spectra. For clarity these were omitted from the previous results as they do not belong to the plasmonic resonances of the nanorods. Instead it was found these intense low energy peaks related to plasmonic modes of the substrate. This is due to part of the substrate breaking off during preparation of the TEM cross section. This gave the substrate a finite length of approximately 2400 nm and as such enabled the substrate to support localised surface plasmon resonances, as seen in Figure 6.27. These LSPR's have spectral features directly resolved at very low energies down to 188 meV (45 THz), and therefore may prove useful in the expanding field of terahertz plasmonics <sup>(257, 258)</sup>.

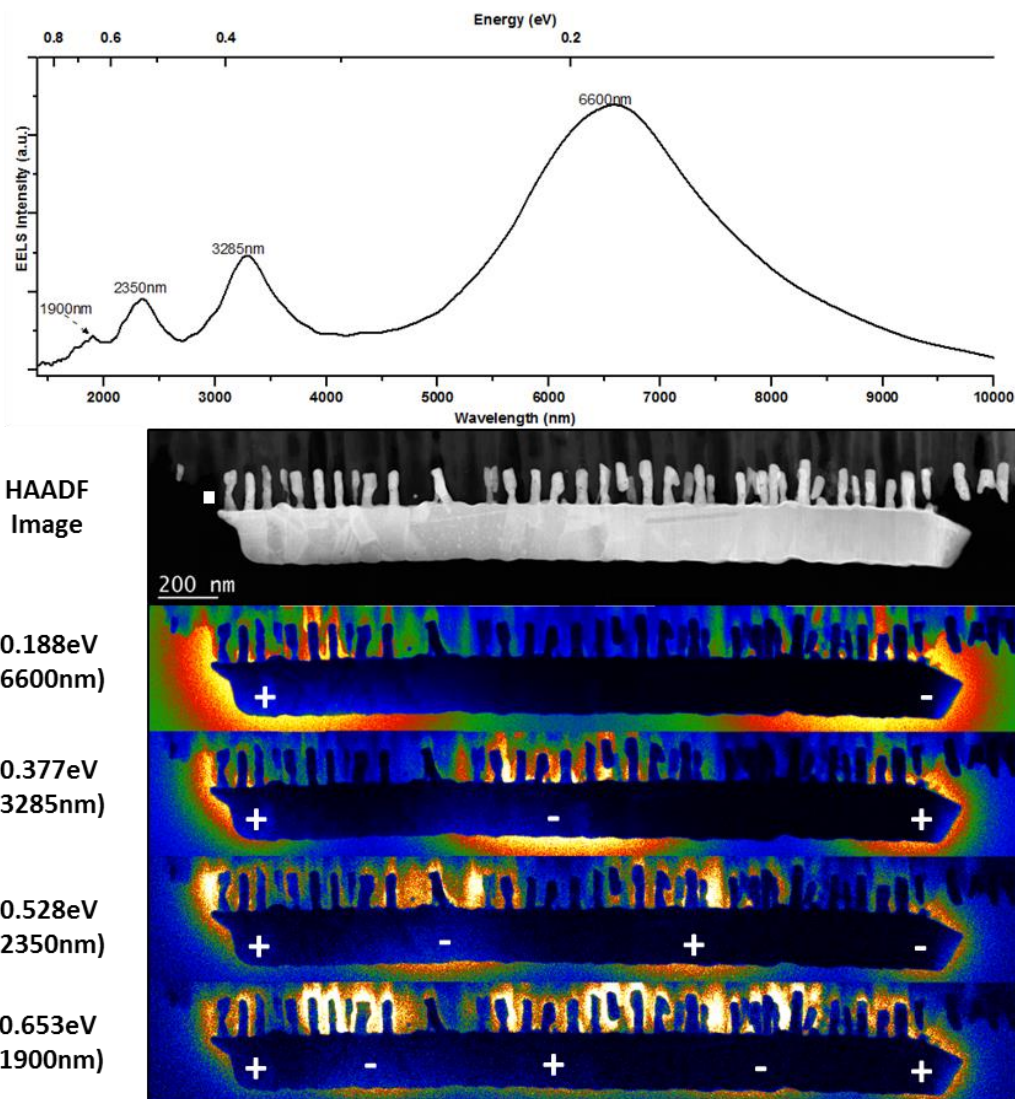


**Figure 6.27:** EELS spectra and SI maps showing the dipole and higher order modes of the gold substrate. The spectra was acquired by integrating the region as shown by the white square in the HAADF image.

## 6.5 Summary of Results

In conclusion, this chapter aimed to characterise the near field properties of the fabricated nanorod arrays using electron energy loss spectroscopy (EELS). This study was particularly interested in assessing whether any coupling was occurring between the nanorods of the array as well as to determine the nature of this coupling. Firstly, to aid with the analysis of the experimental data, a finite element model was produced whereby a current carrying wire (i.e. an electron beam) was used to excite the plasmons, with the energy loss probability then calculated from this, therefore allowing comparisons with the EELS experimental data. Initially, a single isolated nanorod was studied and subsequently modelled. It was found that

to accurately represent the experimental data, both the substrate and any surfactant layer had to be accounted for.

Following this, unsupported nanorod dimers were analysed. It was concluded from the modelling results that the longitudinal mode should split into both a bright and dark mode as the coupling strength increased. This therefore supports the predictions of the plasmon hybridisation model. Unsupported dimers were also analysed using experimental EELS, however no coupling was found for dimers which had a large spacing. Alternatively, as the spacing was reduced it is believed that coupling occurred splitting the longitudinal mode into both bright and dark modes. This was confirmed by analysing EELS spectra by location and noting that the dark mode disappeared when the electron beam was located in the centre of the dimer, as expected based on charge symmetry requirements.

Supported nanorod dimers were then studied both by experimental EELS and modelling. The modelling found that the substrate would lead to a red-shift in the plasmonic resonance due to coupling with its substrate image. It also had the effect however of causing the dipole mode to be stronger and in turn allow coupling between the nanorods up to greater distances. This result was also supported by the experimental data whereby a supported nanorod dimer was found to split into bright and dark modes, and that its resonance position was greatly red-shifted compared to an unsupported nanorod of the same aspect ratio. For supported nanorod dimers of different aspect ratio, it was further found that the dark mode could still be excited within the dimer gap due to the symmetry being broken. In this case, it was determined that coupling was still occurring based on studying the intensities of each mode and noticing that they did not monotonously decrease with increasing distance, as would be expected for uncoupled nanorods.

Furthermore, the effect of going from a dimer to an array of several nanorods was studied. Modelling showed that the longitudinal mode splits into additional modes equal to the number of interacting nanorods. These modes have both symmetric and anti-symmetric configurations of their dipoles and therefore may be considered hybridised bright and dark modes. Experimentally, these multiple peaks were also seen. However, analysing whether coupling had occurred proved challenging. A number of factors relating to the intensities of the modes seen as a function of the location of the electron beam led me to conclude that coupling did occur within the array. This likely led to multiple hybridised modes being formed consisting

of both bright and dark elements. Additionally, there was also evidence that the bright mode of the array may have resulted in the electric field distribution altering to one whereby an oscillation over the width of the nanorods occurred. This therefore matches that found within the modelling work of Chapter 5 for infinite nanorod arrays. Lastly, it was found that a number of very low energy modes (in the terahertz region) occurred within the experimental EELS data. These were due to the substrate being of finite length and therefore it was able to support its own localised surface plasmon resonances.

# 7 NANOROD ARRAYS FOR PHOTOCATALYTIC REACTIONS

So far this thesis has demonstrated the ability to fabricate ordered gold nanorod arrays supported on a substrate by means of using AAO membranes as templates. These nanorod arrays were then characterised by means of UV-Vis, FEM modelling, and EELS so as to ascertain their optical properties. This chapter will address the application of these nanorod arrays in regards to photocatalytic applications. This will begin with a brief review of the concept and motivation behind using plasmonic nanostructures for photocatalytic purposes, before then demonstrating the preliminary results achieved in this work.

## 7.1 Review of Plasmonics for Photocatalytic Reactions

In general terms, a photocatalyst is a semiconductor that absorbs photons in order to produce electron-hole pairs that partake in the reduction and/or oxidation of chemical species <sup>(259)</sup>. With the need to switch to a low carbon society, photocatalysts are expected to play an increasing role within the 21<sup>st</sup> century including applications ranging from the removal of environmental pollutions <sup>(260, 261)</sup>, to the generation of solar fuels such as hydrogen from water splitting <sup>(262, 263)</sup>. Despite this, current issues relating to the photocatalytic efficiency still need to be addressed in order for the technology to reach its full potential. For example, the semiconductors typically used in photocatalysis have bandgaps that absorb only the UV

region, accounting for only 4% of sunlight <sup>(264)</sup>. Additionally, the photogenerated electrons and holes may suffer from recombination thereby also reducing the efficiency <sup>(264)</sup>.

The use of plasmonic metal nanoparticles has shown excellent potential in solving these issues based upon a number of mechanisms. For instance, as has been shown throughout this work, the plasmonic resonances of gold nanoparticles may be tuned throughout the visible and near-infrared spectrum by means of carefully controlling the geometry, size, and coupling of the nanoparticles. These plasmonic resonances give rise to improvements in the optical cross-sections to levels greater than their geometrical equivalent, in addition to the generation of highly localised and enhanced electric field strengths. Furthermore, a typical semiconductor photocatalyst such as TiO<sub>2</sub> will only utilise the UV region of sunlight when placed in isolation owing to its large bandgap of 3.2 eV. With the addition of a plasmonic nanoparticle however, this absorption can be extended into the visible or near-infrared region of light by the metal particle according to the position of its plasmonic resonance. A number of mechanisms may then occur whereby the energy absorbed by the metal nanoparticle is transferred to that of the semiconductor, thereby allowing the utilisation of more of the solar spectrum. The motivation behind plasmonic photocatalysis is therefore to combine these beneficial effects with those of a photocatalytic semiconductor. This is achieved by understanding the different mechanisms by which the plasmons energy is transferred to that of a nearby semiconductor. Although many aspects of these enhancement mechanisms are still under debate, a summary of the current theories will be outlined in addition to experimental results.

### 7.1.1 Increased Plasmonic Scattering

Firstly, it is important to appreciate the various ways a plasmon may decay. After excitation, a plasmon may undergo either radiative decay or non-radiative decay. In the former, a photon is re-emitted from the plasmonic nanoparticle (i.e. scattered) with this primarily occurring for large particles over 100 nm in size <sup>(21)</sup>. This mechanism has predominantly been explored for use in thin-film solar cells whereby the path length of the light may be increased by repeatedly scattering the photons into the active semiconductor layer <sup>(265)</sup>. In contrast, plasmonic scattering for photocatalytic purposes is relatively unexplored and therefore will not be discussed further. Instead the non-radiative decay routes are generally preferred for enhancing photocatalysis and therefore small nanoparticles with high absorption of light are more suited.

## 7.1.2 Hot Electron Transfer

The non-radiative decay of a plasmonic resonance causes the excitation of energetic charge carriers above the Fermi level, resulting in the generation of so called “hot electrons” (or “hot holes”) <sup>(266)</sup>. In an isolated picture these hot electrons initially relax on a timescale of a few hundred femtoseconds by electron-electron scattering, whereby a Fermi-Dirac distribution is regained but at elevated temperature. This elevated temperature is then cooled by subsequent electron-phonon scattering, and finally phonon-phonon relaxation, thereby returning to its original state <sup>(59, 259, 267)</sup>. Alternatively, when a metal nanoparticle is placed in direct contact with a semiconductor (typically n-type in photocatalysis), a potential barrier known as the Schottky barrier forms which inhibits electrons transferring from the metal to the semiconductor. This will be discussed in more detail later, however it is important to note that the barrier height can be significantly lower than the semiconductor’s bandgap <sup>(268)</sup>. Typically, electrons would not have sufficient energy to transfer to the semiconductor, however, under plasmonic resonance the hot electrons generated in the metal nanoparticle may have an energy higher than the Schottky barrier and therefore directly transfer across <sup>(269, 270)</sup>. This occurs in an analogous manner to the working principle of dye-sensitised solar cells and therefore is often termed plasmon sensitisation, however, in this scenario the injected electron / hole can instead partake in redox reactions <sup>(271)</sup>. Importantly, as the photon energy required to generate the hot electrons that subsequently transfer over to the semiconductor is lower than that of the semiconductors bandgap, this allows greater utilisation of the solar spectrum into the visible and even near-infrared regions. This principle is demonstrated in Figure 7.1 below:

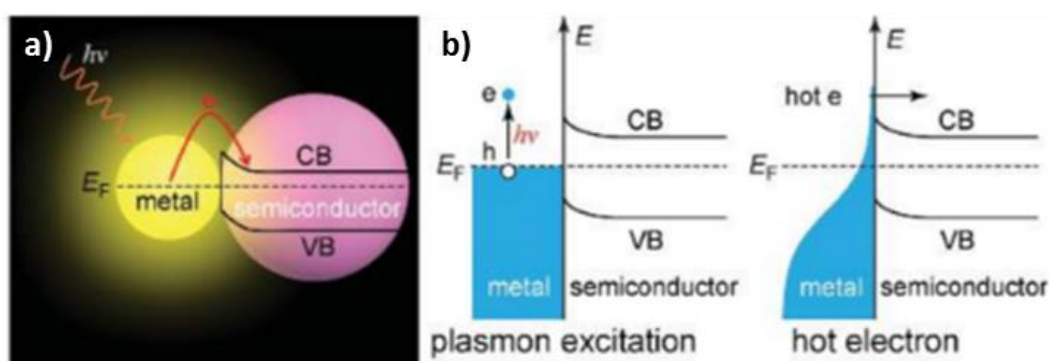


**Figure 7.1: a) Schematic of the generation of a hot electron b) Diagram of hot electron excitation and injection in to an adjacent semiconductor. CB and VB are the conduction and valence bands of the semiconductor respectively, whereas  $E_F$  is the Fermi energy level. Adapted from <sup>(22)</sup>.**

Referring back to the presence of a Schottky barrier, despite this generally acting against the transfer of electrons from the metal to the semiconductor (assuming it is n-type), it may also provide an advantage in photocatalytic applications. This is due to a space charge region forming whereby some electrons in the semiconductor migrate to the metal. This leads to a positively charged region in the semiconductor which in turn generates an internal electric field from the semiconductor to the metal. On generation of charge carriers near the space charge region (including the transferred hot electrons that have overcome the Schottky barrier), the electric field forces separation of the electron-holes whereby the holes are transferred towards the metal nanoparticle and the electrons away, thereby preventing their recombination <sup>(259)</sup>.

Experimentally, hot electron transfer has been demonstrated by Knight *et. al.* <sup>(272)</sup> whereby uncoupled horizontal gold nanorods of various AR were supported on a silicon substrate and attached via a small titanium buffer layer. The titanium layer created the presence of a Schottky barrier with a height of 0.5 eV, which in turn allowed the transfer of hot electrons across when the plasmonic resonances of the nanorods were excited. This transfer of electrons created a photocurrent that could be compared to the incident wavelength and polarisation used. It was found that the photocurrent matched extremely well to the expected resonance conditions for the nanorods according to their aspect ratio and orientation. Additionally, this photocurrent occurred even for the longer aspect nanorods with resonances above 1600 nm (0.77 eV), therefore demonstrating the ability to capture other regions of the solar spectrum <sup>(272)</sup>.

Additionally, Lee *et. al.* <sup>(146)</sup>, and in follow up work, Mubeen *et. al.* <sup>(145)</sup>, fabricated a gold nanorod array using the AAO template method. TiO<sub>2</sub> was deposited on top of the nanorods by electron beam deposition in order to facilitate hydrogen production from water splitting. The TiO<sub>2</sub> was not intended to play a significant role as a photocatalyst, but instead to act as an electron sink where the hot electrons could be collected and transferred to a platinum mesh or attached platinum particles and undergo reduction of hydrogen ions. Additionally, a cobalt/borate oxygen evolution catalyst was electrochemically deposited on the side of the rods to allow oxidation of water thereby completing the other half reaction. The concept was that the electrons received by the oxygen evolution catalyst were then transferred back into the nanorod, filling the positive holes left behind after the hot electron emission. This therefore meant that water splitting could occur on each nanorod individually when illuminated with light. The results showed that hydrogen production was greatly improved in

the visible region as compared to the UV region. The action spectrum (rate of activity vs wavelength) and extinction spectrum of the nanorods also matched very closely, therefore alluding to the plasmonic nature of the reaction. Finally, the photocurrent was seen to increase with decreasing TiO<sub>2</sub> thickness signifying that TiO<sub>2</sub> was not responsible for electron-hole production, but instead that thinner layers resulted in a lower probability of recombination or hot electron thermalisation<sup>(145, 146)</sup>.

Finally, it should also be noted that hot electrons may also participate in the reduction of adsorbates directly on a plasmonic nanoparticle without the need for a Schottky junction. For example, Robotjazi *et. al.*<sup>(273)</sup> created a device for water splitting whereby plasmonic gold nanoparticles were used to generate hot carriers. A p-NiOx substrate layer then separated the carriers by transporting the hot holes away to a counter electrode and blocking the movement of the hot electrons. The hot electrons instead propagate to the surface of the nanoparticle where they are directly transferred into absorbed water molecules to perform the hydrogen evolution reaction<sup>(273)</sup>. This setup has the advantage that a Schottky barrier does not have to be overcome, plus it negates the need for expensive co-catalysts such as platinum.

### 7.1.3 Plasmon-Induced Resonant Energy Transfer (PIRET)

Plasmonic nanoparticles have also been shown to provide enhancements to photocatalytic reactions when the semiconductor is separated from the metal nanoparticle by an insulating layer<sup>(274-276)</sup>. In this scenario, the hot electrons would be unable to transfer to the semiconductor and participate in the reaction, therefore an alternative mechanism is required. It has been proposed by Linic *et. al.*<sup>(277)</sup> that if the plasmonic nanoparticles are sufficiently close to the semiconductor, the strong electric fields surrounding the metal particle may overlap with the semiconductor causing an increased rate of interband transitions and therefore electron-hole production. This process works on the basis that electron-hole generation is proportional to local electric field intensity  $|E|^2$  in the semiconductor<sup>(277)</sup>. This mechanism however also requires that there is an overlap between the semiconductors absorption energy and that of the plasmonic resonance and incident photon<sup>(28)</sup>. This means that the plasmonic resonance needs to have its resonance somewhat towards the UV region, and therefore is typically found for silver nanoparticles. The principle of near-field enhancement can be seen in Figure 7.2.

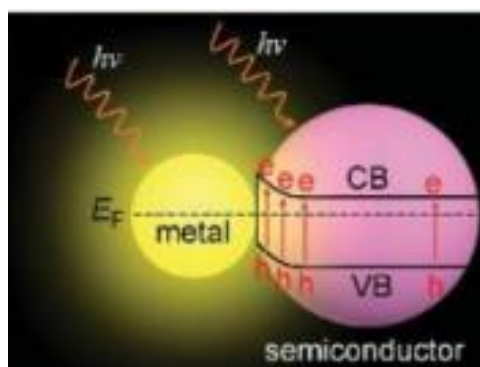


**Figure 7.2: Schematic of the electron-hole formation in a semiconductor based upon plasmonic near field enhancement. Greater electron-hole formation occurs in the region close to the metal nanoparticle. Adapted from <sup>(22)</sup>.**

Although the end effect is identical, an alternate method by which plasmonic nanoparticles are hypothesised to transmit energy to a semiconductor over an insulating layer is that of non-radiative dipole-dipole coupling. As first proposed by Cushing *et. al.* <sup>(278)</sup> in 2012, this states that the non-radiative decay of the surface plasmon dipole directly generates electron-hole pairs in the semiconductor. This occurs in an analogous manner to Förster Resonance Energy Transfer (FRET), however proceeds in the opposite energy direction <sup>(279)</sup>. For example, in FRET a donor dipole transmits its energy to an overlapping lower energy acceptor dipole. In the case of a plasmonic metal – semiconductor system, this therefore results in the quenching of the semiconductor by energy transfer to the metal, and may be considered a back-reaction <sup>(21)</sup>. On the other hand, with PIRET the plasmonic nanoparticle has a very strong dipole and instead acts to transmit the energy to the overlapping higher energy semiconductor <sup>(278)</sup>. These processes are both summarised in Figure 7.3 below:

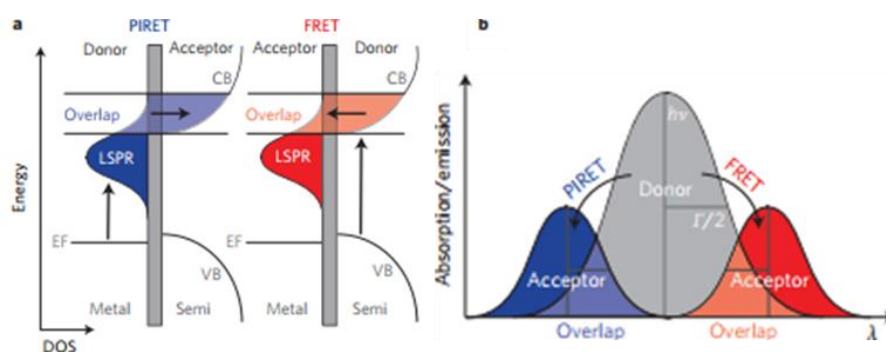


**Figure 7.3: Schematic illustrations of the PIRET and FRET processes. a) In PIRET the LSPR is excited and transfers its energy to an overlapping higher energy semiconductor, whereas in FRET the semiconductor is excited and transfers its energy to the overlapping lower energy metal. b) In both cases the donor has to have an overlapping energy with the acceptor. <sup>(279)</sup>**

Regardless of the exact energy transfer mechanism, a beneficial feature of PIRET is that it not only allows an increased generation of electron-holes, but that these charge carriers also tend to be produced in regions that are close to the surface of the semiconductor (i.e. the metal-semiconductor-liquid interface), as shown in Figure 7.2. This is due to the spatial locality of the electric fields, which varies depending on the geometry, plus its exponential decay in intensity with increasing distance from the metal surface<sup>(277)</sup>. This proximity to the liquid interface and plasmonic nanoparticle is important as it reduces the probability of charge recombination by ensuring shorter diffusion distances to reaction sites, plus it allows the charges produced to be close enough to encounter the effect of plasmonic Schottky barrier charge separation.

Experimentally, Awazu *et. al.*<sup>(274)</sup> found a seven times enhancement in the decomposition of methylene blue for Ag nanoparticles coated in a SiO<sub>2</sub> shell and supported on a TiO<sub>2</sub> layer when illuminated with near UV wavelengths. Additionally, it was found that the enhancement was increased as the SiO<sub>2</sub> shell thickness was reduced, i.e. as the electric field strengths in the TiO<sub>2</sub> increased. Similarly, Kumar *et. al.*<sup>(275)</sup> also reported the degradation of methylene blue using SiO<sub>2</sub> coated Ag nanoparticles on TiO<sub>2</sub>. Once again they reported an increase in photocatalytic performance with decreasing SiO<sub>2</sub> thickness, confirming this to be due to PIRET by means of photocurrent measurements and Raman spectroscopy.

Thomman *et. al.*<sup>(280)</sup> also measured the photocurrent enhancements for 50 nm gold nanoparticles coated in SiO<sub>2</sub> and placed on top of a Fe<sub>2</sub>O<sub>3</sub> semiconductor. A peak enhancement of eleven times was recorded with this enhancement primarily occurring at the plasmonic resonant wavelength. Lastly, Torimoto *et. al.*<sup>(281)</sup> fabricated gold nanoparticles coated in a 17 nm thick SiO<sub>2</sub> layer with CdS semiconductor nanoparticles attached on the outside. They found that compared to CdS nanoparticles without gold, the addition of the plasmonic metal led to higher rates of hydrogen production. Interestingly, it was also noted that when using a thinner layer of SiO<sub>2</sub> (2.8 nm), the hydrogen production rate dropped even compared to the non-plasmonic experiment. This was attributed to FRET transfer from the semiconductor to the gold nanoparticle, thereby quenching the reaction.

#### 7.1.4 Localised Heating by Plasmonic Nanoparticles

Photocatalysis by means of local heating has also been reported<sup>(282, 283)</sup>. This local heating occurs due to the non-radiative decay of a plasmon and can result in significant increases in temperature<sup>(284)</sup>. The exact temperature rise is dictated by the local environment and the

power of the incident light used. For example, when using relatively low power light sources such as mercury or xenon lamps, the heating is believed to be negligible<sup>(22, 285)</sup>. Alternatively, if high powered pulsed lasers are used for illumination, then heating effects are expected to play a major role in enhancing photocatalytic reactions due to an increase in the reaction rate according to the Arrhenius equation<sup>(286)</sup>. This was demonstrated by Bora *et. al.*<sup>(283)</sup> whereby the degradation of methylene blue was achieved by illuminating a ZnO nanowire array coated with gold nanoparticles on top using visible light. The photocatalytic activity was doubled compared to bare ZnO nanorods, with temperatures predicted to reach 300°C, along with a 6x increase in the apparent quantum yield. These results were attributed to heating as opposed to other mechanisms by the authors, however, although localised heating likely played a role, I am doubtful that it was the main contribution compared to the other mechanisms.

Following this outline of the various plasmonic enhancement mechanisms, a brief overview of how these benefits may be transferred to that of the gold nanorod arrays produced in this work is given so as to optimise the design.

### 7.1.5 Plasmonic Photocatalysis in Gold Nanorod Arrays

Considering the above plasmonic photocatalysis enhancement mechanisms, the fabricated gold nanorod arrays produced in this work will now be discussed with regards to optimising them for photocatalytic reactions. Firstly, it is highly desirable to fabricate a photocatalytic platform which is not only efficient at capturing visible light, but also stable in operation and able to be manufactured on a large scale relatively cheaply. By using the AAO template method with gold nanorods, it is hoped the latter two objectives are achieved, however it is also important that the photocatalyst used is also similarly stable. TiO<sub>2</sub> has been widely used since its discovery as a photocatalyst and is well known for its excellent stability<sup>(287)</sup>. This therefore makes a logical choice for use as the semiconductor on the nanorods. Unfortunately, TiO<sub>2</sub> also only absorbs in the UV region of the solar spectrum whereas the gold nanorods primarily have their plasmonic resonance in the visible or near-infrared region. This would mean that an overlap in the spectrum between the TiO<sub>2</sub> and nanorod absorption would likely be inaccessible, and therefore the PIRET mechanism would not enhance the photocatalysis.

On the other hand, the hot electron transfer mechanism is able to utilise the visible spectrum by injecting hot electrons or holes directly into the TiO<sub>2</sub>. Indeed this was shown in the previously discussed work of Lee *et. al.*<sup>(146)</sup>, and Mubeen *et. al.*<sup>(145)</sup>, for hydrogen production by water splitting. Considering this, it is critical to the design that the TiO<sub>2</sub> layer is in direct

contact with that of the gold so that a Schottky barrier is formed. Additionally, it is proposed that the thickness of the layer is not of utmost importance as the TiO<sub>2</sub> is not predominantly responsible for absorption in the hot electron mechanism. Instead thinner semiconductor layers have been shown to lead to higher enhancements due to less charge recombination<sup>(288)</sup>.

To date, the majority of work studying hot electron generation within vertically aligned plasmonic nanorod arrays has been by the Moskovits research group<sup>(289)</sup>. This research however has primarily focussed on the generation of hydrogen via water splitting<sup>(145, 146)</sup> as previously discussed, or alternatively for photovoltaics<sup>(288)</sup>. In contrast, the work on reduction of pollutants by these coated nanorod arrays is significantly less, with an article by Lu *et. al.*<sup>(290)</sup> being the only example. In this work, a gold nanorod array was fabricated in Whatman AAO membranes with resulting diameters of 200-250 nm, and lengths of approximately 900-1000 nm. These were supported on a silver substrate and had 150 nm TiO<sub>2</sub> particles spin coated on the nanorods so that a complete coverage was achieved, resulting in a core shell structure. The array was then illuminated with UV light in order to perform photocatalytic degradation of rhodamine B. A factor of two increase was found for the TiO<sub>2</sub> coated nanorod array compared to TiO<sub>2</sub> in isolation. Similarly, only a 1.3× increase was found for a flat Au TiO<sub>2</sub> film. This enhancement was attributed to efficient separation of carriers due to the presence of a Schottky barrier, plus additionally, a higher surface to volume ratio based on the nanorod geometry<sup>(290)</sup>.

Unfortunately, this work omitted a number of important concepts. For example, the plasmonic nature of the gold nanorods was completely ignored based on illuminating only with UV light. This therefore meant the levels of hot carriers produced by the nanorods would have been very low, plus the semiconductor would not have benefitted from any PIRET mechanisms. Instead the electron-hole generation relied on absorption by the TiO<sub>2</sub>. As this is relatively thin, the absorption would also likely be small and therefore the enhancements noted may have instead relied on other processes. For example, the presence of the silver substrate was also largely neglected however it may have resulted in higher UV absorption, possible PIRET mechanisms, and potentially the formation of hot carriers.

Considering this lack of utilisation of the plasmonic abilities of the nanorods, and the potential visible light benefits it brings, it is therefore believed a gap in the research is present. Namely this would aim to use gold nanorod arrays to perform degradation of pollutants in a similar

manner to the work of Lu *et. al.* <sup>(290)</sup>. In contrast however, visible light should be used whereby the plasmonic resonances of the nanorods are targeted with the aim of producing hot carriers that may transfer to the adjacent TiO<sub>2</sub> layer and participate in the photocatalytic degradation by oxidation/reduction reactions. This research will therefore be the aim of this chapter, with first the characterisation of the deposited TiO<sub>2</sub> performed, before then addressing the degradation of methylene blue over the nanorod array using visible light.

## 7.2 Characterisation of Titanium Dioxide Shell

The methodology behind the deposition of TiO<sub>2</sub> shell using atomic layer deposition (ALD) was previously discussed in Chapter 3, and therefore will not be covered again. Instead this section aims to characterise the deposited layer. This was primarily done by means of electron microscopy and X-ray photoelectron spectroscopy (XPS).

Firstly, SEM images of a nanorod array both before and after TiO<sub>2</sub> deposition are shown in Figure 7.4. It can be seen that the morphology of the nanorods clearly changes whereby the very ordered alignment of the nanorods becomes slightly more disordered, and the surface roughness appears changed going from smooth to somewhat uneven. There is also the suggestion that more of the nanorods are in contact with each other towards their ends, possibly as a result of either increasing in diameter, alterations to their surface charges, or simply due to a different area of the sample being imaged with slightly increased aspect ratio. Despite this, the nanorods are still evidentially still vertically aligned with the majority having open areas surrounding the nanorods that could act as reaction sites. The increased surface roughness is likely due to either the temperatures involved with the ALD deposition causing uneven growth, or due to the pre-treatment steps whereby the sample was rinsed with acetone and isopropanol, before plasma cleaning.

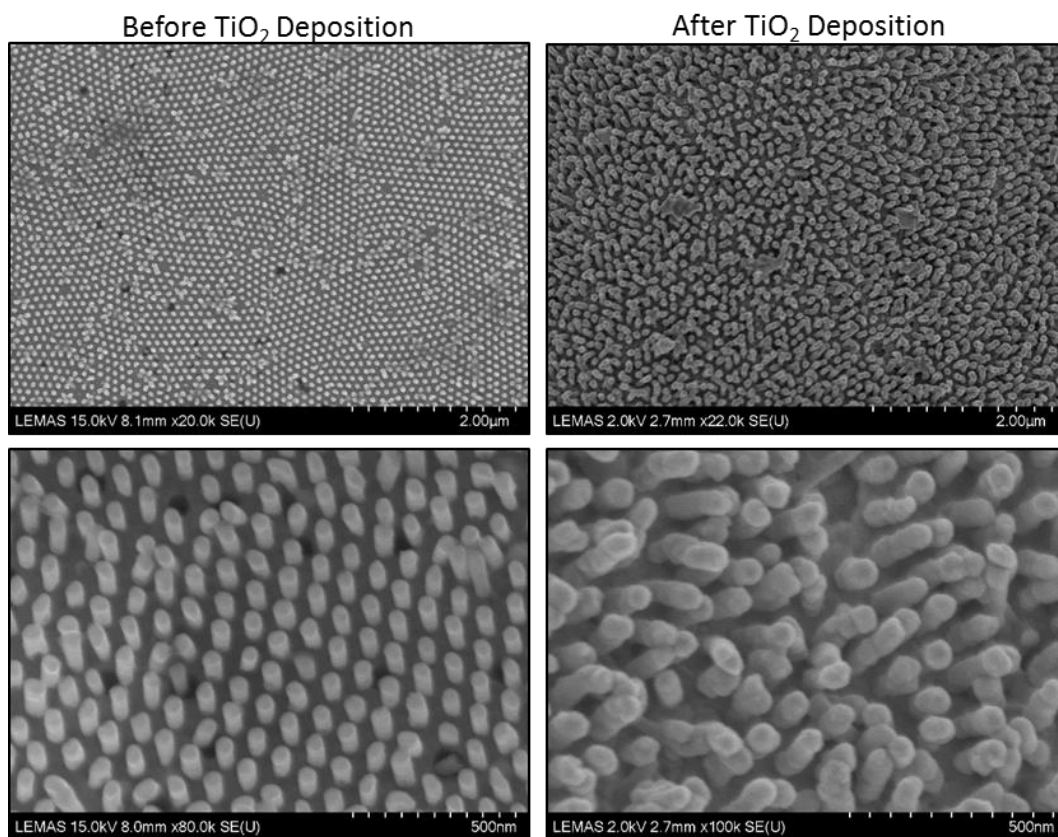


**Figure 7.4: SEM images of a nanorod array both before (left) and after (right) TiO<sub>2</sub> deposition (Sample 1). The top row shows a top down view of the nanorods whereas the bottom row shows a tilted view.**

The diameter of the nanorods shown in Figure 7.4 before TiO<sub>2</sub> deposition is on average 51 nm  $\pm$  6 nm whereas the length is estimated at *ca.* 180 nm (AR = 3.6). Alternatively, following the TiO<sub>2</sub> deposition the diameter is seen to increase to approximately 65 nm  $\pm$  5 nm. This would therefore translate to a diameter increase of  $\sim$ 14 nm, giving a shell thickness of  $\sim$ 7 nm. This sample will be referred to as sample 1 throughout the remainder of this work. Alternatively, a second nanorod array with an average diameter of  $\sim$ 68 nm  $\pm$  2 nm and an AR of 2.3 was also coated in TiO<sub>2</sub>, and will instead be referred to as sample 2. The corresponding SEM images for this sample both before and after ALD can be viewed in appendix 5. In contrast, sample 2 was found to have an average diameter of  $\sim$  68 nm before deposition and  $\sim$  90 nm  $\pm$  4 nm after, therefore giving an estimated shell thickness of  $\sim$ 11 nm.

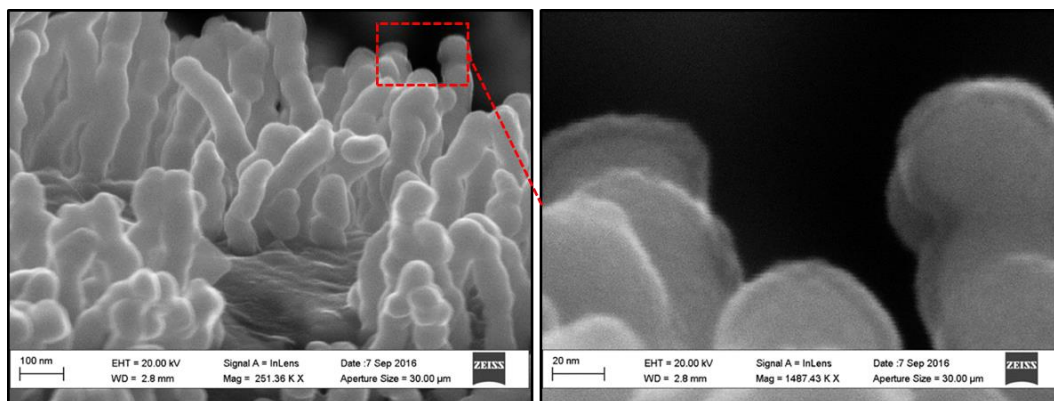


**Figure 7.5: Tilted SEM images of Sample 1 showing the presence of a layer on the surface of the nanorods when using an accelerating voltage of 20 kV. With thanks to Dr. Mark Rosamond, University of Leeds.**

A higher magnification SEM image of Sample 1 at 20 kV and with the sample tilted can be seen in Figure 7.5. This reveals the presence of a layer on the surface of the nanorods that is believed to be the  $\text{TiO}_2$ . It should be noted that at lower accelerating voltages, this layer is no longer visible (*not shown*). Performing measurements of this layer using ImageJ revealed the thickness is relatively even at approximately  $8.38 \text{ nm} \pm 0.46 \text{ nm}$ . This therefore is reasonably close to that estimated by the increase in diameter of the lower magnification SEM images.

To ascertain for certain that the nanorods are coated in  $\text{TiO}_2$  and not some alternate material, a surface sensitive technique is required. For this XPS was chosen due to its excellent ability in determining the surface composition. Furthermore, this is combined with Parallel Angle-Resolved XPS (PAXPS) to reveal additional information regarding how the surface layers change with depth. This was performed on a flat film Au- $\text{TiO}_2$  structure coated under the same conditions as those used for the nanorods arrays. The PAXPS measurements were acquired with thanks to the National EPSRC XPS Users' Service (NEXUS)<sup>(291)</sup> on a Thermo Theta Probe XPS spectrometer. This was performed over angles from  $25^\circ$  to  $75^\circ$ , with a spot size of 400x800 microns, and repeated in three separate areas. Alternatively, the non-angle resolved XPS measurements were acquired on a Thermo Scientific ESCA Lab 250 with a spot size of 500 microns. All data analysis was subsequently performed with CasaXPS software<sup>(292)</sup>. This involved correcting all spectra for charging by setting the adventitious carbon C 1s peak to a binding energy of 284.5 eV.

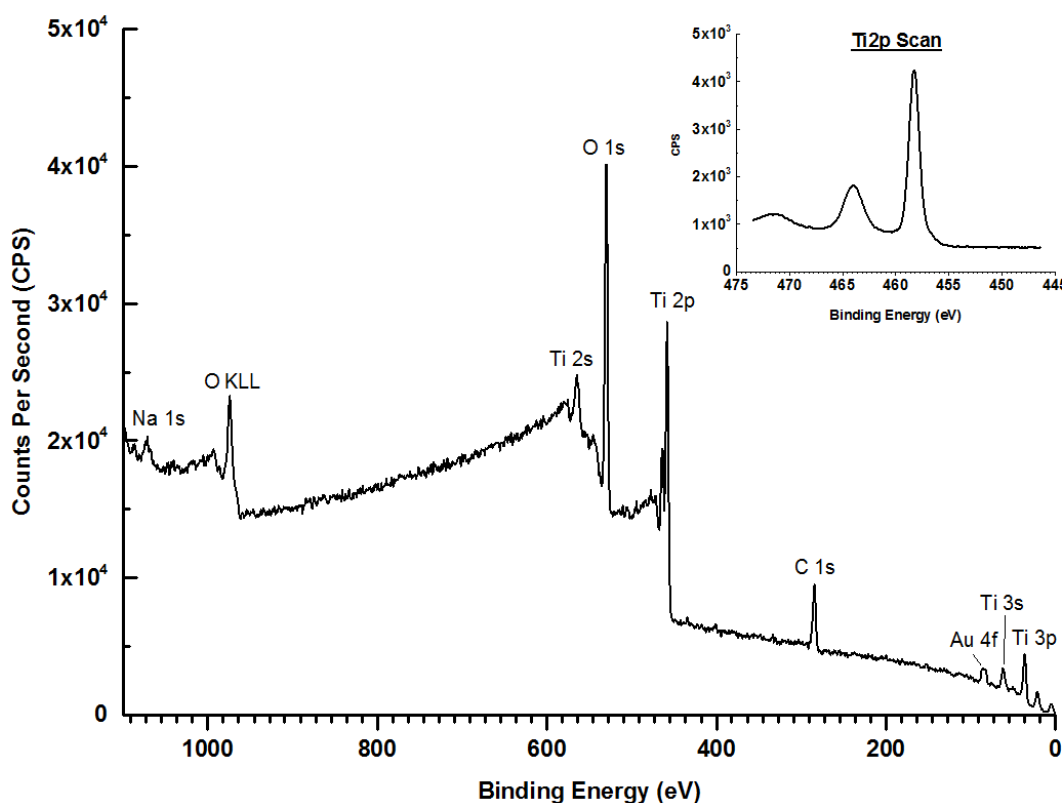


**Figure 7.6:** XPS survey of Sample 2 showing the presence of both titanium and oxygen. The inset shows the corresponding high resolution Ti2p Scan.

The XPS survey for sample 2 can be seen in Figure 7.6, along with an inset showing the higher resolution Ti2p scan. Alternatively the XPS survey and Ti2p scan for Sample 1 is shown in Appendix 6. Both of these surveys show that titanium and oxygen is present within the samples, therefore suggesting TiO<sub>2</sub> was deposited on the surface. Based on the gold counts being relatively small in Sample 2, it is also suggested that almost complete coverage of the nanorods was achieved. This is due to the ALD method being excellent at growing homogeneous thin films, and is expected based on the previously shown SEM images. Sample 1 on the other hand exhibits a more prominent gold peak perhaps due to the TiO<sub>2</sub> layer being estimated from SEM to be thinner, or due to the coverage of the gold not being as high.

In addition to the titanium, oxygen and gold, the survey also reveals small levels of carbon and sodium. The carbon is likely due to contamination from the adhesive copper support as XPS surveys conducted before the acetone and plasma cleaning stage reveal that carbon contamination dominates (see Appendix 7). This therefore shows that it is crucial to remove the adhesive layer from the copper support, or alternatively, use a separate non-contaminating

material before the ALD process. On the other hand, the sodium is likely a result of residue from the NaOH etch of the AAO template.

Studying the high resolution Ti2p scan in the inset of Figure 7.6 in more detail reveals the Ti2p peak is made up of a prominent peak at a binding energy of 458 eV, followed by two further weaker peaks at 464 eV and 472 eV. When comparing these positions to the shifts expected for TiO<sub>2</sub> as obtained from literature<sup>(293, 294)</sup>, the peaks match extremely well therefore signifying that it is in fact TiO<sub>2</sub> present on the surface.

Further information can be gained from the XPS data by performing elemental analysis as shown in Table 4. For this, high resolution spectra were obtained for the carbon, gold, titanium, sodium and oxygen peaks, with Shirley backgrounds fitted to all. Comparing the atomic percent of each element shows that a few differences exist between Sample 1 and Sample 2. For example, Sample 1 has a higher amount of gold and carbon, and a lower amount of oxygen and titanium than Sample 2. This therefore suggests again that the TiO<sub>2</sub> coating on Sample 2 is thicker and perhaps has a higher coverage compared with Sample 1. Additionally, it may also be the case that the pre-cleaning of the copper support was not as successful for Sample 1 leading to higher amounts of carbon contaminating the gold nanorods surface during deposition.

**Table 4: Elemental analysis showing the atomic percent of each element.**

ELEMENTAL ANALYSIS	Au 4f %	C 1s %	Na 1s %	O 1s %	Ti 2p %
Sample 1	5.74	60.6	0.89	27.09	5.67
Sample 2	0.65	29.32	1.92	47.55	20.56

Additionally, the atomic percent's may be normalised to that of titanium, as shown in Table 5. This allows the comparison of the titanium to the oxygen, whereby if all the oxygen was to derive from the TiO<sub>2</sub> you would expect a ratio of 2:1. It is seen that this is nearly the case for Sample 2, once again suggesting that the surface is primarily composed of TiO<sub>2</sub>. Alternatively for Sample 1 the oxygen ratio is 4.78 meaning the oxygen must also be bonded with other species, most likely carbon.

**Table 5: Elemental analysis showing the atomic ratios relative to titanium.**

ELEMENTAL ANALYSIS	Au 4f	C 1s	Na 1s	O 1s	Ti 2p
Sample 1	1.01	10.69	0.16	4.78	1
Sample 2	0.03	1.43	0.09	2.31	1

Lastly, the PAXPS measurements were analysed for a flat gold film with TiO<sub>2</sub> deposited on top using the same ALD conditions as for the samples. In these measurements, the angles quoted are relative to the surface normal. Smaller angles are able to probe deeper into the material and therefore contain more information on the bulk elements, whereas for higher grazing angles, the bulk contributes less. These angle resolved measurements are shown in Figure 7.7 for both the Ti2p and Au4f peaks. These spectra have been normalised based upon their atomic percent concentration and offset from each other so as to identify trends in the peaks. It may be seen that the Ti2p peaks do not vary greatly as the angle is altered as would be expected for a material on the surface. In contrast, the Au4f peak is seen to drastically decrease in intensity at higher angles. As this is when the technique is most surface sensitive, this therefore signifies that the gold is below the titanium and forms the bulk material. Considering this, it is therefore assumed that the gold was successfully coated in a TiO<sub>2</sub> layer. As the XPS technique probes only the top 10 nm or less of the surface, it is therefore believed this TiO<sub>2</sub> layer is approximately slightly less than 10 nm, therefore supporting the results from SEM imaging.

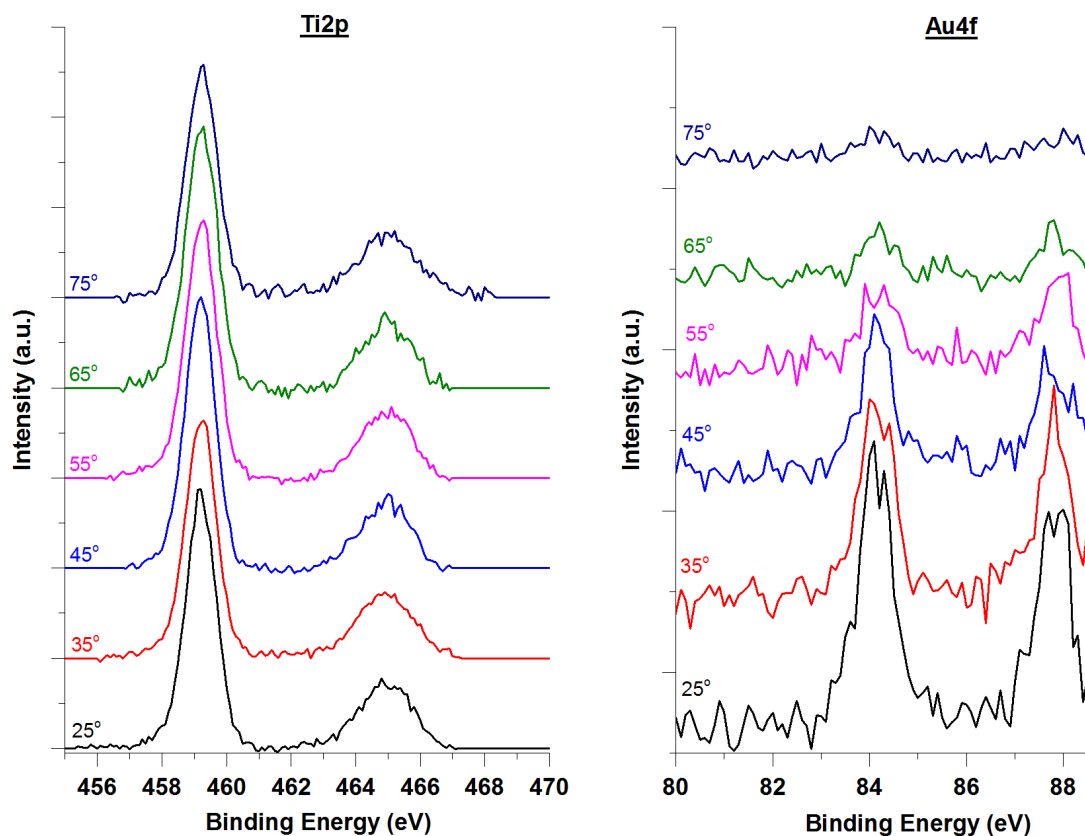


**Figure 7.7:** PAXPS spectra for the Ti2p and Au4f peaks at varying collection angles relative to the surface normal. The spectra have been normalised based upon their atomic percent concentration and offset from each other in the y-direction.

## 7.3 Photocatalytic Abilities of Nanorod Arrays

Following the successful characterisation of the TiO<sub>2</sub> layer, the photocatalytic properties of the nanorod arrays will now be discussed. This will begin with a description of the methodology used in the methylene blue degradation experiments, before then outlining the results with discussion.

### 7.3.1 Methylene Blue Degradation Methodology

The photocatalytic activity of the TiO<sub>2</sub> coated gold nanorod arrays was tested using methylene blue as the organic dye due to its widespread use in other photocatalytic experiments<sup>(295-298)</sup>, its nature as a model dye<sup>(299)</sup>, and lastly due its large use in the textiles industry whereby around 10% is released as a pollutant<sup>(300)</sup>. High purity methylene blue obtained from Alfa Aesar was diluted with ultra-pure water to form a solution with concentration of 0.01 mg/ml. The solution was placed in a Quartz cuvette (supplied by Hellma Analytics) with light path of 2mm and volume of 700  $\mu$ l. This small volume was required due to the size of the samples being relatively small at approximately 0.5 cm<sup>2</sup>. The samples were subsequently placed within

the solution and left for 60 minutes in the dark so as to reach an adsorption-desorption equilibrium.

A 200 W Oriel Instruments 66002 Hg-Xe arc lamp with a 420 nm cut-off filter to remove UV-radiation was used to illuminate the samples. A control experiment was also performed using solely a methylene blue solution at the same concentration without the presence of any sample. The dye degradation was monitored by periodically removing the cuvette and performing UV-Vis measurements between the wavelengths of 300 – 800 nm. The absorption at 663 nm, therefore relating to the methylene blue peak absorption, was recorded and subsequently used to determine the percent degradation according to:

$$\text{Percent Degradation} = 100 * \left( \frac{A_0 - A_t}{A_0} \right) \quad (94)$$

Where  $A_0$  is the absorbance of the initial solution at 663 nm, and  $A_t$  is the absorbance of the solution at the interval time and again at 663 nm. The light intensity reaching the sample was measured using a photometer and initially adjusted to an intensity of 100 mW/cm<sup>2</sup>. Unfortunately, it was found that this power caused rapid photobleaching of the methylene blue solution in the control sample, likely due to the small volumes used. Instead, to obtain a control whereby degradation of the dye was minimal, this intensity was reduced to 5 mW/cm<sup>2</sup>. Despite this reduction in intensity, a small amount of photobleaching was still observed, however, this occurred at much reduced rates.

### 7.3.2 Methylene Blue Degradation Results

The results of the methylene blue degradation are shown in Figure 7.8 for both Sample 1 and Sample 2. The data is presented in relation to the percent degradation of methylene blue compared to its initial starting concentration following the adsorption-desorption phase. It may be seen that in contrast to what is expected, the presence of the samples showed a negligible increase in the degradation of methylene blue compared to the control, over a time period of 1 to 1.5 hours. There is perhaps a suggestion that there is a small enhancement within the first 30 minutes, however following this period, the rate of degradation appears unaltered from the control.

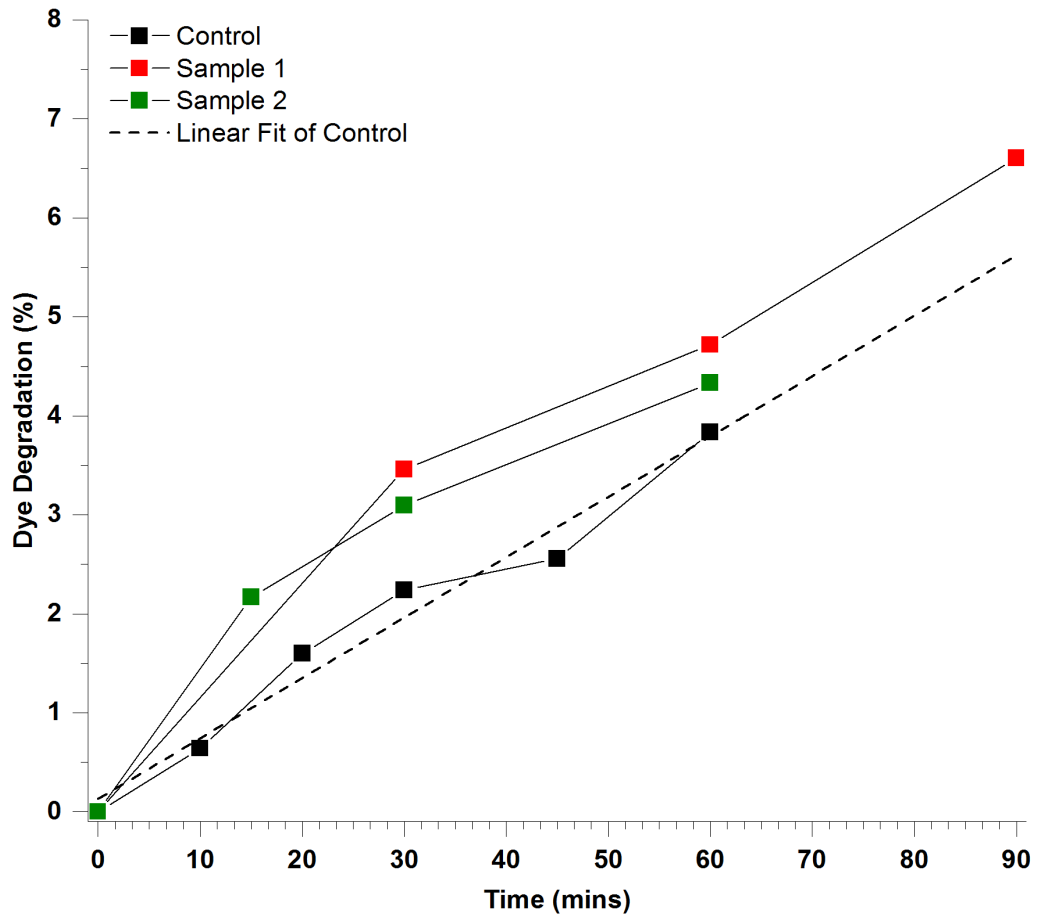


**Figure 7.8: Methylene blue dye degradation percentage for Sample 1, Sample 2 and a control with no sample. A linear fit is added to the control sample so as to clearly see the typical self-degradation rate.**

This result is unexpected as it was predicted that the visible light would excite plasmonic modes of the nanoparticles, which in turn would lead to the generation of hot carriers that are capable of transferring to the TiO<sub>2</sub> and degrading the dye by means of producing highly reactive radicals such as  $\cdot\text{OH}$  and  $\text{O}_2\cdot^-$  <sup>(296)</sup>. Unfortunately, as no appreciable degradation was seen, one or more of these processes must be unable to occur.

An explanation can be found by noting the difference of this experiment compared to that of Lu *et. al.* <sup>(290)</sup> whereby dye degradation was noted for similar gold nanorod TiO<sub>2</sub> arrays. These differences are that Lu *et. al.* did not attempt to utilise the plasmonic hot electron mechanism of the structure to enhance photocatalysis, but instead used UV light to generate electron-hole pairs directly in the TiO<sub>2</sub>. It is therefore assumed that the lack of photocatalytic activity seen in my results arises from either an absence of hot carriers being produced, or an inability for these carriers to transfer to the reaction sites. It is believed the latter is the more likely

explanation due to the findings by Wu *et. al.* <sup>(301)</sup>. In this work the seeded growth method was used to produce gold nanorods which were subsequently coated in TiO<sub>2</sub> with an anisotropic distribution. This coating was such that only the ends of the nanorods were coated in TiO<sub>2</sub> whereas the sides were left exposed (Figure 7.9c). When performing visible light hydrogen production via water splitting (Figure 7.9a), or alternatively methylene blue degradation (Figure 7.9b), it was found the nanorods completely coated in TiO<sub>2</sub> showed little to no activity. This was attributed to the hot carriers being unable to both perform oxidation and reduction reactions. For example, it was proposed that hot carriers were produced due to the plasmonic nature of the nanorods with the hot electrons transferring across the Schottky barrier to the TiO<sub>2</sub> and undertaking reduction reactions. Alternatively the hot holes produced would remain in the gold nanorod, which without access to the solution would be unable to perform any oxidation reactions (Figure 7.9d). This results in the gold nanorod becoming positively charged which in turn would impede further loss of electrons and limit the rate of the reaction to that at which electrons could be resupplied to the particle <sup>(271)</sup>. Alternatively, for nanorods that were not fully coated and instead had a portion of the gold nanorod exposed, excellent visible light photocatalytic ability was noted <sup>(301)</sup>.

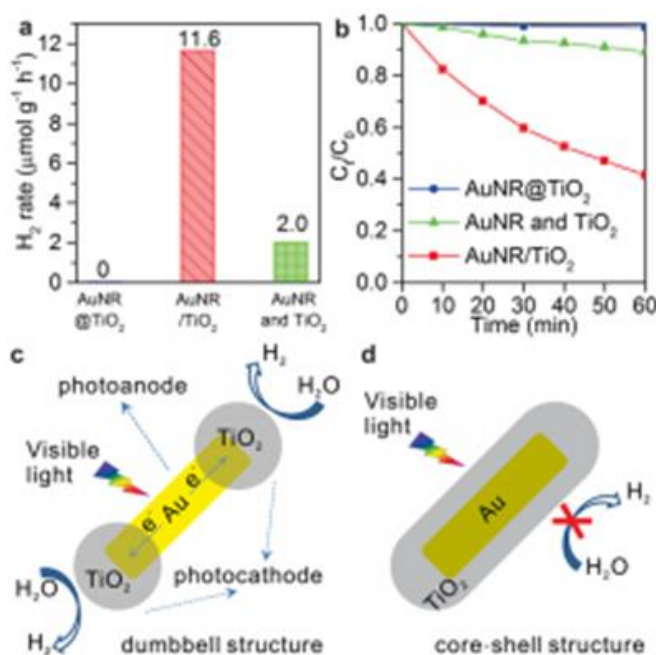


**Figure 7.9:** Wu *et. al.* <sup>(301)</sup> experimental results for a) H<sub>2</sub> production via water splitting and b) methylene blue dye degradation. AuNR@TiO<sub>2</sub> refers to a completely covered core shell particle (see d), AuNR/TiO<sub>2</sub> is for coverage of TiO<sub>2</sub> only the ends (see c), and AuNR and TiO<sub>2</sub> refers to a physical mixture of nanorods and amorphous TiO<sub>2</sub>. c) Schematic illustration of photocatalysis for anisotropic TiO<sub>2</sub> coverage compared to d) lack of photocatalysis for completely coated nanorods.

This explanation may also give insight into why a possible enhancement was seen in my experiments when the samples were first illuminated. For instance, the hot electrons may have successfully been produced and transferred to the TiO<sub>2</sub> to perform reduction reactions whilst the gold nanorod was neutral, thereby giving a small enhancement in degradation rate compared to the control. As electrons were lost however and not replaced by the opposing oxidation reactions, the gold nanorods would have become positively charged. This would have hindered their ability to transfer hot electrons to the TiO<sub>2</sub> and therefore limited the reaction rate to that equal to the photobleaching of the dye.

## 7.4 Summary

To summarise, in this chapter, the various plasmonic photocatalysis mechanisms have been discussed with the hot electron method being deemed the most suitable for application with the gold nanorod arrays. This mechanism was chosen as it is able to utilise visible light without the need for an overlap between the absorption of the semiconductor and the plasmonic resonance. Furthermore, TiO<sub>2</sub> has been successfully coated on the nanorod arrays using ALD, with characterisation achieved using electron microscopy and XPS. It was found that the TiO<sub>2</sub> was between 7-10 nm in thickness and covered the entire surface of the nanorods. Visible light photocatalytic experiments involving the degradation of methylene blue were performed, however, negligible increase in activity compared to the control was found. This is believed to be due to a lack of available sites by which oxidation reactions could occur, therefore impeding the ability of the nanorod to replenish lost electrons, and limiting the rate of the photocatalysis.

## CONCLUSIONS AND FUTURE WORK

As each results chapter within this thesis contained a detailed summary of the conclusions found within that specific chapter, these will not be repeated in full again here. Instead, this section will begin with a brief summary of the novel contributions this work has made, before subsequently highlighting the main conclusions in relation to the original thesis objectives, as outlined in section 1.4.2. This will then conclude with recommendations for future work.

### 7.5 Novelty of Results

This thesis has demonstrated a number of novel results. For example, in the characterisation of nanorod arrays by optical spectroscopy, previous work<sup>(132, 134, 194)</sup> has expressed transmission data in terms of optical extinction due to an inability to distinguish the scattering of the array from that of the absorption. In this work however, the use of an integrating sphere allowed the scattered radiation to be detected, thereby permitting the sole quantification of the absorption. It was found that for a nanorod array of AR=18, the scattering from the array dominated over that of the absorption, therefore signifying that the extinction cannot be assumed to approximate that of the absorption. Additionally, further novel results were also reported based upon the finite element modelling work shown in chapter 5. It was shown that when a gold nanorod array was supported on a gold substrate, coupling occurred between both adjacent nanorods, and in-between the nanorods and the substrate. This resulted in a competing process whereby the particle-particle coupling aimed to blue shift the longitudinal mode, whereas the particle-substrate coupling aimed to red-shift it. This coupling scenario led to a redistribution of the electric fields whereby they localised towards the base of the supported nanorods and appeared to propagate along the array, therefore potentially being useful in wave guiding applications<sup>(133)</sup>.

Furthermore, in regards to analysis of nanoparticle arrays via EELS, to date attention has primarily been restricted to that of nanoparticle dimers<sup>(237, 239, 302-305)</sup>. Although many of these studies have focused on the coupling between nanorods, this has been exclusively addressed to end-to-end orientations of nanorods laid horizontally on a substrate. On the other hand, the study of side-by-side orientated nanorod dimers by EELS has largely been neglected. In addition to this, only a few studies have attempted to characterise the effect of increasing the number of interacting particles. This was typically only extended to a trimer of nanoparticles<sup>(306-308)</sup>, although the work of Barrow *et. al.*<sup>(237, 309)</sup> proved the exception by analysing gold nanoparticles up to chain lengths of five. Similarly, previous studies have also largely omitted

the interaction of the nanoparticle with the substrate. As shown by the modelling results in this work, this can prove very important the case for nanorods stood vertically on a substrate of the same material.

The work shown within chapter 6 of this thesis addresses each of these omissions in previous work by analysing a side-by-side orientated nanorod array stood vertically on a gold substrate and consisting of multiple interacting nanorods. It was found that not only does the substrate lead to a drastic red-shift of the longitudinal mode resonant wavelength, but also as multiple rods interact within an array, additional modes are generated relating to hybridised states of bright and dark modes. It is hoped these novel results reported within this thesis will not only fill gaps within the knowledge, but also stimulate further experiments.

## 7.6 Fulfilment of Research Objectives

The degree of completion of the original research objectives outlined in section 1.4.2 is now addressed.

- 1. To fabricate porous membranes with accurate control over the size, separation and arrangement of the pores for use as templates in the growth of plasmonic nanostructures.**

The methodology and results in chapter 3 and 4 respectively show that AAO templates were successfully produced to a high standard. It was demonstrated that control over the geometry was possible by varying factors such as the electrolyte, its concentration, and the duration of the pore-widening stage. This resulted in control of the pore diameters with a range of between ca. 20 nm and 370 nm possible, and only a small degree of variance between pores. Similarly, the interpore spacing and resulting wall thickness could further be controlled by once again varying the above factors according to the empirical equations listed in chapter 3. Finally, by performing the anodisation on bulk aluminium using a two-step method, the pores were found to be hexagonally arranged with a large degree of order.

- 2. To fabricate regular arrays of plasmonic nanorods using the above mentioned templates, with control over their diameter, aspect ratio, spacing, arrangement and the area over which they are grown.**

It was found that by analysing the SEM images in chapter 4, electrodeposition within the AAO templates led to nanorod arrays being produced with their diameter, spacing, and arrangement governed by the template. Additionally, the aspect ratio of the nanorods was further determined by the duration of electrodeposition, with relatively homogeneous arrays produced with AR's ranging from short nanorods (AR~1) up to much longer nanorods (AR>10). These arrays were electrodeposited over large areas of typically several mm<sup>2</sup>, and in general demonstrated growth in the majority of pores even for the very short AR nanorods.

**3. To characterise the absorption and scattering properties of the nanorod arrays by UV-Vis spectroscopy, and tune the absorption to the visible region of the spectrum.**

By means of performing UV-Vis spectroscopy using an integrating sphere, the absorption, scattering and extinction of the nanorod arrays were determined, as shown in the results of chapter 4. It was found that the coupling within the array led to a large blue-shift of the longitudinal modes resonance wavelength, and highlighted that absorption in the visible region could be achieved by controlling the geometrical factors of the array. This was supported by means of the finite element modelling work in chapter 5, whereby the longitudinal mode was shifted throughout the visible spectrum by varying either the AR or the spacing.

**4. To characterise the near-field electric field enhancements and coupling effects in nanorod arrays by the use of electron energy loss spectroscopy.**

The results in chapter 6 analysed a section of a nanorod array using electron energy loss spectroscopy. Both the electric field distributions and the coupling within the array were characterised. This included cases of both nanorod dimers and more complex longer nanorod arrays, highlighting that both dark and bright modes occurred within the array due to coupling between the nanorods.

**5. To perform thorough simulations on the properties of plasmonic nanospheres and nanorods so as gain a deeper understanding of the fundamental mechanisms of operation and to guide the experimental work.**

The results of chapter 5 began by demonstrating the plasmonic properties of nanospheres and compared them to Mie theory so as to validate the model. It was found that the modelling

matched the theory exceptionally well and therefore validated the model allowing more complex geometries to be studied. This was performed in increasingly complexity going from isolated nanorods, to supported nanorods, before concluding with arrays of both supported and unsupported nanorods. The modelling not only allowed understanding of the fundamental mechanisms within nanorod arrays but also helped analyse the experimental results. For example, the modelling in chapter 5 using plane-waves as an excitation source with the optical cross sections calculated. This therefore allowed comparison to the optical spectroscopy results from chapter 4. Similarly, the modelling in chapter 6 used an electron beam as the excitation source and calculated the energy loss probability, thereby allowing comparison to the EELS experimental results.

#### **6. To coat the nanorod array in a homogeneous thin layer of titanium dioxide.**

The nanorod arrays were coated in a thin layer of TiO<sub>2</sub> by means of ALD as outlined in the methodology of chapter 3 and confirmed by SEM and XPS in chapter 7. This was found to be relatively homogeneous, giving a thin layer of approximately 7-10 nm in thickness with complete coverage over the surface of the nanorods.

#### **7. To perform photocatalytic dye degradation experiments using the TiO<sub>2</sub> coated nanorod arrays and show activation in the visible region of the spectrum due to the plasmonic particles is achievable.**

The TiO<sub>2</sub> coated nanorod arrays were applied to the degradation of a methylene blue solution using visible light. This attempted to utilise the production of hot electrons from the plasmonic nanorods to degrade the dye. Unfortunately, no appreciable degradation was found, attributed to a lack of available sites on the nanorods for oxidation reactions to occur therefore impeding the nanorods from replenishing lost electrons, and limiting its photocatalytic ability.

### **7.7 Recommendations for Future Work**

The work within this thesis has proved to be novel and subsequently led to a number of gaps in the knowledge of nanorod arrays being filled. Despite this, there are a number of areas that would be beneficial for future work, both in terms of increasing our understanding of the complex interactions in nanorod arrays, as well as the their use in photocatalytic applications. Firstly, although it has been shown in this work that the absorption properties of nanorod arrays may be directly ascertained by using an integrating sphere UV-Vis, a systematic analysis of this for a number of different arrays would be beneficial whereby the AR and

spacing was gradually altered. To achieve this, a thin film AAO technique may be more suited due to the relative ease at which UV-Vis data may be collected, even though the nanorods are generally more disordered.

In addition, it would also prove useful to expand the EELS results shown in chapter 6. This is due to a degree of inhomogeneity found between the nanorods in the sample that makes analysis of the results challenging. Although this may highlight how nanorods of different size and spacing may interact in real systems, the EELS analysis is more useful in terms of a fundamental viewpoint due to the excitation by an electron beam unlikely not transferring over to the properties of the system when illuminated by light, as in for their application. Instead, a method such as nanolithography would give a more homogeneous array and therefore allow characterisation of a simplified system.

Lastly, in regards to the use of the arrays in photocatalytic applications, the lack of activity observed due to the complete coverage of the nanorods with  $\text{TiO}_2$  should be addressed. This could be achieved by applying an inhomogeneous coating of  $\text{TiO}_2$  possibly by using atmospheric chemical vapour deposition instead of atomic layer deposition, or potentially masking off an area of the array. If this change in fabrication procedure results in photocatalytic activity being observed, this could then be further expanded to gain deeper insights into the plasmonic photocatalysis process. For example, three identical arrays could be produced with absorption tuned to occur at the same wavelength. One of the arrays could have a thin insulating layer grown on the nanorods, before a semiconductor with overlapping absorption wavelength is deposited. In this scenario, hot electrons would be prohibited from transferring to the semiconductor assuming a thick enough insulating layer, meaning any enhancement in photocatalytic activity would therefore only arise from the PIRET mechanism. Alternatively, in the second array a different semiconductor would be deposited directly on the nanorods whereby its absorption did not overlap with that of the nanorods. This would therefore mean only the hot electron mechanism would contribute to any enhancements seen. Finally, the third nanorod array would have a semiconductor with overlapping absorption directly deposited on the nanorods. In this scenario, both the PIRET and hot electron mechanisms would contribute. This would therefore allow comparison between the different photocatalytic mechanisms, and in my belief would prove both extremely useful in the area of plasmonic photocatalysis.

## BIBLIOGRAPHY

1. FEYNMAN, R.P. Plenty of Room at the Bottom. *In: American Physical Society*, 1960, California Institute of Technology. Caltech Engineering and Science, 1959.
2. OXFORD ENGLISH DICTIONARY. *Oxford Dictionary of English*. Oxford: Oxford University Press, 2010.
3. ROGERS, B., ADAMS, J. and PENNATHUR, S. *Nanotechnology: Understanding Small Systems, Third Edition*. Taylor & Francis, 2014.
4. RAMSDEN, J.J. Chapter 2 - The Nanoscale. *In: Nanotechnology*. Oxford: William Andrew Publishing, 2011, pp.15-34.
5. SUN, K., KOHYAMA, M., TANAKA, S. and TAKEDA, S. Understanding of the activity difference between nanogold and bulk gold by relativistic effects. *Journal of Energy Chemistry*, 2015, **24**(4), pp.485-489.
6. CUENYA, B.R. Synthesis and catalytic properties of metal nanoparticles: Size, shape, support, composition, and oxidation state effects. *Thin Solid Films*, 2010, **518**(12), pp.3127-3150.
7. PHILIPPOT, K. and SERP, P. Concepts in nanocatalysis. *Nanomaterials in Catalysis, First Edition*, pp.1-54.
8. SIGMA ALDRICH. *Gold Nanoparticles: Properties and Applications* [online]. [Accessed 5th December 2016]. Available from: <http://www.sigmaaldrich.com/technical-documents/articles/materials-science/nanomaterials/gold-nanoparticles.html>.
9. ATWATER, H.A. The promise of plasmonics. *Scientific American*, 2007, **296**(4), pp.56-63.
10. BRITISH MUSEUM. *The Lycurgus Cup* [online]. [Accessed 10th July 2014]. Available from: [http://www.britishmuseum.org/explore/highlights/highlight\\_objects/pe\\_mla/t/the\\_lycurgus\\_cup.aspx](http://www.britishmuseum.org/explore/highlights/highlight_objects/pe_mla/t/the_lycurgus_cup.aspx).
11. FREESTONE, I., MEEKS, N., SAX, M. and HIGGITT, C. The Lycurgus Cup — A Roman nanotechnology. *Gold Bulletin*, 2007, **40**(4), pp.270-277.
12. FARADAY, M. The Bakerian Lecture: Experimental Relations of Gold (and Other Metals) to Light. *Philosophical Transactions of the Royal Society of London*, 1857, **147**(ArticleType: research-article / Full publication date: 1857 /), pp.145-181.
13. SHARMA, V., PARK, K. and SRINIVASARAO, M. Colloidal dispersion of gold nanorods: Historical background, optical properties, seed-mediated synthesis, shape separation and self-assembly. *Materials Science and Engineering R: Reports*, 2009, **65**(1-3), pp.1-38.
14. TUDOS, A.J. and SCHASFOORT, R.B. Introduction to surface plasmon resonance. *Handbook of surface Plasmon resonance*, 2008, pp.1-14.

15. HUANG, Y., FANG, Y., ZHANG, Z., ZHU, L. and SUN, M. Nanowire-supported plasmonic waveguide for remote excitation of surface-enhanced Raman scattering. *Light: Science & Applications*, 2014, **3**(8), p.e199.
16. CROZIER, K.B., ZHU, W., WANG, D., LIN, S., BEST, M.D. and CAMDEN, J.P. Plasmonics for surface enhanced raman scattering: Nanoantennas for single molecules. *IEEE Journal of Selected Topics in Quantum Electronics*, 2014, **20**(3), pp.152-162.
17. TAYLOR, A.B. and ZIJLSTRA, P. Single-molecule plasmon sensing: current status and future prospects. *ACS sensors*, 2017, **2**(8), pp.1103-1122.
18. WANG, D.-S. and FAN, S.-K. Microfluidic Surface Plasmon Resonance Sensors: From Principles to Point-of-Care Applications. *Sensors (Basel, Switzerland)*, 2016, **16**(8), p.1175.
19. HIRSCH, L.R., STAFFORD, R.J., BANKSON, J.A., SERSHEN, S.R., RIVERA, B., PRICE, R.E., HAZLE, J.D., HALAS, N.J. and WEST, J.L. Nanoshell-mediated near-infrared thermal therapy of tumors under magnetic resonance guidance. *Proceedings of the National Academy of Sciences of the United States of America*, 2003, **100**(23), pp.13549-13554.
20. GRAMOTNEV, D.K. and BOZHEVOLNYI, S.I. Plasmonics beyond the diffraction limit. *Nat Photon*, 2010, **4**(2), pp.83-91.
21. WARREN, S.C. and THIMSEN, E. Plasmonic solar water splitting. *Energy and Environmental Science*, 2012, **5**(1), pp.5133-5146.
22. JIANG, R., LI, B., FANG, C. and WANG, J. Metal/Semiconductor Hybrid Nanostructures for Plasmon-Enhanced Applications. *Advanced Materials*, 2014, **26**(31), pp.5274-5309.
23. ATWATER, H.A. and POLMAN, A. Plasmonics for improved photovoltaic devices. *Nature Materials*, 2010, **9**(3), pp.205-213.
24. IPCC. *Climate Change 2014: Impacts, Adaption, and Vulnerability. Part A: Global and Sectoral Aspects. Contribution of Working Group II to the Fifth Assessment Report of the Intergovernmental Panel on Climate Change*. Cambridge, United Kingdom, 2014.
25. UNITED NATIONS ENVIRONMENT PROGRAMME (UNEP). *The Emissions Gap Report 2016*. Nairobi, 2016.
26. UNITED NATIONS FRAMEWORK CONVENTION ON CLIMATE CHANGE. The Cancun Agreements. *In: Cancun Climate Change Conference*, Cancun. 2010.
27. ZHOU, X., LIU, G., YU, J. and FAN, W. Surface plasmon resonance-mediated photocatalysis by noble metal-based composites under visible light. *Journal of Materials Chemistry*, 2012, **22**(40), pp.21337-21354.
28. XIAO, M.D., JIANG, R.B., WANG, F., FANG, C.H., WANG, J.F. and YU, J.C. Plasmon-enhanced chemical reactions. *Journal of Materials Chemistry A*, 2013, **1**(19), pp.5790-5805.
29. LOMBARDI, A., DEMETRIADOU, A., WELLER, L., ANDRAE, P., BENZ, F., CHIKKARADDY, R., AIZPURUA, J. and BAUMBERG, J.J. Anomalous

- Spectral Shift of Near- and Far-Field Plasmonic Resonances in Nanogaps. *ACS photonics*, 2016, **3**(3), pp.471-477.
30. MYROSHNYCHENKO, V., RODRÍGUEZ-FERNÁNDEZ, J., PASTORIZA-SANTOS, I., FUNSTON, A.M., NOVO, C., MULVANEY, P., LIZ-MARZÁN, L.M. and DE ABAJO, F.J.G. Modelling the optical response of gold nanoparticles. *Chemical Society Reviews*, 2008, **37**(9), pp.1792-1805.
  31. MAXWELL, J.C. A Dynamical Theory of the Electromagnetic Field. *Philosophical Transactions of the Royal Society of London*, 1865, **155**, pp.459-512.
  32. LEVI, A.F.J. The Lorentz oscillator model. In: *Essential Classical Mechanics for Device Physics*. Morgan & Claypool Publishers, 2016, pp.5-1-5-21.
  33. DRUDE, P. Zur Elektronentheorie der Metalle. *Annalen der Physik*, 1900, **306**(3), pp.566-613.
  34. SWINEHART, D.F. The Beer-Lambert Law. *Journal of Chemical Education*, 1962, **39**(7), p.333.
  35. SOLÍS, D.M., TABOADA, J.M., OBELLEIRO, F., LIZ-MARZÁN, L.M. and GARCÍA DE ABAJO, F.J. Optimization of Nanoparticle-Based SERS Substrates through Large-Scale Realistic Simulations. *ACS photonics*, 2017, **4**(2), pp.329-337.
  36. MAIER, S.A. *Plasmonics: Fundamentals and Applications*. New York: Springer Science + Business Media LLC, 2007.
  37. GANS, R. Über die Form ultramikroskopischer Goldteilchen. *Annalen der Physik*, 1912, **342**(5), pp.881-900.
  38. WAIT, J. Electromagnetic scattering from a radially inhomogeneous sphere. *Applied Scientific Research, Section B*, 1962, **10**(5-6), pp.441-450.
  39. VIDEEN, G. Light scattering from a sphere on or near a surface. *Journal of the Optical Society of America A*, 1991, **8**(3), pp.483-489.
  40. QUINTEN, M. *Optical Properties of Nanoparticle Systems: Mie and Beyond*. Wiley, 2010.
  41. SMOLYANINOV, I.I. Optical microscopy beyond the diffraction limit. *HFSP Journal*, 2008, **2**(3), pp.129-131.
  42. PINES, D. and BOHM, D. A Collective Description of Electron Interactions: II. Collective Individual Particle Aspects of the Interactions. *Physical Review*, 1952, **85**(2), pp.338-353.
  43. RITCHIE, R.H. Plasma Losses by Fast Electrons in Thin Films. *Physical Review*, 1957, **106**(5), pp.874-881.
  44. POWELL, C.J. and SWAN, J.B. Origin of the characteristic electron energy losses in magnesium. *Physical Review*, 1959, **116**(1), pp.81-83.
  45. KELLY, K.L., CORONADO, E., ZHAO, L.L. and SCHATZ, G.C. The optical properties of metal nanoparticles: The influence of size, shape, and dielectric environment. *Journal of Physical Chemistry B*, 2003, **107**(3), pp.668-677.

46. JACKSON, J.D. and JACKSON, J.D. *Classical electrodynamics*. Wiley New York etc., 1962.
47. NIE, S. and EMORY, S.R. Probing single molecules and single nanoparticles by surface-enhanced Raman scattering. *Science*, 1997, **275**(5303), pp.1102-1106.
48. QUINTEN, M. *Optical Properties of Nanoparticle Systems*. Weinheim: Wiley-VCH, 2011.
49. UNDERWOOD, S. and MULVANEY, P. Effect of the Solution Refractive Index on the Color of Gold Colloids. *Langmuir*, 1994, **10**(10), pp.3427-3430.
50. MULVANEY, P., LIZ-MARZAN, L.M., GIERSIG, M. and UNG, T. Silica encapsulation of quantum dots and metal clusters. *Journal of Materials Chemistry*, 2000, **10**(6), pp.1259-1270.
51. PENG, B., ZHANG, Q., LIU, X., JI, Y., DEMIR, H.V., HUAN, C.H.A., SUM, T.C. and XIONG, Q. Fluorophore-Doped Core–Multishell Spherical Plasmonic Nanocavities: Resonant Energy Transfer toward a Loss Compensation. *ACS Nano*, 2012, **6**(7), pp.6250-6259.
52. DU, P., CAO, Y., LI, D., LIU, Z., KONG, X. and SUN, Z. Synthesis of thermally stable Ag@TiO<sub>2</sub> core-shell nanoprisms and plasmon-enhanced optical properties for a P3HT thin film. *RSC Advances*, 2013, **3**(17), pp.6016-6021.
53. THIELE, M., GÖTZ, I., TRAUTMANN, S., MÜLLER, R., CSÁKI, A., HENKEL, T. and FRITZSCHE, W. Wet-chemical Passivation of Anisotropic Plasmonic Nanoparticles for LSPR-sensing by a Silica Shell. *Materials Today: Proceedings*, 2015, **2**(1), pp.33-40.
54. ZHANG, C., HAN, Q., LI, C., ZHANG, M., YAN, L. and ZHENG, H. Metal-enhanced fluorescence of single shell-isolated alloy metal nanoparticle. *Applied Optics*, 2016, **55**(32), pp.9131-9136.
55. XU, X., DU, Q., PENG, B., XIONG, Q., HONG, L., DEMIR, H.V., WONG, T.K.S., KYAW, A.K.K. and SUN, X.W. Effect of shell thickness on small-molecule solar cells enhanced by dual plasmonic gold-silica nanorods. *Applied Physics Letters*, 2014, **105**(11), p.113306.
56. KUZMA, A., WEIS, M., FLICKYNGEROVA, S., JAKABOVIC, J., SATKA, A., DOBROCKA, E., CHLPIK, J., CIRAK, J., DONOVAL, M. and TELEK, P. Influence of surface oxidation on plasmon resonance in monolayer of gold and silver nanoparticles. *Journal of Applied Physics*, 2012, **112**(10), p.103531.
57. LAVEN, P. *MiePlot v 4.3* [Software]. 2017. Available from: <http://www.philiplaven.com/mieplot.htm>.
58. GEDDES, C.D. *Reviews in Plasmonics 2010*. Springer New York, 2011.
59. LINK, S. and EL-SAYED, M.A. Shape and size dependence of radiative, non-radiative and photothermal properties of gold nanocrystals. *International Reviews in Physical Chemistry*, 2000, **19**(3), pp.409-453.

60. PAYNE, E.K., SHUFORD, K.L., PARK, S., SCHATZ, G.C. and MIRKIN, C.A. Multipole Plasmon Resonances in Gold Nanorods. *The journal of physical chemistry. B*, 2006, **110**(5), pp.2150-2154.
61. ALVAREZ, M.M., KHOURY, J.T., SCHAAFF, T.G., SHAFIGULLIN, M.N., VEZMAR, I. and WHETTEN, R.L. Optical Absorption Spectra of Nanocrystal Gold Molecules. *The Journal of Physical Chemistry B*, 1997, **101**(19), pp.3706-3712.
62. KREIBIG, U. and FRAGSTEIN, C.V. The limitation of electron mean free path in small silver particles. *Zeitschrift für Physik*, 1969, **224**(4), pp.307-323.
63. GARCÍA DE ABAJO, F.J. Nonlocal effects in the plasmons of strongly interacting nanoparticles, dimers, and waveguides. *The Journal of Physical Chemistry C*, 2008, **112**(46), pp.17983-17987.
64. RAZA, S., BOZHEVOLNYI, S.I., WUBS, M. and MORTENSEN, N.A. Nonlocal optical response in metallic nanostructures. *Journal of Physics: Condensed Matter*, 2015, **27**(18), p.183204.
65. KREIBIG, U. and VOLLMER, M. *Optical properties of metal clusters*. Springer, 1995.
66. TAO, J., LU, Y.H., ZHENG, R.S., LIN, K.Q., XIE, Z.G., LUO, Z.F., LI, S.L., WANG, P. and MING, H. Effect of aspect ratio distribution on localized surface plasmon resonance extinction spectrum of gold nanorods. *Chinese Physics Letters*, 2008, **25**(12), pp.4459-4462.
67. HU, M., CHEN, J.Y., LI, Z.Y., AU, L., HARTLAND, G.V., LI, X.D., MARQUEZ, M. and XIA, Y.N. Gold nanostructures: engineering their plasmonic properties for biomedical applications. *Chemical Society Reviews*, 2006, **35**(11), pp.1084-1094.
68. KRAHNE, R., MANNA, L., MORELLO, G., FIGUEROLA, A., GEORGE, C. and DEKA, S. *Physical properties of nanorods*. Springer.
69. BRYANT, G.W., GARCÍA DE ABAJO, F.J. and AIZPURUA, J. Mapping the Plasmon Resonances of Metallic Nanoantennas. *Nano Letters*, 2008, **8**(2), pp.631-636.
70. PRESCOTT, S.W. and MULVANEY, P. Gold nanorod extinction spectra. *Journal of Applied Physics*, 2006, **99**(12), p.123504.
71. PECHARROMÁN, C., PÉREZ-JUSTE, J., MATA-OSORO, G., LIZMARZÁN, L.M. and MULVANEY, P. Redshift of surface plasmon modes of small gold rods due to their atomic roughness and end-cap geometry. *Physical Review B*, 2008, **77**(3), p.035418.
72. TRÜGLER, A., TINGUELY, J.-C., KRENN, J.R., HOHENAUF, A. and HOHENESTER, U. Influence of surface roughness on the optical properties of plasmonic nanoparticles. *Physical Review B*, 2011, **83**(8), p.081412.
73. GORDEL, M., PIELA, K., KOŁKOWSKI, R., KOZŁECKI, T., BUCKLE, M. and SAMOĆ, M. End-to-end self-assembly of gold nanorods in isopropanol solution: experimental and theoretical studies. *Journal of Nanoparticle Research*, 2015, **17**, p.477.

74. FUNSTON, A.M., NOVO, C., DAVIS, T.J. and MULVANEY, P. Plasmon Coupling of Gold Nanorods at Short Distances and in Different Geometries. *Nano Letters*, 2009, **9**(4), pp.1651-1658.
75. ANKER, J.N., HALL, W.P., LYANDRES, O., SHAH, N.C., ZHAO, J. and VAN DUYNÉ, R.P. Biosensing with plasmonic nanosensors. *Nat Mater*, 2008, **7**(6), pp.442-453.
76. YONG, Z., LEI, D.Y., LAM, C.H. and WANG, Y. Ultrahigh refractive index sensing performance of plasmonic quadrupole resonances in gold nanoparticles. *Nanoscale Research Letters*, 2014, **9**(1), p.187.
77. BOSMAN, M., ZHANG, L., DUAN, H., TAN, S.F., NIJHUIS, C.A., QIU, C.W. and YANG, J.K.W. Encapsulated Annealing: Enhancing the Plasmon Quality Factor in Lithographically-Defined Nanostructures. *Scientific Reports*, 2014, **4**, p.5537.
78. LIU, C., ZHAO, C., ZHANG, X., GUO, W., LIU, K. and RUAN, S. Unique Gold Nanorods Embedded Active Layer Enabling Strong Plasmonic Effect To Improve the Performance of Polymer Photovoltaic Devices. *The Journal of Physical Chemistry C*, 2016, **120**(11), pp.6198-6205.
79. ZHANG, Z.-Y. and ZHAO, Y.-P. Extinction spectra and electrical field enhancement of Ag nanorods with different topologic shapes. *Journal of Applied Physics*, 2007, **102**(11), p.113308.
80. STURMAN, B., PODIVILOV, E. and GORKUNOV, M. Metal nanoparticles with sharp corners: Universal properties of plasmon resonances. *EPL (Europhysics Letters)*, 2013, **101**(5), p.57009.
81. CAMPION, A. and KAMBHAMPATI, P. Surface-enhanced Raman scattering. *Chemical Society Reviews*, 1998, **27**(4), pp.241-250.
82. DUAN, H., FERNÁNDEZ-DOMÍNGUEZ, A.I., BOSMAN, M., MAIER, S.A. and YANG, J.K.W. Nanoplasmonics: Classical down to the Nanometer Scale. *Nano Letters*, 2012, **12**(3), pp.1683-1689.
83. NICOLETTI, O., DE LA PENA, F., LEARY, R.K., HOLLAND, D.J., DUCATI, C. and MIDGLEY, P.A. Three-dimensional imaging of localized surface plasmon resonances of metal nanoparticles. *nature*, 2013, **502**(7469), pp.80-84.
84. BOSMAN, M., YE, E., TAN, S.F., NIJHUIS, C.A., YANG, J.K., MARTY, R., MLAYAH, A., ARBOUET, A., GIRARD, C. and HAN, M.-Y. Surface plasmon damping quantified with an electron nanoprobe. *Scientific Reports*, 2013, **3**.
85. MOSKOVITS, M. Surface-enhanced spectroscopy. *Reviews of Modern Physics*, 1985, **57**(3), pp.783-826.
86. RUPPIN, R. Effect of non-locality on nanofocusing of surface plasmon field intensity in a conical tip. *Physics Letters A*, 2005, **340**(1), pp.299-302.
87. TOSCANO, G., RAZA, S., XIAO, S., WUBS, M., JAUHO, A.-P., BOZHEVOLNYI, S.I. and MORTENSEN, N.A. Surface-enhanced Raman spectroscopy: nonlocal limitations. *Optics letters*, 2012, **37**(13), pp.2538-2540.

88. WIND, M.M., VLIEGER, J. and BEDEAUX, D. The polarizability of a truncated sphere on a substrate I. *Physica A: Statistical Mechanics and its Applications*, 1987, **141**(1), pp.33-57.
89. JOHNSON, B.R. Calculation of light scattering from a spherical particle on a surface by the multipole expansion method. *Journal of the Optical Society of America A*, 1996, **13**(2), pp.326-337.
90. FUCILE, E., DENTI, P., BORGHESE, F., SAIJA, R. and SINDONI, O.I. Optical properties of a sphere in the vicinity of a plane surface. *Journal of the Optical Society of America A*, 1997, **14**(7), pp.1505-1514.
91. LERMÉ, J., BONNET, C., BROYER, M., COTTANCIN, E., MANCHON, D. and PELLARIN, M. Optical Properties of a Particle above a Dielectric Interface: Cross Sections, Benchmark Calculations, and Analysis of the Intrinsic Substrate Effects. *The Journal of Physical Chemistry C*, 2013, **117**(12), pp.6383-6398.
92. NOGUEZ, C. Surface Plasmons on Metal Nanoparticles: The Influence of Shape and Physical Environment. *The Journal of Physical Chemistry C*, 2007, **111**(10), pp.3806-3819.
93. KADKHODAZADEH, S., CHRISTENSEN, T., BELEGGIA, M., MORTENSEN, N.A. and WAGNER, J.B. The Substrate Effect in Electron Energy-Loss Spectroscopy of Localized Surface Plasmons in Gold and Silver Nanoparticles. *ACS photonics*, 2017, **4**(2), pp.251-261.
94. JENSEN, T.R., DUVAL, M.L., KELLY, K.L., LAZARIDES, A.A., SCHATZ, G.C. and VAN DUYNE, R.P. Nanosphere lithography: effect of the external dielectric medium on the surface plasmon resonance spectrum of a periodic array of silver nanoparticles. *The Journal of Physical Chemistry B*, 1999, **103**(45), pp.9846-9853.
95. YANG, M., LI, J., LI, J. and ZHU, X. Scattering of light by plasmonic nanoparticles on a silicon substrate. *ChemPhysChem*, 2012, **13**(10), pp.2573-2577.
96. RUI, X., XIAO-DONG, W., WEN, L., XIAO-NA, X., YUE-QIANG, L., AN, J., FU-HUA, Y. and JIN-MIN, L. Dielectric layer-dependent surface plasmon effect of metallic nanoparticles on silicon substrate. *Chinese Physics B*, 2012, **21**(2), p.025202.
97. RINGE, E., MCMAHON, J.M., SOHN, K., COBLEY, C., XIA, Y., HUANG, J., SCHATZ, G.C., MARKS, L.D. and VAN DUYNE, R.P. Unraveling the effects of size, composition, and substrate on the localized surface plasmon resonance frequencies of gold and silver nanocubes: a systematic single-particle approach. *The Journal of Physical Chemistry C*, 2010, **114**(29), pp.12511-12516.
98. WU, Y. and NORDLANDER, P. Finite-Difference Time-Domain Modeling of the Optical Properties of Nanoparticles near Dielectric Substrates. *The Journal of Physical Chemistry C*, 2010, **114**(16), pp.7302-7307.
99. KNIGHT, M.W., WU, Y., LASSITER, J.B., NORDLANDER, P. and HALAS, N.J. Substrates Matter: Influence of an Adjacent Dielectric on an Individual Plasmonic Nanoparticle. *Nano Letters*, 2009, **9**(5), pp.2188-2192.

100. HUTTER, T., ELLIOTT, S.R. and MAHAJAN, S. Interaction of metallic nanoparticles with dielectric substrates: effect of optical constants. *Nanotechnology*, 2012, **24**(3), p.035201.
101. CIRACÌ, C., HILL, R.T., MOCK, J.J., URZHUMOV, Y., FERNÁNDEZ-DOMÍNGUEZ, A.I., MAIER, S.A., PENDRY, J.B., CHILKOTI, A. and SMITH, D.R. Probing the Ultimate Limits of Plasmonic Enhancement. *Science (New York, N.Y.)*, 2012, **337**(6098), pp.1072-1074.
102. LINIC, S., CHRISTOPHER, P. and INGRAM, D.B. Plasmonic-metal nanostructures for efficient conversion of solar to chemical energy. *Nat Mater*, 2011, **10**(12), pp.911-921.
103. LI, G., CHERQUI, C., BIGELOW, N.W., DUSCHER, G., STRANEY, P.J., MILLSTONE, J.E., MASIELLO, D.J. and CAMDEN, J.P. Spatially Mapping Energy Transfer from Single Plasmonic Particles to Semiconductor Substrates via STEM/EELS. *Nano Letters*, 2015, **15**(5), pp.3465-3471.
104. PINCHUK, A., HILGER, A., VON PLESSEN, G. and KREIBIG, U. Substrate effect on the optical response of silver nanoparticles. *Nanotechnology*, 2004, **15**(12), p.1890.
105. TANYA, H., STEPHEN, R.E. and SUMEET, M. Interaction of metallic nanoparticles with dielectric substrates: effect of optical constants. *Nanotechnology*, 2013, **24**(3), p.035201.
106. SOBHANI, A., MANJAVACAS, A., CAO, Y., MCCLAIN, M.J., GARCÍA DE ABAJO, F.J., NORDLANDER, P. and HALAS, N.J. Pronounced Linewidth Narrowing of an Aluminum Nanoparticle Plasmon Resonance by Interaction with an Aluminum Metallic Film. *Nano Letters*, 2015, **15**(10), pp.6946-6951.
107. LIU, H., NG, J., WANG, S.B., HANG, Z.H., CHAN, C.T. and ZHU, S.N. Strong plasmon coupling between two gold nanospheres on a gold slab. *New Journal of Physics*, 2011, **13**.
108. TADASHI, T., INOUE, M. and KAZUO, O. Optical Response of a Sphere Coupled to a Metal Substrate. *Journal of the Physical Society of Japan*, 1987, **56**(4), pp.1587-1602.
109. LÉVÊQUE, G. and MARTIN, O.J.F. Optical interactions in a plasmonic particle coupled to a metallic film. *Optics Express*, 2006, **14**(21), pp.9971-9981.
110. MOCK, J.J., HILL, R.T., DEGIRON, A., ZAUSCHER, S., CHILKOTI, A. and SMITH, D.R. Distance-dependent plasmon resonant coupling between a gold nanoparticle and gold film. *Nano Letters*, 2008, **8**(8), pp.2245-2252.
111. PRODAN, E., RADLOFF, C., HALAS, N.J. and NORDLANDER, P. A Hybridization Model for the Plasmon Response of Complex Nanostructures. *Science*, 2003, **302**(5644), pp.419-422.
112. NORDLANDER, P. and PRODAN, E. Plasmon Hybridization in Nanoparticles near Metallic Surfaces. *Nano Letters*, 2004, **4**(11), pp.2209-2213.

113. NORDLANDER, P., OUBRE, C., PRODAN, E., LI, K. and STOCKMAN, M. Plasmon hybridization in nanoparticle dimers. *Nano Letters*, 2004, **4**(5), pp.899-903.
114. HALAS, N.J., LAL, S., CHANG, W.-S., LINK, S. and NORDLANDER, P. Plasmons in strongly coupled metallic nanostructures. *Chemical reviews*, 2011, **111**(6), pp.3913-3961.
115. JAIN, P.K., EUSTIS, S. and EL-SAYED, M.A. Plasmon Coupling in Nanorod Assemblies: Optical Absorption, Discrete Dipole Approximation Simulation, and Exciton-Coupling Model. *The Journal of Physical Chemistry B*, 2006, **110**(37), pp.18243-18253.
116. KASHA, M. Energy Transfer Mechanisms and the Molecular Exciton Model for Molecular Aggregates. *Radiation Research*, 1963, **20**(1), pp.55-70.
117. JAIN, P.K. and EL-SAYED, M.A. Plasmonic coupling in noble metal nanostructures. *Chemical Physics Letters*, 2010, **487**(4-6), pp.153-164.
118. CHEN, H., SHAO, L., LI, Q. and WANG, J. Gold nanorods and their plasmonic properties. *Chemical Society Reviews*, 2013, **42**(7), pp.2679-2724.
119. WILLINGHAM, B., BRANDL, D. and NORDLANDER, P. Plasmon hybridization in nanorod dimers. *Applied Physics B: Lasers and Optics*, 2008, **93**(1), pp.209-216.
120. LEE, A., AHMED, A., DOS SANTOS, D.P., COOMBS, N., PARK, J.I., GORDON, R., BROLO, A.G. and KUMACHEVA, E. Side-by-Side Assembly of Gold Nanorods Reduces Ensemble-Averaged SERS Intensity. *The Journal of Physical Chemistry C*, 2012, **116**(9), pp.5538-5545.
121. N'GOM, M., LI, S., SCHATZ, G., ERNI, R., AGARWAL, A., KOTOV, N. and NORRIS, T.B. Electron-beam mapping of plasmon resonances in electromagnetically interacting gold nanorods. *Physical Review B - Condensed Matter and Materials Physics*, 2009, **80**(11).
122. N'GOM, M., RINGNALDA, J., MANSFIELD, J.F., AGARWAL, A., KOTOV, N., ZALUZEC, N.J. and NORRIS, T.B. Single Particle Plasmon Spectroscopy of Silver Nanowires and Gold Nanorods. *Nano Letters*, 2008, **8**(10), pp.3200-3204.
123. CHENG, Z.-Q., NAN, F., YANG, D.-J., ZHONG, Y.-T., MA, L., HAO, Z.-H., ZHOU, L. and WANG, Q.-Q. Plasmonic nanorod arrays of a two-segment dimer and a coaxial cable with 1 nm gap for large field confinement and enhancement. *Nanoscale*, 2015, **7**(4), pp.1463-1470.
124. LIU, Z., BOLTASSEVA, A., PEDERSEN, R.H., BAKKER, R., KILDISHEV, A.V., DRACHEV, V.P. and SHALAEV, V.M. Plasmonic nanoantenna arrays for the visible. *Metamaterials*, 2008, **2**(1), pp.45-51.
125. WIENER, A., DUAN, H., BOSMAN, M., HORSFIELD, A.P., PENDRY, J.B., YANG, J.K.W., MAIER, S.A. and FERNÁNDEZ-DOMÍNGUEZ, A.I. Electron-Energy Loss Study of Nonlocal Effects in Connected Plasmonic Nanoprisms. *ACS Nano*, 2013, **7**(7), pp.6287-6296.
126. HAYNES, C.L., MCFARLAND, A.D., ZHAO, L., VAN DUYN, R.P., SCHATZ, G.C., GUNNARSSON, L., PRIKULIS, J., KASEMO, B. and

- KÄLL, M. Nanoparticle optics: the importance of radiative dipole coupling in two-dimensional nanoparticle arrays. *The Journal of Physical Chemistry B*, 2003, **107**(30), pp.7337-7342.
127. SMYTHE, E.J., CUBUKCU, E. and CAPASSO, F. Optical properties of surface plasmon resonances of coupled metallic nanorods. *Optics Express*, 2007, **15**(12), pp.7439-7447.
128. FOSS JR, C.A., HORNYAK, G.L., STOCKERT, J.A. and MARTIN, C.R. Optical properties of composite membranes containing arrays of nanoscopic gold cylinders. *The Journal of Physical Chemistry*, 1992, **96**(19), pp.7497-7499.
129. FOSS, C.A., HORNYAK, G.L., STOCKERT, J.A. and MARTIN, C.R. Template-Synthesized Nanoscopic Gold Particles: Optical Spectra and the Effects of Particle Size and Shape. *The Journal of Physical Chemistry*, 1994, **98**(11), pp.2963-2971.
130. HORNYAK, G.L., PATRISSI, C.J. and MARTIN, C.R. Fabrication, Characterization, and Optical Properties of Gold Nanoparticle/Porous Alumina Composites: The Nonscattering Maxwell– Garnett Limit. *The Journal of Physical Chemistry B*, 1997, **101**(9), pp.1548-1555.
131. GARNETT, J.C.M. Colours in Metal Glasses and in Metallic Films. *Philosophical Transactions of the Royal Society of London. Series A, Containing Papers of a Mathematical or Physical Character*, 1904, **203**(359-371), p.385.
132. ATKINSON, R., HENDREN, W.R., WURTZ, G.A., DICKSON, W., ZAYATS, A.V., EVANS, P. and POLLARD, R.J. Anisotropic optical properties of arrays of gold nanorods embedded in alumina. *Physical Review B*, 2006, **73**(23), p.235402.
133. WURTZ, G.A., DICKSON, W., O'CONNOR, D., ATKINSON, R., HENDREN, W., EVANS, P., POLLARD, R. and ZAYATS, A.V. Guided plasmonic modes in nanorod assemblies: strong electromagnetic coupling regime. *Optics Express*, 2008, **16**(10), pp.7460-7470.
134. EVANS, P., HENDREN, W., ATKINSON, R., WURTZ, G., DICKSON, W., ZAYATS, A. and POLLARD, R. Growth and properties of gold and nickel nanorods in thin film alumina. *Nanotechnology*, 2006, **17**(23), p.5746.
135. EVANS, P.R., WURTZ, G.A., ATKINSON, R., HENDREN, W., O'CONNOR, D., DICKSON, W., POLLARD, R.J. and ZAYATS, A.V. Plasmonic Core/Shell Nanorod Arrays: Subattoliter Controlled Geometry and Tunable Optical Properties. *The Journal of Physical Chemistry C*, 2007, **111**(34), pp.12522-12527.
136. FIEHLER, V., PATROVSKY, F., ORTMANN, L., DERENKO, S., HILLE, A. and ENG, L.M. Plasmonic Nanorod Antenna Array: Analysis in Reflection and Transmission. *The Journal of Physical Chemistry C*, 2016, **120**(22), pp.12178-12186.
137. WIEDERRECHT, G. *Handbook of Nanoscale Optics and Electronics*. Elsevier Science, 2010.

138. SHALAEV, V.M., CAI, W., CHETTIAR, U.K., YUAN, H.-K., SARYCHEV, A.K., DRACHEV, V.P. and KILDISHEV, A.V. Negative index of refraction in optical metamaterials. *Optics letters*, 2005, **30**(24), pp.3356-3358.
139. WURTZ, G.A., POLLARD, R., HENDREN, W., WIEDERRECHT, G., GOSZTOLA, D., PODOLSKIY, V. and ZAYATS, A.V. Designed ultrafast optical nonlinearity in a plasmonic nanorod metamaterial enhanced by nonlocality. *Nature Nanotechnology*, 2011, **6**(2), pp.107-111.
140. MCMILLAN, B.G., BERLOUIS, L.E.A., CRUICKSHANK, F.R. and BREVET, P.F. Reflectance and SERS from an ordered array of gold nanorods. *Electrochimica Acta*, 2007, **53**(3), pp.1157-1163.
141. HUANG, Z., MENG, G., HUANG, Q., CHEN, B., ZHU, C. and ZHANG, Z. Large-area Ag nanorod array substrates for SERS: AAO template-assisted fabrication, functionalization, and application in detection PCBs. *Journal of Raman Spectroscopy*, 2013, **44**(2), pp.240-246.
142. DAMM, S., LORDAN, F., MURPHY, A., MCMILLEN, M., POLLARD, R. and RICE, J.H. Application of AAO matrix in aligned gold nanorod array substrates for surface-Enhanced fluorescence and Raman scattering. *Plasmonics*, 2014, **9**(6), pp.1371-1376.
143. FEDELE, S., HAKAMI, M., MURPHY, A., POLLARD, R. and RICE, J. Strong coupling in molecular exciton-plasmon Au nanorod array systems. *Applied Physics Letters*, 2016, **108**(5), p.053102.
144. WURTZ, G.A., EVANS, P.R., HENDREN, W., ATKINSON, R., DICKSON, W., POLLARD, R.J., ZAYATS, A.V., HARRISON, W. and BOWER, C. Molecular Plasmonics with Tunable Exciton– Plasmon Coupling Strength in J-Aggregate Hybridized Au Nanorod Assemblies. *Nano Letters*, 2007, **7**(5), pp.1297-1303.
145. MUBEEN, S., LEE, J., SINGH, N., KRÄMER, S., STUCKY, G.D. and MOSKOVITS, M. An autonomous photosynthetic device in which all charge carriers derive from surface plasmons. *Nature Nanotechnology*, 2013, **8**(4), pp.247-251.
146. LEE, J., MUBEEN, S., JI, X., STUCKY, G.D. and MOSKOVITS, M. Plasmonic photoanodes for solar water splitting with visible light. *Nano Letters*, 2012, **12**(9), pp.5014-5019.
147. JANA, N.R., GEARHEART, L. and MURPHY, C.J. Seed-Mediated Growth Approach for Shape-Controlled Synthesis of Spheroidal and Rod-like Gold Nanoparticles Using a Surfactant Template. *Advanced Materials*, 2001, **13**(18), pp.1389-1393.
148. NIKOOBAKHT, B. and EL-SAYED, M.A. Preparation and growth mechanism of gold nanorods (NRs) using seed-mediated growth method. *Chemistry of Materials*, 2003, **15**(10), pp.1957-1962.
149. TAYLOR, A.B., MICHAUX, P., MOHSIN, A.S.M. and CHON, J.W.M. Electron-beam lithography of plasmonic nanorod arrays for multilayered optical storage. *Optics Express*, 2014, **22**(11), pp.13234-13243.

150. MURPHY, C.J., THOMPSON, L.B., CHERNAK, D.J., YANG, J.A., SIVAPALAN, S.T., BOULOS, S.P., HUANG, J., ALKILANY, A.M. and SISCO, P.N. Gold nanorod crystal growth: From seed-mediated synthesis to nanoscale sculpting. *Current Opinion in Colloid & Interface Science*, 2011, **16**(2), pp.128-134.
151. KRETSCHMER, F., MUEHLIG, S., HOEPPENER, S., WINTER, A., HAGER, M.D., ROCKSTUHL, C., PERTSCH, T. and SCHUBERT, U.S. Survey of Plasmonic Nanoparticles: From Synthesis to Application. *Particle & Particle Systems Characterization*, 2014, **31**(7), pp.721-744.
152. PETRYAYEVA, E. and KRULL, U.J. Localized surface plasmon resonance: nanostructures, bioassays and biosensing—a review. *Analytica chimica acta*, 2011, **706**(1), pp.8-24.
153. POSSIN, G.E. A Method for Forming Very Small Diameter Wires. *Review of Scientific Instruments*, 1970, **41**(5), pp.772-774.
154. WILLIAMS, W.D. and GIORDANO, N. Fabrication of 80 Å metal wires. *Review of Scientific Instruments*, 1984, **55**(3), pp.410-412.
155. HULTEEN, J.C. A general template-based method for the preparation of nanomaterials. *Journal of Materials Chemistry*, 1997, **7**(7), pp.1075-1087.
156. SCHÖNENBERGER, C., VAN DER ZANDE, B.M.I., FOKKINK, L.G.J., HENNY, M., SCHMID, C., KRÜGER, M., BACHTOLD, A., HUBER, R., BIRK, H. and STAUFER, U. Template Synthesis of Nanowires in Porous Polycarbonate Membranes: Electrochemistry and Morphology. *The Journal of Physical Chemistry B*, 1997, **101**(28), pp.5497-5505.
157. BRUMLIK, C.J., MARTIN, C.R. and TOKUDA, K. *Microhole array electrodes based on microporous alumina membranes*. COLORADO STATE UNIV FORT COLLINS DEPT OF CHEMISTRY, 1992.
158. TIERNEY, M.J. and MARTIN, C.R. *Transparent metal microstructures*. TEXAS A AND M UNIV COLLEGE STATION DEPT OF CHEMISTRY, 1987.
159. FOSS, C.A., TIERNEY, M.J. and MARTIN, C.R. Template synthesis of infrared-transparent metal microcylinders: comparison of optical properties with the predictions of effective medium theory. *The Journal of Physical Chemistry*, 1992, **96**(22), pp.9001-9007.
160. LEE, W. and PARK, S.-J. Porous anodic aluminum oxide: anodization and templated synthesis of functional nanostructures. *Chemical reviews*, 2014, **114**(15), pp.7487-7556.
161. CHENG, C. and NGAN, A.H.W. Theoretical Pore Growth Models for Nanoporous Alumina. In: D. LOSIC and A. SANTOS, eds. *Nanoporous Alumina: Fabrication, Structure, Properties and Applications*. Cham: Springer International Publishing, 2015, pp.31-60.
162. SULLIVAN, J.P. and WOOD, G.C. The Morphology and Mechanism of Formation of Porous Anodic Films on Aluminium. *Proceedings of the Royal Society of London. A. Mathematical and Physical Sciences*, 1970, **317**(1531), p.511.

163. SKELDON, P., THOMPSON, G.E., GARCIA-VERGARA, S.J., IGLESIAS-RUBIANES, L. and BLANCO-PINZON, C.E. A Tracer Study of Porous Anodic Alumina. *Electrochemical and Solid-State Letters*, 2006, **9**(11), pp.B47-B51.
164. SU, Z., HÄHNER, G. and ZHOU, W. Investigation of the pore formation in anodic aluminium oxide. *Journal of Materials Chemistry*, 2008, **18**(47), pp.5787-5795.
165. ABDEL-KARIM, R. and WAHEED, A.F. Nanocoatings. *In: Modern Surface Engineering Treatments*. Rijeka: InTech, 2013, p.Ch. 0.
166. CHU, S.Z., WADA, K., INOUE, S., ISOGAI, M., KATSUTA, Y. and YASUMORI, A. Large-Scale Fabrication of Ordered Nanoporous Alumina Films with Arbitrary Pore Intervals by Critical-Potential Anodization. *Journal of The Electrochemical Society*, 2006, **153**(9), pp.B384-B391.
167. LOSIC, D. and SANTOS, A. *Nanoporous Alumina: Fabrication, Structure, Properties and Applications*. Springer International Publishing, 2015.
168. GARCIA, U.M., MENDES, L.F., SANTOS, J.S. and TRIVINHO-STRIXINO, F. COMPARAÇÃO E CONSTRUÇÃO DE REATORES DE "MILD" E "HARD ANÓDISATION" PARA FABRICAÇÃO DE ALUMINA ANÓDICA POROSA. *Química Nova*, 2015, **38**, pp.1112-1116.
169. MASUDA, H. and SATOH, M. Fabrication of gold nanodot array using anodic porous alumina as an evaporation mask. *Japanese Journal of Applied Physics*, 1996, **35**(1B), p.L126.
170. CHU, S.Z., INOUE, S., WADA, K. and KURASHIMA, K. Fabrication of integrated arrays of ultrahigh density magnetic nanowires on glass by anodization and electrodeposition. *Electrochimica Acta*, 2005, **51**(5), pp.820-826.
171. ELAM, J.W., XIONG, G., HAN, C.Y., WANG, H.H., BIRRELL, J.P., WELP, U., HRYN, J.N., PELLIN, M.J., BAUMANN, T.F. and POCO, J.F. Atomic layer deposition for the conformal coating of nanoporous materials. *Journal of Nanomaterials*, 2006, **2006**.
172. NASIRPOURI, F. *Electrodeposition of Nanostructured Materials*. Springer International Publishing, 2016.
173. BHUSHAN, B. *Springer handbook of nanotechnology*. Springer Science & Business Media, 2010.
174. SHARMA, M. and KUANR, B.K. Electrodeposition of Ferromagnetic Nanostructures. *In: Electroplating of Nanostructures*. Rijeka: InTech, 2015, p.Ch. 0.
175. ALAM, K.M., SINGH, A.P., BODEPUDI, S.C. and PRAMANIK, S. Fabrication of hexagonally ordered nanopores in anodic alumina: An alternative pretreatment. *Surface Science*, 2011, **605**(3-4), pp.441-449.
176. ZHANG, J., KIELBASA, J.E. and CARROLL, D.L. Controllable fabrication of porous alumina templates for nanostructures synthesis. *Materials Chemistry and Physics*, 2010, **122**(1), pp.295-300.

177. BANHOLZER, M.J., QIN, L., MILLSTONE, J.E., OSBERG, K.D. and MIRKIN, C.A. On-wire lithography: synthesis, encoding and biological applications. *Nat. Protocols*, 2009, **4**(6), pp.838-848.
178. JOHNSON, L.P. and MATISONS, J.G. Synthesis of high aspect-ratio gold nanowires with highly porous morphology. *ISRN Nanomaterials*, 2012, **2012**.
179. J-LIEW, M., SOBRI, S. and ROY, S. Characterisation of a thiosulphate–sulphite gold electrodeposition process. *Electrochimica Acta*, 2005, **51**(5), pp.877-881.
180. DENG, X.-Q., ZHU, B., LI, X.-S., LIU, J.-L., ZHU, X. and ZHU, A.-M. Visible-light photocatalytic oxidation of CO over plasmonic Au/TiO<sub>2</sub>: Unusual features of oxygen plasma activation. *Applied Catalysis B: Environmental*, 2016, **188**, pp.48-55.
181. TANAKA, A., TERAMURA, K., HOSOKAWA, S., KOMINAMI, H. and TANAKA, T. Visible light-induced water splitting in an aqueous suspension of a plasmonic Au/TiO<sub>2</sub> photocatalyst with metal co-catalysts. *Chemical Science*, 2017.
182. GEORGE, S.M. Atomic layer deposition: an overview. *Chemical reviews*, 2009, **110**(1), pp.111-131.
183. LESKELÄ, M. and RITALA, M. Atomic layer deposition (ALD): from precursors to thin film structures. *Thin Solid Films*, 2002, **409**(1), pp.138-146.
184. JOHNSON, R.W., HULTQVIST, A. and BENT, S.F. A brief review of atomic layer deposition: from fundamentals to applications. *Materials Today*, 2014, **17**(5), pp.236-246.
185. GEORGE, S.M., OTT, A.W. and KLAUS, J.W. Surface Chemistry for Atomic Layer Growth. *The Journal of Physical Chemistry*, 1996, **100**(31), pp.13121-13131.
186. BINDSCHADLER, M. *Pore Image Processor* [Software]. 2009. Available from: [www.urmc.rochester.edu/labs/mcgrath-lab/software/pore-image-processor.aspx](http://www.urmc.rochester.edu/labs/mcgrath-lab/software/pore-image-processor.aspx).
187. SCHNEIDER, C.A., RASBAND, W.S. and ELICEIRI, K.W. NIH Image to ImageJ: 25 years of image analysis. *Nat Meth*, 2012, **9**(7), pp.671-675.
188. LEE, W., JI, R., GOSELE, U. and NIELSCH, K. Fast fabrication of long-range ordered porous alumina membranes by hard anodization. *Nat Mater*, 2006, **5**(9), pp.741-747.
189. NIELSCH, K., CHOI, J., SCHWIRN, K., WEHRSPHORN, R.B. and GÖSELE, U. Self-ordering Regimes of Porous Alumina: The 10 Porosity Rule. *Nano Letters*, 2002, **2**(7), pp.677-680.
190. WANG, H.-W., SHIEH, C.-F., CHEN, H.-Y., SHIU, W.-C., RUSSO, B. and CAO, G. Standing [111] gold nanotube to nanorod arrays via template growth. *Nanotechnology*, 2006, **17**(10), p.2689.
191. DICKEY, M.D., WEISS, E.A., SMYTHE, E.J., CHIECHI, R.C., CAPASSO, F. and WHITESIDES, G.M. Fabrication of arrays of metal and metal oxide nanotubes by shadow evaporation. *ACS Nano*, 2008, **2**(4), pp.800-808.

192. LIANG, Y., ZHEN, C., ZOU, D. and XU, D. Preparation of free-standing nanowire arrays on conductive substrates. *Journal of the American Chemical Society*, 2004, **126**(50), pp.16338-16339.
193. HILL, J.J., HALLER, K., GELFAND, B. and ZIEGLER, K.J. Eliminating Capillary Coalescence of Nanowire Arrays with Applied Electric Fields. *ACS Applied Materials & Interfaces*, 2010, **2**(7), pp.1992-1998.
194. EVANS, P., HENDREN, W., ATKINSON, R. and POLLARD, R. Optical transmission measurements of silver, silver–gold alloy and silver–gold segmented nanorods in thin film alumina. *Nanotechnology*, 2008, **19**(46), p.465708.
195. KULLOCK, R., GRAFSTRÖM, S., EVANS, P.R., POLLARD, R.J. and ENG, L.M. Metallic nanorod arrays: negative refraction and optical properties explained by retarded dipolar interactions. *Journal of the Optical Society of America B*, 2010, **27**(9), pp.1819-1827.
196. MIE, G. Beiträge zur Optik trüber Medien, speziell kolloidaler Metallösungen. *Annalen der Physik*, 1908, **330**(3), pp.377-445.
197. PELTON, M. and BRYANT, G.W. *Introduction to Metal-Nanoparticle Plasmonics*. Wiley, 2013.
198. PARSONS, J., BURROWS, C.P., SAMBLES, J.R. and BARNES, W.L. A comparison of techniques used to simulate the scattering of electromagnetic radiation by metallic nanostructures. *Journal of Modern Optics*, 2010, **57**(5), pp.356-365.
199. DRAINE, B.T. and FLATAU, P.J. Discrete-dipole approximation for scattering calculations. *JOSA A*, 1994, **11**(4), pp.1491-1499.
200. REDDY, J.N. *An introduction to the finite element method*. McGraw-Hill New York, 1993.
201. DONNER, J.S., BAFFOU, G., MCCLOSKEY, D. and QUIDANT, R. Plasmon-assisted optofluidics. *ACS Nano*, 2011, **5**(7), pp.5457-5462.
202. CHU, S. and CHAUDHURI, S. Finite-difference timedomain method for optical waveguide analysis.
203. INAN, U.S. and MARSHALL, R.A. *Numerical electromagnetics: the FDTD method*. Cambridge University Press, 2011.
204. COSTABEL, M. Principles of boundary element methods. *Computer Physics Reports*, 1987, **6**(1), pp.243-274.
205. BREBBIA, C.A. and DOMINGUEZ, J. *Boundary elements: an introductory course*. WIT press, 1994.
206. GARCÍA DE ABAJO, F.J. and HOWIE, A. Retarded field calculation of electron energy loss in inhomogeneous dielectrics. *Physical Review B*, 2002, **65**(11), p.115418.
207. COMSOL MULTIPHYSICS. *Optical Scattering Off of a Gold Nanosphere* [online]. 2012. [Accessed November 2013]. Available from: <http://www.comsol.com/model/optical-scattering-off-of-a-gold-nanosphere-12415>.

208. JOHNSON, P.B. and CHRISTY, R.W. Optical Constants of the Noble Metals. *Physical Review B*, 1972, **6**(12), pp.4370-4379.
209. DEVORE, J.R. Refractive indices of rutile and sphalerite. *JOSA*, 1951, **41**(6), pp.416-419.
210. ZHANG, Q., THRITHAMARASSERY GANGADHARAN, D., LIU, Y., XU, Z., CHAKER, M. and MA, D. Recent advancements in plasmon-enhanced visible light-driven water splitting. *Journal of Materiomics*, 2017, **3**(1), pp.33-50.
211. GAO, M., ZHU, L., ONG, W.L., WANG, J. and HO, G.W. Structural design of TiO<sub>2</sub>-based photocatalyst for H<sub>2</sub> production and degradation applications. *Catalysis Science & Technology*, 2015, **5**(10), pp.4703-4726.
212. BRÉCHIGNAC, C., HOUDY, P. and LAHMANI, M. *Nanomaterials and Nanochemistry*. Springer Berlin Heidelberg, 2008.
213. GÓMEZ, D.E., TEO, Z.Q., ALTISSIMO, M., DAVIS, T.J., EARL, S. and ROBERTS, A. The Dark Side of Plasmonics. *Nano Letters*, 2013, **13**(8), pp.3722-3728.
214. KULLOCK, R., HENDREN, W.R., HILLE, A., GRAFSTRÖM, S., EVANS, P.R., POLLARD, R.J., ATKINSON, R. and ENG, L.M. Polarization conversion through collective surface plasmons in metallic nanorod arrays. *Optics Express*, 2008, **16**(26), pp.21671-21681.
215. LYVERS, D.P., MOON, J.-M., KILDISHEV, A.V., SHALAEV, V.M. and WEI, A. Gold nanorod arrays as plasmonic cavity resonators. *ACS Nano*, 2008, **2**(12), pp.2569-2576.
216. GONG, S.-H., STOLZ, A., MYEONG, G.-H., DOGHECHE, E., GOKARNA, A., RYU, S.-W., DECOSTER, D. and CHO, Y.-H. Effect of varying pore size of AAO films on refractive index and birefringence measured by prism coupling technique. *Optics letters*, 2011, **36**(21), pp.4272-4274.
217. EVANS, P.R., KULLOCK, R., HENDREN, W.R., ATKINSON, R., POLLARD, R.J. and ENG, L.M. Optical Transmission Properties and Electric Field Distribution of Interacting 2D Silver Nanorod Arrays. *Advanced Functional Materials*, 2008, **18**(7), pp.1075-1079.
218. SOLIS, D., WILLINGHAM, B., NAUERT, S.L., SLAUGHTER, L.S., OLSON, J., SWANGLAP, P., PAUL, A., CHANG, W.-S. and LINK, S. Electromagnetic Energy Transport in Nanoparticle Chains via Dark Plasmon Modes. *Nano Letters*, 2012, **12**(3), pp.1349-1353.
219. OMAGHALI, N.E.J., TKACHENKO, V., ANDREONE, A. and ABBATE, G. Optical Sensing Using Dark Mode Excitation in an Asymmetric Dimer Metamaterial. *Sensors (Basel, Switzerland)*, 2014, **14**(1), pp.272-282.
220. BRYDSON, R. *Electron Energy Loss Spectroscopy*. BIOS Scientific Publishers, 2001.
221. WILLIAMS, D.B. and CARTER, C.B. *Transmission Electron Microscopy: A Textbook for Materials Science. Diffraction. II*. Springer, 1996.

222. BRYDSON, R. *Aberration-Corrected Analytical Transmission Electron Microscopy*. Wiley, 2011.
223. BRYDSON, R., BROWN, A., BENNING, L.G. and LIVI, K. Analytical transmission electron microscopy. *Reviews in Mineralogy and Geochemistry*, 2014, **78**(1), pp.219-269.
224. REIMER, L. *Transmission Electron Microscopy: Physics of Image Formation and Microanalysis*. Springer Berlin Heidelberg, 2013.
225. KRIVANEK, O.L., DELLBY, N., SPENCE, A.J., CAMPS, R.A. and BROWN, L.M. Aberration correction in the STEM. In: *Institute of Physics Series 153 (Proceedings of the 1997 Electron Microscopy and Analysis Group Conference)*, University of Cambridge. 1997.
226. BLELOCH, A. and LUPINI, A. Imaging at the picoscale. *Materials Today*, 2004, **7**(12), pp.42-48.
227. RAMASSE, Q.M. Twenty years after: How “Aberration correction in the STEM” truly placed a “A synchrotron in a Microscope”. *Ultramicroscopy*.
228. SEAL, S. *Functional Nanostructures: Processing, Characterization, and Applications*. Springer New York, 2010.
229. PENNYCOOK, S.J. Seeing the atoms more clearly: STEM imaging from the Crewe era to today. *Ultramicroscopy*, 2012, **123**, pp.28-37.
230. HAWKES, P.W. *Advances in Imaging and Electron Physics*. Elsevier Science, 2013.
231. KRIVANEK, O.L., LOVEJOY, T.C., DELLBY, N. and CARPENTER, R.W. Monochromated STEM with a 30 meV-wide, atom-sized electron probe. *Microscopy*, 2013, **62**(1), pp.3-21.
232. RAMASSE, Q.M., SEABOURNE, C.R., KEPAPTSOGLU, D.-M., ZAN, R., BANGERT, U. and SCOTT, A.J. Probing the Bonding and Electronic Structure of Single Atom Dopants in Graphene with Electron Energy Loss Spectroscopy. *Nano Letters*, 2013, **13**(10), pp.4989-4995.
233. CHANTRY, R.L. *Characterising the structure and properties of bimetallic nanoparticles*. thesis, University of Birmingham, 2013.
234. SCOTT, J., THOMAS, P.J., MACKENZIE, M., MCFADZEAN, S., WILBRINK, J., CRAVEN, A.J. and NICHOLSON, W.A.P. Near-simultaneous dual energy range EELS spectrum imaging. *Ultramicroscopy*, 2008, **108**(12), pp.1586-1594.
235. HOHENESTER, U., DITLBACHER, H. and KRENN, J.R. Electron-Energy-Loss Spectra of Plasmonic Nanoparticles. *Physical Review Letters*, 2009, **103**(10), p.106801.
236. NELAYAH, J., KOZIAK, M., STÉPHAN, O., DE ABAJO, F.J.G., TENCÉ, M., HENRARD, L., TAVERNA, D., PASTORIZA-SANTOS, I., LIZMARZÁN, L.M. and COLLIEX, C. Mapping surface plasmons on a single metallic nanoparticle. *Nature Physics*, 2007, **3**(5), pp.348-353.
237. CHU, M.-W., MYROSHNYCHENKO, V., CHEN, C.H., DENG, J.-P., MOU, C.-Y. and GARCÍA DE ABAJO, F.J. Probing Bright and Dark Surface-

- Plasmon Modes in Individual and Coupled Noble Metal Nanoparticles Using an Electron Beam. *Nano Letters*, 2009, **9**(1), pp.399-404.
238. BARROW, S.J., ROSSOUW, D., FUNSTON, A.M., BOTTON, G.A. and MULVANEY, P. Mapping Bright and Dark Modes in Gold Nanoparticle Chains using Electron Energy Loss Spectroscopy. *Nano Letters*, 2014, **14**(7), pp.3799-3808.
239. ALBER, I., SIGLE, W., DEMMING-JANSSEN, F., NEUMANN, R., TRAUTMANN, C., VAN AKEN, P.A. and TOIMIL-MOLARES, M.E. Multipole surface plasmon resonances in conductively coupled metal nanowire dimers. *ACS Nano*, 2012, **6**(11), pp.9711-9717.
240. EGERTON, R.F. *Electron Energy-Loss Spectroscopy in the Electron Microscope*. Springer US, 2012.
241. IBERI, V., MIRSALEH-KOHAN, N. and CAMDEN, J.P. Understanding plasmonic properties in metallic nanostructures by correlating photonic and electronic excitations. *The journal of physical chemistry letters*, 2013, **4**(7), pp.1070-1078.
242. GATAN INC. *Digital Micrograph*,
243. GATAN INC. *STEM Spectrum Imaging Tutorial* [online]. 2001. [Accessed]. Available from: <https://www.ifm.liu.se/materialphysics/thinfilmmaterial/Manualer/gadriell/Gatan%20Manuals/Spectrum%20Imaging%20Tutorial.pdf>.
244. SUPERSTEM. *Instrumentation* [online]. 2017. [Accessed 11/05/2017]. Available from: <http://www.superstem.org/instrumentation>.
245. SIMPORE INC. *Pure Silicon TEM Windows* [online]. 2017. [Accessed 12/05/2017]. Available from: [http://www.temwindows.com/category\\_s/21.htm](http://www.temwindows.com/category_s/21.htm).
246. DE ABAJO, F.G. and KOZIAK, M. Probing the photonic local density of states with electron energy loss spectroscopy. *Physical Review Letters*, 2008, **100**(10), p.106804.
247. RAZA, S., STENGER, N., PORS, A., HOLMGAARD, T., KADKHODAZADEH, S., WAGNER, J.B., PEDERSEN, K., WUBS, M., BOZHEVOLNYI, S.I. and MORTENSEN, N.A. Extremely confined gap surface-plasmon modes excited by electrons. *Nature communications*, 2014, **5**.
248. GÓMEZ-GRAÑA, S., HUBERT, F., TESTARD, F., GUERRERO-MARTÍNEZ, A., GRILLO, I., LIZ-MARZÁN, L.M. and SPALLA, O. Surfactant (Bi)Layers on Gold Nanorods. *Langmuir*, 2012, **28**(2), pp.1453-1459.
249. BOSMAN, M., KEAST, V.J., WATANABE, M., MAAROOOF, A.I. and CORTIE, M.B. Mapping surface plasmons at the nanometre scale with an electron beam. *Nanotechnology*, 2007, **18**(16), p.165505.
250. COLLIEX, C., KOZIAK, M. and STÉPHAN, O. Electron energy loss spectroscopy imaging of surface plasmons at the nanometer scale. *Ultramicroscopy*, 2016, **162**, pp.A1-A24.

251. ASPNES, D.E. and STUDNA, A.A. Dielectric functions and optical parameters of Si, Ge, GaP, GaAs, GaSb, InP, InAs, and InSb from 1.5 to 6.0 eV. *Physical Review B*, 1983, **27**(2), pp.985-1009.
252. TOSCANO, G., RAZA, S., JAUHO, A.-P., MORTENSEN, N.A. and WUBS, M. Modified field enhancement and extinction by plasmonic nanowire dimers due to nonlocal response. *Optics Express*, 2012, **20**(4), pp.4176-4188.
253. KEKICHEFF, P. and SPALLA, O. Refractive Index of Thin Aqueous Films Confined between Two Hydrophobic Surfaces. *Langmuir*, 1994, **10**(5), pp.1584-1591.
254. VERELLEN, N., VAN DORPE, P., VERCRUYSSSE, D., VANDENBOSCH, G.A. and MOSHCHALOV, V.V. Dark and bright localized surface plasmons in nanocrosses. *Optics Express*, 2011, **19**(12), pp.11034-11051.
255. LAN, S., RODRIGUES, S.P., TAGHINEJAD, M. and CAI, W. Dark plasmonic modes in diatomic gratings for plasmoelectronics. *Laser & Photonics Reviews*, 2017, **11**(2), pp.1600312-n/a.
256. MALERBA, M., ALABASTRI, A., MIELE, E., ZILIO, P., PATRINI, M., BAJONI, D., MESSINA, G.C., DIPALO, M., TOMA, A., PROIETTI ZACCARIA, R. and DE ANGELIS, F. 3D vertical nanostructures for enhanced infrared plasmonics. *Scientific Reports*, 2015, **5**, p.16436.
257. MARCO, R., AJAY, N., TAHSIN, A., MIGUEL, B. and MARIO, S. Focus on terahertz plasmonics. *New Journal of Physics*, 2015, **17**(10), p.100201.
258. MITTLEMAN, D.M. Frontiers in terahertz sources and plasmonics. *Nat Photon*, 2013, **7**(9), pp.666-669.
259. XUMING, Z., YU LIM, C., RU-SHI, L. and DIN PING, T. Plasmonic photocatalysis. *Reports on Progress in Physics*, 2013, **76**(4), p.046401.
260. VERBRUGGEN, S.W. TiO<sub>2</sub> photocatalysis for the degradation of pollutants in gas phase: From morphological design to plasmonic enhancement. *Journal of Photochemistry and Photobiology C: Photochemistry Reviews*, 2015, **24**, pp.64-82.
261. CHATTERJEE, D. and DASGUPTA, S. Visible light induced photocatalytic degradation of organic pollutants. *Journal of Photochemistry and Photobiology C: Photochemistry Reviews*, 2005, **6**(2), pp.186-205.
262. FUJISHIMA, A. and HONDA, K. Electrochemical photolysis of water at a semiconductor electrode. *nature*, 1972, **238**(5358), pp.37-38.
263. AHMAD, H., KAMARUDIN, S.K., MINGGU, L.J. and KASSIM, M. Hydrogen from photo-catalytic water splitting process: A review. *Renewable and Sustainable Energy Reviews*, 2015, **43**, pp.599-610.
264. WANG, P., HUANG, B., DAI, Y. and WHANGBO, M.-H. Plasmonic photocatalysts: harvesting visible light with noble metal nanoparticles. *Physical Chemistry Chemical Physics*, 2012, **14**(28), pp.9813-9825.
265. JANG, Y.H., JANG, Y.J., KIM, S., QUAN, L.N., CHUNG, K. and KIM, D.H. Plasmonic Solar Cells: From Rational Design to Mechanism Overview. *Chemical reviews*, 2016, **116**(24), pp.14982-15034.

266. YE, W., LONG, R., HUANG, H. and XIONG, Y. Plasmonic nanostructures in solar energy conversion. *Journal of Materials Chemistry C*, 2017, **5**(5), pp.1008-1021.
267. LINK, S. and EL-SAYED, M.A. Spectral Properties and Relaxation Dynamics of Surface Plasmon Electronic Oscillations in Gold and Silver Nanodots and Nanorods. *The Journal of Physical Chemistry B*, 1999, **103**(40), pp.8410-8426.
268. MOSKOVITS, M. Hot Electrons Cross Boundaries. *Science*, 2011, **332**(6030), pp.676-677.
269. CLAVERO, C. Plasmon-induced hot-electron generation at nanoparticle/metal-oxide interfaces for photovoltaic and photocatalytic devices. *Nat Photon*, 2014, **8**(2), pp.95-103.
270. BESTEIRO, L.V., KONG, X.-T., WANG, Z., HARTLAND, G. and GOVOROV, A.O. Understanding Hot-Electron Generation and Plasmon Relaxation in Metal Nanocrystals: Quantum and Classical Mechanisms. *arXiv preprint arXiv:1707.06125*, 2017.
271. MOSKOVITS, M. The case for plasmon-derived hot carrier devices. *Nat Nano*, 2015, **10**(1), pp.6-8.
272. KNIGHT, M.W., SOBHANI, H., NORDLANDER, P. and HALAS, N.J. Photodetection with Active Optical Antennas. *Science*, 2011, **332**(6030), p.702.
273. ROBATJAZI, H., BAHAUDDIN, S.M., DOIRON, C. and THOMANN, I. Direct Plasmon-Driven Photoelectrocatalysis. *Nano Letters*, 2015, **15**(9), pp.6155-6161.
274. AWAZU, K., FUJIMAKI, M., ROCKSTUHL, C., TOMINAGA, J., MURAKAMI, H., OHKI, Y., YOSHIDA, N. and WATANABE, T. A Plasmonic Photocatalyst Consisting of Silver Nanoparticles Embedded in Titanium Dioxide. *Journal of the American Chemical Society*, 2008, **130**(5), pp.1676-1680.
275. KUMAR, M.K., KRISHNAMOORTHY, S., TAN, L.K., CHIAM, S.Y., TRIPATHY, S. and GAO, H. Field Effects in Plasmonic Photocatalyst by Precise SiO<sub>2</sub> Thickness Control Using Atomic Layer Deposition. *ACS Catalysis*, 2011, **1**(4), pp.300-308.
276. INGRAM, D.B. and LINIC, S. Water Splitting on Composite Plasmonic-Metal/Semiconductor Photoelectrodes: Evidence for Selective Plasmon-Induced Formation of Charge Carriers near the Semiconductor Surface. *Journal of the American Chemical Society*, 2011, **133**(14), pp.5202-5205.
277. LINIC, S., CHRISTOPHER, P. and INGRAM, D.B. Plasmonic-metal nanostructures for efficient conversion of solar to chemical energy. *Nature Materials*, 2011, **10**(12), pp.911-921.
278. CUSHING, S.K., LI, J., MENG, F., SENTY, T.R., SURU, S., ZHI, M., LI, M., BRISTOW, A.D. and WU, N. Photocatalytic activity enhanced by plasmonic resonant energy transfer from metal to semiconductor. *Journal of the American Chemical Society*, 2012, **134**(36), pp.15033-15041.

279. LI, J., CUSHING, S.K., MENG, F., SENTY, T.R., BRISTOW, A.D. and WU, N. Plasmon-induced resonance energy transfer for solar energy conversion. *Nat Photon*, 2015, **9**(9), pp.601-607.
280. THOMANN, I., PINAUD, B.A., CHEN, Z., CLEMENS, B.M., JARAMILLO, T.F. and BRONGERSMA, M.L. Plasmon Enhanced Solar-to-Fuel Energy Conversion. *Nano Letters*, 2011, **11**(8), pp.3440-3446.
281. TORIMOTO, T., HORIBE, H., KAMEYAMA, T., OKAZAKI, K.-I., IKEDA, S., MATSUMURA, M., ISHIKAWA, A. and ISHIHARA, H. Plasmon-Enhanced Photocatalytic Activity of Cadmium Sulfide Nanoparticle Immobilized on Silica-Coated Gold Particles. *The journal of physical chemistry letters*, 2011, **2**(16), pp.2057-2062.
282. CHEN, X., ZHU, H.-Y., ZHAO, J.-C., ZHENG, Z.-F. and GAO, X.-P. Visible-Light-Driven Oxidation of Organic Contaminants in Air with Gold Nanoparticle Catalysts on Oxide Supports. *Angewandte Chemie International Edition*, 2008, **47**(29), pp.5353-5356.
283. BORA, T., ZOEPFL, D. and DUTTA, J. Importance of Plasmonic Heating on Visible Light Driven Photocatalysis of Gold Nanoparticle Decorated Zinc Oxide Nanorods. 2016, **6**, p.26913.
284. GOVOROV, A.O. and RICHARDSON, H.H. Generating heat with metal nanoparticles. *Nano today*, 2007, **2**(1), pp.30-38.
285. LOUIS, C. and PLUCHERY, O. *Gold Nanoparticles for Physics, Chemistry and Biology*. World Scientific Publishing Company, 2017.
286. BAFFOU, G. and QUIDANT, R. Thermo-plasmonics: using metallic nanostructures as nano-sources of heat. *Laser & Photonics Reviews*, 2013, **7**(2), pp.171-187.
287. HASHIMOTO, K., IRIE, H. and FUJISHIMA, A. TiO<sub>2</sub> photocatalysis: a historical overview and future prospects. *Japanese Journal of Applied Physics*, 2005, **44**(12R), p.8269.
288. MUBEEN, S., LEE, J., LEE, W.-R., SINGH, N., STUCKY, G.D. and MOSKOVITS, M. On the Plasmonic Photovoltaic. *ACS Nano*, 2014, **8**(6), pp.6066-6073.
289. MOSKOVITS, M. *Moskovits Research Group* [online]. 2017. [Accessed 21st August 2017]. Available from: <http://www.chem.ucsb.edu/moskovitsgroup/>.
290. LU, Y., CHEN, S., QUAN, X. and YU, H. Fabrication of a TiO<sub>2</sub>/Au Nanorod Array for Enhanced Photocatalysis. *Chinese Journal of Catalysis*, 2011, **32**(11), pp.1838-1843.
291. NEXUS. *National EPSRC XPS Users' Service* [online]. 2017. [Accessed 21st August 2017]. Available from: <http://www.ncl.ac.uk/nexus>.
292. CASAXPS SOFTWARE LTD. *CasaXPS*, 2016. Available from: <http://www.casaxps.com/>.
293. BURKE, A.R., BROWN, C.R., BOWLING, W.C., GLAUB, J.E., KAPSCH, D., LOVE, C.M., WHITAKER, R.B. and MODDEMAN, W.E. Ignition

- mechanism of the titanium–boron pyrotechnic mixture. *Surface and Interface Analysis*, 1988, **11**(6-7), pp.353-358.
294. THERMO SCIENTIFIC XPS. *Titanium* [online]. 2016. [Accessed 22nd August 2017]. Available from: <http://xpssimplified.com/elements/titanium.php>.
  295. SANGPOUR, P., HASHEMI, F. and MOSHFEGH, A.Z. Photoenhanced Degradation of Methylene Blue on Cosputtered M:TiO<sub>2</sub> (M = Au, Ag, Cu) Nanocomposite Systems: A Comparative Study. *The Journal of Physical Chemistry C*, 2010, **114**(33), pp.13955-13961.
  296. TAYADE, R.J., NATARAJAN, T.S. and BAJAJ, H.C. Photocatalytic Degradation of Methylene Blue Dye Using Ultraviolet Light Emitting Diodes. *Industrial & Engineering Chemistry Research*, 2009, **48**(23), pp.10262-10267.
  297. AL-SHAMALI, S.S. Photocatalytic degradation of methylene blue in the presence of TiO<sub>2</sub> catalyst assisted solar radiation. *Australian Journal of Basic and Applied Sciences*, 2013, **7**(4), pp.172-176.
  298. DARIANI, R., ESMAEILI, A., MORTEZAALI, A. and DEHGHANPOUR, S. Photocatalytic reaction and degradation of methylene blue on TiO<sub>2</sub> nano-sized particles. *Optik-International Journal for Light and Electron Optics*, 2016, **127**(18), pp.7143-7154.
  299. JOSEPH, C.G. and ELILARASI, L. Removal of Methylene Blue Dye from Aqueous Solution Using a Newly Synthesized TiO<sub>2</sub>-SiO<sub>2</sub> Photocatalyst in the Presence of Active Chlorine Species. *IOP Conference Series: Materials Science and Engineering*, 2017, **206**(1), p.012090.
  300. PEARCE, C.I., LLOYD, J.R. and GUTHRIE, J.T. The removal of colour from textile wastewater using whole bacterial cells: a review. *Dyes and Pigments*, 2003, **58**(3), pp.179-196.
  301. WU, B., LIU, D., MUBEEN, S., CHUONG, T.T., MOSKOVITS, M. and STUCKY, G.D. Anisotropic Growth of TiO<sub>2</sub> onto Gold Nanorods for Plasmon-Enhanced Hydrogen Production from Water Reduction. *Journal of the American Chemical Society*, 2016, **138**(4), pp.1114-1117.
  302. CHEN, W.-L., LIN, F.-C., LEE, Y.-Y., LI, F.-C., CHANG, Y.-M. and HUANG, J.-S. The modulation effect of transverse, antibonding, and higher-order longitudinal modes on the two-photon photoluminescence of gold plasmonic nanoantennas. *ACS Nano*, 2014, **8**(9), pp.9053-9062.
  303. ALBER, I., SIGLE, W., MÜLLER, S., NEUMANN, R., PICHT, O., RAUBER, M., VAN AKEN, P.A. and TOIMIL-MOLARES, M.E. Visualization of Multipolar Longitudinal and Transversal Surface Plasmon Modes in Nanowire Dimers. *ACS Nano*, 2011, **5**(12), pp.9845-9853.
  304. SLAUGHTER, L.S., WU, Y., WILLINGHAM, B.A., NORDLANDER, P. and LINK, S. Effects of symmetry breaking and conductive contact on the plasmon coupling in gold nanorod dimers. *ACS Nano*, 2010, **4**(8), pp.4657-4666.

305. KOH, A.L., BAO, K., KHAN, I., SMITH, W.E., KOTHLEITNER, G., NORDLANDER, P., MAIER, S.A. and MCCOMB, D.W. Electron energy-loss spectroscopy (EELS) of surface plasmons in single silver nanoparticles and dimers: influence of beam damage and mapping of dark modes. *ACS Nano*, 2009, **3**(10), pp.3015-3022.
306. KLIMOV, V. and GUO, G.-Y. Bright and dark plasmon modes in three nanocylinder cluster. *The Journal of Physical Chemistry C*, 2010, **114**(51), pp.22398-22405.
307. OSBERG, K.D., HARRIS, N., OZEL, T., KU, J.C., SCHATZ, G.C. and MIRKIN, C.A. Systematic study of antibonding modes in gold nanorod dimers and trimers. *Nano Letters*, 2014, **14**(12), pp.6949-6954.
308. GORIS, B., GUZZINATI, G., FERNÁNDEZ-LÓPEZ, C., PÉREZ-JUSTE, J., LIZ-MARZÁN, L.M., TRÜGLER, A., HOHENESTER, U., VERBEECK, J., BALS, S. and VAN TENDELOO, G. Plasmon mapping in Au@ Ag nanocube assemblies. *The Journal of Physical Chemistry C*, 2014, **118**(28), pp.15356-15362.
309. BARROW, S.J., COLLINS, S.M., ROSSOUW, D., FUNSTON, A.M., BOTTON, G.A., MIDGLEY, P.A. and MULVANEY, P. Electron Energy Loss Spectroscopy Investigation into Symmetry in Gold Trimer and Tetramer Plasmonic Nanoparticle Structures. *ACS Nano*, 2016, **10**(9), pp.8552-8563.

# APPENDICES

## Appendix 1

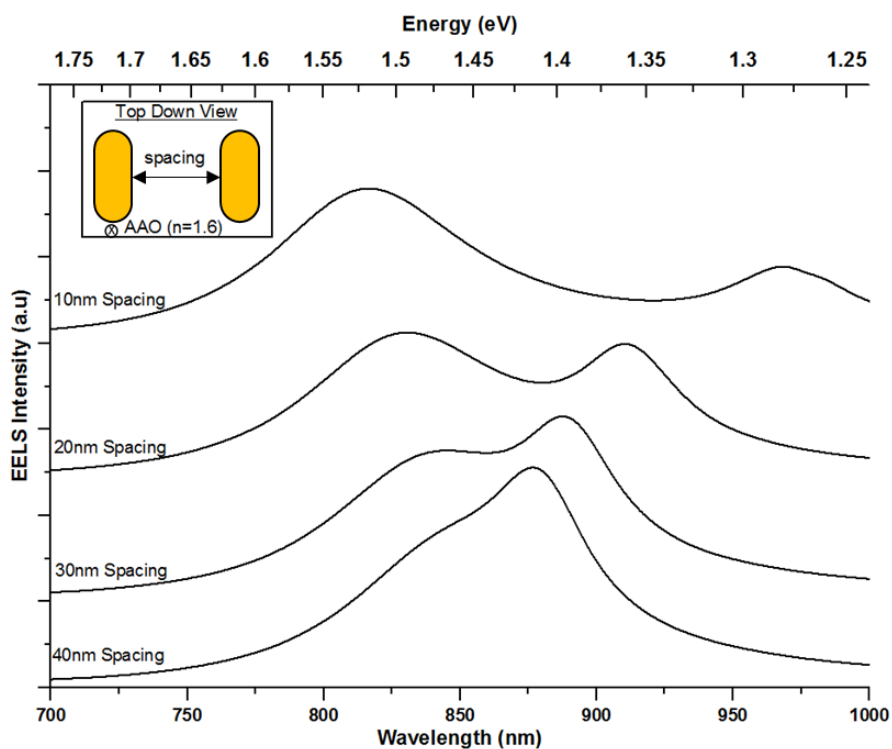


Figure A1: Modelled EELS intensity for a dimer of side-by-side aligned gold nanorods (30 nm x 90 nm) at varying spacing. The nanorods are modelled within AAO with refractive index 1.6 and the electron beam aligned 5 nm above the left nanorod as demonstrated by the cross in the inset. Each curve has been offset in the y-direction.

## Appendix 2

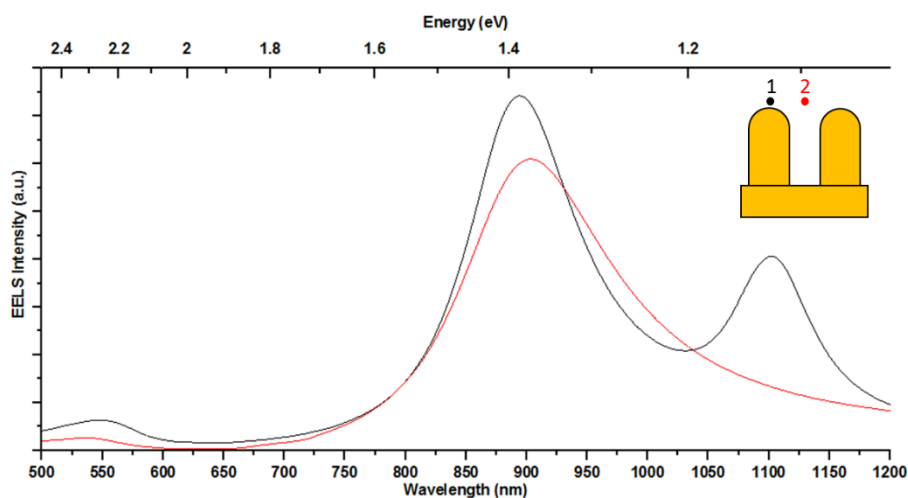
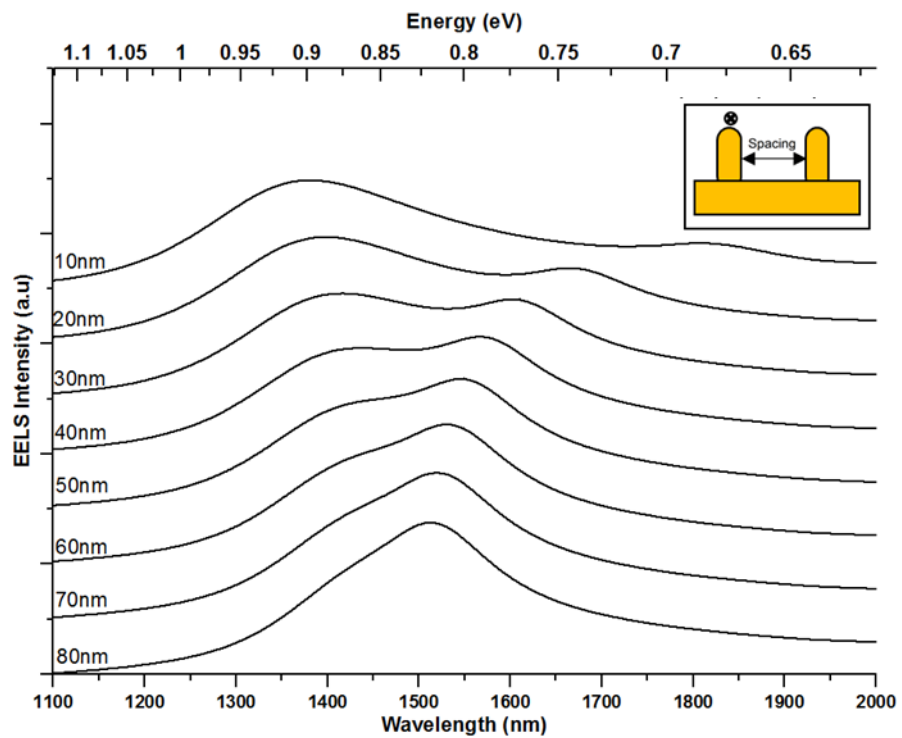


Figure A2: Modelling results for a side by side supported nanorod dimer (AR=3, 20 nm gap) with the E-beam located in different positions.

### Appendix 3



**Figure A3: Modelled EELS intensity for a dimer of side-by-side aligned gold nanorods (30 nm x 90 nm) supported on a 150 nm thick gold substrate at varying spacing and compared to an isolated nanorod. The nanorods are modelled in AAO ( $n=1.6$ ) with the electron beam positioned 5 nm above the left nanorod as demonstrated by the cross in the inset. Each curve has been offset in the y-direction to highlight the development of the modes.**

## Appendix 4

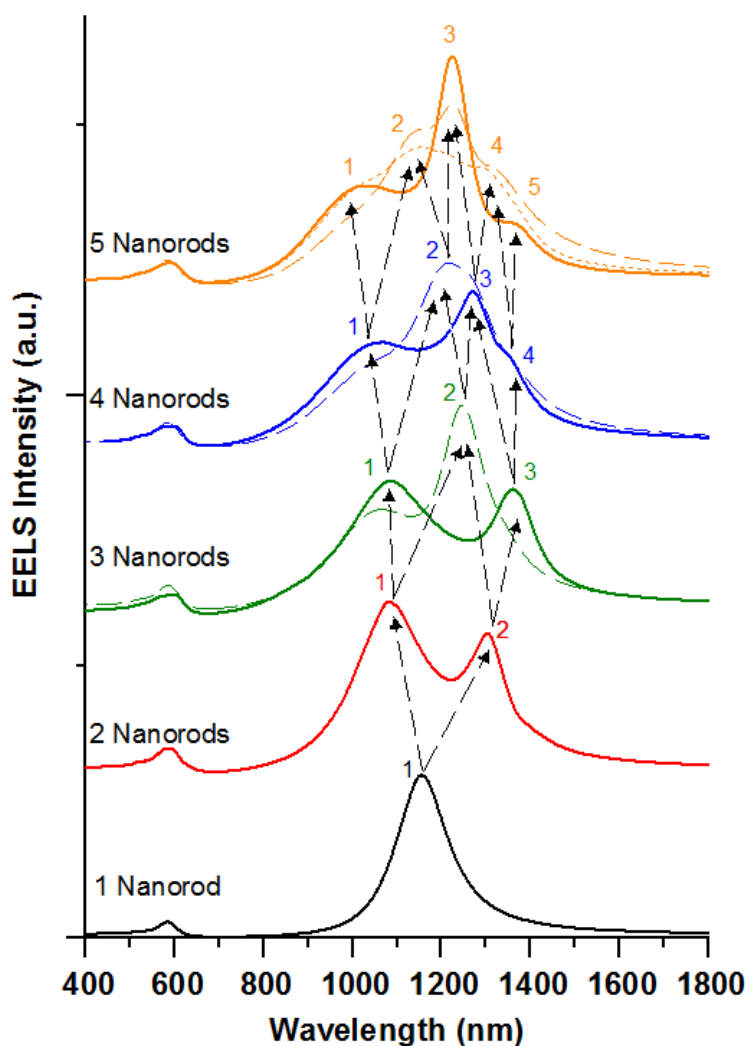


Figure A4: Modelling of EELS spectra for a supported nanorod array with increasing number of interacting nanorods. The solid lines were modelled with the E-beam located above the centre most nanorod in the array, the dashed lines were for the E-beam located above the end nanorod, and the dotted line is with the E-beam above the 2<sup>nd</sup> from the end nanorod. The arrows help show the splitting and hybridisation of the modes with increasing number of nanorods, whereas the numbers aim to help identify the peaks.

## Appendix 5

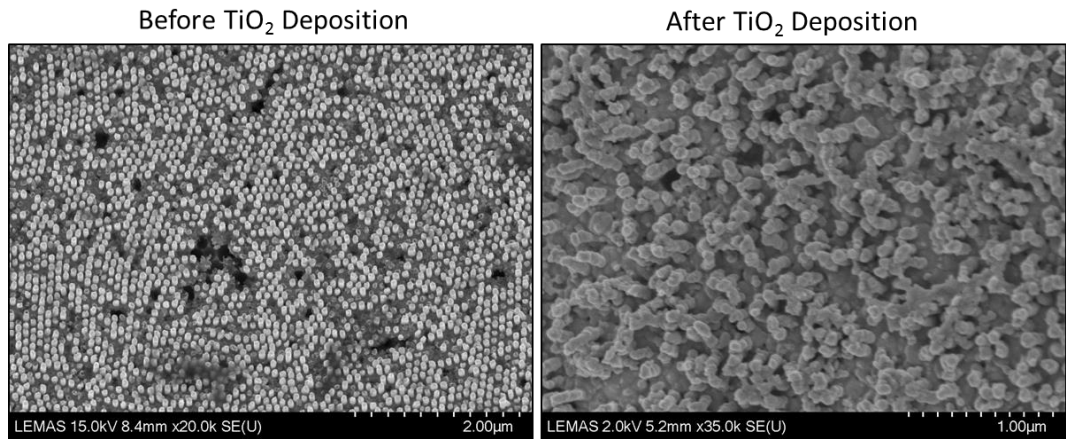


Figure A5: SEM images of Sample 2 both before and after TiO<sub>2</sub> deposition

## Appendix 6

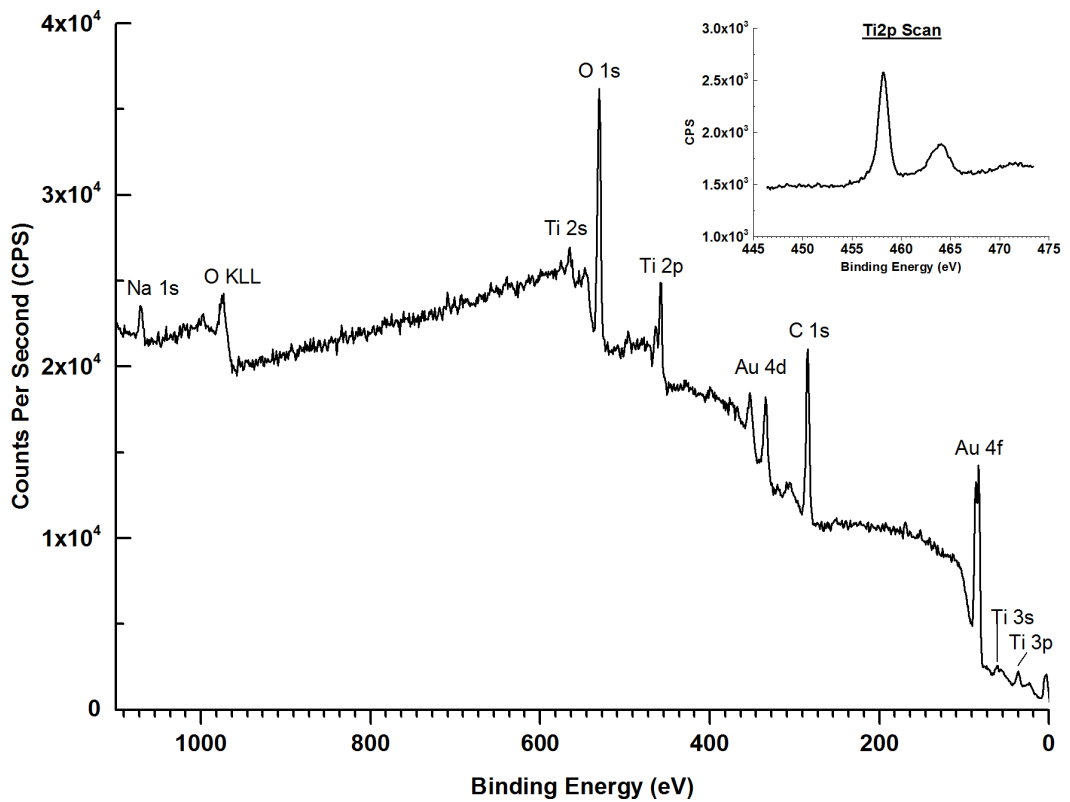
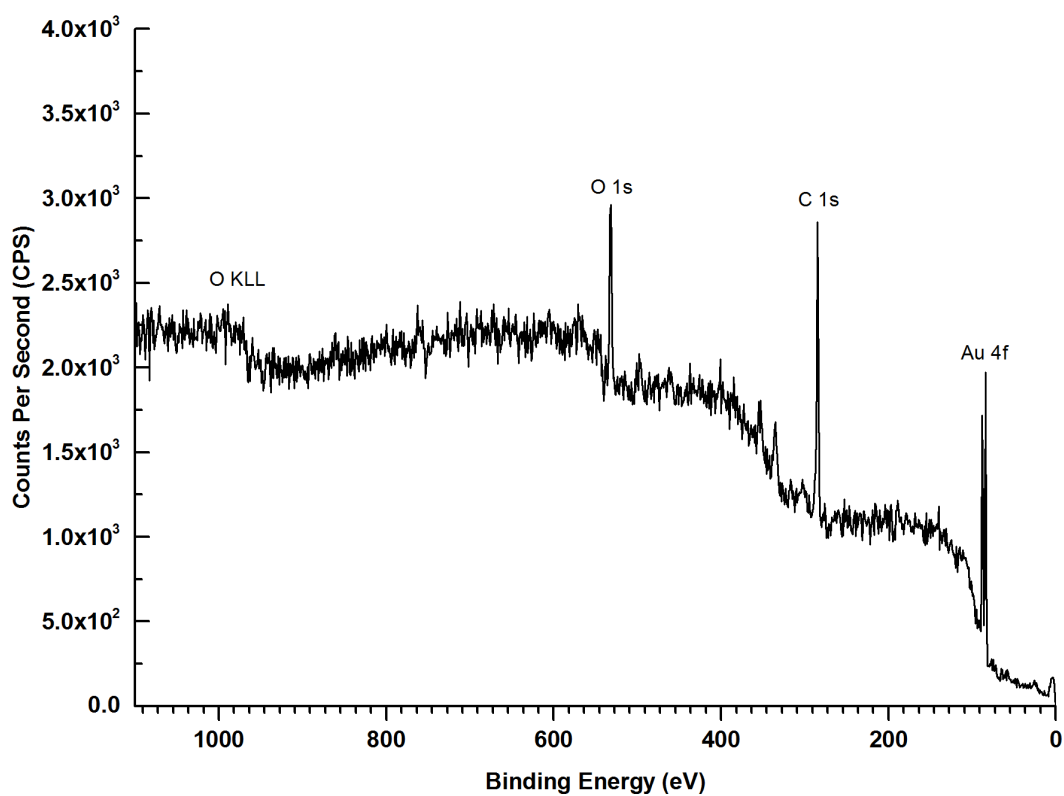


Figure A6: XPS survey of Sample 2 showing the presence of both titanium and oxygen. The inset shows the corresponding high resolution Ti2p Scan.

## Appendix 7



**Figure A7: XPS survey undertaken before pre-cleaning of substrate revealing high levels of carbon contamination.**